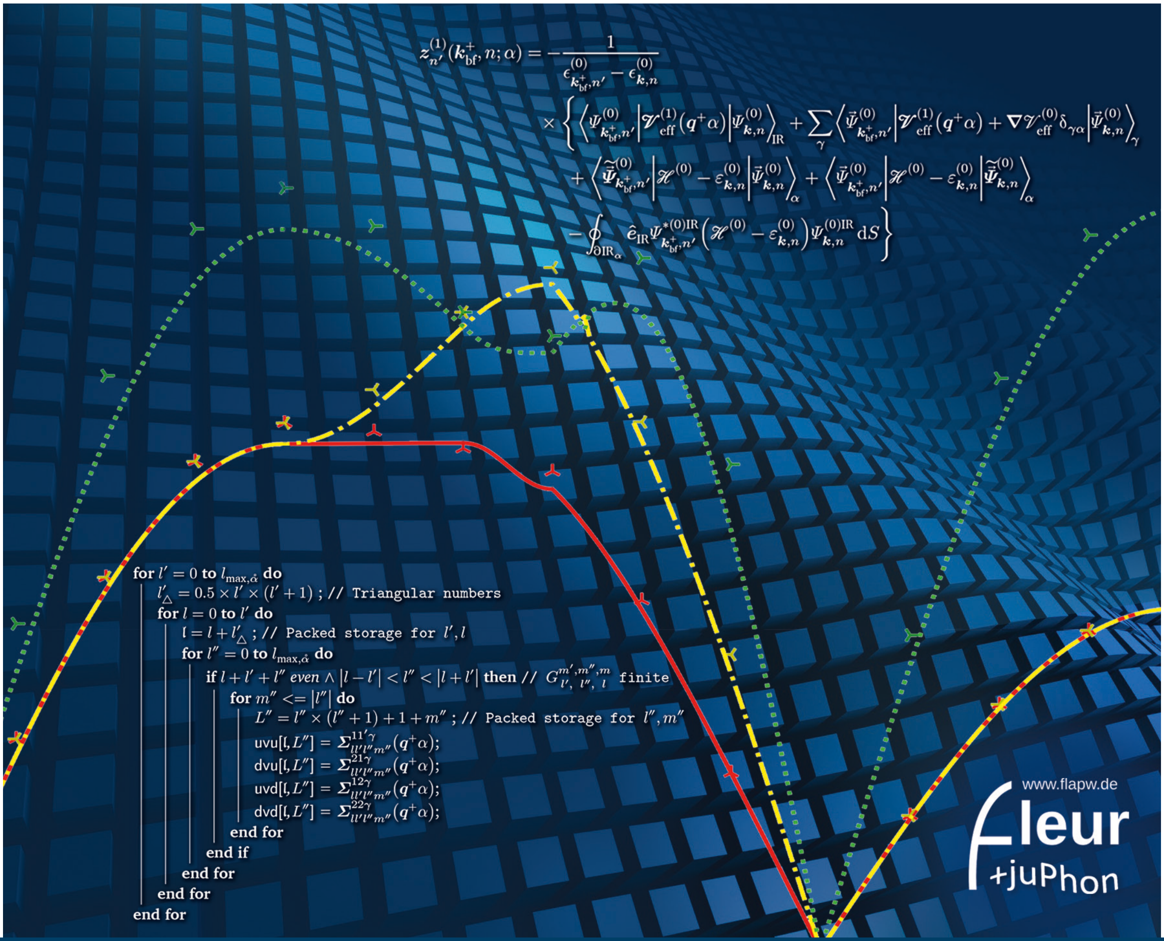

$$z^{(1)}_{n'}(\boldsymbol{k}^{+}_{\mathrm{bf}}, n; \alpha) = -\frac{1}{\epsilon^{(0)}_{\boldsymbol{k}^{+}_{\mathrm{bf}},n'} - \epsilon^{(0)}_{\boldsymbol{k},n}} \times \Bigg\{ \Big\langle \Psi^{(0)}_{\boldsymbol{k}^{+}_{\mathrm{bf}},n'} \Big| \mathscr{V}^{(1)}_{\mathrm{eff}}(\boldsymbol{q}^{+}\alpha) \Big| \Psi^{(0)}_{\boldsymbol{k},n} \Big\rangle_{\mathrm{IR}} + \sum_{\gamma} \Big\langle \vec{\Psi}^{(0)}_{\boldsymbol{k}^{+}_{\mathrm{bf}},n'} \Big| \mathscr{V}^{(1)}_{\mathrm{eff}}(\boldsymbol{q}^{+}\alpha) + \boldsymbol{\nabla}\mathscr{V}^{(0)}_{\mathrm{eff}} \delta_{\gamma\alpha} \Big| \vec{\Psi}^{(0)}_{\boldsymbol{k},n} \Big\rangle_{\gamma} + \Big\langle \widetilde{\vec{\Psi}}^{(0)}_{\boldsymbol{k}^{+}_{\mathrm{bf}},n'} \Big| \mathscr{H}^{(0)} - \varepsilon^{(0)}_{\boldsymbol{k},n} \Big| \vec{\Psi}^{(0)}_{\boldsymbol{k},n} \Big\rangle_{\alpha} + \Big\langle \vec{\Psi}^{(0)}_{\boldsymbol{k}^{+}_{\mathrm{bf}},n'} \Big| \mathscr{H}^{(0)} - \varepsilon^{(0)}_{\boldsymbol{k},n} \Big| \widetilde{\vec{\Psi}}^{(0)}_{\boldsymbol{k},n} \Big\rangle_{\alpha} - \oint_{\partial\mathrm{IR}_{\alpha}} \hat{\boldsymbol{e}}_{\mathrm{IR}} \Psi^{*(0)\mathrm{IR}}_{\boldsymbol{k}^{+}_{\mathrm{bf}},n'} \Big(\mathscr{H}^{(0)} - \varepsilon^{(0)}_{\boldsymbol{k},n} \Big) \Psi^{(0)\mathrm{IR}}_{\boldsymbol{k},n} \, \mathrm{d}S \Bigg\}$$

```
for $l' = 0$ to $l_{\max,\mathring{\alpha}}$ do
    $l'_{\triangle} = 0.5 \times l' \times (l' + 1)$ ; // Triangular numbers
    for $l = 0$ to $l'$ do
        $\mathfrak{l} = l + l'_{\triangle}$ ; // Packed storage for $l', l$
        for $l'' = 0$ to $l_{\max,\mathring{\alpha}}$ do
            if $l + l' + l''$ even $\wedge |l - l'| < l'' < |l + l'|$ then // $G^{m',m'',m}_{l',l'',l}$ finite
                for $m'' <= |l''|$ do
                    $L'' = l'' \times (l'' + 1) + 1 + m''$ ; // Packed storage for $l'', m''$
                    uvu[$\mathfrak{l}, L''$] = $\boldsymbol{\Sigma}^{11'\gamma}_{ll'l''m''}(\boldsymbol{q}^{+}\alpha)$;
                    dvu[$\mathfrak{l}, L''$] = $\boldsymbol{\Sigma}^{21\gamma}_{ll'l''m''}(\boldsymbol{q}^{+}\alpha)$;
                    uvd[$\mathfrak{l}, L''$] = $\boldsymbol{\Sigma}^{12\gamma}_{ll'l''m''}(\boldsymbol{q}^{+}\alpha)$;
                    dvd[$\mathfrak{l}, L''$] = $\boldsymbol{\Sigma}^{22\gamma}_{ll'l''m''}(\boldsymbol{q}^{+}\alpha)$;
                end for
            end if
        end for
    end for
end for
```

Density-Functional Perturbation Theory within the All-Electron Full-Potential Linearized Augmented Plane-Wave Method: Application to Phonons

Christian-Roman Gerhorst

Schlüsseltechnologien / Key Technologies
Band / Volume 259
ISBN 978-3-95806-649-6

Mitglied der Helmholtz-Gemeinschaft

JÜLICH
Forschungszentrum

Schriften des Forschungszentrums Jülich
Reihe Schlüsseltechnologien / Key Technologies Band / Volume 259

Forschungszentrum Jülich GmbH
Peter Grünberg Institut (PGI)
Quanten-Theorie der Materialien (PGI-1/IAS-1)

Density-Functional Perturbation Theory within the All-Electron Full-Potential Linearized Augmented Plane-Wave Method: Application to Phonons

Christian-Roman Gerhorst

Schriften des Forschungszentrums Jülich
Reihe Schlüsseltechnologien / Key Technologies Band / Volume 259

ISSN 1866-1807 ISBN 978-3-95806-649-6

Bibliografische Information der Deutschen Nationalbibliothek.
Die Deutsche Nationalbibliothek verzeichnet diese Publikation in der
Deutschen Nationalbibliografie; detaillierte Bibliografische Daten
sind im Internet über http://dnb.d-nb.de abrufbar.

Herausgeber und Vertrieb: Forschungszentrum Jülich GmbH
Zentralbibliothek, Verlag
52425 Jülich
Tel.: +49 2461 61-5368
Fax: +49 2461 61-6103
zb-publikation@fz-juelich.de
www.fz-juelich.de/zb

Umschlaggestaltung: Grafische Medien, Forschungszentrum Jülich GmbH

Druck: Grafische Medien, Forschungszentrum Jülich GmbH

Schriften des Forschungszentrums Jülich
Reihe Schlüsseltechnologien / Key Technologies, Band / Volume 259

D 82 (Diss. RWTH Aachen University, 2022)

ISSN 1866-1807
ISBN 978-3-95806-649-6

Vollständig frei verfügbar über das Publikationsportal des Forschungszentrums Jülich (JuSER)
unter www.fz-juelich.de/zb/openaccess.

“*Information is not knowledge. The only source of knowledge is experience. You need experience to gain wisdom.*”

commonly attributed to Albert Einstein (1879 - 1955)

Abstract

Solids consisting of periodic lattice structures exhibit vibrational modes of their atomic nuclei. In the context of a quantum-mechanical description, the excitations of the collective lattice vibrations are quantized and behave like particles. These quasiparticles are called phonons and essential for describing a diverse spectrum of central solid properties and phenomena. Density-Functional Theory (DFT) according to Kohn and Sham has established itself as a very successful, state-of-the-art, material-specific, theoretical, and computational framework. It enables us to calculate the phonon modes with very high predictive power from the first principles of quantum mechanics for describing electrons and ions. Two different approaches to obtaining phonon properties are employed: (i) the Finite Displacement (FD) ansatz, where the second-order derivatives of the total energy with respect to atomic displacements are approximated by difference quotients that involve the forces exerted on the atoms due to their finite displacement, and (ii) the Density-Functional Perturbation Theory (DFPT), a variational approach delivering the desired second-order derivatives from linear responses to an infinitesimal displacement wave. The ambition of this dissertation is to pursue a DFPT beyond the common frameworks with plane-wave basis functions. It is realized by means of the Full-Potential Linearized Augmented Plane-Wave (FLAPW) method, an all-electron electronic-structure method based on muffin-tin (MT) spheres circumscribing the atomic nuclei. The FLAPW method is known for providing the density-functional answer to arbitrary material systems, i.e., independent of which chemical element in the periodic table is chosen. I report on the implementation and validation of the DFPT approach within the FLAPW method in terms of the newly-developed computer program `juPhon`. Its algorithm describes the properties of phonons in harmonic approximation and is based on the input of the `FLEUR` code, which is a DFT implementation utilizing the aforementioned FLAPW ansatz. In detail, I elucidate the numerical challenges and show how they have been surmounted enabling us to reliably set up a dynamical matrix, the associated phonon energies of which are many orders of magnitude smaller than the ground-state energy of a crystal. This covers (i) implementing the self-consistent Sternheimer equation, which determines the first-order variations of the charge density as well as the effective potential due to the presence of the displacement wave, and (ii) accounting for the features of the LAPW basis-set. Owing to the displaced atoms, the latter entails considering both Pulay basis-set corrections and discontinuities at the MT-sphere surfaces in the section-wise defined LAPW basis and the potentials. While the Pulay terms compensate for the representation of the wave functions outside the Hilbert space spanned by the finite LAPW basis-set, the discontinuities require the introduction of surface integral contributions. Decisive has amongst others been a sustainable programming paradigm, making `juPhon` become a complex and sophisticated testing and application software. Within this thesis, I finally benchmark the `juPhon` phonon dispersions of bulk fcc Cu, Au, Al, Ne, and Ar as well as bcc Mo by comparing them with respective FD computations and experimental reference data. These results show a good agreement.

Kurzzusammenfassung

Festkörper mit periodischen Gitterstrukturen weisen Atomkern-Schwingungsmoden auf. Bei einer quantenmechanischen Beschreibung sind die Anregungen der kollektiven Gitterschwingungen quantisiert und verhalten sich wie Teilchen. Diese Quasi-Teilchen heißen Phononen und sind wesentlich, um ein vielfältiges Spektrum zentraler Festkörpereigenschaften und -phänomene zu beschreiben. Die Dichtefunktionaltheorie (DFT) nach Kohn und Sham hat sich als sehr erfolgreiches, modernes, materialspezifisches, theoretisches und numerisches Konzept etabliert. Sie ermöglicht die Berechnung der Phononenmoden mit sehr hoher Vorhersagekraft aus den ersten Prinzipien der Quantenmechanik zur Beschreibung von Elektronen und Ionen. Üblich sind zwei verschiedene Methoden, um Phononeneigenschaften zu berechnen: (i) der Finite Displacement (FD)-Ansatz, der die zweiten Ableitungen der Gesamtenergie nach den Atomverschiebungen durch Differenzenquotienten, die die Kräfte auf die Atome aufgrund ihrer Verschiebungen beinhalten, nähert, und (ii) die Dichtefunktionalstörungstheorie (DFPT), ein Variationsansatz, der die gewünschten zweiten Ableitungen mittels linearer Antwortgrößen auf eine infinitesimale Verschiebungswelle liefert. Ziel dieser Dissertation ist es, eine DFPT jenseits der üblichen Herangehensweise mit ebenen Wellen als Basisfunktionen zu verfolgen. Es wird mit der Full-Potential Linearized Augmented Plane-Wave (FLAPW)-Methode für eine vollständige Elektronenstruktur realisiert, der Atomkerne umschreibende Muffin-tin (MT)-Kugeln zugrunde liegen und die bekanntlich eine Dichtefunktionalantwort für beliebige Materialien, also unabhängig vom gewählten chemischen Element im Periodensystem, liefert. Ich berichte über die Implementierung und Validierung des DFPT-Ansatzes innerhalb der FLAPW-Methode mithilfe der neu entwickelten Software `juPhon`. Deren Algorithmus beschreibt die Phononeneigenschaften in harmonischer Näherung und basiert auf dem Input des `FLEUR`-Codes, der eine DFT-Implementierung mithilfe der FLAPW-Methodik ist. Ich beleuchte detailliert die numerischen Herausforderungen inklusive deren Überwindung, was das verlässliche Aufsetzen einer dynamischen Matrix erlaubt, deren zugehörige Phononenenergien um viele Größenordnungen kleiner sind als die Grundzustandsenergie eines Kristalls. Dies umfasst (i) die Implementierung der selbstkonsistenten Sternheimergleichung, die die ersten Variationen der Ladungsdichte und des effektiven Potentials aufgrund der präsenten Verschiebungswelle bestimmt und (ii) den Besonderheiten des LAPW-Basissatzes Rechnung zu tragen. Aufgrund der verschobenen Atome birgt letzteres sowohl das Beachten von Pulay-Basiskorrekturen als auch von Unstetigkeiten auf den MT-Kugeloberflächen in der abschnittsweise definierten LAPW-Basis und in den Potentialen. Während die Pulay-Terme die Darstellung der Wellenfunktionen außerhalb des durch den endlichen FLAPW-Basissatz aufgespannten Hilbert-Raums kompensieren, erfordern die Unstetigkeiten Oberflächenintegrale. Entscheidend ist unter anderem ein nachhaltiges Programmierparadigma gewesen, durch das `juPhon` zu einer komplexen und anspruchsvollen Test- und Anwendungssoftware geworden ist. In dieser Thesis benchmarke ich schließlich die mit `juPhon` berechneten Phononendispersionen von fcc Cu, Au, Al, Ne und Ar, sowie bcc Mo, indem ich sie mit FD-Berechnungen oder experimentellen Referenzdaten vergleiche. Die Ergebnisse zeigen eine gute Übereinstimmung.

Contents

List of Figures ix

List of Tables xi

List of Algorithms xii

Abbreviations and Acronyms xiii

Physical Constants xvi

Annotation on Typography and Nomenclature xvi

1 Introduction 1

2 Density-Functional Theory 7
- 2.1 Hohenberg–Kohn Theorems . . . 8
- 2.2 Kohn–Sham System . . . 9
  - 2.2.1 Kohn–Sham Equations . . . 10
  - 2.2.2 Common Approximations for the Exchange-Correlation Potential . . . 11
  - 2.2.3 Self-Consistency and Mixing of the Charge Density . . . 13
- 2.3 Brief Overview of DFT Generalizations . . . 16

3 Phonons 19
- 3.1 Basic Theory . . . 20
- 3.2 Direct Ab-Initio Approach to Phonon Physics . . . 23

4 Density-Functional Perturbation Theory 27
- 4.1 Response Functions and Total Energy Derivatives . . . 28
  - 4.1.1 Perturbation Theory and Hellmann–Feynman Theorem . . . 29
  - 4.1.2 General Second-Order Derivative of the Total Energy . . . 31
  - 4.1.3 $2n+1$ Theorem . . . 33
- 4.2 Development of Density-Functional Perturbation Theory . . . 33
  - 4.2.1 Dielectric Approach . . . 33
  - 4.2.2 Framework of the Green Function Method . . . 35
- 4.3 Viable Types of Perturbations . . . 37

5 All-Electron Full-Potential Linearized Augmented Plane-Wave Method 41
5.1 Augmented Plane-Wave Concept . . . 44
5.2 Linearized Augmented Plane-Wave Basis . . . 47
5.3 All-Electron and Full-Potential Calculations . . . 52
5.4 Local Orbitals . . . 54
5.5 Determining the Charge Density . . . 56
  5.5.1 Core Contribution and the Origin of Core Tails . . . 57
  5.5.2 Valence Contribution . . . 58
5.6 Calculating the Full Effective Potential . . . 59
  5.6.1 The Method of Weinert for the Coulomb Potential . . . 60
  5.6.2 Exchange-Correlation Potential . . . 62
5.7 Exploiting Symmetry . . . 62
  5.7.1 Muffin-Tin Sphere Coordinates and Irreducible Brillouin Zone . . . 63
  5.7.2 Charge Density and Effective Potential . . . 64
5.8 Constructing the Kohn–Sham Hamiltonian . . . 65
  5.8.1 Interstitial Contribution . . . 65
  5.8.2 Muffin-Tin Contribution . . . 67
5.9 Finding the Total Energy of the Ground State . . . 70
5.10 Varying the Kohn–Sham Wave Functions . . . 71
5.11 Coping with the Discontinuity at the Muffin-Tin Boundary . . . 74
5.12 Ab-Initio Atomic Forces . . . 76

6 Dynamical Matrix from Density-Functional Perturbation Theory Employing the All-Electron Full-Potential Linearized Augmented Plane-Wave Method 79
6.1 Preamble . . . 80
  6.1.1 Recapitulation with Emphasis on Phonons . . . 81
  6.1.2 Road Map to Phonon Dispersions . . . 84
6.2 Charge Density Variations . . . 86
  6.2.1 Gradient of the Unperturbed Charge Density . . . 87
  6.2.2 First-Order Variation of the Charge Density . . . 88
6.3 Potential Variations . . . 89
  6.3.1 Linear Variations of the External Potential . . . 90
  6.3.2 Linear Variations of the Hartree Potential . . . 92
  6.3.3 Linear Variations of the Exchange-Correlation Potential . . . 94
  6.3.4 Second-Order Variation of the Ion–Ion Interaction . . . 95
6.4 Sternheimer Equation . . . 100
  6.4.1 Derivation . . . 100
  6.4.2 First-Order Variation of the Kohn–Sham Energies . . . 103
  6.4.3 Self-Consistency Cycle . . . 103
6.5 Dynamical Matrix . . . 104
  6.5.1 Hellmann–Feynman Contribution . . . 104
  6.5.2 Pulay Corrections . . . 104
  6.5.3 Surface-Term Corrections . . . 106

7 Implementation and Results 109
7.1 Setting the Stage . . . 112
  7.1.1 Test Suite . . . 112

7.1.2 Numerical Accuracy 114
7.1.3 Performance 117
7.1.4 Relativistic Corrections 121
7.1.5 Dealing with Broken Symmetry 121
7.1.6 Initialization of `juPhon` and Integrity Tests of its Starting Data 121
7.2 Linear Charge-Density Variations 132
7.2.1 Gradient of the Unperturbed Charge Density 133
7.2.2 Core-Tail Corrections 137
7.2.3 First-Order Charge Density Variation 140
7.2.4 Visualization 146
7.2.5 Tests 147
7.3 Linear Potential Variations 158
7.3.1 Coulomb Potential 159
7.3.2 Exchange-Correlation Potential 165
7.3.3 Visualization 170
7.3.4 Tests 175
7.4 Solving the Sternheimer Equation 180
7.4.1 Facilitating the Numerics 181
7.4.2 Optimized Hellmann–Feynman Contribution 185
7.4.3 Optimized Pulay Corrections 191
7.4.4 Optimized Surface-Integral Correction 198
7.4.5 Mixing 200
7.4.6 Self-Consistency Cycle 202
7.4.7 Tests 205
7.5 Second-Order Variation of the Ion–Ion Interaction 210
7.5.1 Algorithm 211
7.5.2 Visualization 212
7.5.3 Tests 215
7.6 Dynamical matrix 219
7.6.1 Determining the Phonon Frequencies 220
7.6.2 Expanding under Time Reversal Symmetry 222
7.6.3 Circumventing Hessian Contributions 227
7.6.4 Goldstone Condition 234
7.6.5 Canceling Gradient Pulay Matrix-Elements with Surface Integrals 241
7.6.6 Alleviating Muffin-Tin Integrands 243
7.6.7 Avoiding Second-Order Terms Already Vanishing in First Order 246
7.6.8 Final Expressions 249
7.6.9 Tests 259
7.7 Phonon Dispersions 261
7.7.1 Evolution 262
7.7.2 Status Quo 267

8 Conclusion **275**

9 Outlook **277**

A Installing and Employing `juPhon` **279**

B Applied Input Files 281

C Gradient of a Muffin-Tin Function 287

D Analytical Solution of the Monoatomic Sternheimer Equation for $q = 0$ 291

E Outer-Product Divergence Theorem 293

Bibliography 295

List of Figures

2.1 Flow chart of the Kohn–Sham self-consistency cycle. 14
2.2 Jacob's ladder of xc-functional approximations. 17

3.1 Visualization of an exemplary phonon commensurate with a supercell. 25

5.1 Partitioning of a unit cell within the Full-Potential Linearized Augmented Plane-Wave method. 45
5.2 Symmetry-related muffin-tin spheres feature similar local coordinate systems, which are embedded in the global coordinate system Ξ^{g} of the unit cell. . . . 63

7.1 Flowchart summarizing the central steps for calculating phonon energies with the computer code `juPhon`. 111
7.2 Schematic visualization of the relation between $\boldsymbol{k}+\boldsymbol{q}$, that is in a second Brillouin zone, and a (translation-)symmetry related $\boldsymbol{k}^{+}_{\mathrm{bf}}$, that is in the first Brillouin zone and connected to the second Brillouin zone by a back-folding vector $\boldsymbol{G}_{\mathrm{bf}}$. 125
7.3 Benchmark of the muffin-tin gradient subroutine utilized in the `juPhon` code by differentiating the toy function $r_{\nu}^{-1}\mathrm{Y}_{00}$ 138
7.4 Real-space plot of the first-order density variation for fcc Ne. 148
7.5 Real-space plot of the first-order density variation for fcc Al. 149
7.6 Check of the radial derivative subroutine employed in `juPhon`. 151
7.7 Heat maps contrasting the first-order density variation from the `juPhon` code with a benchmark using a difference quotient method based on the `FLEUR` program, for a sc Ne system and a longitudinal phonon with $\boldsymbol{q}=(0,0,0.25)^{\top}$. 155
7.8 Heat maps contrasting the first-order density variation from the `juPhon` code with a benchmark using a difference quotient method based on the `FLEUR` program, for a sc Ne system and a phonon with $\boldsymbol{q}=(0,0.25,0.5)^{\top}$. 156
7.9 Absolute error 1D-analysis of figure 7.7 and figure 7.8 on the complete mesh and along horizontal lines between the muffin-tin extrema. 157
7.10 2D-slices of first-order effective, exchange-correlation, Hartree, and external potential variations for fcc Ne and $\boldsymbol{q}=({}^{1}\!/\!{}_{4},{}^{1}\!/\!{}_{4},0)^{\top}$. 171
7.11 2D-slices of first-order effective, exchange-correlation, Hartree, and external potential variations for fcc Al and $\boldsymbol{q}=({}^{1}\!/\!{}_{4},{}^{1}\!/\!{}_{4},0)^{\top}$. 172

7.12 3D isosurfaces of unperturbed effective-, exchange-correlation-, Hartree-, and external-potential gradients for fcc Ne. 173
7.13 3D isosurfaces of unperturbed effective-, exchange-correlation-, Hartree-, and external-potential gradients for fcc Al. 174
7.14 Difference between the Weinert and the numerical gradient methods, using the example of the effective potential gradient ($\boldsymbol{q} = \boldsymbol{0}$) for fcc Ne and fcc Al. . 177
7.15 Defining the lower and upper parts of the matrix elements $\boldsymbol{t}^{\text{full},pp'\gamma}_{\eta(l'm'lm)}(\boldsymbol{q}^{+}\alpha)$. . . 190
7.16 Mixing distances of first-order density variation as a function of iteration steps for fcc Ne and fcc Al. 203
7.17 Flow chart of the implemented Sternheimer self-consistency cycle. 204
7.18 Behavior of the second-order ion–ion interaction $\underline{E}^{(2)}_{\text{ii}}$ from `juPhon` for fcc Al on a typical path, incorporating fcc high-symmetry points. 213
7.19 Behavior of the second-order ion–ion interaction $\underline{E}^{(2)}_{\text{ii}}$ from `juPhon` for bcc Na on a typical path, incorporating bcc high-symmetry points. 214
7.20 Absolute error of second-order ion–ion interaction $\underline{E}^{(2)}_{\text{ii}}$ for fcc Al on a typical path, incorporating fcc high-symmetry points. 217
7.21 Absolute error of second-order ion–ion interaction $\underline{E}^{(2)}_{\text{ii}}$ for bcc Na on a typical path, incorporating bcc high-symmetry points. 218
7.22 Dispersion relation of `juPhon` for fcc Ne according to section 7.6.4. 263
7.23 Dispersion relation of `juPhon` for fcc Al according to section 7.6.4. 264
7.24 Dispersion relation of `juPhon` for fcc Ne according to the formalism after section 7.6.5. 265
7.25 Dispersion relation of `juPhon` for fcc Al according to the formalism after section 7.6.5. 266
7.26 Final `juPhon` dispersion relation for fcc Cu, compared with Finite Displacement data. 268
7.27 Final `juPhon` phonon dispersion-relation for fcc Au, compared with Finite Displacement data. 269
7.28 Final `juPhon` phonon dispersion-relation for fcc Al, compared with Finite Displacement data. 270
7.29 Final `juPhon` phonon dispersion-relation for bcc Mo, compared with Finite Displacement and experimental reference data. 271
7.30 Final `juPhon` phonon dispersion-relation for fcc Ne, compared with Finite Displacement data. 273
7.31 Final `juPhon` phonon dispersion-relation for fcc Ar, compared with Finite Displacement data. 274

List of Tables

7.1 Overview of the 39 tests in the `juPhon` code (1/2). 115
7.2 Overview of the 39 tests in the `juPhon` code (2/2). 116
7.3 Files stemming from the `FLEUR` computation before the `juPhon` calculation. . . 122
7.4 List of tests that require files apart from those given in table 7.3. 123
7.5 Input data of the Birch–Murnaghan fit for Ne and Al. 124
7.6 Results of the Birch–Murnaghan fit for Ne and Al. 124
7.7 Relating Kronecker deltas in equation (7.39b) and variable names in `juPhon`. 146
7.8 Legend of high-symmetry points for fcc and bcc lattice structures. 212
7.9 Atomic weights utilized in this thesis. 222

List of Algorithms

1 Rough runtime analysis of the `juPhon` program (1/3: initialization). 118

2 Rough runtime analysis of the `juPhon` program (2/3: Sternheimer loop). . . . 119

3 Rough runtime analysis of the `juPhon` program (3/3: dynamical matrix). . . . 120

4 Loop structure for converting symmetrized to unsymmetrized expansions. . . . 127

5 Gradient of the unperturbed Coulomb, Hartree, or external potential. 163

6 First-order variation of the Coulomb, Hartree, and external potential. 165

7 Convolution of kernel and unperturbed interstitial density gradient. 167

8 Optimized interstitial Hellmann–Feynman term in the Sternheimer equation. . 188

9 Lower and upper matrix elements $\boldsymbol{t}^{\mathrm{L},pp'\gamma}_{\eta(l'm'lm)}(\boldsymbol{q}^{+}\alpha)$ and $\boldsymbol{t}^{\mathrm{U},pp'\gamma}_{\eta(l'm'lm)}(\boldsymbol{q}^{+}\alpha)$. 192

10 Outsourced part of algorithm 9 (multiplying the Gaunt coefficients). 193

11 Outsourced part of algorithm 9 (mapping array and logical matrix). 194

12 Optimized muffin-tin Hellmann–Feynman term in the Sternheimer equation. . 195

Abbreviations and Acronyms

a	analytical
APW	Augmented Plane-Wave
b	bra
bf	back-fold
bk	braket
BO	Born–Oppenheimer
BSE	Bethe–Salpeter Equation
c	core
CI	Configuration Interaction
Cou	Coulomb
crt	cartesian
ct	core tail
ctC	core-tail correction
DFPT	Density-Functional Perturbation Theory
DFT	Density-Functional Theory
diff	differing
dp	density-potential
eff	effective
ext	external
f	fold
FD	Finite Displacement
FFT	Fast Fourier Transform
FLAPW	Full-Potential Linearized Augmented Plane-Wave
GEA	Generalized Expansion Approximation
GGA	Generalized Gradient Approximation
gs	ground state

HF	Hellmann–Feynman
HK	Hohenberg–Kohn
HSP	High-symmetry points
Htr	Hartree
Hxc	Hartree and exchange-correlation
IBC	Incomplete Basis Correction
IBZ	Irreducible wedge of the Brillouin Zone
ii	ion–ion
in	input
int	internal
IR	Interstitial region
k	ket
KKR	Korringa–Kohn–Rostocker
KS	Kohn–Sham
L	lower
LDA	Local Density Approximation
LMTO	Linearized Muffin-tin Orbital
LO	Local Orbital
mb	many body
MT	Muffin-tin
n	numerical
$\mathfrak{n}$	natural
ni	non-interacting
nsph	non-spherical
O	optimized
occ	occupied
opt	optimal
out	output
Pl	Pulay
ps	pseudo
QMD	Quantum Molecular Dynamics
RPA	Random Phase Approximation
SCC	Self-Consistency Cycle
SCDFT	Superconducting Density-Functional Theory

sf	surface
Sh	Sternheimer
SIC	Self-Interaction Correction
SOC	Spin–Orbit Coupling
sph	spherical
stbl	stable
TDDFT	Time-Dependent Density-Functional Theory
tot	total
TRS	Time Reversal Symmetry
U	upper
v	valence
vol	volume
X	Exchange
xc	Exchange-correlation

Physical Constants

a_0	Bohr Radius
e	Charge of one electron
ϵ_0	Dielectric constant
E_h	Hartree energy
m_e	Mass of one electron
$\hbar$	Planck constant divided by 2π

Annotation on Typography and Nomenclature

The nomenclature in this dissertation is guided by the standard *ISO 80000 (Quantities and units — Part 2: Mathematics)* [1]. Regarding the notation, I am fully aware of the fact that it could be condensed on some pages for the sake of a better overview, e.g. by introducing aggregate indices such as L instead of lm. However, the focus of this thesis is on the implementation. Therefore, I decided in favor of typesetting more elongated equations, explicitly containing all indices relevant for the programming. Doing so, facilitates a direct translation of the equations into source code, without possibly rewriting them to avoid confusion.

Chapter 1

Introduction

Fundamental many-body Hamiltonian

The fascinating richness of static, dynamic, thermodynamic, transport, and excitation phenomena in solid-state physics is ultimately attributed to the properties of two different constituent particles: electrons and nuclei. Both electrons and nuclei primarily interact via the well-known Coulomb interaction and there are vast quantities of them in a solid [2]. Their kinetic energies and interactions are quantum-mechanically described by the famous and fundamental many-body Hamiltonian operator of solid-state physics[1]:

$$\mathscr{H}_{\mathrm{mb}} = -\sum_{\mathfrak{p}} \frac{\Delta_{\mathfrak{p}}}{2} - \sum_{\gamma} \frac{\Delta_\gamma}{2M_\gamma} + \frac{1}{2}\sum_{\substack{\mathfrak{p},\mathfrak{p}'| \\ \mathfrak{p}\neq\mathfrak{p}'}} \frac{1}{\left|\boldsymbol{r}_{\mathfrak{p}} - \boldsymbol{r}_{\mathfrak{p}'}\right|} + \frac{1}{2} \sum_{\substack{\gamma,\gamma'| \\ \gamma\neq\gamma'}} \frac{Z_\gamma Z_{\gamma'}}{\left|\boldsymbol{\tau}_\gamma - \boldsymbol{\tau}_{\gamma'}\right|} - \sum_{\mathfrak{p},\gamma}\frac{Z_\gamma}{\left|\boldsymbol{r}_{\mathfrak{p}}-\boldsymbol{\tau}_\gamma\right|} . \tag{1.1}$$

Its first two terms are the kinetic energy operators of every electron $\mathfrak{p}$ at position $\boldsymbol{r}_{\mathfrak{p}}$, and of every nucleus γ with mass M_γ expressed in the units of the electron mass located at $\boldsymbol{\tau}_\gamma$. In the third and fourth terms, the mutually repulsive Coulomb interactions between (i) the electrons and (ii) the nuclei of the chemical elements characterized by the nuclear numbers Z_γ and $Z_{\gamma'}$ are taken into account, while excluding the self-interaction. The last term represents the attractive Coulomb interaction between the electrons and the nuclei. Additional external electromagnetic fields or relativistic effects, such as spin–orbit coupling are neglected for the sake of brevity. It is fascinating to acknowledge that only two parameters, the relative mass of the nuclei and the nuclear charge of the ions, are sufficient to describe all intricate properties of all minerals, crystalline solids, as well as structural and functional materials in one, two, or three spatial dimensions. [3]

Quasiparticles

The Hamiltonian (1.1) and its appropriate many-body wave functions $\Psi\big(\{\boldsymbol{r}_{\mathfrak{p}}\},\{\boldsymbol{\tau}_\gamma\}\big)$ describe apart from static (e.g. structural) properties likewise collective excitations of the electrons and nuclei: examples are excitons, plasmons, magnons, or phonons, to name but a few prominent ones. These excitations and the manner of modeling them bear a similarity to particles, provided they are approached by quantum-field theory [4]. Therefore, these

---

[1] This Hamiltonian is given in Hartree atomic units: $m_{\mathrm{e}} = 1$, $(4\pi\epsilon_0)^{-1} = 1$, $\hbar = 1$, $e = 1$ [3]. Furthermore, the symbol $|$ in the sum specifications is borrowed from the nomenclature of set theory and stands for “such that” in the following.

excitations are usually denoted as quasiparticles, specified by their crystal momentum[2] $\boldsymbol{q}$ and their energy transfer in quanta of $\hbar\omega$ [4]. [5]

Phonons

In this dissertation, the focus is on phonon[3] quasiparticles, i.e., collective modes of atomic nuclei, which vibrate around their equilibrium position in a crystal [7]. Each phonon can be attributed a specific displacement pattern of the atoms with a particular displacement direction along which the vibrations of the atoms take place [8]. In the history of solid-state physics, investigations of phonons can be traced back to its beginnings roughly one hundred years ago. The pioneer Igor Yevgenyevich Tamm is typically credited with quantum-mechanically describing sound waves in elastic media, and publishing it in the year 1932 [9, 10]. Since then, phonons have widely been studied in solid-state physics and many findings are meanwhile textbook knowledge [4, 11, 12]. For instance, phonons are the main contribution to the specific heat in a material, and pivotal ingredients for explaining heat conductivity, thermal expansion, ohmic resistance (regarding electrical currents) due to electron–phonon scattering, or BCS superconductivity (for which the electron-phonon coupling is an important driving mechanism). Overall, phonons remain a central theme in solid-state research. Among the much discussed scientific questions is the understanding of the coupling of the lattice vibrations to the spin degree of freedom via the relativistic spin–orbit interaction [13] or to the magnetic sublattice [14]. The former is responsible for spin-relaxation processes, spin-flip lifetime, depolarization of spin-currents [15], or angular momentum transfer in ultrafast magnetization processes [16]. The latter is a prerequisite for dynamical Dzyaloshinskii–Moriya interactions in centro-symmetric solids [17]. In the context of orbitronics [18], the coupling of the phonons to the orbital degrees of freedom is relevant. Making progress along these lines requires describing the phonon properties of chemically, structurally, and electronically complex solids in a materials-specific fashion.

Valence electrons and ions

Considering the overwhelming number of electrons and nuclei as well as their mutual correlation in typical solid-state systems, it is practically impossible to study phonons and their subsequent physics by a direct solution of equation (1.1) [2]. So, introducing a number of approximations or practical reformulations are the key to success [2]. Firstly, one available option in periodic solids is to reduce the electronic degrees of freedom to the so-called valence electrons [19]. Since at least some of the electrons are so strongly bonded to the nuclei that they are normally only marginally involved in the aforementioned solid-state phenomena, their role is restricted to screen the charge of the atomic cores [19]. The entities of nuclei and localized core electrons are denoted as *ions*, provided their screened charge differs from the atomic number of the incorporated nuclei, and these ions are sometimes effectively considered as “nuclei” [19]. The remaining negatively charged particles are known as *valence electrons* and, e.g., responsible for chemical bonding. They rearrange, which enables the atoms or ions to bond with each other, creating solid matter that is organized in a certain order (usually in periodic lattices) [19]. In periodic systems with their translational symmetry, these spin-carrying valence electrons induce an electronic structure. It manifests itself in the form of the band structures, which are subject to certain symmetries and can be classified by topological quantities. The electronic structure determines the total energy, the forces acting on atoms, and also gives rise to interesting magnetic, optical, and electrical phenomena in materials to name but a few examples. [3]

---

[2] Given excitons, choosing the symbol $\boldsymbol{k}$ instead of $\boldsymbol{q}$ is more common.

[3] The classical Greek word “φωνή” can be translated into “sound” [6].

Adiabatic approximation

When neglecting phenomena like the electron–phonon interaction, the adiabatic or Born–Oppenheimer (BO) approximation [20] (see also reference [21]) can be invoked. This further common yet powerful approximation is grounded on the assumption that electronic and nuclear degrees of freedom can independently be considered, because it is based on the large mass difference between electrons and nuclei[4]. This fact reflects itself in the definition of the small perturbation parameter $\lambda = \sqrt[4]{1/M_\gamma}$. To lowest order, i.e., in the limit of an infinite ion mass M_γ ($\lambda \to 0$), the complete electron–ion wave-function uncorrelates. It thus factorizes in (i) electron wave-functions, satisfying Schrödinger equations of the Hamiltonian (1.1) with vanishing ion momenta (second term) and quasi-fixed ion-positions $\boldsymbol{\tau}_\gamma$ as parameters, and (ii) nuclear wave-functions $\Psi\big(\{\boldsymbol{\tau}_\gamma\}\big)$, solving

$$\left(-\sum_\gamma \frac{\Delta_\gamma^2}{2M_\gamma} + E_{\mathrm{BO}}\Big(\{\boldsymbol{\tau}_\gamma\}\Big) \right) \Psi\Big(\{\boldsymbol{\tau}_\gamma\}\Big) = E\Psi\Big(\{\boldsymbol{\tau}_\gamma\}\Big) . \tag{1.2}$$

The potential energy function $E_{\mathrm{BO}}\big(\{\boldsymbol{\tau}_\gamma\}\big)$ of the interacting ions in this differential equation, called the BO energy, is an energy surface over the coordinates $\{\boldsymbol{\tau}_\gamma\}$, and the total ground-state energy of the aforementioned Hamiltonian (1.1) for $M_\gamma \to \infty$ [22]. By using the BO approximation, the account of the phonons will only focus on the nuclear degrees of freedom (and just indirectly on the electronic ones). But averaging the BO energy over the BO surface of typical phonon amplitudes, the resulting mean $\bar{E}_{\mathrm{BO}}$ is in practice many orders of magnitude larger than the variation $\Delta E_{\mathrm{BO}} = \max_{\{\boldsymbol{\tau}_\gamma\}} \big| E_{\mathrm{BO}}(\{\boldsymbol{\tau}_\gamma\}) - \bar{E}_{\mathrm{BO}} \big|$, i.e., $\Delta E_{\mathrm{BO}} / \bar{E}_{\mathrm{BO}} \approx \mathcal{O}\big(10^{-7}\big)$. Therefore, reliably determining the BO surface presents a formidable challenge. [3]

Harmonic approximation

One typically assumes that the atomic displacements of phonons in the vicinity of the equilibrium structure $\{\boldsymbol{\tau}_\gamma^{(0)}\}$ are small relative to the interatomic distances. This allows for Taylor-expanding the BO surface in orders of the atomic displacements and dropping terms above second order, known as the harmonic approximation. In the harmonic approximation, the BO surface is replaced by a quadratic form,

$$E_{\mathrm{BO}}\Big(\{\boldsymbol{\tau}_\gamma\}\Big) \to \Big(\{\boldsymbol{\tau}_\gamma\} - \{\boldsymbol{\tau}_\gamma^{(0)}\}\Big)^{\top} \underline{D}\Big(\{\boldsymbol{\tau}_\gamma^{(0)}\}\Big) \Big(\{\boldsymbol{\tau}_\gamma\} - \{\boldsymbol{\tau}_\gamma^{(0)}\}\Big) , \tag{1.3}$$

(the first-order term vanishes for the optimized lattice structure) and equation (1.2) reduces to a differential equation of coupled harmonic oscillators [3]. Its solution is analytical and usually found by means of computers, i.e., quasi-analytically [3]. The remaining challenge to be faced is determining the dynamical matrix $\underline{D}$, which contains the Hessian matrix of second-order derivatives, acting on E_{BO} with respect to the position of the ions from equation (1.1) [7]. [23]

Approximating the system of electrons

Even in the limit of $M \to \infty$, the general solution of the Hamiltonian (1.1) is basically not feasible [2]. This can be attributed to the Coulomb interaction between the electrons, which correlates the electrons, and prohibits writing electron wave-functions as a product of single-particle wave-functions describing non-interacting electrons [3]. For the last 100 years, it has in fact been a general task and research field of condensed matter physics (i) to develop an understanding of the phenomena underlying equation (1.1), (ii) to search for effective approximations, (iii) to synthesize simplifying and effective models, or (iv) to establish new theoretical concepts and algorithms [2, 3, 24–38].

Density-Functional Theory

In this dissertation, we resort to Density-Functional Theory (DFT) [39] in the formulation of Kohn and Sham [40], which has been developed in the mid-1960s. It is an exact

---

[4] The proton mass is about $1.836 \cdot 10^3 \times$ times larger than the electron mass [12].

reformulation of the eigenvalue problem, given by the Hamiltonian (1.1), in terms of the electron-charge density instead of many-electron wave functions. But, the solution of this reformulation is subject to knowing the generally unknown quantum-mechanical exchange-correlation (xc) energy inherent in DFT. The electron-charge density is not only a much simpler mathematical and computational object than the many-electrons wave function [41, 42], but equally important, experience has shown that rather simple yet powerful approximations to the unknown xc energy, like the Local Density Approximation (LDA) [40] or the Generalized Gradient Approximation (GGA) [43–45], provide excellent results. The predictive power of these results becomes obvious for wide classes of materials and for many physical or chemical properties. Kohn–Sham DFT with its many developments in various directions, (i) like Hedin's formulation of many-body perturbation theory in terms of the $\mathcal{GW}$-approximation for mastering excited states [46], (ii) such as the Time-Dependent Density-Functional Theory (TDDFT) [47, 48], (iii) towards higher quantum mechanical precision, and (iv) towards the description of strongly correlated electron systems by the development of hybrid functionals or amending functionals by static or dynamic Coulomb interactions (e.g. LDA + U [49] or LDA + DMFT [50]), is considered *the* computational standard model for the first-principles calculation of electronic and structural properties in solid-state physics, materials science, nanoscience, mineralogy, as well as parts of chemistry, and bio-chemistry. For a broader view see for instance references [3, 51–54]. [3]

Full-Potential Linearized Augmented Plane-Wave method

The DFT approach is realized in electronic-structure methods, which solve the Kohn–Sham equations to obtain the ground-state electron density and subsequent electronic properties. Implementing these methods requires very advanced and complex state-of-the-art computer algorithms (see e.g. Martin [3] for an overview). Typically, electronic-structure methods are classified according to the type of basis functions into which the Kohn–Sham orbitals are expanded. In the context of phonon calculations in crystalline solids, plane-wave based methods are the first and foremost (see for instance `ABINIT` [55–57], `VASP` [58], `QUANTUM ESPRESSO` [59–61], and the mixed basis method [62]). They are either based on the pseudopotential approximation to describe the interaction of valence electrons at the ion core or utilize the Projector-Augmented Plane Wave (PAW) method [3, 63]. Within this dissertation, in contrast, I work with the Full-Potential Linearized Augmented Plane-Wave (FLAPW) method [64–68], as implemented in the electronic-structure code `FLEUR` [69]. It is an all-electron approach, treating core electrons on the same footing as valence electrons. But, the nuclear charge produces a Coulomb singularity and thereby associated rapid variations of the charge density in the vicinity of the nucleus. In order to deal with this singularity, the space of the unit cell is partitioned into muffin-tin (MT) spheres, in which wave functions, charge densities, as well as potentials are represented in real space, and an interstitial region (IR) with a plane-wave representation of the aforesaid quantities. This ansatz is often considered the gold standard among the electronic structure methods [70], applicable to solids with open- and closed-packed structures, and to unit cells incorporating any naturally-occurring chemical element of the periodic table. However, this approach bears likewise particular challenges due to different definitions of basis functions in different regions of space, matching at the MT sphere boundary. [3, 71]

Calculating the dynamical matrix

In combination with DFT, two complementary computational approaches have been developed to determine the dynamical matrix $\underline{D}$: (i) the Finite Displacement (FD) method [3, 72–75] and (ii) the Density-Functional Perturbation Theory (DFPT) [3, 68, 76–87]. In the FD method, the dynamic matrix or the second-order energy derivatives are replaced by corresponding quotients of first-order differences, whose nominators contain differences of forces acting on the atoms due to different displacement patterns. The dynamical matrix is calculated for finite grids of wave vectors $\boldsymbol{q}$ in the Brillouin zone, with a grid size that depends on the size of the supercell, which must in turn be chosen adequate for the respective displacement patterns (as for instance in reference [88]). According to the literature, this direct ab-initio approach to determining the dynamical matrix, or especially the phonon-dispersion and thermal properties, has become the standard [3]. This status-quo has mainly be fostered by the advent of precise force calculations, especially those based on plane-wave basis sets, as well as the increase of computational capacity in combination with numerical efficiency regarding the electronic-structure methods, making the evaluation of larger unit cells (super cells) feasible [3]. On the other hand, DFPT, pioneered by Zein [76], Baroni, Giannozzi, and Testa [80], as well as Gonze et al. [81–85], allows for computing the dynamical matrix and the phonon properties for any selected phonon wave-vector $\boldsymbol{q}$, using *only* the chemical unit cell [3, 68]. Analytically applying the Rayleigh–Schrödinger perturbation theory to the Kohn–Sham Hamiltonian, the finite displacements are replaced by infinitesimal ones. The Sternheimer equation can then be invoked to self-consistently determine the linear charge-density response to the aforementioned infinitesimal displacement pattern [3]. Determining phonon dispersion-relations from the DFPT, is conceptually and algorithmically much more complex than from the FD method. Solving only the Sternheimer equation, is already (at least) as complicated as the self-consistent solution of the Kohn–Sham equation, but allows a fine-tracing of the phonon dispersion. For instance, this can be necessary for investigating the interaction of phonons with other degrees of freedom, such as magnons [89], where the dispersion relations show a crossing or anticrossing behavior within a finite region of wave vectors $\boldsymbol{q}$ [90, 91]. [22, 23, 87, 92]

Achievements in this dissertation

In this dissertation I report on the successful realization of the DFPT for calculating the dynamical matrix $\underline{D}$ in harmonic approximation by means of the all-electron FLAPW electronic-structure method. The algorithm has been implemented from scratch in the open-source code `juPhon`, which is compatible with the input data from the all-electron FLAPW code `FLEUR` (see page 112 for details). Employing `juPhon`, I have computed phonon dispersion-relations for a set of simple bulk systems: fcc Cu, fcc Au, fcc Al, bcc Mo, fcc Ne, and fcc Ar. These are validated against computational benchmarks obtained from the FD ansatz and experimental data, where the former are also based on the `FLEUR` code (cf. page 261). From a more general perspective and in concert with the `exciting` [93], `flair` [94, 95], and `Elk` [96] codes, this thesis extends the applicability of the DFPT, which can not only be applied to phonons, but also magnons or electric fields [22], to the FLAPW method. Important groundwork was done by Aaron Klüppelberg [88]. He refined the calculation of forces in `FLEUR` to the necessary precision that enables us nowadays to generate versatile phonon dispersion-relations from the FD approach. Learning from published linear-response formulations of MT-based electronic-structure methods [93–95, 97–99], Klüppelberg [88] provides in his doctoral thesis an analytical mathematical formulation of the DFPT approach for the FLAPW method. We translated this to a functioning code, where the word translation also implies reformulations to guarantee analytical cancellations of large terms. The FLAPW method is also employed in alternative electronic-structure frameworks: `WIEN2k` [100], `Elk` [96], `flair` [101], or `exciting` [102]. The corresponding DFPT implementations can be found in the codes `exciting` [93], `flair` [94, 95], or `Elk` [96]. Overall, the results of these implementations are scarce and an evaluation of the accuracy and computational efficiency is incomplete, if not lacking.

Outline of the dissertation

The thesis is organized in 9 chapters and 5 Appendices. The first six chapters can be considered as introductory chapters introducing: the DFT (chapter 2); the standard theory of harmonic phonons, the dynamical matrix, and the concept of the direct method for the phonon dispersion (chapter 3); the DFPT including the $2n+1$ theorem (chapter 4); and the FLAPW method (chapter 5). In chapter 6, an excerpt of the analytical DFPT formulation for the FLAPW method by Klüppelberg [88] is given. In these chapters, the emphasis is on the insights and quantities needed to implement the DFPT method and to calculate phonons by using the FLAPW method in chapter 7. We briefly conclude in chapter 8 and provide a potential outlook in chapter 9. Within the first two appendices, I address the installation as well as the general usage of `juPhon` (appendix A), and list the input parameters used for the results of this dissertation (appendix B). The three remaining appendices elucidate the theoretical background of three relations referred to hereinafter, i.e., the gradient of a function expanded in the MT spheres (appendix C), the analytical solution of the Sternheimer equation for $\boldsymbol{q} = \mathbf{0}$ (appendix D), and an outer-product extension of the divergence theorem (appendix E).

Summary of central chapter

The essential part of this dissertation is chapter 7. Here, I describe `juPhon`, the successful elaborate implementation of the DFPT, in detail and validate it by presenting successful results, in particular the aforementioned phonon dispersion-relations. But, it likewise contains intermediate outcomes of first- and second-order quantities, which I calculated with `juPhon` and which are required for the dynamical matrices. I address our concepts for resolving the considerable difficulties encountered in such a complex project. The formidable challenge of achieving a sufficient numerical accuracy within the implemented framework, incorporating multitudinous Pulay [68, 103] and surface [88] terms due to the position-dependent, incomplete and discontinuous LAPW basis, often required solutions surpassing naive implementations. Some of these optimizations were already suggested by Klüppelberg [88] concentrating on providing a comprehensive *theoretical* framework. But translating a theoretical formalism of this complexity into a functioning numerical algorithm is a challenging task. Imponderable numerics require consistency checks of the equations, occasionally rederivations or changes of formulations. In fact, the implementation of the dynamical matrix has required radical reformulations, before an acceptable result could be generated. Only indispensable terms have remained, further optimizations intend to exploit the principle of analytical error cancelation. Still, the overall involved intricate programming effort has been considerable. Central in this highly sophisticated framework has been the development of test concepts, ensuring reliable intermediate results. Often this has turned out to be hard, because cross-checking is only possible in very few cases. With the help of this comprehensive test suite, new features can be added or approximations can be relaxed in a safe way. All fundamental problems are solved now. Based on the presented results, there is a clear proof of concept. This allows for enhancing the versatility of `juPhon` in a straight-forward and quick way.

Chapter 2

Density-Functional Theory

2.1 Hohenberg–Kohn Theorems 8
2.2 Kohn–Sham System 9
2.3 Brief Overview of DFT Generalizations 16

Charge density instead of wave function

DFT expresses the (ground-state) properties of a complicated many-body system as functionals of its ground-state particle density $n_{\mathrm{gs}}(\boldsymbol{r})$. In solid-state physics, the many-body system is described by the Hamiltonian in equation (1.1). Hence, the *ground-state electron-charge density* $\rho_{\mathrm{gs}}(\boldsymbol{r}) = q_{\mathrm{e}} n_{\mathrm{gs}}(\boldsymbol{r})$, with the charge of an electron q_{e}, represents the aforementioned particle density. By confining to the charge density, the formulation of DFT circumvents the handling of the intractable many-body wave function [41]. Dealing with this wave function is tough or impossible because it scales with the number of particles N, whose quantum state is described ($N \geq 100$ given small molecules and $N \approx 10^{23}$ in a solid) [41]. Even though the many-body wave function provides much more information compared to the charge density, the latter offers access to plenty of calculable quantities which otherwise are hard to obtain [104]. [3]

Kohn–Sham Density-Functional Theory

Moreover, DFT (based on the concept of Kohn and Sham [40]) is in principle an exact ab-initio method for tackling the interacting many-body system [3]. It is mapped to an auxiliary non-interacting one-particle problem having the same ground-state density as the interacting many-body system, while all many-body effects are put into an exchange–correlation (xc) functional. However, the fact that a universal explicit form of this xc functional is not known, constitutes a shortcoming decisive for the accuracy of the DFT method. Nevertheless, this has sparked the development of various xc-functional approximations. Although treating notably highly-correlated materials and band gaps proves challenging, even simple xc-functional approximations convince by being impressively in line with experimental results. With the awarding of half of the Nobel Prize in chemistry to Walter Kohn in 1998 [105, 52] “for his development of the density-functional theory,” even greater significance was attached to DFT. Today, DFT has established itself as a state-of-the-art method, predominantly, to calculate the ground-state properties of the interacting many-body electronic system (forecasting of stable structures, band structure, ground-state energy and the quantities deriving from it, etc. [104]). Setting up databases for material design with DFT results and applying the disruptive technology of machine learning to it [106], allows us to stay excited at the prospect of DFT. [3]

References

Throughout the history of DFT, certain publications appear as important milestones, only a small selection of which can be discussed within the scope of this thesis. The overview paper of Jones [54], for example, provides an in-depth analysis and the standard textbook of Martin [3] contains a comprehensive discussion of the history and all aspects of DFT, including further literature. Therefore, the latter book will serve as the main reference for the whole of chapter 2.

Outline

Section 2.1 briefly summarizes the work of Hohenberg and Kohn [39]. They formulated and proved two theorems providing the fundamentals of modern DFT, after the pioneering work of Thomas [107], Fermi [108] and Dirac [109]. These theorems allow us to consider the total energy of the aforementioned interacting many-body system as a functional of the charge density that reaches its unique minimum by inserting the *ground-state* charge density. Despite the fact that the publication of Hohenberg and Kohn [39] has been ranked seminal, it does not provide an explicit how-to for calculating the total energy. The situation has changed with the work of Kohn and Sham [40], who introduce the auxiliary non-interacting one-particle system (Kohn–Sham system) which section 2.2 is devoted to. This major breakthrough, together with the development of reliable xc functionals, enabled DFT to develop into a dominant method for electronic-structure calculations. The increasing success of DFT is generating more and more interest and has given rise to generalizations of which a small selection shall be listed in section 2.3. [3]

2.1 Hohenberg–Kohn Theorems

Applicability

Hohenberg and Kohn [39] have managed to provide a formulation of DFT that constitutes an exact theory of any many-body problem with N interacting particles, which react to the influence of an arbitrary external potential. Without loss of generality, the focus here is on the many-body Hamiltonian in equation (1.1) to which the approximation of Born and Oppenheimer [20] has been applied (see chapter 1). Therefore, the movement of the electron particles is governed by the Coulomb interaction among each other and with the ions, which give rise to a static potential. [3]

Central theorems

Pivotal in the paper of Hohenberg and Kohn are two theorems: The *first theorem* states that for non-degenerate ground states, the ground-state particle density uniquely determines the external potential apart from a constant. This entails the complete electronic many-body Hamiltonian to be specified by the ground-state charge(-particle) density ρ_{gs}. The same holds true for the eigenfunctions and eigenvalues of this Hamiltonian [3, 41]. Therefore, the total energy of the system, and any observable that is a functional of the external potential, are also unique functionals of the ground-state charge density [3, 41]. Such a total energy functional can be defined as

$$E_{\mathrm{HK}}\big[\rho_{\mathrm{gs}}(\boldsymbol{r})\big] := F\big[\rho_{\mathrm{gs}}(\boldsymbol{r})\big] + \int V_{\mathrm{ext}}(\boldsymbol{r})\rho_{\mathrm{gs}}(\boldsymbol{r})\,\mathrm{d}^3r + E_{\mathrm{ii}}\,. \tag{2.1}$$

While V_{ext} is the external potential, the functional F contains the internal[1] contributions of the total energy and is therefore called universal [104] (equal for all systems [41]). The variable E_{ii} represents the ion–ion interaction. The *second theorem* states that, in the case of charge conservation [41] and with any external potential, the ground-state charge density globally minimizes a general total energy functional as in equation (2.1). This results in the exact ground-state total energy and ground-state density of the many-body system. The textbook of Martin [3], for instance, provides proofs of the theorems and a detailed discussion including further literature. Finally, it must be stressed that, although Hohenberg and Kohn have provided the basis for many achievements in modern DFT, they do *not* instruct explicitly how to calculate the functional F. [3]

Extensions and generalizations

The theorems of Hohenberg and Kohn are generalized and reformulated by Levy et al. [110–112] as well as by Lieb et al. [113–115], giving more insight into the functional and also including degeneracy. Moreover, Mermin [116] has published an extension of the Hohenberg–Kohn theory for canonical and grand canonical ensembles at finite temperature. But, it has not led to many applications as they are harder to find. [3]

2.2 Kohn–Sham System

Concept

In the quest for finding a method to determine the energy functional (2.1) of Hohenberg and Kohn in the context of the aforesaid many-body system, the publication of Kohn and Sham [40] represents a major breakthrough. It has paved the way for the incredible success of modern DFT. In a nutshell, Kohn and Sham substitute the complicated many-body problem with an auxiliary non-interacting single-particle system, while restricting themselves to only reveal the *ground-state* features of the real system. This auxiliary Kohn–Sham system is to exhibit the same ground-state charge density ρ_{gs} as the many-body problem. Moreover, they suggest the total energy functional

$$E_{\text{KS}}\left[\rho_{\text{gs}}(\boldsymbol{r})\right] = T_{\text{ni}}\left[\rho_{\text{gs}}(\boldsymbol{r})\right] + \int V_{\text{ext}}(\boldsymbol{r})\rho_{\text{gs}}(\boldsymbol{r})\,\mathrm{d}^3 r + E_{\text{Htr}}\left[\rho_{\text{gs}}(\boldsymbol{r})\right] + E_{\text{ii}} + E_{\text{xc}}\left[\rho_{\text{gs}}(\boldsymbol{r})\right] , \quad (2.2\text{a})$$

where T_{ni} is the kinetic energy of the auxiliary non-interacting electrons, V_{ext} the external potential resulting from the nuclei or other external fields, E_{Htr} the Hartree contribution, and E_{ii} the interaction between the nuclei. The last functional E_{xc} contains all remaining contributions to the total energy that are attributed to many-body effects, such as exchange and correlation. This leads to its name exchange–correlation energy. [3]

Outline

Section 2.2.1 presents the details of the Kohn–Sham total energy (2.2a) and the Kohn–Sham equations that can be derived from it. Typical categories of xc-functional approximations are sketched in section 2.2.2. Finally, the basic strategy to self-consistently solve the independent-particle Kohn–Sham equations, including prominent classes of mathematical minimization procedures being employed in this context, are briefly described in section 2.2.3. Overall, the discussion within this section 2.2 does not involve spin-polarization, time-dependence, temperatures beyond zero, or any relativistic effects.

---

[1] They are *not* dependent on the external potential V_{ext} [3].

2.2.1 Kohn–Sham Equations

Kohn–Sham energy functional

The idea to map the complex many-body problem, with a given ground-state density, to an auxiliary system with non-interacting particles, featuring exactly the same ground-state density[2], leads to a set of N single-particle equations[3]. These Kohn–Sham equations are significantly easier to solve than those resulting from the Hamiltonian of the many-body problem. Aiming for this set of Kohn–Sham equations, the general Kohn–Sham version of the total energy (2.1) shall now be discussed more explicitly, using Hartree atomic units (see footnote on page 1). The kinetic energy [68, 117] of the non-interacting particles is given by

$$T_{\mathrm{ni}}\left[\rho_{\mathrm{gs}}(\boldsymbol{r})\right] = -\frac{1}{2}\sum_{o}\int \Psi_o^*(\boldsymbol{r})\overleftarrow{\nabla}\overrightarrow{\nabla}\Psi_o(\boldsymbol{r})\,\mathrm{d}^3r = -\frac{1}{2}\sum_{o}\int \left|\nabla\Psi_o(\boldsymbol{r})\right|^2\mathrm{d}^3r\ , \tag{2.2b}$$

where $\Psi_o(\boldsymbol{r})$ are the one-particle wave functions of an occupied[4] orbital o, and the arrows above the gradients indicate the application direction of the derivative operators [3]. Although the kinetic energy in equation (2.2b) is a functional of the ground-state density (cf. section 2.1), this dependence does not explicitly appear in the proposal of Kohn and Sham [40]. Nonetheless, choosing such a representation of the single-particle kinetic energy as one term in the Kohn–Sham total energy (2.2a) gives one reason why the Kohn–Sham DFT has been applied successfully so many times. Furthermore, the Hartree energy in the Kohn–Sham total energy (2.2a) is given by the classical Coulomb interaction between the ground-state charge densities evaluated at different locations $\boldsymbol{r}$ and $\boldsymbol{r}'$

$$E_{\mathrm{Htr}}\left[\rho_{\mathrm{gs}}(\boldsymbol{r})\right] = \frac{1}{2}\int \frac{\rho_{\mathrm{gs}}(\boldsymbol{r})\rho_{\mathrm{gs}}(\boldsymbol{r}')}{|\boldsymbol{r}-\boldsymbol{r}'|}\,\mathrm{d}^3r'\,\mathrm{d}^3r\ . \tag{2.2c}$$

The potential due to the Coulomb-like interaction between the ions, located at $\boldsymbol{\tau}$ and $\boldsymbol{\tau}'$ with respective proton numbers Z and Z', reads

$$E_{\mathrm{ii}} = \frac{1}{2}\sum_{\boldsymbol{\tau}\boldsymbol{\tau}'}\frac{ZZ'}{|\boldsymbol{\tau}-\boldsymbol{\tau}'|}\ . \tag{2.2d}$$

Kohn and Sham also do not give an explicit formulation[5] for the xc functional in the Kohn–Sham total energy (2.2a), nevertheless they have simplified searching for approximations. Although the task of developing good approximations that live up to the variety and subtleties of real systems in some cases poses a challenge, fortunately, this can often be achieved fairly accurately. This discussion is postponed until section 2.2.2. [3]

Properties of Kohn–Sham equations

The orthogonal one-particle wave functions of orbital o appearing in equation (2.2b) are called the Kohn–Sham eigenfunctions of the single-particle Kohn–Sham equation

$$\left(-\frac{\Delta}{2} + V_{\mathrm{eff}}(\boldsymbol{r})\right)\Psi_o(\boldsymbol{r}) = \varepsilon_o\Psi_o(\boldsymbol{r})\ . \tag{2.3a}$$

---

[2] This mapping is exactly fulfilled for the homogeneous gas, however, no hard evidence has been provided that such an auxiliary system with the same ground-state density as the real system can be found in general. Still, the success of DFT is beyond dispute. [3]

[3] Consider additional factor of two for degenerate spin.

[4] According to the Pauli principle, every orbital is fully occupied with one spin-up and one spin-down electron, starting from the orbital with lowest energy up to the Fermi energy. However, we suppress the spin-index within the current section, keep in mind a spin-degeneracy factor of 2, and refer to section 2.3 for the integration of the spin-polarization into the Kohn–Sham DFT formalism.

[5] If the exact form of the xc functional were known, the ground-state density and the ground-state total energy would be exact.

While the corresponding Kohn–Sham eigenenergies are denoted by ε_o, $V_{\text{eff}}(\boldsymbol{r})$ is an effective local potential acting on one electron located at $\boldsymbol{r}$. As the Kohn–Sham equation can be derived from the Kohn–Sham total energy in a variational approach (2.2a), the Kohn–Sham eigenenergies are the Lagrange parameters of the condition for the Kohn–Sham wave functions to be orthonormal. Moreover, the effective potential is defined as

$$V_{\text{eff}}\Big[\rho_{\text{gs}}(\boldsymbol{r});\boldsymbol{r}\Big] := V_{\text{ext}}(\boldsymbol{r}) + \int \frac{\rho_{\text{gs}}(\boldsymbol{r}')}{|\boldsymbol{r}-\boldsymbol{r}'|}\,\mathrm{d}^3 r' + V_{\text{xc}}\Big[\rho_{\text{gs}}(\boldsymbol{r})\Big] \,. \tag{2.3b}$$

The first term is the external potential. The second term is the Hartree potential, which is the functional derivative of the Hartree energy in equation (2.2c) with respect to the ground-state density. The last term is the so-called xc potential, which is also defined as the functional derivative of the xc energy with respect to the ground-state density. This xc potential requires approximations of which the most common ones are given an overview of in section 2.2.2 and further classes are mentioned in section 2.3. In principle, the effective potential is chosen so that the ground-state density of the non-interacting Kohn–Sham system actually corresponds to the ground-state density of the interacting many-body problem. One is able to adjust this, as well as possible, only by the choice of the xc-potential approximation. Having determined the Kohn–Sham eigenfunctions $\Psi_o(\boldsymbol{r})$ by using the Kohn–Sham equations, the ground-state charge density can easily be gained

$$\rho_{\text{gs}}(\boldsymbol{r}) = \sum_o \big|\Psi_o(\boldsymbol{r})\big|^2 \,. \tag{2.4}$$

Both the effective potential and the ground-state charge density stem from a minimization procedure and are stationary as far as slight deviations are concerned [3, 118]. It must be clear that such a variational solution is only in line with an exact pointwise solution of an analytically solvable system on average [119]. Important consequences shall be elaborated in further chapters of this dissertation. Finally, it must be stressed that the Kohn–Sham eigenvalues are, strictly speaking, purely auxiliary quantities without any physical relevance. An exception is the highest eigenvalue approximating the negative ionization energy [120] as accurately as the approximation to the xc energy. Still, employing the Kohn–Sham eigenvalues in general allows for calculating trustworthy physical quantities (an overview is for instance provided by Martin [3]). [3]

Self-consistent solution

The Kohn–Sham equations require a self-consistent approach to be solved due to the fact that the effective potential (2.3b) is not known in the beginning. It depends on the ground-state density (2.4) which in turn depends on the Kohn–Sham wave functions (2.3a). In order to calculate the Kohn–Sham wave functions, one requires the calculated effective potential which sets up the self-consistency cycle. Section 2.2.3 is concerned with shedding more light on this aspect. [3]

2.2.2 Common Approximations for the Exchange-Correlation Potential

Theoretical background

The xc energy is governed by the xc hole, expressing the extent to which the Pauli exclusion principle and correlation due to the Coulomb interaction lower the probability of one electron being located in the vicinity of another. This circumstance leads to more sophisticated properties than, for instance, those known from the Hartree potential. Setting the Hohenberg–Kohn total energy formulation in equation (2.1) equal to the total energy expression of Kohn and Sham in equation (2.2a) yields

$$E_{\mathrm{xc}}\Big[\rho_{\mathrm{gs}}(\boldsymbol{r})\Big] = \langle T\rangle - T_{\mathrm{ni}}\Big[\rho_{\mathrm{gs}}(\boldsymbol{r})\Big] + \langle V_{\mathrm{int}}\rangle - E_{\mathrm{Htr}} \,, \tag{2.5}$$

where $\langle T\rangle$ and $\langle V_{\mathrm{int}}\rangle$ are the expectation values of the kinetic energy and the internal potential energy[6] in the real many-body system, respectively. Furthermore, $T_{\mathrm{ni}}\Big[\rho_{\mathrm{gs}}(\boldsymbol{r})\Big]$ is the single-particle kinetic energy of the auxiliary system and E_{Htr} is the Hartree energy. Equation (2.5) elucidates the energy difference between the real many-body system and the auxiliary system, and exposes the challenges to find a general form for this xc energy. Thus in practice, approximations are decisive. Meanwhile, there exists a plethora of it also covering the xc potential

$$V_{\mathrm{xc}}\Big[\rho_{\mathrm{gs}}(\boldsymbol{r})\Big] = \frac{\delta E_{\mathrm{xc}}\Big[\rho_{\mathrm{gs}}(\boldsymbol{r})\Big]}{\delta\rho_{\mathrm{gs}}(\boldsymbol{r})} \,, \tag{2.6}$$

which has been defined in section 2.2.1. Their success, among others, is due to the xc energy constituting a significantly smaller contribution of the total energy to be approximated relative to the Hohenberg–Kohn energy functional $F\Big[\rho_{\mathrm{gs}}(\boldsymbol{r})\Big]$ in equation (2.1) [104]. This draws from the fact that especially the kinetic energy of the auxiliary non-interacting electrons has been split off [104]. [3]

Local Density Approximation

While the functionals occurring in the Hohenberg–Kohn theorems (see section 2.1) depend non-locally on the ground-state density, Kohn and Sham [40] mention that for solids the xc functional can, often in a good approximation, be written as

$$E^{\mathrm{LDA}}_{\mathrm{xc}}\Big[\rho_{\mathrm{gs}}(\boldsymbol{r})\Big] = \int \rho_{\mathrm{gs}}(\boldsymbol{r})\varepsilon^{\mathrm{LDA}}_{\mathrm{xc}}\Big(\rho_{\mathrm{gs}}(\boldsymbol{r})\Big)\,\mathrm{d}^3 r \,, \tag{2.7}$$

with an xc energy density $\varepsilon^{\mathrm{LDA}}_{\mathrm{xc}}\Big(\rho_{\mathrm{gs}}(\boldsymbol{r})\Big)$ (it is equal to the xc energy density of the homogeneous gas and is therefore a function instead of a density functional) [3, 41]. In the so-called Local Density Approximation (LDA), the xc energy-density is usually composed of an analytical exchange part of the homogeneous gas and a correlation part [3, 41]. The latter has been determined by Monte Carlo methods [121] or, as in the references [43, 122], has been parameterized [3, 41]. Vital for the justification of LDA, which is exact for a homogeneous gas, is comparison with experiment. Although a rather simple construction, the correspondence of LDA with experiment is astonishing. For example, lattice constants differ between experimental and theoretical results not more than a few percent. [3]

$X\alpha$ approximation

Within the scope of this thesis the $X\alpha$ approximation becomes relevant due to its simple derivative of the respective xc potential, which is needed for the gradient or the first-order variation of the xc potential (see section 6.3.3 for an explicit form). Its origin dates back to the publication of Slater [123], who proposed an exchange potential for the homogeneous gas which features the same $\rho^{1/3}$ behavior, but a prefactor differing from the suggestion of Kohn and Sham. The prefactor of the exchange (X) potential is usually called α[7] and typically ranges between 1 and $4/3$. Varying α can compensate for contributions which have been neglected, if only the exchange potential of the homogeneous gas without correlation corrections has been used. A thorough discussion of the $X\alpha$ method can for example be found in the publication of Connolly [125]. [3]

---

[6] This includes all potential contributions not stemming from an external potential [3].

[7] The historical development of this parameter is pointed out, for example, by Zope and Dunlap [124].

Gradient approximations

An improvement to the LDA represents the class of xc potentials which additionally include the charge density gradient

$$E_{\mathrm{xc}}^{\mathrm{GGA}}\big[\rho_{\mathrm{gs}}(\boldsymbol{r})\big] = \int \rho_{\mathrm{gs}}(\boldsymbol{r})\,\varepsilon_{\mathrm{xc}}^{\mathrm{GGA}}\big(\rho_{\mathrm{gs}}(\boldsymbol{r}), \boldsymbol{\nabla}\rho_{\mathrm{gs}}(\boldsymbol{r})\big)\, \mathrm{d}^3 r \ , \tag{2.8}$$

and is called the Generalized Gradient Approximation (GGA). In comparison to the Gradient Expansion Approximation (GEA) proposed by Kohn and Sham [40] which can fail, for example in fulfilling sum rules, and is all in all not better than the LDA [126], the representatives of the GGA have more control over the gradients of the density. Particularly in real materials, these gradients become hard to handle. Prominent GGA representatives are the PBE functional [43], the PW91 functional [44], or the B88 functional [45]. In many situations GGA functionals can be more accurate than LDA functionals when compared to experiments and enable reliable calculations for even more material classes. [3]

More elaborate approximations

Although LDA and GGA functionals are the default in today's DFT calculations, they fail in some cases, such as in materials with strong correlation or van der Waals interaction [3]. Two chapters in the textbook of Martin [3] are devoted to LDA, GGA or more advanced xc functionals. There, further (overview) literature is also provided introducing new functionals or ranking and comparing them with respect to different material classes. A quick overview of what exists beyond LDA and GGA is the subject of section 2.3.

2.2.3 Self-Consistency and Mixing of the Charge Density

Abstraction

From an abstract point of view, finding the self-consistent solution of the Kohn–Sham equations[8] is in line with a numerical minimization procedure for either the effective potential or the charge density. As far as the `FLEUR` code [69] is concerned, the change of the density is minimized [127]. So, no additional constant must be accounted for, which would have been present for the minimization of the potential. From another point of view, one can interpret the minimization as a fixed-point problem obeying

$$\mathfrak{F}\big[\rho_{\mathrm{gs}}(\boldsymbol{r})\big] - \rho_{\mathrm{gs}}(\boldsymbol{r}) =: \mathcal{F}\big[\rho_{\mathrm{gs}}(\boldsymbol{r})\big] = 0 \, , \tag{2.9a}$$

where

$$\mathfrak{F}\big[\rho^{\mathrm{i}}(\boldsymbol{r})\big] = \rho^{\mathrm{i}+1}(\boldsymbol{r}) \tag{2.9b}$$

is a map between two sequential iterations i and $\mathrm{i}+1$ of the self-consistency cycle [128]. Furthermore, the ground-state density represents the fixed-point [128]. [3]

Concept

The scheme for the Kohn–Sham self-consistency cycle is depicted in figure 2.1. It starts with a well-educated guess of the input ground-state density. For solids, the density resulting from an overlap of all atomic densities (see also section 5.5.1) often corresponds quite well to the actual density. Therefore, such a density construction represents a good starting point for the minimization procedure. This input charge density gives a related effective input potential, which sets up a Hamiltonian. The Hamiltonian is diagonalized resulting in output Kohn–Sham eigenfunctions and Kohn–Sham eigenenergies which can be used to set up an output potential and an output charge density. The change of the output density compared to

---

[8] This means the effective potential results from the ground-state density and vice versa.

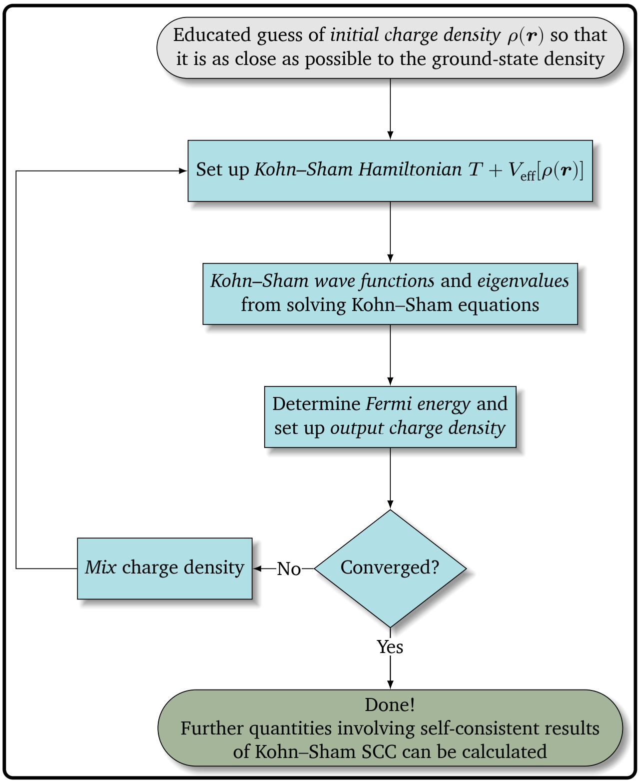

Figure 2.1: Flowchart of the Kohn–Sham self-consistency cycle (based on reference [128, figure 4]). Starting with an educated guess of the input charge density, the Kohn–Sham Hamiltonian is set up and diagonalized giving the Kohn–Sham eigenfunctions and eigenvalues. The latter can be used to find the Fermi energy and calculate the output charge density. If the output charge density differs from the input charge density of the iteration the output charge density resulted from, input and output charge densities will be mixed to determine a new input charge density and initiate a new iteration step. If, up to some numerical threshold, the charge density is self-consistent with the effective potential, the Kohn–Sham self-consistency cycle (SCC) has converged and is terminated. This state sets the stage for further calculations employing the resulting quantities of the Kohn–Sham SCC.

the input density, due to an input effective potential, can also be interpreted as the Kohn–Sham susceptibility [119]. Further discussion of the latter is delayed until section 4.2.1. The difference [128] between the output and input charge-density can be defined as

$$\left\| \mathcal{F}\left[\rho^{\mathrm{i}}(\boldsymbol{r})\right] \right\| . \tag{2.10}$$

Equation (2.10) is a measure for the self-consistency of the Kohn–Sham system. Thus, reaching the minimum is equal to a vanishing distance between the output and input charge-density. It is the way, that the output density contributes to the new input density, which categorizes the mathematical minimization (mixing) procedures [41]. They differ in how fast they converge or how successful they are in damping emerging oscillations [41]. Setting the output density as the new input density without any mixing procedure lets the fixed-point problem diverge in general [128]. [3]

Linear mixing

The concept of linear mixing [128] is summarized by

$$\rho^{\mathrm{i}+1}_{\mathrm{in}} = \alpha\rho^{\mathrm{i}}_{\mathrm{out}} + (1-\alpha)\rho^{\mathrm{i}}_{\mathrm{in}} = \rho^{\mathrm{i}}_{\mathrm{in}} + \alpha\left(\rho^{\mathrm{i}}_{\mathrm{out}} - \rho^{\mathrm{i}}_{\mathrm{in}}\right) = \rho^{\mathrm{i}}_{\mathrm{in}} + \alpha\mathcal{F}\left[\rho^{\mathrm{i}}_{\mathrm{in}}\right] . \tag{2.11}$$

In equation (2.11), the difference of the output and input charge density related to the same iteration is sort of a first derivative and enters with a certain percentage determined by α into the new input charge density (can approximately be seen as the steepest descent). Linear mixing does not need much information except for the input and output quantities. This might be an advantage, but can also be interpreted as a disadvantage as far as the speed of convergence is concerned. Linear mixing counts as the slowest-converging mixing method. Also, increasing α, i.e., adding more information to the new input density about the steepest descent, does not work well in every case. Nevertheless, when setting a small α, the iteration mostly converges, but slowly and linearly [128]. [3]

Newton–Raphson mixing

More optimal are Newton–Raphson methods, where the first-order of the expansion

$$\mathcal{F}\left[\rho(\boldsymbol{r})\right] = \mathcal{F}\left[\rho^{\mathrm{i}}(\boldsymbol{r})\right] + \mathcal{J}\left[\rho^{\mathrm{i}}(\boldsymbol{r})\right]\left(\rho(\boldsymbol{r}) - \rho^{\mathrm{i}}(\boldsymbol{r})\right) \tag{2.12a}$$

is used and the Jacobian is defined as

$$\mathcal{J}\left[\rho^{\mathrm{i}}(\boldsymbol{r})\right] = \left.\frac{\partial\mathcal{F}[\rho(\boldsymbol{r})]}{\partial\rho(\boldsymbol{r}')}\right|_{\rho^{\mathrm{i}}(\boldsymbol{r})} . \tag{2.12b}$$

Setting $\rho(\boldsymbol{r}) = \rho^{\mathrm{i}+1}(\boldsymbol{r})$ and $\mathcal{F}\left[\rho^{\mathrm{i}+1}(\boldsymbol{r})\right] = 0$ in equation (2.12a) leads to the condition

$$\rho^{\mathrm{i}+1}_{\mathrm{in}} = \rho^{\mathrm{i}}_{\mathrm{in}} - \mathcal{J}^{-1}\left[\rho^{\mathrm{i}}_{\mathrm{in}}\right]\mathcal{F}\left[\rho^{\mathrm{i}}_{\mathrm{in}}\right] . \tag{2.12c}$$

The high computational costs of evaluating or inverting the large matrix representation of the Jacobian and the small convergence radius of this method outweigh its quadratic convergence behavior and have led to the development of quasi-Newton methods, which try to overcome the aforementioned disadvantages. [128]

Quasi-Newton mixing

The quasi-Newton methods circumvent fully determining the Jacobian in every iteration. This is beneficial for situations in which the Jacobian has large dimensions or cannot totally be set up. All representatives of this mixing category have the quasi-Newton condition

$$\Delta\rho^{\mathrm{i}}_{\mathrm{in}} = \mathcal{J}^{-1}\left[\rho^{\mathrm{i}}_{\mathrm{in}}\right]\Delta\mathcal{F}\left[\rho^{\mathrm{i}}_{\mathrm{in}}\right] \tag{2.13a}$$

with

$$\Delta\rho_{\text{in}}^{\text{i}} := \rho_{\text{in}}^{\text{i}} - \rho_{\text{in}}^{\text{i}-1} \tag{2.13b}$$

and

$$\Delta\mathcal{F}\left[\rho_{\text{in}}^{\text{i}}\right] := \mathcal{F}\left[\rho_{\text{in}}^{\text{i}}\right] - \mathcal{F}\left[\rho_{\text{in}}^{\text{i}-1}\right] \tag{2.13c}$$

in common. However, it is an underdetermined set of equations which is coped with differently by the procedures counting among the quasi-Newton methods. While the charge density approaches its minimum super-linearly in sequential iterations, the inverse Jacobian is evaluated stepwise and is constantly improving after every iteration [3]. This results in a history of previous mixing steps. If some of these steps have been less effective in reaching the minimum, the convergence behavior might be worsened [128, 129]. This is due to the fact that quasi-Newton mixing-step suggestions correlate more with their history than they do in the Newton–Raphson method, where only the last iteration step is used [128, 129]. Although the convergence radius is larger relative to the Newton–Raphson methods, the starting density might still be too far away from the fixed-point. Provided this situation or when numerical parameters are altered during the minimization procedure, the convergence slows down and the quasi-Newton method should be started from the beginning. The speed of convergence can even be increased more with generalized Newton methods involving preconditioning [130–132]. [128]

Numerics

A comprehensive discussion about mixing procedures and further literature can be found in [3, 129]. When calculating derived quantities from the results of the Kohn–Sham self-consistency cycle, one must keep in mind that, due to numerical noise, the self-consistency can be achieved only up to a certain accuracy. As a consequence, the effective potential and the ground-state density are not exactly self-consistent. In the case of the total energy, for example, it proved convenient to use the input ground-state density and the effective potential which result from it together with the Kohn–Sham eigenfunctions and eigenvalues that result from the diagonalization of the Hamiltonian (see section 5.9 and section 7.1.6). [3]

2.3 Brief Overview of DFT Generalizations

Spin Density-Functional Theory

Up to now, the spin degree of freedom has been neglected in the current chapter, as within the scope of the thesis only spin-degenerated systems are treated. Here, it is sufficient to just multiply by a factor of 2 in the end to account for the spin-up or spin-down character of the electrons. For magnetic materials, admittedly, the ground-state density can, in principle, be determined using the formalism introduced above in the current chapter. However, the magnetization, a functional of the ground-state density according to the Hohenberg–Kohn theorems (see section 2.1), is unknown. In order to shed light on it, one can resort to Spin Density-Functional Theory that is based on a generalization of the aforementioned Hohenberg–Kohn theorems. Within this theory, for example, the effective potential and the ground-state density become spin-dependent, a magnetization density of which can be formed to enable research in magnetic phenomena. An introduction in the treatment of magnetism is, for example, given by Blügel [133] or Bihlmayer [134]. [3]

Superconducting Density-Functional Theory

A generalization that appears interesting in the context of phonons is the DFT of superconductivity or alternatively called the Superconducting Density-Functional Theory (SCDFT) [135–137], in which e.g. Sanna [138] provides an introduction. This theory is characterized by integrating an anomalous pair density (consistent with the spin density that was mentioned in the previous paragraph) and bases its formulation on the electron–phonon interaction. [3]

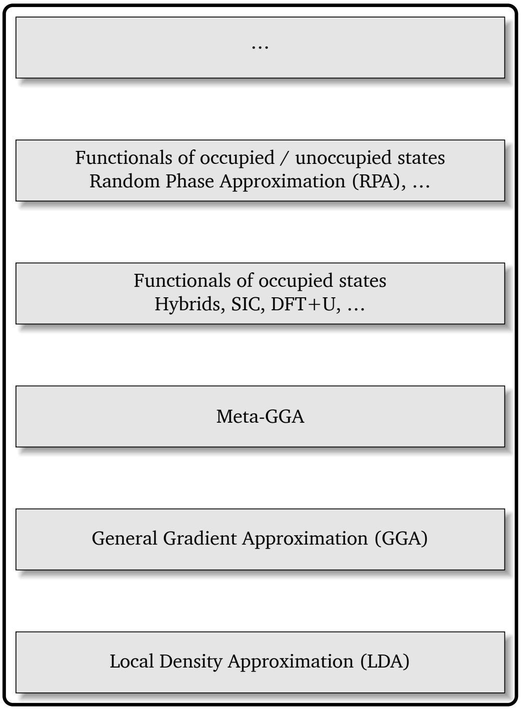

Figure 2.2: Jacob's ladder of xc-functional approximations (based on reference [3, figure 9.1]). The categories of xc functionals are ranked by complexity, starting with the simplest approximation, the LDA, at the lowest rung of the ladder. The increased complexity of the functionals is justified by their power and accuracy [3].

Jacob's ladder

Beyond the popular local density and general gradient approximations that have been discussed in section 2.2.2, many other functionals have been proposed. They try to overcome the disadvantages of LDA or GGA approaches for cases in which the local approximation is insufficient, examples are van der Waals interactions or polarizability. In addition to the ground-state density and the gradient of the ground-state density, functionals can also be dependent on wave functions as well as on kinetic-energy densities, formed by wave function derivatives. The density can likewise be averaged or weighted. A popular categorization is achieved by Jacob's ladder, which can be found in figure 2.2. It ranks the functionals according to the information used and their accuracy compared to the real xc functional. After LDA, the GGA follows, as it also contains the gradient of the ground-state density. Going up the ladder, there are meta-GGA with an additional kinetic energy density. Hybrid functionals, SIC, and

DFT+U ensue, using wave functions of occupied states or, such as in RPA, wave functions of occupied and unoccupied states. [3]

Development of new functionals

It is hard to stay updated among all the functionals that have been developed [53, 139] and there is not a single functional that is best for all situations. Otherwise, a general form for the xc functional defined in section 2.2 would have been found. Instead, each situation, phenomenon, or material has one or a set of functionals that are well-suited. In order to find new functionals that are not derived from theoretical considerations, chemical databases have been fitted and one applies artificial intelligence [140, 141]. Artificial intelligence recognizes patterns and relations that might be nonobvious or are extremely tricky to understand. On the one hand, this can lead to powerful functionals, but on the other hand, one cannot explain why they are working so well. [3]

Beyond the ground state

The Hohenberg–Kohn theorems do not exclude the description of excitations as the ground-state density sets up the full Hamiltonian (see section 2.1). For that reason, many-body calculations such as Configuration Interaction (CI), Monte Carlo, $\mathcal{GW}$, or the Bethe–Salpeter Equation (BSE) are based on the Kohn–Sham eigenfunctions. [3]

Chapter 3

Phonons

3.1 Basic Theory 20
3.2 Direct Ab-Initio Approach to Phonon Physics 23

Setting the stage

After having discussed how to use DFT to cope with interacting electrons in the static potential of the ions, this chapter deals with the vibrating ions moving in the Born–Oppenheimer (BO) potential, given a fixed electronic configuration. Thereby, the adiabatic approximation of the many-body Hamiltonian in equation (1.1) is applied (cf. chapter 1). Furthermore, the focus is again on bulk solids with a periodic lattice structure. Lattice vibrations, which can, for example, be excited by a compressional wave such as sound or by electromagnetic waves in the infrared spectrum [7, 142], are usually referred to as *phonon* quasiparticles in the context of quantum mechanics [5].

Relevance

The importance of (quantized) lattice dynamics becomes obvious in a huge class of material-specific phenomena. Among them are the transport of heat and sound, elastic properties, or the interaction and scattering of neutrons or electromagnetic waves in solids (the latter waves exhibit frequencies in the visible or X-ray spectrum) [4, 5, 7]. Furthermore, vibrating ions interact with spin-carrying electrons and hence e.g. play a role in electrical resistance, heat capacity, or can give rise to superconductivity at low temperatures by enabling an effective electron–electron attraction [4]. Such interactions of phonons with photons or spin-carrying electrons underlie the definitions of quasiparticles like polaritons or polarons [5]. Moreover, phonons govern dielectric and piezoelectric material properties [87]. In addition, phenomena such as those described by thermal expansion coefficients, as well as phase transitions from solid to liquid or between lattice structures (martensitic transitions) [4] involve phonons [8]. However, all phenomena in the previous sentence, and the functional dependences of the electrical resistance or the phonon frequencies on temperature or other parameters require theories beyond the harmonic approximation (see section 3.1 for a definition) [8]. The subjects of current research are also exotic acoustic metamaterials, so-called phononic crystals [143, 144]. Within these metamaterials sound waves can be directed, filtered due to band gaps in the phonon dispersions, or manipulated in a certain way similar to light or electrons in crystals [143, 144]. All in all, research on phonons promises new and innovative high-tech applications in the future.

Measuring dispersion relations

The central phonon dispersion relations inform about the phonon frequencies as functions of the phonon wave vector. Usually, these phonon frequencies are within an interval from 0 to 10–$30\,\mathrm{THz}$. Experimental methods to measure them partially or completely range from inelastic incoherent neutron scattering [145–147], or X-ray diffraction and Brillouin light scattering [148–150], to infrared absorptions or Raman spectroscopy [151, 152] [3, 7]. An overview of experimental techniques notably focusing on surface phonons is given by Fritsch and Schröder [153] [23]. [142]

Theoretical methods

Theoretical approaches to understanding how phonons contribute to physical effects include, for example, semiclassical theories or operator techniques in models and perturbative approaches, such as those using Feynman diagrams [5, 8]. Particularly for finite temperatures, the physics of phonons can be investigated with molecular dynamics simulations [154–157].

Outline

Section 3.1 is devoted to summarizing the basic parts of phonon theory, relevant within the scope of this thesis, to clarify the associated terminology and to describe the assumptions this dissertation rests on. In addition to analytical methods, numerical methods have also been established and augment the access to regimes beyond the cut-offs of analytical calculations. Within section 3.2, the class of so-called direct ab-initio methods is presented. They offer an alternative to the class of perturbative methods, such as Density-Functional Perturbation Theory (DFPT), in order to calculate phonon frequencies.

3.1 Basic Theory

Literature

The equations of lattice dynamics are part of standard textbooks about solid-state physics today. This section mainly refers to the textbooks of Galsin [7] and Mahan [5], and also to the concise lecture notes of Heid [23]. One of the first standard textbooks in the context of lattice dynamics has been published by Born and Huang [21].

Minimal Born–Oppenheimer energy

The definition of the BO energy $E_{\mathrm{BO}}(\{\boldsymbol{\tau}\})$ (1.3) sets the stage for outlining the central points in the theory of lattice dynamics. Starting with a common DFT calculation (as discussed in chapter 2), it is feasible to calculate the minimum E_{BO} of the BO energy [22]. This minimum is characterized by the equilibrium configuration $\{\boldsymbol{\tau}^{(0)}\}$ of the ions at temperature $T = 0\,\mathrm{K}$. [23]

Taylor-expanding the Born–Oppenheimer energy

In a next step, the ensemble of coupled ions might undergo a set of small[1] displacements, described individually for an atom (ion) γ by $\boldsymbol{w}_\gamma$. Thus, the new locations $\{\boldsymbol{\tau}\} = \{\boldsymbol{\tau}^{(0)}\} + \{\boldsymbol{w}\}$ of the nuclei (ions) are in the close vicinity of the equilibrium configuration $\{\boldsymbol{\tau}^{(0)}\}$. In this particular case, the expansion of the BO energy

$$E_{\mathrm{BO}}\Big(\{\boldsymbol{\tau}\}\Big) = E_{\mathrm{BO}}\Big(\{\boldsymbol{\tau}^{(0)}\}\Big) + \sum_{\gamma} \boldsymbol{\Phi}_\gamma^\top \boldsymbol{w}_\gamma + \frac{1}{2}\sum_{\gamma\gamma'} \boldsymbol{w}_\gamma^\top \underline{\Phi_{\gamma\gamma'}}\, \boldsymbol{w}_{\gamma'} + \ldots \tag{3.1a}$$

reveals dynamic features of the underlying system. Cutting off third- or higher-order terms, which is acceptable whenever the displacements are small enough, is known as the *harmonic approximation*, and shall be adhered to henceforth. Within equation (3.1a), the ith component

---

[1] This means small relative to the distances between the ions [7].

of the vector

$$\varPhi_{\gamma,i} := \left.\frac{\partial E_{\text{BO}}}{\partial \tau_{\gamma,i}}\right|_{\boldsymbol{w}_\gamma=\boldsymbol{0}} =: -F^{(1)}_{\gamma,i} \tag{3.1b}$$

represents minus the ith coordinate of the first-order *interatomic force* $F^{(1)}_{\gamma,i}$. This force acts on atom γ in a direction given by the cartesian unit vector $\hat{\boldsymbol{e}}_i$, and results from the effective BO energy in the case of a displacement given by the vector components $w_{\gamma,i}$. Since the equilibrium configuration of the ions ($\{\boldsymbol{w}\} = \boldsymbol{0}$) minimizes the effective BO energy in equation (3.1a), its first derivative with respect to each $\boldsymbol{\tau}_\gamma$ is zero, and so is every force[2] $F^{(1)}_{\gamma,i}$ in this case. In contrast

$$\left[\underline{\varPhi_{\gamma\gamma'}}\right]_{ij} := \left.\frac{\partial^2 E_{\text{BO}}}{\partial \tau_{\gamma,i}\,\partial \tau_{\gamma',j}}\right|_{\boldsymbol{w}_\gamma=\boldsymbol{w}_{\gamma'}=\boldsymbol{0}} \tag{3.1c}$$

does not vanish in general in this context and is named the *harmonic force-constant matrix*. One can use it, to harmonic order, to approximate the force in direction i on an ion γ, which is held fixed, provided an ion γ' is displaced by $w_{\gamma',j}$ in direction j

$$F^{(2)}_{\gamma,i} = -\sum_{\gamma',j}\left[\underline{\varPhi_{\gamma\gamma'}}\right]_{ij} w_{\gamma',j}\,. \tag{3.2}$$

With equation (3.2), the analogy of the harmonic force-constant matrix to a spring constant (Hooke's law) becomes obvious. [23]

Sum rules

Furthermore, if every atom is displaced by the same amount $\boldsymbol{w}_{\text{const}}$ in the same direction, i.e., $\boldsymbol{w}_{\gamma'} = \boldsymbol{w}_{\text{const}}$, the whole crystal will be shifted without varying interatomic distances. Therefore, the ions will remain in their equilibrium configuration causing the BO energy to be minimal, which can only be fulfilled for

$$\sum_\gamma \boldsymbol{\varPhi}_\gamma = \boldsymbol{0} \quad \wedge \quad \sum_{\gamma\gamma'} \underline{\varPhi_{\gamma\gamma'}} = \underline{0_\gamma} \tag{3.3a}$$

in harmonic order. By making the same argument for equation (3.2),

$$\sum_{\gamma'} \underline{\varPhi_{\gamma\gamma'}} = \underline{0_\gamma} \tag{3.3b}$$

follows. [7]

Harmonic dynamics

In order to cast light on the dynamics of the ions, in the sense of classical mechanics, the force in equation (3.2) is inserted into the second fundamental law of Newton

$$M_\gamma \frac{\partial^2 w_{\gamma,i}(t)}{\partial t^2} = F^{(2)}_{\gamma,i}(t) = -\sum_{\gamma',j}\left[\underline{\varPhi_{\gamma\gamma'}}\right]_{ij} w_{\gamma' j}(t)\,. \tag{3.4}$$

In this expression, M_γ is the mass of an nucleus γ, vibrating periodically in time around its equilibrium position with the amplitude $\left|\boldsymbol{w}_{\gamma'}\right|$. Given a crystal with a periodic lattice

---

[2] This circumstance forms the basis of algorithms for relaxing material structures, using forces based on DFT calculations [3]. The challenges presented by actual numerical calculations, especially when choosing the FLAPW method, are the subject of section 5.10, section 5.11, and section 5.12.

structure fulfilling translational symmetry, the Bloch theorem [20] can be exploited in order to circumvent dealing with an infinite set of coupled differential equations in equation (3.4). As a consequence, the displacements $\boldsymbol{w}_{\gamma_{\boldsymbol{R}}}$ of every atom γ, which now is located in and attributed to a unit cell addressed by $\boldsymbol{R}$, fall into categories labeled by the vector $\boldsymbol{q}$

$$\boldsymbol{w}^{\boldsymbol{q}}_{\gamma_{\boldsymbol{R}}}(t) = \boldsymbol{Q}_{\gamma_{\boldsymbol{R}}}(\boldsymbol{q}, t)\mathrm{e}^{\mathrm{i}\boldsymbol{q}\cdot\boldsymbol{R}} + \boldsymbol{Q}^{*}_{\gamma_{\boldsymbol{R}}}(\boldsymbol{q}, t)\mathrm{e}^{-\mathrm{i}\boldsymbol{q}\cdot\boldsymbol{R}} \tag{3.5a}$$

$$=: \boldsymbol{w}^{\boldsymbol{q}^{+}}_{\gamma_{\boldsymbol{R}}}(t) + \boldsymbol{w}^{\boldsymbol{q}^{-}}_{\gamma_{\boldsymbol{R}}}(t)\ , \tag{3.5b}$$

Modes

decoupling the infinitely large set of differential equations (3.4) into $3N_{\gamma_{\boldsymbol{R}}}$ equations of independent one-dimensional (harmonic) oscillators ($N_{\gamma_{\boldsymbol{R}}}$ is the number of atoms attributed to the unit cell $\boldsymbol{R}$) [3, 88]. Therefore, the ansatz [8] is made that the *polarization vector*

$$\boldsymbol{Q}_{\gamma_{\boldsymbol{R}}}(\boldsymbol{q}, t) = \frac{1}{\sqrt{M_\gamma}}\boldsymbol{Q}_{\gamma_{\boldsymbol{R}}}(\boldsymbol{q})\mathrm{e}^{\mathrm{i}\omega_\iota(\boldsymbol{q})t} \tag{3.6a}$$

$$\Leftrightarrow Q_\iota(\boldsymbol{q}, t) = \frac{1}{\sqrt{M_\gamma}}Q_\iota(\boldsymbol{q})\mathrm{e}^{\mathrm{i}\omega_\iota(\boldsymbol{q})t} \tag{3.6b}$$

Dynamical matrix

is periodic in time with $\iota \in [1, 3N]$ indexing the *branches* or *modes*, which are called *longitudinal* for $\boldsymbol{q} \parallel \boldsymbol{Q}_{\gamma_{\boldsymbol{R}}}(\boldsymbol{q})$ and *transversal* given $\boldsymbol{q} \perp \boldsymbol{Q}_{\gamma_{\boldsymbol{R}}}(\boldsymbol{q})$. This completes the picture of a wave with wave vector $\boldsymbol{q}$ propagating through the lattice and fulfills the eigenvalue equation

$$\underline{D_{\gamma\gamma'}}(\boldsymbol{q})\boldsymbol{Q}_{\gamma'}(\boldsymbol{q}) = \omega_\iota^2(\boldsymbol{q})\boldsymbol{Q}_\gamma(\boldsymbol{q})\ , \tag{3.7a}$$

or after replacing the atom index and displacement direction by the branch index

$$\underline{D}(\boldsymbol{q})\boldsymbol{Q}_\iota(\boldsymbol{q}) = \omega_\iota^2(\boldsymbol{q})\boldsymbol{Q}_\iota(\boldsymbol{q})\ , \tag{3.7b}$$

for the *dynamical matrix*

$$\left[\underline{D_{\gamma\gamma'}(\boldsymbol{q})}\right]_{ij} =: \frac{1}{\sqrt{M_\gamma M_{\gamma'}}}\sum_{\boldsymbol{R}'}\left[\underline{\mathit{\Phi}_{\gamma_{\boldsymbol{0}}\gamma'_{\boldsymbol{R}'}}}\right]_{ij}\mathrm{e}^{\mathrm{i}\boldsymbol{q}\boldsymbol{R}'}\ . \tag{3.8a}$$

In the previous definition the periodicity of the lattice has been used ($\boldsymbol{R} = \boldsymbol{0}$ and $\boldsymbol{R}' - \boldsymbol{R} = \boldsymbol{R}'$). Inserting equation (3.1c) yields

$$\left[\underline{D_{\gamma\gamma'}(\boldsymbol{q})}\right]_{ij} =: \frac{1}{\sqrt{M_\kappa M_{\kappa'}}}\sum_{\boldsymbol{R}'}\left.\frac{\partial^2 E_{\mathrm{BO}}}{\partial\tau_{\gamma_{\boldsymbol{0}},i}\,\partial\tau_{\gamma'_{\boldsymbol{R}'},j}}\right|_{\boldsymbol{w}_{\gamma_{\boldsymbol{0}}}=\boldsymbol{w}_{\gamma'_{\boldsymbol{R}'}}=\boldsymbol{0}}\mathrm{e}^{\mathrm{i}\boldsymbol{q}\boldsymbol{R}'}\ . \tag{3.8b}$$

Dispersion relation

Equations (3.7) result from inserting the first term of equation (3.5a) with either equation (3.6a) or equation (3.6b) into equation (3.4) (inserting the second term of equation (3.5a) in the aforementioned way, results in the complex conjugate of equations (3.7)). Equations (3.7) mirror the polarization vectors to be the eigenvectors or normal vectors of the dynamical matrix (3.8). As a consequence, the modes ι are also called *normal modes*. Furthermore, equations (3.7) define the *dispersion relations* $\omega_\iota(\boldsymbol{q})$ to be the eigenvalues of the $3N \times 3N$ dynamical matrix. In polyatomic systems, i.e., the unit cell contains more than one atom, the normal modes subdivide into 3 acoustic[3] and $3N-3$ optical[4] modes, whereas only 3 acoustic branches emerge for systems with only one atom per unit cell (monoatomic). Moreover, the Hermitian character of the dynamical matrix ensures real squares of frequencies as eigenvalues. Usually, the latter are positive. Negative squares of frequencies result in imaginary dispersion relations, indicating instabilities in the underlying structure. The Time Reversal Symmetry (TRS) holds for the dynamical matrix, hence also for the polarizations and dispersion relations. Thereby, the latter fulfill $\omega_\iota(-\boldsymbol{q}) = \omega_\iota^*(\boldsymbol{q})$ (for stable structures $\omega_\iota^*(\boldsymbol{q}) = \omega_\iota(\boldsymbol{q})$ holds in addition due to real frequencies). [7]

Quantum-mechanical description

When discussing displacements and momenta in atomic orders of magnitude, quantum mechanical effects come into play, governed by the fundamental commutator

$$\left[\boldsymbol{w}_{\gamma_{\boldsymbol{R}},i}, M_{\gamma'_{\boldsymbol{R}'}} \frac{\partial \boldsymbol{w}_{\gamma'_{\boldsymbol{R}'},j}}{\partial t} \right] = \mathrm{i}\hbar\delta_{ij}\delta_{\gamma_{\boldsymbol{R}}\gamma'_{\boldsymbol{R}'}} . \tag{3.9}$$

Introducing the second quantization, as the Coulomb interaction underlies the exchange of quantized photons, the quantized lattice vibrations are integrated into a quasiparticle concept of quantum field theory [4]. They satisfy the Bose–Einstein statistics, and are named *phonons* for which bosonic ladder operators are defined. These operators enable creation or annihilation of a phonon quasiparticle, i.e., in the wave picture to add quanta to or subtract quanta from the quantized amplitude of the lattice vibration. However, the frequencies remain equivalent compared to classical mechanics and define the energy of a phonon quasiparticle as $\hbar\omega_\iota(\boldsymbol{q})$ [8]. Against the background of ab-initio DFT calculations, quantum-mechanical effects are inherent in the xc energy and xc potential (cf. chapter 2). [5]

Goldstone modes

The acoustic normal modes of phonons with a wave vector $\boldsymbol{q} = \boldsymbol{0}$ are named *Goldstone modes* [158, 159], denoting the phonons to be in the limit of an infinite wavelength [4, 160]. This is consistent with the whole crystal shifted without a change of interatomic distances, as already stated above in the current section [4, 160]. It entails the dynamical matrix at the Γ-point to be zero and to possess vanishing eigenvalues[5] [4, 160]. Consistently for $\boldsymbol{q} = \boldsymbol{0}$, the sum rule in equation (3.3b) can only be fulfilled for the dynamical matrix (3.8), provided its diagonal features vanishing entries [8]. Moreover, close to the Γ-point, acoustic modes show a linear behavior, while optical modes usually tend to a constant value there [5]. The textbook of Grosso and Parravicini [8] offers an overview of typical dispersion relations for some important material classes.

3.2 Direct Ab-Initio Approach to Phonon Physics

Principle

Basically, all *direct methods* to calculate the phonon dispersion or the dynamical matrix, respectively, use changes of quantities obtained by standard DFT calculations with a displaced or the equilibrium configuration of the ions. Keeping the ions fixed to determine the total

---

[3] These modes are responsible for the transport of sound in a medium [4]. For long wavelengths, the speed of sound is the proportionality constant between the dispersion and the wave-vector $\boldsymbol{q}$ [4].

[4] Optical branches couple with electric fields, which can be understood from the optical mode of a diatomic-chain model with the first and second atom having charges and amplitudes with opposite sign, effectively forming a dipole [4, 8].

[5] This can also be derived from the sum rule in equation (3.3b) (see reference [8]).

energy is why such algorithms are also known as *frozen phonon* methods [3]. Throughout the last decades, many papers have been published, presenting dispersion relations from ab-initio based direct-methods. A good overview can, for example, be found in the paper of Fritsch and Schröder [153]. [23]

Pioneering approaches

One of the early works by Yin and Cohen [161] presents phonon frequencies at the Γ- and X-points for which the normal modes, mirroring the respective displaced ion configuration, have been determined by group theoretical considerations based on the underlying symmetry. Given known normal modes, the related frequencies can be extracted from equations (3.7). Another approach [162, 163] is to extract frequencies from curvatures of calculated total energies as a function of displacement [3]. However, an educated guess cannot always be made in advance. In general, the normal modes result from a diagonalization of the dynamical matrix. [23]

Finite Displacement method

In the Finite Displacement (FD) method [72–75] an improvement is made by using equation (3.2), one requires only the force on one atom while displacing another atom and no longer the normal modes [3]. According to the intrinsic symmetry of the examined system, a set of displacements is chosen to determine the whole force-constant matrix via difference quotients (3.1c) (each of these displacements determines one row of this matrix) [3]. That means without symmetry optimizations and for a unit cell of N atoms, one needs $3N$ independent self-consistency calculations that can completely independently be executed in parallel. Each of these calculations scales proportional to N^3 regarding the computational time. The displacement contains one free parameter which is the amplitude of the displacement. Depending on the amplitude, one remains in the harmonic regime or is already in the anharmonic one. This can be tested as a function of the amplitude or in comparison with the DFPT results, which we derive explicitly and discuss later. After a Fourier transform of the force-constant matrix into the dynamical matrix (see equations (3.8)), the frequencies and all normal modes can be determined by its diagonalization [88]. Ideally, the force calculation is based on the Hellmann–Feynman theorem, which shall be introduced in section 4.1.1. In practice, one needs corrections terms to the Hellmann–Feynman force, whose computational effort is in general much larger than the Hellmann–Feynman forces themselves. Also, more accurate methods such as the FLAPW approach entail a more sophisticated calculation of the forces (see section 5.12). [23]

Advantages

On the one hand, the actual theoretical concept and the effort of implementation to obtain phonon dispersions from direct ab-initio methods are easier than perturbative techniques such as DFPT (apart from the aforementioned challenges concerning accurate forces) [3]. This especially holds true for third- or higher-order derivatives of the BO energy in equation (3.1a). [23]

Disadvantages

On the other hand, when compiling the complete dynamical matrix, it is essential to include one complete phonon wave period into the DFT calculations beyond the Goldstone modes. So for instance for the wave-vector $(0, 0.25, 0.5)^\top$, without loss of generality, one period expands through one unit cell in the x-direction, four unit cells in the y-direction, and two unit cells in the z-direction, which increases the time to self-consistency by a factor 512 compared to the $\boldsymbol{q} = \mathbf{0}$-modes. Such a phonon is called commensurate to a $1 \times 4 \times 2$ supercell and this scenario is illustrated in figure 3.1. It becomes obvious that the computational effort to calculate certain wave-vectors (for example with small coordinates) immensely grows or can even exceed available computer resources. The prerequisite of phonons being commensurate

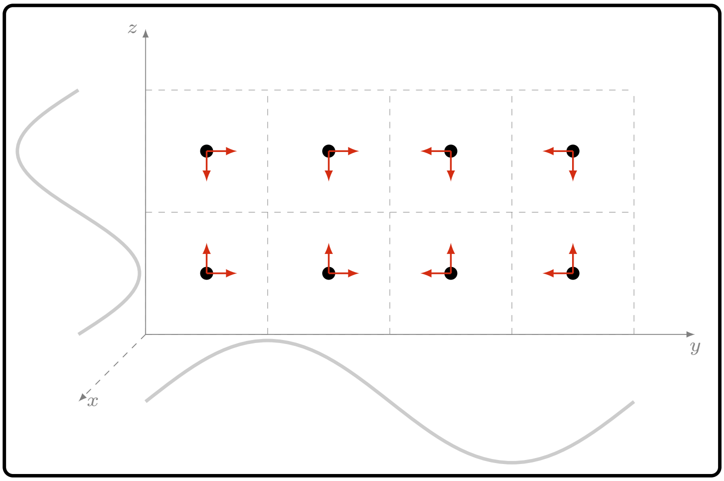

Figure 3.1: For a phonon wave vector $\boldsymbol{q} = (0, 0.25, 0.5)^\top 2\pi/a_{\text{lat}}$ with lattice constant a_{lat}, a commensurate supercell of one unit cell in the x-direction, four unit cells in the y-direction, and two unit cells in the z-direction is required to enclose the complete period of the related phonon modes (based on reference [88, figure 5.1]). The periods in the y- and z-directions are illustrated by the grayish sine waves. The red arrows indicate the directions of the infinitesimal displacements from the equilibrium position.

with the supercell setup restricts the application of this method to phonon wave-vectors, the components of which must be rational numbers. A further problem of a large supercell consists in the fact that the number of $\boldsymbol{k}$-sampling points must be inversely proportional to the size of the supercell to ensure comparable $\boldsymbol{k}$-sets for different phonon vectors $\boldsymbol{q}$. Finally, a problem occurs at some point when the effective range of lattice interactions becomes smaller than the size of the supercell [23]. Today, the FD approach is applied by many first-principles programs and sophisticated tools have been developed to suggest an irreducible set of displacement patterns in conjunction with the crystal symmetry of the lattice. Well-known is the `phonopy` tool [164], which we base on the first-principle implementation `FLEUR` [69] in order to generate benchmark data that is contrasted with my results in section 7.7. [87, 88]

Chapter 4

Density-Functional Perturbation Theory

4.1 Response Functions and Total Energy Derivatives 28
4.2 Development of Density-Functional Perturbation Theory 33
4.3 Viable Types of Perturbations 37

Motivation

DFT has established itself as a reliable and effective method, in particular to determine the ground-state charge density and the ground-state total energy of the interacting many-particle problem for various systems (see chapter 2). Consequently, it appears worthwhile to place a method for investigating responses of the many-body system to perturbations on a similar footing. But at first glance, dealing with perturbations might *not* connote seeking inspiration in a framework for electronic ground-state quantities. Nevertheless a perturbation which has a strength so small as to leave the electronic system almost in its ground state, suggests basing the method, which analyzes many-body system responses to such a perturbation, on the convincing Density-Functional Theory. Hence, it seems reasonable to name it Density-Functional Perturbation Theory (DFPT). [22]

Origin

DFPT is usually[1] attributed to Baroni, Giannozzi, and Testa [80], who utilize Green functions in their method [68], an alternative but equal formulation [3] is given by Gonze et al. [81–85]. So DFPT can either be derived in the former way by applying Rayleigh–Schrödinger perturbation theory to a perturbed Kohn–Sham Hamiltonian, while the perturbation is normally expressed by the external potential (this approach guides the discussion in this chapter). Alternatively, it is deducible in the latter manner by applying a variational ansatz[2] to the total energy, which is expanded to a respective order (involving the Euler–Lagrange equations) [68]. [22]

Purpose and success story

Thus, DFPT integrates organically into DFT and delivers any order of total energy derivatives with respect to characteristic perturbation parameters (cf. the methods in section 3.2 resorting to difference quotients or accurate forces). Both pure derivatives and mixed derivatives are feasible [3]. Nowadays, numerous papers report on the good agreement of

---

[1] Even before, there has been a publication of DFPT by Zein [76] in the Soviet Union [87].

[2] One historically important application of the variational ansatz already took place in 1930 when Hylleraas [165] calculated the two-electron problem [3].

DFPT calculations with experimental data, and evince a broad spectrum of different calculated response quantities as well as materials [3, 87]. This substantiates the significance and efficiency of DFPT [23]. Among others, one reason for the success of DFPT is that total energy variations are usually easier to calculate than the total energy itself [3]. A comprehensive overview is given by the review papers of Baroni et al. [87] as well as Gonze, Rignanese, and Caracas [92]. Moreover, a list of established DFPT implementations is already given in chapter 1. [22]

Outline

Section 4.1 is concerned with summarizing central aspects of Rayleigh–Schrödinger perturbation theory and response functions, especially regarding linear response. Furthermore, it presents a second-order derivative of the total energy with respect to a general perturbation parameter, as well as a fundamental connection between the order of response quantities and the order of total energy derivatives. This sets the stage for section 4.2. Confined to insulators, an introduction to the main concepts of DFPT is combined there with a comparison to an alternative response method, building upon the dielectric matrix. Throughout this section, technical implementation details are not given. Finally, section 4.3 illustrates the versatility of DFPT by addressing various perturbations it can be applied to. Due to its formulation, DFPT constitutes a highly efficient and powerful method to calculate phonon quantities, in particular, compared to the methods discussed in section 3.2. At this point however, it must be underlined that phonon response is separately addressed in chapter 6 and chapter 7. Therefore, it is not the main focus of the current chapter.

4.1 Response Functions and Total Energy Derivatives

Motivation

Various exciting phenomena we experience when carrying out experiments can be interpreted as a reaction or response to an applied perturbation. This perturbation might be a mechanical stimulus, or the application of electric or magnetic fields, to name but a few. From another perspective, the design of high-tech materials incorporates the selection of samples whose response fits best to the desired response properties. In physics, understanding a new system by perturbing it and examining its response is actually rather intuitive and quantified by so-called response functions. Focusing on condensed matter systems, it turns out that many of these response functions are connected to first- or higher-order derivatives of the ground-state total energy with respect to one or more perturbations. To list a few: with first-order derivatives one can examine dipole moments [166] or forces; research on phonon dynamical matrices, piezoelectricity and elastic constants can be carried out from second-order derivatives; third-order derivatives are related to phonon–phonon interaction [167], Grüneisen parameters and anharmonic force constants (see also Baroni et al. [87] and references therein). The extent to which the respective orders of total energy derivatives are relevant correlates both with the intensity or amplitude of the perturbations (categorizing them as first, second or higher order[3]) and with the phenomenon intended to be explored (e.g. thermal expansion [168]). [22]

Outline

Section 4.1.1 contains the essentials of Rayleigh–Schrödinger perturbation theory, which are required hereinafter. In this context, parallels to the Hellmann–Feynman theorem [169, 170] are drawn, the orthogonality relations between wave-function variations are discussed, and the connections to the total energy derivatives with respect to an arbitrary parameter are

---

[3] It is also common to subdivide into linear, harmonic, and anharmonic effects.

established. The discussion of further aspects, that can result from the introduction of basis sets, is postponed to section 5.10, section 5.11, and section 5.12 as well as chapter 6 and chapter 7. Section 4.1.2 presents the second-order derivative of the total energy with respect to a general perturbation parameter, motivating the calculation of the first-order charge-density variation. In fact, *only* the first order of the charge-density variation is required for the third-order total energy variation. This is a direct consequence of the fundamental $2n+1$ theorem which shall be elucidated, but not proven, in section 4.1.3.

4.1.1 Perturbation Theory and Hellmann–Feynman Theorem

Literature

The basics of perturbation theory can be found within every standard quantum mechanics textbook. Nonetheless, e.g. Verstraete and Zanolli [22] have published a comprehensive discussion of this topic in the context of DFPT, which is referred to within this subsection unless cited differently.

Rayleigh–Schrödinger perturbation theory

Perturbation theory postulates that the perturbation, whose strength is expressed by a parameter λ, is small enough for an arbitrary perturbed quantity $g(\lambda)$ to be expandable in a rapidly enough converging Taylor series

$$g(\lambda) = \sum_{\mathfrak{o}=0}^{\infty} \lambda^{\mathfrak{o}} g^{(\mathfrak{o})}(\lambda) \,, \tag{4.1a}$$

in which

$$g^{(\mathfrak{o})}(\lambda) = \frac{1}{\mathfrak{o}!} \left. \frac{\mathrm{d}^{\mathfrak{o}} g(\lambda)}{\mathrm{d}\lambda^{\mathfrak{o}}} \right|_{\lambda=0} \tag{4.1b}$$

and $\mathfrak{o}$ indicates the order of perturbation. Perturbations (considered static in the following) are usually applied to an unperturbed system with diagonalized Hamiltonian $\mathscr{H}^{(0)}$ and orthonormal eigenfunctions. Formally, perturbations are described by an external potential as a function of a perturbation strength λ, so that the Hamiltonian of the perturbed system reads

$$\mathscr{H}(\lambda) = \mathscr{H}^{(0)} + \mathscr{V}_{\text{ext}}(\lambda) \,. \tag{4.2}$$

This Hamiltonian satisfies the Schrödinger equation

$$\Big(\mathscr{H}(\lambda) - \epsilon_{\mathfrak{p}}(\lambda)\Big)\Big|\mathit{\Psi}_{\mathfrak{p}}(\lambda)\Big\rangle = 0 \,, \tag{4.3a}$$

where $\mathfrak{p}$ enumerates the perturbed but unknown eigenfunctions $\Big|\mathit{\Psi}_{\mathfrak{p}}(\lambda)\Big\rangle$ and eigenenergies $\epsilon_{\mathfrak{p}}(\lambda)$. Expanding all functions of λ according to equations (4.1) yields

$$\left(\sum_{\mathfrak{o}''=0}^{\infty} \lambda^{\mathfrak{o}''} \mathscr{H}^{(\mathfrak{o}'')}(\lambda) - \sum_{\mathfrak{o}''=0}^{\infty} \lambda^{\mathfrak{o}''} \epsilon_{\mathfrak{p}}^{(\mathfrak{o}'')}(\lambda) \right) \sum_{\mathfrak{o}'''=0}^{\infty} \lambda^{\mathfrak{o}'''} \left| \mathit{\Psi}_{\mathfrak{p}}^{(\mathfrak{o}''')}(\lambda) \right\rangle = 0 \,, \tag{4.3b}$$

or reordered according to the orders of perturbation indicated by $\mathfrak{o}$

$$\sum_{\mathfrak{o}=0}^{\infty} \lambda^{\mathfrak{o}} \left(\sum_{\mathfrak{o}'=0}^{\mathfrak{o}} \left(\mathscr{H}^{(\mathfrak{o}')} - \epsilon_{\mathfrak{p}}^{(\mathfrak{o}')} \right) \left| \mathit{\Psi}_{\mathfrak{p}}^{(\mathfrak{o}-\mathfrak{o}')} \right\rangle \right) = 0 \,. \tag{4.3c}$$

Sternheimer equation

The zeroth order ($\mathfrak{o} = 0$) of this expression is trivially fulfilled. For the linear response theory, focusing on the first order $\mathfrak{o} = 1$ of the Schrödinger equation is sufficient and results in

$$\left(\mathscr{H}^{(0)} - \epsilon_{\mathfrak{p}}^{(0)}\right)\left|\Psi_{\mathfrak{p}}^{(1)}\right\rangle = -\left(\mathscr{H}^{(1)} - \epsilon_{\mathfrak{p}}^{(1)}\right)\left|\Psi_{\mathfrak{p}}^{(0)}\right\rangle . \tag{4.4}$$

Equation (4.4) is called the Sternheimer equation according to Sternheimer [171], who published it first in the context of ion polarizabilities. If one desires to determine the first-order variation of the wave function, the Sternheimer equation can be rewritten to exclude singularities (see reference [22]). Projecting equation (4.4) onto a normalized unperturbed eigenfunction $\Psi_{\mathfrak{p}}^{(0)}$ lets the left-hand side of the Sternheimer equation vanish if the self-adjoint Hamiltonian $\mathscr{H}^{(0)}$ acts on the left and results in the relation for the first-order eigenenergy change

$$\epsilon_{\mathfrak{p}}^{(1)} = \left\langle \Psi_{\mathfrak{p}}^{(0)} \middle| \mathscr{H}^{(1)} \middle| \Psi_{\mathfrak{p}}^{(0)} \right\rangle_{\Omega} . \tag{4.5}$$

Hellmann–Feynman theorem

The variable Ω indicates the volume of the perturbed system. Exploiting equation (4.1b) in (4.5) reveals the consistency with the Hellmann–Feynman theorem [169, 170] given normalized eigenfunctions $\Psi_{\mathfrak{p}}^{(0)}$ of eigenvalue $\epsilon_{\mathfrak{p}}$ for a Hamiltonian $\mathscr{H}$

$$\frac{\mathrm{d}\epsilon_{\mathfrak{p}}(\lambda)}{\mathrm{d}\lambda} = \int_{\Omega} \Psi_{\mathfrak{p}}^{(0)*}(\boldsymbol{r}) \frac{\mathrm{d}\mathscr{H}(\lambda)}{\mathrm{d}\lambda} \Psi_{\mathfrak{p}}^{(0)}(\boldsymbol{r})\, \mathrm{d}^3 r = \left\langle \Psi_{\mathfrak{p}}^{(0)} \middle| \frac{\mathrm{d}\mathscr{H}(\lambda)}{\mathrm{d}\lambda} \middle| \Psi_{\mathfrak{p}}^{(0)} \right\rangle_{\Omega} \tag{4.6a}$$

$$= \left\langle \Psi_{\mathfrak{p}}^{(0)} \middle| \frac{\mathrm{d}\mathscr{V}(\lambda)}{\mathrm{d}\lambda} \middle| \Psi_{\mathfrak{p}}^{(0)} \right\rangle_{\Omega} . \tag{4.6b}$$

The equivalence of equations (4.6a) and (4.6b) holds if $\mathscr{H}(\lambda) = \mathscr{T} + \mathscr{V}(\lambda)$ can be subdivided into a kinetic energy operator $\mathscr{T}$ and a potential operator $\mathscr{V}(\lambda)$. A simple proof of the Hellmann–Feynman theorem [170] uses the product rule, the orthonormality of the eigenfunctions and the self-adjointness of the Hamiltonian operator. The Hamiltonian operator is not self-adjoint in general, especially if the basis is section-wise defined [88], which is often the case in numerical calculations. Similar to the first-order eigenenergies (4.5), for the second-order eigenenergies, the second-order terms in (4.3c) are extracted and projected onto $\Psi_{\mathfrak{p}}^{(0)}$ leading to

$$\epsilon_{\mathfrak{p}}^{(2)} = \left\langle \Psi_{\mathfrak{p}}^{(0)} \middle| \mathscr{H}^{(2)} \middle| \Psi_{\mathfrak{p}}^{(0)} \right\rangle_{\Omega} + \left\langle \Psi_{\mathfrak{p}}^{(0)} \middle| \mathscr{H}^{(1)} - \epsilon_{\mathfrak{p}}^{(1)} \middle| \Psi_{\mathfrak{p}}^{(1)} \right\rangle_{\Omega} . \tag{4.7}$$

This equation displays that the second-order eigenenergy is only dependent on the first-order (variation) and the zeroth-order wave functions, which is the result of the fundamental $2n+1$-theorem discussed in section 4.1.3.

First-order wave function

In order to evaluate this first-order wave function correction, it is expanded[4] using the orthonormal and complete basis[5] of the unperturbed wave function

$$\left|\Psi_{\mathfrak{p}}^{(1)}\right\rangle = \sum_{\mathfrak{p}'} c_{\mathfrak{p}\mathfrak{p}'}^{(1)} \left|\Psi_{\mathfrak{p}'}^{(0)}\right\rangle . \tag{4.8a}$$

---

[4] Apart from this variational ansatz, some scenarios allow for formulating differential equations that deliver the pointwise first-order wave-function correction.

[5] This is possible because the first-order wave function lies completely within the Hilbert space spanned by the unperturbed wave functions. However, chapter 6 addresses an example where the first-order wave function cannot be described by the Hilbert space of the unperturbed wave functions anymore. [88]

The coefficients $c^{(1)}_{\mathfrak{p}\mathfrak{p}'}$ which satisfy $\mathfrak{p} = \mathfrak{p}'$ are zero and subsequently discussed to the case $\mathfrak{p} \neq \mathfrak{p}'$. Putting equation (4.8a) into the Sternheimer equation (4.4), enables one to evaluate the action of the Hamiltonian and delivers

$$\sum_{\mathfrak{p}'|\mathfrak{p}'\in \mathrm{P}^{\perp}} \left(\epsilon^{(0)}_{\mathfrak{p}'} - \epsilon^{(0)}_{\mathfrak{p}}\right) c^{(1)}_{\mathfrak{p}\mathfrak{p}'} \left|\Psi^{(0)}_{\mathfrak{p}'}\right\rangle = -\left(\mathscr{H}^{(1)} - \epsilon^{(1)}_{\mathfrak{p}}\right)\left|\Psi^{(0)}_{\mathfrak{p}}\right\rangle . \tag{4.8b}$$

In this equation, $\mathrm{P}^{\perp}$ is the subspace of all occupied and unoccupied states orthogonal to the set of wave functions belonging to the eigenvalue $\epsilon_{\mathfrak{p}}$. Hence excluding the complementary subspace P, prevents the difference of energies on the left-hand side from becoming zero. Inserting a completeness relation on both sides results in

$$\left|\Psi^{(1)}_{\mathfrak{p}}\right\rangle = \sum_{\mathfrak{p}'|\mathfrak{p}'\in \mathrm{P}^{\perp}} \left|\Psi^{(0)}_{\mathfrak{p}'}\right\rangle \frac{\left\langle \Psi^{(0)}_{\mathfrak{p}'} \middle| \mathscr{H}^{(1)} \middle| \Psi^{(0)}_{\mathfrak{p}} \right\rangle_{\Omega}}{\epsilon^{(0)}_{\mathfrak{p}} - \epsilon^{(0)}_{\mathfrak{p}'}} , \tag{4.8c}$$

General-order orthogonality

the well-known relation for the first-order perturbation of the wave function from Rayleigh–Schrödinger perturbation theory. The wave functions as part of the Schrödinger equation for the perturbed system (4.3a) are demanded to fulfill

$$\left\langle \Psi_{\mathfrak{p}}(\lambda) \middle| \Psi_{\mathfrak{p}}(\lambda) \right\rangle_{\Omega} = 1 . \tag{4.9a}$$

Using equations (4.1) and subtracting

$$\left\langle \Psi^{(0)}_{\mathfrak{p}}(0) \middle| \Psi^{(0)}_{\mathfrak{p}}(0) \right\rangle_{\Omega} = 1 \tag{4.9b}$$

yields the orthogonality of the wave-function variations to any order $\mathfrak{o} > 0$ of the perturbation parameter λ

$$\sum_{\mathfrak{o}'=0}^{\mathfrak{o}} \left\langle \Psi^{(\mathfrak{o}')}_{\mathfrak{p}}(\lambda) \middle| \Psi^{(\mathfrak{o}-\mathfrak{o}')}_{\mathfrak{p}}(\lambda) \right\rangle_{\Omega} = 0 . \tag{4.9c}$$

Due to the gauge freedom of the wave function phase, $\mathrm{Im}\, c_{\mathfrak{p}\mathfrak{p}} = 0$ holds so that equation (4.8c) remains valid. The variable Ω for the volume is suppressed in the following sections of this chapter.

4.1.2 General Second-Order Derivative of the Total Energy

Literature

The total energy (2.1) shall now be differentiated twice with respect to general perturbation parameters. A more detailed discussion can be found in the lecture notes of Heid [23], which section 4.1.2 adheres to.

Generalization

First, the external potential (4.2) is further generalized, so that it is a function of a set of $\mathfrak{b}$ adiabatic perturbation parameters $\mathbb{L} = \left\{\lambda_b : b \in [1, \mathfrak{b}]\right\}$. Such an external potential $V^{\mathbb{L}}_{\text{ext}}(\boldsymbol{r})$ leads to a ground-state density $\rho^{\mathbb{L}}_{\text{gs}}(\boldsymbol{r})$, minimizing a total energy

$$E^{\mathbb{L}}_{\text{tot}} = F\left[\rho^{\mathbb{L}}_{\text{gs}}\right] + \int \rho^{\mathbb{L}}_{\text{gs}}(\boldsymbol{r}) V^{\mathbb{L}}_{\text{ext}}(\boldsymbol{r})\, \mathrm{d}^3 r + E^{\mathbb{L}}_{\text{ii}} , \tag{4.10}$$

which incorporates the universal functional $F\left[\rho^{\mathbb{L}}_{\text{gs}}\right]$ and the ion–ion interaction $E^{\mathbb{L}}_{\text{ii}}$. In equation (4.10) the perturbation comes into play directly through the external potential and implicitly through the ground-state density from the self-consistent DFT calculation. Differentiating with respect to a perturbation parameter λ_b ($b \in \mathbb{L}$) therefore results in

First-order derivative

$$\frac{\partial E^{\mathbb{L}}_{\text{tot}}}{\partial\lambda_b} = \underbrace{\int \frac{\delta E^{\mathbb{L}}_{\text{tot}}}{\delta\rho^{\mathbb{L}}_{\text{gs}}(\boldsymbol{r})}\frac{\partial\rho^{\mathbb{L}}_{\text{gs}}(\boldsymbol{r})}{\partial\lambda_b}\,\mathrm{d}^3r}_{=0} + \int \rho^{\mathbb{L}}_{\text{gs}}(\boldsymbol{r})\frac{\partial V^{\mathbb{L}}_{\text{ext}}(\boldsymbol{r})}{\partial\lambda_b}\,\mathrm{d}^3r + \frac{\partial E^{\mathbb{L}}_{\text{ii}}}{\partial\lambda_b}\,. \tag{4.11}$$

Second-order derivative

As $\rho^{\mathbb{L}}_{\text{gs}}(\boldsymbol{r})$ minimizes $E^{\mathbb{L}}_{\text{tot}}$, the first functional derivative vanishes so that equation (4.11) is consistent with the Hellmann–Feynman theorem (4.6). Differentiating again with respect to $\lambda_{b'}$ ($b' \in \mathbb{L}$) yields

$$\frac{\partial^2 E^{\mathbb{L}}_{\text{tot}}}{\partial\lambda_{b'}\partial\lambda_b} = \int \rho^{\mathbb{L}}_{\text{gs}}(\boldsymbol{r})\frac{\partial^2 V^{\mathbb{L}}_{\text{ext}}(\boldsymbol{r})}{\partial\lambda_{b'}\partial\lambda_b}\,\mathrm{d}^3r + \int \frac{\partial\rho^{\mathbb{L}}_{\text{gs}}(\boldsymbol{r})}{\partial\lambda_{b'}}\frac{\partial V^{\mathbb{L}}_{\text{ext}}(\boldsymbol{r})}{\partial\lambda_b}\,\mathrm{d}^3r + \frac{\partial^2 E^{\mathbb{L}}_{\text{ii}}}{\partial\lambda_{b'}\,\partial\lambda_b} \tag{4.12a}$$

in which, by means of the chain rule, the second term can be symmetrized [79, 172]

$$= \int \rho^{\mathbb{L}}_{\text{gs}}(\boldsymbol{r})\frac{\partial^2 V^{\mathbb{L}}_{\text{ext}}(\boldsymbol{r})}{\partial\lambda_{b'}\partial\lambda_b}\,\mathrm{d}^3r + \int \frac{\partial V^{\mathbb{L}}_{\text{ext}}(\boldsymbol{r})}{\partial\lambda_{b'}}\int \underbrace{\frac{\delta\rho^{\mathbb{L}}_{\text{gs}}(\boldsymbol{r})}{\delta V^{\mathbb{L}}_{\text{ext}}(\boldsymbol{r}')}}_{\chi^{\mathbb{L}}_{\text{ext}}(\boldsymbol{r},\boldsymbol{r}')}\frac{\partial V^{\mathbb{L}}_{\text{ext}}(\boldsymbol{r})}{\partial\lambda_b}\,\mathrm{d}^3r'\,\mathrm{d}^3r + \frac{\partial^2 E^{\mathbb{L}}_{\text{ii}}}{\partial\lambda_{b'}\,\partial\lambda_b}\,, \tag{4.12b}$$

Susceptibility

revealing the susceptibility $\chi_{\text{ext}}(\boldsymbol{r},\boldsymbol{r}')$. From the definition [88]

$$=: \int \rho^{(0)\mathbb{L}}_{\text{gs}}(\boldsymbol{r})V^{(2)\mathbb{L}}_{\text{ext}}(\boldsymbol{r})\,\mathrm{d}^3r + \int V^{(1)\mathbb{L}}_{\text{ext}}(\boldsymbol{r})\rho^{(1)\mathbb{L}}(\boldsymbol{r})\,\mathrm{d}^3r + E^{(2)\mathbb{L}}_{\text{ii}}\,, \tag{4.12c}$$

the relation between this susceptibility and the first-order response of the charge density to an external field

$$\rho^{(1)\mathbb{L}}(\boldsymbol{r}) = \int \chi^{\mathbb{L}}_{\text{ext}}(\boldsymbol{r},\boldsymbol{r}')V^{(1)\mathbb{L}}_{\text{ext}}(\boldsymbol{r}')\,\mathrm{d}^3r' \tag{4.13a}$$

becomes obvious [172]. The experienced external field stems from the first-order variation of the external potential $V^{(1)\mathbb{L}}_{\text{ext}}$ with respect to the general perturbation parameters. Equation (4.12c) also includes the second-order variation of the external potential $V^{(2)\mathbb{L}}_{\text{ext}}(\boldsymbol{r})$ and the second-order variation of the ion–ion interaction $E^{(2)\mathbb{L}}_{\text{ii}}$. Moreover, the susceptibility $\chi^{\mathbb{L}}_{\text{ext}}(\boldsymbol{r},\boldsymbol{r}')$ must not be confused with the Kohn–Sham susceptibility $\chi_{\text{KS}}(\boldsymbol{r},\boldsymbol{r}')$ [3]. The latter relates to the former and allows for another expression of the first-order charge density variation, involving the dielectric matrix $\underline{\epsilon}^{-1}$ [3]. This discussion is delayed until section 4.2.1. Alternatively, it is feasible to express the first-order variation of the charge density as

Relevant definition of first-order density variation

$$\rho^{(1)\mathbb{L}}(\boldsymbol{r}) = \sum_{\mathfrak{p}} f^{(0)}_{\mathfrak{p}}\left[\mathit{\Psi}^{*(0)\mathbb{L}}_{\mathfrak{p}}(\boldsymbol{r})\mathit{\Psi}^{(1)\mathbb{L}}_{\mathfrak{p}}(\boldsymbol{r}) + \mathit{\Psi}^{*(1)\mathbb{L}}_{\mathfrak{p}}(\boldsymbol{r})\mathit{\Psi}^{(0)\mathbb{L}}_{\mathfrak{p}}(\boldsymbol{r})\right], \tag{4.13b}$$

by applying the product rule to the unperturbed density in equation (2.4), while $f^{(0)}_{\mathfrak{p}}$ indicates the occupation of the state $\mathfrak{p}$. The first-order variation of the wave functions and its complex conjugate can be obtained from perturbation theory (see equation (4.8c)).

Resume

All in all, equation (4.11) thus exhibits that the *first*-order derivative (variation) of the total ground-state energy is a functional of the *unperturbed* ground-state density. Moreover, equation (4.12) displays the *second-order* derivative (variation) of the total energy to be a functional of the *first*-order variation of the electronic density. Both observations underlie the fundamental $2n+1$ theorem outlined in the following.

4.1.3 $2n+1$ Theorem

The $2n+1$ theorem is an implication of the variational principle [22] ensuring that the wave functions from 0-th up to n-th order give access to quantities related to the $2n$-th and $(2n+1)$-th derivatives of the total energy with respect to one or more adiabatic perturbation parameters. Consequently, given e.g. the first derivative of the wave function, the third-order derivative of the total energy (including its related response functions) is also available, avoiding significant additional effort. A general proof will not be given here but can be found in reference [81] making use of the fact that the energy functional is variational with respect to the wave functions and their variations. [22, 23]

4.2 Development of Density-Functional Perturbation Theory

Outline and literature

An important example for the second-order derivative of the total energy, on which this dissertation focuses, is determining the harmonic phonon frequencies, given the perturbation parameter is an ion displacement. Section 4.2.1, in which the central ideas of the dielectric approach [79, 173] are presented, describes the first application of linear response calculations in the context of phonons [87]. The name of the approach suggests employing the dielectric matrix as a quantity for calculating the desired first-order charge-density response. As the use of the dielectric matrix, however, has proven impracticable, progress has been made with the DFPT, also known as the Green function method [23]. DFPT circumvents vital employment of the dielectric matrix [23]. An introduction to its key aspects and a comparison with the dielectric approach is the subject of section 4.2.2. Section 4.2 mainly refers to Heid [23] if not cited differently.

4.2.1 Dielectric Approach

Concept

The dielectric approach exploits the fact that the first-order response of the electron density is characterized by a shift of the electrons screening the external potential. This effect is quantified by the dielectric matrix $\underline{\epsilon}$ and the external potential variation represents the perturbation. Consequently, the first-order variation of the effective potential reads

$$\begin{aligned} V_{\text{eff}}^{(1)}(\boldsymbol{r}) &= V_{\text{ext}}^{(1)}(\boldsymbol{r}) + V_{\text{Hxc}}^{(1)}(\boldsymbol{r}) && \text{(4.14a)} \\ &= V_{\text{ext}}^{(1)}(\boldsymbol{r}) + \int \left(\frac{\delta V_{\text{Htr}}^{(0)}(\boldsymbol{r})}{\delta \rho^{(0)}(\boldsymbol{r}')} + \frac{\delta V_{\text{xc}}^{(0)}(\boldsymbol{r})}{\delta \rho^{(0)}(\boldsymbol{r}')} \right) \rho^{(1)}(\boldsymbol{r}')\, \mathrm{d}^3 r' && \text{(4.14b)} \\ &= V_{\text{ext}}^{(1)}(\boldsymbol{r}) + \int \left(\frac{1}{|\boldsymbol{r}-\boldsymbol{r}'|} + \frac{\delta^2 E_{\text{xc}}^{(0)}(\boldsymbol{r})}{\delta \rho^{(0)}(\boldsymbol{r}')\delta \rho^{(0)}(\boldsymbol{r})} \right) \rho^{(1)}(\boldsymbol{r}')\, \mathrm{d}^3 r' && \text{(4.14c)} \end{aligned}$$

and is a functional of the ground-state density in the context of DFT (the index gs is suppressed hereinafter). Usually, the Hartree and xc kernel $K_{\text{Hxc}}(\boldsymbol{r},\boldsymbol{r}')$ is introduced [119]

$$V_{\text{eff}}^{(1)}(\boldsymbol{r}) =: V_{\text{ext}}^{(1)}(\boldsymbol{r}) + \int K_{\text{Hxc}}(\boldsymbol{r},\boldsymbol{r}')\rho^{(1)}(\boldsymbol{r}')\, \mathrm{d}^3 r' \ . \tag{4.14d}$$

The first-order variation of the density (4.13a) can be further reformulated here. For factoring out, the indices $\mathfrak{p}$ and $\mathfrak{p}'$ in its second term are interchanged resulting in

$$\rho^{(1)}(\boldsymbol{r}) = \sum_{\mathfrak{p}'|\mathfrak{p}'\in\mathrm{P}^{\perp}} \frac{f^{(0)}_{\mathfrak{p}} - f^{(0)}_{\mathfrak{p}'}}{\epsilon^{(0)}_{\mathfrak{p}} - \epsilon^{(0)}_{\mathfrak{p}'}} \left\langle \Psi^{(0)}_{\mathfrak{p}'} \middle| V^{(1)}_{\mathrm{eff}} \middle| \Psi^{(0)}_{\mathfrak{p}} \right\rangle \Psi^{*(0)}_{\mathfrak{p}}(\boldsymbol{r}) \Psi^{(0)}_{\mathfrak{p}'}(\boldsymbol{r}) \,, \tag{4.14e}$$

which connects the first-order variations of the effective potential and of the electron density.

Kohn–Sham susceptibility

Finally, one can also rewrite the first-order variation of the density into

$$\rho^{(1)}(\boldsymbol{r}) = \int \chi_{\mathrm{KS}}(\boldsymbol{r}, \boldsymbol{r}') V^{(1)}_{\mathrm{eff}}(\boldsymbol{r}') \, \mathrm{d}^3 r' \;, \tag{4.14f}$$

incorporating the non-interacting charge-density susceptibility [172], also known as the *Kohn–Sham susceptibility* [119]

$$\chi_{\mathrm{KS}}(\boldsymbol{r}, \boldsymbol{r}') := \frac{\delta \rho^{(0)}(\boldsymbol{r})}{\delta V^{(0)}_{\mathrm{eff}}(\boldsymbol{r}')} \,. \tag{4.15a}$$

Its representation in terms of wave functions can be identified in equation (4.14e)

$$=: \sum_{\mathfrak{p}'|\mathfrak{p}'\in\mathrm{P}^{\perp}} \frac{f^{(0)}_{\mathfrak{p}} - f^{(0)}_{\mathfrak{p}'}}{\epsilon^{(0)}_{\mathfrak{p}} - \epsilon^{(0)}_{\mathfrak{p}'}} \Psi^{*(0)}_{\mathfrak{p}}(\boldsymbol{r}) \Psi^{(0)}_{\mathfrak{p}'}(\boldsymbol{r}) \Psi^{*(0)}_{\mathfrak{p}'}(\boldsymbol{r}') \Psi^{(0)}_{\mathfrak{p}}(\boldsymbol{r}') \tag{4.15b}$$

and contains the independent-particle Green function [3]

$$\mathcal{G}^{\mathrm{ni}(0)}_{\mathfrak{p}}(\boldsymbol{r}, \boldsymbol{r}') = \sum_{\mathfrak{p}'|\mathfrak{p}'\in\mathrm{P}^{\perp}}^{\infty} \frac{\Psi^{(0)}_{\mathfrak{p}'}(\boldsymbol{r}) \Psi^{*(0)}_{\mathfrak{p}'}(\boldsymbol{r}')}{\epsilon^{(0)}_{\mathfrak{p}} - \epsilon^{(0)}_{\mathfrak{p}'}} \,. \tag{4.16}$$

The Kohn–Sham susceptibility describes the modification of the Kohn–Sham charge density given an altering effective Kohn–Sham potential [3]. In the context of DFT, Hybertsen and Louie [174] first published this perturbative derivation of the charge susceptibility. Its form itself had been developed earlier by Adler [175] and Wiser [176] for periodic systems to calculate dielectric constants in the context of band theory. In the DFT framework, the Kohn–Sham charge susceptibility (4.15) only incorporates ground-state Kohn–Sham wave functions describing the non-interacting Kohn–Sham system and is therefore an exact quantity. The

Dielectric matrix

dielectric matrix results from pasting (4.14f) into (4.14d) so that

$$V^{(1)}_{\mathrm{eff}}(\boldsymbol{r}) = V^{(1)}_{\mathrm{ext}}(\boldsymbol{r}) + \int K_{\mathrm{Hxc}}(\boldsymbol{r}, \boldsymbol{r}') \int \chi_{\mathrm{KS}}(\boldsymbol{r}', \boldsymbol{r}'') V^{(1)}_{\mathrm{eff}}(\boldsymbol{r}'') \, \mathrm{d}^3 r'' \, \mathrm{d}^3 r' \;. \tag{4.17a}$$

Expressed in a matrix-vector-component notation, in which equal indices are contracted (Einstein notation), the first-order effective potential variation reads

$$\left[V^{(1)}_{\mathrm{eff}}\right]_{\boldsymbol{r}} = \left[V^{(1)}_{\mathrm{ext}}\right]_{\boldsymbol{r}} + \left[I\right]_{\boldsymbol{r}\boldsymbol{r}'} \left[\chi_0\right]_{\boldsymbol{r}'\boldsymbol{r}''} \left[V^{(1)}_{\mathrm{eff}}\right]_{\boldsymbol{r}''} \,, \tag{4.17b}$$

equivalent to

$$\left[V^{(1)}_{\mathrm{eff}}\right]_{\boldsymbol{r}} = \left[1 - I\chi_0\right]^{-1}_{\boldsymbol{r}\boldsymbol{r}'} \left[V^{(1)}_{\mathrm{ext}}\right]_{\boldsymbol{r}'} =: \left[\epsilon\right]^{-1}_{\boldsymbol{r}\boldsymbol{r}'} \left[V^{(1)}_{\mathrm{ext}}\right]_{\boldsymbol{r}'} \,. \tag{4.17c}$$

Algorithm

In equation (4.17c), one identifies the inverse of the dielectric matrix $\underline{\epsilon}^{-1}$. Switching back to the integral notation and inserting equation (4.17c) into equation (4.14f) yields

$$\rho^{(1)}(\boldsymbol{r}) = \int \chi_{\mathrm{KS}}(\boldsymbol{r},\boldsymbol{r}')\big(1 - K_{\mathrm{Hxc}}(\boldsymbol{r},\boldsymbol{r}')\big)^{-1} V_{\mathrm{ext}}^{(0)}(\boldsymbol{r}')\,\mathrm{d}^3 r' \;. \tag{4.18}$$

By comparing equation (4.18) with equation (4.13a) (and suppressing $\mathbb{L}$ because of only one perturbation parameter), the relation

$$\chi_{\mathrm{ext}}(\boldsymbol{r},\boldsymbol{r}') = \chi_{\mathrm{KS}}(\boldsymbol{r},\boldsymbol{r}')\big(1 - K_{\mathrm{Hxc}}(\boldsymbol{r},\boldsymbol{r}')\big)^{-1} \tag{4.19}$$

becomes apparent [3, 5, 177, 178]. Thus, calculating the first-order charge-density variation in this way [79, 173] involves determining the dielectric matrix, inverting it, calculating the first-order response of the effective potential (see equation (4.17c)), and then using the charge susceptibility (4.15) for calculating the first-order density variation (4.14f). This first-order variation of the density can then be used for the second- or third-order variation of the total energy, e.g. in order to calculate phonon properties [87]. Sometimes, it works well to simplify the dielectric matrix by approximations such as the scalar and analytic Lindhard dielectric function [172]. In general, however, for practical purposes this method has an unfavorable computational performance since the setup of the dielectric matrix is rather costly[6] [3]. Furthermore, the inversion of the matrix is frequently impossible, irrespective of the choice of basis set, i.e., whether the basis set is in Fourier space or in real space using Wannier functions [3]. Since equation (4.15) assumes the availability of unoccupied orbitals, pursuing the dielectric approach requires advanced concepts to determine the unoccupied states for methods with very efficient basis sets (for instance LMTO).

Pros and cons

4.2.2 Framework of the Green Function Method

Advantages

DFPT, also known as the Green function method, avoids calculating the dielectric matrix and only requires summing over occupied states. Therefore, this method accomplishes a better numerical performance than the procedure presented in section 4.2.1 [3]. Furthermore, DFPT can be adjusted to deliver a desired response function to a certain type of perturbation [3]. In this sense, DFPT is more specific relative to a dielectric matrix method which might have several contributions in general [3]. To set up the DFPT formalism with restriction to non-metallic systems[7], one can start from equation (4.14e). In this case, the density variations become zero if both summation indices $\mathfrak{p}$ and $\mathfrak{p}'$ label either a conduction state with index u (the occupation numbers vanish) or a valence state with index o (the difference of both occupation numbers being 1 is 0). Therefore, equation (4.14e) simplifies to

Formalism
(non-metallic)

$$\begin{aligned}\rho^{(1)}(\boldsymbol{r}) &= \sum_{ou} \frac{f_o^{(0)}}{\epsilon_o^{(0)} - \epsilon_u^{(0)}} \Big\langle \varPsi_u^{(0)} \Big| V_{\mathrm{eff}}^{(1)} \Big| \varPsi_o^{(0)} \Big\rangle \varPsi_u^{*(0)}(\boldsymbol{r}) \varPsi_o^{(0)}(\boldsymbol{r}) \\ &+ \sum_{ou} \frac{-f_o^{(0)}}{\epsilon_u^{(0)} - \epsilon_o^{(0)}} \Big\langle \varPsi_o^{(0)} \Big| V_{\mathrm{eff}}^{(1)} \Big| \varPsi_u^{(0)} \Big\rangle \varPsi_o^{*(0)}(\boldsymbol{r}) \varPsi_u^{(0)}(\boldsymbol{r}) \,.\end{aligned} \tag{4.20a}$$

---

[6] This can, for example, also be done [179] with ab-initio direct supercell methods similar to the methods described for phonons in section 3.2 [3].

[7] In metallic systems the occupation numbers are generally affected by the perturbation [22, 86].

TRS allows for exploiting $\Psi = \Psi^*$ [180] so that

$$\rho^{(1)}(\boldsymbol{r}) = 2 \sum_{ou} \frac{f_o^{(0)}}{\epsilon_o^{(0)} - \epsilon_u^{(0)}} \left\langle \Psi_u^{(0)} \middle| V_\text{eff}^{(1)} \middle| \Psi_o^{(0)} \right\rangle \Psi_o^{*(0)}(\boldsymbol{r}) \Psi_u^{(0)}(\boldsymbol{r}) \, . \tag{4.20b}$$

Separating the sum over the conduction bands defines

$$\Psi_o^{(1)}(\boldsymbol{r}) := \sum_u \frac{1}{\epsilon_o^{(0)} - \epsilon_u^{(0)}} \Psi_u^{(0)}(\boldsymbol{r}) \left\langle \Psi_u^{(0)} \middle| V_\text{eff}^{(1)} \middle| \Psi_o^{(0)} \right\rangle \, , \tag{4.20c}$$

in which the Green function from equation (4.16) can be identified

$$\Psi_o^{(1)}(\boldsymbol{r}) := \int \mathcal{G}_o^{\text{ni}(0)}(\boldsymbol{r}, \boldsymbol{r}') V_\text{eff}^{(1)}(\boldsymbol{r}') \Psi_o^{(0)}(\boldsymbol{r}') \, \mathrm{d}^3 r' \, . \tag{4.20d}$$

This definition leads to a simplified form of the first-order density variation

$$\rho^{(1)}(\boldsymbol{r}) = 2 \sum_o \Psi_o^{*(0)}(\boldsymbol{r}) \Psi_o^{(1)}(\boldsymbol{r}) \, , \tag{4.20e}$$

which for TRS is consistent with combining equation (4.13b) (for one perturbation parameter, suppressing $\mathbb{L}$) with equation (4.8c). The first-order variation of the wave function is determined by solving the Sternheimer equation (see section 4.1.1)

$$\left(\mathscr{H}^{(0)} - \epsilon_o^{(0)} \right) \left| \Psi_o^{(1)} \right\rangle = - \sum_u \left| \Psi_u^{(0)} \right\rangle \left\langle \Psi_u^{(0)} \middle| V_\text{eff}^{(1)}(\boldsymbol{r}) \middle| \Psi_o^{(0)} \right\rangle = - \mathscr{P}_\mathrm{u} V_\text{eff}^{(1)} \left| \Psi_o^{(0)} \right\rangle \tag{4.21a}$$

$$= \left(\mathscr{P}_\mathrm{o} - 1 \right) V_\text{eff}^{(1)} \left| \Psi_o^{(0)} \right\rangle \tag{4.21b}$$

in which $\mathscr{P}_\mathrm{u}$ is the projector to the unoccupied subspace and $\mathscr{P}_\mathrm{o}$ projects onto the occupied subspace. It should be emphasized again that only summing over the occupied valence state and not over all conduction bands is sufficient, significantly increasing computer performance. In order to obtain the first-order variation of the Kohn–Sham wave functions, the Hamiltonian $\mathscr{H}^{(0)}$ in the Sternheimer equation (4.4) must be the Kohn–Sham Hamiltonian [22].

Alternative derivation

Another way [81, 82, 85], likewise resulting in the Sternheimer equation, illustrates the variational character of the first-order Kohn–Sham wave functions. By using the Euler–Lagrange equations, the second variation of the electronic total energy (the total energy without ionic degrees of freedom) is minimized with regard to the set of first-order wave functions so that the unperturbed wave functions are orthogonal to the first-order variation of the wave functions (see equation (4.9c)). [22]

Variational character

The variational character of the first-order wave functions is consistent with the variational character of the unperturbed Kohn–Sham wave functions. The latter result from the self-consistent solution of the Kohn–Sham equations and are only on average, and not pointwise, equal to the real wave functions of the Kohn–Sham system (see chapter 2) [119]. Due to its variational background, DFPT is a stable method, so small errors cannot induce large variations of the results [97]. Furthermore, analogously to the Kohn–Sham equations, the Sternheimer equation can be solved by a minimization procedure (see section 2.2.3). This is based on the idea that the internal degrees of freedom, determining the static response of the charge density to the perturbation, are to arrange in such a way that the second variation of the electronic total energy becomes minimal [3]. Finally, the prerequisite [22] to employing DFPT is that the external perturbation is small relative to excitations of the electrons. According to equation (4.1), this means [22]

Theory cutoff

$$\left|\Psi_{\mathfrak{p}}^{(0)}\right\rangle \gg \lambda\left|\Psi_{\mathfrak{p}}^{(1)}\right\rangle \tag{4.22a}$$

or as an implication of equation (4.8c)

$$\left\langle\Psi_{\mathfrak{p}'}^{(0)}\middle|\mathscr{H}^{(1)}\middle|\Psi_{\mathfrak{p}}^{(0)}\right\rangle \ll \left(\epsilon_{\mathfrak{p}}^{(0)} - \epsilon_{\mathfrak{p}'}^{(0)}\right). \tag{4.22b}$$

4.3 Viable Types of Perturbations

Literature

DFPT opens up the opportunity to conduct research into systems responding to manifold perturbations. An overview is for example given in the lecture notes of Verstraete and Zanolli [22], serving as the main reference for section 4.3 unless cited differently. Even broader overviews are, for instance, offered in the publications of Baroni et al. [87] and Gonze, Rignanese, and Caracas [92].

Phonons

Prominent in the literature [87] is the application of DFPT to a phonon perturbation intending to shed light on the respective charge density response, phonon dispersion relations, and normal modes resulting from the dynamical matrix in the harmonic approximation (see section 3.1). The induced variation of the charge density can guide one through developing a well-educated initial guess for starting densities in an ab-initio structure-optimization algorithm (see section 5.12), significantly enhancing its computational performance [119]. But, the comprehensive discussion of setting up the dynamical matrix by means of DFPT is deferred to chapter 6 and chapter 7 in order to firstly introduce the Full-Potential Linearized Augmented Plane-Wave (FLAPW) method in chapter 5. Apart from the theoretical understanding of material instabilities (see section 3.1) and of experiments such as inelastic incoherent neutron scattering, infrared absorption, or other experiments listed in the introduction of chapter 3, phonon dispersion relations also enable one to determine phonon densities of states. The latter provide insight into thermodynamical quantities like, for example, entropy, free energy, and specific heat at constant volume (see [92, 181] and references therein). Furthermore, equipped with the self-consistent effective Kohn–Sham potential, utilizing phonon dispersions, and the related phonon displacements, Savrasov and Savrasov [182] have succeeded in calculating a matrix element for the electron–phonon interaction [183, 184] from DFPT. This matrix element in combination with Fermi's Golden Rule can be used to calculate lifetimes for phonons and electrons, or to determine the Eliashberg [185] function for forecasting superconducting critical temperatures (for example as in [186] or [187]) [3]. Moreover, the matrix element serves as a basis for calculations [182] concerning electron transport using the Boltzmann transport equation [188–190].

Electrical fields

A second noteworthy type of perturbation that DFPT can be used for is given by a macroscopic electric field $\boldsymbol{E}$ (in the following the discussion is limited to static electric fields which some insulator is exposed to). Its response to such a field is called the electrical dipole moment or polarization, and is implicitly contained in a variation of the Kohn–Sham wave function as well as in a variation of the charge density. In addition, an explicit function of the electric field describing its thermodynamical coupling to a polarization must be added to the

Born–Oppenheimer Hamiltonian reading $\mathscr{V}_{\text{ext}}(\boldsymbol{r}) = q\boldsymbol{E} \cdot \boldsymbol{r}$, with the position operator $\boldsymbol{r}$ [87]. It turns out that the position operator conflicts with the periodic Born–von-Kármán boundary conditions, and the external potential has no lower boundary, so matrix elements involving the problematic position operator disagree likewise [87]. At the same time, wave functions fulfilling these periodic boundary conditions are also not well-defined [87]. In linear response, however, a well-defined self-consistent scheme to calculate the polarization $\boldsymbol{P}$ can be set up [87, 191]. Another ansatz works with finite-wavelength responses [79, 192] before executing $\boldsymbol{q} \to \boldsymbol{0}$ analytically [3]. The polarization is caused by a shift of the ions from their equilibrium position due to a force which, in linear approximation, is proportional to the electric field [92]. Alternatively, polarization can be induced by phonon displacements and, in linear order, polarization is proportional to the displacement [92]. The proportionality is governed by the *Born effective charge* tensor

$$Z_{ij}^{*\gamma} = \Omega \frac{\partial P_i}{\partial w_{\gamma j}(\boldsymbol{q} = \boldsymbol{0})} = \frac{\partial F_{\gamma j}}{\partial E_i} = -\frac{\partial^2 E_{\text{BO}}}{\partial E_i \, \partial w_{\gamma j}(\boldsymbol{q} = \boldsymbol{0})} \,, \tag{4.23}$$

which is a mixed second-order derivative of the Born–Oppenheimer energy E_{BO} (1.3) with added electric field dependence, while Ω is the unit cell volume [92]. The displacement $\boldsymbol{w}_\gamma$ and the force $\boldsymbol{F}_\gamma$ are addressed in section 3.1. By using the partial derivative of the polarization with respect to the electric field, the electronic part of the dielectric permittivity tensor

$$\epsilon_{ij}^{\infty} = \delta_{ij} + 4\pi \frac{\partial P_i}{\partial E_j} \tag{4.24}$$

can be defined. For displacements parallel to the phonon vector $\boldsymbol{q}$ in ionic materials, a frequency shift, which is a function of the Born effective charges and the dielectric permittivity, occurs due to the formation of a macroscopic polarization. This leads to the so-called *LO-TO splitting*[8] in dispersion relations as far as optical branches at the Γ-point are concerned. Born and Huang [21] published a theory for cubic and tetrahedral lattices consisting of two atoms, which was later generalized by Böttger [193] and is concisely summarized by Baroni et al. [87].

Homogeneous mechanical deformation

If the perturbation consists in a macroscopic homogeneous mechanical deformation, DFPT can be applied to evaluate piezoelectric tensors or certain elastic constants. But in an infinite crystal, the macroscopic deformation leads to different boundary conditions between the Hamiltonians of the perturbed and unperturbed case [87]. The unit cell angles, the cell parameters, and therefore the basis set, are influenced by the strain. In section 4.1.1, it was shown that there must be one common basis set for the perturbed and unperturbed cases. Therefore, one idea [194] is to apply a unitary transformation to the unperturbed Hamiltonian, so that the resulting auxiliary Hamiltonian describes its energy difference to the unperturbed system, but not yet the correct energy difference between the unperturbed and real physical perturbed cases [87]. However, as the boundary conditions are the same for the real and the auxiliary perturbed Hamiltonian, DFPT can be used to determine the remaining energy difference between the auxiliary and real perturbed systems [87]. This method does not account for an individual rearrangement (phonon modes) of the atoms in their unit cell to minimize their total energy if a strain is applied [87]. Still, this phenomenon can also be described using DFPT [87]. The discussed work-around becomes obsolete with a more

---

[8] The abbreviation LO means longitudinal optical whereas TO denotes transversal optical.

general formulation by Hamann et al. [195]. Another application area of DFPT is piezoelectric tensors, which express the change of the macroscopic electric polarization resulting from a homogeneous strain without a macroscopic field [87]. A more modern way to systematically evaluate responses to displacements, strains, or electric fields, or their combinations, using DFPT is given in the publication of Wu, Vanderbilt, and Hamann [196] [22].

Magnetic fields

In which way a system responds to a magnetic field is expressed by the magnetic susceptibility. However, its calculation for diamagnetic materials proves to be a formidable challenge, whereas the calculation of (anti)ferromagnetic response, manifesting itself in magnon quasiparticles which are basically spin waves, has been worked out by Savrasov [197]. In addition, for magnon dispersions, there are more performant and established methods suggested in the literature. A more detailed discussion related to this topic and about the relativistic effect of spin–orbit coupling can be found in the lecture notes of Verstraete and Zanolli [22].

Third-order quantities

The $2n+1$ theorem (see section 4.1.3) takes considerable effort out of handling third-order quantities such as Raman intensity tensors, electro-optic coefficients, thermal expansion, heat transport, or anharmonic inter-atomic force constants. A comprehensive overview of quantities related to the third variation of the total energy is given by Baroni et al. [87] or by Verstraete and Zanolli [22].

Chapter 5

All-Electron Full-Potential Linearized Augmented Plane-Wave Method

5.1 Augmented Plane-Wave Concept 44
5.2 Linearized Augmented Plane-Wave Basis 47
5.3 All-Electron and Full-Potential Calculations 52
5.4 Local Orbitals 54
5.5 Determining the Charge Density 56
5.6 Calculating the Full Effective Potential 59
5.7 Exploiting Symmetry 62
5.8 Constructing the Kohn–Sham Hamiltonian 65
5.9 Finding the Total Energy of the Ground State 70
5.10 Varying the Kohn–Sham Wave Functions 71
5.11 Coping with the Discontinuity at the Muffin-Tin Boundary 74
5.12 Ab-Initio Atomic Forces 76

Motivation of basis-sets

For obtaining self-consistency in the variational Kohn–Sham equations, their numerical solution is central to every iteration step (cf. section 2.2). The search for the most efficient way to determine the eigenenergies and eigenstates of these Kohn–Sham equations has sparked the development of many fruitful electronic-structure methods. Hereby, different kinds of (material) systems, phenomena or computational infrastructures impose various challenging requirements. Provided such a method utilizes a basis set for expanding the Kohn–Sham wave functions, this basis set can often be adapted to keep up with the aforementioned demands and the choice of the basis set constitutes one criterion for classifying electronic structure methods [68]. Martin [3] provides a comprehensive categorization and discussion of this topic. [71]

Generalized eigenvalue problem in periodic systems

Periodic bulk systems suggest expanding the unperturbed[1] Kohn–Sham wave functions

$$\Psi^{(0)}_{\boldsymbol{k},n}(\boldsymbol{r}) = \sum_{\mathrm{j}=1}^{N} z^{(0)}_{\mathrm{j}}(\boldsymbol{k},n)\phi^{(0)}_{\boldsymbol{k},\mathrm{j}}(\boldsymbol{r}) \tag{5.1}$$

for the band n as Bloch functions [198] with a Bloch vector $\boldsymbol{k}$, using a set of N unperturbed basis functions $\phi^{(0)}_{\boldsymbol{k},\mathrm{j}}(\boldsymbol{r})$ at position $\boldsymbol{r}$, and unperturbed expansion coefficients $z^{(0)}_{\mathrm{j}}(\boldsymbol{k},n)$ [3]. This expansion employing a basis set ensures the variational character of the Kohn–Sham wave functions. Therewith, the Kohn–Sham equation (2.3a) with its effective potential (2.3b), reads

$$\left(-\frac{\Delta}{2} + V^{(0)}_{\mathrm{Htr}}(\boldsymbol{r}) + V^{(0)}_{\mathrm{ext}}(\boldsymbol{r}) + V^{(0)}_{\mathrm{xc}}(\boldsymbol{r})\right)\Psi^{(0)}_{\boldsymbol{k},n}(\boldsymbol{r}) = \varepsilon^{(0)}_{\boldsymbol{k},n}\Psi^{(0)}_{\boldsymbol{k},n}(\boldsymbol{r})\,. \tag{5.2a}$$

Inserting and projecting onto equation (5.1) leads to a generalized eigenvalue problem

$$\boldsymbol{z}^{\dagger(0)}(\boldsymbol{k},n)\left(\underline{H}^{(0)}(\boldsymbol{k}) - \epsilon^{(0)}_{\boldsymbol{k},n}\underline{S}^{(0)}(\boldsymbol{k})\right)\boldsymbol{z}^{(0)}(\boldsymbol{k},n) = 0\,, \tag{5.2b}$$

with the *Hamiltonian matrix* elements in the Brillouin zone Ω given by

$$H^{(0)}_{\mathrm{j}',\mathrm{j}}(\boldsymbol{k}) = \int_{\Omega} \phi^{*(0)}_{\boldsymbol{k},\mathrm{j}'}(\boldsymbol{r})\left(-\frac{\Delta}{2} + V^{(0)}_{\mathrm{Htr}}(\boldsymbol{r}) + V^{(0)}_{\mathrm{ext}}(\boldsymbol{r}) + V^{(0)}_{\mathrm{xc}}(\boldsymbol{r})\right)\phi^{(0)}_{\boldsymbol{k},\mathrm{j}}(\boldsymbol{r})\,\mathrm{d}^3r\ , \tag{5.2c}$$

and consequently the *overlap matrix* elements defined as

$$S^{(0)}_{\mathrm{j}',\mathrm{j}}(\boldsymbol{k}) = \int_{\Omega} \phi^{*(0)}_{\boldsymbol{k},\mathrm{j}'}(\boldsymbol{r})\phi^{(0)}_{\boldsymbol{k},\mathrm{j}}(\boldsymbol{r})\,\mathrm{d}^3r\ . \tag{5.2d}$$

Both the Hamiltonian and the overlap matrix are Hermitian (or symmetric if real). The $\boldsymbol{k}$-vectors are generally discretized on a mesh spreading across the Brillouin zone. When further specifying the generic basis functions in equation (5.1), reaching a decision on its explicit form is guided by the requirements that the basis set should be tractable on the one hand [132]. On the other hand, it should efficiently enable the expanded variational wave function to behave as similarly as possible relative to the exact pointwise solution [132]. [71]

Plane-wave basis

A popular choice in this context are the orthonormal plane waves

$$\Psi^{(0)}_{\boldsymbol{k},n}(\boldsymbol{r}) = \frac{1}{\sqrt{\Omega}}\sum_{\boldsymbol{G}} z^{(0)}_{\boldsymbol{G}}(\boldsymbol{k},n)\mathrm{e}^{\mathrm{i}(\boldsymbol{k}+\boldsymbol{G})\cdot\boldsymbol{r}}\ , \tag{5.3}$$

for which the overlap matrix, equation (5.2d), becomes the unity matrix $\underline{1}$. They are indexed by the reciprocal lattice vectors $\boldsymbol{G}$, up to a particular cutoff. Furthermore, they are eigenfunctions of a Hamiltonian incorporating the kinetic energy and a constant potential. As a consequence, the first term in equation (5.2c) forms a diagonal matrix and in general such a plane-wave basis is easy to implement. [132]

Overview of chapter

However close to the nuclei, the singular $^1/_r$-potential behavior induces a rapid wave-function change, although the position $\boldsymbol{r}$ varies only slightly. Hence, the efficiency of the plane-waves basis set in equation (5.3) drastically declines, due to the number of plane waves

---

[1] Henceforth, the index for the order of perturbation is attached for sake of consistency, after introducing it in chapter 4.

required for a reasonably accurate description[2] of the aforementioned singularity. Slater [201] has resolved this issue by introducing the Augmented Plane-Wave (APW) method [3, 202–205] to which section 5.1 is devoted. In spheres around the atoms, this method implements atomic solutions (substituting the radial Bessel functions of a plane-wave expansion in spherical harmonics), while outside the spheres the plane-wave basis remains untouched. By exploiting these solutions of the radial Schrödinger equation with a spherical potential inside the spheres, a more efficient basis set results. But, this is at the expense of solving non-linear equations in order to match the wave functions expanded in both partitions of the basis set. The development has proceeded [206] with introducing linearization [207–210], leading to the *Linearized Augmented Plane-Wave* (LAPW) method which is presented in section 5.2. Especially for systems incorporating heavy chemical elements or whenever relativistic effects are of interest, the LAPW method can be extended to employ solutions of the relativistic Pauli–Dirac equation [127, 211], organically including the spin and its coupling to the orbital angular momentum (spin–orbit coupling or SOC) [68, 212]. Within the `FLEUR` program [69], the Scalar-Relativistic Approximation (SRA) [213–217] is implemented to simplify the evaluation of the sophisticated Pauli–Dirac equation if possible. Elucidating the integration of relativistic corrections finalizes section 5.2. The LAPW framework makes calculations feasible that take all electrons [67] of the atom into account and handle the full potential without shape approximations [64, 218]. This has paved the way for the *all-electron Full-potential Linearized Augmented Plane-Wave* (FLAPW) calculations [65, 66] which are specified in section 5.3. Accounting for every electron can lead to scenarios in which the LAPW basis cannot ensure an adequate description of all states [68]. For coping with many of these scenarios, the concept of introducing “Local Orbitals” (LOs) [219] has prevailed in the electronic-structure community. LOs, which shall be set up in section 5.4, can extend the APW concept (APW + LO [220]), effectively implying less basis functions, or its linearized version (LAPW + LO [219]) [68]. In general, the FLAPW method relies on an accurate all-electron charge density, which is introduced in equation (2.4) as an integral constituent of the self-consistent Kohn–Sham system. A guide for implementing this full density is outlined in section 5.5. In addition, a precise calculation of the effective potential, addressed in section 5.6, represents the premise that the LAPW method delivers accurate results [3]. This section summarizes the decisive method of Weinert [64], which delivers the Coulomb potential and provides an alternative to the well-known Ewald summation. Also, this section deals with the setup of the exchange-correlation potential. The efficiency of describing systems with significant and sophisticated non-spherical contributions to the charge density and the potential can be increased, depending on how much symmetry underlies the investigated system. Such symmetry optimizations, inhering in the `FLEUR` code [69] results, are presented in section 5.7. The remaining part of a self-consistent iteration step (see section 2.2) consists in the setup of the Hamiltonian matrix elements, defined in equation (5.2c), and the overlap matrix elements, given by equation (5.2d). Section 5.8 is concerned with it. One reason why the FLAPW method has successfully established itself is the accuracy of total energy calculations [3, 66, 70]. Therefore, the usual setup of the total energy in the FLAPW framework is briefly presented in section 5.9. In order to set the stage for chapter 6 and chapter 7, as well as to provide the background to section 5.12, section 5.10 gives an introduction into the principles and subtleties of varying the Kohn–Sham wave functions expanded in the LAPW

---

[2] Still, plane-wave basis sets are common in codes substituting the real potential by a pseudopotential, permitting at least a precise mimicking among the atoms [71, 199, 200].

basis, especially due to a displacement of the nuclei. This section predominantly puts forward the Pulay [103] corrections, emerging from the incompleteness of the LAPW basis and drawing from the fact that the Kohn–Sham wave functions are variational (see equation (5.1)) [68, 88]. Moreover in practice, numerical discontinuities in the position-dependent LAPW basis arise, propagating to the charge density and to the effective potential [68, 88]. Section 5.11 expands upon implications for spatial derivatives of integrals over the unit cell, involving the latter discontinuous quantities, in particular against the background of phonons and forces [88]. Furthermore, a reformulation of the kinetic Laplace operator into a symmetric form is discussed, which is already applied in the APW method (see e.g. [68, 220, 221]). Finally, section 5.12 summarizes the central concepts for the implementation of ab-initio forces, mainly having been brought to the fore by Soler and Williams [222, 223] as well as Yu, Singh, and Krakauer [224]. Based upon the latter publication, Klüppelberg [88] has significantly refined the force formalism improving the numerical results for FLAPW ab-initio forces, especially for complex materials. Grasping ab-initio forces, whose relation to phonons has already been anticipated in section 3.1, elucidates analogous ideas entering into the DFPT realization of phonons within the FLAPW framework, on which chapter 6 and chapter 7 elaborate. [71]

Relevance and literature

To put it in a nutshell, applications employing any kind of APW-basis sets (especially the FLAPW framework) are manifold and exhibit in the multitude of strategies having been developed to master sophisticated phenomena such as non-collinear magnetism [225] or transport and scattering [226–228]. Likewise, quasiparticle self-energies are for instance determined within the $\mathcal{G}W$ approximation [229, 230] or lower-dimensional geometries (e.g. [231, 232]) are investigated. In principle, almost any material comprising of chemical elements with arbitrary atomic numbers less than 138 [127] is tractable. But particularly for systems containing rare earths or transition metals, the (F)LAPW (or alternatively the LMTO [206]) method is well suited [68]. The efficiency and accuracy the FLAPW method exhibits, excel in particular for nuclear quantities [67] (relative to approximating methods employing pseudopotentials [199, 200]) and have made it the benchmark [70] among electronic structure methods [3, 68]. A comprehensive overview of the FLAPW method and its implementation is given by Blügel and Bihlmayer [71] or Singh and Nordström [68], further subtleties of the `FLEUR` [69] program can for instance be found in Kurz [233, 234]. Finally, the textbook of Martin [3] provides a comprehensive overview and categorization of further electronic structure methods. [71]

5.1 Augmented Plane-Wave Concept

Motivation and literature

Basis sets should on the one hand allow for a satisfying approximation to the actual eigenfunctions, and on the other hand enable a maximum of computational performance, which usually mirrors in a minimal amount of required basis functions [132]. Although in general this can be hard to realize, it stands to reason that those basis sets perform best, which include the intrinsic physical properties of the system under investigation [132]. In the context of solid state physics, Slater [201, 204] has introduced the APW concept which is concisely summarized in the textbook of Singh and Nordström [68], serving as main reference for the current section unless cited differently. Further progress in the APW method was made by Slater and Saffren [3, 202, 203]. Also, the textbook of Loucks [205] is a standard reference for the APW method.

Partioning concept

In order to live up to the inherently inhomogeneous potential landscape in periodic solids, the APW method basically subdivides it into two regions: (i) spheres, called *muffin-tins* (MTs), centrally incorporating the ions as well as their immediate surroundings, and (ii) the remaining *interstitial region* (IR). Figure 5.1 depicts the aforementioned division of the unit cell. The radii of the MTs are to be set so that the spheres do not overlap. But at the same time, the MT spheres should nearly[3] take up all the available space of the unit cell [71].

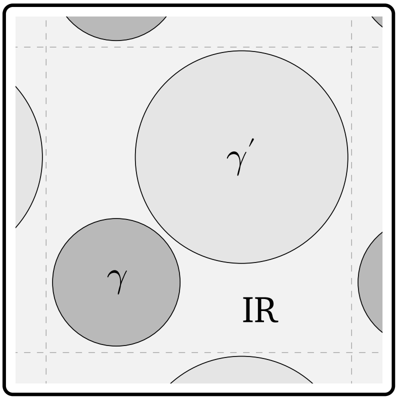

Figure 5.1: Partitioning of a unit cell within the FLAPW method into different muffin-tin (MT) spheres γ and γ', as well as the interstitial region (IR). The MT-sphere radii are chosen so that the spheres do not overlap and there remains a little space between them to make a relaxation of the lattice structure possible. This scheme is based on reference [71, figure 7].

Deduction of basis set

While the IR features a rather smooth potential, the potential becomes stronger the smaller the distance is to the ions. Therefore, the wave function rapidly changes its value as a function of the position, especially in the central region of the MT spheres, while it behaves significantly steadier in the IR. Based on the fact that plane waves form the solution of a Schrödinger equation with a constant potential, Slater proposes them as the basis set for the IR [3]. The linear combination of plane waves must describe the IR wave function fairly well, in particular its additional variation as a result of the matching to the MT wave function [3]. In the MT spheres, Slater particularly exploits the predominantly spherical behavior of the potential in the vicinity of the nuclei. It justifies his ansatz of the radial Schrödinger equation for a local, spherical atomic problem (in Hartree units [234]) with energy E_l^γ and orbital quantum number l

$$\left[-\frac{1}{2}\frac{\partial^2}{\partial r_\gamma^2}+\frac{1}{2}\frac{l(l+1)}{r_\gamma^2}+V_{\text{eff, sph}}^{(0)}\left(r_\gamma\right)-E_l^\gamma\right]r_\gamma u_{l1}^\gamma\left(r_\gamma\right)=0\,. \tag{5.4}$$

Its solutions $u_{l1}^\gamma\left(r_\gamma\right)$ mimic the radial behavior of the MT wave function in the MT sphere γ. However, their index 1 can be ignored in the remaining section, because it is actually not required in the context of APW. Instead, the index simplifies referring to the previous equation in the following discussion and anticipates a distinction that must be made within the

---

[3] Leaving some narrow space between the MT spheres, one can optimize the atomic space in a relaxation procedure aiming to get rid of intra-atomic forces (see section 3.1 and section 5.12)[128].

LAPW method[4]. As far as equation (5.4) is concerned within the APW method, the energy parameter E^γ_l in general differs from the Kohn–Sham eigenenergy. Furthermore, an intrinsic orthogonality exists between the $u^\gamma_{l1}\left(r_\gamma\right)$ and arbitrary eigenstates of the Hamiltonian in equation (5.4), which are zero at the MT sphere boundary [206]. The eigenenergies of the latter are typically so low (core states) that the probability density of these electrons features its significant contribution close to and around the core of the atoms. Their wave functions thus ideally vanish when approaching the boundary to the IR. The isotropic potential $V^{(0)}_{\text{eff, sph}}\left(r_\gamma\right)$ is represented by the spherical part of the unperturbed Kohn–Sham effective potential. Both assumptions, the constant potential in the IR and the spherical potential in the MT spheres, are known as *shape approximations* or *MT potential* [3] and are practiced in many APW implementations [71]. Several publications utilizing shape approximations concern transition metals or transition metal compounds and particularly systems featuring a close packing (hcp, whose lattice-parameter ratio reads $^c/_a = \sqrt{^8/_3}$, or fcc) deliver the best results. Often, other configurations can still be handled with an acceptable outcome, which, however, worsens when less symmetry is available.

Definition of basis functions

The name "Augmented Plane-Wave" owes its origins to the plane-wave expansion

$$\mathrm{e}^{\mathrm{i}\boldsymbol{G}\cdot\boldsymbol{r}} = 4\pi\mathrm{e}^{\mathrm{i}\boldsymbol{G}\cdot\boldsymbol{\tau}_\gamma}\sum_{lm}\mathrm{i}^l\mathrm{j}_l\left(Gr_\gamma\right)\mathrm{Y}^*_{lm}\left(\hat{\boldsymbol{G}}\right)\mathrm{Y}_{lm}\left(\hat{\boldsymbol{r}}_\gamma\right) \tag{5.5}$$

in spherical harmonics Y_{lm} (also known as Rayleigh decomposition [71]), in which m is the magnetic quantum number. Herein, the transformation $\boldsymbol{r}_\gamma = \boldsymbol{r} - \boldsymbol{\tau}_\gamma$ from the global coordinate system of the unit cell into a spherical coordinate system of the MT sphere, surrounding atom γ located at $\boldsymbol{\tau}_\gamma$, is used. Therewith, equation (5.5) delivers the value of the plane waves given $\left|\boldsymbol{r}_\gamma\right|$ equals the MT radius R_γ [71]. By substituting the Bessel function $\mathrm{j}_l\left(Gr_\gamma\right)$ in this equation with the radial solution $u^\gamma_{l1}\left(r_\gamma\right)$ from equation (5.4), and matching the value of the latter to that of the former at $\left|\boldsymbol{r}_\gamma\right| = R^\gamma_{\mathrm{MT}}$, the plane wave is augmented into the MT sphere [71]. So, all in all the APW basis set is defined as [71]

$$\phi^{\mathrm{APW}}_{\boldsymbol{k},\boldsymbol{G}}(\boldsymbol{r}) := \begin{cases} \dfrac{1}{\sqrt{\Omega}}\mathrm{e}^{\mathrm{i}(\boldsymbol{k}+\boldsymbol{G})\cdot\boldsymbol{r}}, & \mathrm{IR} \\ \displaystyle\sum_{lm} a^{\boldsymbol{Gk}\gamma}_{lm1}u^\gamma_{l1}(r_{\nu^\gamma})\mathrm{Y}_{lm}\left(\hat{\boldsymbol{r}}_\gamma\right), & \mathrm{MT}_\gamma \end{cases} . \tag{5.6}$$

Normally, the MT basis function is set up on a logarithmic mesh with mesh points ν^γ, individually adjustable for each MT sphere γ, so that the behavior of the MT wave function is optimally accounted for in integrals or differential equations. It is of paramount importance to choose the matching coefficients $a^{\boldsymbol{Gk}\gamma}_{lm1}$ such that the basis functions are continuous on the surface of the spheres, in order to ensure that the kinetic energy (see also section 5.11) is correctly defined. In the APW framework, this prerequisite is satisfied by the choice [71]

$$a^{\boldsymbol{Gk}\gamma}_{lm1} = \frac{4\pi\mathrm{i}^l}{\sqrt{\Omega}}\mathrm{e}^{\mathrm{i}(\boldsymbol{k}+\boldsymbol{G})\cdot\boldsymbol{\tau}_\gamma}\mathrm{Y}^*_{lm}\left(\widehat{\boldsymbol{k}+\boldsymbol{G}}\right)\frac{\mathrm{j}_l\left(|\boldsymbol{k}+\boldsymbol{G}|R_\gamma\right)}{u^\gamma_{l1}\left(R_\gamma\right)} . \tag{5.7}$$

Non-linearity

The workflow of the APW method requires adjusting the energy parameter E_l in equation (5.4) to the initially unknown band energy as accurately as possible [71]. However,

---

[4] In the LAPW method, solutions from a differentiated version of equation (5.4) also become relevant and shall be indicated with the index 2.

since the radial functions also depend on the energy and the matching conditions must be fulfilled for every eigenenergy, the solution of the eigenvalue problem turns into a nonlinear problem, rather than a simple diagonalization [71]. A detailed discussion of this aspect is provided in the textbook of Martin [3].

Further drawbacks

Including the full effective potential into the formalism (instead of resorting to shape approximations) presents a tough challenge, still, it is in principle possible [235, 236]. Nonetheless concerning this aspect, linearized methods work better and are more established [3]. Furthermore, for some combinations of the energy parameters E_l and the MT sphere radii R_γ [88], the radial functions u^γ_{l1} become zero on the MT sphere surfaces. Thus, the plane waves in the IR decouple from the MT basis functions and numerical issues occur, known as the *asymptote problem*. Finally by construction, the discontinuous slope of the wave functions at the MT sphere boundary implies additional surface integrals (5.77), because of the Laplace operator in the kinetic energy [71].

5.2 Linearized Augmented Plane-Wave Basis

Principle and literature

Determined efforts to overcome the problems of the APW concept had been taken early on (see reference [68] for details). Eventually and apart from matching the radial solution at E_l, Andersen [206] has introduced an additional first-order energy derivative of the radial solution into the basis set, calculated at the energy parameter E_l (cf. also reference [208]). Assuring the continuity for both of the radial solutions gives rise to the Linearized Augmented Plane-Wave (LAPW) method, the setup of which in this section adheres to the discussion in the textbook of Singh and Nordström [68] unless differently quoted.

Linearized basis functions

The LAPW method underlies the Taylor expansion at E_l of the energy-dependent radial function in equation (5.6)[5]

$$u^\gamma_{l1}\big(\epsilon; r_\gamma\big) = u^\gamma_{l1}\big(E^\gamma_l; r_\gamma\big) + \big(\epsilon - E^\gamma_l\big)\frac{\partial u^\gamma_{l1}\big(\epsilon; r_\gamma\big)}{\partial\epsilon}\bigg|_{\epsilon=E^\gamma_l} + \mathcal{O}\Big(\big(\epsilon - E^\gamma_l\big)^2\Big) \tag{5.8a}$$

$$=: u^\gamma_{l1}\big(E^\gamma_l; r_\gamma\big) + \big(\epsilon - E^\gamma_l\big)u^\gamma_{l2}\big(E^\gamma_l; r_\gamma\big) + \mathcal{O}\Big(\big(\epsilon - E^\gamma_l\big)^2\Big) \tag{5.8b}$$

with a general energy parameter ϵ, up to linear order [71]. In the MT spheres, relative to the APW basis (5.6), its linearized version comprises not only $u^\gamma_{l1}\big(E_l, r_\gamma\big)$ anymore, but $u^\gamma_{l1}\big(E_l; r_\gamma\big)$ and $u^\gamma_{l2}\big(E_l; r_\gamma\big)$ [71]. Each of them is related to the energy parameter E_l, but in the LAPW basis E_l is considered constant (and suppressed hereinafter) [71]. Thus for all band energies lying close to E_l, the same energy parameter can be chosen so that a simple eigenvalue problem with a single diagonalization results, instead of the nonlinear problem in section 5.1. All in all, the LAPW basis reads

$$\phi^{\text{LAPW}}_{\boldsymbol{k},\boldsymbol{G}}(\boldsymbol{r}) := \begin{cases} \dfrac{1}{\sqrt{\Omega}}\mathrm{e}^{\mathrm{i}(\boldsymbol{k}+\boldsymbol{G})\cdot\boldsymbol{r}}, & \boldsymbol{r} \in \text{IR} \\ \sum\limits_{lmp} a^{\boldsymbol{G}\boldsymbol{k}\gamma}_{lmp} u^\gamma_{lp}\big(r_\gamma\big)\mathrm{Y}_{lm}\big(\hat{\boldsymbol{r}}_\gamma\big), & \boldsymbol{r} \in \text{MT}_\gamma \end{cases} \tag{5.9}$$

---

[5] The argument indicating the energy dependence of u^γ_{l1} is suppressed in section 5.1.

with the index p equalling 1 or 2. The function $u^{\gamma}_{l2}\left(r_{\gamma}\right)$ is calculated from the energy derivative of equation (5.4) [234]

$$\left[-\frac{1}{2}\frac{\partial^2}{\partial r_{\gamma}^2}+\frac{1}{2}\frac{l(l+1)}{r_{\gamma}^2}+V^{(0)}_{\text{eff, sph}}\left(r_{\gamma}\right)-E^{\gamma}_{l}\right]r_{\gamma}u^{\gamma}_{l2}\left(r_{\gamma}\right)=r_{\gamma}u^{\gamma}_{l1}\left(r_{\gamma}\right). \tag{5.10}$$

Furthermore, the energy parameter E_l is equally chosen, both in equations (5.4) and (5.10). Postulating the normalization condition

$$\int_0^{R_{\gamma}}\left(r_{\gamma}u^{\gamma}_{l1}\left(r_{\gamma}\right)\right)^2\mathrm{d}r=1 \tag{5.11}$$

of the solutions from equation (5.4), results in the orthogonality between $u^{\gamma}_{l1}(r)$ and $u^{\gamma}_{l2}(r)$. In fact, this orthogonality is not vital, but simplifies the setup of the (F)LAPW framework. The LAPW basis is utilized for the valence states and constructed orthogonal to states within deeper lying energy spectra (see core states in section 5.3 and section 5.5.1). Having ordered the LAPW-expansion terms of the MT wave-function according to the absolute value of the vectors $\boldsymbol{G}$, a truncated expansion, with already a small number of terms, approximates the sophisticated behavior of the true MT wave-function fairly well. This is implied by the aforementioned orthogonality. The matching parameter $a^{\boldsymbol{Gk}\gamma}_{lm1}$ is again determined (at E^{γ}_{l}) as in equation (5.7), which analogously can likewise be used for obtaining the additional $a^{\boldsymbol{Gk}\gamma}_{lm2}$. However, introducing the latter condition leads to a larger basis set than in the APW framework.

Errors

The LAPW scheme induces the errors $\left(\epsilon-E^{\gamma}_{l}\right)^2$ and $\left(\epsilon-E^{\gamma}_{l}\right)^4$ for the wave functions and the eigenvalues, respectively. Equipped with the $2n+1$ theorem (section 4.1.3), estimating errors of higher-order variations becomes also feasible [3]. In practice, E_l is set in a way so that the aforementioned errors are minimized [71]. This results in E_l lying in the middle of an interval enclosing the bands of l-like character [71]. But, the wider range of Kohn–Sham energies, which can be described with a single choice of E_l in the LAPW method, comes at a price. Urging the first-order energy derivative to be continuous leads to a stiffness and worse behavior of the basis for Kohn–Sham energies near to E_l. Therefore relative to the APW method, a larger set of plane waves is required to converge the resulting quantities. Nevertheless, provided a converged LAPW basis set, actually only the linearization error remains [3]. Apart from that, the matching of even higher derivatives [237] does not bring benefit, but worsens the variational properties of the wave functions [71]. Furthermore, it requires more plane waves within the basis so that the calculation converges. Generally, a remedy for avoiding higher plane-wave cut-offs can be achieved by local orbitals, which section 5.4 is devoted to.

Relativistic corrections

The kinetic energy of some electrons close to the nuclei requires involving relativistic corrections. In particular [234], this holds true for systems containing elements with a large proton number. Apart from that, many phenomena of growing interest are due to relativistic effects such as Spin–Orbit Coupling (SOC) or the spin itself [212]. The spin inheres organically in the bi-spinors $\mathit{\Psi}$, and relativistic effects are governed by the gauge-invariant and covariant Dirac equation for electrons of mass m_{e} (see e.g. the textbook of Peskin and Schroeder [238])

$$\left(\mathrm{i}\hbar\not{\mathcal{D}}-m_{\mathrm{e}}c^2\right)\mathit{\Psi}=-\gamma^0 q_{\mathrm{e}}\mathscr{V}^{(0)}_{\text{eff}}\mathit{\Psi}\,. \tag{5.12a}$$

This equation contains the speed of light c (approximately equalling 137.036 in atomic (Hartree) units [239]) and the effective Kohn–Sham potential operator $\mathscr{V}^{(0)}_{\text{eff}}$ multiplied by the electronic charge q_{e}. The notation $\not{\mathscr{D}}$ [238] is a common abbreviation for

$$\left(\mathrm{i}\hbar\gamma^{\varsigma}\mathscr{D}_{\varsigma} - m_{\mathrm{e}}c^2\right)\Psi = -\gamma^0 q_{\mathrm{e}}\mathscr{V}^{(0)}_{\mathrm{eff}}\Psi\,, \tag{5.12b}$$

while the index ς indicates the components of the vectors in Minkowski space (Einstein notation is assumed in the Dirac equation). Contracting the gauge invariant derivative operator $\mathscr{D}_{\varsigma}$ [238] with the Dirac γ matrices results in

$$\left(\mathrm{i}\hbar\gamma^0\frac{\partial\Psi}{\partial t} + \mathrm{i}\hbar c\boldsymbol{\gamma}\cdot\left(\boldsymbol{\nabla} + \mathrm{i}\frac{q_{\mathrm{e}}}{\hbar c}\boldsymbol{\mathscr{A}}\right) - m_{\mathrm{e}}c^2\right)\Psi = -\gamma^0 q_{\mathrm{e}}\mathscr{V}^{(0)}_{\mathrm{eff}}\Psi\,, \tag{5.12c}$$

with the vector potential operator $\boldsymbol{\mathscr{A}}$. The 4×4 Dirac γ matrices [240] are defined as

$$\gamma^{\mu} = \left(\gamma^0, \boldsymbol{\gamma}\right) = \left(\beta, \beta\boldsymbol{\alpha}\right) = \left(\gamma^0, \gamma^1, \gamma^2, \gamma^3\right)\,, \tag{5.12d}$$

$$\boldsymbol{\alpha} = \begin{pmatrix} 0 & \boldsymbol{\sigma} \\ \boldsymbol{\sigma} & 0 \end{pmatrix} = \left(\begin{pmatrix} 0 & \underline{\sigma}_1 \\ \underline{\sigma}_1 & 0 \end{pmatrix}, \begin{pmatrix} 0 & \underline{\sigma}_2 \\ \underline{\sigma}_2 & 0 \end{pmatrix}, \begin{pmatrix} 0 & \underline{\sigma}_3 \\ \underline{\sigma}_3 & 0 \end{pmatrix}\right)^{\top}\,, \quad \beta = \begin{pmatrix} \underline{1}_2 & 0 \\ 0 & -\underline{1}_2 \end{pmatrix}\,, \tag{5.12e}$$

$$\underline{\sigma}_1 = \begin{pmatrix} 0 & 1 \\ 1 & 0 \end{pmatrix}\,, \quad \underline{\sigma}_2 = \begin{pmatrix} 0 & -\mathrm{i} \\ \mathrm{i} & 0 \end{pmatrix}\,, \quad \underline{\sigma}_3 = \begin{pmatrix} 1 & 0 \\ 0 & -1 \end{pmatrix}\,, \tag{5.12f}$$

while $\underline{\sigma}_i$ are the 2×2 Pauli spin matrices in the Hilbert space spanned by the spin-up and spin-down states. Rewriting equation (5.12c) by using the 4×4 matrices α and β in the Dirac–Pauli representation [240] from equation (5.12e) reads

$$\left(-\mathrm{i}\hbar c\beta\boldsymbol{\alpha}\cdot\left(\boldsymbol{\nabla} + \mathrm{i}\frac{q_{\mathrm{e}}}{\hbar c}\boldsymbol{\mathscr{A}}\right) + \beta^2 m_{\mathrm{e}}c^2 - \beta q_{\mathrm{e}}\mathscr{V}^{(0)}_{\mathrm{eff}}\right)\Psi = \beta\mathrm{i}\hbar\frac{\partial\Psi}{\partial t}\,, \tag{5.12g}$$

which can be multiplied by β

$$\left(\boldsymbol{\alpha}\cdot\left(-\mathrm{i}\hbar c\boldsymbol{\nabla} + q_{\mathrm{e}}\boldsymbol{\mathscr{A}}\right) + \beta m_{\mathrm{e}}c^2 - q_{\mathrm{e}}\mathscr{V}^{(0)}_{\mathrm{eff}}\right)\Psi = \mathrm{i}\hbar\frac{\partial\Psi}{\partial t}\,, \tag{5.12h}$$

and transfered into the stationary form [212]

$$\left(\boldsymbol{\alpha}\cdot\left(c\boldsymbol{\mathscr{p}} + q_{\mathrm{e}}\boldsymbol{\mathscr{A}}\right) + \beta m_{\mathrm{e}}c^2 - q_{\mathrm{e}}\mathscr{V}^{(0)}_{\mathrm{eff}}\right)\Psi = \epsilon'\Psi\,. \tag{5.12i}$$

In the previous equation, $\boldsymbol{\mathscr{p}}$ is the momentum operator, and $\epsilon' = \epsilon + m_{\mathrm{e}}c^2$ the energy from which the rest energy $m_{\mathrm{e}}c^2$ can be split off [212].

Non-relativistic limit expansion

The bi-spinor $\Psi = (\psi, \chi)^{\top}$, as this name hints at, is composed of two spinors: the so-called large spinor ψ and the so-called small one χ, which both are of the dimension 2×1. If the momentum operator $\boldsymbol{\mathscr{p}}$ acts on the bi-spinor, the momentum $\boldsymbol{p}$ of the particle will be measured. Furthermore when acting on the bi-spinor, the effective potential operator $\mathscr{V}^{(0)}_{\mathrm{eff}}$ and the vector potential operator $\boldsymbol{\mathscr{A}}$ deliver the respective values of the effective potential $V^{(0)}_{\mathrm{eff}}(\boldsymbol{r})$ or the vector potential $\boldsymbol{A}(\boldsymbol{r})$ in position space. Starting from the Dirac equation, focussing on the large spinor ψ, and exploiting $q_{\mathrm{e}}V^{(0)}_{\mathrm{eff}} \ll \epsilon' + m_{\mathrm{e}}c^2 \approx 2m_{\mathrm{e}}c^2$ within the non-relativistic limit, it is possible to expand

$$\Bigg(\epsilon + q_{\mathrm{e}}V^{(0)}_{\mathrm{eff}}(\boldsymbol{r}) - \frac{1}{2m_{\mathrm{e}}}\left(\boldsymbol{p} + \frac{q_{\mathrm{e}}}{c}\boldsymbol{A}(\boldsymbol{r})\right)^2 + \frac{1}{2m_{\mathrm{e}}c^2}\left(\epsilon + q_{\mathrm{e}}V^{(0)}_{\mathrm{eff}}(\boldsymbol{r})\right)^2 + \mathrm{i}\frac{q_{\mathrm{e}}}{(2m_{\mathrm{e}}c)^2}\boldsymbol{E}(\boldsymbol{r})\cdot\boldsymbol{p} - \frac{q_{\mathrm{e}}}{(2m_{\mathrm{e}}c)^2}\underline{\boldsymbol{\sigma}}\cdot\left(\boldsymbol{E}(\boldsymbol{r})\times\boldsymbol{p}\right) - \frac{q_{\mathrm{e}}}{2m_{\mathrm{e}}c}\underline{\boldsymbol{\sigma}}\cdot\boldsymbol{B}(\boldsymbol{r})\Bigg]\psi = 0 \tag{5.13}$$

in orders of ${}^{v}/_{c}$, while v is the velocity of the electron and $\boldsymbol{E}(\boldsymbol{r})$ denotes the electric field[6]. The Schrödinger equation can be identified in the first three terms, the relativistic change of the mass due to a finite velocity (mass-velocity term) is considered in the fourth term, and the fifth term is called the Darwin term. These five terms are attributed to the group of *scalar-relativistic* contributions. Their decisive difference relative to the last two terms in equation (5.13), which represent the spin–orbit interaction and the coupling between the spin and a magnetic field $\boldsymbol{B}(\boldsymbol{r})$, is the lack of any spin matrices $\underline{\boldsymbol{\sigma}}$. In order to simplify solving equation (5.13) for ϵ, this energy in the mass-velocity can be approximately replaced by the energy parameter E_l. [212]

Scalar-relativistic approximation

Since a full-relativistic description of the electrons significantly increases the computational effort, resorting to the scalar-relativistic approximation [213], which includes only the aforementioned scalar-relativistic terms, appears attractive when not considering SOC. The original quantum numbers can be further used, because a coupling of spin and spatial coordinates is avoided, decoupling the spin-up and spin-down channels. Nonetheless, provided small atomic numbers, the SOC contribution is so small that in some cases it can be subsequently added on top of the scalar-relativistic solutions, using the second variation method [217] [68, 71]. Henceforth, the scalar-relativistic approximation is preferred for the valence electrons. As in equations (5.4) and (5.10), the `FLEUR` [69] program implements the scalar-relativistic Dirac equation with restricting to the spherical part of the effective Kohn–Sham potential. Determining the scalar-relativistic radial functions for the spin channels indexed by σ requires solving a set of coupled differential equations, e.g. for $p = 1$ they read [234]

$$\begin{pmatrix} \frac{l(l+1)}{2r_\gamma^2\left(m_\mathrm{e}+\left(\sqrt{2}c\right)^{-2}\left(E-V^{(0)\sigma}_{\text{eff, sph}}\left(r_\gamma\right)\right)\right)} + V^{(0)\sigma}_{\text{eff, sph}}\left(r_\gamma\right) & -\frac{2c}{r_\gamma} - c\frac{\partial}{\partial r_\gamma} \\ c\frac{\partial}{\partial r_\gamma} & -2m_\mathrm{e}c^2 + V^{(0)\sigma}_{\text{eff, sph}}\left(r_\gamma\right) \end{pmatrix} \vec{u}^{\gamma\sigma}_{l1}\left(r_\gamma\right) = E\,\vec{u}^{\gamma\sigma}_{l1}\left(r_\gamma\right) \quad (5.14)$$

(the spin index σ is suppressed hereinafter due to the focus on spin-degenerate systems). Although the $\vec{u}^{\gamma}_{lp}\left(r_\gamma\right)$ have a vectorial character and their two components are also called large and small, they do not directly correspond to the large ψ and the small χ of the bi-spinor Ψ. Additionally, since elements of the Euclidian vector space are written in bold font within this dissertation, the vector composed of the large and the small components in $\vec{u}^{\gamma}_{lp}\left(r_\gamma\right)$ is indicated by a small arrow, and its components are indexed by s. Details of deriving the previous equation and the scalar-relativistic formalism are provided in the dissertation of Kurz [234]. Further information can be found in the paper of Koelling and Harmon [213] and the textbook of Singh and Nordström [68]. As far as the matching coefficients are concerned, only the large component solution is involved in the matching to the IR wave function. The contribution of the small component close to the MT sphere boundary is too small to be relevant for this procedure. In this sense, the small component depends on the large component and in general, the contribution of the former is smaller than that of the latter. Finally, the MT basis set in the scalar-relativistic approximation can be written as

$$\vec{\phi}^{(0)\gamma}_{\boldsymbol{k},\boldsymbol{G}}(\boldsymbol{r}) := \sum_{lmp} a^{\boldsymbol{Gk}\gamma}_{lmp} \begin{pmatrix} u^{1\gamma}_{lp}\left(r_\gamma\right) \\ u^{2\gamma}_{lp}\left(r_\gamma\right) \end{pmatrix} \mathrm{Y}_{lm}\left(\hat{\boldsymbol{r}}_\gamma\right) =: \sum_{lmp} a^{\boldsymbol{Gk}\gamma}_{lmp} \vec{u}^{\gamma}_{lp}\left(r_\gamma\right) \mathrm{Y}_{lm}\left(\hat{\boldsymbol{r}}_\gamma\right) , \qquad (5.15)$$

---

[6] An extension with less approximations [127] is e.g. the work of Yamagami [241].

relative to the non-relativistic MT part of equation (5.9). In order to be consistent with the non-relativistic basis set, the scalar-relativistic radial solutions obey the orthonormality condition

$$\int_0^{R_\gamma} r_\gamma^2 \sum_s u^{s\gamma}_{lp'}\big(r_\gamma\big) u^{s\gamma}_{lp}\big(r_\gamma\big)\,\mathrm{d}r_\gamma = \delta_{p'p}\,. \tag{5.16}$$

Moreover, the IR plane-wave basis stays unaffected, because relativistic corrections are not significant in this region. In summary, the unperturbed scalar-relativistic LAPW basis set, in which the logarithmic radial MT mesh ν is no longer suppressed, reads[7]

$$\phi^{(0)}_{\boldsymbol{k},\boldsymbol{G}}(\boldsymbol{r}) := \begin{cases} \dfrac{1}{\sqrt{\Omega}} \mathrm{e}^{\mathrm{i}(\boldsymbol{k}+\boldsymbol{G})\cdot\boldsymbol{r}}, & \boldsymbol{r} \in \mathrm{IR} \\ \displaystyle\sum_{lmp} a^{\boldsymbol{G}\boldsymbol{k}\gamma}_{lmp} \vec{u}^{\gamma}_{lp}(r_{\nu^\gamma}) \mathrm{Y}_{lm}\big(\hat{\boldsymbol{r}}_\gamma\big), & \boldsymbol{r} \in \mathrm{MT}_\gamma \end{cases} \tag{5.17a}$$

$$\phi^{(0)}_{\boldsymbol{k},\boldsymbol{G}}(\boldsymbol{r}) =: \begin{cases} \dfrac{1}{\sqrt{\Omega}} \mathrm{e}^{\mathrm{i}(\boldsymbol{k}+\boldsymbol{G})\cdot\boldsymbol{r}}, & \boldsymbol{r} \in \mathrm{IR} \\ \displaystyle\sum_{lmp} a^{\boldsymbol{G}\boldsymbol{k}\gamma}_{lmp} \vec{\varphi}^{\gamma}_{lmp}(\boldsymbol{r}_{\nu^\gamma}), & \boldsymbol{r} \in \mathrm{MT}_\gamma \end{cases} =: \begin{cases} \phi^{(0)\mathrm{IR}}_{\boldsymbol{k},\boldsymbol{G}}(\boldsymbol{r}) \\ \vec{\phi}^{(0)\gamma}_{\boldsymbol{k},\boldsymbol{G}}(\boldsymbol{r}_{\nu^\gamma}) \end{cases} . \tag{5.17b}$$

It must be emphasized that the scalar-relativistic approximation does not lead to a larger basis set and can therefore be considered highly efficient if applicable. [234]

Pros and cons

Although additional complexity arises in the LAPW basis relative to the plane-wave basis from a separate treatment of the MT spheres, and the number of LAPW basis functions exceeds those of the nonlinear KKR method [242], or the linear LMTO [206] method, the advantages of the LAPW method preponderate [3, 71]. Its convergence behavior surpasses that of a pure plane-wave basis in the demanding potential landscape of a bulk solid, film systems, chain structures, and single atoms. In addition, the asymptote problem of the APW basis is resolved, as the decoupling of the IR and MT wave function is avoided by the continuity of the radial or energy first-order derivative applied to the radial functions $u^{\gamma}_{l1}(r)$. Due to this continuity the surface integrals mentioned at the end of section 5.1 and displayed in equation (5.77) also vanish [71]. However, the introduction of the additional energy derivatives causes linearization errors [3]. Altogether, the LAPW basis enables widespread applications to arbitrary systems (see e.g. Singh and Nordström [68] or Martin [3] for an overview) by solving an efficient linear eigenvalue problem. Its high accuracy excels and also implies from the possibility and simplicity (non-linearity is avoided) of flexibly integrating all electrons and the complete effective potential with overcoming any shape approximations (see section 5.6 and especially section 5.3) [3]. Particularly prominent are calculations of systems incorporating transition metals and rare earth elements in which magnetic order or distorting the lattice induce slight energy differences underlying interesting features [3]. Likewise, the LAPW method has convinced with calculations involving surface and adsorbate structures [71, 243].

---

[7] As the small component of the MT basis does practically not contribute at the MT sphere boundary and the IR does not feature relativistic corrections, the small arrow is only on top of the MT basis functions.

5.3 All-Electron and Full-Potential Calculations

Density and potential expansions

Facing the challenge of rigorous calculations in complex systems, approximations at some point reach their limit leading to unsatisfactory results. One notable example is provided by the $1/r$ singularity of the potential close to the nuclei. In this area, the expansion of the wave function in a plane-wave basis only poorly works due to its bad convergence behavior, as noted in the introduction of the current chapter. Furthermore, it is not compatible with a variational approach, such as DFT described in chapter 2. The LAPW basis (see section 5.2) circumvents this problem, as in the MT spheres, the exact solutions of a Schrödinger equation, with potential relativistic corrections (Dirac equation), form the pivotal contribution. In addition, matching the interstitial partition to the MT spheres only requires solving linear equations, in contrast to the APW basis presented in section 5.1. It must be stressed that the choice of a more adequate basis set for the wave function mirrors likewise in the properties of the charge density and the potential [68]. Hence, a similar partitioning and expansion in plane wave or spherical harmonics appears and proves adequate (the index ν indicates the discrete MT mesh to set the stage for the following chapters)

$$\rho^{(0)}(\boldsymbol{r}) = \underbrace{\sum_{\boldsymbol{G}} \rho_{\mathrm{IR}}^{(0)}(\boldsymbol{G})\mathrm{e}^{\mathrm{i}\boldsymbol{G}\cdot\boldsymbol{r}}}_{\rho_{\mathrm{IR}}^{(0)}(\boldsymbol{r})} + \sum_{\gamma} \underbrace{\sum_{lm} \left[\rho_{\gamma}^{(0)}(r_{\nu\gamma})\right]_{lm} \mathrm{Y}_{lm}\left(\hat{\boldsymbol{r}}_{\gamma}\right)}_{\rho_{\gamma}^{(0)}(\boldsymbol{r})}, \tag{5.18}$$

$$V_{\mathrm{eff}}^{(0)}(\boldsymbol{r}) = \overbrace{\sum_{\boldsymbol{G}} V_{\mathrm{eff}}^{(0)\mathrm{IR}}(\boldsymbol{G})\mathrm{e}^{\mathrm{i}\boldsymbol{G}\cdot\boldsymbol{r}}}^{V_{\mathrm{eff}}^{(0)\mathrm{IR}}(\boldsymbol{r})} + \sum_{\gamma} \overbrace{\sum_{lm} \left[V_{\mathrm{eff}}^{(0)\gamma}(r_{\nu\gamma})\right]_{lm} \mathrm{Y}_{lm}\left(\hat{\boldsymbol{r}}_{\gamma}\right)}^{V_{\mathrm{eff}}^{(0)\gamma}(\boldsymbol{r})}. \tag{5.19}$$

Concept

These two expansions in combination with the LAPW basis for the wave functions enable one to treat *all electrons* accurately. Moreover, choosing the LAPW basis circumvents the use of shape approximations done in the potential and density, and instead involves the more rigorous *all-electron* charge density as well as the *full potential* (as described in section 5.5 and section 5.6) in the whole unit cell. Although the radial solutions are still determined with only the spherical part of the total effective MT potential, the Hamiltonian incorporates the complete potential and thereby the aforementioned singularity (see section 5.8). This elaborate concept is denoted as the *All-Electron Full-Potential Linearized Augmented Plane-Wave (All-Electron FLAPW)* [65, 218] method. [71]

Core- & valence-electron basis

The electrons are subdivided into core electrons and valence electrons. Core electrons feature eigenenergies lying so many Rydberg units below the Fermi energy that they are centered around the nucleus, as close as basically not to experience a non-spherical contribution of the potential. The core wave-functions are ideally (exceptions are addressed in section 5.5.1) localized to their MT spheres [71] and therefore not involved in bondings to other atoms [88] or overlapping with core electrons from neighboring MT spheres. Consequently, instead of expanding them in the LAPW basis, they are obtained from a Hamiltonian with a spherically symmetric potential, which describes an isolated atom, by utilizing a numeric shooting method. In general, they are calculated from the Dirac equation (see section 5.2) [68]. Finally, the core wave functions are usually orthogonal to the valence wave functions [68]. In contrast, the valence electrons are influenced by possible non-spherical contributions, correlated with the fact that their wave functions extend across the IR and MT spheres. Thus, they are described by the LAPW basis and the Hamiltonian setup employs the full effective potential. With their dependency on the spherical or the full effective potential, both the valence *and* the core electrons are included into the self-consistency iteration [68]. [71]

Core tails

Due to the theoretically stringent localization of the core wave functions in their MT spheres, the latter and the respective core energies do not depend[8] on the Bloch vector $\boldsymbol{k}$ and would therefore feature a constant dispersion relation [88]. In fact however, as a consequence of the long-range Coulomb interaction, tails, i.e., tiny contributions of the core wave functions, reach out of the MT spheres. Hence, they oppose the requirement of the aforementioned orthogonality between the MT valence and core state of the same orbital quantum number l to a certain extent. Large overlaps between core and valence states are usually given for semi-core states[9]. They feature a relatively short energy separation to valence states compared to the other core states (see section 5.4). These finite overlaps can result in "ghost bands" [244] above the actual core state energy, and indicate a significant core state contribution in a valence state. Ghost bands depend on the LAPW energy parameter E_l and result from its disadvantageous choice for a certain MT sphere radius, culminating in inappropriate radial solutions (see section 5.2) to describe the semi-core states in the valence band. However, ghost bands can be spotted by (i) a nearly constant dispersion, (ii) their orbital quantum number being identical to the respective core state, and (iii) the ghost-band-affected valence function being substantially confined to the MT sphere. The extension with LOs (see section 5.4) turns out to be the best way to overcome these difficulties. [68]

Basis parameters

Which states are attributed to the valence or the core spectrum can be steered, among other options, by the choice of E_l. A separate treatment of valence and core electrons excludes the core states from the dispersion relations so that the LAPW cutoff parameter can be chosen smaller. Intricate all-electron FLAPW implementations can feature plenty of parameters as a result of optimizations or their versatility. Nevertheless, some of those parameters are pivotal, in particular to control the LAPW basis or cutoffs of the density and the potential. Essentially in `FLEUR`, the number of plane-waves in the LAPW basis is set by $K_{\text{max}} \geq |\boldsymbol{k}+\boldsymbol{G}|$, while the number of IR expansion coefficients of the density in equation (5.18) and the potential in equation (5.19) is operated by $2K_{\text{max}} \leq G_{\text{max}} \geq |\boldsymbol{G}|$ [68, 88]. Furthermore, the number of spherical harmonics used is controlled by a maximal orbital quantum number $l_{\text{max},\gamma}$, and the partitioning of the LAPW basis set influenced by the MT sphere radii R_γ. A usual choice of R_γ is guided by (i) considering that the core states are restricted to the MT spheres as well as possible, (ii) the wave function, potential and density are optimally described by their IR or MT expansion, and (iii) discontinuities at the MT spheres are minimized [88]. A rule of thumb is given by the relation $l_{\text{max},\gamma} = R_\gamma K_{\text{max}}$ which ensures a balanced number of plane waves and spherical harmonics. Other key parameters are responsible for the density of the logarithmic radial meshes, both for the MT valence and the core states. Further refinements of the aforementioned parameters are addressed within the next sections, provided they become significantly relevant. Nonetheless, in order to ensure that outcomes of the FLAPW calculations are comparable, in particular the cutoff parameters must be converged, i.e., the results should not differ significantly anymore when further increasing those parameters. [68]

---

[8] Outside the representative unit cell, e.g. for supercells, Klüppelberg [88] introduces an additional factor $\exp(i\boldsymbol{k}\cdot\boldsymbol{R})$, entailing an artificial dependence on the Bloch factor $\boldsymbol{k}$. However, this index is suppressed hereinafter as the focus lies predominantly on the representative unit cell.

[9] They are typically relevant in materials involving rare earths, alkali metals, actinides or some transition metals. [68]

Benefits and relevance

As a consequence of the all-electron character, magnetism, nuclear quantities (for example hyperfine field, isomer and core-level shift) as well as 3d- and 4f-electrons are accurately dealt with. In addition, correlation, which is possibly insufficiently treated by the LDA, is organically integrated [128]. Apart from that, the general all-electron FLAPW method can be applied in various scenarios with basically any natural chemical elements from the periodic table involved. Several geometries beyond bulk systems, such as surfaces, organic and inorganic molecules, 1D geometries, to name but a few, or symmetries pose no problem [3]. Although ranked among the more elaborate electronic structure methods, the all-electron FLAPW method has acquired the reputation to represent the current benchmark for other methods [3, 70]. This is because of its highest accuracy as well as its general and widespread applicability in electronic structure calculations [3]. [71]

5.4 Local Orbitals

Motivation

Often, it proves reasonable to set the energy parameter E_l (see equations (5.4) and (5.10), as well as section 5.3) to a value lying close to the average of the relevant band ensemble. However, some systems feature core states, the energy of which is so high that they are not as localized as the other core states. For example, this is the case if 4f inner-transition metals or elements on the left-hand side of the periodic table are involved [71, 219]. Consequently, neglecting the non-spherical component of the effective potential for these core states turns out to be a bad approximation, especially as far as total energy calculations are concerned. Furthermore, semi-core states form bands with a low energy in the dispersion and hinder finding an optimal energy parameter which lives up to an accurate description of both the valence and the semi-core bands. In other scenarios, the energy distance of the highest and lowest lying bands (to be covered by the energy parameter E_l) can lead to a non-acceptable linearization error (see equation (5.8)), in particular for the bands with the largest energy difference to E_l. [68]

Alternative

In order to address the aforementioned problems, either several energy parameter sets are introduced (each attributed to one "window," cutting out a certain energy interval of the spectrum [71, 245]) or the LAPW basis set is extended by *Local Orbitals* (LOs) [219]. The former is obsolete and further details can be found in Singh and Nordström [68], whereas the more powerful and better-performing LO solution is well-established in the `FLEUR` code [69][10] and other implementations. Using LOs provides more variational freedom and can facilitate or allow for converging the basis set. [68]

Concept

The basis function of an LO is given by the linear combination

$$\phi^{\gamma l_{\tilde{p}}}_{\boldsymbol{k},\boldsymbol{G}_{\tilde{p}}}\left(\boldsymbol{r}_{\gamma}\right) = \sum_{m}\left(a^{\boldsymbol{G}_{\tilde{p}}\boldsymbol{k}\gamma}_{lm1}u^{\gamma}_{l1}(r_{\nu^{\gamma}}) + a^{\boldsymbol{G}_{\tilde{p}}\boldsymbol{k}\gamma}_{lm2}u^{\gamma}_{l2}(r_{\nu^{\gamma}}) + a^{\boldsymbol{G}_{\tilde{p}}\boldsymbol{k}\gamma}_{lm\tilde{p}}u^{\gamma}_{l\tilde{p}}(r_{\nu^{\gamma}})\right)\mathrm{Y}_{lm}\left(\hat{\boldsymbol{r}}_{\gamma}\right). \tag{5.20}$$

Since LOs are not relevant in this thesis, the scalar-relativistic approximation is not considered at this point. Comparing it with the muffin-tin LAPW basis function in equation (5.9), a third radial function $u^{\gamma}_{l\tilde{p}}\left(R_{\gamma}\right)$ with its own energy parameter, which can be set to the energy of the problematic states, is added. The matching coefficients standing in front of the latter radial

---

[10] In the `FLEUR` code, LOs have basically been programmed by Kurz [233].

solutions are subject to the conditions

$$\mathfrak{a}_{lm1}^{\tilde{p}\boldsymbol{k}\gamma} u_{l1}^{\gamma}\big(R_\gamma\big) + \mathfrak{a}_{lm2}^{\tilde{p}\boldsymbol{k}\gamma} u_{l2}^{\gamma}\big(R_\gamma\big) + \mathfrak{a}_{lm3}^{\tilde{p}\boldsymbol{k}\gamma} u_{l\tilde{p}}^{\gamma}\big(R_\gamma\big) = 0 \tag{5.21a}$$

$$\mathfrak{a}_{lm1}^{\tilde{p}\boldsymbol{k}\gamma} \frac{\partial u_{l1}^{\gamma}(r_{\nu^\gamma})}{\partial r_{\nu^\gamma}}\bigg|_{r_{\nu^\gamma}=R_\gamma} + \mathfrak{a}_{lm2}^{\tilde{p}\boldsymbol{k}\gamma} \frac{\partial u_{l2}^{\gamma}(r_{\nu^\gamma})}{\partial r_{\nu^\gamma}}\bigg|_{r_{\nu^\gamma}=R_\gamma} + \mathfrak{a}_{lm3}^{\tilde{p}\boldsymbol{k}\gamma} \frac{\partial u_{l\tilde{p}}^{\gamma}(r_{\nu^\gamma})}{\partial r_{\nu^\gamma}}\bigg|_{r_{\nu^\gamma}=R_\gamma} = 0 \tag{5.21b}$$

$$\int_0^{R_\gamma} r_{\nu^\gamma}^2 \Big(\mathfrak{a}_{lm1}^{\tilde{p}\boldsymbol{k}\gamma} u_{l1}^{\gamma}(r_{\nu^\gamma}) + \mathfrak{a}_{lm2}^{\tilde{p}\boldsymbol{k}\gamma} u_{l2}^{\gamma}(r_{\nu^\gamma}) + \mathfrak{a}_{lm3}^{\tilde{p}\boldsymbol{k}\gamma} u_{l\tilde{p}}^{\gamma}(r_{\nu^\gamma})\Big)\, \mathrm{d}r_{\nu^\gamma} = 1\,. \tag{5.21c}$$

The LO basis set which is fully located within the MT sphere boundary must vanish at the MT sphere boundary, as ensured by equation (5.21a). Furthermore, the same holds true for the radial derivative of the LO basis set, evaluated at the MT sphere boundary as stated by equation (5.21b). Moreover, the LO basis is normed which is ensured by the condition in equation (5.21c). This set of three equations (5.21) uniquely determines the three matching coefficients contained within, therefore the LO extension does not require new boundary conditions. [71]

Symmetry optimizations

However, in the `FLEUR` implementation, the symmetry of lattices can be exploited to speed up calculations. Exploiting inversion symmetry, the local orbitals must exhibit the same transformation behavior as plane-waves, which is ensured by [71]

$$a_{lm1}^{\boldsymbol{G}_{\tilde{p}}\boldsymbol{k}\gamma} = \mathrm{e}^{\mathrm{i}\left(\boldsymbol{k}+\boldsymbol{G}_{\tilde{p}}\right)\cdot\boldsymbol{\tau}_\gamma} \mathfrak{a}_{lm1}^{\tilde{p}\boldsymbol{k}\gamma} 4\pi \frac{1}{W} \mathrm{i}^l \mathrm{Y}_{lm}^{*}\Big(\widehat{\boldsymbol{k}+\boldsymbol{G}_{\tilde{p}}}\Big) \tag{5.22a}$$

$$a_{lm2}^{\boldsymbol{G}_{\tilde{p}}\boldsymbol{k}\gamma} = \mathrm{e}^{\mathrm{i}\left(\boldsymbol{k}+\boldsymbol{G}_{\tilde{p}}\right)\cdot\boldsymbol{\tau}_\gamma} \mathfrak{a}_{lm2}^{\tilde{p}\boldsymbol{k}\gamma} 4\pi \frac{1}{W} \mathrm{i}^l \mathrm{Y}_{lm}^{*}\Big(\widehat{\boldsymbol{k}+\boldsymbol{G}_{\tilde{p}}}\Big) \tag{5.22b}$$

$$a_{lm\tilde{p}}^{\boldsymbol{G}_{\tilde{p}}\boldsymbol{k}\gamma} = \mathrm{e}^{\mathrm{i}\left(\boldsymbol{k}+\boldsymbol{G}_{\tilde{p}}\right)\cdot\boldsymbol{\tau}_\gamma} \mathfrak{a}_{lm3}^{\tilde{p}\boldsymbol{k}\gamma} 4\pi \frac{1}{W} \mathrm{i}^l \mathrm{Y}_{lm}^{*}\Big(\widehat{\boldsymbol{k}+\boldsymbol{G}_{\tilde{p}}}\Big)\,, \tag{5.22c}$$

where

$$W = \left(\frac{\partial u_{l1}^{\gamma}(r_{\nu^\gamma})}{\partial r_{\nu^\gamma}}\bigg|_{r_{\nu^\gamma}=R_\gamma} u_{l2}\big(R_\gamma\big) - u_{l1}\big(R_\gamma\big) \frac{\partial u_{l2}^{\gamma}(r_{\nu^\gamma})}{\partial r_{\nu^\gamma}}\bigg|_{r_{\nu^\gamma}=R_\gamma} \right)\,, \tag{5.22d}$$

and the final matching coefficients on the left sides define those in equation (5.20). Equations (5.22) connect the local orbitals to the angular part of the virtual plane-waves, which is extracted utilizing the plane-wave expansion in equation (5.5). Each local orbital requires one virtual plane wave. The latter is labelled by an additional reciprocal basis vector $\boldsymbol{G}_{\tilde{p}}$, and within the complete set of virtual plane waves, they must be linearly independent.

Properties

Furthermore, each LO comprises of $2l+1$ basis functions, due to the dependence of the spherical harmonics on both the orbital quantum number l and the magnetic quantum number m [88]. The orthogonality of the LO basis functions with respect to the LAPW basis functions is not ensured, because on the one hand the complete radial part in equation (5.20) does not fulfill an equation analogous to equation (5.10). On the other hand, all radial functions in equation (5.20) have a finite contribution in general [88]. Within the scope of this dissertation, only systems that do not necessarily require LOs are of relevance. Therefore, LOs are not considered within the following sections and chapters. Details of the LO extension within the FLAPW implementation `FLEUR` are for instance provided by Kurz [233]. [68]

5.5 Determining the Charge Density

Occupation number and $\boldsymbol{k}$-set

In periodic structures, the valence electron charge density is obtained from the Kohn–Sham wave functions (5.1) with Bloch character $\boldsymbol{k}$ and can therefore be evaluated by the integral

$$\rho^{(0)}(\boldsymbol{r}) = \frac{2}{\Omega}\int_{\Omega}\sum_{n|\epsilon_{\boldsymbol{k},n}<E_{\mathrm{F}}}\left|\Psi^{(0)}_{\boldsymbol{k},\boldsymbol{n}}(\boldsymbol{r})\right|^2 \mathrm{d}^3k \rightarrow 2\sum_{\boldsymbol{k},n} f^{(0)}_{\boldsymbol{k},n}\Psi^{*(0)}_{\boldsymbol{k},n}(\boldsymbol{r})\Psi^{(0)}_{\boldsymbol{k},n}(\boldsymbol{r}) \tag{5.23}$$

over the Brillouin zone Ω with its volume Ω. The integration over the $\boldsymbol{k}$-point continuum is normally either realized by the tetrahedron method [246–248] or the special points [249] method. In the latter case (indicated by the → in equation (5.23)), a specific grid of $\boldsymbol{k}$-points is determined, on the mesh points of which the valence charge density is evaluated. Afterwards, all these results are weighted by $f^{(0)}_{\boldsymbol{k},n}$ and summed (additional symmetry optimizations are discussed in section 5.7). Relevant are those Kohn–Sham wave functions, whose Kohn–Sham eigenvalues $\epsilon_{\boldsymbol{k},n}$ (see section 2.2.1) are smaller than the Fermi energy[11] E_{F}. Moreover, the occupation of band n expresses through a binary integer for insulators and semiconductors (both material classes are characterized by an energy band gap, incorporating the Fermi energy between valence and conduction bands), reflecting the step-function character of the Fermi function at temperature $T = 0$ [88]. In contrast, metals feature bands crossing the Fermi energy, i.e., depending on the Bloch vector $\boldsymbol{k}$, sudden changes between occupied and unoccupied states occur [88]. This badly harmonizes with the discrete sum in the special points method, because actually the special points method requires the integrands to be periodic and feature no rapid variations. Consequently, a larger set of $\boldsymbol{k}$-points becomes necessary to converge the summation in equation (5.23). However, a temperature broadening of the Fermi function implies fractional occupation numbers, smoothens the transition from occupied to unoccupied states and enhances the convergence for the aforementioned case [88]. Furthermore, the charge density should be independent of $N_{\boldsymbol{k}}$, the number of terms in the $\boldsymbol{k}$-point sum [68]. Therefore, the occupation factor is divided by $N_{\boldsymbol{k}}$, yielding the weighted occupation factor $f^{(0)}_{\boldsymbol{k},n}$ [68]. Further technical details are for instance provided in the textbook of Singh and Nordström [68]. Finally, due to the spin degeneracy this dissertation restricts to, a factor of 2 is multiplied in equation (5.23). [71]

Outline

As mentioned in particular within section 5.3, the core states are not expanded in the LAPW basis in contrast to the valence states (see section 5.2). This suggests splitting the charge density

$$\rho^{(0)}(\boldsymbol{r}) = \rho^{(0)}_{\mathrm{c}}(\boldsymbol{r}) + 2\sum_{\boldsymbol{k},n} f^{(0)}_{\boldsymbol{k},n}\sum_{\boldsymbol{G}'\boldsymbol{G}} z^{*(0)}_{\boldsymbol{G}'}(\boldsymbol{k},n) z^{(0)}_{\boldsymbol{G}}(\boldsymbol{k},n)\phi^{(0)*}_{\boldsymbol{k},\boldsymbol{G}'}(\boldsymbol{r})\phi^{(0)}_{\boldsymbol{k},\boldsymbol{G}}(\boldsymbol{r})\,. \tag{5.24}$$

into a core part $\rho^{(0)}_{\mathrm{c}}(\boldsymbol{r})$ which is discussed in section 5.5.1. The remaining valence part is addressed in section 5.5.2, while the LAPW basis functions $\phi^{(0)}_{\boldsymbol{k},\boldsymbol{G}}(\boldsymbol{r})$ are given by equations (5.17).

---

[11] The technical details of determining the Fermi energy E_{F} are for example provided by the textbook of Singh and Nordström [68].

5.5.1 Core Contribution and the Origin of Core Tails

Core-electron density

The core contribution of the charge density

$$\rho_{\mathrm{c}}^{(0)}(\boldsymbol{r}) = \sum_{\gamma}\sum_{\mathfrak{p}}\left|\Psi_{\mathfrak{p}}^{\gamma}\left(\boldsymbol{r}_{\nu_{\mathrm{c}}^{\gamma}}\right)\right|^{2} \tag{5.25a}$$

$$= \sum_{\gamma}\rho_{\gamma,\mathrm{c}}^{(0)}\left(r_{\nu_{\mathrm{c}}^{\gamma}}\right)\mathrm{Y}_{00}\left(\hat{\boldsymbol{r}}_{\gamma}\right) \tag{5.25b}$$

derives from the core states $\Psi_{\mathfrak{p}}^{\gamma}\left(\boldsymbol{r}_{\nu_{\mathrm{c}}^{\gamma}}\right)$ of MT γ (see section 5.3). The index $\mathfrak{p}$ summarizes all quantum numbers arising in the spherical problem and simply enumerates the core states according to their energy. Moreover expanding the charge density in a series of spherical harmonics, the constant Y_{00} suffices, because the core wave functions are eigenstates of a Hamiltonian with a spherical potential. Within the `FLEUR` implementation [69], the numerical solution of the differential equation for the core states takes place on a radial mesh $r_{\nu_{\mathrm{c}}^{\gamma}}$, exceeding the separate radial mesh of the LAPW basis $r_{\nu^{\gamma}}$ in the MT spheres [88]. The complete core density $\rho_{\mathrm{c}}^{(0)}(\boldsymbol{r})$ contains the core densities $(4\pi)^{-1/2}\rho_{\gamma,\mathrm{c}}^{(0)}\left(r_{\nu_{\mathrm{c}}^{\gamma}}\right)$ of every MT γ in the unit cell. In systems with core tails [250], an additional contribution to the valence density both in the IR and the MT spheres must be accounted for [68]. [88]

Core tails

Due to their construction, core states enable differentiation of arbitrary order not featuring any discontinuity [88]. In order to calculate the IR contribution resulting from a core state in MT γ, its underlying spherical potential is augmented to the IR on condition that it is matched continuously at the MT sphere boundary. In the `FLEUR` program this spherical potential approximates a zero asymptote for large $r_{\nu_{\mathrm{c}}^{\gamma}}$, possibly already intersecting with the IR [88]. Furthermore, the real charge density in the MT sphere is substituted by a pseudo charge-density [88]. The latter has the requirement of equalling the real charge density in the IR, but to have a faster converging Fourier expansion so that [88]

$$\rho_{\mathrm{IR,ct}}^{(0)}(\boldsymbol{G}) = \frac{1}{\Omega}\int_{\gamma}\rho_{\mathrm{c}}^{(0),\mathrm{ps}}\left(\boldsymbol{r}_{\gamma}\right)\mathrm{e}^{-\mathrm{i}\boldsymbol{G}\cdot\boldsymbol{r}}\,\mathrm{d}^{3}r \tag{5.26a}$$

$$= \sum_{\gamma}\underbrace{\mathrm{e}^{-\mathrm{i}\boldsymbol{G}\cdot\boldsymbol{\tau}_{\gamma}}}_{S_{\gamma}(\boldsymbol{G})}\underbrace{\frac{1}{\Omega}\int_{\gamma}\rho_{\mathrm{c},\gamma}^{(0),\mathrm{ps}}\left(\boldsymbol{r}_{\gamma}\right)\mathrm{e}^{-\mathrm{i}\boldsymbol{G}\cdot\boldsymbol{r}_{\gamma}}\,\mathrm{d}^{3}r}_{F_{\gamma}(\boldsymbol{G})}\ . \tag{5.26b}$$

Within the last equation, a coordinate transformation to the local coordinate system of the MT spheres $\boldsymbol{r}_{\gamma} = \boldsymbol{r} - \boldsymbol{\tau}_{\gamma}$ is exploited, and leads to a definition of the structure factor $S_{\gamma}(\boldsymbol{G})$ as well as the form factor $F_{\gamma}(\boldsymbol{G})$ [88]. The complete IR core-tail density sums up the IR core-tail contributions of all MT spheres γ. Once given the plane-wave representation, it can be augmented to the neighboring MT spheres with the Rayleigh expansion in equation (5.5) [88]. The coefficients of the spherical harmonic expansion read [88]

$$\left[\rho_{\gamma,\mathrm{ct}}^{(0)\gamma'}\left(r_{\nu^{\gamma}}\right)\right]_{lm} = \sum_{\boldsymbol{G}}S_{\gamma'}(\boldsymbol{G})F_{\gamma'}(\boldsymbol{G})\oint_{\partial\gamma}\mathrm{Y}_{lm}^{*}\left(\hat{\boldsymbol{r}}_{\gamma}\right)\mathrm{e}^{\mathrm{i}\boldsymbol{G}\cdot\boldsymbol{r}}\,\mathrm{d}S \tag{5.27a}$$

$$= 4\pi\mathrm{i}^{l}\sum_{\boldsymbol{G}}S_{\gamma'}(\boldsymbol{G})F_{\gamma'}(\boldsymbol{G})S_{\gamma}^{*}(\boldsymbol{G})\mathrm{Y}_{lm}^{*}\left(\hat{\boldsymbol{G}}\right)\mathrm{j}_{l}\left(Gr_{\nu^{\gamma}}\right)\ . \tag{5.27b}$$

The superposition of all core-tails entering the MT sphere γ and originating from any other MT γ' leads to the MT core-tail contribution $\rho_{\gamma,\mathrm{ct}}^{(0)}(\boldsymbol{r}_{\nu^{\gamma}})$. At this point, attention must be paid to subtract the pseudo charge-density and add the actual charge density in the MT sphere γ. Technical details of the core charge-density implementation are for example provided in the appendix of reference [88]. [68]

5.5.2 Valence Contribution

Interstitial part

The IR part of the charge density

$$\rho^{(0)}_{\mathrm{IR}}(\boldsymbol{r}) = \rho^{(0)}_{\mathrm{IR,\ v}}(\boldsymbol{r}) + \rho^{(0)}_{\mathrm{IR,\ ct}}(\boldsymbol{r}) \tag{5.28}$$

subdivides into a valence part with Kohn–Sham wave-function expansion coefficients, and a potential core-tail part [68]. While the latter is set up in section 5.5.1, the former

$$\rho^{(0)}_{\mathrm{IR,\ v}}(\boldsymbol{r}) = \frac{2}{\Omega}\sum_{\boldsymbol{k},n} f^{(0)}_{\boldsymbol{k},n} \sum_{\boldsymbol{G}'} z^{*(0)}_{\boldsymbol{G}'}(\boldsymbol{k},n)\mathrm{e}^{-\mathrm{i}(\boldsymbol{k}+\boldsymbol{G}')\cdot\boldsymbol{r}} \sum_{\boldsymbol{G}} z^{(0)}_{\boldsymbol{G}}(\boldsymbol{k},n)\mathrm{e}^{\mathrm{i}(\boldsymbol{k}+\boldsymbol{G})\cdot\boldsymbol{r}} \tag{5.29a}$$

derives from equation (5.24) by inserting the LAPW basis from equation (5.17). Next, an index $\boldsymbol{G}'' := \boldsymbol{G} - \boldsymbol{G}'$ is defined so that the index $\boldsymbol{G}$ can be substituted

$$\rho^{(0)}_{\mathrm{IR,\ v}}(\boldsymbol{r}) = \frac{2}{\Omega}\sum_{\boldsymbol{k},n} f^{(0)}_{\boldsymbol{k},n} \sum_{\boldsymbol{G}'} \sum_{\boldsymbol{G}''+\boldsymbol{G}'} z^{*(0)}_{\boldsymbol{G}'}(\boldsymbol{k},n) z^{(0)}_{\boldsymbol{G}''+\boldsymbol{G}'}(\boldsymbol{k}',n)\mathrm{e}^{\mathrm{i}\boldsymbol{G}''\cdot\boldsymbol{r}} \,. \tag{5.29b}$$

Using a FFT algorithm for exploiting the convolution theorem, the wave-function expansion coefficients can be combined to the IR expansion coefficients of the charge density

$$\rho^{(0)}_{\mathrm{IR,\ v}}(\boldsymbol{r}) =: \sum_{\boldsymbol{G}''} \rho^{(0)}_{\mathrm{IR,\ v}}(\boldsymbol{G}'')\mathrm{e}^{\mathrm{i}\boldsymbol{G}''\cdot\boldsymbol{r}} \,. \tag{5.29c}$$

An alternative to the FFT method is to simply evaluate the sums in equation (5.29b). [71]

Numerical cutoffs

Since an infinite basis set is impossible to realize in the computation, only those $\boldsymbol{G}$ and $\boldsymbol{G}'$ in equations (5.29) fulfilling $|\boldsymbol{k}+\boldsymbol{G}| \leq K_{\text{max}}$ or $|\boldsymbol{k}+\boldsymbol{G}'| \leq K_{\text{max}}$ are considered, as already touched in section 5.3. In turn, the IR charge density is a product of two quantities, whose expansion is truncated at K_{max}, implying its cutoff condition $|\boldsymbol{G}''| \leq 2K_{\text{max}}$ [71]. However, the core-tail contribution $\boldsymbol{\rho}^{(0)}_{\mathrm{IR,\ ct}}(\boldsymbol{r})$ can have contributions in its plane-wave expansions for $2K_{\text{max}} < |\boldsymbol{G}''| \leq G_{\text{max}}$ [127]. Therefore in practice, the expansion in equation (5.18) fulfills $|\boldsymbol{G}| \leq G_{\text{max}}$.

Scalar large matching coefficients

For the MT coefficients of the charge density in atom γ

$$A^{\boldsymbol{k}\gamma n}_{lmp} := \sum_{\boldsymbol{G}} z^{(0)}_{\boldsymbol{G}}(\boldsymbol{k},n) a^{\boldsymbol{G}\boldsymbol{k}\gamma}_{lmp} \tag{5.30}$$

is defined, consisting of MT matching coefficients (see equation (5.9)) and the Kohn–Sham wave-function expansion coefficients. Basically, the reciprocal lattice vectors $\boldsymbol{G}$ are contracted and substituted by the bands n. This is motivated by the fact that the number of bands required in a calculation is approximately tenth of the number of reciprocal lattice-vectors [127]. Similar to the IR contribution of the charge density, the MT charge density again has two parts [68]

Muffin-tin part

$$\rho^{(0)}_{\gamma}(\boldsymbol{r}) = \rho^{(0)}_{\gamma,\mathrm{v}}(\boldsymbol{r}) + \rho^{(0)}_{\gamma,\mathrm{ct}}(\boldsymbol{r}) \,. \tag{5.31}$$

The first one is the valence contribution, the second part is the overlap of core-tails reaching into MT γ and originating from the neighboring MT spheres (cf. section 5.5.1) [68]. In order to gain the valence expansion coefficient of the spherical harmonic expansion in equation (5.18), the charge density in MT γ (see equation (5.24)) is projected onto an arbitrary spherical harmonic $\mathrm{Y}_{lm}\left(\hat{\boldsymbol{r}}_\gamma\right)$

$$\left[\rho^{(0)}_{\gamma,\mathrm{v}}(\boldsymbol{r}_{\nu\gamma})\right]_{lm} = \oint_{\partial\gamma} \mathrm{Y}^*_{lm}\left(\hat{\boldsymbol{r}}_\gamma\right)\rho^{(0)}_{\gamma,\mathrm{v}}(\boldsymbol{r}_{\nu\gamma})\,\mathrm{d}\Omega\ . \tag{5.32a}$$

By using equation (5.17) and expressing the scalar product, due to the scalar-relativistic approximation (cf. equation (5.2)), in the sum over s, this yields

$$\begin{aligned}\left[\rho^{(0)}_{\gamma,\mathrm{v}}(\boldsymbol{r}_{\nu\gamma})\right]_{lm} = &\sum_{l''m''p''}\sum_{l'm'p'} 2\sum_{\boldsymbol{k},n} f^{(0)}_{\boldsymbol{k},n} A^{*\boldsymbol{k}\gamma n}_{l'm'p'} A^{\boldsymbol{k}\gamma n}_{l''m''p''} \oint_{\partial\gamma} \mathrm{Y}^*_{lm}\left(\hat{\boldsymbol{r}}_\gamma\right)\sum_{s} \\ &\times \left(\sum_{l'm'p'} u^{s\gamma}_{l'p'}(r_{\nu\gamma})\mathrm{Y}^*_{l'm'}\left(\hat{\boldsymbol{r}}_\gamma\right)\right)\left(\sum_{l''m''p''} u^{s\gamma}_{l''p''}(r_{\nu\gamma})\mathrm{Y}^*_{l''m''}\left(\hat{\boldsymbol{r}}_\gamma\right)\right)\mathrm{d}\Omega\ . \end{aligned} \tag{5.32b}$$

Finally, reordering results in

$$\left[\rho^{(0)}_{\gamma,\mathrm{v}}(\boldsymbol{r}_{\nu\gamma})\right]_{lm} = \sum_{l'p'l''p''}\sum_{s} u^{s\gamma}_{l'p'}(r_{\nu\gamma})u^{s\gamma}_{l''p''}(r_{\nu\gamma}) \sum_{m'm''} G^{m''\,m\,m'}_{l''\,\,l\,\,l'}\, 2\sum_{\boldsymbol{k},n} f^{(0)}_{\boldsymbol{k},n} A^{*\boldsymbol{k}\gamma n}_{l'm'p'} A^{\boldsymbol{k}\gamma n}_{l''m''p''} \tag{5.32c}$$

which contains the Gaunt coefficients

$$G^{m''\,m\,m'}_{l''\,\,l\,\,l'} = \oint_{\partial\gamma} \mathrm{Y}^*_{l''m''}\left(\hat{\boldsymbol{r}}_\gamma\right)\mathrm{Y}_{lm}\left(\hat{\boldsymbol{r}}_\gamma\right)\mathrm{Y}_{l'm'}\left(\hat{\boldsymbol{r}}_\gamma\right)\mathrm{d}S\ , \tag{5.32d}$$

the properties of which can e.g. be found in the textbooks of Martin [3] or Singh and Nordström [68]. Since this dissertation discusses only results of systems in which LOs are not urgently required, the implementation of LOs to the charge density in `FLEUR` is not addressed at this point, but can for instance be found in the work of Kurz [233]. All sums in equations (5.32) over orbital or magnetic quantum numbers are governed by the cutoff $l_{\mathrm{max},\gamma}$ mentioned in section 5.3. [71]

5.6 Calculating the Full Effective Potential

Outline

Similarly to the charge density, addressed in section 5.5, the effective potential requires an accurate expansion [3] in plane waves and spherical harmonics, as displayed by equation (5.19). The effective potential is defined in equation (2.3b) as a sum of the external, the Hartree and the xc potentials. In turn, the sum of the Hartree potential and the external potential is known as the Coulomb potential [68]

$$V^{(0)}_{\mathrm{Cou}}(\boldsymbol{r}) = \int \frac{\rho(\boldsymbol{r}')}{|\boldsymbol{r}-\boldsymbol{r}'|}\,\mathrm{d}^3r' - \sum_{\gamma\boldsymbol{R}} \frac{Z}{\left|\boldsymbol{r}-\left(\boldsymbol{\tau}_{\gamma_{\boldsymbol{R}}}+\boldsymbol{R}\right)\right|}\ . \tag{5.33}$$

In the all-electron FLAPW implementation `FLEUR` [69], the plane-wave and spherical-harmonic expansion coefficients of the Coulomb potential are determined with a method developed by Weinert [64], which is outlined in section 5.6.1 [234]. Further details of the xc-potential expansion coefficients are given in section 5.6.2.

5.6.1 The Method of Weinert for the Coulomb Potential

Motivation

The Coulomb potential is related to the charge density by the Poisson equation

$$\Delta V^{(0)}_{\mathrm{Cou}}(\boldsymbol{r}) = -4\pi\rho^{(0)}(\boldsymbol{r}) \,, \tag{5.34}$$

determining the Coulomb potential as

$$V^{(0)}_{\mathrm{Cou}}(\boldsymbol{r}) = \sum_{\boldsymbol{G}} \frac{4\pi\rho^{(0)}(\boldsymbol{G})}{|\boldsymbol{G}|^2} \mathrm{e}^{\mathrm{i}\boldsymbol{G}\cdot\boldsymbol{r}} \,, \tag{5.35}$$

with the Fourier coefficients of the charge density $\rho^{(0)}(\boldsymbol{G})$. In the all-electron FLAPW method (cf. section 5.3), the precise description of the Coulomb potential proves to be a tough challenge, because the plane-wave expansion does not converge near the nuclei. But Weinert [64] has developed a method meeting the challenges of the rapidly varying core-electron charge density or the point-like charge density of the nuclei, and constituting an alternative to the widespread Ewald summation method. [68]

Concept

Weinert utilizes the fact that different charge densities in a MT γ can have the same multipole moments

$$\mathfrak{q}^{\gamma}_{lm} = \int_{\gamma} \mathrm{Y}^{*}_{lm}(\hat{\boldsymbol{r}}) r^{l} \rho^{(0)}(\boldsymbol{r}) \,\mathrm{d}^3 r \,, \tag{5.36}$$

which define the same expansion

$$V^{(0)}_{\mathrm{Cou}}(\boldsymbol{r}) = \sum_{lm} \frac{4\pi}{2l+1} \frac{\mathfrak{q}_{lm}}{r^{l+1}} \mathrm{Y}_{lm}(\hat{\boldsymbol{r}}) \tag{5.37}$$

of the Coulomb potential in spherical harmonics. Furthermore, the genuine charge density

$$\rho^{(0)}(\boldsymbol{r}) = \rho^{(0)}_{\mathrm{IR}}(\boldsymbol{r})\Theta(\boldsymbol{r} \in \mathrm{IR}) + \sum_{\gamma} \rho^{(0)}_{\gamma}(\boldsymbol{r})\Theta\big(\boldsymbol{r} \in \mathrm{MT}_{\gamma}\big) \tag{5.38a}$$

$$= \rho^{(0)}_{\mathrm{IR}}(\boldsymbol{r}) + \left(\sum_{\gamma} \rho^{(0)}_{\gamma}(\boldsymbol{r}) - \rho^{(0)}_{\mathrm{IR}}(\boldsymbol{r})\right)\Theta\big(\boldsymbol{r} \in \mathrm{MT}_{\gamma}\big) \tag{5.38b}$$

can be subdivided according to the known LAPW partitioning, while the step functions confine terms to the IR and the MT spheres. For a more comfortable derivation, the IR representation of the charge density is in addition evaluated in the whole unit cell, and afterwards subtracted from all MTs γ. [64]

Interstitial part

It turns out that the real charge density in the MT spheres has a badly-converging Fourier expansion [64]. Therefore, it is substituted by a more adequate pseudo charge-density to set up the IR plane-wave expansion of the Coulomb potential [64]. Its multipole moments (based on equations (5.38b) and (5.36)) are given by

$$\mathfrak{q}^{\gamma,\mathrm{ps}}_{lm} = \mathfrak{q}^{\gamma}_{lm} - \mathfrak{q}^{\gamma,\mathrm{IR}}_{lm} \,, \tag{5.39}$$

where

$$\mathfrak{q}^{\gamma,\mathrm{IR}}_{lm} = \frac{\sqrt{4\pi}}{3} R^{3}_{\gamma} \rho^{(0)}_{\mathrm{IR}}(\boldsymbol{G}=\boldsymbol{0})\delta_{l0}\delta_{m0} + 4\pi\mathrm{i}^{l} R^{l+3}_{\gamma} \sum_{\boldsymbol{G}|\boldsymbol{G}\neq\boldsymbol{0}} \rho^{(0)}_{\mathrm{IR}}(\boldsymbol{G}) \frac{\mathrm{j}_{l+1}\big(|\boldsymbol{G}|R_{\gamma}\big)}{|\boldsymbol{G}|R_{\gamma}} \mathrm{e}^{\mathrm{i}\boldsymbol{G}\cdot\boldsymbol{\tau}_{\gamma}} \mathrm{Y}^{*}_{lm}\big(\hat{\boldsymbol{G}}\big) \tag{5.40}$$

is obtained from the Rayleigh decomposition (5.5) of the IR charge density (5.28) in the MT spheres. The sum over the reciprocal $\boldsymbol{G}$ features the condition (indicated by $|$ hereinafter, which is borrowed from the nomenclature of sets) that $\boldsymbol{G} = \boldsymbol{0}$ is excluded. It is feasible to find a pseudo-density sharing the same multipole moments (5.39) with the original charge density in the MT sphere. However, the pseudo-density features a significantly rapider convergence in reciprocal space relative to the true density. The Fourier coefficients of this pseudo-density

$$n_{\mathrm{Cou}}^{\mathrm{ps}}(\boldsymbol{G}) = \rho_{\mathrm{IR}}^{(0)}(\boldsymbol{G}) + \delta_{\boldsymbol{G}\boldsymbol{0}}\delta_{l0}\delta_{m0}\frac{\sqrt{4\pi}}{\Omega}\sum_{\gamma}\mathfrak{q}_{lm}^{\gamma,\mathrm{ps}} \tag{5.41}$$
$$+\left(1-\delta_{\boldsymbol{G}\boldsymbol{0}}\right)\frac{4\pi}{\Omega}\sum_{lm\gamma}\frac{(-\mathrm{i})^{l}(2l+2N+3)!!}{(2l+1)!!}\frac{\mathrm{j}_{l+N+1}\left(|\boldsymbol{G}|R_{\gamma}\right)}{\left(|\boldsymbol{G}|R_{\gamma}\right)^{N+1}}\mathrm{e}^{-\mathrm{i}\boldsymbol{G}\cdot\boldsymbol{\tau}_{\gamma}}\mathrm{Y}_{lm}\left(\hat{\boldsymbol{G}}\right)\mathfrak{q}_{lm}^{\gamma,\mathrm{ps}}$$

are inserted into the solution of the Poisson equation in equation (5.35) yielding the true Coulomb potential in the IR

$$V_{\mathrm{Cou}}^{(0)\mathrm{IR}}(\boldsymbol{r}) = \sum_{\boldsymbol{G}|\boldsymbol{G}\neq\boldsymbol{0}}\frac{4\pi n_{\mathrm{Cou}}^{\mathrm{ps}}(\boldsymbol{G})}{|\boldsymbol{G}|^{2}}\mathrm{e}^{\mathrm{i}\boldsymbol{G}\cdot\boldsymbol{r}} =: \sum_{\boldsymbol{G}\neq\boldsymbol{0}}V_{\mathrm{Cou}}^{(0)\mathrm{IR}}(\boldsymbol{G})\mathrm{e}^{\mathrm{i}\boldsymbol{G}\cdot\boldsymbol{r}}\,. \tag{5.42}$$

Furthermore, the pseudo charge-density incorporates a parameter N, which Weinert introduces and examines in his publication [64, 68]. `FLEUR` [69] stores the optimal parameters in combination with the orbital quantum number l, hence N is constant within a respective MT sphere. Moreover, the Fourier transform of equation (5.34) reveals that an average charge neutrality $\rho_{\mathrm{IR}}^{(0)}(\boldsymbol{G}=\boldsymbol{0})$ must be imposed. Despite $V_{\mathrm{Cou}}^{(0)\mathrm{IR}}(\boldsymbol{G}=\boldsymbol{0})$ is not set, due to the periodic bulk system, this arbitrary shift of the potential is in general fixed to zero [71]. [88]

Muffin-tin part

The MT coefficients of the Coulomb potential in the MT sphere of atom γ are determined by the Dirichlet boundary value problem, utilizing the IR Coulomb potential at its MT sphere boundary

$$V_{\mathrm{Cou}}^{(0)\gamma}(\boldsymbol{r}) = \int_{\gamma}\left(\rho_{\gamma}^{(0)}(\boldsymbol{r}') - Z\mathrm{Y}_{00}\right)\mathcal{G}\left(\boldsymbol{r}_{\gamma},\boldsymbol{r}'_{\gamma}\right)\mathrm{d}^{3}r' - \frac{R_{\gamma}^{2}}{4\pi}\oint_{\partial\gamma}V_{\mathrm{Cou}}^{(0)\mathrm{IR}}\left(R_{\gamma}\right)\frac{\partial\mathcal{G}\left(\boldsymbol{r}_{\gamma},\boldsymbol{r}'_{\gamma}\right)}{\partial n}\,\mathrm{d}\Omega \tag{5.43a}$$

with the Green function ($r_{\gamma,<} := \min\left(r_{\gamma}, r'_{\gamma}\right)$ and $r_{\gamma,>} := \max\left(r_{\gamma}, r'_{\gamma}\right)$)

$$\mathcal{G}\left(\boldsymbol{r}_{\gamma},\boldsymbol{r}'_{\gamma}\right) = 4\pi\sum_{lm}\frac{\mathrm{Y}_{lm}^{*}\left(\hat{\boldsymbol{r}}'_{\gamma}\right)\mathrm{Y}_{lm}\left(\hat{\boldsymbol{r}}_{\gamma}\right)}{2l+1}\frac{r_{\gamma,<}^{l}}{r_{\gamma,>}^{l+1}}\left[1-\left(\frac{r_{\gamma,>}}{R_{\gamma}}\right)^{2l+1}\right] \tag{5.43b}$$

and the derivative

$$\left.\frac{\partial\mathcal{G}\left(\boldsymbol{r}_{\gamma},\boldsymbol{r}'_{\gamma}\right)}{\partial r'}\right|_{r'=R_{\gamma}} = -\frac{4\pi}{R_{\gamma}^{2}}\sum_{lm}\left(\frac{r_{\gamma}}{R_{\gamma}}\right)^{l}\mathrm{Y}_{lm}^{*}\left(\hat{\boldsymbol{r}}'_{\gamma}\right)\mathrm{Y}_{lm}\left(\hat{\boldsymbol{r}}_{\gamma}\right)\,. \tag{5.43c}$$

Decisive at this point is using the real charge which is composed of the nuclear charge Z and the charges of the electrons in the MT sphere, given by the MT charge density (see section 5.5). [88]

5.6.2 Exchange-Correlation Potential

Interstitial part

The calculation of the exchange-correlation (xc) potential strongly depends on the technical details of the xc-potential approximation chosen (see section 2.2.2). Generally however, it is calculated in real space due to its non-linear dependence on the charge density. Hence, the charge density is needed in its real space representation. Within a `FLEUR` [69] calculation, the charge density is given by its expansion coefficients, according to equation (5.18). Therefore, in the IR a FFT is used to transform the Fourier coefficients of the charge density to real space and to determine the Fourier expansion of the xc potential from real space. As there is a non-linear relation between the xc potential and the density, the cutoff $G_{\text{max}}^{\text{xc}} > G_{\text{max}}$ must be introduced for a better convergence of the calculation [88]. [71]

Muffin-tin part

For the MT region, the charge density is evaluated on the radial grid points and a set of well-chosen angular mesh points to make it available in real space. This enables one to find the real space representation of the xc potential in the MT spheres, which then can be projected onto a spherical harmonic with orbital quantum number l and magnetic quantum number m. Equations revealing more technical details are provided in the context of section 7.3.2. [71]

5.7 Exploiting Symmetry

Possible symmetry optimizations

The `FLEUR` program optimizes the representation of the LAPW wave function (section 5.2), Brillouin zone integrations (section 5.5), the charge density (section 5.5), and the effective potential (section 5.6), by considering the symmetries given by the system under investigation [234]. The latter fall into space group symmetries in the IR and point-group symmetries (not altering the atomic position) within the MT spheres. Furthermore, inversion symmetry makes complex quantities real, or symmetry operations can connect MT spheres containing the same atom type (equal atomic number). All these symmetries can on the one hand be encoded into the expansions of the charge density and the potential, and on the other hand into the matching coefficients of the wave functions or the set of discrete $\boldsymbol{k}$-points. However if possible, inversion symmetry in lattices is taken into account already in the setup of the system, namely by a well-educated choice of the unit cell-origin, serving as input for the DFT calculation. The adaptations of the LAPW basis coefficients in the MT relative to those introduced in equation (5.7) are postponed to section 5.8.2.

Outline

Section 5.7.1 presents the symmetry improvements to the Brillouin zone integrations such as in equation (5.5). The set of symmetrized basis functions for the charge density and the potential are called stars in the IR and lattice harmonics in the MT. Both are described in section 5.7.2. Although additionally considering symmetry in the DFT implementation involves certain effort, the benefit derived, e.g. a speed-up of run-time, better convergence, or decreased demand of storage, clearly outweighs. Redundant, i.e., equal or vanishing expansion coefficients, related or spotted by symmetry, are avoided, leading to an irreducible set of coefficients. [68]

5.7.1 Muffin-Tin Sphere Coordinates and Irreducible Brillouin Zone

Local coordinate system

In order to live up to the geometry of the MT spheres and exploit symmetry, a local spherical coordinate system is defined within them so that the MT centers are the origins of the local coordinate systems. Furthermore, the transformation from the global coordinate system of the unit cell (used for the IR) is given by $\boldsymbol{r}_{\gamma} = \boldsymbol{r} - \boldsymbol{\tau}_{\gamma}$. In polyatomic systems, the space group symmetry of the system can induce some of the MT spheres to have similar scalar fields, only differing by a rotation from the perspective of the global coordinate system in the unit cell. From the set of symmetry-related MT spheres, one can be identified as *representative* on condition that the remaining MT coordinate systems can be derived from it by a space group operation so that all atoms of this set have the same atom type [68, 71]. This aspect is depicted in figure 5.2. [68]

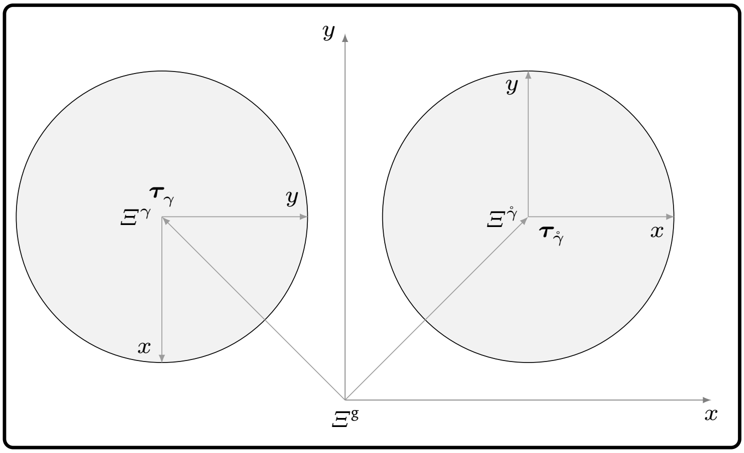

Figure 5.2: Symmetry-related MT spheres feature similar local coordinate systems, which are embedded in the global coordinate system $\varXi^{\mathrm{g}}$ of the unit cell. The local coordinate system $\varXi^{\gamma}$, the origin of which is located at $\boldsymbol{\tau}_{\gamma}$, differs from the local coordinate system $\varXi^{\mathring{\gamma}}$ of the representative MT sphere, whose origin is at $\boldsymbol{\tau}_{\mathring{\gamma}}$, in this example by a rotation of $^{3\pi}/_{2}$. The coordinate transformation from $\varXi^{\mathrm{g}}$ to e.g. $\varXi^{\mathring{\gamma}}$ is given by $\boldsymbol{r}_{\mathring{\gamma}} = \boldsymbol{r} - \boldsymbol{\tau}_{\mathring{\gamma}}$ [68]. Usually within the spheres, a spherical coordinate system is chosen. This 2D scheme is based on reference [71, figure 11].

Irreducible Brillouin zone

The special-point Brillouin-zone integration addressed in section 5.5 utilizes the rotational part of the point group symmetry to find an irreducible set of $\boldsymbol{k}$-points, the so-called *Irreducible wedge of the Brillouin Zone* (IBZ) [71]. Every $\boldsymbol{k}$-point of this IBZ is a representative $\boldsymbol{k}$-point so that all $\boldsymbol{k}$-points of the remaining zone can be derived from the IBZ. Due to the underlying symmetry, functions of the $\boldsymbol{k}$-point feature the same value for related $\boldsymbol{k}$-points. Therefore, a $\boldsymbol{k}$-point weight (depending on the number of symmetry-connected $\boldsymbol{k}$-points) is introduced so that sums, such as in equation (5.23), are correctly evaluated, despite the reduced number of summands because of the IBZ. The factors $f^{(0)}_{\boldsymbol{k},n}$ are thus composed of the (integer or fractional) occupation factor, the $\boldsymbol{k}$-point weight factor and the reciprocal number of $\boldsymbol{k}$-points $N_{\boldsymbol{k}}$ in the $\boldsymbol{k}$-point mesh. [68]

5.7.2 Charge Density and Effective Potential

Stars

The charge density and the effective potential can be expanded in a symmetry-optimized way by stars and lattice harmonics. The orthogonal stars basis functions are given by

$$\phi_{\mathrm{s}} = \frac{1}{N_{\mathrm{op}}} \sum_{\underline{\mathfrak{R}}} \mathrm{e}^{\mathrm{i}\left(\underline{\mathfrak{R}}\boldsymbol{G}\right)\cdot\left(\boldsymbol{r}-\boldsymbol{t}_{\underline{\mathfrak{R}}}\right)} \tag{5.44a}$$

which can be rewritten as

$$\phi_{\mathrm{s}} = \frac{1}{m_{\mathrm{s}}} \sum_{m} \varphi_m \mathrm{e}^{\mathrm{i}\left(\underline{\mathfrak{R}}_m \boldsymbol{G}\right)\cdot\boldsymbol{r}} \tag{5.44b}$$

with the phases

$$\varphi_m = \frac{m_s}{N_{\mathrm{op}}} \sum_{\underline{\mathfrak{R}}|\underline{\mathfrak{R}}\in\mathbb{m}} \mathrm{e}^{-\mathrm{i}\left(\underline{\mathfrak{R}}\boldsymbol{G}\right)\cdot\boldsymbol{t}_{\underline{\mathfrak{R}}}} \,. \tag{5.44c}$$

Stars basis functions are governed by N_{op} space group operations

$$\left\{\underline{\mathfrak{R}} \mid \boldsymbol{t}\right\}\boldsymbol{r} = \underline{\mathfrak{R}}\boldsymbol{r} + \boldsymbol{t}\,, \tag{5.45}$$

which are composed of a rotation matrix $\underline{\mathfrak{R}}$ and a translation $\boldsymbol{t}$ to mimic the symmetry of the lattice. The rotation can be a unit matrix, and the translation a vector with a vanishing l^2-norm. Given all $\boldsymbol{t} = \boldsymbol{0}$, the space group is called symorphic [71]. As shown in equation (5.44b), each plane-wave basis function labeled by its reciprocal lattice vector $\boldsymbol{G}$ can be attributed to exactly one specific group of $m_{\mathrm{s}} \leq N_{\mathrm{op}}$ plane waves, called a *star*. A star features a representative $\boldsymbol{G}$ to which all other $\boldsymbol{G}'$ in this star are connected by a pure rotation matrix $\underline{\mathfrak{R}}_{\mathbb{m}}$. The set $\mathbb{m}$ in equation (5.44c) contains all space group operations connecting the representative $\boldsymbol{G}$ with the symmetry equivalent $\underline{\mathfrak{R}}_{\mathbb{m}}\boldsymbol{G}$. This implies all reciprocal lattice vectors in a star have the same Euclidian norm. However, it must be underlined at this point that in general two plane waves with their labels $\boldsymbol{G}$ and $\boldsymbol{G}'$, both having the same length, can belong to different stars. In addition, the more symmetry operations inhere the lattice of interest, the fewer stars are required to expand the density or the potential[12] in stars, while the star members increase. If the lattice of interest shows inversion symmetry and the location of the unit cell origin equals the inversion site, certain phases ensure that the potential or density star coefficients, as well as the stars, become real. In general however, the star expansion coefficients are complex, but lead to real charge densities and potentials[13]. [68]

Lattice harmonics

Given a converged basis set in the MT spheres, the spherical harmonics, which are used for expanding the charge density or the potential in a specific MT sphere γ, can be grouped into lattice harmonics, characterized by the linear combination

$$\mathfrak{Y}^{\gamma}_{\lambda}\left(\hat{\boldsymbol{r}}_{\gamma}\right) = \sum_{\mu} \mathfrak{c}^{\gamma}_{\lambda\mu} \mathrm{Y}_{l(\lambda),m(\mu)}\left(\hat{\boldsymbol{r}}_{\gamma}\right) . \tag{5.46}$$

This expansion, with its coefficients $\mathfrak{c}^{\gamma}_{\lambda\mu}$, exploits the symmetry between related MT spheres, analogously to section 5.7.1. Thus, it suffices to store the lattice-harmonic expansion coefficients of a representative MT sphere. Furthermore, redundant or vanishing contributions are

---

[12] This also holds true for any other function living up to the lattice symmetry.

[13] Charge densities and potentials must be real anyway, since they are observables.

not considered so that a minimal set of relevant orbital quantum numbers λ and magnetic quantum numbers μ results, which normally is significantly smaller than the set of l and m. Usually, the coefficients attributed to a lattice harmonic $\mathfrak{Y}^{\gamma}_{\lambda}\left(\hat{\boldsymbol{r}}_{\gamma}\right)$ are called members [127, 251]. In the `FLEUR` code, a lattice harmonic characterized by a specific λ is unique, i.e., there is only one lattice harmonic per λ [127]. The expansion coefficients of the charge density or the potential in a symmetry-related MT sphere can be derived by applying the connecting symmetry operation to the expansion coefficients of the representative MT sphere. Technical details for determining the lattice-harmonic coefficients are discussed in the textbook of Singh and Nordström [68]. Moreover, the coefficients $\mathfrak{c}^{\gamma}_{\lambda\mu}$ are chosen so as to ensure that the lattice harmonics are real and orthonormal to each other. [68]

5.8 Constructing the Kohn–Sham Hamiltonian

Partitioning

During the self-consistency cycle, an essential part of one iteration step consists in determining the Kohn–Sham eigenfunctions and Kohn–Sham eigenenergies from the Kohn–Sham Hamiltonian (see section 2.2). A variational ansatz typically implies introducing a basis set, and deciding for the LAPW basis-set leads to a representation of the Hamiltonian matrix, which inheres in a division into an IR and the ensemble of MT spheres [71]

$$\left\langle \Psi^{(0)}_{\boldsymbol{k},n} \middle| \mathscr{H}^{(0)} - \epsilon^{(0)}_{\boldsymbol{k},n} \middle| \Psi^{(0)}_{\boldsymbol{k},n} \right\rangle_{\Omega} = \left\langle \Psi^{(0)}_{\boldsymbol{k},n} \middle| \mathscr{H}^{(0)} - \epsilon^{(0)}_{\boldsymbol{k},n} \middle| \Psi^{(0)}_{\boldsymbol{k},n} \right\rangle_{\mathrm{IR}} + \sum_{\gamma} \left\langle \Psi^{(0)}_{\boldsymbol{k},n} \middle| \mathscr{H}^{(0)} - \epsilon^{(0)}_{\boldsymbol{k},n} \middle| \Psi^{(0)}_{\boldsymbol{k},n} \right\rangle_{\gamma} . \tag{5.47}$$

It must be stressed at this point that the `FLEUR` code [69] implements equation (5.47) in terms of basis functions. However, for the sake of reducing redundancy, this representation is chosen so that it is possible to refer to it from the following chapters.

Outline

The IR term of equation (5.47) is addressed in section 5.8.1, while section 5.8.2 is devoted to the MT contributions. For both subsections, the discussion closely adheres to the publication of Blügel and Bihlmayer [71].

5.8.1 Interstitial Contribution

Step function

In the FLAPW method, the Heaviside step function

$$\Theta(\boldsymbol{r}) = \begin{cases} 1, & \text{IR} \\ 0, & \text{MT} \end{cases} \tag{5.48a}$$

with its plane-wave representation

$$\Theta(\boldsymbol{r}) = \sum_{\boldsymbol{G}''} \underbrace{\left(\delta_{\boldsymbol{G}'',\boldsymbol{0}} - \left(1 - \delta_{\boldsymbol{G}'',\boldsymbol{0}}\right) \sum_{\gamma} \frac{4\pi R_{\gamma}^{3}}{\Omega} \mathrm{e}^{-\mathrm{i}\boldsymbol{G}''\cdot\boldsymbol{\tau}_{\gamma}} \frac{\mathrm{j}_1\left(|\boldsymbol{G}''|R_{\gamma}\right)}{|\boldsymbol{G}''|R_{\gamma}} \right)}_{\Theta(\boldsymbol{G}'')} \mathrm{e}^{\mathrm{i}\boldsymbol{G}''\cdot\boldsymbol{r}} \tag{5.48b}$$

Subdivision

is utilized for IR quantities, because as a factor it excludes the MT spheres from the unit cell volume. Equipped with the aforementioned step function, equation (5.47) is usually subdivided into three parts, (i) the action of the kinetic energy operator, (ii) the action of the effective potential operator and (iii) the overlap of the Kohn–Sham wave (LAPW basis) functions. Furthermore, inserting a completeness relation of the position basis enables one to use the LAPW basis functions for the IR, as given in equation (5.17). At the same time, the integral is restricted to the IR by multiplying by the aforementioned Heaviside step function

$$\begin{aligned}
&\left\langle \mathit{\Psi}^{(0)}_{\boldsymbol{k},n} \middle| \mathscr{H}^{(0)} - \epsilon^{(0)}_{\mathrm{k},n} \middle| \mathit{\Psi}^{(0)}_{\boldsymbol{k},n} \right\rangle_{\mathrm{IR}} \\
&\quad = \frac{1}{\mathit{\Omega}} \sum_{\boldsymbol{G}'\boldsymbol{G}} z^{*(0)}_{\boldsymbol{G}'}(\boldsymbol{k},n) z^{(0)}_{\boldsymbol{G}}(\boldsymbol{k},n) \int_{\mathit{\Omega}} \Theta(\boldsymbol{r}) \mathrm{e}^{-\mathrm{i}\left(\boldsymbol{k}+\boldsymbol{G}'\right)\cdot\boldsymbol{r}} \left[\left(-\frac{\Delta}{2} + \mathscr{V}^{(0)}_{\mathrm{eff}} - \epsilon^{(0)}_{\mathrm{k},n} \right) \mathrm{e}^{\mathrm{i}(\boldsymbol{k}+\boldsymbol{G})\cdot\boldsymbol{r}} \right] \mathrm{d}^3 r \qquad (5.49\mathrm{a}) \\
&\quad = \frac{1}{\mathit{\Omega}} \sum_{\boldsymbol{G}'\boldsymbol{G}} z^{*(0)}_{\boldsymbol{G}'}(\boldsymbol{k},n) z^{(0)}_{\boldsymbol{G}}(\boldsymbol{k},n) \int_{\mathit{\Omega}} \mathrm{e}^{-\mathrm{i}\left(\boldsymbol{G}'-\boldsymbol{G}\right)\cdot\boldsymbol{r}} \Theta(\boldsymbol{r}) \left(\frac{|\boldsymbol{k}+\boldsymbol{G}|^2}{2} + V^{(0)}_{\mathrm{eff}}(\boldsymbol{r}) - \epsilon^{(0)}_{\mathrm{k},n} \right) \mathrm{d}^3 r \qquad (5.49\mathrm{b}) \\
&\quad =: \sum_{\boldsymbol{G}'\boldsymbol{G}} z^{*(0)}_{\boldsymbol{G}'}(\boldsymbol{k},n) \left(\left[H^{\mathrm{IR}}(\boldsymbol{k}) \right]_{\boldsymbol{G}'\boldsymbol{G}} - \epsilon^{(0)}_{\mathrm{k},n} \left[S^{\mathrm{IR}} \right]_{\boldsymbol{G}'\boldsymbol{G}} \right) z^{(0)}_{\boldsymbol{G}}(\boldsymbol{k},n) \,. \qquad (5.49\mathrm{c})
\end{aligned}$$

Again, it must be stressed that only the part within the parentheses is relevant for the DFT calculation, i.e., the sums and the wave-function expansion coefficients are not required.

Final forms

Applying the Laplace and the potential operator $\mathscr{V}^{(0)}_{\mathrm{eff}}$ to the plane-wave, results in the known kinetic energy of a free particle and the effective potential evaluated at position $\boldsymbol{r}$ in equation (5.49b). In order to ensure a Hermitian matrix, the Laplace operator can be split into a gradient acting on the ket and a gradient acting on the bra, using integration by parts [68]. However as a result, additional surface integrals (5.76) sustain given discontinuous derivatives of the wave functions [68]. They are not considered in `FLEUR`, because for the LAPW basis with converged parameters, its continuity by construction makes such surface integrals practically irrelevant (their contribution is too small to be significant or completely vanishes). As a consequence, an equivalence of both kinetic energy representations is implied. Still, the kinetic energy is made Hermitian in `FLEUR` by averaging the action of the Laplace operator on the bra and the ket basis functions. Finally in equation (5.49c), a Fourier transform of the Hamiltonian at Bloch vector $\boldsymbol{k}$

$$\begin{aligned}
\left[H^{\mathrm{IR}}(\boldsymbol{k}) \right]_{\boldsymbol{G}'\boldsymbol{G}} &:= \frac{1}{\mathit{\Omega}} \int_{\mathit{\Omega}} \mathrm{e}^{-\mathrm{i}\left(\boldsymbol{G}'-\boldsymbol{G}\right)\cdot\boldsymbol{r}} \Theta(\boldsymbol{r}) \left(\frac{|\boldsymbol{k}+\boldsymbol{G}|^2}{2} + V^{(0)}_{\mathrm{eff}}(\boldsymbol{r}) \right) \mathrm{d}^3 r && (5.50\mathrm{a}) \\
&= \frac{|\boldsymbol{k}+\boldsymbol{G}'|^2 + |\boldsymbol{k}+\boldsymbol{G}|^2}{4} \Theta(\boldsymbol{G}'-\boldsymbol{G}) + [V\Theta](\boldsymbol{G}'-\boldsymbol{G}) && (5.50\mathrm{b}) \\
&=: \frac{|\boldsymbol{k}+\boldsymbol{G}'|^2 + |\boldsymbol{k}+\boldsymbol{G}|^2}{4} \Theta(\boldsymbol{G}'') + [V\Theta](\boldsymbol{G}'') && (5.50\mathrm{c})
\end{aligned}$$

and the overlap of the IR Kohn–Sham wave (LAPW basis) functions

$$\begin{aligned}
\left[S^{\mathrm{IR}} \right]_{\boldsymbol{G}'\boldsymbol{G}} &:= \frac{1}{\mathit{\Omega}} \int_{\mathit{\Omega}} \mathrm{e}^{-\mathrm{i}\left(\boldsymbol{G}'-\boldsymbol{G}\right)\cdot\boldsymbol{r}} \Theta(\boldsymbol{r}) \, \mathrm{d}^3 r && (5.51\mathrm{a}) \\
&= \Theta(\boldsymbol{G}'-\boldsymbol{G}) && (5.51\mathrm{b}) \\
&=: \Theta(\boldsymbol{G}'') && (5.51\mathrm{c})
\end{aligned}$$

result, while a new reciprocal lattice vector $\boldsymbol{G}'' =: \boldsymbol{G}' - \boldsymbol{G}$ is defined. It simplifies the definition of the Fourier coefficients for the so-called *warped* effective potential

$$[V\Theta](\boldsymbol{G}'') = \sum_{\boldsymbol{G}'''} V(\boldsymbol{G}''') \Theta(\boldsymbol{G}'' - \boldsymbol{G}''') \,. \qquad (5.52)$$

The step function Fourier coefficients in equation (5.48b) are analytically determined fulfilling $\boldsymbol{G}'' \leq 2G_{\text{max}}$. These coefficients together with the IR effective potential are subject to a Fast Fourier Transform (FFT) so that both the step function and the potential are given in real space, as exact as their chosen cutoffs. The real-space effective potential and step function are multiplied to exploit the convolution theorem. After a back-transformation with the FFT, the Fourier coefficients on the left-hand side of equation (5.52) result.

5.8.2 Muffin-Tin Contribution

Basis-function representation

In a similar way to the IR, the variational wave-function expansion coefficients of the Kohn–Sham wave function can be excluded. So, they enclose a sum of the MT Hamiltonian matrix elements and the MT overlap matrix elements for a Bloch vector $\boldsymbol{k}$, which are dependent on the reciprocal lattice vectors $\boldsymbol{G}$ and $\boldsymbol{G}'$:

$$\left\langle \vec{\Psi}^{(0)}_{\boldsymbol{k},n} \middle| \mathscr{H}^{(0)} - \epsilon^{(0)}_{\boldsymbol{k},n} \middle| \vec{\Psi}^{(0)}_{\boldsymbol{k},n} \right\rangle_{\gamma} = \sum_{\boldsymbol{G}'\boldsymbol{G}} z^{*(0)}_{\boldsymbol{G}'}(\boldsymbol{k},n) \Big([H^{\gamma}(\boldsymbol{k})]_{\boldsymbol{G}'\boldsymbol{G}} - \epsilon^{(0)}_{\boldsymbol{k},n} [S^{\gamma}(\boldsymbol{k})]_{\boldsymbol{G}'\boldsymbol{G}} \Big) z^{(0)}_{\boldsymbol{G}}(\boldsymbol{k},n) \,. \tag{5.53}$$

The small arrows above the Kohn–Sham wave function indicate the scalar-relativistic character.

Symmetry optimization

Before proceeding, it is necessary to discuss another symmetry optimization of the `FLEUR` implementation that becomes relevant in this context. In section 5.7, it is stated that inhering space group symmetries can relate certain MT spheres to each other, enabling one to define a representative MT sphere $\mathring{\gamma}$ [68]. Hence, it suffices to store the lattice-harmonic expansion coefficients of the effective potential within this special sphere, because the effective potential in the related spheres could be derived by applying the symmetry operations underlying the investigated system [68]. But actually, it is not implemented in this way [127]. Instead of rotating the effective potential from the representative MT sphere to the symmetry-related ones, the MT wave functions are rotated from the latter to the former with the respective rotation matrices $\mathfrak{R}$ [68, 127]. This requires including them in the Rayleigh expansion (5.5), in order to rotate the vector to the atomic positions $\boldsymbol{\tau}_{\gamma}$ and the $\boldsymbol{k}$-vectors, resulting in

$$\mathrm{e}^{\mathrm{i}\left(\underline{\mathfrak{R}}(\boldsymbol{k}+\boldsymbol{G})\right)\cdot\left(\boldsymbol{r}+\underline{\mathfrak{R}}\boldsymbol{\tau}_{\gamma}\right)} = \mathrm{e}^{\mathrm{i}(\boldsymbol{k}+\boldsymbol{G})\cdot\boldsymbol{\tau}_{\gamma}} 4\pi \sum_{lm} \mathrm{i}^{l} \mathrm{j}_{l}(|\boldsymbol{k}+\boldsymbol{G}|r) \mathrm{Y}^{*}_{lm}\Big(\widehat{\underline{\mathfrak{R}}(\boldsymbol{k}+\boldsymbol{G})}\Big) \mathrm{Y}_{lm}(\hat{\boldsymbol{r}}) \,. \tag{5.54}$$

Consequently, the matching coefficients allowing for focussing only on the representative unit cell read (cf. equation (5.7))

$$a^{\boldsymbol{G}\boldsymbol{k}\gamma}_{lm1} = \mathrm{e}^{\mathrm{i}(\boldsymbol{k}+\boldsymbol{G})\cdot\boldsymbol{\tau}_{\gamma}} 4\pi \mathrm{i}^{l} \frac{1}{W} \mathrm{Y}^{*}_{lm}\Big(\widehat{\underline{\mathfrak{R}}(\boldsymbol{k}+\boldsymbol{G})}\Big) \tag{5.55a}$$

$$\times \left[u^{1\gamma}_{l2}\big(R_{\gamma}\big) |\boldsymbol{k}+\boldsymbol{G}| \frac{\partial \mathrm{j}_{l}\big(|\boldsymbol{k}+\boldsymbol{G}|r_{\gamma}\big)}{\partial r_{\gamma}}\bigg|_{r_{\gamma}=R_{\gamma}} - \frac{\partial u^{1\gamma}_{l2}\big(r_{\gamma}\big)}{\partial r_{\gamma}}\bigg|_{r_{\gamma}=R_{\gamma}} \mathrm{j}_{l}\big(|\boldsymbol{k}+\boldsymbol{G}|R_{\gamma}\big) \right]$$

$$a^{\boldsymbol{G}\boldsymbol{k}\gamma}_{lm2} = \mathrm{e}^{\mathrm{i}(\boldsymbol{k}+\boldsymbol{G})\cdot\boldsymbol{\tau}_{\gamma}} 4\pi \mathrm{i}^{l} \frac{1}{W} \mathrm{Y}^{*}_{lm}\Big(\widehat{\underline{\mathfrak{R}}(\boldsymbol{k}+\boldsymbol{G})}\Big) \tag{5.55b}$$

$$\times \left[\frac{\partial u^{1\gamma}_{l1}\big(r_{\gamma}\big)}{\partial r_{\gamma}}\bigg|_{r_{\gamma}=R_{\gamma}} \mathrm{j}_{l}\big(|\boldsymbol{k}+\boldsymbol{G}|R_{\gamma}\big) - u^{1\gamma}_{l1}\big(R_{\gamma}\big) |\boldsymbol{k}+\boldsymbol{G}| \frac{\partial \mathrm{j}_{l}\big(|\boldsymbol{k}+\boldsymbol{G}|r_{\gamma}\big)}{\partial r_{\gamma}}\bigg|_{r_{\gamma}=R_{\gamma}} \right]$$

with the definition of the Wronskian matrix.

$$W = u^{1\gamma}_{l2}\big(R_{\gamma}\big) \frac{\partial u^{1\gamma}_{l1}\big(r_{\gamma}\big)}{\partial r_{\gamma}}\bigg|_{r_{\gamma}=R_{\gamma}} - u^{1\gamma}_{l1}\big(R_{\gamma}\big) \frac{\partial u^{1\gamma}_{l2}\big(r_{\gamma}\big)}{\partial r_{\gamma}}\bigg|_{r_{\gamma}=R_{\gamma}} \tag{5.55c}$$

Final form of overlap

For the overlap matrix elements from equation (5.53), the muffin-tin LAPW basis functions from equation (5.17b) are inserted so that

$$[S^{\gamma}(\boldsymbol{k})]_{\boldsymbol{G}'\boldsymbol{G}} = \sum_{l'm'p'} \sum_{lmp} a^{*\boldsymbol{G}'\boldsymbol{k}\gamma}_{lmp} a^{\boldsymbol{G}\boldsymbol{k}\gamma}_{lmp} \int_{\mathring{\gamma}} \sum_{s} \varphi^{*s\mathring{\gamma}}_{l'm'p'}(\boldsymbol{r}_{\nu\mathring{\gamma}}) \varphi^{s\mathring{\gamma}}_{lmp}(\boldsymbol{r}_{\nu\mathring{\gamma}}) \, \mathrm{d}^3 r_{\nu\mathring{\gamma}} \ . \tag{5.56}$$

This integral, which is independent of the Bloch vectors $\boldsymbol{k}$ and the reciprocal lattice vectors $\boldsymbol{G}$ and $\boldsymbol{G}'$, shall be further reformulated. The MT basis functions with excluded matching coefficients are substituted by their definition, yielding products of radial solutions and spherical harmonics. This suggests introducing spherical coordinates

$$\int_{\mathring{\gamma}} \sum_{s} \varphi^{*s\mathring{\gamma}}_{l'm'p'}(\boldsymbol{r}_{\nu\mathring{\gamma}}) \varphi^{s\mathring{\gamma}}_{lmp}(\boldsymbol{r}_{\nu\mathring{\gamma}}) \, \mathrm{d}^3 r_{\nu\mathring{\gamma}} \tag{5.57a}$$

$$= \int_{\mathring{\gamma}} \sum_{s} u^{s\mathring{\gamma}}_{l'p'}(r_{\nu\mathring{\gamma}}) \mathrm{Y}^{*}_{l'm'}\big(\hat{\boldsymbol{r}}_{\mathring{\gamma}}\big) u^{s\mathring{\gamma}}_{lp}(r_{\nu\mathring{\gamma}}) \mathrm{Y}_{lm}\big(\hat{\boldsymbol{r}}_{\mathring{\gamma}}\big) \, \mathrm{d}^3 r_{\nu\mathring{\gamma}}$$

$$= \int_{0^+}^{R_{\mathring{\gamma}}} \sum_{s} r^2_{\nu\mathring{\gamma}} u^{s\mathring{\gamma}}_{l'p'}(r_{\nu\mathring{\gamma}}) u^{s\mathring{\gamma}}_{lp}(r_{\nu\mathring{\gamma}}) \oint_{\partial\mathring{\gamma}} \mathrm{Y}^{*}_{l'm'}\big(\hat{\boldsymbol{r}}_{\mathring{\gamma}}\big) \mathrm{Y}_{lm}\big(\hat{\boldsymbol{r}}_{\mathring{\gamma}}\big) \, \mathrm{d}\Omega \, \mathrm{d}r_{\nu\mathring{\gamma}} \ . \tag{5.57b}$$

Reordering the terms reveals in equation (5.57b) that the orthogonality relation of the spherical harmonics can be used. This reflects in the product of Kronecker deltas, possessing indices of orbital and magnetic quantum numbers, in the following equation

$$= \delta_{ll'} \delta_{mm'} \int_{0^+}^{R_{\mathring{\gamma}}} \sum_{s} r_{\nu\mathring{\gamma}} u^{s\mathring{\gamma}}_{l'p'}(r_{\nu\mathring{\gamma}}) r_{\nu\mathring{\gamma}} u^{s\mathring{\gamma}}_{lp}(r_{\nu\mathring{\gamma}}) \, \mathrm{d}r_{\nu\mathring{\gamma}} \ . \tag{5.57c}$$

Finally, the properties of the radial solutions can be used, which have already been discussed in section 5.2

$$= \begin{cases} \delta_{ll'} \delta_{mm'}, & p = 1 \wedge p' = 1 \\ \delta_{ll'} \delta_{mm'} \displaystyle\int_{0^+}^{R_{\mathring{\gamma}}} \sum_{s} r_{\nu\mathring{\gamma}} u^{s\mathring{\gamma}}_{l'2}(r_{\nu\mathring{\gamma}}) r_{\nu\mathring{\gamma}} u^{s\mathring{\gamma}}_{l2}(r_{\nu\mathring{\gamma}}) \, \mathrm{d}r_{\nu\mathring{\gamma}} \, , & p = 2 \wedge p' = 2 \\ 0, & p \neq p' \end{cases} \tag{5.57d}$$

$$=: \begin{cases} \delta_{ll'} \delta_{mm'}, & p = 1 \wedge p' = 1 \\ \delta_{ll'} \delta_{mm'} N^{\mathring{\gamma}}_{ll'}, & p = 2 \wedge p' = 2 \ . \\ 0, & p \neq p' \end{cases} \tag{5.57e}$$

Having evaluated the integrals, equation (5.56) simplifies to

$$-\epsilon^{(0)}_{\boldsymbol{k},n} \sum_{l'm'p'} \sum_{lmp} a^{*\boldsymbol{G}'\boldsymbol{k}\gamma}_{l'm'p'} a^{\boldsymbol{G}\boldsymbol{k}\gamma}_{lmp} \int_{\mathring{\gamma}} \sum_{s} \varphi^{*s\mathring{\gamma}}_{l'm'p'}(\boldsymbol{r}_{\nu\mathring{\gamma}}) \varphi^{s\mathring{\gamma}}_{lmp}(\boldsymbol{r}_{\nu\mathring{\gamma}}) \, \mathrm{d}^3 r_{\nu\mathring{\gamma}} \tag{5.58}$$

$$= -\epsilon^{(0)}_{\boldsymbol{k},n} \sum_{lm} \left(a^{*\boldsymbol{G}'\boldsymbol{k}\gamma}_{lm1} a^{\boldsymbol{G}\boldsymbol{k}\gamma}_{lm1} + a^{*\boldsymbol{G}'\boldsymbol{k}\gamma}_{lm2} a^{\boldsymbol{G}\boldsymbol{k}\gamma}_{lm2} N^{\mathring{\gamma}}_{ll} \right) .$$

Subdividing the Hamiltonian

The partitioning of the Hamiltonian in the MT spheres differs from the way it is done in the IR (see section 5.8.1). While in the IR the kinetic energy is separated from the effective potential, in the MT spheres the spherical part of the effective potential operator is summarized with the kinetic energy operator to a spherical Hamiltonian operator. This avoids dealing with the singularity at $\boldsymbol{r}_{\gamma} = \boldsymbol{0}$. Consequently, the remaining contribution is represented by the non-spherical effective potential. In order to achieve the explicit Hermiticity of this Hamiltonian matrix-element part, the spherical Hamiltonian must be made Hermitian while the non-spherical part is invariant under this operation [68]. Therefore, in the `FLEUR` code [69] the spherical Hamiltonian is realized as

$$[H^{\gamma}(\boldsymbol{k})]_{\boldsymbol{G}'\boldsymbol{G}} = \sum_{l'm'p'} \sum_{lmp} a_{lmp}^{*\boldsymbol{G}'\boldsymbol{k}\gamma} \Bigg(\int_{\mathring{\gamma}} \sum_{s} \varphi_{l'm'p'}^{*s\mathring{\gamma}}(\boldsymbol{r}_{\nu\mathring{\gamma}}) \frac{1}{2} \left(\overset{\leftharpoondown}{\mathscr{H}}{}^{(0)}_{\text{sph}} + \overset{\rightharpoonup}{\mathscr{H}}{}^{(0)}_{\text{sph}} \right) \varphi_{lmp}^{s\mathring{\gamma}}(\boldsymbol{r}_{\nu\mathring{\gamma}})\, \mathrm{d}^3 r_{\nu\mathring{\gamma}} \\ + \int_{\mathring{\gamma}} \sum_{s} \varphi_{l'm'p'}^{*s\mathring{\gamma}}(\boldsymbol{r}_{\nu\mathring{\gamma}}) \left[V_{\text{eff,nsph}}^{(0)\mathring{\gamma}}(\boldsymbol{r}_{\nu\mathring{\gamma}}) \varphi_{lmp}^{s\mathring{\gamma}}(\boldsymbol{r}_{\nu\mathring{\gamma}}) \right] \mathrm{d}^3 r_{\nu\mathring{\gamma}} \Bigg) a_{lmp}^{\boldsymbol{G}\boldsymbol{k}\gamma} \,. \tag{5.59}$$

The symbols $\leftharpoondown$ and $\rightharpoonup$ indicate the application direction of the Hamiltonian operator.

Final spherical Hamiltonian

For revealing the action of the Hamiltonian operator, only the Hamiltonian operator acting to the right is discussed now, its action to the left works analogously. After applying again the orthonormality relation of the spherical harmonics, the spherical Hamiltonian acts according to the eigenvalue equations (5.4) and (5.10) of the radial solutions yielding

$$\int_{\mathring{\gamma}} \sum_{s} \varphi_{l'm'p'}^{*s\mathring{\gamma}}(\boldsymbol{r}_{\nu\mathring{\gamma}}) \left(\overset{\rightharpoonup}{\mathscr{H}}{}^{(0)}_{\text{sph}} \varphi_{lmp}^{s\mathring{\gamma}}(\boldsymbol{r}_{\nu\mathring{\gamma}}) \right) \mathrm{d}^3 r_{\nu\mathring{\gamma}} \tag{5.60a}$$

$$= \delta_{ll'} \delta_{mm'} \int_{0^+}^{R_{\mathring{\gamma}}} \sum_{s} r_{\nu\mathring{\gamma}}^2 u_{l'p'}^{s\mathring{\gamma}}(r_{\nu\mathring{\gamma}}) \left(\overset{\rightharpoonup}{\mathscr{H}}{}^{(0)}_{\text{sph}} u_{lp}^{s\mathring{\gamma}}(r_{\nu\mathring{\gamma}}) \right) \mathrm{d}r_{\nu\mathring{\gamma}}$$

$$= \delta_{ll'} \delta_{mm'} \int_{0^+}^{R_{\mathring{\gamma}}} \sum_{s} r_{\nu\mathring{\gamma}} u_{l'p'}^{s\mathring{\gamma}}(r_{\nu\mathring{\gamma}}) \tag{5.60b}$$

$$\times \left(\delta_{p1} E_l^{\mathring{\gamma}} r_{\nu\mathring{\gamma}} u_{l1}^{s\mathring{\gamma}}(r_{\nu\mathring{\gamma}}) + \delta_{p2} \left(r_{\nu\mathring{\gamma}} u_{l1}^{s\mathring{\gamma}}(r_{\nu\mathring{\gamma}}) + E_l^{\mathring{\gamma}} r_{\nu\mathring{\gamma}} u_{l2}^{s\mathring{\gamma}}(r_{\nu\mathring{\gamma}}) \right) \right) \mathrm{d}r_{\nu\mathring{\gamma}} \,.$$

This result (and its analogous counterpart) can be inserted again into the first term of the right-hand side in equation (5.59) so that

$$\sum_{l'm'p'} \sum_{lmp} a_{l'm'p'}^{*\boldsymbol{G}'\boldsymbol{k}\gamma} a_{lmp}^{\boldsymbol{G}\boldsymbol{k}\gamma} \int_{\mathring{\gamma}} \sum_{s} \varphi_{l'm'p'}^{*s\mathring{\gamma}}(\boldsymbol{r}_{\nu\mathring{\gamma}}) \frac{1}{2} \left(\overset{\leftharpoondown}{\mathscr{H}}{}^{(0)}_{\text{sph}} + \overset{\rightharpoonup}{\mathscr{H}}{}^{(0)}_{\text{sph}} \right) \varphi_{lmp}^{s\mathring{\gamma}}(\boldsymbol{r}_{\nu\mathring{\gamma}})\, \mathrm{d}^3 r_{\nu\mathring{\gamma}} \tag{5.61a}$$

$$= \sum_{lm} \left(E_l^{\mathring{\gamma}} a_{lm1}^{*\boldsymbol{G}'\boldsymbol{k}\gamma} a_{lm1}^{\boldsymbol{G}\boldsymbol{k}\gamma} + \frac{1}{2} \left(a_{lm1}^{*\boldsymbol{G}'\boldsymbol{k}\gamma} a_{lm2}^{\boldsymbol{G}\boldsymbol{k}\gamma} + a_{lm2}^{*\boldsymbol{G}'\boldsymbol{k}\gamma} a_{lm1}^{\boldsymbol{G}\boldsymbol{k}\gamma} \right) + N_{ll}^{\mathring{\gamma}} a_{lm2}^{*\boldsymbol{G}'\boldsymbol{k}\gamma} a_{lm2}^{\boldsymbol{G}\boldsymbol{k}\gamma} E_l^{\mathring{\gamma}} \right)$$

$$= \sum_{lm} E_l^{\mathring{\gamma}} \left(a_{lm1}^{*\boldsymbol{G}'\boldsymbol{k}\gamma} a_{lm1}^{\boldsymbol{G}\boldsymbol{k}\gamma} + N_{ll}^{\mathring{\gamma}} a_{lm2}^{*\boldsymbol{G}'\boldsymbol{k}\gamma} a_{lm2}^{\boldsymbol{G}\boldsymbol{k}\gamma} \right) + \frac{1}{2} \left(a_{lm1}^{*\boldsymbol{G}'\boldsymbol{k}\gamma} a_{lm2}^{\boldsymbol{G}\boldsymbol{k}\gamma} + a_{lm2}^{*\boldsymbol{G}'\boldsymbol{k}\gamma} a_{lm1}^{\boldsymbol{G}\boldsymbol{k}\gamma} \right) . \tag{5.61b}$$

Final non-spherical Hamiltonian

The integral in equation (5.59) containing the non-spherical potential is also separately considered now. The orthonormality condition of the spherical harmonics cannot be used anymore here, since the non-spherical potential is additionally expanded in spherical harmonics, leading to three separate orbital and magnetic quantum-number indices. However, the surface integral in equation (5.62a) has already been defined in equation (5.32d) to be the Gaunt coefficient. It is finally multiplied by the radial integrals $\Sigma_{ll'l''m''}^{pp'\mathring{\gamma}}\left[V_{\text{eff,nsph}}^{(0)\gamma}(r_{\nu\mathring{\gamma}})\right]$ to result in the $\boldsymbol{k}$-independent matrix elements

$$\begin{aligned}
&\int_{\mathring{\gamma}} \sum_{s} \varphi^{*s\mathring{\gamma}}_{l'm'p'}(\boldsymbol{r}_{\nu\mathring{\gamma}}) V^{(0)\mathring{\gamma}}_{\text{eff,nsph}}(\boldsymbol{r}_{\nu\mathring{\gamma}}) \varphi^{s\mathring{\gamma}}_{lmp}(\boldsymbol{r}_{\nu\mathring{\gamma}})\, \mathrm{d}^3 r_{\nu\mathring{\gamma}} && \text{(5.62a)}\\
&\quad = \int_{0^+}^{R_{\mathring{\gamma}}} r^2_{\nu\mathring{\gamma}} \sum_{s} u^{s\mathring{\gamma}}_{l'p'}(r_{\nu\mathring{\gamma}}) \sum_{\lambda\mu} \left[V^{(0)\mathring{\gamma}}_{\text{eff,nsph}}(r_{\nu\mathring{\gamma}})\right]_{\lambda\mu} u^{s\mathring{\gamma}}_{lp}(r_{\nu\mathring{\gamma}})\\
&\qquad\qquad \times \oint_{\partial\mathring{\gamma}} \mathrm{Y}^{*}_{l'm'}\left(\hat{\boldsymbol{r}}_{\mathring{\gamma}}\right) \mathrm{Y}_{l''(\lambda)\, m''(\mu)}\left(\hat{\boldsymbol{r}}_{\mathring{\gamma}}\right) \mathrm{Y}_{lm}\left(\hat{\boldsymbol{r}}_{\mathring{\gamma}}\right) \mathrm{d}\Omega\, \mathrm{d}r_{\nu\mathring{\gamma}}\\
&\quad = \sum_{\lambda\mu} G^{m'\, m''(\mu)\, m}_{l'\; l''(\lambda)\; l} \int_{0^+}^{R_{\mathring{\gamma}}} \left[V^{(0)\mathring{\gamma}}_{\text{eff,nsph}}(r_{\nu\mathring{\gamma}})\right]_{\lambda\mu} \sum_{s} r_{\nu\mathring{\gamma}} u^{s\mathring{\gamma}}_{l'p'}(r_{\nu\mathring{\gamma}}) r_{\nu\mathring{\gamma}} u^{s\mathring{\gamma}}_{lp}(r_{\nu\mathring{\gamma}})\, \mathrm{d}r_{\nu\mathring{\gamma}} && \text{(5.62b)}\\
&\quad := \sum_{\lambda\mu} G^{m'\, m''(\mu)\, m}_{l'\; l''(\lambda)\; l} \left[\Sigma^{pp'\mathring{\gamma}}_{ll'l''m''}\left[V^{(0)\mathring{\gamma}}_{\text{eff,nsph}}(r_{\nu\mathring{\gamma}})\right]\right]_{\lambda\mu} && \text{(5.62c)}\\
&\quad := t^{\text{full},pp'\mathring{\gamma}}_{\eta(l'm'lm)} \left[V^{(0)\mathring{\gamma}}_{\text{eff,nsph}}(\boldsymbol{r}_{\nu\mathring{\gamma}})\right]. && \text{(5.62d)}
\end{aligned}$$

Symmetry nomenclature

The symmetry optimizations, discussed in the beginning of this subsection and in section 5.7, manifest themselves in the lattice harmonic coefficients (5.46) of the effective potential and the small circles above the atom index $\mathring{\gamma}$. Furthermore, the functions $l''(\lambda)$ and $m''(\mu)$ deliver the respective orbital and magnetic quantum number given the index λ of the lattice harmonic or of its member with quantum number μ. If the evaluation only takes place in the representative MT sphere, it is important to multiply a factor $N_{\mathring{\gamma}}$ representing the number of equivalent MT spheres, which are related to the representative MT sphere $\mathring{\gamma}$.

5.9 Finding the Total Energy of the Ground State

Derivation

The total energy in the FLAPW method is derived from the Kohn–Sham total energy functional given in equation (2.2a) [71]. Basically, the total energy

$$\begin{aligned}
&E^{(0)}_{\text{KS}}\left[\rho^{(0)}(\boldsymbol{r})\right] = && \text{(5.63a)}\\
&\qquad T_{\text{ni}}\left[\rho^{(0)}(\boldsymbol{r})\right] + E^{(0)}_{\text{Htr}}\left[\rho^{(0)}(\boldsymbol{r})\right] + \int_{\Omega} V^{(0)}_{\text{ext}}(\boldsymbol{r}) \rho^{(0)}(\boldsymbol{r})\, \mathrm{d}^3 r + E^{(0)}_{\text{xc}}\left[\rho^{(0)}(\boldsymbol{r})\right] + E^{(0)}_{\text{ii}}
\end{aligned}$$

is composed of the kinetic energy $T_{\text{ni}}[\rho^{(0)}(\boldsymbol{r})]$, the Hartree energy, the contribution incorporating the external potential $V^{(0)}_{\text{ext}}(\boldsymbol{r})$, the xc energy $E^{(0)}_{\text{xc}}[\rho^{(0)}(\boldsymbol{r})]$, and the ion–ion interaction $E^{(0)}_{\text{ii}}$. Furthermore, it is implicitly assumed that the charge density, the Hartree energy and the xc energy are self-consistent, i.e., they are zeroth-order or unperturbed ground-state quantities and stem from a converged DFT calculation. By rearranging the Kohn–Sham equations (2.3a), the independent-particle kinetic energy can be formulated as

$$T_{\text{ni}}\left[\rho^{(0)}(\boldsymbol{r})\right] = \sum_{\boldsymbol{k},n} \varepsilon^{(0)}_{\boldsymbol{k},n} - \int_{\Omega} V^{(0)}_{\text{eff}}(\boldsymbol{r}) \rho^{(0)}(\boldsymbol{r})\, \mathrm{d}^3 r \tag{5.63b}$$

with the Kohn–Sham energies

$$\varepsilon^{(0)}_{\boldsymbol{k},n} = \left\langle \Psi^{(0)}_{\boldsymbol{k},n} \middle| H_{\text{KS}} \middle| \Psi^{(0)}_{\boldsymbol{k},n} \right\rangle . \tag{5.63c}$$

Using this independent-particle kinetic energy within the total energy (5.63a) reads

$$\begin{aligned} E_{\mathrm{KS}}^{(0)}\left[\rho^{(0)}(\boldsymbol{r})\right] &= \sum_{\boldsymbol{k},n} f_{\boldsymbol{k},n}^{(0)} \varepsilon_{\boldsymbol{k},n}^{(0)} - \int_{\Omega} V_{\mathrm{eff}}^{(0)}(\boldsymbol{r}) \rho^{(0)}(\boldsymbol{r}) \,\mathrm{d}^3 r + \int_{\Omega} V_{\mathrm{ext}}^{(0)}(\boldsymbol{r}) \rho^{(0)}(\boldsymbol{r}) \,\mathrm{d}^3 r + E_{\mathrm{ii}}^{(0)} \\ &+ \frac{1}{2} \int_{\Omega} \frac{\rho^{(0)}(\boldsymbol{r}) \rho^{(0)}(\boldsymbol{r}')}{|\boldsymbol{r} - \boldsymbol{r}'|} \,\mathrm{d}^3 r' \,\mathrm{d}^3 r + \int_{\Omega} \rho^{(0)}(\boldsymbol{r}) \varepsilon_{\mathrm{xc}}^{(0)}[\rho(\boldsymbol{r})] \,\mathrm{d}^3 r \;. \qquad (5.63\mathrm{d}) \end{aligned}$$

In comparison to other DFT methods, the total energy functional within the all-electron FLAPW method transcends by including both the real $1/r$ singularity and all electrons, hence, also the core-electrons (see section 5.3). [3]

Numeric strategies

It is important to develop a strategy so that the Coulomb singularity is reasonably coped with [68]. One way is for instance presented in the publication of Weinert, Wimmer, and Freeman [66]. They introduce a Madelung potential, which represents a Coulomb potential including both all the electron and all the nuclear charges in the crystal volume. However, the nuclear charge at the position the potential is evaluated at is not a part of the Madelung potential. It allows for a reformulation of the total energy, avoiding a singularity and only containing quantities which are available after a DFT calculation without significant effort. As already mentioned in section 2.2.3, best results for the total energy can be achieved in practice by using the input potential and the output charge density of one self-consistent iteration step, because the numerical convergence can only be performed up to a certain threshold, due to numerical reasons [3].

Metals

Analogously to section 5.5, metals require fractional occupation numbers in equation (5.63d). In order to sustain the variational character of the total energy in this case, slight adjustments of the total energy become necessary. They can be found in the publication of Weinert and Davenport [252]. [88]

5.10 Varying the Kohn–Sham Wave Functions

Preface

In order to set the stage for employing the FLAPW method to evaluate ab-initio forces or harmonic phonon properties from DFPT, it is imperative to elucidate the impact of displaced nuclei on the induced LAPW basis variations. The following nomenclature anticipates that of the phonon formalism set up in chapter 6 and chapter 7. Nevertheless, the discussion in this section can be adjusted to forces, because it exhibits all essential analogies. This is for instance done within the dissertation of Klüppelberg [88], to which this complete section refers unless differently cited.

Recapitulation

Section 3.1 has already addressed that on the one hand the first-order derivative of the BO energy with respect to the atomic position is related to the ab-initio forces, and on the other hand, the second-order derivative of the BO energy is connected to the dynamical matrix. Section 4.1.2, in turn, has clarified that the first derivative of the BO energy with respect to a general perturbation parameter is a functional of the unperturbed charge density. Furthermore, the second-order derivative of the BO energy with respect to the general perturbation parameter requires calculating the first variation of the charge density. Both facts are supported by the $2n + 1$ theorem mentioned in section 4.1.3. Moreover, equation (4.20e) shows the first-order charge-density variation to be dependent on the first-order variation of the Kohn–Sham wave function. However, forces (as shown in section 5.12) additionally require a first-order derivative of the wave functions with respect to the nuclei positions. Analogously, the setup of the dynamical matrix involves a second-order derivative of the wave functions (see for instance section 6.5.2). Still, these demands do not violate the $2n+1$ theorem, since only the derivative or variation of the LAPW *basis* is finally needed.

Incomplete Basis Corrections

Due to its decisive property of being dependent on $\boldsymbol{r}$, the variation of the wave functions expanded in the LAPW basis (cf. equation (5.17)) presents a challenge if the inducing external perturbation entails a displacement of the nuclei. Apart from the expansion coefficients, such an external perturbation in particular affects the location of the MT spheres and thus the LAPW basis. Analogously to section 4.1.1, the perturbed LAPW Kohn–Sham wave function can be expanded in orders of the perturbation parameter λ

$$\begin{aligned}\varPsi^{\text{pert}}_{\boldsymbol{k},n}(\boldsymbol{r}) &= \sum_{\boldsymbol{G}} z^{(0)}_{\boldsymbol{G}}(\boldsymbol{k},n)\phi^{(0)}_{\boldsymbol{k},\boldsymbol{G}}(\boldsymbol{r}) + \lambda \sum_{\tilde{\boldsymbol{k}},\boldsymbol{G}} \left(z^{(1)}_{\boldsymbol{G}}\left(\tilde{\boldsymbol{k}},n\right)\phi^{(0)}_{\tilde{\boldsymbol{k}},\boldsymbol{G}}(\boldsymbol{r}) + z^{(0)}_{\boldsymbol{G}}(\boldsymbol{k},n)\phi^{(1)}_{\boldsymbol{k},\boldsymbol{G}}(\boldsymbol{r})\right) \\ &\quad + \frac{\lambda^2}{2!}\sum_{\tilde{\boldsymbol{k}},\boldsymbol{G}}\left[z^{(2)}_{\boldsymbol{G}}\left(\tilde{\boldsymbol{k}},n\right)\phi^{(0)}_{\tilde{\boldsymbol{k}},\boldsymbol{G}}(\boldsymbol{r}) + 2z^{(1)}_{\boldsymbol{G}}\left(\tilde{\boldsymbol{k}},n\right)\phi^{(1)}_{\tilde{\boldsymbol{k}},\boldsymbol{G}}(\boldsymbol{r}) + z^{(0)}_{\boldsymbol{G}}(\boldsymbol{k},n)\phi^{(2)}_{\tilde{\boldsymbol{k}},\boldsymbol{G}}(\boldsymbol{r})\right] \\ &\quad + \mathcal{O}\left(\lambda^3\right) \qquad (5.64a) \\ &=: \varPsi^{(0)}_{\boldsymbol{k},n}(\boldsymbol{r}) + \lambda\varPsi^{(1)}_{\boldsymbol{k},n}(\boldsymbol{r}) + \frac{\lambda^2}{2}\varPsi^{(2)}_{\boldsymbol{k},n}(\boldsymbol{r}) + \mathcal{O}\left(\lambda^3\right). \qquad (5.64b)\end{aligned}$$

The tilde above the Bloch vector $\tilde{\boldsymbol{k}}$ indicates the possible impact on the Bloch character as a result of the perturbation (details are postponed to section 6.1.1). In order to build upon the successful features of the LAPW basis, the Kohn–Sham wave-function variations should be a linear combination of the basis functions spanning the LAPW Hilbert space. This means, all terms which are *not* proportional to $\phi^{(0)}$ in the equations (5.64) vanish. However, especially for phonons and forces, the LAPW basis must be adjusted by so-called Incomplete Basis Corrections (IBC) (see in particular the publication of Betzinger et al. [99]). They can be subdivided into a basis response and a Pulay contribution [103]. The former results from the variation of the $\vec{u}^{\gamma}_{lp}(r_{\nu^\gamma})$ in equation (5.17), due to the variation of the effective potential given a perturbation. For forces, Yu, Singh, and Krakauer [224] ranked the benefit of this contribution too small to be significant, especially against the background of the effort it takes to implement the basis response. With regards to phonons, this can likewise be assumed [68], therefore the focus henceforth is on the Pulay correction. Neglecting the basis response within the frozen-augmentation approximation can be compensated by employing LOs [68].

Origin of Pulay corrections

Without loss of generality, the first variation of the Kohn–Sham wave function

$$\begin{aligned}\varPsi^{(1)}_{\boldsymbol{k},n}(\boldsymbol{r}) &= \sum_{\tilde{\boldsymbol{k}},\boldsymbol{G}} z^{(1)}_{\boldsymbol{G}}\left(\tilde{\boldsymbol{k}},n\right)\phi^{(0)}_{\boldsymbol{k},\boldsymbol{G}}(\boldsymbol{r}) + \sum_{\tilde{\boldsymbol{k}},\boldsymbol{G}} z^{(0)}_{\boldsymbol{G}}\left(\tilde{\boldsymbol{k}},n\right)\phi^{(1)}_{\boldsymbol{k},\boldsymbol{G}}(\boldsymbol{r}) \qquad (5.65a) \\ &=: \varPsi^{(1),\in\text{HS}}_{\boldsymbol{k},n} + \varPsi^{(1),\notin\text{HS}}_{\boldsymbol{k},n} \qquad (5.65b)\end{aligned}$$

thus subdivides into two terms. While the first one is proportional to $\phi^{(0)}_{\boldsymbol{k},\boldsymbol{G}}(\boldsymbol{r})$ and is therefore fully within the LAPW Hilbert space, the second is partly or completely orthogonal to the aforementioned Hilbert space. As a consequence,

$$\left\langle \varPsi^{(1)}_{\boldsymbol{k},n}\middle|\mathscr{H}^{(0)}\middle|\varPsi^{(0)}_{\boldsymbol{k},n}\right\rangle \qquad (5.66)$$

features a finite overlap between the part of the wave-function variation outside the Hilbert space, and especially the kinetic Laplace operator in the Hamiltonian applied to the ket. Naively, this matrix element should actually vanish.

Furthermore, the Hellmann–Feynman theorem in equation (4.6) must be revisited:

$$\frac{\partial \epsilon^{(0)}_{\boldsymbol{k},n}}{\partial \boldsymbol{\tau}_\alpha} = \frac{\partial}{\partial \boldsymbol{\tau}_\alpha} \int \Psi^{*(0)}_{\boldsymbol{k},n}(\boldsymbol{r})\mathscr{H}^{(0)}\Psi^{(0)}_{\boldsymbol{k},n}(\boldsymbol{r})\,\mathrm{d}^3 r \tag{5.67a}$$

$$= \int \frac{\partial \Psi^{*(0)}_{\boldsymbol{k},n}}{\partial \boldsymbol{\tau}_\alpha}\mathscr{H}^{(0)}\Psi^{(0)}_{\boldsymbol{k},n}\,\mathrm{d}^3 r + \int \Psi^{*(0)}_{\boldsymbol{k},n}\frac{\partial \mathscr{H}^{(0)}}{\partial \boldsymbol{\tau}_\alpha}\Psi^{(0)}_{\boldsymbol{k},n}\,\mathrm{d}^3 r + \int \Psi^{*(0)}_{\boldsymbol{k},n}\mathscr{H}^{(0)}\frac{\partial \Psi^{(0)}_{\boldsymbol{k},n}}{\partial \boldsymbol{\tau}_\alpha}\,\mathrm{d}^3 r \tag{5.67b}$$

$$=: \int \boldsymbol{\Psi}^{*(1)}_{\boldsymbol{k},n}\mathscr{H}^{(0)}\Psi^{(0)}_{\boldsymbol{k},n}\,\mathrm{d}^3 r + \int \Psi^{*(0)}_{\boldsymbol{k},n}\boldsymbol{\mathscr{H}}^{(1)}\Psi^{(0)}_{\boldsymbol{k},n}\,\mathrm{d}^3 r + \int \Psi^{*(0)}_{\boldsymbol{k},n}\mathscr{H}^{(0)}\boldsymbol{\Psi}^{(1)}_{\boldsymbol{k},n}\,\mathrm{d}^3 r \tag{5.67c}$$

$$=: \epsilon^{(1)}_{\boldsymbol{k},n} \,. \tag{5.67d}$$

Due to finite contributions from matrix elements such as in equation (5.66), the first and third terms in equation (5.67b) do not vanish anymore. An in-depth analysis reveals that the Kohn–Sham wave functions are variational and only on average equal the correct pointwise solution of the Kohn–Sham system. For a displacing perturbation, it turns out that the LAPW basis set is not sufficient, i.e., *not complete* to describe the perturbed Kohn–Sham system. This implies the aforementioned Pulay corrections. If it had been complete, extending the LAPW basis by enlarging the number of its basis functions would have gradually made the part of the first-order wave-function variation $\notin$ HS in equation (5.65b) irrelevant to any precision [68].

Deducing its explicit form

For expounding on the explicit form of the Pulay correction, the transformation to the MT[14] local coordinate system $\boldsymbol{r}_\alpha = \boldsymbol{r} - \boldsymbol{\tau}_\alpha$ becomes important. Furthermore, given a displacement $\boldsymbol{w}_\alpha$ of the nuclei (see section 3.1), be it due to forces or phonons, the MT spheres surrounding the latter follow, justifying the generalization $\boldsymbol{r}_\alpha = \boldsymbol{r} - \boldsymbol{\tau}_\alpha - \boldsymbol{w}_\alpha$. Thus, the derivative with respect to $\boldsymbol{w}_\alpha$ can be redirected to $\boldsymbol{\tau}_\alpha$ or $\boldsymbol{r}$, obeying

$$\boldsymbol{\nabla}_{\boldsymbol{w}_\alpha}\phi^{(0)\alpha}_{\boldsymbol{k},\boldsymbol{G}}(\boldsymbol{r}) = \boldsymbol{\nabla}_{\boldsymbol{\tau}_\alpha}\phi^{(0)\alpha}_{\boldsymbol{k},\boldsymbol{G}}(\boldsymbol{r}) = -\boldsymbol{\nabla}_{\boldsymbol{r}}\phi^{(0)\alpha}_{\boldsymbol{k},\boldsymbol{G}}(\boldsymbol{r}) \equiv -\boldsymbol{\nabla}\phi^{(0)\alpha}_{\boldsymbol{k},\boldsymbol{G}}(\boldsymbol{r}) \,. \tag{5.68}$$

In the MT spheres α, all constituents of the basis functions $\phi^{\alpha}_{\boldsymbol{k},\boldsymbol{G}}(\boldsymbol{r})$ (see equation (5.9)) are sensitive to a displacement leading to

$$\boldsymbol{\nabla}_{\boldsymbol{w}_\alpha}\phi^{(0)\alpha}_{\boldsymbol{k},\boldsymbol{G}}(\boldsymbol{r}) = [\mathrm{i}(\boldsymbol{k}+\boldsymbol{G}) - \boldsymbol{\nabla}]\phi^{(0)\alpha}_{\boldsymbol{kG}}(\boldsymbol{r}) \quad . \tag{5.69}$$

The matching coefficients $a^{\boldsymbol{Gk}\alpha}_{lmp}$ are given explicitly in equation (5.55), however, incorporate the rotation to the representative local coordinate systems. In order to simplify the following discussion, the rotation matrices $\underline{R} \equiv \underline{1}$ are set to the unit matrix. Differentiating the matching coefficients with respect to the atomic equilibrium position $\boldsymbol{\tau}_\alpha$ results in the first term of the previous equation due to the phase factors. For the remaining basis function, the differential operator with respect to $\boldsymbol{w}$ is rewritten using equation (5.68), ensuing a minus sign. Both the radial solutions and the spherical harmonics are affected by the gradient with respect to $\boldsymbol{r}$ (see appendix C) and therefore contribute to the remaining Pulay correction.

Raison d'être

While the term stemming from the matching coefficients in equation (5.69) can again be expressed with the original MT basis functions $\phi^{\alpha}_{\boldsymbol{k},\boldsymbol{G}}(\boldsymbol{r})$, the remaining part of equation (5.69)

---

[14] Displaced atoms are attributed the indices α and β hereinafter, instead of the general atom index γ.

requires the gradients of the MT basis functions. Consequently, the complete variation of the MT basis function is not fully contained in the Hilbert space the LAPW basis functions span. In contrast, the IR plane waves are not dependent on the atomic positions and applying a derivative with respect to $\boldsymbol{r}$ yields

$$\nabla \mathrm{e}^{\mathrm{i}(\boldsymbol{k}+\boldsymbol{G})\cdot\boldsymbol{r}} = -\mathrm{i}(\boldsymbol{k}+\boldsymbol{G})\mathrm{e}^{\mathrm{i}(\boldsymbol{k}+\boldsymbol{G})\cdot\boldsymbol{r}}\,. \tag{5.70}$$

This means that every variation of the IR LAPW basis function $\phi^{\mathrm{IR}}_{\boldsymbol{k},\boldsymbol{G}}$ can be described by a basis function of the LAPW Hilbert space again.

Utilized basis corrections

All in all, the LAPW basis set does not suffice anymore in cases where the nuclei undergo a slight or infinitesimal shift, although for the undisplaced system it performs in an excellent way. Furthermore, the Pulay terms to compensate the incompleteness of the LAPW basis, when expanding variations of the Kohn–Sham wave function, restrict to the MT and read

$$\phi^{(1)\boldsymbol{w}_\alpha}_{\boldsymbol{kG}}(\boldsymbol{r}) = \begin{cases} 0, & \mathrm{IR} \\ \boldsymbol{w}_\alpha^\top\left[\mathrm{i}(\boldsymbol{k}+\boldsymbol{G}) - \nabla\right]\phi^{(0)\alpha}_{\boldsymbol{kG}}(\boldsymbol{r}), & \mathrm{MT}_\alpha \end{cases}. \tag{5.71}$$

In order to conceal the vectorial character of the last equation, it is projected onto the displacement $\boldsymbol{w}_\alpha$. The second-order variation of the LAPW basis function is given by

$$\phi^{(2)\boldsymbol{w}_\alpha}_{\boldsymbol{kG}}(\boldsymbol{r}) = \begin{cases} 0, & \mathrm{IR} \\ \boldsymbol{w}_\alpha^\top\left[\mathrm{i}(\boldsymbol{k}+\boldsymbol{G}) - \nabla\right]\left[\mathrm{i}(\boldsymbol{k}+\boldsymbol{G}) - \nabla\right]^\top\phi^{(0)\alpha}_{\boldsymbol{kG}}(\boldsymbol{r})\,\boldsymbol{w}_\alpha, & \mathrm{MT}_\alpha \end{cases}. \tag{5.72}$$

In this equation, the dyadic product of gradients applied to the MT basis function is surrounded by the $\boldsymbol{w}_\alpha$. This both leads to a scalar expression and picks out the relevant components of the intermediate matrix-like expression.

Non-self-adjoint Hamiltonian

Finally, it must be considered that Hamiltonian operators acting on the kets in matrix elements of the form (cf. for instance also the last term of equation (5.67c))

$$\left\langle \vec{\varphi}^{\gamma}_{l'm'p'} \middle| \mathscr{H}^{(0)} - \epsilon^{(0)}_{\boldsymbol{k},n} \middle| \nabla\vec{\varphi}^{\gamma}_{lmp} \right\rangle_\gamma \tag{5.73a}$$

$$\left\langle \vec{\varphi}^{\gamma}_{l'm'p'} \middle| \mathscr{H}^{(0)} - \epsilon^{(0)}_{\boldsymbol{k},n} \middle| \nabla\nabla^\top\vec{\varphi}^{\gamma}_{lmp} \right\rangle_\gamma \tag{5.73b}$$

cannot be simply applied to the bras (for example to let the matrix elements cancel by exploiting the Kohn–Sham equations (2.3a)). The matrix elements are evaluated in the MT sphere of atom γ and the $\vec{\varphi}$ are defined as in equation (5.17b). In this sense, the Hamiltonian operator is *not* self-adjoint in general. An application to the left would cause correction terms which are further specified in appendix E, because their detailed discussion anticipates too much and is too technical at this point. If only basis functions inside the LAPW Hilbert space had been involved in these matrix elements, i.e., no gradient had been applied to the basis functions, the Hamiltonian matrix-elements would have been self-adjoint [251].

5.11 Coping with the Discontinuity at the Muffin-Tin Boundary

Origin of discontinuities

The MT matching coefficients $a^{\boldsymbol{Gk}\gamma}_{lmp}$ of the LAPW basis (equation (5.17)) are constructed such as to enable a smooth continuation of the basis functions and their energy derivatives, when crossing the boundary between the IR and the MT spheres (MT sphere boundary hereinafter). In practice however, the impossibility of implementing infinite basis sets restricts these quantities to be continuous at the MT sphere boundary [88]. As a consequence, the charge density (see section 5.5.2) constructed from LAPW wave functions, and the effective potential (see section 2.2.1 and section 5.6) as a functional of the charge density likewise feature such a discontinuity [88]. The discontinuity of the effective potential predominantly originates from the xc potential (section 5.6.2), whereas the Coulomb potential (see section 5.6.1), provided converged parameters of the Rayleigh expansion, features the best continuity by construction [251]. In general, the smoothness of the LAPW basis can also be influenced by the FLAPW parameters (K_{max}, G_{max}, $l_{\text{max},\mathring{\gamma}}$ to name but a few) as discussed in section 5.3.

First-order surface integral corrections

A direct consequence of the LAPW basis set being a function of the position $\boldsymbol{r}$ is that the boundaries of the basis-set partitions also depend on $\boldsymbol{r}$. Since they move, whenever phenomena are considered entailing a displacement of the atoms, the aforementioned discontinuities impact upon integrals over the unit cell volume (they are typically subdivided into IR and MT spheres contributions reflecting the partitions of the LAPW[15] basis set). If these integrals are differentiated with respect to the atomic positions[16] $\boldsymbol{\tau}_\gamma$, and their integrands are formed of a universal but discontinuous unperturbed quantity $g^{(0)}$ expanded in the LAPW basis,

$$\frac{\mathrm{d}}{\mathrm{d}\boldsymbol{\tau}_\alpha}\int_\Omega g^{(0)}(\boldsymbol{r})\,\mathrm{d}^3r = \left[\int_{\text{IR}} \frac{\mathrm{d}g^{(0)}_{\text{IR}}(\boldsymbol{r})}{\mathrm{d}\boldsymbol{\tau}_\alpha}\,\mathrm{d}^3r + \sum_\gamma \int_\gamma \frac{\mathrm{d}g^{(0)}_\gamma(\boldsymbol{r})}{\mathrm{d}\boldsymbol{\tau}_\alpha}\,\mathrm{d}^3r\right] + \oint_{\partial\alpha}\left[g^{(0)}_\alpha(\boldsymbol{r}) - g^{(0)}_{\text{IR}}(\boldsymbol{r})\right]\hat{\boldsymbol{r}}\,\mathrm{d}S \tag{5.74}$$

must be obeyed. The previous equation depicts that apart from the first and second terms, in which the IR representation g_{IR} and its MT equivalent g_γ are differentiated, a surface integral over the MT sphere boundary emerges. It accounts for the change of the integral boundaries under a variation of $\boldsymbol{\tau}_\alpha$, and contains a difference of the MT representation g_{MT} and g_{IR} expanded in the IR basis set, which vanishes as soon as g is perfectly continuous. In practice, it might prove successful sometimes to make the aforementioned surface integrals less relevant by achieving a better continuity with converging $l_{\text{max},\mathring{\gamma}}$ (while balancing k_{max}). [88]

Second-order surface integral corrections

Phonons necessitate the calculation of the second-order total energy variation (see section 4.1.2 and section 5.9). Therefore, also a second-order expression

$$\begin{aligned}
&\sum_\alpha \boldsymbol{w}_\alpha^\top \left(\oint_{\partial\alpha}\left[g^{(0)}_\alpha(\boldsymbol{r}) - g^{(0)}_{\text{IR}}(\boldsymbol{r})\right]\hat{\boldsymbol{r}}\,\mathrm{d}S\right)^{(1)} &(5.75\text{a})\\
&\quad= \sum_\alpha \boldsymbol{w}_\alpha^\top \left(\int_\alpha \boldsymbol{\nabla}\left[g^{(0)}_\alpha(\boldsymbol{r}) - g^{(0)}_{\text{IR}}(\boldsymbol{r})\right]\mathrm{d}^3r\right)^{(1)}\\
&\quad= \sum_\alpha \boldsymbol{w}_\alpha^\top \oint_{\partial\alpha}\boldsymbol{\nabla}\left[g^{(0)}_\alpha(\boldsymbol{r}) - g^{(0)}_{\text{IR}}(\boldsymbol{r})\right]\hat{\boldsymbol{r}}^\top\,\mathrm{d}S\;\boldsymbol{w}_\alpha + \sum_\alpha \boldsymbol{w}_\alpha^\top \oint_{\partial\alpha}\left[g^{(1)}_\alpha(\boldsymbol{r}) - g^{(1)}_{\text{IR}}(\boldsymbol{r})\right]\hat{\boldsymbol{r}}\,\mathrm{d}S &(5.75\text{b})
\end{aligned}$$

of equation (5.74) is required. Within equations (5.75), the divergence theorem communicates between volume integrals of the sphere α and its surface integrals. Just as in the first variation, the volume integral is completely varied by varying the integral boundaries (first term) and varying the integrand (second term). All integrals, be they of a vectorial or matrix-like character, are projected onto the displacement $\boldsymbol{w}_\alpha$ (see section 3.1). [88]

---

[15] This consideration transfers analogously to similar methods, e.g. LMTO [206]. [88]

[16] The subindex $\boldsymbol{R}$ indicating the unit cell, as in section 3.1, is suppressed henceforth because the focus lies on periodic structures in the following.

Corrected overlap

One application constitutes in varying the overlap of two Kohn–Sham wave functions

$$\left\langle \Psi^{(1)}_{\boldsymbol{k}',n'} \middle| \Psi^{(0)}_{\boldsymbol{k},n} \right\rangle + \left\langle \Psi^{(1)}_{\boldsymbol{k}',n'} \middle| \Psi^{(0)}_{\boldsymbol{k},n} \right\rangle + \sum_{\alpha} \boldsymbol{w}^{\top}_{\alpha} \oint_{\partial\alpha} \hat{\boldsymbol{r}} \left(\Psi^{*(1)\alpha}_{\boldsymbol{k}',n'}(\boldsymbol{r}) \Psi^{(0)\alpha}_{\boldsymbol{k},n}(\boldsymbol{r}) - \Psi^{*(0)\mathrm{IR}}_{\boldsymbol{k}',n'}(\boldsymbol{r}) \Psi^{(1)\mathrm{IR}}_{\boldsymbol{k},n}(\boldsymbol{r}) \right) \mathrm{d}S \,. \tag{5.76}$$

Beyond the first two terms resulting from the product rule, the aforementioned surface integrals occur. This must be considered, for instance, when calculating whether the number of electrons in the systems changes as a result of the perturbation, which causes the variation of the Kohn–Sham wave functions. [88]

Symmetric kinetic energy

Finally, if the Laplace operator is applied to a wave function expanded in the LAPW basis, discontinuities at the MT sphere boundary occur since the LAPW basis is theoretically only continuous up to linear order [68]. An alternative for the Laplace operator can be gained from reviewing the form of the kinetic energy, as it is usually implemented in APW codes. It is given by the left-hand side of

$$\begin{aligned} \frac{1}{2} \int_{\Omega} \left[\boldsymbol{\nabla} \Psi^{(0)}_{\boldsymbol{k},n}(\boldsymbol{r}) \right]^{\dagger} \boldsymbol{\nabla} \Psi^{(0)}_{\boldsymbol{k},n}(\boldsymbol{r}) \, \mathrm{d}V = & \frac{1}{2} \int_{\Omega} \Psi^{*(0)}_{\boldsymbol{k},n}(\boldsymbol{r}) \Delta \Psi^{(0)}_{\boldsymbol{k},n}(\boldsymbol{r}) \, \mathrm{d}V \\ & + \frac{1}{2} \oint_{\partial\gamma} \Psi^{*(0)}_{\boldsymbol{k},n}(\boldsymbol{r}) \sum_{\gamma} \left(\boldsymbol{\nabla}^{\top} \Psi^{(0)\gamma}_{\boldsymbol{k},n}(\boldsymbol{r}) - \boldsymbol{\nabla}^{\top} \Psi^{(0)\mathrm{IR}}_{\boldsymbol{k},n}(\boldsymbol{r}) \right) \mathrm{d}\boldsymbol{S} \,, \end{aligned} \tag{5.77}$$

and according to Slater [201] the more original form based on the variational principle, underlying the derivation of the Schrödinger equation. In equation (5.77), the first identity of Green (see for instance the textbook of Hanson [253]) can be recognized. It states that the Laplacian and the symmetric form of the double derivative differ, given discontinuous wave functions or gradients of wave functions at the MT sphere boundaries. Actually, the LAPW basis is constructed to ensure both the continuity of the wave function and its gradient. Nevertheless, due to the aforementioned cutoffs in numerics, the surface integrals in equation (5.77) might become relevant and are at least numerically more correct. The `FLEUR` [69] code realizes the kinetic energy operator as an average of a Laplacian acting to the left and to the right. Furthermore, because of the LAPW basis set, the surface terms in equation (5.77) are ignored. Still, `FLEUR` implements the APW+LO basis, where the symmetric form is used, a thorough discussion on this topic is provided by Sjöstedt et al. [220, 221].

5.12 Ab-Initio Atomic Forces

Motivation

One output of a DFT calculation with the FLAPW method is the total or BO energy from equation (5.63d) [71]. The derivative of this BO energy with respect to the ion positions is linked[17] in equation (3.1b) to the first-order interatomic force [3]. Ab-initio forces have independently been developed by Soler and Williams [222, 223] as well as Yu, Singh, and Krakauer [224], both formalisms have proven to be equivalent [68, 71]. Furthermore, as already pointed out in section 3.1, the BO energy becomes minimal given vanishing first-order interatomic forces. Hence, apart from numerical subtleties, finite forces resulting from a calculation based on self-consistent DFT quantities indicate the atomic positions are not optimal [88]. This

---

[17] This relation between the first-order energy derivative with respect to the ion position and the expectation value of the acceleration operator was already given by Ehrenfest [254] in the early days of quantum mechanics, further history of the Hellmann–Feynman theorem is outlined in the textbook of Martin [3].

aspect can be exploited to optimize the underlying lattice structure [71]. Therefore, the DFT algorithm to relax structures iterates displacing the atoms and updating the forces after a new DFT calculation until the forces have vanished [71]. These relaxing algorithms can be made more efficient by employing mathematical optimization or minimization methods [88]. As discussed already in section 3.2, the force formalism, provided highly precise forces, can be employed to calculate phonon properties.

Hellmann–Feynman contribution

Putting forward the argument that in the ground state the total energy is extremal as far as all feasible wave function variations and hence the density variations are concerned, justifies cancelling the first and third integrals in equation (5.67b) in a first approximation. This leads to the Hellmann–Feynman force

$$\boldsymbol{F}_{\alpha}^{\mathrm{HF}} = -\int \left.\frac{\partial V_{\text{ext}}^{(0)}(\boldsymbol{r})}{\partial \boldsymbol{\tau}_{\alpha}}\right|_{\boldsymbol{w}_{\alpha}=\boldsymbol{0}} \rho^{(0)}(\boldsymbol{r})\,\mathrm{d}^3 r - \left.\frac{\partial E_{\mathrm{ii}}^{(0)}}{\partial \boldsymbol{\tau}_{\alpha}}\right|_{\boldsymbol{w}_{\alpha}=\boldsymbol{0}}, \tag{5.78}$$

the terms of which result from terms in the total energy exhibiting an explicit dependence on the nuclei positions. [3, 88]

Basis-induced corrections

The prerequisite of the Hellmann–Feynman theorem is an exact pointwise eigenstate solution. However, as analyzed already in section 5.10, the LAPW basis does not suffice, and does not fulfill this requirement when dealing with variations of wave functions expanded in it. In particular, this holds true for variations with respect to the atomic positions. Both initially mentioned groups figured out additional force terms functioning as an incomplete basis correction, which are known as Pulay [103] forces. They result from reformulating the neglected terms in equation (5.67) to

$$\boldsymbol{F}_{\alpha}^{\mathrm{Pl}} = \sum_{\boldsymbol{k},n} 2 f_{\boldsymbol{k},n}^{(0)} \left(\left\langle \frac{\mathrm{d}\mathit{\Psi}_{\boldsymbol{k},n}^{(0)}}{\mathrm{d}\boldsymbol{\tau}_{\alpha}} \middle| \mathscr{H}^{(0)} - \epsilon_{\boldsymbol{k},n}^{(0)} \middle| \mathit{\Psi}_{\boldsymbol{k},n}^{(0)} \right\rangle + \left\langle \mathit{\Psi}_{\boldsymbol{k},n}^{(0)} \middle| \mathscr{H}^{(0)} - \epsilon_{\boldsymbol{k},n}^{(0)} \middle| \frac{\mathrm{d}\mathit{\Psi}_{\boldsymbol{k},n}^{(0)}}{\mathrm{d}\boldsymbol{\tau}_{\alpha}} \right\rangle \right), \tag{5.79}$$

including a sum over the occupied states. Based on reference [224], Klüppelberg [88] additionally considers core-tail corrections in the entire unit cell and the surface terms from section 5.11, significantly refining the numerics of ab-initio forces. [88]

Chapter 6

Dynamical Matrix from Density-Functional Perturbation Theory Employing the All-Electron Full-Potential Linearized Augmented Plane-Wave Method

6.1 Preamble 80
6.2 Charge Density Variations 86
6.3 Potential Variations 89
6.4 Sternheimer Equation 100
6.5 Dynamical Matrix 104

Motivation

DFPT is introduced in chapter 4 as a tremendous and highly efficient method surpassing especially frozen-phonon methods in exploring harmonic phonon physics. Additionally inspired by the current benchmark status of the all-electron FLAPW framework (cf. chapter 5), a fusion of the latter with the former appears to be extremely auspicious for obtaining highly precise dynamical matrices in manifold materials. However, only a tiny number of respective publications are available and already expounded in chapter 1.

Outline

This chapter presents the outstanding work of Klüppelberg [88], who has developed a comprehensive formalism for dynamical matrices, accounting for the many subtleties that ensue from the aforementioned combination in the case of linear phonon response. Before discussing the central points of his work in detail, section 6.1 recapitulates the previous chapters and covers a sketch of his concept. Thus, the basic and intricate information essential for his approach and previously mentioned in this dissertation is unified. Afterwards, the calculation of the linear[1] charge-density variations is addressed in section 6.2. They form, e.g., an indispensable part of the linear Hartree- and xc-potential variations. Section 6.3 is devoted to these and all other potential variations required for phonon dispersion relations.

---

[1] For the sake of readability, hereinafter I use the umbrella term “linear” to denote both the first-order variation and the gradient of any unperturbed quantity.

Furthermore, both the first-order potential and charge-density variation communicate via the Sternheimer equation, the setup of which is the topic of section 6.4. Finally, the preceding sections allow for composing the dynamical matrix in section 6.5.

Chapter scope

At this point, it remains to be underlined, that this chapter cannot deliver every detail in the theory of Klüppelberg. Nevertheless, it still aspires to elucidate its cohesion, identify errors, and provide the background knowledge for chapter 7.

6.1 Preamble

Analogies

In analogy to a DFT calculation, utilizing the all-electron FLAPW method within DFPT pursues the goal of ensuring a highly rigorous representation of the (full) linear charge-density and effective-potential variations. Furthermore, both the valence and the core electrons are involved. For unperturbed quantities from a DFT calculation, this is predominantly achieved by employing the LAPW basis (plus local orbitals) for the valence electrons, the Weinert method for the Coulomb potential, the relativistic pointwise description of the core wave-functions, and by considering core-tail contributions to the charge density.

Incomplete basis corrections

It turns out that the LAPW basis is incomplete whenever expanding first- (or higher-) order changes of the variational Kohn–Sham wave functions, mirroring the phonon response. Therefore, it is imperative to include incomplete basis-set corrections, which fall into basis response and Pulay contributions. While Klüppelberg assumes the former to be small (according to experiences of Yu, Singh, and Krakauer [224] in force calculations), and hence neglects it within the *frozen-augmentation approximation*, he consistently incorporates the latter. Furthermore, he also extends the frozen-augmentation approximation of the LAPW basis to the pointwise core-electron solutions within the *frozen-core approximation*. Although LOs can compensate the neglected basis response in regimes or systems for which the frozen-augmentation approximation is poor, reference [88] only marginally addresses their integration.

Surface term corrections

Additionally, this reference reveals numerous surface terms, arising from a variation of the integral boundaries due to a displacement of the MT spheres, with each of their integrands discontinuous at the respective MT sphere boundary. The LAPW basis is constructed to be continuous up to the first-order energy derivative. But in practice, the Kohn–Sham wave functions, the charge density, and the xc quantities show a small discontinuity due to a finite $l_{\mathrm{max},\mathring{\gamma}}$ cutoff. In contrast, the Coulomb potential is continuous by the Weinert construction [251].

Potentials and core-tail corrections

In order to live up to the accurate unperturbed Coulomb-potential calculation, Klüppelberg extends the Weinert formalism to both the required linear Coulomb-potential variations and the second-order variation of the ion–ion interaction. The latter is traditionally calculated by Ewald summation methods (see for instance Gonze and Lee [255]). Finally, he explicitly describes the variations of the core-tails as a consequence of the MT spheres leaving their equilibrium positions.

Scope of theory

Among the enormous variety of systems which are covered by the combination of the DFT, the DFPT, and the all-electron FLAPW methods, reference [88] selects, as a first step, 3D bulk systems with a periodic lattice structure. Furthermore, (non-)collinear magnetism is not dealt with, since it introduces an additional level of complexity. In principle, however, it is possible to integrate it into the presented formalism. As part of future work, this will in particular derive even more benefit from the FLAPW method. The same holds true for the SOC, legitimating the scalar-relativistic approximation for obtaining the radial functions in the muffin-tin LAPW basis set. Hereinafter, a spin degeneracy (for example emerging in diamagnetic materials) is assumed, enabling one to suppress the spin index, provided a factor of two is considered.

Outline

In the following, section 6.1.1 recaps on the underlying phonon theory, because many essential equations at this point are still too generally formulated or information is partly isolated among the previous chapters. In order to frame this chapter and give an orientation for its remaining sections, section 6.1.2 delivers a road map, starting from the results of a preceding DFT calculation and ending with a phonon dispersion from DFPT.

6.1.1 Recapitulation with Emphasis on Phonons

Adiabatic approximation

Phonon quasiparticles constitute the quantum-mechanical approach for describing the physics of lattice vibrations in a solid, which basically subdivides into electrons and nuclei. By applying the Born–Oppenheimer approximation, the electrons decouple from the nuclei at lowest order. This enables one to deal with the electronic many-body system in the field of fixed nuclei, and vice versa to learn about the dynamics of the nuclei in the BO potential given the total energy of an electronic configuration. The total ground-state energy (BO potential) can be determined from the well-established Kohn–Sham DFT.

Linear response, harmonic frequencies

It changes slightly provided infinitesimal collective displacements, i.e., phonons alter the external potential

$$V_{\text{ext}}^{(0)}(\boldsymbol{r}) = -\sum_{\gamma} \frac{Z_{\gamma_{\boldsymbol{R}}}}{\left|\boldsymbol{r} - \boldsymbol{\tau}_{\gamma_{\boldsymbol{R}}}\right|} , \tag{6.1}$$

with $Z_{\gamma_{\boldsymbol{R}}}$ indicating the nuclear charge, and $\boldsymbol{\tau}_{\gamma_{\boldsymbol{R}}}$ denoting the position of an atom $\gamma_{\boldsymbol{R}}$ in the unit cell addressed by $\boldsymbol{R}$ (cf. the electron–ion potential in equation (1.1)). This variation of the external potential represents a phonon perturbation inducing an associated response. In linear order, this response of the electrons constitutes an integral part of the dynamical matrix which deduces from the second-order term in a perturbation series of the total energy. Diagonalizing the dynamical matrix results in the polarization vectors and the harmonic frequencies of the phonon. These three quantities relate to each other in the eigenvalue problem given by equations (3.7). As far as the Hohenberg–Kohn total energy in equation (2.1) is concerned, it is still correct because of the universality of its general functional, likewise holding true for systems undergoing such a perturbation [3]. Therefore, varying this ground-state functional is legitimate and yields valid results [3]. For vanishing forces the configuration of the nuclei minimizes the total energy. Its harmonic perturbation-series term represents the lowest-order correction, and one truncates higher-order terms within the harmonic approximation. Against this background, the general perturbation parameters used in chapter 3 and chapter 4 specify to $\boldsymbol{\tau}_{\gamma_{\boldsymbol{R}}}$ (see e.g. references [77, 79, 87]).

Density-Functional Perturbation Theory

In an elegant fashion, the linear response quantities for the dynamical matrix are self-consistently obtained from DFPT. Supported by the $2n+1$ theorem, higher-order variations of electronic quantities can be considered irrelevant for setting up the dynamical matrix.

In addition, Klüppelberg formulates his theory such that the polarization vectors surround the desired quantities, but they need not be determined before they become known anyway through the diagonalization of the dynamical matrix. Furthermore, it is generally feasible to choose any real number for each component of the phonon wave vector $\boldsymbol{q}$ without any additional effort. In periodic structures, DFPT namely allows for concentrating on a *single* representative unit cell with the volume Ω.

Bloch theorem

Periodic systems in which the potential fulfills

$$V^{(0)}(\boldsymbol{r}+\boldsymbol{R}) = V^{(0)}(\boldsymbol{r}) \tag{6.2}$$

allow for exploiting the Bloch theorem [198], resulting in eigenfunctions with Bloch character $\boldsymbol{k}$. However, a phonon displacing atoms $\alpha_{\boldsymbol{R}}$ impacts the periodic structure of the unperturbed lattice [22] so that

$$V^{(1)}(\boldsymbol{r}+\boldsymbol{R};\boldsymbol{q}\alpha) = \mathrm{e}^{\mathrm{i}\boldsymbol{q}\cdot\boldsymbol{R}} V^{(1)}(\boldsymbol{r};\boldsymbol{q}\alpha)\,. \tag{6.3}$$

Hence for every additional variation, a Bloch character shift by $\pm\boldsymbol{q}$ occurs, relative to the original Bloch character.

Linearized Augmented Plane-Wave basis

The LAPW basis is directly affected by the displacements of atoms $\alpha_{\boldsymbol{R}}$. Based on equation (5.17b), the transformation from the global to the local coordinate system of the MT spheres can be generalized to

$$\boldsymbol{r}_{\text{center}}^{\alpha,\boldsymbol{R},\boldsymbol{w}} = \boldsymbol{\tau}_{\alpha_{\boldsymbol{R}}} + \boldsymbol{R} + \boldsymbol{w}_{\alpha_{\boldsymbol{R}}}^{\boldsymbol{q}}\,. \tag{6.4}$$

This means the $\boldsymbol{\tau}_{\alpha_{\boldsymbol{R}}}$ are defined to be fixed in their equilibrium positions in the following, and the infinitesimal displacements

$$\begin{align}
\boldsymbol{w}_{\alpha_{\boldsymbol{R}}}^{\boldsymbol{q}} &= \boldsymbol{Q}_{\alpha_{\boldsymbol{R}}} \mathrm{e}^{\mathrm{i}\boldsymbol{q}\cdot\boldsymbol{R}} + \boldsymbol{Q}_{\alpha_{\boldsymbol{R}}}^{*} \mathrm{e}^{-\mathrm{i}\boldsymbol{q}\cdot\boldsymbol{R}} \tag{6.5a}\\
&=: \boldsymbol{w}_{\alpha_{\boldsymbol{R}}}^{\boldsymbol{q}^{+}} + \boldsymbol{w}_{\alpha_{\boldsymbol{R}}}^{\boldsymbol{q}^{-}} \tag{6.5b}
\end{align}$$

derive from a phonon with wave vector $\boldsymbol{q}$ and polarization $\boldsymbol{Q}_{\alpha_{\boldsymbol{R}}}$. They are composed of a complex "+"-summand and a complex conjugate "−"-summand, in order to avoid an unphysical complex-valued displacement. Relative to equation (3.5b), this displacement is time-independent, and the dependency of the polarization vectors on $\boldsymbol{q}$ inheres in the choice of generally indicating them by capital $\boldsymbol{Q}$ (in accordance[2] with reference [88]). It should be stressed that this concept of two counter-propagating phonons in equations (6.5) pervades the complete subsequent formalism. All in all, the LAPW basis (5.17) can thus be written as

$$\phi_{\boldsymbol{k},\boldsymbol{G},\boldsymbol{R}}^{(0),\boldsymbol{w}_{\alpha_{\boldsymbol{R}}}^{\boldsymbol{q}}}(\boldsymbol{r}) := \begin{cases}
\dfrac{1}{\sqrt{\Omega}}\mathrm{e}^{\mathrm{i}(\boldsymbol{k}+\boldsymbol{G})\cdot\boldsymbol{r}}, & \boldsymbol{r}\in \mathrm{IR}\\[2ex]
\displaystyle\sum_{lmp} a_{lmp}^{\boldsymbol{G}\boldsymbol{k}\gamma_{\boldsymbol{R}}} \vec{u}_{lp}^{\gamma\boldsymbol{R}}\left(\left|\boldsymbol{r}-\boldsymbol{r}_{\text{center}}^{\alpha,\boldsymbol{R},\boldsymbol{w}^{\boldsymbol{0}}}\right|_{\nu\gamma}\right)\mathrm{Y}_{lm}\left(\frac{\boldsymbol{r}-\boldsymbol{r}_{\text{center}}^{\alpha,\boldsymbol{R},\boldsymbol{w}^{\boldsymbol{0}}}}{\left|\boldsymbol{r}-\boldsymbol{r}_{\text{center}}^{\alpha,\boldsymbol{R},\boldsymbol{w}^{\boldsymbol{0}}}\right|}\right), & \boldsymbol{r}\in \mathrm{MT}_{\gamma_{\boldsymbol{R}}\neq\alpha_{\boldsymbol{R}}}\\[2ex]
\displaystyle\sum_{lmp} a_{lmp}^{\boldsymbol{G}\boldsymbol{k}\alpha\boldsymbol{R}} \vec{u}_{lp}^{\alpha\boldsymbol{R}}\left(\left|\boldsymbol{r}-\boldsymbol{r}_{\text{center}}^{\alpha,\boldsymbol{R},\boldsymbol{w}^{\boldsymbol{q}}}\right|_{\nu\alpha}\right)\mathrm{Y}_{lm}\left(\frac{\boldsymbol{r}-\boldsymbol{r}_{\text{center}}^{\alpha,\boldsymbol{R},\boldsymbol{w}^{\boldsymbol{q}}}}{\left|\boldsymbol{r}-\boldsymbol{r}_{\text{center}}^{\alpha,\boldsymbol{R},\boldsymbol{w}^{\boldsymbol{q}}}\right|}\right), & \boldsymbol{r}\in \mathrm{MT}_{\alpha_{\boldsymbol{R}}}\,,
\end{cases} \tag{6.6}$$

---

[2] Within this dissertation, a reasonable part of the nomenclature is borrowed from reference [88], in order to minimize confusion.

employing the previous two equations and setting $\boldsymbol{w} = \mathbf{0}$ in the undisplaced atom $\gamma_{\boldsymbol{R}} \neq \alpha_{\boldsymbol{R}}$. Without loss of generality, hereinafter the unit cell $\boldsymbol{R} = \mathbf{0}$ is chosen to be the representative unit cell with the volume Ω in order to suppress the index $\boldsymbol{R}$. However, in some cases (for instance equations (6.7)) the $\mathbf{0}$ is not inserted, e.g. if the Bloch character is thought to manifest itself.

Pulay corrections

From equation (6.6), it becomes obvious that the LAPW basis is expected to also describe the displaced MT sphere surrounding an atom α. Inserting equation (6.5a) into equation (5.71) yields the aforementioned Pulay correction

$$\begin{aligned}\phi^{(1)\alpha}_{\boldsymbol{k},\boldsymbol{G}}(\boldsymbol{r}) &= \boldsymbol{Q}^{\top}_{\alpha}\,[\mathrm{i}(\boldsymbol{k}+\boldsymbol{G}) - \boldsymbol{\nabla}]\phi^{(0)\alpha}_{\boldsymbol{k},\boldsymbol{G}}(\boldsymbol{r})\mathrm{e}^{\mathrm{i}\boldsymbol{q}\cdot\boldsymbol{R}} + \boldsymbol{Q}^{\dagger}_{\alpha}\,[\mathrm{i}(\boldsymbol{k}+\boldsymbol{G}) - \boldsymbol{\nabla}]\phi^{(0)\alpha}_{\boldsymbol{k},\boldsymbol{G}}(\boldsymbol{r})\mathrm{e}^{-\mathrm{i}\boldsymbol{q}\cdot\boldsymbol{R}} && (6.7\mathrm{a})\\ &=: \boldsymbol{Q}^{\top}_{\alpha}\,\boldsymbol{\phi}^{(1)\alpha+}_{\boldsymbol{k},\boldsymbol{G}}(\boldsymbol{r}) + \boldsymbol{Q}^{\dagger}_{\alpha}\,\boldsymbol{\phi}^{(1)\alpha-}_{\boldsymbol{k},\boldsymbol{G}}(\boldsymbol{r})\,. && (6.7\mathrm{b})\end{aligned}$$

The Bloch character of this basis correction is expressed by the additional superscripts $\pm$ denoting a shift by $\pm\boldsymbol{q}$.

First-order wave-function variation

Reviewing equation (5.64), the discussed variation of the Bloch character resolves $\tilde{\boldsymbol{k}}$ such that each term of $\Psi^{(1)}_{\boldsymbol{k},n}$ has Bloch character $\boldsymbol{k} \pm \boldsymbol{q}$. Explicitly, this yields

$$\begin{aligned}\Psi^{(1)}_{\boldsymbol{k},n}(\boldsymbol{r};\boldsymbol{q}) &= \sum_{\alpha}\Bigg(\boldsymbol{Q}^{\top}_{\alpha}\sum_{\boldsymbol{G}}\Big(\boldsymbol{z}^{(1)}_{\boldsymbol{G}}(\boldsymbol{k},n;\boldsymbol{q}\alpha)\phi^{(0)}_{\boldsymbol{k}+\boldsymbol{q},\boldsymbol{G}}(\boldsymbol{r}) + z^{(0)}_{\boldsymbol{G}}(\boldsymbol{k},n)\boldsymbol{\phi}^{(1)\alpha+}_{\boldsymbol{k},\boldsymbol{G}}(\boldsymbol{r})\Big) && (6.8\mathrm{a})\\ &\qquad + \boldsymbol{Q}^{\dagger}_{\alpha}\sum_{\boldsymbol{G}}\Big(\boldsymbol{z}^{(1)}_{\boldsymbol{G}}(\boldsymbol{k},n;-\boldsymbol{q}\alpha)\phi^{(0)}_{\boldsymbol{k}-\boldsymbol{q},\boldsymbol{G}}(\boldsymbol{r}) + z^{(0)}_{\boldsymbol{G}}(\boldsymbol{k},n)\boldsymbol{\phi}^{(1)\alpha-}_{\boldsymbol{k},\boldsymbol{G}}(\boldsymbol{r})\Big)\Bigg)\\ &:= \sum_{\alpha}\boldsymbol{Q}^{\top}_{\alpha}\,\boldsymbol{\Psi}^{(1)+}_{\boldsymbol{k},n}(\boldsymbol{r};\alpha) + \boldsymbol{Q}^{\dagger}_{\alpha}\,\boldsymbol{\Psi}^{(1)-}_{\boldsymbol{k},n}(\boldsymbol{r};\alpha)\,. && (6.8\mathrm{b})\end{aligned}$$

The basis functions or their variations must be evaluated at the same vector in reciprocal space as the wave-function expansion coefficients or their variations. Therefore, the variations of the MT basis functions are evaluated at $\boldsymbol{k}$, but still feature a Bloch character $\boldsymbol{k} \pm \boldsymbol{q}$, motivating the additional notation with $\pm$. Additionally, only the MT basis functions of the displaced atom α are to be corrected, the plane-wave basis in the IR remains complete under the emergence of phonons (cf. section 5.10).

Second-order wave function variation

Another variation to second-order, in which now atom β is displaced, leads to terms featuring a Bloch character of $\boldsymbol{k}$ and $\boldsymbol{k} \pm 2\boldsymbol{q}$. It shall turn out to suffice if only discussing the part of $\Psi^{(2)}_{\boldsymbol{k},n}$ which is of Bloch character $\boldsymbol{k}$, i.e., $\boldsymbol{q}$ equals $\mathbf{0}$ so that the matrix elements for the displaced atoms β and α read

$$\begin{aligned}&\Big[\Psi^{(2)\mathbf{0}}_{\boldsymbol{k},n}(\boldsymbol{r})\Big]_{\beta\alpha} && (6.9)\\ &\quad= \boldsymbol{Q}^{\dagger}_{\beta}\sum_{\boldsymbol{G}}\Big[\underline{z}^{(2)}_{\boldsymbol{G}}(\boldsymbol{k},n)\phi^{(0)}_{\boldsymbol{k},\boldsymbol{G}}(\boldsymbol{r}) + \boldsymbol{z}^{(1)}_{\boldsymbol{G}}(\boldsymbol{k},n;\boldsymbol{q}\alpha)\Big[\boldsymbol{\phi}^{(1)\beta-}_{\boldsymbol{k}+\boldsymbol{q},\boldsymbol{G}}(\boldsymbol{r})\Big]^{\top} + z^{(0)}_{\boldsymbol{G}}(\boldsymbol{k},n)\underline{\phi}^{(2)\mathbf{0}}_{\boldsymbol{k},\boldsymbol{G}}(\boldsymbol{r})\Big]\,\boldsymbol{Q}_{\alpha}\\ &\qquad+ \boldsymbol{Q}^{\top}_{\beta}\sum_{\boldsymbol{G}}\Big[\underline{z}^{(2)}_{\boldsymbol{G}}(\boldsymbol{k},n)\phi^{(0)}_{\boldsymbol{k},\boldsymbol{G}}(\boldsymbol{r}) + \boldsymbol{z}^{(1)}_{\boldsymbol{G}}(\boldsymbol{k},n;-\boldsymbol{q}\alpha)\Big[\boldsymbol{\phi}^{(1)+}_{\boldsymbol{k}-\boldsymbol{q},\boldsymbol{G}}(\boldsymbol{r})\Big]^{\top} + z^{(0)}_{\boldsymbol{G}}(\boldsymbol{k},n)\underline{\phi}^{(2)\mathbf{0}}_{\boldsymbol{k},\boldsymbol{G}}(\boldsymbol{r})\Big]\,\boldsymbol{Q}^{*}_{\alpha}\,.\end{aligned}$$

Charge variation

One assumes charge neutrality in an unperturbed system, meaning the number of electrons

$$N_{\mathrm{e}} = \int_{\Omega}\rho^{(0)}(\boldsymbol{r})\,\mathrm{d}^3r = \int_{\Omega}\sum_{\boldsymbol{k},n}f^{(0)}_{\boldsymbol{k},n}\Psi^{(0)*}_{\boldsymbol{k},n}(\boldsymbol{r})\Psi^{(0)}_{\boldsymbol{k},n}(\boldsymbol{r})\,\mathrm{d}^3r \qquad (6.10)$$

is equal to the sum of atom core charges $\sum_\gamma Z_\gamma$ and arranged in all unit cells so that a zero net charge results. Indeed, a phonon including its response changes the arrangement of electrons and ions to one another, nevertheless the number of electrons remains unaffected. In order to express this fact, equation (5.76) can be specified to equal bands n and $\boldsymbol{k}$-vectors and used as a constituent in the first-order variation of the electron number

$$\begin{aligned} 0 &= N_{\mathrm{e}}^{(1)} \qquad (6.11)\\ &:= \sum_\alpha \boldsymbol{Q}_\alpha^\top \left(\sum_{\boldsymbol{k},n} f_{\boldsymbol{k},n}^{(0)} \left[\left\langle \boldsymbol{\Psi}_{\boldsymbol{k},n}^{(1)+}(\alpha) \middle| \Psi_{\boldsymbol{k},n}^{(0)} \right\rangle + \left\langle \Psi_{\boldsymbol{k},n}^{(0)} \middle| \boldsymbol{\Psi}_{\boldsymbol{k},n}^{(1)+}(\alpha) \right\rangle \right] + \oint_{\partial\alpha} \hat{\boldsymbol{e}} \left[\rho_\alpha^{(0)}(\boldsymbol{r}) - \rho_{\mathrm{IR}}^{(0)}(\boldsymbol{r}) \right] \mathrm{d}S \right) \\ &+ \sum_\alpha \boldsymbol{Q}_\alpha^\dagger \left(\sum_{\boldsymbol{k},n} f_{\boldsymbol{k},n}^{(0)} \left[\left\langle \boldsymbol{\Psi}_{\boldsymbol{k},n}^{(1)-}(\alpha) \middle| \Psi_{\boldsymbol{k},n}^{(0)} \right\rangle + \left\langle \Psi_{\boldsymbol{k},n}^{(0)} \middle| \boldsymbol{\Psi}_{\boldsymbol{k},n}^{(1)-}(\alpha) \right\rangle \right] + \oint_{\partial\alpha} \hat{\boldsymbol{e}} \left[\rho_\alpha^{(0)}(\boldsymbol{r}) - \rho_{\mathrm{IR}}^{(0)}(\boldsymbol{r}) \right] \mathrm{d}S \right) . \end{aligned}$$

Occupation-number variation

Finally, Klüppelberg omits terms which are proportional to the variation of the occupation number. This is reasonable for insulators and semiconductors. But for metals, which in general have fractional occupation numbers, he assumes that the occupation numbers vanish for the first-order variation of the total energy (see Weinert and Davenport [252]). In second-order, i.e., regarding phonons, he rests on references [87, 97] for this statement to hold true, provided $\boldsymbol{q} \neq \boldsymbol{0}$. However for the Goldstone modes, additional terms [68, 86] become necessary in metals[3].

6.1.2 Road Map to Phonon Dispersions

Dynamical matrix

The dynamical matrix, which becomes diagonal in the vector space spanned by the polarization vectors $\boldsymbol{Q}$, relates to the second-order variation of the total energy by[4] [97]

$$E_{\mathrm{tot}}^{(2)}(\boldsymbol{q}) = \sum_{\beta\alpha} \boldsymbol{Q}_\beta^\dagger \underline{D}^{\beta\alpha}(\boldsymbol{q}^{+-}) \boldsymbol{Q}_\alpha + \boldsymbol{Q}_\beta^\top \underline{D}^{\beta\alpha}(\boldsymbol{q}^{-+}) \boldsymbol{Q}_\alpha^* \, . \qquad (6.12)$$

According to Savrasov [97], only these terms contribute to the dynamical matrix $\underline{D}$ that have a vanishing Bloch character[5], i.e., that have a product of terms with Bloch character $\boldsymbol{q}^+$ and $\boldsymbol{q}^-$. These mixed terms are indicated hereinafter by $\underline{D}(\boldsymbol{q}^{+-})$ or $\underline{D}(\boldsymbol{q}^{-+})$. As a function of $\boldsymbol{q}$, the eigenvalues of the dynamical matrix form the branches of the phonon dispersion-relation of interest. Therefore, the strategy is to vary the total energy in equation (5.63d) in order to identify the required constituents.

Total-energy variations

The first variation is given by [256]

$$\begin{aligned} E_{\mathrm{tot}}^{(1)} &= \sum_{\boldsymbol{k},n} \left(f_{\boldsymbol{k},n}^{(0)} \epsilon_{\boldsymbol{k},n}^{(1)} \right) - \int_\Omega \rho^{(0)}(\boldsymbol{r}) V_{\mathrm{eff}}^{(1)}(\boldsymbol{r}) \, \mathrm{d}^3 r + \int_\Omega \rho^{(0)}(\boldsymbol{r}) V_{\mathrm{ext}}^{(1)}(\boldsymbol{r}) \, \mathrm{d}^3 r + E_{\mathrm{ii}}^{(1)} \qquad (6.13) \\ &+ \sum_\beta \left[\boldsymbol{w}_\beta^{\boldsymbol{q}} \right]^\top \oint_{\partial\beta} \hat{\boldsymbol{r}} \left[\rho_\beta^{(0)}(\boldsymbol{r}) \left(\epsilon_{\mathrm{xc}}^{(0)\beta}(\boldsymbol{r}) - V_{\mathrm{xc}}^{(0)\beta}(\boldsymbol{r}) \right) - \rho_{\mathrm{IR}}^{(0)}(\boldsymbol{r}) \left(\epsilon_{\mathrm{xc}}^{(0)\mathrm{IR}}(\boldsymbol{r}) - V_{\mathrm{xc}}^{(0)\mathrm{IR}}(\boldsymbol{r}) \right) \right] \mathrm{d}S \, . \end{aligned}$$

---

[3] Neukirchen has derived these terms as an extension to the formalism [88] and finds that they only become relevant for metals with a polyatomic basis (unpublished).

[4] The Bloch character indicated in the dynamical matrices will be clarified within this chapter.

[5] The pure terms $\underline{D}(\boldsymbol{q}^{++})$ and $\underline{D}(\boldsymbol{q}^{--})$ would be proportional to $\exp(\pm \mathrm{i} 2\boldsymbol{q} \cdot \boldsymbol{R})$ and deliver contributions for $E_{\mathrm{tot}}^{(2)}(2\boldsymbol{q})$, although the investigation of $E_{\mathrm{tot}}^{(2)}(\boldsymbol{q})$ is intended [97].

Varying again yields the second-order variation [256]

$$\begin{aligned} E_{\text{tot}}^{(2)} = {} & \sum_{\boldsymbol{k},n} \Big(f_{\boldsymbol{k},n}^{(0)} \epsilon_{\boldsymbol{k},n}^{(2)} + f_{\boldsymbol{k},n}^{(1)} \epsilon_{\boldsymbol{k},n}^{(1)} \Big) - \int_{\varOmega} \rho^{(1)}(\boldsymbol{r}) V_{\text{eff}}^{(1)}(\boldsymbol{r})\, \mathrm{d}^3 r - \int_{\varOmega} \rho^{(0)}(\boldsymbol{r}) V_{\text{eff}}^{(2)}(\boldsymbol{r})\, \mathrm{d}^3 r \\ & + \int_{\varOmega} \rho^{(1)}(\boldsymbol{r}) V_{\text{ext}}^{(1)}(\boldsymbol{r})\, \mathrm{d}^3 r + \int_{\varOmega} \rho^{(0)}(\boldsymbol{r}) V_{\text{ext}}^{(2)}(\boldsymbol{r})\, \mathrm{d}^3 r + E_{\text{ii}}^{(2)} + E_{\text{tot,sf}}^{(2)} \,. \end{aligned} \tag{6.14a}$$

According to the arguments given in section 6.1.1, terms containing variations of occupation numbers in any variation of the total energy are dropped in the following. A closer inspection of the second-order Kohn–Sham energies lets them fall into three categories

$$\epsilon_{\boldsymbol{k},n}^{(2)} = \epsilon_{\boldsymbol{k},n}^{(2)\text{HF}} + \epsilon_{\boldsymbol{k},n}^{(2)\text{Pl}} + \epsilon_{\boldsymbol{k},n}^{(2)\text{sf}} \,, \tag{6.14b}$$

the Hellmann–Feynman (HF), the Pulay (Pl), and the surface (sf) terms. The HF and Pl terms are given by

$$\sum_{\boldsymbol{k},n} f_{\boldsymbol{k},n}^{(0)} \epsilon_{\boldsymbol{k},n}^{(2)\text{HF}} = \sum_{\boldsymbol{k},n} f_{\boldsymbol{k},n}^{(0)} \Big\langle \varPsi_{\boldsymbol{k},n}^{(0)} \Big| V_{\text{eff}}^{(2)} \Big| \varPsi_{\boldsymbol{k},n}^{(0)} \Big\rangle + \int_{\varOmega} \rho^{(1)}(\boldsymbol{r}) V_{\text{ext}}^{(1)}(\boldsymbol{r})\, \mathrm{d}^3 r \;, \tag{6.14c}$$

$$\begin{aligned} \sum_{\boldsymbol{k},n} f_{\boldsymbol{k},n}^{(0)} \epsilon_{\boldsymbol{k},n}^{(2)\text{Pl}} = {} & \sum_{\boldsymbol{k},n} f_{\boldsymbol{k},n}^{(0)} \Big\langle \varPsi_{\boldsymbol{k},n}^{(0)} \Big| V_{\text{eff}}^{(2)} \Big| \varPsi_{\boldsymbol{k},n}^{(0)} \Big\rangle + 2 \int_{\varOmega} \rho^{(1)}(\boldsymbol{r}) V_{\text{eff}}^{(1)}(\boldsymbol{r})\, \mathrm{d}^3 r \\ & + \sum_{\boldsymbol{k},n} f_{\boldsymbol{k},n}^{(0)} \bigg(\Big\langle \varPsi_{\boldsymbol{k},n}^{(2)} \Big| \mathscr{H}^{(0)} - \epsilon_{\boldsymbol{k},n}^{(0)} \Big| \varPsi_{\boldsymbol{k},n}^{(0)} \Big\rangle + \Big\langle \varPsi_{\boldsymbol{k},n}^{(0)} \Big| \mathscr{H}^{(0)} - \epsilon_{\boldsymbol{k},n}^{(0)} \Big| \varPsi_{\boldsymbol{k},n}^{(2)} \Big\rangle \\ & \qquad + 2 \Big\langle \varPsi_{\boldsymbol{k},n}^{(1)} \Big| \mathscr{H}^{(0)} - \epsilon_{\boldsymbol{k},n}^{(0)} \Big| \varPsi_{\boldsymbol{k},n}^{(1)} \Big\rangle \bigg) \,. \end{aligned} \tag{6.14d}$$

All surface terms that result from the second-order variation of the total energy (section 5.11), i.e., also including $\epsilon_{\boldsymbol{k},n}^{(2)\text{sf}}$, are attributed to

$$\begin{aligned} E_{\text{tot,sf}}^{(2)} = \sum_{\beta} \Big[\boldsymbol{w}_{\beta}^{\boldsymbol{q}} \Big]^{\top} \Bigg\{ & 2 \sum_{\boldsymbol{k},n} f_{\boldsymbol{k},n}^{(0)} \oint_{\partial\beta} \hat{\boldsymbol{r}} \Big[\varPsi_{\boldsymbol{k},n}^{*(1)\beta}(\boldsymbol{r}) \Big(\mathscr{H}^{(0)} - \epsilon_{\boldsymbol{k},n}^{(0)} \Big) \varPsi_{\boldsymbol{k},n}^{(0)\beta}(\boldsymbol{r}) \\ & \qquad - \varPsi_{\boldsymbol{k},n}^{*(1)\text{IR}}(\boldsymbol{r}) \Big(\mathscr{H}^{(0)} - \epsilon_{\boldsymbol{k},n}^{(0)} \Big) \varPsi_{\boldsymbol{k},n}^{(0)\text{IR}}(\boldsymbol{r}) \Big]\, \mathrm{d}S \\ & + 2 \sum_{\boldsymbol{k},n} f_{\boldsymbol{k},n}^{(0)} \oint_{\partial\beta} \hat{\boldsymbol{r}} \Big[\varPsi_{\boldsymbol{k},n}^{*(0)\beta}(\boldsymbol{r}) \Big(\mathscr{H}^{(0)} - \epsilon_{\boldsymbol{k},n}^{(0)} \Big) \varPsi_{\boldsymbol{k},n}^{(1)\beta}(\boldsymbol{r}) \\ & \qquad - \varPsi_{\boldsymbol{k},n}^{*(0)\text{IR}}(\boldsymbol{r}) \Big(\mathscr{H}^{(0)} - \epsilon_{\boldsymbol{k},n}^{(0)} \Big) \varPsi_{\boldsymbol{k},n}^{(1)\text{IR}}(\boldsymbol{r}) \Big]\, \mathrm{d}S \\ & + \delta_{\beta\alpha} \sum_{\alpha} \sum_{\boldsymbol{k},n} f_{\boldsymbol{k},n}^{(0)} \oint_{\partial\beta} \bigg[\boldsymbol{\nabla} \Big(\varPsi_{\boldsymbol{k},n}^{*(0)\beta}(\boldsymbol{r}) \Big(\mathscr{H}^{(0)} - \epsilon_{\boldsymbol{k},n}^{(0)} \Big) \varPsi_{\boldsymbol{k},n}^{(0)\beta}(\boldsymbol{r}) \Big) \\ & \qquad - \boldsymbol{\nabla} \Big(\varPsi_{\boldsymbol{k},n}^{*(0)\text{IR}}(\boldsymbol{r}) \Big(\mathscr{H}^{(0)} - \epsilon_{\boldsymbol{k},n}^{(0)} \Big) \varPsi_{\boldsymbol{k},n}^{(0)\text{IR}}(\boldsymbol{r}) \Big) \bigg] \hat{\boldsymbol{r}}^{\top}\, \mathrm{d}S\; \boldsymbol{w}_{\alpha}^{\boldsymbol{q}} \\ & + \delta_{\beta\alpha} \sum_{\alpha} \oint_{\partial\beta} \bigg[\boldsymbol{\nabla} \Big(\rho_{\beta}^{(0)}(\boldsymbol{r}) \Big(\epsilon_{\text{xc}}^{(0)\beta}(\boldsymbol{r}) - \mu_{\text{xc}}^{(0)\beta}(\boldsymbol{r}) \Big) \Big) \\ & \qquad - \boldsymbol{\nabla} \Big(\rho_{\text{IR}}^{(0)}(\boldsymbol{r}) \Big(\epsilon_{\text{xc}}^{(0)\text{IR}}(\boldsymbol{r}) - V_{\text{xc}}^{(0)\text{IR}}(\boldsymbol{r}) \Big) \Big) \bigg] \hat{\boldsymbol{r}}^{\top}\, \mathrm{d}S\; \boldsymbol{w}_{\alpha}^{\boldsymbol{q}} \\ & + \delta_{\beta\alpha} \oint_{\partial\beta} \hat{\boldsymbol{r}} \Big[\rho_{\beta}^{(0)}(\boldsymbol{r}) \Big(2 V_{\text{ext}}^{(1)\beta}(\boldsymbol{r}) + V_{\text{Htr}}^{(1)\beta}(\boldsymbol{r}) \Big) \\ & \qquad - \rho_{\text{IR}}^{(0)}(\boldsymbol{r}) \Big(2 V_{\text{ext}}^{(1)\text{IR}}(\boldsymbol{r}) + V_{\text{Htr}}^{(1)\text{IR}}(\boldsymbol{r}) \Big) \Big]\, \mathrm{d}S \Bigg\} \,. \end{aligned} \tag{6.14e}$$

Some of these terms result from additional variations of surface terms, such as the surface integral in equation (6.13). The way of calculating it is already discussed around equation (5.75). Inserting the HF (6.14c) and Pl (6.14d) contributions of the second-order Kohn–Sham energy variation into equation (6.14a), enables one to further evaluate the second-order variation of the total energy so that it is finally composed of

$$E^{(2)}_{\text{tot}} = E^{(2)}_{\text{tot,HF}} + E^{(2)}_{\text{tot,Pl}} + E^{(2)}_{\text{tot,sf}} \,, \tag{6.15a}$$

while

$$E^{(2)}_{\text{tot,HF}} = \int_{\Omega} \rho^{(1)}(\boldsymbol{r}) V^{(1)}_{\text{ext}}(\boldsymbol{r})\, \mathrm{d}^3 r + \int_{\Omega} \rho^{(0)}(\boldsymbol{r}) V^{(2)}_{\text{ext}}(\boldsymbol{r})\, \mathrm{d}^3 r + E^{(2)}_{\text{ii}} \tag{6.15b}$$

and

$$\begin{aligned} E^{(2)}_{\text{tot,Pl}} = & \int_{\Omega} \rho^{(1)}(\boldsymbol{r}) V^{(1)}_{\text{eff}}(\boldsymbol{r})\, \mathrm{d}^3 r + 2 \sum_{\boldsymbol{k},n} f^{(0)}_{\boldsymbol{k},n} \Big(\Big\langle \varPsi^{(2)}_{\boldsymbol{k},n} \Big| \mathscr{H}^{(0)} - \epsilon^{(0)}_{\boldsymbol{k},n} \Big| \varPsi^{(0)}_{\boldsymbol{k},n} \Big\rangle + \Big\langle \varPsi^{(0)}_{\boldsymbol{k},n} \Big| \mathscr{H}^{(0)} - \epsilon^{(0)}_{\boldsymbol{k},n} \Big| \varPsi^{(2)}_{\boldsymbol{k},n} \Big\rangle \\ & + 2 \Big\langle \varPsi^{(1)}_{\boldsymbol{k},n} \Big| \mathscr{H}^{(0)} - \epsilon^{(0)}_{\boldsymbol{k},n} \Big| \varPsi^{(1)}_{\boldsymbol{k},n} \Big\rangle \Big) \,. \end{aligned} \tag{6.15c}$$

The third term in equation (6.15a) is still given by equation (6.14e).

Required quantities

Equations (6.15) stimulate the introduction of the concept for the following discussion. It immediately becomes obvious that unperturbed quantities are required such as the charge density $\rho^{(0)}(\boldsymbol{r})$, the unperturbed Kohn–Sham wave functions $\varPsi^{(0)}_{\boldsymbol{k},n}$, the Kohn–Sham energies $\epsilon^{(0)}_{\boldsymbol{k},n}$, the effective potential $V^{(0)\beta}_{\text{eff}}(\boldsymbol{r})$ (or only the xc part), and the xc energy density $\epsilon^{(0)\beta}_{\text{xc}}(\boldsymbol{r})$. These are typical results of a classical DFT calculation preceding the application of the DFPT method. Quantities necessitated in the first-order variation are the charge-density variation $\rho^{(1)}(\boldsymbol{r})$, and therefore also the first-order variation of the Kohn–Sham energy $\epsilon^{(1)}_{\boldsymbol{k},n}$, as well as the variation of the effective potential $V^{(1)}_{\text{eff}}(\boldsymbol{r})$ (or parts of it). All of these first-order electronic quantities can be obtained from DFPT. What remains are the second-order variation of the external potential $V^{(2)}_{\text{ext}}(\boldsymbol{r})$, the second-order variation of the ion–ion interaction $E^{(2)}_{\text{ii}}$, and the part of the second-order wave function $\varPsi^{(2)\boldsymbol{0}}_{\boldsymbol{k}n}(\boldsymbol{r})$ with Bloch character $\boldsymbol{k}$. In contrast to the first-order quantities, the required second-order variations are related to the nuclei and hence do not involve employing a self-consistent approach. As soon as all quantities are available, the dynamical matrix can be calculated and diagonalized for a specific $\boldsymbol{q}$. This procedure can be repeated for any further arbitrary $\boldsymbol{q}$. However, in practice one tends to calculate only certain desired or high-symmetry points of the dispersion and interpolate the rest [92, 255, 257].

6.2 Charge Density Variations

Outline

Variations of the electron charge density are only required up to linear order. However, the linear change of the charge density can either be represented by a numerical gradient, which acts onto the unperturbed charge density, or by a first-order variation. The former is discussed in section 6.2.1 while the latter is the subject of section 6.2.2. In this context, equation (5.68) is to be considered.

6.2.1 Gradient of the Unperturbed Charge Density

Interstitial region

In the IR, one can apply the gradient with respect to $\boldsymbol{r}$ to the first term at the right-hand side of equation (5.18). Since there is no position dependency in the Fourier coefficients, the gradient only affects the plane waves so that

$$\boldsymbol{\nabla}\rho_{\mathrm{IR}}^{(0)}(\boldsymbol{r}) = \sum_{\boldsymbol{G}} \mathrm{i}\boldsymbol{G}\rho_{\mathrm{IR}}^{(0)}(\boldsymbol{G})\mathrm{e}^{\mathrm{i}\boldsymbol{G}\cdot\boldsymbol{r}} \,. \tag{6.16}$$

Muffin-tin spheres

The analytical gradient of the charge density in the MT spheres of atoms γ (second term at the right-hand side of equation (5.18)) turns out to be more sophisticated. Due to the product rule, both the radial expansion coefficients and the spherical harmonics in

$$\boldsymbol{\nabla}\rho_{\gamma}^{(0)}(\boldsymbol{r}) = \sum_{lm} \boldsymbol{\nabla}\left(\left[\rho_{\gamma}^{(0)}(r)\right]_{lm} \mathrm{Y}_{lm}(\hat{\boldsymbol{r}})\right) \tag{6.17a}$$

are subject to the application of the gradient. An elongated derivation, which can be found in appendix C, finally leads to

$$\begin{aligned}\boldsymbol{\nabla}\rho_{\gamma}^{(0)}\left(\boldsymbol{r}_{\gamma}\right) = \underline{T} \sum_{m''=-1}^{1} \hat{\boldsymbol{e}}_{m''}(-1)^{m''}\sqrt{\frac{4\pi}{3}} \sum_{lm} \mathrm{Y}_{lm}\left(\hat{\boldsymbol{r}}_{\gamma}\right) \sum_{l''|l''\in\{-1,1\}} G_{l,\;\;l+l'',\;\;1}^{m,\;m+m'',\;-m''} \\ \times \left[\frac{\partial\left[\rho_{\gamma}^{(0)}\left(r_{\gamma}\right)\right]_{l+l'',m'+m''}}{\partial r_{\gamma}} - \left(-l''l + \frac{\left(\mathrm{i}\sqrt{3}\right)^{l''+1}l'' - 1}{2}\right)\frac{\left[\rho_{\gamma}^{(0)}\left(r_{\gamma}\right)\right]_{l+l'',m'+m''}}{r_{\gamma}}\right] .\end{aligned} \tag{6.17b}$$

Correcting Klüppelberg [88]

This relation almost corresponds to Klüppelberg [88, equation (4.17)], apart from some differences concerning indices or prefactors. An implementation of his equation (4.17) does not deliver correct results and lets consistency checks fail, this discussion is postponed to section 7.2. In addition, Klüppelberg reuses this incorrect formula for the MT gradient in [88, equation (7.59)]. Since in equation (6.17b) the MT gradient is applied in a special coordinate system spanned by the unit vectors $\hat{\boldsymbol{e}}_{m''}$ (see appendix C), it must be transformed back to a cartesian gradient of a MT function by the transformation matrix

$$\underline{T} = \frac{1}{\sqrt{2}}\begin{pmatrix} 1 & 0 & -1 \\ -\mathrm{i} & 0 & -\mathrm{i} \\ 0 & \sqrt{2} & 0 \end{pmatrix} . \tag{6.17c}$$

It likewise differs from a wrong suggestion in [88, equation (4.18)].

Continuity

The LAPW basis ensures continuity up to $l_{\mathrm{max},\mathring{\gamma}}$ for a wave function expanded in it [68]. Applying the gradient to a function expanded in spherical harmonics lets contributions in the orbital quantum-number channel l scatter to the neighboring channels $l \pm 1$ [68]. Therefore, the continuity of a gradient quantity is strictly speaking restricted up to $l_{\mathrm{max},\mathring{\gamma}} - 1$ [68]. Furthermore, the gradient of the unperturbed charge density is influenced by the fact that there are discontinuities in the first-order derivatives of the wave functions leading to cusps for the charge density in the center of the MT spheres (see for example reference [258]). However, with the logarithmic mesh which is used in the MT sphere, the atomic position is only approximated, but never reached. Still, apart from relativistic effects the cusps result in a respective noncontinuous behavior of the unperturbed charge density, its gradient or quantities depending on them.

6.2.2 First-Order Variation of the Charge Density

Simplifications

The first-order variation of the density is already defined by equation (4.20e) in a compact way. In general, however, the product rule also implies the variation of the occupation numbers so that the first-order charge density variation for a spin-degenerate system (considered by a factor 2)[6] is given by

$$
\begin{aligned}
\rho^{(1)}(\boldsymbol{r};\boldsymbol{q}) &= 2\sum_{\boldsymbol{k},n} f^{(1)}_{\boldsymbol{k},n}(\boldsymbol{q})\mathit{\Psi}^{*(0)}_{\boldsymbol{k},n}(\boldsymbol{r})\mathit{\Psi}^{(0)}_{\boldsymbol{k},n}(\boldsymbol{r}) && \text{(6.18a)}\\
&\quad + 2\sum_{\boldsymbol{k},n} f^{(0)}_{\boldsymbol{k},n}\Big(\mathit{\Psi}^{*(1)}_{\boldsymbol{k},n}(\boldsymbol{r};\boldsymbol{q})\mathit{\Psi}^{(0)}_{\boldsymbol{k},n}(\boldsymbol{r}) + \mathit{\Psi}^{*(0)}_{\boldsymbol{k},n}(\boldsymbol{r})\mathit{\Psi}^{(1)}_{\boldsymbol{k},n}(\boldsymbol{r};\boldsymbol{q})\Big)\\
&= 2\sum_{\boldsymbol{k},n}\left(f^{(1)}_{\boldsymbol{k},n}(\boldsymbol{q})\mathit{\Psi}^{*(0)}_{\boldsymbol{k},n}(\boldsymbol{r})\mathit{\Psi}^{(0)}_{\boldsymbol{k},n}(\boldsymbol{r}) + 2\sum_{\boldsymbol{k},n} f^{(0)}_{\boldsymbol{k},n}\mathit{\Psi}^{*(0)}_{\boldsymbol{k},n}(\boldsymbol{r})\mathit{\Psi}^{(1)}_{\boldsymbol{k},n}(\boldsymbol{r};\boldsymbol{q})\right) . && \text{(6.18b)}
\end{aligned}
$$

In accordance with section 6.1.1, focussing on insulators, semiconductors, and metals with a monoatomic basis set, allows for only concentrating on the terms proportional to the unperturbed occupation number. Therewith, the second term in equation (6.18a) transforms into the respective term in equation (6.18b) (incorporating a factor 2) by exploiting

$$
\mathit{\Psi}^{(0)}_{-\boldsymbol{k},n}(\boldsymbol{r}) = \mathit{\Psi}^{*(0)}_{\boldsymbol{k},n}(\boldsymbol{r}) \, , \tag{6.19}
$$

according to the TRS [180]. In each system relevant within this thesis TRS holds[7], therefore the following discussion rests on TRS being obeyed.

Subdivision

In order to progress in terms of the all-electron FLAPW method, the states in equations (6.18) are subdivided into core states and valence states. Since the core density is ideally strictly confined within the MT spheres, its variation can be expressed by the gradient of the pointwise core wave-functions. Additionally, a phase factor dependent on $\boldsymbol{q}$ is required so that the description lives up to the displacements of the MT spheres, occurring for a phonon with wave vector $\pm\boldsymbol{q}$. In the valence spectrum, the LAPW basis (5.17) is utilized and corrected by Pulay contributions. Due to the TRS, it is sufficient to restrict the discussion to the first term in

$$
\rho^{(1)}(\boldsymbol{r};\boldsymbol{q}) = \sum_{\alpha} \boldsymbol{Q}^{\top}_{\alpha}\,\boldsymbol{\rho}^{(1)}\big(\boldsymbol{r};\boldsymbol{q}^{+}\alpha\big) + \boldsymbol{Q}^{\dagger}_{\alpha}\,\boldsymbol{\rho}^{(1)}\big(\boldsymbol{r};\boldsymbol{q}^{-}\alpha\big) \, , \tag{6.20}
$$

because the second one can be obtained from the first by a complex conjugation, switching also the Bloch character from $\boldsymbol{q}^{+}$ to $\boldsymbol{q}^{-}$ (cf. equation (6.19)). Equation (6.20) originates from inserting equation (6.8b) (including equations (6.7)) into the last term of equation (6.18b). The vectorial character of

$$
\begin{aligned}
\boldsymbol{\rho}^{(1)}\big(\boldsymbol{r};\boldsymbol{q}^{\pm}\alpha\big) &= -2\sum_{\boldsymbol{R}} \mathrm{e}^{\pm\mathrm{i}\boldsymbol{q}\cdot\boldsymbol{R}}\boldsymbol{\nabla}\rho^{(0)}_{\alpha}(\boldsymbol{r}) && \text{(6.21)}\\
&\quad + 4\sum_{\boldsymbol{k},n} f^{(0)}_{\boldsymbol{k},n}\sum_{\boldsymbol{G}'\boldsymbol{G}}\Big(z^{*(0)}_{\boldsymbol{G}'}(\boldsymbol{k},n)\boldsymbol{z}^{(1)}_{\boldsymbol{G}}(\boldsymbol{k},n;\pm\boldsymbol{q}\alpha)\phi^{*(0)}_{\boldsymbol{k},\boldsymbol{G}'}(\boldsymbol{r})\phi^{(0)}_{\boldsymbol{k}\pm\boldsymbol{q},\boldsymbol{G}}(\boldsymbol{r})\\
&\qquad + \sum_{\boldsymbol{R}}\Theta\Big(R^{\mathrm{MT}}_{\alpha} - \big|\boldsymbol{r}-\boldsymbol{\tau}_{\alpha}-\boldsymbol{R}\big|\Big)\mathrm{e}^{\pm\mathrm{i}\boldsymbol{q}\cdot\boldsymbol{R}}\\
&\qquad \times z^{*(0)}_{\boldsymbol{G}'}(\boldsymbol{k},n)z^{(0)}_{\boldsymbol{G}}(\boldsymbol{k},n)\phi^{*(0)}_{\boldsymbol{k},\boldsymbol{G}'}(\boldsymbol{r})\big(\mathrm{i}(\boldsymbol{k}+\boldsymbol{G})-\boldsymbol{\nabla}\big)\phi^{(0)}_{\boldsymbol{k},\boldsymbol{G}}(\boldsymbol{r})\Big)
\end{aligned}
$$

---

[6] In contrast, Klüppelberg includes the spin-degeneracy factor within the occupation numbers.

[7] TRS for instance is broken for crystals in a ferromagnetic order [133, 180].

derives from the cartesian directions in which a MT sphere, surrounding an ion, can be displaced. Further details can be considered as technical subtleties of the implementation and are therefore shifted to chapter 7.

6.3 Potential Variations

Overview

Throughout the formalism, the linear variations of the effective potential, the second-order variation of the ion–ion interaction, and the second-order variation of the external potential are necessitated. In first-order, the effective potential variation

$$\boldsymbol{V}_{\text{eff}}^{(1)}(\boldsymbol{r};\boldsymbol{q}^{\pm}\alpha) = \boldsymbol{V}_{\text{ext}}^{(1)}(\boldsymbol{r};\boldsymbol{q}^{\pm}\alpha) + \boldsymbol{V}_{\text{Htr}}^{(1)}(\boldsymbol{r};\boldsymbol{q}^{\pm}\alpha) + \boldsymbol{V}_{\text{xc}}^{(1)}(\boldsymbol{r};\boldsymbol{q}^{\pm}\alpha) \tag{6.22}$$

subdivides into the external, the Hartree, and the xc contribution. In the same manner as for instance in equation (6.20), equation (6.22) is part of

$$V_{\text{eff}}^{(1)}(\boldsymbol{r};\boldsymbol{q}) = \sum_{\alpha}\left(\boldsymbol{Q}_{\alpha}^{\top}\,\boldsymbol{V}_{\text{eff}}^{(1)}(\boldsymbol{r};\boldsymbol{q}^{+}\alpha) + \boldsymbol{Q}_{\alpha}^{\dagger}\,\boldsymbol{V}_{\text{eff}}^{(1)}(\boldsymbol{r};\boldsymbol{q}^{-}\alpha)\right). \tag{6.23}$$

The "+"-term and the "−"-term relate to each other like in equation (6.20). While the Hartree and xc potentials are purely electron-related, the first variation of the external potential in equation (6.1) is also dependent on the charges and the positions of the nuclei. However, $\boldsymbol{V}_{\text{ext}}^{(1)}(\boldsymbol{r};\boldsymbol{q}^{\pm}\alpha)$ does not incorporate a variation of the charge density, enabling one to vary it again in accordance with the $2n+1$ theorem. This results in the second-order variation of the external potential which can be decomposed into

$$\begin{aligned} V_{\text{ext}}^{(2)}(\boldsymbol{r};\boldsymbol{q}) = \sum_{\beta\alpha\boldsymbol{R}}\Big[&\boldsymbol{Q}_{\beta}^{\top}\left(\boldsymbol{\nabla}\boldsymbol{\nabla}^{\top}V_{\text{ext}}^{(0)\boldsymbol{R}}(\boldsymbol{r})\right)\boldsymbol{Q}_{\alpha}\mathrm{e}^{2\mathrm{i}\boldsymbol{q}\cdot\boldsymbol{R}} + \boldsymbol{Q}_{\beta}^{\dagger}\left(\boldsymbol{\nabla}\boldsymbol{\nabla}^{\top}V_{\text{ext}}^{\beta\boldsymbol{R}}(\boldsymbol{r})\right)\boldsymbol{Q}_{\alpha}^{*}\mathrm{e}^{-2\mathrm{i}\boldsymbol{q}\cdot\boldsymbol{R}} \\ &+ \boldsymbol{Q}_{\beta}^{\top}\left(\boldsymbol{\nabla}\boldsymbol{\nabla}^{\top}V_{\text{ext}}^{\beta\boldsymbol{R}}(\boldsymbol{r})\right)\boldsymbol{Q}_{\alpha}^{*} + \boldsymbol{Q}_{\beta}^{\dagger}\left(\boldsymbol{\nabla}\boldsymbol{\nabla}^{\top}V_{\text{ext}}^{\beta\boldsymbol{R}}(\boldsymbol{r})\right)\boldsymbol{Q}_{\alpha}\Big]. \end{aligned} \tag{6.24}$$

But its calculation entails numerical drawbacks, urging one to circumvent the evaluation of this potential, further details are provided in section 7.6.3. For this reason, the derivation of the potential $V_{\text{ext}}^{(2)}(\boldsymbol{r})$ is not reviewed hereinafter. Finally, the second-order ion–ion interaction involves only the nuclei.

General concept

All potential variations in the work of Klüppelberg are set up in analogy either to the Weinert construction of the Coulomb potential in section 5.6.1, or the xc potential in section 5.6.2. The essential differences are that for the Hartree and the xc parts, the unperturbed charge density is substituted by a gradient, or the first-order variation of the charge density. Furthermore, concerning the external potential, a gradient is applied to the Dirac delta-distribution which describes the point charge. Additionally, the calculation of the second-order ion–ion-interaction variation in particular differs from the usually-employed Ewald summation. Klüppelberg bases his proposal on a publication of Weinert, Wimmer, and Freeman [66] which suggests a similar approach as for the Coulomb potential.

Outline

The linear variations of the external potential are the subject of section 6.3.1, the setup of the linear Hartree potential variations is addressed in section 6.3.2, and the linear xc-potential variations are dealt with in section 6.3.3. Section 6.3.4 concludes with the setup of the second-order ion–ion interaction.

6.3.1 Linear Variations of the External Potential

The linear external potential variations are handled in the same way as the Coulomb potential in section 5.6.1. Therefore, a separate consideration of the IR and the MT spheres ensues.

Interstitial contribution

Real charge

Due to the phonon, the point charges undergo a shift which is expressed by applying the gradient to a position-dependent Dirac delta-distribution. If the displacement amplitudes of the MT spheres must live up to modulation with a finite $\boldsymbol{q}$, an additional phase factor $\exp(\mathrm{i}\tilde{\boldsymbol{q}}\cdot\boldsymbol{R})$ becomes necessary. For the sake of avoiding redundancy, the notation $\tilde{\boldsymbol{q}}$ of Klüppelberg is introduced. Expressions containing a $\tilde{\boldsymbol{q}}$ are valid for gradients ($\tilde{\boldsymbol{q}} = \boldsymbol{0}$) or first-order variations with an arbitrary $\boldsymbol{q}^{\pm} = \tilde{\boldsymbol{q}}$. Provided the bare gradient of the external potential is of interest, the aforementioned phase factor becomes the neutral element of multiplication. Hence, the charge variation for the linear variation of the external potential is assumed to be

$$\boldsymbol{n}_{\text{ext}}(\boldsymbol{r}, \tilde{\boldsymbol{q}}\alpha_{\boldsymbol{R}}) = \sum_{\boldsymbol{R}} Z_{\alpha}\mathrm{e}^{\pm\mathrm{i}\tilde{\boldsymbol{q}}\cdot\boldsymbol{R}}\boldsymbol{\nabla}\delta\left(\boldsymbol{r} - \boldsymbol{\tau}_{\alpha_{\boldsymbol{R}}} - \boldsymbol{R}\right). \tag{6.25}$$

Multipole moments

One immediately envisages that a plane-wave expansion does not work well in this case. Therefore, one can avoid the gradient with respect to the Dirac delta distribution by employing integration by parts. The boundary terms vanish because the Dirac delta distribution only contributes at the MT sphere centers of the displaced atoms α and not at their MT sphere boundaries. This leads to the multipole moments

$$\boldsymbol{\mathsf{q}}_{lm}^{\gamma\boldsymbol{R}'}(\tilde{\boldsymbol{q}}\alpha) = -Z_{\alpha}\mathrm{e}^{\pm\mathrm{i}\tilde{\boldsymbol{q}}\cdot\boldsymbol{R}'}\delta_{\gamma\alpha}\boldsymbol{\nabla}\left[r^{l}\mathrm{Y}_{lm}^{*}(\hat{\boldsymbol{r}})\right]_{\boldsymbol{r}=\boldsymbol{0}} \tag{6.26}$$

Pseudo-density

for MT sphere γ in the unit cell $\boldsymbol{R}'$, if atom α (and its images, which is implicitly assumed hereinafter) is displaced to satisfy a phonon with wave vector $\tilde{\boldsymbol{q}}$. Due to the Kronecker delta in the last relation, a pseudo-charge is only located in the displaced atom α. Moreover, Klüppelberg shows that only the channel with orbital quantum number $l = 1$ delivers a contribution, as equation (6.26) is evaluated at the MT sphere center. Since this form of the multipole moments is not easily tractable (cf. section 6.2.1), Klüppelberg suggests the reformulation

$$\sum_{m=-1}^{1}\left(\boldsymbol{\nabla}_{\boldsymbol{s}}\left[s\mathrm{Y}_{1m}^{*}(\hat{\boldsymbol{s}})\right]_{\boldsymbol{s}=\boldsymbol{0}}\right)\mathrm{Y}_{1m}(\hat{\boldsymbol{r}}_{\alpha}) = \frac{3}{4\pi}\hat{\boldsymbol{r}}_{\alpha} \tag{6.27a}$$

$$= \sum_{i=1}^{3}\hat{\boldsymbol{e}}_{i}\sum_{m=-1}^{1}\frac{3}{4\pi}\zeta_{im}\mathrm{Y}_{1m}(\hat{\boldsymbol{r}}_{\alpha}), \tag{6.27b}$$

with the matrix elements

$$\underline{\zeta} = \sqrt{\frac{2\pi}{3}}\begin{pmatrix} 1 & 0 & -1 \\ \mathrm{i} & 0 & \mathrm{i} \\ 0 & \sqrt{2} & 0 \end{pmatrix}, \tag{6.27c}$$

defining the linear combination of spherical harmonics for the vector $\boldsymbol{r}$. This form (6.27b) leads to the pseudo-density

$$\begin{aligned} \boldsymbol{n}^{\text{ps}}_{\text{ext}}(\boldsymbol{G};\tilde{\boldsymbol{q}}\alpha) &= -\frac{4\pi}{\Omega}\sum_{m=-1}^{1}\frac{\mathrm{i}(2+2N+3)!!}{(2+1)!!R_\alpha}\frac{\mathrm{j}_{1+N+1}(|\boldsymbol{G}\pm\tilde{\boldsymbol{q}}|R_\alpha)}{(|\boldsymbol{G}\pm\tilde{\boldsymbol{q}}|R_\alpha)^{N+1}}\mathrm{e}^{-\mathrm{i}(\boldsymbol{G}\pm\tilde{\boldsymbol{q}})\cdot\boldsymbol{\tau}_\alpha} && \text{(6.28a)} \\ &\qquad\times \mathrm{Y}_{1m}\left(\widehat{\boldsymbol{G}\pm\tilde{\boldsymbol{q}}}\right)\mathbf{q}^{\alpha\boldsymbol{0}}_{1m}(\tilde{\boldsymbol{q}}\alpha) \\ &= \mathrm{i}\frac{Z_\alpha}{\Omega}(2N+5)!!\frac{(\boldsymbol{G}\pm\tilde{\boldsymbol{q}})\mathrm{e}^{-\mathrm{i}(\boldsymbol{G}\pm\tilde{\boldsymbol{q}})\cdot\boldsymbol{\tau}_\alpha}}{(|\boldsymbol{G}\pm\tilde{\boldsymbol{q}}|R_\alpha)^{N+2}}\mathrm{j}_{N+2}(|\boldsymbol{G}\pm\tilde{\boldsymbol{q}}|R_\alpha) && \text{(6.28b)} \\ \boldsymbol{n}^{\text{ps}}_{\text{ext}}(\boldsymbol{0};\tilde{\boldsymbol{q}}\alpha) &= \boldsymbol{0}\,. && \text{(6.28c)} \end{aligned}$$

Now, both the first-order variation of the external potential

Potentials

$$\begin{aligned} \boldsymbol{V}^{(1)}_{\text{ext}}(\boldsymbol{r};\boldsymbol{q}^{\pm}\alpha) &= \sum_{\boldsymbol{G}|\boldsymbol{G}\pm\boldsymbol{q}\neq\boldsymbol{0}} 4\pi\frac{\boldsymbol{n}^{\text{ps}}_{\text{ext}}(\boldsymbol{G};\boldsymbol{q}^{\pm}\alpha)}{|\boldsymbol{G}\pm\boldsymbol{q}|^2}\mathrm{e}^{\mathrm{i}(\boldsymbol{G}\pm\boldsymbol{q})\cdot\boldsymbol{r}} && \text{(6.29a)} \\ &=: \sum_{\boldsymbol{G}|\boldsymbol{G}\pm\boldsymbol{q}\neq\boldsymbol{0}} \boldsymbol{V}^{(1)}_{\text{ext}}(\boldsymbol{G};\boldsymbol{q}^{\pm}\alpha)\mathrm{e}^{\mathrm{i}(\boldsymbol{G}\pm\boldsymbol{q})\cdot\boldsymbol{r}} && \text{(6.29b)} \end{aligned}$$

and the gradient of the first-order variation can be separately set up by solving the Poisson equation. The gradient is in line with a collective displacement of all atoms, without a $\boldsymbol{q}$-modulation, therefore an additional sum over all atoms implies

$$\begin{aligned} \boldsymbol{\nabla}V^{(0)}_{\text{ext}}(\boldsymbol{r}) &= -\sum_{\boldsymbol{G}|\boldsymbol{G}\neq\boldsymbol{0}}\sum_{\alpha} 4\pi\frac{\boldsymbol{n}^{\text{ps}}_{\text{ext}}(\boldsymbol{G};\alpha)}{|\boldsymbol{G}|^2}\mathrm{e}^{\mathrm{i}\boldsymbol{G}\cdot\boldsymbol{r}} && \text{(6.30a)} \\ &=: \sum_{\boldsymbol{G}|\boldsymbol{G}\neq\boldsymbol{0}}\left[\boldsymbol{\nabla}V^{(0)}_{\text{ext}}\right](\boldsymbol{G})\mathrm{e}^{\mathrm{i}\boldsymbol{G}\cdot\boldsymbol{r}}\,. && \text{(6.30b)} \end{aligned}$$

Muffin-tin contribution

After the IR representation for the first-order variation of the external potential and the gradient of the external potential have been found, a Dirichlet boundary-value problem is solved. As a consequence, the spherical harmonic coefficients of the MT first-order external-potential variation are given by

$$\begin{aligned} &\left[\boldsymbol{V}^{(1)}_{\text{ext}}\left(\boldsymbol{r}_\gamma+\boldsymbol{\tau}_\gamma+\boldsymbol{R}';\boldsymbol{q}^{\pm}\alpha\right)\right]_{lm} && \text{(6.31)} \\ &\quad= \mathrm{e}^{\pm\mathrm{i}\boldsymbol{q}\cdot\boldsymbol{R}'}\sum_{\boldsymbol{G}|\boldsymbol{G}\pm\boldsymbol{q}\neq\boldsymbol{0}} \mathrm{e}^{\mathrm{i}(\boldsymbol{G}\pm\boldsymbol{q})\cdot\boldsymbol{\tau}_\gamma}\boldsymbol{V}^{(1)}_{\text{ext}}(\boldsymbol{G};\boldsymbol{q}^{\pm}\alpha)\left(\frac{r_\gamma}{R_\gamma}\right)^{l}4\pi\mathrm{i}^l\mathrm{Y}^{*}_{lm}\left(\widehat{\boldsymbol{G}\pm\boldsymbol{q}}\right)\mathrm{j}_l\left(|\boldsymbol{G}\pm\boldsymbol{q}|R_\gamma\right) \\ &\qquad - \mathrm{e}^{\pm\mathrm{i}\boldsymbol{q}\cdot\boldsymbol{R}'}Z_\alpha\delta_{\gamma\alpha}\frac{4\pi}{3}\frac{1}{r_\alpha^2}\left(1-\left(\frac{r_\alpha}{R_\alpha}\right)^{3}\right)\sum_{m=-1}^{1}\frac{3}{4\pi}\sum_i\hat{\boldsymbol{e}}_i\zeta_{im}\,. \end{aligned}$$

Furthermore, the gradient of the unperturbed external potential in the MT spheres reads

$$\begin{aligned} \left[\boldsymbol{\nabla}V^{(0)}_{\text{ext}}\left(\boldsymbol{r}_\gamma+\boldsymbol{\tau}_\gamma+\boldsymbol{R}'\right)\right]_{lm} &= \sum_{\boldsymbol{G}|\boldsymbol{G}\neq\boldsymbol{0}}\mathrm{e}^{\mathrm{i}\boldsymbol{G}\cdot\boldsymbol{\tau}_\gamma}\left[\boldsymbol{\nabla}V^{(0)}_{\text{ext}}\right](\boldsymbol{G})\left(\frac{r_\gamma}{R_\gamma}\right)^{l}4\pi\mathrm{i}^l\mathrm{Y}^{*}_{lm}\left(\hat{\boldsymbol{G}}\right)\mathrm{j}_l\left(|\boldsymbol{G}|R_\gamma\right) \\ &\quad + Z_\alpha\delta_{\gamma\alpha}\frac{4\pi}{3}\frac{1}{r_\alpha^2}\left(1-\left(\frac{r_\alpha}{R_\alpha}\right)^{3}\right)\sum_{m=-1}^{1}\frac{3}{4\pi}\sum_i\hat{\boldsymbol{e}}_i\zeta_{im}\,. && \text{(6.32)} \end{aligned}$$

6.3.2 Linear Variations of the Hartree Potential

Motivation

Calculating the linear variations of the Hartree potential seems less sophisticated, because no gradients of Dirac delta distributions are involved. Nevertheless, the linear all-electron charge-density variations are still not well-describable in a Fourier expansion, especially in the vicinity of the nuclei. Therefore, Klüppelberg again applies the Coulomb potential scheme of Weinert, which is why this section subdivides into the setup of the IR and MT contributions of the linear Hartree variations.

Interstitial contribution

Multipole moments

When calculating the multipole moments, one must account for the charge density variation given in the MT spheres as well as in the IR. Klüppelberg therefore derives for the multipole moments of the first-order Hartree potential variation

$$\begin{aligned}&\left[\mathbf{q}^{\gamma\boldsymbol{R}'}_{\delta\rho}\left(\boldsymbol{q}^{\pm}\alpha\right)\right]_{lm} \qquad (6.33)\\ &= \mathrm{e}^{\pm\mathrm{i}\boldsymbol{q}\cdot\boldsymbol{R}'}\int_0^{R_{\mathring{\gamma}}} r_{\nu\mathring{\gamma}}^{l+2}\left[\boldsymbol{\rho}^{(1)}_{\gamma,\mathrm{full}}\left(r_{\nu\mathring{\gamma}};\boldsymbol{q}^{\pm}\alpha\right)\right]_{lm}\mathrm{d}r_{\nu\mathring{\gamma}}\\ &\quad - 4\pi\mathrm{i}^l R_{\mathring{\gamma}}^{l+3}\mathrm{e}^{\pm\mathrm{i}\boldsymbol{q}\cdot\boldsymbol{R}'}\sum_{\boldsymbol{G}|\boldsymbol{G}+\boldsymbol{q}\neq\boldsymbol{0}}\boldsymbol{\rho}^{(1)}_{\mathrm{IR}}(\boldsymbol{G};\boldsymbol{q}^{\pm}\alpha)\mathrm{e}^{\mathrm{i}(\boldsymbol{G}\pm\boldsymbol{q})\cdot\boldsymbol{\tau}_\gamma}\mathrm{Y}^*_{lm}\left(\widehat{\boldsymbol{G}\pm\boldsymbol{q}}\right)\frac{\mathrm{j}_{l+1}\left(|\boldsymbol{G}\pm\boldsymbol{q}|R_{\mathring{\gamma}}\right)}{|\boldsymbol{G}\pm\boldsymbol{q}|R_{\mathring{\gamma}}}\,,\end{aligned}$$

while the multipole moments for the gradient of the Hartree potential variation read

$$\begin{aligned}\left[\mathbf{q}^{\gamma\boldsymbol{R}'}_{\boldsymbol{\nabla}\rho}\right]_{lm} &= \int_0^{R_{\mathring{\gamma}}} r_{\nu\mathring{\gamma}}^{l+2}\left[\boldsymbol{\nabla}\rho^{(0)}_{\gamma}\left(r_{\nu\mathring{\gamma}}\right)\right]_{lm}\mathrm{d}r_{\nu\mathring{\gamma}} \qquad (6.34)\\ &\quad - 4\pi\mathrm{i}^l R_{\mathring{\gamma}}^{l+3}\sum_{\boldsymbol{G}|\boldsymbol{G}\neq\boldsymbol{0}}\left[\boldsymbol{\nabla}\rho^{(0)}_{\mathrm{IR}}\right](\boldsymbol{G})\mathrm{e}^{\mathrm{i}\boldsymbol{G}\cdot\boldsymbol{\tau}_\gamma}\mathrm{Y}^*_{lm}\left(\hat{\boldsymbol{G}}\right)\frac{\mathrm{j}_{l+1}\left(|\boldsymbol{G}|R_{\mathring{\gamma}}\right)}{|\boldsymbol{G}|R_{\mathring{\gamma}}}\,.\end{aligned}$$

Both multipole moments exhibit analogies to the Hartree multipole moments in section 5.6.1, particularly because the contributions of the IR charge-density variation and that of the MT sphere are subtracted from each other. Moreover, since equations (6.33) and (6.34) need no further reformulation for the implementation, I anticipate the nomenclature of chapter 7, and already indicate the discrete logarithmic MT mesh $r_{\nu\mathring{\gamma}}$ of atom γ at this point. Furthermore, some quantities remain equal in all MT spheres of the same atom type, and thus must only be stored once for the representative MT sphere $\mathring{\gamma}$ (see section 5.7). This I display by a small circle above the atom indices hereinafter. Due to the discontinuity of the charge density an additional surface term

Surface-term multipole correction

$$\left[\mathbf{q}^{\gamma\boldsymbol{R}'}_{\mathrm{surf}}(\tilde{\boldsymbol{q}}\alpha)\right]_{lm} = \delta_{\gamma\alpha}\mathrm{e}^{\pm\mathrm{i}\tilde{\boldsymbol{q}}\cdot\boldsymbol{R}'}\oint_{\partial\alpha}\hat{\boldsymbol{e}}\mathrm{Y}^*_{lm}(\hat{\boldsymbol{r}}_\alpha)r_\alpha^l\left(\rho^{(0)}_\alpha(\boldsymbol{r}_\alpha+\boldsymbol{\tau}_\alpha)-\rho^{(0)}_{\mathrm{IR}}(\boldsymbol{r}_\alpha+\boldsymbol{\tau}_\alpha)\right)\mathrm{d}S \qquad (6.35)$$

with the aforementioned $\tilde{\boldsymbol{q}}$ notation must be included into the calculation of the multipole moments. In order to calculate this term, the charge density response

$$\boldsymbol{n}_{\mathrm{surf}}(\tilde{\boldsymbol{q}}\alpha) = \left(\rho^{(0)}_\alpha(\boldsymbol{r})-\rho^{(0)}_{\mathrm{IR}}(\boldsymbol{r})\right)\Big|_{\partial\alpha}\sum_{\boldsymbol{R}}\mathrm{e}^{\pm\mathrm{i}\tilde{\boldsymbol{q}}\cdot\boldsymbol{R}}\frac{\boldsymbol{r}-\boldsymbol{\tau}_{\alpha_{\boldsymbol{R}}}-\boldsymbol{R}}{\left|\boldsymbol{r}-\boldsymbol{\tau}_{\alpha_{\boldsymbol{R}}}-\boldsymbol{R}\right|}\delta\left(R_\alpha-\left|\boldsymbol{r}-\boldsymbol{\tau}_{\alpha_{\boldsymbol{R}}}-\boldsymbol{R}\right|\right) \qquad (6.36)$$

can be assumed. The surface contribution is a function of the electron charge density discontinuity and usually less relevant than the remaining contributions of the multipole moments. All in all, the aforementioned multipole moments contributions for the first-order variation of the Hartree potential combine to

Pseudo-densities

$$\left[\mathfrak{q}^{\gamma\boldsymbol{R}'}_{\delta\rho,\text{tot}}\left(\boldsymbol{q}^{\pm}\alpha\right)\right]_{lm} = \left[\mathfrak{q}^{\gamma\boldsymbol{R}'}_{\delta\rho}\left(\boldsymbol{q}^{\pm}\alpha\right)\right]_{lm} + \left[\mathfrak{q}^{\gamma\boldsymbol{R}'}_{\text{surf}}\left(\boldsymbol{q}^{\pm}\alpha\right)\right]_{lm} \tag{6.37}$$

and the pseudo-density with these multipole moments is given by

$$\begin{aligned} \boldsymbol{n}^{\text{ps},\delta\rho}_{\text{Htr}}\left(\boldsymbol{G};\boldsymbol{q}^{\pm}\alpha\right) = \boldsymbol{\rho}^{(1)}_{\text{IR}}\left(\boldsymbol{G};\boldsymbol{q}^{\pm}\alpha\right) + \frac{4\pi}{\Omega}\sum_{\gamma}\sum_{lm}\frac{(-\mathrm{i})^{l}(2l+2N+3)!!}{(2l+1)!!R^{l}_{\gamma}}\frac{\mathrm{j}_{l+N+1}\left(|\boldsymbol{G}\pm\boldsymbol{q}|R_{\gamma}\right)}{\left(|\boldsymbol{G}\pm\boldsymbol{q}|R_{\gamma}\right)^{N+1}} \\ \times\, \mathrm{e}^{-\mathrm{i}(\boldsymbol{G}\pm\boldsymbol{q})\cdot\tau_{\gamma}}\mathrm{Y}_{lm}\left(\widehat{\boldsymbol{G}\pm\boldsymbol{q}}\right)\left[\boldsymbol{q}^{\gamma\boldsymbol{R}'}_{\delta\rho,\text{tot}}\left(\boldsymbol{q}^{\pm}\alpha\right)\right]_{lm}. \end{aligned} \tag{6.38}$$

The multipole moments for the gradient of the unperturbed Hartree potential, with the Kronecker delta in the surface contribution already evaluated, are given by

$$\left[\mathfrak{q}^{\gamma\boldsymbol{R}'}_{\boldsymbol{\nabla}\rho,\text{tot}}\right]_{lm} = \left[\mathfrak{q}^{\gamma\boldsymbol{R}'}_{\boldsymbol{\nabla}\rho}\right]_{lm} - \sum_{\alpha}\left[\mathfrak{q}^{\gamma\boldsymbol{R}'}_{\text{surf}}\left(\tilde{\boldsymbol{q}}^{\pm}\alpha\right)\right]_{lm} \tag{6.39}$$

so that the pseudo-charges yield

$$\begin{aligned} \boldsymbol{n}^{\text{ps},\boldsymbol{\nabla}}_{\text{Htr}}(\boldsymbol{G}) = \boldsymbol{\nabla}\rho^{(0)}_{\text{IR}}(\boldsymbol{G}) + \frac{4\pi}{\Omega}\sum_{\gamma}\sum_{lm}\frac{(-\mathrm{i})^{l}(2l+2N+3)!!}{(2l+1)!!R^{l}_{\gamma}}\frac{\mathrm{j}_{l+N+1}\left(|\boldsymbol{G}|R_{\gamma}\right)}{\left(|\boldsymbol{G}|R_{\gamma}\right)^{N+1}} \\ \times\, \mathrm{e}^{-\mathrm{i}\boldsymbol{G}\cdot\boldsymbol{\tau}_{\gamma}}\mathrm{Y}_{lm}\left(\hat{\boldsymbol{G}}\right)\left[\mathfrak{q}^{\gamma\boldsymbol{R}'}_{\boldsymbol{\nabla}\rho,\text{tot}}\right]_{lm}. \end{aligned} \tag{6.40}$$

These pseudo-densities can be used to solve the Poisson equation and obtain the IR representation of the first-order Hartree potential variation

Potentials

$$\boldsymbol{V}^{(1)}_{\text{Htr}}\left(\boldsymbol{r};\boldsymbol{q}^{\pm}\alpha\right) = \sum_{\boldsymbol{G}|\boldsymbol{G}\pm\boldsymbol{q}\neq\boldsymbol{0}} 4\pi\frac{\boldsymbol{n}^{\text{ps},\delta\rho}_{\text{Htr}}\left(\boldsymbol{G};\boldsymbol{q}^{\pm}\alpha\right)}{|\boldsymbol{G}\pm\boldsymbol{q}|^{2}}\mathrm{e}^{\mathrm{i}(\boldsymbol{G}\pm\boldsymbol{q})\cdot\boldsymbol{r}} \tag{6.41a}$$

$$:= \sum_{\boldsymbol{G}|\boldsymbol{G}\pm\boldsymbol{q}\neq\boldsymbol{0}} \boldsymbol{V}^{(1)}_{\text{Htr}}\left(\boldsymbol{G};\boldsymbol{q}^{\pm}\alpha\right)\mathrm{e}^{\mathrm{i}(\boldsymbol{G}\pm\boldsymbol{q})\cdot\boldsymbol{r}}. \tag{6.41b}$$

The IR representation for the gradient of the unperturbed Hartree potential reads

$$\boldsymbol{\nabla}V^{(0)}_{\text{Htr}}(\boldsymbol{r}) = \sum_{\boldsymbol{G}|\boldsymbol{G}\neq\boldsymbol{0}} 4\pi\frac{\boldsymbol{n}^{\text{ps}\boldsymbol{\nabla}}_{\text{Htr}}(\boldsymbol{G})}{|\boldsymbol{G}|^{2}}\mathrm{e}^{\mathrm{i}\boldsymbol{G}\cdot\boldsymbol{r}} \tag{6.42a}$$

$$:= \sum_{\boldsymbol{G}|\boldsymbol{G}\neq\boldsymbol{0}} \left[\boldsymbol{\nabla}V^{(0)}_{\text{Htr}}\right](\boldsymbol{G})\mathrm{e}^{\mathrm{i}\boldsymbol{G}\cdot\boldsymbol{r}}. \tag{6.42b}$$

Muffin-tin contribution

Analogously to the linear external potential variations, the Dirichlet boundary value problem is solved. This results in the MT representation of the first-order Hartree potential variation

$$\begin{aligned}&\left[\boldsymbol{V}^{(1)}_{\text{Htr}}\left(\boldsymbol{r}_\gamma+\boldsymbol{\tau}_\gamma;\boldsymbol{q}^{\pm}\alpha\right)\right]_{lm} \\ &\quad= \frac{4\pi}{2l+1}\int_0^{R_\gamma} s_\gamma^2\left[\boldsymbol{\rho}^{(1)}_{\gamma,\text{full}}\left(\boldsymbol{r}_\gamma;\boldsymbol{q}^{\pm}\alpha\right)\right]_{lm}\frac{r_<^l}{r_>^{l+1}}\left(1-\left(\frac{r_>}{R_\gamma}\right)^{2l+1}\right)\mathrm{d}s_\gamma \\ &\qquad+\left(\frac{r_\gamma}{R_\gamma}\right)^l\sum_{\boldsymbol{G}|\boldsymbol{G}\pm\boldsymbol{q}\neq\boldsymbol{0}}\mathrm{e}^{\mathrm{i}(\boldsymbol{G}\pm\boldsymbol{q})\cdot\boldsymbol{\tau}_\gamma}\boldsymbol{V}^{(1)}_{\text{Htr}}(\boldsymbol{G};\boldsymbol{q}^{\pm}\alpha)4\pi\mathrm{i}^l\mathrm{Y}^*_{lm}\left(\widehat{\boldsymbol{G}\pm\boldsymbol{q}}\right)\mathrm{j}_l\left(|\boldsymbol{G}\pm\boldsymbol{q}|R_\gamma\right).\end{aligned} \tag{6.43}$$

Furthermore, it leads to the gradient of the unperturbed Hartree potential in the MT spheres

$$\begin{aligned}\left[\boldsymbol{\nabla}V^{(0)}_{\text{Htr}}\left(\boldsymbol{r}_\gamma+\boldsymbol{\tau}_\gamma\right)\right]_{lm} &= \frac{4\pi}{2l+1}\int_0^{R_\gamma} s_\gamma^2\left[\boldsymbol{\nabla}\rho^{(0)}_\gamma\left(\boldsymbol{r}_\gamma\right)\right]_{lm}\frac{r_<^l}{r_>^{l+1}}\left(1-\left(\frac{r_>}{R_\gamma}\right)^{2l+1}\right)\mathrm{d}s_\gamma \\ &\quad+\left(\frac{r_\gamma}{R_\gamma}\right)^l\sum_{\boldsymbol{G}|\boldsymbol{G}\neq\boldsymbol{0}}\mathrm{e}^{\mathrm{i}\boldsymbol{G}\cdot\boldsymbol{\tau}_\gamma}\left[\boldsymbol{\nabla}V^{(0)}_{\text{Htr}}\right](\boldsymbol{G})4\pi\mathrm{i}^l\mathrm{Y}^*_{lm}\left(\hat{\boldsymbol{G}}\right)\mathrm{j}_l\left(|\boldsymbol{G}|R_\gamma\right).\end{aligned} \tag{6.44}$$

6.3.3 Linear Variations of the Exchange-Correlation Potential

The linear variations of the xc potential result from a functional derivative of the xc potential

$$\boldsymbol{\nabla}V^{(0)}_{\text{xc}}(\boldsymbol{r}) = \boldsymbol{\nabla}\rho^{(0)}(\boldsymbol{r})\left.\frac{\delta V^{(0)}_{\text{xc}}[\rho(\boldsymbol{r})]}{\delta\rho(\boldsymbol{r})}\right|_{\rho(\boldsymbol{r})=\rho^{(0)}(\boldsymbol{r})} \tag{6.45}$$

$$\boldsymbol{V}^{(1)}_{\text{xc}}\left(\boldsymbol{r};\boldsymbol{q}^{\pm}\alpha\right) = \boldsymbol{\rho}^{(1)}\left(\boldsymbol{r};\boldsymbol{q}^{\pm}\alpha\right)\left.\frac{\delta V^{(0)}_{\text{xc}}[\rho(\boldsymbol{r})]}{\delta\rho(\boldsymbol{r})}\right|_{\rho(\boldsymbol{r})=\rho^{(0)}(\boldsymbol{r})}, \tag{6.46}$$

where in equation (6.45) the inner derivative is expressed by the gradient of the charge density and in equation (6.46) by the first-order variation of the charge density.

Interstitial contribution

In the IR, both the functional derivative of the xc kernel with respect to the charge density and the gradient of the charge density (first-order variation of the charge density) are expanded in plane waves. It is imperative to find the Fourier expansion coefficients of the interstitial xc potential which is composed of the products

$$\boldsymbol{\nabla}V^{(0)}_{\text{xc}}(\boldsymbol{r}) = \sum_{\boldsymbol{G}\boldsymbol{G}'}\boldsymbol{\nabla}\rho^{(0)}_{\text{IR}}(\boldsymbol{G})\frac{\delta V^{(0)}_{\text{xc}}[\rho(\boldsymbol{r})]}{\delta\rho(\boldsymbol{r})}(\boldsymbol{G}')\mathrm{e}^{\mathrm{i}(\boldsymbol{G}+\boldsymbol{G}')\cdot\boldsymbol{r}} \tag{6.47}$$

$$\boldsymbol{V}^{(1)}_{\text{xc}}\left(\boldsymbol{r};\boldsymbol{q}^{\pm}\alpha\right) = \sum_{\boldsymbol{G}\boldsymbol{G}'}\boldsymbol{\rho}^{(1)}_{\text{IR}}\left(\boldsymbol{G};\boldsymbol{q}^{\pm}\alpha\right)\frac{\delta V^{(0)}_{\text{xc}}[\rho(\boldsymbol{r})]}{\delta\rho(\boldsymbol{r})}(\boldsymbol{G}')\mathrm{e}^{\mathrm{i}(\boldsymbol{G}+\boldsymbol{G}'\pm\boldsymbol{q})\cdot\boldsymbol{r}}. \tag{6.48}$$

Further details are given in the IR part of section 7.3.2.

Muffin-tin contribution

In the MT spheres, the constituents of the xc-potential variations are expanded in spherical harmonics. The aim constitutes in finding the expansion coefficients for the spherical harmonic expansion of the product, which for the gradient of the unperturbed xc potential yields

$$\boldsymbol{\nabla} V_{\mathrm{xc}}^{(0)\gamma}(\boldsymbol{r}) = \left(\sum_{lm}\left[\boldsymbol{\nabla}\rho_{\gamma}^{(0)}(r)\right]_{lm} \mathrm{Y}_{lm}(\hat{\boldsymbol{r}})\right)\left(\sum_{l'm'}\left[\frac{\delta V_{\mathrm{xc}}^{(0)}\left[\rho^{(0)}(\boldsymbol{r})\right]}{\delta\rho^{(0)}(\boldsymbol{r})}(r)\right]_{l'm'} \mathrm{Y}_{l'm'}(\hat{\boldsymbol{r}})\right), \tag{6.49}$$

and the first-order variation of the xc potential is

$$\boldsymbol{V}_{\mathrm{xc}}^{(1)\gamma}(\boldsymbol{r};\boldsymbol{q}^{\pm}\alpha) = \left(\sum_{lm}\left[\boldsymbol{\rho}_{\gamma}^{(1)}(r;\boldsymbol{q}^{\pm}\alpha)\right]_{lm} \mathrm{Y}_{lm}(\hat{\boldsymbol{r}})\right)\left(\sum_{l'm'}\left[\frac{\delta V_{\mathrm{xc}}^{(0)}\left[\rho^{(0)}(\boldsymbol{r})\right]}{\delta\rho^{(0)}(\boldsymbol{r})}(r)\right]_{l'm'} \mathrm{Y}_{l'm'}(\hat{\boldsymbol{r}})\right). \tag{6.50}$$

Further details are provided by the MT part of section 7.3.2.

6.3.4 Second-Order Variation of the Ion–Ion Interaction

Periodic lattice structure

In order to determine the second-order ion–ion energy variation $E_{\mathrm{ii}}^{(2)}$ for equation (6.14a), the ion–ion interaction of zeroth order, in equation (2.2d), is reformulated in the sense of a periodic lattice structure. Within this lattice, a phonon with wave vector $\boldsymbol{q}$ displaces the nuclei. This means an atom α (β) is located in unit cell $\boldsymbol{R}$ ($\boldsymbol{R}'$) at the position $\boldsymbol{\tau}_{\alpha_{\boldsymbol{R}}}$ ($\boldsymbol{\tau}_{\beta_{\boldsymbol{R}'}}$) and displaced by $\boldsymbol{w}^{\boldsymbol{q}}_{\alpha_{\boldsymbol{R}}}$ ($\boldsymbol{w}^{\boldsymbol{q}}_{\beta_{\boldsymbol{R}'}}$) resulting in

$$E_{\mathrm{ii}}^{(0)}(\boldsymbol{q}) = \frac{1}{2}\sum_{\alpha\beta}\sum_{\substack{\boldsymbol{R}\boldsymbol{R}'|\\ \boldsymbol{R}\neq\boldsymbol{R}'}} \frac{Z_{\alpha}Z_{\beta}}{\left|\boldsymbol{\tau}_{\alpha_{\boldsymbol{R}}} + \boldsymbol{R} + \boldsymbol{w}^{\boldsymbol{q}}_{\alpha_{\boldsymbol{R}}} - \boldsymbol{\tau}_{\beta_{\boldsymbol{R}'}} - \boldsymbol{R}' - \boldsymbol{w}^{\boldsymbol{q}}_{\beta_{\boldsymbol{R}'}}\right|}. \tag{6.51}$$

The $\boldsymbol{\tau}$ are now expressed in the global coordinate system of the unit cell, and the displacements are defined in equation (6.5). Relative to equation (2.2d), a combination of three vectors (cf. equation (6.4)) now points to the center of the respective MT sphere.

Derivation

The ansatz for the second-order response of the ion–ion energy

$$E_{\mathrm{ii}}^{(2)}(\boldsymbol{q}) = \frac{1}{2}\sum_{\alpha'\beta'}\sum_{\boldsymbol{R}''\boldsymbol{R}'''} \boldsymbol{w}^{\top\boldsymbol{q}}_{\alpha'_{\boldsymbol{R}''}}\left[\boldsymbol{\nabla}_{\boldsymbol{w}^{\boldsymbol{q}}_{\alpha'_{\boldsymbol{R}''}}}\boldsymbol{\nabla}^{\top}_{\boldsymbol{w}^{\boldsymbol{q}}_{\beta'_{\boldsymbol{R}'''}}} E_{\mathrm{ii}}^{(0)}(\boldsymbol{q})\right]_{\boldsymbol{w}^{\boldsymbol{q}}=\boldsymbol{0}} \boldsymbol{w}^{\boldsymbol{q}}_{\beta'_{\boldsymbol{R}'''}} \tag{6.52a}$$

exhibits analogies to the second-order term in a Taylor series of a scalar function with a multi-dimensional argument, which in this case is given by the displacement. Each gradient addresses the displacement of a general atom α' or β' in the unit cells to which $\boldsymbol{R}''$ or $\boldsymbol{R}'''$ point, respectively. According to the product rule, this leads to the four terms

$$\begin{aligned} E_{\mathrm{ii}}^{(2)}(\boldsymbol{q}) = \frac{1}{2}\sum_{\alpha'\beta'}\sum_{\boldsymbol{R}''\boldsymbol{R}'''} \boldsymbol{w}^{\top\boldsymbol{q}}_{\alpha'_{\boldsymbol{R}''}} \Bigg[&\left(\delta_{\alpha'\alpha}\delta_{\boldsymbol{R}''\boldsymbol{R}} + \delta_{\alpha'\beta}\delta_{\boldsymbol{R}''\boldsymbol{R}'}\right)\left(\delta_{\beta'\alpha}\delta_{\boldsymbol{R}'''\boldsymbol{R}} + \delta_{\beta'\beta}\delta_{\boldsymbol{R}'''\boldsymbol{R}'}\right) \\ &\times \boldsymbol{\nabla}_{\boldsymbol{w}^{\boldsymbol{q}}_{\alpha'_{\boldsymbol{R}''}}}\boldsymbol{\nabla}^{\top}_{\boldsymbol{w}^{\boldsymbol{q}}_{\beta'_{\boldsymbol{R}'''}}} E_{\mathrm{ii}}^{(2)}(\boldsymbol{q})\Bigg]_{\boldsymbol{w}^{\boldsymbol{q}}=\boldsymbol{0}} \boldsymbol{w}^{\boldsymbol{q}}_{\beta'_{\boldsymbol{R}'''}}. \end{aligned} \tag{6.52b}$$

As soon as the derivative sets α' or β' to either α or to β, respectively, this also fixes $\boldsymbol{R}''$ or $\boldsymbol{R}'''$ to either $\boldsymbol{R}$ or $\boldsymbol{R}'$, mirroring in the products of Kronecker deltas. Applying the Kronecker deltas, redirecting the application of the gradients from the displacements $\boldsymbol{w}^{\boldsymbol{q}}$ to the atomic positions $\boldsymbol{\tau}$ (see equation (5.68)), and evaluating $\boldsymbol{w} = \boldsymbol{0}$ yields

$$\begin{aligned} E^{(2)}_{\text{ii}}(\boldsymbol{q}) = \frac{1}{2}\sum_{\alpha\beta}\sum_{\substack{\boldsymbol{R}\boldsymbol{R}'| \\ \boldsymbol{R}\neq\boldsymbol{R}'}} Z_\alpha Z_\beta \Bigg(& \boldsymbol{w}^{\top\boldsymbol{q}}_{\alpha_{\boldsymbol{R}}}\, \boldsymbol{\nabla}_{\boldsymbol{\tau}_{\alpha_{\boldsymbol{R}}}} \boldsymbol{\nabla}^{\top}_{\boldsymbol{\tau}_{\alpha_{\boldsymbol{R}}}} \frac{1}{\left|\boldsymbol{\tau}_{\alpha_{\boldsymbol{R}}} + \boldsymbol{R} - \boldsymbol{\tau}_{\beta_{\boldsymbol{R}'}} - \boldsymbol{R}'\right|}\, \boldsymbol{w}^{\boldsymbol{q}}_{\alpha_{\boldsymbol{R}}} \\ & + \boldsymbol{w}^{\top\boldsymbol{q}}_{\alpha_{\boldsymbol{R}}}\, \boldsymbol{\nabla}_{\boldsymbol{\tau}_{\alpha_{\boldsymbol{R}}}} \boldsymbol{\nabla}^{\top}_{\boldsymbol{\tau}_{\beta_{\boldsymbol{R}'}}} \frac{1}{\left|\boldsymbol{\tau}_{\alpha_{\boldsymbol{R}}} + \boldsymbol{R} - \boldsymbol{\tau}_{\beta_{\boldsymbol{R}'}} - \boldsymbol{R}'\right|}\, \boldsymbol{w}^{\boldsymbol{q}}_{\beta_{\boldsymbol{R}'}} \\ & + \boldsymbol{w}^{\top\boldsymbol{q}}_{\beta_{\boldsymbol{R}'}}\, \boldsymbol{\nabla}_{\boldsymbol{\tau}_{\beta_{\boldsymbol{R}'}}} \boldsymbol{\nabla}^{\top}_{\boldsymbol{\tau}_{\alpha_{\boldsymbol{R}}}} \frac{1}{\left|\boldsymbol{\tau}_{\alpha_{\boldsymbol{R}}} + \boldsymbol{R} - \boldsymbol{\tau}_{\beta_{\boldsymbol{R}'}} - \boldsymbol{R}'\right|}\, \boldsymbol{w}^{\boldsymbol{q}}_{\alpha_{\boldsymbol{R}}} \\ & + \boldsymbol{w}^{\top\boldsymbol{q}}_{\beta_{\boldsymbol{R}}} \boldsymbol{\nabla}_{\boldsymbol{\tau}_{\beta_{\boldsymbol{R}'}}} \boldsymbol{\nabla}^{\top}_{\boldsymbol{\tau}_{\beta_{\boldsymbol{R}'}}} \frac{1}{\left|\boldsymbol{\tau}_{\alpha_{\boldsymbol{R}}} + \boldsymbol{R} - \boldsymbol{\tau}_{\beta_{\boldsymbol{R}'}} - \boldsymbol{R}'\right|}\, \boldsymbol{w}^{\boldsymbol{q}}_{\beta_{\boldsymbol{R}'}} \Bigg)\,. \end{aligned} \tag{6.52c}$$

By renaming $\alpha_{\boldsymbol{R}}$ to $\beta_{\boldsymbol{R}'}$ and vice versa, and doing the same with $\boldsymbol{R}$ and $\boldsymbol{R}'$, the last two lines are equalized to the first two lines but the denominators remain effectively the same so that

$$\begin{aligned} E^{(2)}_{\text{ii}}(\boldsymbol{q}) = \sum_{\alpha\beta}\sum_{\substack{\boldsymbol{R}\boldsymbol{R}'| \\ \boldsymbol{R}\neq\boldsymbol{R}'}} Z_\alpha Z_\beta \Bigg(& \boldsymbol{w}^{\top\boldsymbol{q}}_{\alpha_{\boldsymbol{R}}}\, \boldsymbol{\nabla}_{\boldsymbol{\tau}_{\alpha_{\boldsymbol{R}}}} \boldsymbol{\nabla}^{\top}_{\boldsymbol{\tau}_{\alpha_{\boldsymbol{R}}}} \frac{1}{\left|\boldsymbol{\tau}_{\alpha_{\boldsymbol{R}}} + \boldsymbol{R} - \boldsymbol{\tau}_{\beta_{\boldsymbol{R}'}} - \boldsymbol{R}'\right|}\, \boldsymbol{w}^{\boldsymbol{q}}_{\alpha_{\boldsymbol{R}}} \\ & + \boldsymbol{w}^{\top\boldsymbol{q}}_{\alpha_{\boldsymbol{R}}}\, \boldsymbol{\nabla}_{\boldsymbol{\tau}_{\alpha_{\boldsymbol{R}}}} \boldsymbol{\nabla}^{\top}_{\boldsymbol{\tau}_{\beta_{\boldsymbol{R}'}}} \frac{1}{\left|\boldsymbol{\tau}_{\alpha_{\boldsymbol{R}}} + \boldsymbol{R} - \boldsymbol{\tau}_{\beta_{\boldsymbol{R}'}} - \boldsymbol{R}'\right|}\, \boldsymbol{w}^{\boldsymbol{q}}_{\beta_{\boldsymbol{R}'}} \Bigg)\,. \end{aligned} \tag{6.52d}$$

If now inserting the definitions of the displacements (6.5), and substituting the $\boldsymbol{R}$ and $\boldsymbol{R}'$ by the definitions $\boldsymbol{R}'' \coloneqq \boldsymbol{R}' - \boldsymbol{R}$ as well as $\boldsymbol{R}''' = \boldsymbol{R}'$ (which are both decoupled from the $\boldsymbol{R}''$ and $\boldsymbol{R}'''$ introduced in equation (6.52a)),

$$\begin{aligned} E^{(2)}_{\text{ii}}(\boldsymbol{q}) = \sum_{\alpha\beta} Z_\alpha Z_\beta \Bigg\{ & \left(\sum_{\boldsymbol{R}'''} \mathrm{e}^{-2\mathrm{i}\boldsymbol{q}\cdot\boldsymbol{R}'''}\right) \Bigg(\boldsymbol{Q}^{\dagger}_{\alpha} \sum_{\substack{\boldsymbol{R}''|\boldsymbol{R}''\neq\boldsymbol{0}, \\ \text{if } \alpha=\beta}} \boldsymbol{\nabla}_{\boldsymbol{\tau}_\alpha} \boldsymbol{\nabla}^{\top}_{\boldsymbol{\tau}_\alpha} \frac{\mathrm{e}^{2\mathrm{i}\boldsymbol{q}\cdot\boldsymbol{R}''}}{\left|\boldsymbol{\tau}_\alpha - \boldsymbol{\tau}_\beta - \boldsymbol{R}''\right|}\, \boldsymbol{Q}^{*}_{\alpha} \\ & \qquad + \boldsymbol{Q}^{\dagger}_{\beta} \sum_{\substack{\boldsymbol{R}''|\boldsymbol{R}''\neq\boldsymbol{0}, \\ \text{if } \alpha=\beta}} \boldsymbol{\nabla}_{\boldsymbol{\tau}_\alpha} \boldsymbol{\nabla}^{\top}_{\boldsymbol{\tau}_\beta} \frac{\mathrm{e}^{\mathrm{i}\boldsymbol{q}\cdot\boldsymbol{R}''}}{\left|\boldsymbol{\tau}_\alpha - \boldsymbol{\tau}_\beta - \boldsymbol{R}''\right|}\, \boldsymbol{Q}^{*}_{\alpha} \Bigg) \\ & + \left(\sum_{\boldsymbol{R}'''} \mathrm{e}^{2\mathrm{i}\boldsymbol{q}\cdot\boldsymbol{R}'''}\right) \Bigg(\boldsymbol{Q}^{\top}_{\alpha} \sum_{\substack{\boldsymbol{R}''|\boldsymbol{R}''\neq\boldsymbol{0}, \\ \text{if } \alpha=\beta}} \boldsymbol{\nabla}_{\boldsymbol{\tau}_\alpha} \boldsymbol{\nabla}^{\top}_{\boldsymbol{\tau}_\alpha} \frac{\mathrm{e}^{-2\mathrm{i}\boldsymbol{q}\cdot\boldsymbol{R}''}}{\left|\boldsymbol{\tau}_\alpha - \boldsymbol{\tau}_\beta - \boldsymbol{R}''\right|}\, \boldsymbol{Q}_{\alpha} \\ & \qquad + \boldsymbol{Q}^{\top}_{\beta} \sum_{\substack{\boldsymbol{R}''|\boldsymbol{R}''\neq\boldsymbol{0}, \\ \text{if } \alpha=\beta}} \boldsymbol{\nabla}_{\boldsymbol{\tau}_\alpha} \boldsymbol{\nabla}^{\top}_{\boldsymbol{\tau}_\beta} \frac{\mathrm{e}^{-\mathrm{i}\boldsymbol{q}\cdot\boldsymbol{R}''}}{\left|\boldsymbol{\tau}_\alpha - \boldsymbol{\tau}_\beta - \boldsymbol{R}''\right|}\, \boldsymbol{Q}_{\alpha} \Bigg) \end{aligned}$$

$$
\left.
\begin{aligned}
&+ N\boldsymbol{Q}_\alpha^\top \sum_{\substack{\boldsymbol{R}''|\boldsymbol{R}''\neq\boldsymbol{0},\\ \text{if }\alpha=\beta}} \boldsymbol{\nabla}_{\boldsymbol{\tau}_\alpha}\boldsymbol{\nabla}_{\boldsymbol{\tau}_\alpha}^\top \frac{1}{|\boldsymbol{\tau}_\alpha-\boldsymbol{\tau}_\beta-\boldsymbol{R}''|}\boldsymbol{Q}_\alpha \\
&+ N\boldsymbol{Q}_\beta^\top \sum_{\substack{\boldsymbol{R}''|\boldsymbol{R}''\neq\boldsymbol{0},\\ \text{if }\alpha=\beta}} \boldsymbol{\nabla}_{\boldsymbol{\tau}_\alpha}\boldsymbol{\nabla}_{\boldsymbol{\tau}_\beta}^\top \frac{\mathrm{e}^{\mathrm{i}\boldsymbol{q}\cdot\boldsymbol{R}''}}{|\boldsymbol{\tau}_\alpha-\boldsymbol{\tau}_\beta-\boldsymbol{R}''|}\boldsymbol{Q}_\alpha \\
&+ N\boldsymbol{Q}_\alpha^\dagger \sum_{\substack{\boldsymbol{R}''|\boldsymbol{R}''\neq\boldsymbol{0},\\ \text{if }\alpha=\beta}} \boldsymbol{\nabla}_{\boldsymbol{\tau}_\alpha}\boldsymbol{\nabla}_{\boldsymbol{\tau}_\alpha}^\top \frac{1}{|\boldsymbol{\tau}_\alpha-\boldsymbol{\tau}_\beta-\boldsymbol{R}''|}\boldsymbol{Q}_\alpha^* \\
&+ N\boldsymbol{Q}_\beta^\dagger \sum_{\substack{\boldsymbol{R}''|\boldsymbol{R}''\neq\boldsymbol{0},\\ \text{if }\alpha=\beta}} \boldsymbol{\nabla}_{\boldsymbol{\tau}_\alpha}\boldsymbol{\nabla}_{\boldsymbol{\tau}_\beta}^\top \frac{\mathrm{e}^{-\mathrm{i}\boldsymbol{q}\cdot\boldsymbol{R}''}}{|\boldsymbol{\tau}_\alpha-\boldsymbol{\tau}_\beta-\boldsymbol{R}''|}\boldsymbol{Q}_\alpha^*
\end{aligned}
\right\} \tag{6.52e}
$$

results. Self-interaction is avoided by excluding the terms $\boldsymbol{R}'' = \boldsymbol{0}$ for the case $\alpha = \beta$. The sums in parentheses within the first and third lines yield either 0 (if $2\boldsymbol{q}$ is a reciprocal lattice vector $\boldsymbol{G}$) or N, the number of unit cells (else). Due to equation (6.12), only the last four lines of the previous equation are of interest, as the other lines contain either pairs of $\boldsymbol{Q}^\dagger$ and $\boldsymbol{Q}^*$ or $\boldsymbol{Q}^\top$ and $\boldsymbol{Q}$, respectively. Furthermore, the indices $\boldsymbol{R}$ and $\boldsymbol{R}'$ of the atom indices α or β can be dropped, because $\boldsymbol{R}''$ now indicates the distance between the unit cells the atoms α or β are located in.

Reformulation for Weinert method

Consistent with the prevailing nomenclature and exploiting the lattice periodicity to focus on a single unit cell (which implies dividing by N), Klüppelberg [88] defines

$$
E_{\text{ii}}^{(2)}(\boldsymbol{q}^{+-}) := \sum_{\alpha\beta} Z_\alpha Z_\beta \sum_{\substack{\boldsymbol{R}''|\boldsymbol{R}''\neq\boldsymbol{0},\\ \text{if }\alpha=\beta}} \left(\boldsymbol{Q}_\alpha^\top\, \boldsymbol{\nabla}_{\boldsymbol{\tau}_\alpha}\boldsymbol{\nabla}_{\boldsymbol{\tau}_\alpha}^\top \frac{1}{|\boldsymbol{\tau}_\alpha-\boldsymbol{\tau}_\beta-\boldsymbol{R}''|}\boldsymbol{Q}_\alpha^* + \boldsymbol{Q}_\beta^\top\, \boldsymbol{\nabla}_{\boldsymbol{\tau}_\alpha}\boldsymbol{\nabla}_{\boldsymbol{\tau}_\beta}^\top \frac{\mathrm{e}^{\mathrm{i}\boldsymbol{q}\cdot\boldsymbol{R}''}}{|\boldsymbol{\tau}_\alpha-\boldsymbol{\tau}_\beta-\boldsymbol{R}''|}\boldsymbol{Q}_\alpha^* \right) \tag{6.53a}
$$

$$
E_{\text{ii}}^{(2)}(\boldsymbol{q}^{-+}) := \sum_{\alpha\beta} Z_\alpha Z_\beta \sum_{\substack{\boldsymbol{R}''|\boldsymbol{R}''\neq\boldsymbol{0},\\ \text{if }\alpha=\beta}} \left(\boldsymbol{Q}_\alpha^\dagger\, \boldsymbol{\nabla}_{\boldsymbol{\tau}_\alpha}\boldsymbol{\nabla}_{\boldsymbol{\tau}_\alpha}^\top \frac{1}{|\boldsymbol{\tau}_\alpha-\boldsymbol{\tau}_\beta-\boldsymbol{R}''|}\boldsymbol{Q}_\alpha + \boldsymbol{Q}_\beta^\dagger\, \boldsymbol{\nabla}_{\boldsymbol{\tau}_\alpha}\boldsymbol{\nabla}_{\boldsymbol{\tau}_\beta}^\top \frac{\mathrm{e}^{-\mathrm{i}\boldsymbol{q}\cdot\boldsymbol{R}''}}{|\boldsymbol{\tau}_\alpha-\boldsymbol{\tau}_\beta-\boldsymbol{R}''|}\boldsymbol{Q}_\alpha \right) . \tag{6.53b}
$$

It is obvious that $E_{\text{ii}}^{(2)}(\boldsymbol{q}^{+-}) = E_{\text{ii}}^{*(2)}(\boldsymbol{q}^{-+})$. Moreover, the gradient with respect to $\boldsymbol{\tau}_\beta$ differs from that with respect to $\boldsymbol{\tau}_\alpha$ only by the sign of its inner derivative. Consequently

$$
E_{\text{ii}}^{(2)}(\boldsymbol{q}^{-+}) = \sum_{\alpha\beta} Z_\alpha Z_\beta \sum_{\substack{\boldsymbol{R}''|\boldsymbol{R}''\neq\boldsymbol{0},\\ \text{if }\alpha=\beta}} \left(\boldsymbol{Q}_\alpha^\dagger\, \boldsymbol{\nabla}_{\boldsymbol{\tau}_\alpha}\boldsymbol{\nabla}_{\boldsymbol{\tau}_\alpha}^\top \frac{1}{|\boldsymbol{\tau}_\alpha-\boldsymbol{\tau}_\beta-\boldsymbol{R}''|}\boldsymbol{Q}_\alpha - \boldsymbol{Q}_\beta^\dagger\, \boldsymbol{\nabla}_{\boldsymbol{\tau}_\alpha}\boldsymbol{\nabla}_{\boldsymbol{\tau}_\alpha}^\top \frac{\mathrm{e}^{-\mathrm{i}\boldsymbol{q}\cdot\boldsymbol{R}''}}{|\boldsymbol{\tau}_\alpha-\boldsymbol{\tau}_\beta-\boldsymbol{R}''|}\boldsymbol{Q}_\alpha \right) \tag{6.54a}
$$

$$=: \sum_{\alpha\beta} \boldsymbol{Q}^{\dagger}_{\beta}\, \underline{E}^{(2)\beta\alpha}_{\mathrm{ii}}\left(\boldsymbol{q}^{-+}\right) \boldsymbol{Q}_{\alpha} - \boldsymbol{Q}^{\dagger}_{\alpha}\, \underline{E}^{(2)\beta\alpha}_{\mathrm{ii}}\left(\boldsymbol{0}^{-+}\right) \boldsymbol{Q}_{\alpha} \tag{6.54b}$$

holds and reveals that its second term equals minus the first term for $\boldsymbol{q} = \boldsymbol{0}$, ignoring the polarization vectors. This means that these terms obviously only cancel each other for the 3×3 submatrices located in the diagonal of the $3N \times 3N$ dynamical matrix. Hence, in the following it is imperative to find a way to calculate

$$\underline{E}^{(2)\beta\alpha}_{\mathrm{ii}}\left(\boldsymbol{q}^{-+}\right) = -Z_{\alpha} \sum_{\substack{\boldsymbol{R}''|\boldsymbol{R}''\neq\boldsymbol{0},\\ \text{if } \alpha=\beta}} \boldsymbol{\nabla}_{\boldsymbol{\tau}_{\alpha}} \boldsymbol{\nabla}^{\top}_{\boldsymbol{\tau}_{\alpha}} \frac{Z_{\beta}\mathrm{e}^{-\mathrm{i}\boldsymbol{q}\cdot\boldsymbol{R}''}}{\left|\boldsymbol{\tau}_{\alpha} - \boldsymbol{\tau}_{\beta} - \boldsymbol{R}''\right|} \tag{6.55a}$$

$$= -Z_{\alpha} \lim_{\boldsymbol{r}\to\boldsymbol{\tau}_{\alpha}} \sum_{\substack{\boldsymbol{R}''|\boldsymbol{R}''\neq\boldsymbol{0},\\ \text{if } \alpha=\beta}} \boldsymbol{\nabla}\boldsymbol{\nabla}^{\top} \frac{Z_{\beta}\mathrm{e}^{-\mathrm{i}\boldsymbol{q}\cdot\boldsymbol{R}''}}{\left|\boldsymbol{r} - \boldsymbol{\tau}_{\beta} - \boldsymbol{R}''\right|} \tag{6.55b}$$

and sufficient to solely focus on it. In equation (6.55b), a limit is introduced, implying the gradients should be redirected to $\boldsymbol{r}$ instead of $\boldsymbol{\tau}_{\alpha}$. By utilizing the Dirac delta distribution, an integral representation becomes feasible. However, the gradients still act on $\boldsymbol{r}$, i.e., on the denominator of the fraction. With two applications of integrations by parts, the gradients are redirected to $\boldsymbol{r}'$, yielding

$$\underline{E}^{(2)\beta\alpha}_{\mathrm{ii}}\left(\boldsymbol{q}^{-+}\right) = Z_{\alpha} \lim_{\boldsymbol{r}\to\boldsymbol{\tau}_{\alpha}} \int_{\Omega} \sum_{\substack{\boldsymbol{R}''|\boldsymbol{R}''\neq\boldsymbol{0},\\ \text{if } \alpha=\beta}} \frac{-Z_{\beta}\mathrm{e}^{-\mathrm{i}\boldsymbol{q}\cdot\boldsymbol{R}''} \boldsymbol{\nabla}_{\boldsymbol{r}'} \boldsymbol{\nabla}^{\top}_{\boldsymbol{r}'} \delta\left(\boldsymbol{r}' - \left(\boldsymbol{\tau}'_{\beta} + \boldsymbol{R}''\right)\right)}{\left|\boldsymbol{r} - \boldsymbol{r}'\right|} \,\mathrm{d}^3 r' \ . \tag{6.55c}$$

Thereby, the boundary terms vanish because of the Dirac delta distribution in the limit as its argument approaches infinity, and the two minus signs emerging in front of the volume integral cancel each other. For this integral in equation (6.55c), Klüppelberg has developed a framework which is in line with the Weinert [64] formalism for calculating the Coulomb potential and its first variations. However, his theory borrows some concepts from the publication of Weinert, Wimmer, and Freeman [66]. The condition underlying the sum over $\boldsymbol{R}''$, from equation (6.52e) on, is relaxed while calculating the IR contribution of equations (6.55). Thus, the sum in equation (6.55c) runs over all $\boldsymbol{R}''$, also for $\alpha = \beta$, in order to not violate the periodicity of the lattice [127]. This must be considered later in the MT region.

Multipole moments

In this sense, from equation (6.55c) the true charge density

$$\underline{n}^{\beta}\left(\boldsymbol{r}'; \boldsymbol{q}^{-+}\right) = -Z_{\beta} \sum_{\boldsymbol{R}''} \mathrm{e}^{-\mathrm{i}\boldsymbol{q}\cdot\boldsymbol{R}''} \boldsymbol{\nabla}_{\boldsymbol{r}'} \boldsymbol{\nabla}^{\top}_{\boldsymbol{r}'} \delta\left(\boldsymbol{r}' - \left(\boldsymbol{\tau}_{\beta} + \boldsymbol{R}''\right)\right) \tag{6.56a}$$

can be extracted. Renaming the indices $\boldsymbol{R}''$ to $\boldsymbol{R}'''$ and β to β' yields

$$\underline{n}^{\beta'}\left(\boldsymbol{r}'; \boldsymbol{q}^{-+}\right) = -Z_{\beta'} \sum_{\boldsymbol{R}'''} \mathrm{e}^{-\mathrm{i}\boldsymbol{q}\cdot\boldsymbol{R}'''} \boldsymbol{\nabla}_{\boldsymbol{r}_{\beta'}} \boldsymbol{\nabla}^{\top}_{\boldsymbol{r}_{\beta'}} \delta\left(\boldsymbol{r}' - \left(\boldsymbol{\tau}_{\beta'} + \boldsymbol{R}'''\right)\right) \tag{6.56b}$$

and is used to find the multipole moments. They are given by the MT integral

$$\underline{\mathfrak{q}}^{\beta\boldsymbol{R}''}_{lm}\left(\boldsymbol{q}^{-+}\right) = \int_{\beta_{\boldsymbol{R}''}} \mathrm{Y}^{*}_{lm}\left(\widehat{\boldsymbol{r}' - \boldsymbol{\tau}_{\beta} - \boldsymbol{R}''}\right) \left|\boldsymbol{r}' - \boldsymbol{\tau}_{\beta} - \boldsymbol{R}''\right|^{l} \underline{n}^{\beta'}\left(\boldsymbol{r}_{\beta} + \tau_{\beta} + \boldsymbol{R}; \boldsymbol{q}^{-+}\right) \mathrm{d}^3 r_{\beta} \tag{6.57a}$$

and are evaluated in the local coordinate system with its transformation $\boldsymbol{r}_\beta = \boldsymbol{r}' - \boldsymbol{\tau}_\beta - \boldsymbol{R}$. Inserting equation (6.56a) leads to

$$\underline{\mathrm{q}}_{lm}^{\beta\boldsymbol{R}''}\left(\boldsymbol{q}^{-+}\right) = \sum_{\boldsymbol{R}'''} Z_{\beta'}\mathrm{e}^{-\mathrm{i}\boldsymbol{q}\cdot\boldsymbol{R}'''} \int_{\beta_{\boldsymbol{R}''}} \mathrm{Y}_{lm}^{*}\left(\hat{\boldsymbol{r}}_\beta\right)\left|\boldsymbol{r}'_\beta\right|^{l} \times \boldsymbol{\nabla}_{\boldsymbol{r}_\beta}\boldsymbol{\nabla}_{\boldsymbol{r}_\beta}^{\top}\delta\left(\boldsymbol{r}_\beta - \left(\boldsymbol{\tau}_{\beta'} - \boldsymbol{\tau}_\beta\right) - \left(\boldsymbol{R}''' - \boldsymbol{R}''\right)\right)\mathrm{d}^3 r_\beta \ , \tag{6.57b}$$

which fixes $\boldsymbol{\tau}_{\beta'} \equiv \boldsymbol{\tau}_\beta$ and $\boldsymbol{R}''' \equiv \boldsymbol{R}''$, collapsing the sum over $\boldsymbol{R}'''$. Circumventing the gradients acting on the Dirac delta by integrating by parts twice, results in a classical Dirac delta integral which can be evaluated so that

$$\underline{\mathrm{q}}_{lm}^{\beta\boldsymbol{R}''}\left(\boldsymbol{q}^{-+}\right) = -Z_\beta \mathrm{e}^{-\mathrm{i}\boldsymbol{q}\cdot\boldsymbol{R}''}\boldsymbol{\nabla}_{\boldsymbol{r}_\beta}\boldsymbol{\nabla}_{\boldsymbol{r}_\beta}^{\top}\left[r_\beta^l \mathrm{Y}_{lm}^{*}\left(\hat{\boldsymbol{r}}_\beta\right)\right]_{\boldsymbol{r}_\beta=\boldsymbol{0}} . \tag{6.57c}$$

Pseudo-density

The boundary terms vanish because the Dirac delta and its gradient are zero at the MT sphere boundary, and analogously to section 6.3.1, equation (6.57c) implies that $l = 2$ gives the only contribution. This leads to the pseudo-density

$$\underline{n}_{\mathrm{ps}}^{\beta}\left(\boldsymbol{G};\boldsymbol{q}^{-+}\right) = \frac{Z_\beta}{\mathit{\Omega}}(2N+7)!!\frac{\mathrm{j}_{N+3}\left(|\boldsymbol{G}-\boldsymbol{q}|R_\beta\right)}{\left(|\boldsymbol{G}-\boldsymbol{q}|R_\beta\right)^{N+3}}\mathrm{e}^{-\mathrm{i}(\boldsymbol{G}-\boldsymbol{q})\cdot\boldsymbol{\tau}_\beta} \times \left((\boldsymbol{G}-\boldsymbol{q})(\boldsymbol{G}-\boldsymbol{q})^{\top} - \frac{|\boldsymbol{G}-\boldsymbol{q}|^2}{3}\underline{1}\right) , \tag{6.58}$$

Beyond displaced muffin-tin sphere

provided $\boldsymbol{G} - \boldsymbol{q} \neq \boldsymbol{0}$, otherwise there is no contribution. Now it is possible to formulate the IR contribution as

$$Z_\alpha \lim_{\boldsymbol{r}\to\boldsymbol{\tau}_\alpha}\int_{\mathit{\Omega}}\sum_{\substack{\boldsymbol{R}''|\boldsymbol{R}''\neq\boldsymbol{0},\\ \text{if } \alpha=\beta}} \frac{-Z_\beta \mathrm{e}^{-\mathrm{i}\boldsymbol{q}\cdot\boldsymbol{R}''}\boldsymbol{\nabla}_{\boldsymbol{r}'}\boldsymbol{\nabla}_{\boldsymbol{r}'}^{\top}\delta\left(\boldsymbol{r}' - \left(\boldsymbol{\tau}'_\beta + \boldsymbol{R}''\right)\right)}{|\boldsymbol{r}-\boldsymbol{r}'|}\mathrm{d}^3 r' \tag{6.59a}$$

$$= \sum_{\boldsymbol{G}|\boldsymbol{G}-\boldsymbol{q}\neq\boldsymbol{0}} Z_\alpha \lim_{\boldsymbol{r}\to\boldsymbol{\tau}_\alpha}\frac{4\pi\underline{n}^{\beta}\left(\boldsymbol{G};\boldsymbol{q}^{-+}\right)}{|\boldsymbol{G}-\boldsymbol{q}|^2}\mathrm{e}^{\mathrm{i}(\boldsymbol{G}-\boldsymbol{q})\cdot\boldsymbol{r}}$$

$$= \sum_{\boldsymbol{G}|\boldsymbol{G}-\boldsymbol{q}\neq\boldsymbol{0}} Z_\alpha \frac{4\pi\underline{n}^{\beta}\left(\boldsymbol{G};\boldsymbol{q}^{-+}\right)}{|\boldsymbol{G}-\boldsymbol{q}|^2}\mathrm{e}^{\mathrm{i}(\boldsymbol{G}-\boldsymbol{q})\cdot\boldsymbol{\tau}_\alpha} , \tag{6.59b}$$

while in this context IR means everything beyond the MT spheres β (and their images), i.e., also the MT spheres $\beta \neq \alpha$. Thus, there is no danger that self-interaction is considered in this case.

Displaced muffin-tin sphere

Given the MT sphere $\beta = \alpha$ at $\boldsymbol{R} = 0$, a Dirichlet boundary value problem is set up. To avoid self interaction in the volume integral, the ion charge at $\boldsymbol{R} = \boldsymbol{0}$ is excluded by an appropriate sum. Therefore, the Dirac delta in the volume integral always yields zero as the condition $\boldsymbol{R} = \boldsymbol{0}$ is never fulfilled. Within the surface integral, the pseudo-density (6.58), in which $\boldsymbol{R} = \boldsymbol{0}$ is included, is corrected by subtracting the contribution from the problematic ionic charge again. All in all, this yields

$$
\begin{aligned}
&Z_\alpha \lim_{\boldsymbol{r}\to\boldsymbol{\tau}_\alpha} \int_\Omega \sum_{\substack{\boldsymbol{R}''|\boldsymbol{R}''\neq\boldsymbol{0},\\ \text{if } \alpha=\beta}} \frac{-Z_\beta \mathrm{e}^{-\mathrm{i}\boldsymbol{q}\cdot\boldsymbol{R}''} \boldsymbol{\nabla}_{\boldsymbol{r}'} \boldsymbol{\nabla}_{\boldsymbol{r}'}^\top \delta\Big(\boldsymbol{r}' - \Big(\boldsymbol{\tau}_\beta' + \boldsymbol{R}''\Big)\Big)}{|\boldsymbol{r} - \boldsymbol{r}'|} \,\mathrm{d}^3 r' \qquad (6.60)\\
&= -Z_\alpha \int Z_\beta \sum_{\boldsymbol{R}''|\boldsymbol{R}''\neq\boldsymbol{0}} \mathrm{e}^{-\mathrm{i}\boldsymbol{q}\cdot\boldsymbol{R}''} \boldsymbol{\nabla}_{\boldsymbol{s}_\beta} \boldsymbol{\nabla}_{\boldsymbol{s}_\beta}^\top \delta\big(\boldsymbol{s}_\beta - (\boldsymbol{R}'' - \boldsymbol{0})\big) \mathcal{G}\big(\boldsymbol{r}_\beta, \boldsymbol{s}_\beta\big) \,\mathrm{d}^3 s_\beta \\
&\quad - Z_\alpha \oint \int \frac{Z_\beta \sum_{\boldsymbol{R}''} \mathrm{e}^{-\mathrm{i}\boldsymbol{q}\cdot\boldsymbol{R}''} \boldsymbol{\nabla}_{\boldsymbol{r}'} \boldsymbol{\nabla}_{\boldsymbol{r}'}^\top \delta\big(\boldsymbol{r}' - \boldsymbol{\tau}_\beta - \boldsymbol{R}''\big) - Z_\beta \boldsymbol{\nabla}_{\boldsymbol{r}'} \boldsymbol{\nabla}_{\boldsymbol{r}'}^\top \delta\big(\boldsymbol{r}' - \boldsymbol{\tau}_\beta\big)}{\big|R_\beta \boldsymbol{s} + \boldsymbol{\tau}_\beta - \boldsymbol{r}'\big|} \,\mathrm{d}^3 r' \\
&\qquad \times \sum_{lm} \left(\frac{r_\beta}{R_\beta}\right)^l \mathrm{Y}_{lm}^*(\hat{\boldsymbol{s}}) \mathrm{Y}_{lm}^*\big(\hat{\boldsymbol{r}}_\beta\big) \,\mathrm{d}S
\end{aligned}
$$

with $\mathcal{G}\big(\boldsymbol{r}_\beta, \boldsymbol{s}_\beta\big)$ defined in equation (5.43b).

6.4 Sternheimer Equation

Outline

The Sternheimer equation delivers the first-order variation of the Kohn–Sham wave-function expansion coefficients. Therefore, the former is derived and motivated in section 6.4.1. It shall become apparent that most of the quantities required for the Sternheimer equation are already set up or are available from a DFT calculation conducted in advance. This includes the unperturbed and the first-order variation of the effective potential, the unperturbed and the first-order variation of the Kohn–Sham wave function, and the unperturbed Kohn–Sham energies. What remains is the detailed form of the first-order Kohn–Sham energy variation, which is given in section 6.4.2. Finally, section 6.4.3 is devoted to the self-consistent iteration procedure which inheres in the DFPT.

6.4.1 Derivation

The form of the Sternheimer equation, as found in Klüppelberg [88, equation (7.19)] can be motivated starting from the Schrödinger equation

$$
\Big(\mathscr{H}^{(0)} - \varepsilon_{\boldsymbol{k},n}^{(0)}\Big)\Big|\Psi_{\boldsymbol{k},n}^{(0)}\Big\rangle = 0\,. \qquad (6.61a)
$$

In a first step, a projection of the Schrödinger equation onto the LAPW basis functions, evaluated at a general reciprocal wave vector $\tilde{\boldsymbol{k}}$ specified at the end of this section,

$$
\Big\langle \phi_{\tilde{\boldsymbol{k}},\boldsymbol{G}'}^{(0)} \Big| \mathscr{H}^{(0)} - \varepsilon_{\boldsymbol{k},n}^{(0)} \Big| \Psi_{\boldsymbol{k},n}^{(0)} \Big\rangle_\Omega = 0 \qquad (6.61b)
$$

is performed. This results in an additional integral over the unit cell with the volume Ω. If the wave function in the ket is then expanded in the LAPW basis, the central Kohn–Sham matrix element of a DFT calculation (5.47) manifests itself. Adhering to the product rule, the bra, the inner part, and the ket of this matrix element are varied. Afterwards, equation (6.8) for the first-variation of the Kohn–Sham wave function, and equations (6.7) for the first-variation of the LAPW basis (Pulay corrections) are inserted. Varying the integral boundaries yields surface terms (see equation (5.74)) which are projected onto the displacement vector displayed by equations (6.5). Since the kinetic energy operator is not sensitive to the external-potential perturbation, it is excluded from variation [68]. Hence, only the effective-potential part of the Hamiltonian undergoes a variation, suggesting the insertion of equation (6.23). In the same manner as the already-introduced varied quantities, the variation of the Kohn–Sham energy is split into

$$\epsilon^{(1)}_{\boldsymbol{k},n}(\boldsymbol{q}) = \sum_{\alpha}\Big(\boldsymbol{Q}^{\top}_{\alpha}\,\boldsymbol{\epsilon}^{(1)}_{\boldsymbol{k},n}(\boldsymbol{q}^{+}\alpha) + \boldsymbol{Q}^{\dagger}_{\alpha}\,\boldsymbol{\epsilon}^{(1)}_{\boldsymbol{k},n}(\boldsymbol{q}^{-}\alpha)\Big)\,. \tag{6.61c}$$

It can be shown (see for instance reference [88]) that the first-order variation of the Kohn–Sham energy must only be evaluated for the Goldstone modes. The explicit form of the former is given in section 6.4.2. Finally for obtaining the expression

$$\begin{aligned}
&\Big\langle \phi^{(0)}_{\tilde{\boldsymbol{k}},\boldsymbol{G}'}\Big|\mathscr{H}^{(0)} - \varepsilon^{(0)}_{\boldsymbol{k},n}\Big|\boldsymbol{Q}^{\top}\,\boldsymbol{z}^{(1)}_{\boldsymbol{G}}(\boldsymbol{k},n;\boldsymbol{q}\alpha)\phi^{(0)}_{\boldsymbol{k}+\boldsymbol{q},\boldsymbol{G}} + \boldsymbol{Q}^{\dagger}\,\boldsymbol{z}^{(1)}_{\boldsymbol{G}}(\boldsymbol{k},n;-\boldsymbol{q}\alpha)\phi^{(0)}_{\boldsymbol{k}-\boldsymbol{q},\boldsymbol{G}}\Big\rangle_{\Omega} \qquad (6.61\text{d})\\
&\quad = -\Big\langle \boldsymbol{Q}^{\top}\,\boldsymbol{\phi}^{(1)\alpha+}_{\tilde{\boldsymbol{k}},\boldsymbol{G}'} + \boldsymbol{Q}^{\dagger}\,\boldsymbol{\phi}^{(1)\alpha-}_{\tilde{\boldsymbol{k}},\boldsymbol{G}'}\Big|\mathscr{H}^{(0)} - \varepsilon^{(0)}_{\boldsymbol{k},n}\Big|\Psi^{(0)}_{\boldsymbol{k},n}\Big\rangle_{\alpha}\\
&- \Big\langle \phi^{(0)}_{\tilde{\boldsymbol{k}},\boldsymbol{G}'}\Big|\boldsymbol{Q}^{\top}\Big(\boldsymbol{\mathscr{V}}^{(1)}_{\text{eff}}(\boldsymbol{q}^{+}\alpha) - \delta_{\boldsymbol{q}\boldsymbol{0}}\boldsymbol{\epsilon}^{(1)}_{\boldsymbol{k},n}(\boldsymbol{q}^{+}\alpha)\Big) + \boldsymbol{Q}^{\dagger}\Big(\boldsymbol{\mathscr{V}}^{(1)}_{\text{eff}}(\boldsymbol{q}^{-}\alpha) - \delta_{\boldsymbol{q}\boldsymbol{0}}\boldsymbol{\epsilon}^{(1)}_{\boldsymbol{k},n}(\boldsymbol{q}^{\pm}\alpha)\Big)\Big|\Psi^{(0)}_{\boldsymbol{k},n}\Big\rangle_{\Omega}\\
&\quad - \Big\langle \phi^{(0)}_{\tilde{\boldsymbol{k}},\boldsymbol{G}'}\Big|\mathscr{H}^{(0)} - \varepsilon^{(0)}_{\boldsymbol{k},n}\Big|\sum_{\boldsymbol{G}} z^{(0)}_{\boldsymbol{G}}(\boldsymbol{k},n)\Big(\boldsymbol{Q}^{\top}\,\boldsymbol{\phi}^{(1)\alpha+}_{\boldsymbol{k},\boldsymbol{G}} + \boldsymbol{Q}^{\dagger}\,\boldsymbol{\phi}^{(1)\alpha-}_{\boldsymbol{k},\boldsymbol{G}}\Big)\Big\rangle_{\alpha}\\
&\quad - \boldsymbol{Q}^{\top}\sum_{\boldsymbol{R}}\mathrm{e}^{\mathrm{i}\boldsymbol{q}\cdot\boldsymbol{R}}\oint_{\partial\alpha_{\boldsymbol{R}}}\phi^{*(0)\alpha}_{\tilde{\boldsymbol{k}},\boldsymbol{G}'}(\boldsymbol{r})\Big(\mathscr{H}^{(0)} - \varepsilon^{(0)}_{\boldsymbol{k},n}\Big)\Psi^{(0)\alpha}_{\boldsymbol{k},n}(\boldsymbol{r})\,\mathrm{d}\boldsymbol{S}\\
&\quad + \boldsymbol{Q}^{\top}\sum_{\boldsymbol{R}}\mathrm{e}^{\mathrm{i}\boldsymbol{q}\cdot\boldsymbol{R}}\oint_{\partial\alpha_{\boldsymbol{R}}}\phi^{*(0)\mathrm{IR}}_{\tilde{\boldsymbol{k}},\boldsymbol{G}'}(\boldsymbol{r})\Big(\mathscr{H}^{(0)} - \varepsilon^{(0)}_{\boldsymbol{k},n}\Big)\Psi^{(0)\mathrm{IR}}_{\boldsymbol{k},n}(\boldsymbol{r})\,\mathrm{d}\boldsymbol{S}\\
&\quad - \boldsymbol{Q}^{\dagger}\sum_{\boldsymbol{R}}\mathrm{e}^{-\mathrm{i}\boldsymbol{q}\cdot\boldsymbol{R}}\oint_{\partial\alpha_{\boldsymbol{R}}}\phi^{*(0)\alpha}_{\tilde{\boldsymbol{k}},\boldsymbol{G}'}(\boldsymbol{r})\Big(\mathscr{H}^{(0)} - \varepsilon^{(0)}_{\boldsymbol{k},n}\Big)\Psi^{(0)\alpha}_{\boldsymbol{k},n}(\boldsymbol{r})\,\mathrm{d}\boldsymbol{S}\\
&\quad + \boldsymbol{Q}^{\dagger}\sum_{\boldsymbol{R}}\mathrm{e}^{-\mathrm{i}\boldsymbol{q}\cdot\boldsymbol{R}}\oint_{\partial\alpha_{\boldsymbol{R}}}\phi^{*(0)\mathrm{IR}}_{\tilde{\boldsymbol{k}},\boldsymbol{G}'}(\boldsymbol{r})\Big(\mathscr{H}^{(0)} - \varepsilon^{(0)}_{\boldsymbol{k},n}\Big)\Psi^{(0)\mathrm{IR}}_{\boldsymbol{k},n}(\boldsymbol{r})\,\mathrm{d}\boldsymbol{S}\ ,
\end{aligned}$$

those terms in which the bra, partially the ket, and the middle of the braket, i.e., the Hamiltonian operator and the Kohn–Sham energies, are varied, are subtracted on both sides and thus shifted to the right-hand side of the equation.

Analysis

On the left-hand side, there remains the term with the quantity of interest. These are the first-order variation of the Kohn–Sham expansion coefficients multiplied with a matrix which must be inverted to obtain the varied expansion coefficients. On the right-hand side, the terms fall into a Hellmann–Feynman contribution in which the Hamiltonian and the Kohn–Sham energies are varied, Pulay terms in which the basis functions are varied, and surface integrals to consider the variation of the integral boundaries, provided a displacement of the MT spheres in atom α. The Pulay terms are confined from the complete unit cell to the MT spheres of the displaced atom α, since only there the Pulay correction of the LAPW basis has a contribution. The essential matrix relation at the representative unit cell $\boldsymbol{R} = \boldsymbol{0}$ (this $\boldsymbol{0}$

is suppressed hereinafter) can be extracted from equation (6.61d) and formulated as

$$\begin{aligned}
&\sum_{\boldsymbol{G}} \left\langle \phi^{(0)}_{\boldsymbol{k}\pm\boldsymbol{q},\boldsymbol{G}'} \middle| \mathscr{H}^{(0)} - \varepsilon^{(0)}_{\boldsymbol{k},n} \middle| \phi^{(0)}_{\boldsymbol{k}\pm\boldsymbol{q},\boldsymbol{G}} \right\rangle_{\Omega} \boldsymbol{z}^{(1)}_{\boldsymbol{G}}(\boldsymbol{k}, n; \pm\boldsymbol{q}\alpha) \qquad (6.61\mathrm{e})\\
&\quad = -\sum_{\boldsymbol{G}} \Bigg\{ \left\langle \phi^{(0)}_{\boldsymbol{k}\pm\boldsymbol{q},\boldsymbol{G}'} \middle| \boldsymbol{\mathscr{V}}^{(1)}_{\text{eff}}(\boldsymbol{q}^{\pm}\alpha) - \delta_{\boldsymbol{q}\boldsymbol{0}} \boldsymbol{\epsilon}^{(1)}_{\boldsymbol{k},n}(\boldsymbol{q}^{\pm}\alpha) \middle| \phi^{(0)}_{\boldsymbol{k},\boldsymbol{G}} \right\rangle_{\Omega}\\
&\qquad + \left\langle \boldsymbol{\phi}^{(1)\alpha\mp}_{\boldsymbol{k}\pm\boldsymbol{q},\boldsymbol{G}'} \middle| \mathscr{H}^{(0)} - \varepsilon^{(0)}_{\boldsymbol{k},n} \middle| \phi^{(0)}_{\boldsymbol{k},\boldsymbol{G}} \right\rangle_{\alpha} + \left\langle \phi^{(0)}_{\boldsymbol{k}\pm\boldsymbol{q},\boldsymbol{G}'} \middle| \mathscr{H}^{(0)} - \varepsilon^{(0)}_{\boldsymbol{k},n} \middle| \boldsymbol{\phi}^{(1)\alpha\pm}_{\boldsymbol{k},\boldsymbol{G}} \right\rangle_{\alpha}\\
&\qquad + \oint_{\partial\alpha} \phi^{*(0)\alpha}_{\boldsymbol{k}\pm\boldsymbol{q},\boldsymbol{G}'}(\boldsymbol{r}) \left(\mathscr{H}^{(0)} - \varepsilon^{(0)}_{\boldsymbol{k},n} \right) \phi^{(0)\alpha}_{\boldsymbol{k},\boldsymbol{G}}(\boldsymbol{r})\, \mathrm{d}\boldsymbol{S}\\
&\qquad - \oint_{\partial\alpha} \phi^{*(0)\mathrm{IR}}_{\boldsymbol{k}\pm\boldsymbol{q},\boldsymbol{G}'}(\boldsymbol{r}) \left(\mathscr{H}^{(0)} - \varepsilon^{(0)}_{\boldsymbol{k},n} \right) \phi^{(0)\mathrm{IR}}_{\boldsymbol{k},\boldsymbol{G}}(\boldsymbol{r})\, \mathrm{d}\boldsymbol{S} \Bigg\} z^{(0)}_{\boldsymbol{G}}(\boldsymbol{k}, n)\,.
\end{aligned}$$

Bloch character

Within the previous equation n is the band index, $\boldsymbol{k}$ is the momentum of the electrons, $\boldsymbol{q}$ is the phonon wave-vector and $\boldsymbol{G}$ and $\boldsymbol{G}'$ are the reciprocal lattice vectors. Due to the dependency of the first-order expansion coefficient on $\boldsymbol{k} \pm \boldsymbol{q}$ on the left-hand side of equation (6.61e), the basis function must feature the Bloch character $\boldsymbol{k} \pm \boldsymbol{q}$. On condition that the Bloch character must vanish in an integral over the unit cell, the basis function in the bra must have the same Bloch character, i.e., $\boldsymbol{k} \pm \boldsymbol{q}$. This uniquely fixes also the general vector $\tilde{\boldsymbol{k}}$ on the right-hand side of equation (6.61d). Then, each of the remaining matrix elements on this side features a vanishing Bloch character. The Bloch character $\boldsymbol{q}$ of the first-order potential variation in the HF term compensates for the $-\boldsymbol{q}$ character of the basis-function in the bra, which is implicitly complex conjugated. In the first Pulay term (third line of (6.61e)), the basis function variation is evaluated at $\boldsymbol{k} \pm \boldsymbol{q}$, inducing an additional Bloch-character shift of $\pm\boldsymbol{q}$ which compensates for the phase factor shift $\mp\boldsymbol{q}$ indicated by the superscript. Furthermore, in the second Pulay term, the Bloch characters of the bra and the ket cancel each other. As far as the surface integral is concerned, the $\mp\boldsymbol{q}$ of the complex conjugated LAPW basis-function has its counter part in the phase factor, which has been suppressed due to $\boldsymbol{R} = \boldsymbol{0}$ and actually contains a $\pm\boldsymbol{q}$. As a consequence of the TRS, the Sternheimer equations, in which $\tilde{\boldsymbol{k}} = \boldsymbol{k} + \boldsymbol{q}$ and $\tilde{\boldsymbol{k}} = \boldsymbol{k} - \boldsymbol{q}$ are almost related to each other by a complex conjugation. Applying the TRS also shifts $\boldsymbol{k} \rightarrow -\boldsymbol{k}$. This can later be compensated by summing over all $\boldsymbol{k}$, e.g. for obtaining the charge-density variation [251]. If all wave vectors $\boldsymbol{k}$ are symmetrically located within the Brillouin zone, it makes no difference whether the sum is performed over $\boldsymbol{k}$ or $-\boldsymbol{k}$ and the index can adequately be interchanged. In this case, the $\pm\boldsymbol{q}$ solutions of the Sternheimer equation are in fact related to each other by a complex conjugation. Hence analogously to the previous procedure, only the solution with $\tilde{\boldsymbol{k}} = \boldsymbol{k} + \boldsymbol{q}$ shall be discussed further.

Time Reversal Symmetry

Analytical solution for $\boldsymbol{q} = \boldsymbol{0}$

Finally, it must be underlined that there exists an analytical solution of equation (6.61e) for the Goldstone modes [251]. This discussion is postponed to section 7.4, but in appendix D, I prove this for an optimized version of equation (6.61e).

6.4.2 First-Order Variation of the Kohn–Sham Energies

General form

The Sternheimer equation (6.61e) requires the first-order change of the Kohn–Sham energies for the Goldstone modes. Klüppelberg suggests using

$$\begin{aligned}\boldsymbol{\epsilon}^{(1)}_{\boldsymbol{k},n}(\mathbf{0}^{\pm}\alpha) = {} & \left\langle \Psi^{(0)}_{\boldsymbol{k},n} \middle| \boldsymbol{\mathscr{V}}^{(1)}_{\text{eff}}(\mathbf{0}^{\pm}\alpha) \middle| \Psi^{(0)}_{\boldsymbol{k},n} \right\rangle_{\Omega} \\ & + \sum_{\boldsymbol{G}'} z^{*(0)}_{\boldsymbol{G}'}(\boldsymbol{k},n) \left\langle \boldsymbol{\phi}^{(1)\mp}_{\boldsymbol{k},\boldsymbol{G}'}(\mathbf{0}\alpha) \middle| \mathscr{H}^{(0)} - \epsilon^{(0)}_{\boldsymbol{k},n} \middle| \Psi^{(0)}_{\boldsymbol{k},n} \right\rangle_{\Omega} \\ & + \sum_{\boldsymbol{G}} \left\langle \Psi^{(0)}_{\boldsymbol{k},n} \middle| \mathscr{H}^{(0)} - \epsilon^{(0)}_{\boldsymbol{k},n} \middle| \boldsymbol{\phi}^{(1)\pm}_{\boldsymbol{k},\boldsymbol{G}}(\mathbf{0}\alpha) \right\rangle_{\Omega} z^{(0)}_{\boldsymbol{G}}(\boldsymbol{k},n) \\ & + \oint_{\partial\alpha} \hat{\boldsymbol{r}} \left[\sum_{\gamma} \Psi^{*(0)\gamma}_{\boldsymbol{k},n}(\boldsymbol{r}) \left(\mathscr{H}^{(0)} - \epsilon^{(0)}_{\boldsymbol{k},n} \right) \Psi^{(0)\gamma}_{\boldsymbol{k},n}(\boldsymbol{r}) \right. \\ & \qquad \left. - \Psi^{*(0)\text{IR}}_{\boldsymbol{k},n}(\boldsymbol{r}) \left(\mathscr{H}^{(0)} - \epsilon^{(0)}_{\boldsymbol{k},n} \right) \Psi^{(0)\text{IR}}_{\boldsymbol{k},n}(\boldsymbol{r}) \right] \mathrm{d}S \; . \end{aligned} \tag{6.62}$$

Comparing equation (6.62) with the Sternheimer equation (6.61e), a similarity reveals itself. However in contrast to the Sternheimer equation, the matrix elements are diagonal in the bands and the reciprocal vectors $\boldsymbol{k}$.

Case $\boldsymbol{q} = \mathbf{0}$

For $\boldsymbol{q} = \mathbf{0}$, the change of the Kohn–Sham energies is zero if the material features monoatomic unit cells, because the crystal is only rigidly shifted. There is no reason that a variation should have been induced. But in polyatomic systems, an inner breathing mode within the unit cells is possible so that equation (6.62) does not vanish in general anymore. Coincidently, the center-of-mass movement still equals the shift of the whole crystal such as in the monoatomic case. In ionic materials this scenario leads to a LO-TO splitting in optical branches (cf. section 4.3). For finite $\boldsymbol{q}$, Klüppelberg shows that the first-order variation of the Kohn–Sham energies vanishes.

6.4.3 Self-Consistency Cycle

Theoretical background

The self-consistency cycle of the DFPT is already partly motivated at the end of section 4.2.2. Applied to phonons, the minimum of the dynamical matrix, which is a functional of the first-order charge-density and effective-potential variation, must be found. If the external potential changes, implying a perturbation of the system, the electrons are induced to move, varying the charge density. It happens until the electrons again screen the external potential adjusted to the moved ions (cf. section 4.2.1). This is a self-consistent scenario, because the first-order variations of the Hartree and the xc potentials are again functionals of the first-order charge-density variation. An in-depth analysis originates this from the fact that the Kohn–Sham DFT and the DFPT are effective mean-field theories [3]. Hence, apart from the response function or susceptibility (see chapter 4), e.g. the charge density variation due to a phonon, the electronic potentials, i.e., the Hartree and the xc contributions also vary [3]. Details of the concrete self-consistency cycle are shifted to chapter 7 to avoid redundancy.

6.5 Dynamical Matrix

Outline

The contributions to the dynamical matrix have already been derived in section 6.1.2, but are discussed in more detail now. Essentially they are grouped into three categories, the Hellmann–Feynman contributions $\underline{D}_{\text{HF}}(\boldsymbol{q})$ (see section 6.5.1), the Pulay contributions $\underline{D}_{\text{Pl}}(\boldsymbol{q})$ as discussed in section 6.5.2, and finally the surface-term contributions $\underline{D}_{\text{sf}}(\boldsymbol{q})$, which are addressed in section 6.5.3

$$D^{\beta\alpha}(\boldsymbol{q}) = D^{\beta\alpha}_{\text{HF}}(\boldsymbol{q}) + D^{\beta\alpha}_{\text{Pl}}(\boldsymbol{q}) + D^{\beta\alpha}_{\text{sf}}(\boldsymbol{q})\,. \tag{6.63}$$

6.5.1 Hellmann–Feynman Contribution

Deduction

According to equation (6.15b), equation (6.12), and equation (6.63) the Hellmann–Feynman contributions to the dynamical matrix comprises the first-order charge-density variation, the first-order external potential, the unperturbed charge density, the second-order variation of the external potential, and the second-order variation of the ion–ion interaction. All of these quantities have been discussed in the previous sections. Hence, equation (6.20), the external part of equation (6.23), equation (6.24), and equations (6.53) can be inserted so that

$$\begin{aligned} D^{\beta\alpha}_{\text{HF}}(\boldsymbol{q}) = \int_{\Omega} &\Big(\boldsymbol{Q}^{\top}_{\beta}\,\boldsymbol{\rho}^{(1)}(\boldsymbol{r};\boldsymbol{q}^{+}\beta) + \boldsymbol{Q}^{\dagger}_{\beta}\,\boldsymbol{\rho}^{(1)}(\boldsymbol{r};\boldsymbol{q}^{-}\beta)\Big) \qquad (6.64\text{a}) \\ &\qquad \times \Big(\Big[\boldsymbol{V}^{(1)}_{\text{ext}}(\boldsymbol{r};\boldsymbol{q}^{+}\alpha)\Big]^{\top}\boldsymbol{Q}_{\alpha} + \Big[\boldsymbol{V}^{(1)}_{\text{ext}}(\boldsymbol{r};\boldsymbol{q}^{-}\alpha)\Big]^{\top}\boldsymbol{Q}^{*}_{\alpha}\Big)\,\mathrm{d}^3r \\ &+ \int_{\Omega}\rho^{(0)}(\boldsymbol{r})\Big(\boldsymbol{Q}^{\top}_{\beta}\mathrm{e}^{\mathrm{i}\boldsymbol{q}\cdot\boldsymbol{R}} + \boldsymbol{Q}^{\dagger}_{\beta}\mathrm{e}^{-\mathrm{i}\boldsymbol{q}\cdot\boldsymbol{R}}\Big)\,\delta_{\beta\alpha}\boldsymbol{\nabla}\boldsymbol{\nabla}^{\top}V^{(0)}_{\text{ext}}(\boldsymbol{r})\Big(\boldsymbol{Q}_{\alpha}\mathrm{e}^{\mathrm{i}\boldsymbol{q}\cdot\boldsymbol{R}} + \boldsymbol{Q}^{*}_{\alpha}\mathrm{e}^{-\mathrm{i}\boldsymbol{q}\cdot\boldsymbol{R}}\Big)\,\mathrm{d}^3r \\ &+ E^{(2)}_{\text{ii}}(\boldsymbol{q}^{-+}) + E^{(2)}_{\text{ii}}(\boldsymbol{q}^{+-}) \end{aligned}$$

results. As mentioned in section 6.1.2 and section 6.3.4, only terms with effectively vanishing Bloch character remain. Therefore, the complete HF contribution to the dynamical matrix is given by

$$\begin{aligned} D^{\beta\alpha}_{\text{HF}}(\boldsymbol{q}) &= \boldsymbol{Q}^{\dagger}_{\beta}\left(\int_{\Omega}\boldsymbol{\rho}^{(1)}(\boldsymbol{r};\boldsymbol{q}^{-}\beta)\Big[\boldsymbol{V}^{(1)}_{\text{ext}}(\boldsymbol{r};\boldsymbol{q}^{+}\alpha)\Big]^{\top}\mathrm{d}^3r + \delta_{\beta\alpha}\int_{\Omega}\rho^{(0)}(\boldsymbol{r})\boldsymbol{\nabla}\boldsymbol{\nabla}^{\top}V^{(0)}_{\text{ext}}(\boldsymbol{r})\,\mathrm{d}^3r\right)\boldsymbol{Q}_{\alpha} \\ &\quad + \boldsymbol{Q}^{\top}_{\beta}\left(\int_{\Omega}\boldsymbol{\rho}^{(1)}(\boldsymbol{r};\boldsymbol{q}^{+}\beta)\Big[\boldsymbol{V}^{(1)}_{\text{ext}}(\boldsymbol{r};\boldsymbol{q}^{-}\alpha)\Big]^{\top}\mathrm{d}^3r + \delta_{\beta\alpha}\int_{\Omega}\rho^{(0)}(\boldsymbol{r})\boldsymbol{\nabla}\boldsymbol{\nabla}^{\top}V^{(0)}_{\text{ext}}(\boldsymbol{r})\,\mathrm{d}^3r\right)\boldsymbol{Q}^{*}_{\alpha} \\ &\quad + \boldsymbol{Q}^{\dagger}_{\beta}\,\underline{E}^{(2)\beta\alpha}_{\text{ii}}(\boldsymbol{q}^{-+})\,\boldsymbol{Q}_{\alpha} + \delta_{\boldsymbol{Q}_{\beta}\boldsymbol{Q}_{\alpha}}\boldsymbol{Q}^{\dagger}_{\beta}\,\underline{E}^{(2)\beta\alpha}_{\text{ii}}(\boldsymbol{0}^{-+})\,\boldsymbol{Q}_{\alpha} \\ &\quad + \boldsymbol{Q}^{\top}_{\beta}\,\underline{E}^{(2)\beta\alpha}_{\text{ii}}(\boldsymbol{q}^{+-})\,\boldsymbol{Q}_{\alpha} + \delta_{\boldsymbol{Q}_{\beta}\boldsymbol{Q}_{\alpha}}\boldsymbol{Q}^{\top}_{\beta}\,\underline{E}^{(2)\beta\alpha}_{\text{ii}}(\boldsymbol{0}^{+-})\,\boldsymbol{Q}_{\alpha} \qquad (6.64\text{b}) \\ &=: \boldsymbol{Q}^{\dagger}_{\beta}\,\underline{D}^{\beta\alpha}_{\text{HF}}(\boldsymbol{q}^{-+})\,\boldsymbol{Q}_{\alpha} + \boldsymbol{Q}^{\top}_{\beta}\,\underline{D}^{\beta\alpha}_{\text{HF}}(\boldsymbol{q}^{+-})\,\boldsymbol{Q}_{\alpha}\,. \qquad (6.64\text{c}) \end{aligned}$$

6.5.2 Pulay Corrections

Subdivision

It proves convenient to separate the following discussion of equation (6.15c) into two parts. First, the unit-cell integral is expounded on, the integrand of which is a product of the first-order charge-density and effective potential variation. After this, the remaining matrix elements, which depend on the wave vector $\boldsymbol{k}$, are further specified. Consequently the Pulay contribution of the dynamical matrix can be subdivided into

$$D^{\beta\alpha}_{\text{Pl}}(\boldsymbol{q}) = D^{\beta\alpha}_{\text{Pl,dp}}(\boldsymbol{q}) + D^{\beta\alpha}_{\text{Pl,bk}}(\boldsymbol{q}) \,. \tag{6.65}$$

Unit-Cell Integral

The unit-cell integral of the Pulay contribution to the dynamical matrix is the first integral in equation (6.14a) and given by

$$\begin{aligned}
D^{\beta\alpha}_{\text{Pl,dp}}(\boldsymbol{q}) &= \int_{\Omega} \Big(\boldsymbol{Q}^{\top}_{\beta}\, \boldsymbol{\rho}^{(1)}(\boldsymbol{r}; \boldsymbol{q}^{+}\beta) + \boldsymbol{Q}^{\dagger}_{\beta}\, \boldsymbol{\rho}^{(1)}(\boldsymbol{r}; \boldsymbol{q}^{-}\beta) \Big) && \text{(6.66a)} \\
&\qquad \times \Big(\Big[\boldsymbol{V}^{(1)}_{\text{eff}}(\boldsymbol{r}, \boldsymbol{q}^{+}\alpha) \Big]^{\top} \boldsymbol{Q}_{\alpha} + \Big[\boldsymbol{V}^{(1)}_{\text{eff}}(\boldsymbol{r}, \boldsymbol{q}^{-}\alpha) \Big]^{\dagger} \boldsymbol{Q}^{*}_{\alpha} \Big)\, \mathrm{d}^3 r \\
&= \boldsymbol{Q}^{\dagger}_{\beta} \int_{\Omega} \boldsymbol{\rho}^{(1)}(\boldsymbol{r}; \boldsymbol{q}^{-}\beta) \Big[\boldsymbol{V}^{(1)}_{\text{eff}}(\boldsymbol{r}; \boldsymbol{q}^{+}\alpha) \Big]^{\top} \mathrm{d}^3 r \; \boldsymbol{Q}_{\alpha} && \text{(6.66b)} \\
&\quad + \boldsymbol{Q}^{\top}_{\beta} \int_{\Omega} \boldsymbol{\rho}^{(1)}(\boldsymbol{r}; \boldsymbol{q}^{+}\beta) \Big[\boldsymbol{V}^{(1)}_{\text{eff}}(\boldsymbol{r}; \boldsymbol{q}^{-}\alpha) \Big]^{\top} \mathrm{d}^3 r \; \boldsymbol{Q}^{*}_{\alpha} \,. \\
&=: \boldsymbol{Q}^{\dagger}_{\beta}\, \underline{D}^{\beta\alpha}_{\text{Pl,dp}}(\boldsymbol{q}^{-+})\, \boldsymbol{Q}_{\alpha} + \boldsymbol{Q}^{\top}_{\beta}\, \underline{D}^{\beta\alpha}_{\text{Pl,dp}}(\boldsymbol{q}^{+-})\, \boldsymbol{Q}_{\alpha} && \text{(6.66c)}
\end{aligned}$$

Here, equations (6.20) and (6.23) are inserted into the respective integral of equations (6.66). Relative to the Hellmann–Feynman contribution in equation (6.64b), it does not only contain the first-order variation of the external potential, but also that of the Hartree and the xc potentials.

Matrix Elements

Derivation and nomenclature

Compared to the unit-cell integral contribution in the previous equation, the matrix element contributions take significantly more effort to calculate. This is a consequence of using the challenging all-electron FLAPW method. They are given by the terms behind the second sum in equation (6.14d). When inserting the variations of the Kohn–Sham wave functions from equation (6.8) and equation (6.9), which are expanded in the LAPW basis, the following abbreviations are introduced: If the second-order variation of the Kohn–Sham wave function stands in the bra, the contribution is denoted as “2b.” Provided the ket contains the second-order variation, “2k” is used. And when the first-order variation of the wave function is incorporated both in the bra and in the ket, it is indicated by “1bk.”

General expressions

Expanding the matrix elements therefore results in

$$\begin{aligned}
D^{\beta\alpha}_{\text{Pl,bk}}(\boldsymbol{q}) := \sum_{\boldsymbol{k},n} \Big(& \boldsymbol{Q}^{\dagger}_{\beta}\, 2 f^{(0)}_{\boldsymbol{k},n} \underline{D}^{\boldsymbol{k}n\beta\alpha}_{\text{Pu2b}}(\boldsymbol{q}^{+-})\, \boldsymbol{Q}_{\alpha} + \boldsymbol{Q}^{\dagger}_{\beta}\, 2 f^{(0)}_{\boldsymbol{k},n} \underline{D}^{\boldsymbol{k}n\beta\alpha}_{\text{Pu2k}}(\boldsymbol{q}^{-+})\, \boldsymbol{Q}_{\alpha} && \text{(6.67a)} \\
&+ \boldsymbol{Q}^{\dagger}_{\beta}\, 4 f^{(0)}_{\boldsymbol{k},n} \underline{D}^{\boldsymbol{k}n\beta\alpha}_{\text{Pu1bk}}(\boldsymbol{q}^{++})\, \boldsymbol{Q}_{\alpha} + \boldsymbol{Q}^{\top}_{\beta}\, 4 f^{(0)}_{\boldsymbol{k},n} \underline{D}^{\boldsymbol{k}n\beta\alpha}_{\text{Pu1bk}}(\boldsymbol{q}^{--})\, \boldsymbol{Q}^{*}_{\alpha} \\
&+ \boldsymbol{Q}^{\top}_{\beta}\, 2 f^{(0)}_{\boldsymbol{k},n} \underline{D}^{\boldsymbol{k}n\beta\alpha}_{\text{Pu2b}}(\boldsymbol{q}^{-+})\, \boldsymbol{Q}^{*}_{\alpha} + \boldsymbol{Q}^{\top}_{\beta}\, 2 f^{(0)}_{\boldsymbol{k},n} \underline{D}^{\boldsymbol{k}n\beta\alpha}_{\text{Pu2k}}(\boldsymbol{q}^{+-})\, \boldsymbol{Q}^{*}_{\alpha} \Big)
\end{aligned}$$

with

$$\begin{aligned}\underline{D}^{\boldsymbol{k}n\beta\alpha}_{\text{Pu2b}}(\boldsymbol{q}^{\pm\mp}) := {}& \left\langle 2\sum_{\boldsymbol{G}'} \boldsymbol{z}^{(1)}_{\boldsymbol{G}'}(\boldsymbol{k},n;\pm\boldsymbol{q}\beta)\left[\vec{\boldsymbol{\phi}}^{(1)\alpha\mp}_{\boldsymbol{k}\pm\boldsymbol{q},\boldsymbol{G}'}\right]^{\top}\middle|\mathscr{H}^{(0)}-\epsilon^{(0)}_{\boldsymbol{k},n}\middle|\sum_{\boldsymbol{G}} z^{(0)}_{\boldsymbol{G}}(\boldsymbol{k},n)\phi^{(0)}_{\boldsymbol{k},\boldsymbol{G}}\right\rangle \\ &+\left\langle \sum_{\boldsymbol{G}'} z^{(0)}_{\boldsymbol{G}'}(\boldsymbol{k},n)\underline{\vec{\phi}}^{(2)\beta\pm\mp}_{\boldsymbol{k}+\boldsymbol{0},\boldsymbol{G}'}\delta_{\beta\alpha}\middle|\mathscr{H}^{(0)}-\epsilon^{(0)}_{\boldsymbol{k},n}\middle|\sum_{\boldsymbol{G}} z^{(0)}_{\boldsymbol{G}}(\boldsymbol{k},n)\phi^{(0)}_{\boldsymbol{k},\boldsymbol{G}}\right\rangle ,\end{aligned}\tag{6.67b}$$

$$\begin{aligned}\underline{D}^{\boldsymbol{k}n\beta\alpha}_{\text{Pu2k}}(\boldsymbol{q}^{\mp\pm}) := {}& \left\langle \sum_{\boldsymbol{G}'} z^{(0)}_{\boldsymbol{G}'}(\boldsymbol{k},n)\phi^{(0)}_{\boldsymbol{k},\boldsymbol{G}'}\middle|\mathscr{H}^{(0)}-\epsilon^{(0)}_{\boldsymbol{k},n}\middle|2\sum_{\boldsymbol{G}} \boldsymbol{z}^{(1)}_{\boldsymbol{G}}(\boldsymbol{k},n;\mp\boldsymbol{q}\beta)\left[\vec{\boldsymbol{\phi}}^{(1)\alpha\pm}_{\boldsymbol{k}\mp\boldsymbol{q},\boldsymbol{G}}\right]^{\top}\right\rangle \\ &+\left\langle \sum_{\boldsymbol{G}'} z^{(0)}_{\boldsymbol{G}'}(\boldsymbol{k},n)\phi^{(0)}_{\boldsymbol{k},\boldsymbol{G}'}\middle|\mathscr{H}^{(0)}-\epsilon^{(0)}_{\boldsymbol{k},n}\middle|\sum_{\boldsymbol{G}} z^{(0)}_{\boldsymbol{G}}(\boldsymbol{k},n)\underline{\vec{\phi}}^{(2)\beta\mp\pm}_{\boldsymbol{k}+\boldsymbol{0},\boldsymbol{G}}\delta_{\beta\alpha}\right\rangle ,\end{aligned}\tag{6.67c}$$

and

$$\begin{aligned}\underline{D}^{\boldsymbol{k}n\beta\alpha}_{\text{Pu1bk}}(\boldsymbol{q}^{\pm\pm}) := {}& \left\langle \sum_{\boldsymbol{G}'} \boldsymbol{z}^{(1)}_{\boldsymbol{G}'}(\boldsymbol{k},n;\pm\boldsymbol{q}\beta)\phi^{(0)}_{\boldsymbol{k}\pm\boldsymbol{q},\boldsymbol{G}'}\middle|\mathscr{H}^{(0)}-\epsilon^{(0)}_{\boldsymbol{k},n}\middle|\sum_{\boldsymbol{G}}\left[\boldsymbol{z}^{(1)}_{\boldsymbol{G}}(\boldsymbol{k},n;\pm\boldsymbol{q}\alpha)\right]^{\top}\phi^{(0)}_{\boldsymbol{k}\pm\boldsymbol{q},\boldsymbol{G}}\right\rangle \\ &+\left\langle \sum_{\boldsymbol{G}'} \boldsymbol{z}^{(1)}_{\boldsymbol{G}'}(\boldsymbol{k},n;\pm\boldsymbol{q}\beta)\phi^{(0)}_{\boldsymbol{k}\pm\boldsymbol{q},\boldsymbol{G}'}\middle|\mathscr{H}^{(0)}-\epsilon^{(0)}_{\boldsymbol{k},n}\middle|\sum_{\boldsymbol{G}} z^{(0)}_{\boldsymbol{G}}(\boldsymbol{k},n)\left[\vec{\boldsymbol{\phi}}^{(1)\alpha\pm}_{\boldsymbol{k},\boldsymbol{G}}\right]^{\top}\right\rangle \\ &+\left\langle \sum_{\boldsymbol{G}'} z^{(0)}_{\boldsymbol{G}'}(\boldsymbol{k},n)\vec{\boldsymbol{\phi}}^{(1)\beta\pm}_{\boldsymbol{k},\boldsymbol{G}'}\middle|\mathscr{H}^{(0)}-\epsilon^{(0)}_{\boldsymbol{k},n}\middle|\sum_{\boldsymbol{G}}\left[\boldsymbol{z}^{(1)}_{\boldsymbol{G}}(\boldsymbol{k},n;\pm\boldsymbol{q}\alpha)\right]^{\top}\phi^{(0)}_{\boldsymbol{k}\pm\boldsymbol{q},\boldsymbol{G}}\right\rangle \\ &+\left\langle \sum_{\boldsymbol{G}'} z^{(0)}_{\boldsymbol{G}'}(\boldsymbol{k},n)\vec{\boldsymbol{\phi}}^{(1)\beta\pm}_{\boldsymbol{k},\boldsymbol{G}'}\middle|\mathscr{H}^{(0)}-\epsilon^{(0)}_{\boldsymbol{k},n}\middle|\sum_{\boldsymbol{G}} z^{(0)}_{\boldsymbol{G}}(\boldsymbol{k},n)\left[\vec{\boldsymbol{\phi}}^{(1)\alpha\pm}_{\boldsymbol{k},\boldsymbol{G}}\right]^{\top}\right\rangle .\end{aligned}\tag{6.67d}$$

It becomes directly obvious that no second-order variation of the wave-function expansion coefficients is required. This is because they are combined with a classical unperturbed basis function. Hence, both the bra and the ket are completely covered by the LAPW Hilbert space. As a consequence, the Hamiltonian fulfills the Kohn–Sham equation variationally and its application to the unperturbed Kohn–Sham wave function results in the Kohn–Sham energy so that these matrix elements cancel. Ultimately, this constitutes the reason why the $2n+1$ theorem is not violated.

6.5.3 Surface-Term Corrections

Derivation

The surface-term contributions from section 6.1.2 are further evaluated and the displacement (6.5) inserted. Moreover, it is necessary to employ the first-order wave function variations from equations (6.8) with the first-order basis-function variation from equations (6.7). Furthermore, equation (6.23) with the external and Hartree part of equation (6.22) are required. They are pointed out in section 6.3.1 and section 6.3.2, respectively. All of them subdivide into contributions with Bloch characters $\boldsymbol{q}$ and $-\boldsymbol{q}$ so that

$$
\begin{aligned}
\underline{D}_{\text{sf}}^{\beta\alpha}(\boldsymbol{q}) = \left(\boldsymbol{Q}_{\beta}^{\top} + \boldsymbol{Q}_{\beta}^{\dagger}\right) \Bigg\{ \sum_{\boldsymbol{k},n} f_{\boldsymbol{k},n}^{(0)} \Bigg\{ & \\
& 2 \oint_{\partial\beta} \hat{\boldsymbol{r}} \Bigg[\left(\left[\boldsymbol{\Psi}_{\boldsymbol{k},n}^{(1)\beta+}(\boldsymbol{r};\alpha)\right]^{\top} \boldsymbol{Q}_{\alpha} + \left[\boldsymbol{\Psi}_{\boldsymbol{k},n}^{(1)\beta-}(\boldsymbol{r};\alpha)\right]^{\top} \boldsymbol{Q}_{\alpha}^{*} \right)^{*} \left(\mathscr{H}^{(0)} - \epsilon_{\boldsymbol{k},n}^{(0)}\right) \Psi_{\boldsymbol{k},n}^{(0)\beta}(\boldsymbol{r}) \\
& \qquad - \left(\left[\boldsymbol{\Psi}_{\boldsymbol{k},n}^{(1)\text{IR}+}(\boldsymbol{r};\alpha)\right]^{\top} \boldsymbol{Q}_{\alpha} + \left[\boldsymbol{\Psi}_{\boldsymbol{k},n}^{(1)\text{IR}-}(\boldsymbol{r};\alpha)\right]^{\top} \boldsymbol{Q}_{\alpha}^{*} \right)^{*} \left(\mathscr{H}^{(0)} - \epsilon_{\boldsymbol{k},n}^{(0)}\right) \Psi_{\boldsymbol{k},n}^{(0)\text{IR}}(\boldsymbol{r}) \Bigg] \,\mathrm{d}S \\
& + 2 \oint_{\partial\beta} \hat{\boldsymbol{r}} \Bigg[\Psi_{\boldsymbol{k},n}^{*(0)\beta}(\boldsymbol{r}) \left(\mathscr{H}^{(0)} - \epsilon_{\boldsymbol{k},n}^{(0)}\right) \left(\left[\boldsymbol{\Psi}_{\boldsymbol{k},n}^{(1)\beta+}(\boldsymbol{r};\alpha)\right]^{\top} \boldsymbol{Q}_{\alpha} + \left[\boldsymbol{\Psi}_{\boldsymbol{k},n}^{(1)\beta-}(\boldsymbol{r};\alpha)\right]^{\top} \boldsymbol{Q}_{\alpha}^{*} \right) \\
& \qquad - \Psi_{\boldsymbol{k},n}^{*(0)\text{IR}}(\boldsymbol{r}) \left(\mathscr{H}^{(0)} - \epsilon_{\boldsymbol{k},n}^{(0)}\right) \left(\left[\boldsymbol{\Psi}_{\boldsymbol{k},n}^{(1)\text{IR}+}(\boldsymbol{r};\alpha)\right]^{\top} \boldsymbol{Q}_{\alpha} + \left[\boldsymbol{\Psi}_{\boldsymbol{k},n}^{(1)\text{IR}-}(\boldsymbol{r};\alpha)\right]^{\top} \boldsymbol{Q}_{\alpha}^{*} \right) \Bigg] \,\mathrm{d}S \\
& + \delta_{\beta\alpha} \oint_{\partial\beta} \Bigg[\boldsymbol{\nabla} \left(\Psi_{\boldsymbol{k},n}^{*(0)\beta}(\boldsymbol{r}) \left(\mathscr{H}^{(0)} - \epsilon_{\boldsymbol{k},n}^{(0)}\right) \Psi_{\boldsymbol{k},n}^{(0)\beta}(\boldsymbol{r}) \right) \\
& \qquad - \boldsymbol{\nabla} \left(\Psi_{\boldsymbol{k},n}^{*(0)\text{IR}}(\boldsymbol{r}) \left(\mathscr{H}^{(0)} - \epsilon_{\boldsymbol{k},n}^{(0)}\right) \Psi_{\boldsymbol{k},n}^{(0)\text{IR}}(\boldsymbol{r}) \right) \Bigg] \hat{\boldsymbol{r}}^{\top} \,\mathrm{d}S \, \left(\boldsymbol{Q}_{\beta} + \boldsymbol{Q}_{\alpha}^{*}\right) \Bigg\} \\
& + \delta_{\beta\alpha} \oint_{\partial\beta} \Bigg[\boldsymbol{\nabla} \left(\rho_{\beta}^{(0)}(\boldsymbol{r}) \left(\epsilon_{\text{xc}}^{(0)\beta}(\boldsymbol{r}) - V_{\text{xc}}^{(0)\beta}(\boldsymbol{r}) \right) \right) \\
& \qquad - \boldsymbol{\nabla} \left(\rho_{\text{IR}}^{(0)}(\boldsymbol{r}) \left(\epsilon_{\text{xc}}^{(0)\text{IR}}(\boldsymbol{r}) - V_{\text{xc}}^{(0)\text{IR}}(\boldsymbol{r}) \right) \right) \Bigg] \hat{\boldsymbol{r}}^{\top} \,\mathrm{d}S \, \left(\boldsymbol{Q}_{\beta} + \boldsymbol{Q}_{\alpha}^{*}\right) \\
& + \delta_{\beta\alpha} \oint_{\partial\beta} \hat{\boldsymbol{r}} \Bigg[\rho_{\beta}^{(0)}(\boldsymbol{r}) \Bigg(\left(2\left[\boldsymbol{V}_{\text{ext}}^{(1)\beta}(\boldsymbol{r};\boldsymbol{q}^{+}\alpha)\right]^{\top} + \left[\boldsymbol{V}_{\text{Htr}}^{(1)\beta}(\boldsymbol{r};\boldsymbol{q}^{+}\alpha)\right]^{\top} \right) \boldsymbol{Q}_{\alpha} \\
& \qquad + \left(2\left[\boldsymbol{V}_{\text{ext}}^{(1)\beta}(\boldsymbol{r};\boldsymbol{q}^{-}\alpha)\right]^{\dagger} + \left[\boldsymbol{V}_{\text{Htr}}^{(1)\beta}(\boldsymbol{r};\boldsymbol{q}^{-}\alpha)\right]^{\dagger} \right) \boldsymbol{Q}_{\alpha}^{*} \Bigg) \Bigg] \,\mathrm{d}S \\
& + \delta_{\beta\alpha} \oint_{\partial\beta} \hat{\boldsymbol{r}} \Bigg[\rho_{\text{IR}}^{(0)}(\boldsymbol{r}) \Bigg(\left(2\left[\boldsymbol{V}_{\text{ext}}^{(1)\text{IR}}(\boldsymbol{r};\boldsymbol{q}^{+}\alpha)\right]^{\top} + \left[\boldsymbol{V}_{\text{Htr}}^{(1)\text{IR}}(\boldsymbol{r};\boldsymbol{q}^{+}\alpha)\right]^{\top} \right) \boldsymbol{Q}_{\alpha} \\
& \qquad + \left(2\left[\boldsymbol{V}_{\text{ext}}^{(1)\text{IR}}(\boldsymbol{r};\boldsymbol{q}^{-}\alpha)\right]^{\dagger} + \left[\boldsymbol{V}_{\text{Htr}}^{(1)\text{IR}}(\boldsymbol{r};\boldsymbol{q}^{-}\alpha)\right]^{\dagger} \right) \boldsymbol{Q}_{\alpha}^{*} \Bigg) \Bigg] \,\mathrm{d}S \Bigg\}
\end{aligned}
\tag{6.68a}
$$

According to section 6.1.2 only the terms are relevant which have a Bloch character of $\pm\boldsymbol{q}$. Therefore, the previous equation simplifies to

Time Reversal Symmetry

$$
D_{\text{sf}}^{\beta\alpha}(\boldsymbol{q}) =: \sum_{\beta\alpha} \left(\boldsymbol{Q}_{\beta}^{\dagger} \, \underline{D}_{\text{sf}}^{\beta\alpha}(\boldsymbol{q}^{+}) \, \boldsymbol{Q}_{\alpha} + \boldsymbol{Q}_{\beta}^{\top} \, \underline{D}_{\text{sf}}^{\beta\alpha}(\boldsymbol{q}^{-}) \, \boldsymbol{Q}_{\alpha}^{*} \right) . \tag{6.68b}
$$

with

$$
\begin{aligned}
\underline{D}_{\mathrm{sf}}^{\beta\alpha}(\boldsymbol{q}^{\pm}) := \sum_{\boldsymbol{k},n} f_{\boldsymbol{k},n}^{(0)} \Bigg\{ 2 \oint_{\partial\beta} \hat{\boldsymbol{r}} \Bigg[& \Big[\boldsymbol{\Psi}_{\boldsymbol{k},n}^{(1)\beta\mp}(\boldsymbol{r};\alpha)\Big]^{\dagger} \Big(\mathscr{H}^{(0)} - \epsilon_{\boldsymbol{k},n}^{(0)}\Big) \Psi_{\boldsymbol{k},n}^{(0)\beta}(\boldsymbol{r}) \\
& - \Big[\boldsymbol{\Psi}_{\boldsymbol{k},n}^{(1)\mathrm{IR}\mp}(\boldsymbol{r};\alpha)\Big]^{\dagger} \Big(\mathscr{H}^{(0)} - \epsilon_{\boldsymbol{k},n}^{(0)}\Big) \Psi_{\boldsymbol{k},n}^{(0)\mathrm{IR}}(\boldsymbol{r}) \Bigg] \, \mathrm{d}S \\
& + 2 \oint_{\partial\beta} \hat{\boldsymbol{r}} \Bigg[\Psi_{\boldsymbol{k},n}^{*(0)\beta}(\boldsymbol{r}) \Big(\mathscr{H}^{(0)} - \epsilon_{\boldsymbol{k},n}^{(0)}\Big) \Big[\boldsymbol{\Psi}_{\boldsymbol{k},n}^{(1)\beta\pm}(\boldsymbol{r};\alpha)\Big]^{\top} \\
& - \Psi_{\boldsymbol{k},n}^{*(0)\mathrm{IR}}(\boldsymbol{r}) \Big(\mathscr{H}^{(0)} - \epsilon_{\boldsymbol{k},n}^{(0)}\Big) \Big[\boldsymbol{\Psi}_{\boldsymbol{k},n}^{(1)\mathrm{IR}\pm}(\boldsymbol{r};\alpha)\Big]^{\top} \Bigg] \, \mathrm{d}S \\
& + \delta_{\beta\alpha} \oint_{\partial\beta} \Bigg[\boldsymbol{\nabla} \Big(\Psi_{\boldsymbol{k},n}^{*(0)\beta}(\boldsymbol{r}) \Big(\mathscr{H}^{(0)} - \epsilon_{\boldsymbol{k},n}^{(0)}\Big) \Psi_{\boldsymbol{k},n}^{(0)\beta}(\boldsymbol{r}) \Big) \\
& - \boldsymbol{\nabla} \Big(\Psi_{\boldsymbol{k},n}^{*(0)\mathrm{IR}}(\boldsymbol{r}) \Big(\mathscr{H}^{(0)} - \epsilon_{\boldsymbol{k},n}^{(0)}\Big) \Psi_{\boldsymbol{k},n}^{(0)\mathrm{IR}}(\boldsymbol{r}) \Big) \Bigg] \hat{\boldsymbol{r}}^{\top} \, \mathrm{d}S \Bigg\} \\
+ \delta_{\beta\alpha} \oint_{\partial\beta} \Bigg[& \boldsymbol{\nabla} \Big(\rho_{\beta}^{(0)}(\boldsymbol{r}) \Big(\epsilon_{\mathrm{xc}}^{(0)\beta}(\boldsymbol{r}) - V_{\mathrm{xc}}^{(0)\beta}(\boldsymbol{r}) \Big) \Big) \\
& - \boldsymbol{\nabla} \Big(\rho_{\mathrm{IR}}^{(0)}(\boldsymbol{r}) \Big(\epsilon_{\mathrm{xc}}^{(0)\mathrm{IR}}(\boldsymbol{r}) - V_{\mathrm{xc}}^{(0)\mathrm{IR}}(\boldsymbol{r}) \Big) \Big) \Bigg] \hat{\boldsymbol{r}}^{\top} \, \mathrm{d}S \\
+ \delta_{\beta\alpha} \oint_{\partial\beta} \hat{\boldsymbol{r}} \Bigg[& \rho_{\beta}^{(0)}(\boldsymbol{r}) \Big(2 \Big[\boldsymbol{V}_{\mathrm{ext}}^{(1)\beta}(\boldsymbol{r};\boldsymbol{q}^{\pm}\alpha)\Big]^{\top} + \Big[\boldsymbol{V}_{\mathrm{Htr}}^{(1)\beta}(\boldsymbol{r};\boldsymbol{q}^{\pm}\alpha)\Big]^{\top} \Big) \\
& - \rho_{\mathrm{IR}}^{(0)}(\boldsymbol{r}) \Big(2 \Big[\boldsymbol{V}_{\mathrm{ext}}^{(1)\mathrm{IR}}(\boldsymbol{r};\boldsymbol{q}^{\pm}\alpha)\Big]^{\top} + \Big[\boldsymbol{V}_{\mathrm{Htr}}^{(1)\mathrm{IR}}(\boldsymbol{r};\boldsymbol{q}^{\pm}\alpha)\Big]^{\top} \Big) \Bigg] \, \mathrm{d}S \; .
\end{aligned}
\tag{6.68c}
$$

Further technical details of the implementation are pointed out in section 7.6.

Chapter 7

Implementation and Results

7.1 Setting the Stage . . . 112
7.2 Linear Charge-Density Variations . . . 132
7.3 Linear Potential Variations . . . 158
7.4 Solving the Sternheimer Equation . . . 180
7.5 Second-Order Variation of the Ion–Ion Interaction . . . 210
7.6 Dynamical matrix . . . 219
7.7 Phonon Dispersions . . . 261

Intention of chapter

In chapter 6 (and preceding chapters), a theory is introduced to calculate phonon dispersion-relations from a combination of the DFPT and the FLAPW method. Hereinafter, I elucidate `juPhon`, our implementation of this approach. This covers (i) an explanation of the algorithms used to address the multitudinous numerical challenges, (ii) an overview of all conducted validity tests and (iii) a presentation of the `juPhon` results. Already realizing the Sternheimer equation is comparable to, or even more intricate than, a standard self-consistent DFT algorithm for determining the total energy. Currently, the `juPhon` code overall contains approximately 50 000 lines of real source code, i.e., excluding comments, documentation, and blank lines [259].

Assistance received

This is a huge project that cannot be completed alone within a restricted time frame of a PhD program. I was therefore supported by some members of the institute for the Quantum Theory of Materials. It is part of the Peter Grünberg Institute and the Institute of Advanced Simulation, which both maintain a long-standing tradition in developing sophisticated research software. While I have essentially programmed each line of `juPhon`, many of the applied concepts, pointed out in the following, have resulted from discussions [119, 127, 251, 256, 260, 261]. Furthermore, I was supported by my advisors in debugging and inventing testing strategies [119, 127, 251]. Due to the large scale of the project, this initial implementation adopted some concepts rather than tackling each problem from scratch. A few algorithms thus adhere to adequate snippets of the `FLEUR` code [69][1] or suggestions of Klüppelberg [88].

---

[1] Whenever reasonable, the most current version of the `FLEUR` code served as inspiration.

Code philosophy

However, therein lies the danger that these ideas might turn out to only be a quick-fix solution[2] or even not work at all. The former entails a refactoring, which must sometimes be postponed due to restricted time resources (in this case, the quality of the source code is worsened). But, the probability of facing the latter will be much higher if everything is realized from scratch. Moreover, reinventing the wheel, i.e., a dissipation of time is avoided by initially analyzing whether issues have already been resolved. I have followed the guidelines of adjusting recycled code snippets in the first instance as little as possible, in order to maximize the probability of retaining their functionality. However, this delays the aforementioned refactoring in favor of an earlier-working implementation.

Chapter overview flow-chart

Apart from the succeeding outline of this chapter, the flow chart in figure 7.1 is supposed to additionally facilitate the navigation through chapter 7, and establish a connection to chapter 6. This figure provides an overview of the central steps that characterize the algorithm of `juPhon` for a specific phonon vector $\boldsymbol{q}$. It includes the initialization (grayish), the Sternheimer self-consistency cycle (blueish), determining the second-order variation of the ion–ion interaction due to a phonon (reddish), as well as the setup of the dynamical matrix (yellowish). Diagonalizing the dynamical matrix and processing this scheme for a special set of $\boldsymbol{q}$-vectors, phonon dispersion relations (greenish) can be computed.

Outline of chapter 7

In more detail and consecutive order, section 7.1 starts with general remarks on what to consider as important for the implementation, and elaborates on the initialization of `juPhon`. In section 7.2, the implementation of the linear charge-density variations is discussed and 2D plots of the first-order charge-density variation are provided for selected $\boldsymbol{q}$-vectors. Section 7.3 then presents the implementation of the linear potential variations and their visualizations. While the potential gradients are given as isosurfaces in 3D, the first-order variations are illustrated again in 2D for the same $\boldsymbol{q}$-values as chosen in section 7.2. Our way of achieving the self-consistency of the Sternheimer equation is explained in section 7.4. Section 7.5 discusses the realized implementation of the second-order ion–ion interaction. In particular from a numerical point of view, the implementation of the dynamical matrix has proven to be highly demanding. Enlarging upon it and elucidating our implementation strategy is the subject of section 7.6. Finally, I contrast my phonon-dispersions results from DFPT with benchmark FD-computations and experimental data in section 7.7.

---

[2] Some snippets are more complicated than necessary, because in former times the architecture of the hardware required a way of programming which is obsolete or even self-defeating today. Furthermore, it is often impossible to organically absorb foreign original code snippets into the present `juPhon` code structure. Finally, important numerical issues might have been ignored heretofore.

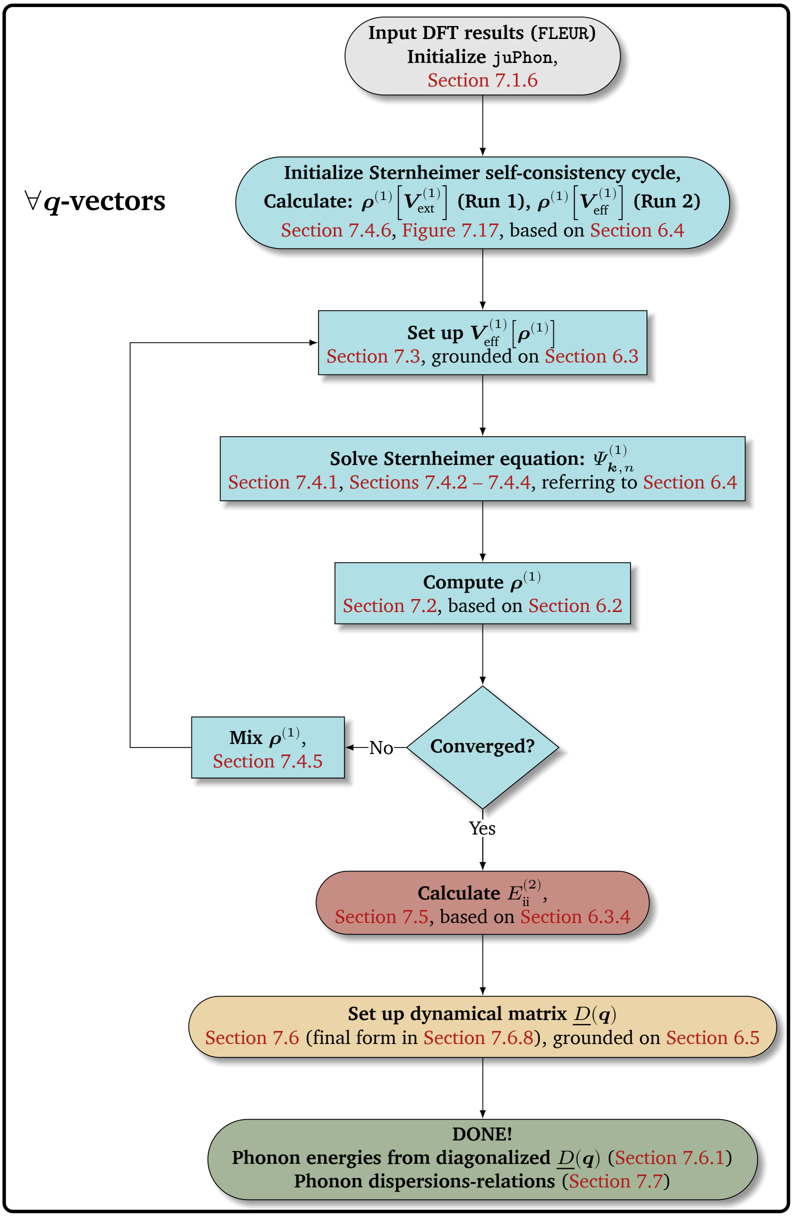

Figure 7.1: Flowchart summarizing the central steps for calculating phonon energies with the computer code `juPhon`. For each step, the sections containing the details of the implementation (chapter 7) and of the theory (chapter 6) are indicated. The order of variation due to a phonon is expressed by an upper index in parentheses.

7.1 Setting the Stage

Compatibility of `juPhon`

In principle, a `juPhon` calculation can be based on an arbitrary DFT all-electron FLAPW calculation (cf. chapter 1). This however requires an interface for `juPhon`, which I have programmed for the `FLEUR` code version 26[3]. It enables me to employ the read-in results of the aforementioned `FLEUR` version for every `juPhon` calculation[4]. During the course of developing `juPhon`, `FLEUR` has significantly been modernized, refactored, and improved so that my interface requires adjustments. Thus, I always refer to this old version of the `FLEUR` code, unless differently stated. This is because the new version had not been stable and reliable for a long time during the development of `juPhon`. Now, switching to the latest `FLEUR` version is possible and updating my interface is part of future work.

Outline

Various general aspects must be considered for the realization of a project as big as that of phonon-dispersion relations. During the implementation, I have faced the challenge that it involves sustained programming efforts before physically relevant results can be achieved. Such physics data is comparable to published benchmarks, coming either from experiments or from other electronic-structure codes. Consequently, we are convinced that establishing a comprehensive testing framework is of utmost importance [119, 127, 251]. This suite of testing subroutines is introduced in section 7.1.1 and serves, among others, to verify the reliability of (intermediate) results from `juPhon`. In particular, the combination of the DFPT and FLAPW methods inevitably requires developing strategies for handling the numerics. Section 7.1.2 addresses the applied concepts for reaching the desired precision. Moreover, a first naive implementation, especially of such an intricate framework, often results in a poor computational performance. In section 7.1.3, I roughly estimate the runtime of `juPhon` and describe the procedure I have followed for improving it. In this context, starting points for implementing a future parallelization are likewise presented. Section 7.1.4 and section 7.1.5 are devoted to simplifications underlying in order to reduce the level of complexity in the first implementation. These cover the symmetry optimizations and relativistic corrections (cf. in particular section 5.2 and section 5.7), respectively. Finally, section 7.1.6 defines the `FLEUR` input, points out the initialization algorithm of `juPhon`, and presents a set of tests that check the integrity of the input and initialization quantities `juPhon` relies on.

7.1.1 Test Suite

Motivation

The implementation of the DFPT framework presented in the previous chapters proves to be highly elaborate and urges the development of sophisticated optimizations. Consequently adhering to the principle of "divide and conquer," the algorithm must be reasonably split into coherent subprocedures that calculate intermediate quantities. Doing this, it is naive to assume that each subtlety is always considered, and human nature inevitably leads to software bugs at some point. All the more, it is of paramount importance to develop a suite of testing subroutines, which substantiates the reliability of `juPhon` and helps to identify problems. Possible errors can originate from (i) fundamentally incorrect assumptions or calculations

---

[3] The version referred to (see reference [69] for its documentation) is given in the repository oldfleur4juphon when searching for the hash `1332f354af36cab1086ac5c3aeba345b852367e0` .

[4] The results of `juPhon` discussed in the following (except for those in section 7.7.1) are generated by the version stored in the repository `juPhon` with the hash `e7c50ff83e44aeb32a63741e1bb5ae4ac2e8aaaa`. Furthermore, both `FLEUR` and `juPhon` are compiled with the Intel Fortran compiler [262] (version 19.1.0.166).

in the underlying theory, (ii) typos in reference [88], (iii) bugs within its implementation, or (iv) numerical reasons. The more intricate the algorithm, the harder it is to spot such errors. But at least for the cases (ii), (iii), and (iv), tests allow for highlighting the causing issues. Numerical inaccuracies are often tricky to find, especially when one does not ponder their existence. Nevertheless, their impact must not be underestimated, because violations of central mathematical relations such as the Divergence Theorem are possible.

Raison d'être

The development of a comprehensive test framework is costly and not often rewarded in science. But improving the reliability and preserving the reproducibility or functionality are actually pivotal for a good scientific practice. In the long term, a test suite drastically simplifies the maintenance and extension of the code [263, 264]. Without consistent testing, optimizations can corrupt recent achievements and errors accumulate [263, 264]. Such optimizations range from obtaining and retaining a clean code according to Martin [263], to increasing the computational performance or the numerical stability (e.g. after having devised new features). Hence, automating the manual execution of the test is beneficial [263, 264]. Still, in a first poor man's version, the `juPhon` test suite must be started manually. It must be stressed that a subset of these checks should always, or at least regularly, be conducted before the actual `juPhon` calculation. Especially, this holds true when new parameters for this computation have been set. In a next step, the poor man's testing framework will be automated so that for every commit it will be executed by the server, which stores the `juPhon` repository.

Test types

Basically, the constituents of the `juPhon` test suite fall into two categories. Either the inherent consistency of subroutines is validated or their return values are compared to expected values. The former tests ensure that two contributions cancel each other or a certain sum adds up to e.g. one. Concerning the latter test type, many return values of subroutines are not always known in the beginning. In particular, this holds true when either the correctness of this subroutine has not been proven before or intermediate quantities are not measurable in the experiment, due to the basic principles of quantum mechanics. Phonon observables are primarily their dispersion relations. But in principle, the charge-density responses or certain sorts of potentials likewise belong to the former. Nevertheless, sometimes it is feasible to find limiting cases for which the result(s) of a subroutine is (are) clear, concurrently accepting this to not cover all possible outcomes of the subroutine. Another more fruitful option consists of utilizing the results of already-established electronic-structure programs. They can ideally calculate phonon-dispersion relations from DFPT within the FLAPW method in the same way `juPhon` does. But, such a program does not exist, although the `Elk` [96] project[5] and the `exciting` [102] code are closest to this requirement (see chapter 1). However, since it takes considerable effort to make the intermediate quantities of two codes comparable, I mainly resort to the aforesaid alternative test concepts. Still for final results, such as the dispersion relations or the second-order ion–ion interaction, it is interesting to contrast them with outcomes obtained from other numerical methods. Especially the former quantities can be compared to calculations from code frameworks listed in chapter 1. Apart from that, I benchmark our Weinert implementation of the latter with an Ewald-inspired method, realized in the subroutines of the `ABINIT` [55–57, 255, 265] package. Finally, in some cases it is possible to manipulate the subroutines of `juPhon` such that their return values can be compared with intermediate results of the `FLEUR` code. Further tests of `juPhon` involve using

---

[5] Neukirchen verified the Sternheimer self-consistency cycle for Al and the second-order ion–ion interaction by comparing it to the Elk results as far as possible (unpublished).

debug programs like `TotalView` [266] and `Valgrind` [267–269], or employing compilers that are different from the Intel Fortran Compiler [262]. Many of the test concepts are not obvious and their development has been influenced by discussions [119, 127, 251], but I have been driving this test-suite development, and I have programmed all tests.

Limits and overview

All in all, the integrity of `juPhon` would be optimally tested provided (almost) every possible result of the code is checked. But as a consequence of the aforementioned reasons, reaching a full coverage[6] is in fact hard, in particular for finite $\boldsymbol{q}$ values. Furthermore, the details and subtleties of all tests are not described here, but in the following sections. This is in order to ensure that they are discussed in the context of the quantities they check. Nonetheless, table 7.1 and table 7.2 provide an overview of all tests in this chapter and include also references to the pages they can be found on.

7.1.2 Numerical Accuracy

Challenges and motivation

In the end, it stands to reason that the valid significant figures in the phonon frequencies should be maximized [127]. However, the absolute numerical value of the total energy is about five orders of magnitude[7] larger than that of typical phonon frequencies. This fact can probably be ranked as the most formidable numerical challenge [119]. It is exacerbated by the circumstance that these small energies are planned to be obtained from sums of gradient quantities, and gradient operations are roughening operations in the field of numerical mathematics [119]. They can feature enormously larger values, in particular close around the nuclei. In a nutshell, very small numbers must be calculated from the sum or difference of very large numbers. It has turned out that relying on a naive handling of numerics in this context inevitably fails. On the contrary, it must be considered pivotal to strive for the required numerical accuracy of intermediate results so that an sufficiently accurate result can be obtained in the end.

Avoiding error sources

Answering the question which accuracy is technically achievable and reasonable is guided by various aspects. In general, numerical errors fall into three categories: (i) rounding errors, (ii) truncation errors, and (iii) discretization errors [270, 271]. Additionally, non-numerical approximation errors such as for the xc quantities (cf. section 2.2.2) or the linearization error of the LAPW basis (5.2) should be kept in mind [271]. Category (i) depends on the length of the floating-point significand [270]. The measure adopted from the `FLEUR` code is likewise to use an $8\,\mathrm{byte}$ representation of the floating-point number in `juPhon`, doubling the default $4\,\mathrm{byte}$ precision in `FORTRAN`. The former is known as the IEEE format and allows for a *machine precision* of approximately 10^{-16} as an upper limit for the relative error of rounding [271]. Nevertheless, the floating-point precision can drastically be lowered by the propagation of rounding errors $\varepsilon_{\boldsymbol{x}}$ of a variable vector $\boldsymbol{x}$ with i components

$$\varepsilon_{\mathfrak{g}} = \sum_i \left| \frac{x_i}{\mathfrak{g}(\boldsymbol{x})} \frac{\partial \mathfrak{g}(\boldsymbol{x})}{\partial \boldsymbol{x}} \right| \varepsilon_{x_i} \,, \tag{7.1}$$

if a general function $\mathfrak{g}(\boldsymbol{x})$ is applied [270]. This propagated error $\varepsilon_{\mathfrak{g}}$ becomes huge, provided the result of the function is close to zero [270]. For instance, this happens if subtracting two similar numbers [270]. Such problematic operations should be performed as soon as possible

---

[6] The coverage will be visualized by respective tools in the near future.

[7] This ratio is exact for Ne and Al.

Table 7.1: Overview of the 39 tests in the `juPhon` code (1/2). The abbreviations I/O, LDV, and LPV denote input/output, linear density variation, and linear potential variation, respectively.

#	Class	Name	Page
1	I/O	The $\boldsymbol{k}$-point generator and the `kpts` file	128
2	I/O	Consistency of the `eig` file using `Fermie`	128
3	I/O	Continuities of the wave functions (`eig`), the charge density (`cdn1`), and the effective potential (`pottot_unwarped`) from `FLEUR`	128
4	I/O	Properties of the radial functions from the LAPW basis set	130
5	I/O	Orthogonality of the Kohn–Sham wave functions (`eig`)	130
6	I/O	Comparing the log files of `FLEUR` and `juPhon`	131
7	I/O	Abandoning the rotations of the local coordinate systems	132
8	LDV	Radial derivatives	150
9	LDV	Gaunt coefficients	150
10	LDV	Trivial muffin-tin gradient	152
11	LDV	Reproducing the unperturbed charge density	152
12	LDV	First-order density variation for the Goldstone modes	153
13	LDV	Continuity of density gradient and first-order density variation	153
14	LDV	First-order charge-density variation from difference quotients	154
15	LPV	Alternative for the gradient of the unperturbed Coulomb potential	175
16	LPV	Alternative of pseudo-density for the external-potential variations	176
17	LPV	Continuity of the linear potential variations	178
18	LPV	Reproducing the unperturbed `FLEUR` potentials	178
19	LPV	The first-order effective-potential variations for $\boldsymbol{q} = \boldsymbol{0}$	179
20	LPV	Time Reversal Symmetry	179

Table 7.2: Overview of the 39 tests in the `juPhon` code (2/2). The abbreviations SHE, EI2, and DMS mean Sternheimer equation, second-order ion–ion interaction, and dynamical-matrix setup, respectively.

#	Class	Name	Page
21	SHE	Hellmann–Feynman Sternheimer equation	205
22	SHE	Hellmann–Feynman matrix element for $\boldsymbol{q} = \mathbf{0}$	206
23	SHE	Vanishing of the first-order Kohn–Sham energy	206
24	SHE	Cross-checking the Pulay contributions	207
25	SHE	Muffin-tin sphere complement of IR surface integral	208
26	SHE	Converge Sternheimer equation from analytical Goldstone-modes solution	209
27	SHE	Comparing converged result to analytical solution for $\boldsymbol{q} = \mathbf{0}$	209
28	SHE	First-order density variation from occupied-occupied band combinations	210
29	SHE	Time Reversal Symmetry of converged quantities	209
30	EI2	Alternative method for pseudo-density Fourier coefficients	215
31	EI2	Time Reversal Symmetry	215
32	EI2	Cross-checking of Weinert method (`juPhon`) with Ewald method (`ABINIT`)	215
33	DMS	Converged parameter for interstitial step function	259
34	DMS	Converged parameter for convolution of potential and step function	259
35	DMS	Cross-checking the MT Hamiltonian and overlap matrix element	260
36	DMS	Adding the IR part to the MT Hamiltonian and overlap matrix element	260
37	DMS	Cross-checking with Sternheimer surface integral	260
38	DMS	Cross-checking of surface integrals with almost continuous Integrands	260
39	DMS	Analytical Goldstone-modes solution for correction terms	261

in an evaluation of an expression [271]. But, it is better to avoid them and sometimes this can be achieved by a rearrangement of the problematic terms [270]. Furthermore, the accuracy of the integrals used in `FLEUR` or `juPhon` is around 10^{-7} in units of the integrands [251]. This impacts on the significant digits of the phonon frequencies. Generally, the choice of the integration or differentiation methods governs the numerical accuracy, see e.g. classical difference quotient versus the symmetric one [271]. Details on the methods used and the arisen problems are provided in the following sections. Finally, the truncation error can be mitigated by optimizing the set of input parameters, such as G_{max}, k_{max}, $l_{\text{max},\mathring{\gamma}}$, $R_{\mathring{\gamma}}$, and the discrete MT mesh, to name but a few.

General strategy

As a consequence, our approach is guided by an analytical reformulation of the terms in Klüppelberg [88], such that numerical pitfalls are minimized [119, 127, 251, 270]. Essentially, this means being critical and vigilant about the cancellation of sums or fulfillment of mathematical relations from a numerical point of view, even though this may seem superfluous from an analytical standpoint [251]. Each of the aforesaid error categories (i) to (iii) must be contemplated. All in all, the numerical errors (noise) should not influence the final results significantly (numerical stability) [270, 271].

7.1.3 Performance

Prioritization

For the first implementation, I have prioritized obtaining a working realization of the DFPT in reference [88]. Therefore, the main focus has not been on achieving a cutting-edge performance. Nonetheless, sometimes the implementation has turned out to be too naive for pursuing the aforementioned strategy. Enhancements have become necessary, when the runtime of `juPhon` had become too large for an efficient debugging in reasonable time. But, enormous potential can still be unleashed, in order to achieve a significantly better computational performance.

Possible optimizations

Important examples constitute in employing parallelization or further adjusting the recycled `FLEUR` subroutines. Usually, they do not feature an optimal performance yet within their new environment of `juPhon` subroutines, or are already improved in the latest version of the `FLEUR` code. Furthermore, the order and size of some array dimensions can be optimized to ensure a contiguous run through the storage. Apart from that, the evaluation of some quantities have become redundant during the implementation process, which will be fixed in a future refactoring. However, an overall analysis of the most severe performance bottlenecks ensued by a respective prioritization should always precede this kind of fixes.

Runtime assumptions

In algorithm 1, algorithm 2, and algorithm 3, I estimate lower asymptotes $\Omega(.)$ for the runtime of `juPhon` as a function of the LAPW cutoffs or of the material parameters. These lower boundaries originate from the essential loop structure of `juPhon`. Due to the scope of the complete algorithm, it is subdivided into an initialization part in algorithm 1, a Sternheimer part in algorithm 2, and a dynamical-matrix part in algorithm 3. For the FFT, I assume in general a performance of $\Omega(n\lg(n))$ ($\lg(n) \equiv \log_2(n)$), and for the diagonalization of the dynamical matrix a performance of $\Omega\left(n^3\right)$ [272]. In this estimate, n is the number of coefficients undergoing the FFT, or one dimension of the quadratic dynamical matrix, respectively [272]. Furthermore, $\xi_{\text{I/O}}$ in the first line of algorithm 1 is a not further specified runtime constant for the interface to the DFT calculation in advance. The exact meaning of “general initialization” in algorithm 1 is the subject of section 7.1.6. Moreover, I refer to the average performances in a DFT calculation, concerning the setups of the unperturbed charge density and the effective potential, as well as the number of cycles required to reach self-consistency [92]. This for instance takes place in the second line of algorithm 1, in which the runtime is specified in units of setting up either an unperturbed (Coulomb) potential with the Weinert method or an unperturbed xc potential. Additionally and e.g. in line 3 of algorithm 1, the performance depends on the number of MT sphere mesh points $\#\nu$ (see section 5.1). Within the algorithms, the abbreviations Sh, Pl, ctC, sf, HF denote Sternheimer, Pulay, core-tail correction, surface, and Hellmann–Feynman, respectively. Finally, I include expressions defined in section 7.4.1 to section 7.4.6 for the Sternheimer, and in section 7.6.8 for the dynamical matrix part.

Algorithm 1: Rough runtime analysis of the `juPhon` program (1/3: initialization).

```
1 General initialization ; // $\Omega\left(\xi_{\mathrm{I/O}}\right)$
2 All potential and density gradients ;
    // $\Omega\Big(3\#G_{\mathrm{max}} + 9l_{\mathrm{max},\mathring{\gamma}}\big(2l_{\mathrm{max},\mathring{\alpha}}+1\big)\#\mathrm{atoms} + 4V^{(0)}_{\mathrm{Weinert}} + 2V^{(0)}_{\mathrm{xc}}\Big)$
3 Prepare Sh Pl ; // $\Omega\Big(2\#\nu^{\mathring{\gamma}}\Big(l_{\mathrm{max},\mathring{\alpha}}\big(2l_{\mathrm{max},\mathring{\alpha}}+1\big)\Big)^3\#\mathrm{atoms}\Big)$
4 Prepare Sh ctC ; // $\Omega\Big(\Big(\#G_{\mathrm{max}}\big(1+\#\nu^{\mathring{\gamma}}\big)+10\#\nu^{\mathring{\gamma}}\Big)\#\mathrm{atoms}\Big)$
```

Runtime factors

In summary, the algorithms reveal that the runtime can be influenced by the typical FLAPW cutoff parameters $l_{\mathrm{max},\mathring{\gamma}}$, G_{max}, k_{max}, and $\#\nu^{\mathring{\gamma}}$. Particularly the Sternheimer self-consistency cycle however scales with $\Omega(\#\mathrm{atoms}^2)$, a factor of 3 for the three displacement directions, the product of occupied and unoccupied bands, and the size of the $\boldsymbol{k}$-set and $\boldsymbol{q}$-set. It must be considered that $\boldsymbol{k}+\boldsymbol{q}$ must again be in the group of $\boldsymbol{k}$-vectors utilized during the `juPhon` calculation. Therefore, if choosing a $\boldsymbol{q}$ which does not fulfill this property, the aforesaid condition must be restored by adding more $\boldsymbol{k}$-vectors to the set at hand [251]. The setup of the dynamical matrix scales with the number of $\boldsymbol{q}$ and $\boldsymbol{k}$ vectors, with $\Omega\big(\#\mathrm{atoms}^2\big)$, the squared number of displacement directions $\Omega(9)$, but only with the number of occupied bands, which are few relative to the unoccupied bands.

Comparison with Finite Displacement

Assuming that the number of bands is proportional to the number of atoms [119], the Sternheimer self-consistency cycle scales with $\mathrm{Omega}(\#\mathrm{atoms}^4)$, i.e., also the DFPT method. This is faster than the FD technique, which scales with $\mathrm{Omega}(\#\mathrm{atoms}^5)$ because of the DFT diagonalization scaling with $\mathrm{Omega}(\#\mathrm{atoms}^3)$. Furthermore, due to the requirement of supercells, the DFPT approach outperforms the FD method for a general $\boldsymbol{q}$-vector.

Parallelization strategy

For the parallelization of algorithm 2, I suggest[8] that pairs of fixed phonon vectors $\boldsymbol{q}$ and displaced atoms α are ideally qualified to be calculated on distinct nodes. This is because these pairs are independent from each other and basically do not require any data transfer with other nodes during their calculation. In principle, one could also reformulate the Sternheimer algorithm to only calculate one displacement direction, which then is provided as a parameter. In this case, there would be a triple of displacement direction i, displaced atom α and $\boldsymbol{q}$-vector per node. In my opinion, all remaining loops should be parallelized on the same node. In contrast, for the setup of the dynamical matrix in algorithm 3, only the $\boldsymbol{q}$ loop should be

---

[8] Similar considerations have already been done before by others on a theoretical level or for different codes. This paragraph refers explicitly to the `juPhon` code.

Algorithm 2: Rough runtime analysis of the `juPhon` program (2/3: Sternheimer loop).

```
foreach $\boldsymbol{q}$ do // $\Omega(\#\boldsymbol{q})$
    foreach $\alpha$ do // $\Omega(\#\mathrm{atoms})$
        Calculate ctC; // $\Omega\left(l_{\mathrm{max},\mathring{\gamma}} + 3\#\nu^{\mathring{\gamma}}\left(\#G_{\mathrm{max}} + \left(2l_{\mathrm{max},\mathring{\gamma}} + 1\right)l_{\mathrm{max},\mathring{\gamma}}\#\mathrm{atoms}\right)\right)$
        Prepare Sh sf ; // $\Omega\left(9\#G_{\mathrm{max}}l_{\mathrm{max},\mathring{\alpha}}\left(2l_{\mathrm{max},\mathring{\alpha}} + 1\right)\right)$
        repeat// $\approx \Omega(\#\mathrm{DFT\ SCC\ iterations})$
            Calculate Sh potentials ;
              // $\approx \Omega\left(V^{(0)}_{\mathrm{Weinert}} + V^{(0)}_{\mathrm{xc}} + 3\#\nu^{\mathring{\gamma}}l_{\mathrm{max},\mathring{\alpha}}\left(2l_{\mathrm{max},\mathring{\alpha}} + 1\right)\#\mathrm{atoms}\right)$
            Prepare Sh HF ; // $\Omega\left(12\#\nu^{\mathring{\gamma}}\left(l_{\mathrm{max},\mathring{\alpha}}\left(2l_{\mathrm{max},\mathring{\alpha}} + 1\right)\right)^3\#\mathrm{atoms}\right)$
            foreach $\boldsymbol{k}$ do // $\Omega(\#\boldsymbol{k})$
                foreach $i$ do // $\Omega(3)$
                    Prepare ket matching coefficients;
                      // $\Omega\left(8\mathrm{k}_{\mathrm{max}}l_{\mathrm{max},\mathring{\gamma}}\left(2l_{\mathrm{max},\mathring{\alpha}} + 1\right)\#\mathrm{atoms}\#\mathrm{occ.\ val.\ bands}\right)$
                    Prepare bra matching coefficients;
                      // $\Omega\left(8\mathrm{k}_{\mathrm{max}}l_{\mathrm{max},\mathring{\gamma}}\left(2l_{\mathrm{max},\mathring{\alpha}} + 1\right)\#\mathrm{atoms}\#\mathrm{all\ val.\ bands}\right)$
                    foreach $n$ do // $\Omega(\#\mathrm{occupied\ valence\ bands})$
                        foreach $n'$ do // $\Omega(\#\mathrm{all\ valence\ bands})$
                            HF IR ; // $\Omega\left(3^4\,\#G^3_{\mathrm{max}}\lg\left(3^3\#G^3_{\mathrm{max}}\right)\right)$
                            HF MT ; // $\Omega\left(2^4\#\nu^{\mathring{\gamma}}\left(\left(2l_{\mathrm{max},\mathring{\gamma}} + 1\right)l_{\mathrm{max},\mathring{\gamma}}\right)^3\#\mathrm{atoms}\right)$
                            Pl ;
                              // $\Omega\left(2^2l_{\mathrm{max},\mathring{\alpha}}\left(2l_{\mathrm{max},\mathring{\alpha}} + 1\right)\left(6 + 2^3\left(l_{\mathrm{max},\mathring{\alpha}}\left(2l_{\mathrm{max},\mathring{\alpha}} + 1\right)\right)^2\right)\right)$
                            sf; // $\Omega\left(3\mathrm{k}^2_{\mathrm{max}}\left(3 + \left(l_{\mathrm{max},\mathring{\gamma}}\right)^3\left(2l_{\mathrm{max},\mathring{\alpha}} + 1\right)^2\right)\right)$
                        end foreach
                    end foreach
                end foreach
            end foreach
            Calculate and mix Sh $\rho^{(1)}$ ; // $\approx \Omega\left(3\rho^{(0)}_{\mathrm{DFT}}\right)$
        until self-consistent;
        Calculate full $\rho^{(1)}$ ; // $\approx \Omega\left(3\rho^{(0)}_{\mathrm{DFT}}\right)$
    end foreach
end foreach
```

Algorithm 3: Rough runtime analysis of the `juPhon` program (3/3: dynamical matrix).

```
foreach $\boldsymbol{q}$ do // $\Omega(\#\boldsymbol{q})$
    foreach $\alpha$ do // $\Omega(\#\text{atoms})$
        foreach $\beta$ do // $\Omega(\#\text{atoms})$
            foreach $i$ do // $\Omega(3)$
                foreach $j$ do // $\Omega(3)$
                    Calculate $D^{\beta\alpha}_{\text{HF}}(\boldsymbol{q})$ ;
                      // $\Omega\Big(162\,\#G^{4}_{\text{max}}\lg\big(3^{3}\#G^{3}_{\text{max}}\big) + 27\,\#G^{3}_{\text{max}} + 2V^{(0)}_{\text{Weinert}}\Big) +$
                      $\Omega\bigg(\Big(9\Big(\big(2l_{\text{max},\mathring{\gamma}} + 1\big)l_{\text{max},\mathring{\gamma}}\Big)^{2} + 6\#\nu^{\mathring{\gamma}}\big(2l_{\text{max},\mathring{\gamma}} + 1\big)l_{\text{max},\mathring{\gamma}}\Big)\#\text{atoms}\bigg) +$
                      $\Omega\Big(3\#\nu^{\mathring{\gamma}}\big(2l_{\text{max},\mathring{\gamma}} + 1\big)l_{\text{max},\mathring{\gamma}}\Big)$
                    Calculate $D^{\beta\alpha}_{\text{Pl,dp}}(\boldsymbol{q})$; // $\Omega\Big(6\#\nu^{\mathring{\gamma}}\big(2l_{\text{max},\mathring{\gamma}} + 1\big)l_{\text{max},\mathring{\gamma}}\#\text{atoms}\Big)$
                    foreach $\boldsymbol{k}$ do // $\Omega(\#\boldsymbol{k})$
                        foreach $n$ do // $\Omega(\#\text{occucpied valence bands})$
                            Calculate $D^{\beta\alpha}_{\text{Pl,bk}}(\boldsymbol{q})$ ; // $\Omega\bigg(60\mathrm{k}^{2}_{\text{max}}\Big(l_{\text{max},\mathring{\alpha}}\big(2l_{\text{max},\mathring{\alpha}} + 1\big)\Big)^{2}\bigg)$
                            Calculate $\boldsymbol{k}$- and $n$-dependent $\underline{D}^{\beta\alpha}_{\text{sf}}(\boldsymbol{q})$ ; // $\Omega\big(216\#k^{2}_{\text{max}}\big)$
                        end foreach
                    end foreach
                    Calculate rest of IR $\underline{D}^{\beta\alpha}_{\text{sf}}(\boldsymbol{q})$ ; // $\Omega\big(27\#G^{2}_{\text{max}}\big)$
                    Calculate rest of MT $\underline{D}^{\beta\alpha}_{\text{sf}}(\boldsymbol{q})$ ; // $\Omega\bigg(18\Big(l_{\text{max},\mathring{\alpha}}\big(2l_{\text{max},\mathring{\alpha}} + 1\big)\Big)^{2}\bigg)$
                    Hermitization ; // $\Omega(1)$
                end foreach
            end foreach
        end foreach
    end foreach
    Diagonalization ; // $\Omega\big(3^{3}(\#\text{atoms})^{3}\big)$
    Post Processing ; // $\Omega(1)$
end foreach
```

distributed to different nodes. The iterations in the loop over the $\boldsymbol{k}$-points are essentially independent from each other. They are summed in the end to determine corrections to the dynamical matrix, which can likewise be exploited for the parallelization. In general, it is beneficial to exclude every calculation of $\boldsymbol{k}$-independent quantities from the $\boldsymbol{k}$-point loop, because the number of $\boldsymbol{k}$-points becomes large when converging demanding materials [251]. The same holds true for the loop over all valence bands. Further more specific optimizations are proposed throughout the rest of the chapter.

7.1.4 Relativistic Corrections

Approximation

According to chapter 5, the wave functions in the matrix-element Pulay corrections (6.67) subdivide into a valence contribution and a core contribution. Klüppelberg [88] has developed a way to integrate the latter into the dynamical matrix. But we are of the opinion that this is not properly done, because Klüppelberg [88, equation (7.115)] does not sufficiently take the relativistic Dirac character of the core states into account [127, 251]. Still, for the first implementation, we decided to resort to the Schrödinger equation, decreasing the level of complexity. In order to achieve this, I increase the constant for the speed of light by three orders of magnitude, both within the variables of the `FLEUR` and the `juPhon` code [127, 251]. This reduces the significance of the small component in the LAPW basis [119, 127, 251]. However, it leads to unphysical results the more relativistic corrections become relevant (heavy elements).

7.1.5 Dealing with Broken Symmetry

Simplification

Phonons, which displace atoms from their equilibrium positions, break certain symmetries, depending on the respective phonon mode. This requires adjusting the symmetry optimizations, such as the irreducible wedge of the $\boldsymbol{k}$-point set (see for instance Singh and Nordström [68]). However, the unperturbed quantities remain unaffected by the symmetry breaking of the phonons so that the symmetry optimizations are still valid [251]. Despite the advantages in computational performance and numerical stability that entail from exploiting the remaining symmetries (see section 5.7), we decided against it in a first approach [119, 127, 251]. This allows for postponing the evaluation of the remaining symmetries and their correct implementation, as well as reducing the complexity. As a consequence, all symmetry optimizations which are done in `FLEUR` and are described in chapter 5 are abandoned. But, these optimizations also inhere in the results that `juPhon` uses as its starting point. Therefore, a back-transformation becomes necessary of which the details are pointed out in section 7.1.6.

7.1.6 Initialization of `juPhon` and Integrity Tests of its Starting Data

Outline

This section contains more technical details about obtaining the required input quantities (see section 6.1.2) and further initialization data after a `FLEUR` calculation. More details can be found in appendix A. It results in various files required for the `juPhon` calculation and listed in table 7.3, which only indicates their relevant content. In addition, table 7.4 shows all tests requiring files beyond those in table 7.3, including the pages where these tests are specified.

Table 7.3: Files stemming from the `FLEUR` computation that precedes the `juPhon` calculation. Some of them contain more (irrelevant) information than indicated here. The last five files are necessitated by the recycled `FLEUR` subroutine `Fleur_init`. By the term "warping", I denote convoluting an IR quantity with the IR step function. This is explicitly *not* done in the files `pottot_unwarped`, `excpw_uw_fleur`, and `vxc0_uw_fleur`.

File Name	Contained Information
`cdn1`	$\rho^{(0)}_{\mathrm{IR}}(\boldsymbol{G})$, $\rho^{(0)}_{\mathring{\gamma}}(r_{\nu\mathring{\gamma}})$
`kpts`	$\boldsymbol{k}$, $\boldsymbol{q}$
`pottot`	$\left[\Theta\ V^{(0)\mathrm{IR}}_{\mathrm{eff}}\right](\boldsymbol{G}), V^{(0)\mathring{\gamma}}_{\mathrm{eff}}(r_{\nu\mathring{\gamma}})$
`eig`	$\lvert\boldsymbol{G}\rvert < k_{\mathrm{max}}, E_l, \epsilon^{(0)}_{\boldsymbol{k},n},\ z^{(0)}_{\boldsymbol{G}}(\boldsymbol{k},n)$
`pottot_unwarped`	$V^{(0)\mathrm{IR}}_{\mathrm{eff}}(\boldsymbol{G}), V^{(0)\gamma}_{\mathrm{eff}}(r_{\nu\mathring{\gamma}})$
`enpara`	E_l
`excpw_uw_fleur`	$\epsilon^{(0)\mathrm{IR}}_{\mathrm{xc}}(\boldsymbol{G})$
`excr_fleur`	$\epsilon^{(0)\gamma}_{\mathrm{xc}}(r_{\nu\mathring{\gamma}})$
`vxc0_uw_fleur`	$V^{(0)\mathrm{IR}}_{\mathrm{xc}}(\boldsymbol{G}), V^{(0)\gamma}_{\mathrm{xc}}(r_{\nu\mathring{\gamma}})$
`JuPhon.inp`	input parameters of `juPhon`
`inp` for `Fleur_init`	(parameters)
`sym.out` for `Fleur_init`	(symmetries)
`f17para` for `Fleur_init`	(parameters)
`stars` for `Fleur_init`	ϕ_{s}
`wkf2` for `Fleur_init`	$\Theta(\boldsymbol{G})$, $\Theta(\boldsymbol{r})$

Fleur_init

Table 7.3 incorporates the expression `Fleur_init`. It refers to the recycled and equally-named subroutine, which initializes a `FLEUR` calculation, as well as to its recycled subroutine dependencies. In contrast to the usual procedure, these subroutines are taken from an early stage of the modernized `FLEUR` version[9]. This is because a significant change between version 26 and newer versions of `FLEUR` consists in the introduction of `FORTRAN` types. Employing them is in line with fulfilling my ambition of a modern `FORTRAN` code. Furthermore, borrowing the version of `Fleur_init` containing `FORTRAN` types is tolerable, because data that results can easily and comprehensively be tested. These tests, the concept of which has been developed by Betzinger [251] or is inspired by checks of the `FLEUR` code, shall be discussed at the end of this section. First, however, the initialization part of `juPhon` is described in detail.

Table 7.4: List of tests that require files apart from those given in table 7.3.

#	Name	Page
7	Abandoning the rotations of the local coordinate systems	132
11	Reproducing the unperturbed charge density	152
14	First-order charge-density variation from difference quotients	154
18	Reproducing the unperturbed `FLEUR` potentials	178
24	Cross-checking the Pulay contributions	207
32	Cross-checking of Weinert method (`juPhon`) with Ewald method (`ABINIT`)	215
34	Converged parameter for convolution of potential and step function	259

Initialization

Birch–Murnaghan fit

Before starting a regular `juPhon` calculation, the files in table 7.3 must be available and the `juPhon` parameters must be set (see appendix A and appendix B for the applied input parameters). In particular for phonon calculations, the curve fit to the Birch–Murnaghan equation of state [3, 273, 274] or in general the relaxation of the lattice structure is decisive [119, 127]. It ensures that the total energy is minimal, the forces vanish, and the harmonic contribution of the total energy is the leading order of correction (cf. section 3.1). This should actually already be the case when employing the experimental lattice parameters a_{exp} ($4.42\,\text{Å}$ for Ne [275] and $4.05\,\text{Å}$ for Al [276, 277]). However, applying approximations, e.g. for the xc potential, in turn leads to deviations and requires a relaxation of the lattice structure. This particularly holds true for the simple Xα potential (cf. section 2.2.2). For the aforesaid systems, the input data and the results of the Birch–Murnaghan curve fit are listed in table 7.5 and table 7.6,

---

[9] Within the repository of the `FLEUR` code, the commit of the referred version is addressed by the hash `f02ffa2e8b1e374ac78118d94f00c88cf7ecb95b`.

respectively. The input data points are symmetrically distributed around the resulting lattice constant a_{DFT}, which is taken for the `juPhon` calculation and features the minimum total energy. For Ne $a_{\mathrm{DFT}} = 4.19\,\mathrm{Å}$ is found and for Al the result is $a_{\mathrm{DFT}} = 4.09\,\mathrm{Å}$. The former outcome of the fit is $5.1\,\%$ smaller and the latter $0.9\,\%$ larger than the respective experimental value a_{exp}. I have assumed that $1\,\mathrm{Å} = 1.889\,726\,124\,57\,a_0$.

Table 7.5: Input data of the Birch–Murnaghan fit for Ne and Al. The first and third columns contain the ratios between the lattice constants a_{DFT} set for the calculation, and the respective experimental lattice constants a_{exp}. The remaining columns incorporate the resulting total energies of the `FLEUR` calculation in units of the Hartree energy E_{h}.

$a^{\mathrm{Ne}}_{\mathrm{DFT}}/a^{\mathrm{Ne}}_{\mathrm{exp}}$	$E^{(0)}_{\mathrm{tot,Ne}}$ / E_{h}	$a^{\mathrm{Al}}_{\mathrm{DFT}}/a^{\mathrm{Al}}_{\mathrm{exp}}$	$E^{(0)}_{\mathrm{tot,Al}}$ / E_{h}
0.90	−127.491 987 565 3	0.96	−240.474 247 058 5
0.91	−127.492 091 132 5	0.97	−240.475 449 453 0
0.92	−127.492 162 748 9	0.98	−240.476 312 634 2
0.93	−127.492 209 570 0	0.99	−240.476 878 436 4
0.94	−127.492 235 157 5	1.00	−240.477 158 030 3
0.95	−127.492 242 873 8	1.01	−240.477 170 153 0
0.96	−127.492 235 152 6	1.02	−240.476 941 193 6
0.97	−127.492 216 436 8	1.03	−240.476 496 078 0
0.98	−127.492 187 887 9	1.04	−240.475 857 888 1
0.99	−127.492 151 474 6	1.05	−240.475 046 912 4
1.00	−127.492 109 503 1	1.06	−240.474 106 645 2

Table 7.6: Results of the Birch–Murnaghan fit for Ne and Al.

fit results	Ne	Al
$a_{\mathrm{DFT}}/a_{\mathrm{exp}}$	0.948 925 2	1.009 627 7
B_0 / mbar	0.037 25	0.685 08
B_0' / mbar	7.443 05	4.224 59

Input data interface

At the start of the `juPhon` calculation, the subroutine `InitializeJuPhon` is called. Thus, the subroutine `ReadInpFile` is executed, which reads in `JuPhon.inp` and is based on the parameter management of the `SpeX` [230] code. Furthermore, the setup of the $\boldsymbol{k}$ and $\boldsymbol{q}$ set is inspired by the $\boldsymbol{k}$-point generator in `FLEUR` and will be unified with it in the future. The $\boldsymbol{q}$-point set is constructed such that it is a subset of the $\boldsymbol{k}$-point set in order to ensure that all required wave-functions expansion coefficients are available [88]. At the same time, a mapping array is determined which stores the index of the $\boldsymbol{k}$-vector being the result of $\boldsymbol{k}+\boldsymbol{q}$ [251]. If $\boldsymbol{k}+\boldsymbol{q}$ leaves the first Brillouin zone, the resulting sum of the vectors is back-folded by a reciprocal lattice vector $\boldsymbol{G}_{\mathrm{bf}}$ as sketched in figure 7.2 [251]. The setup of the Bloch vectors needs `First_glance`, `Rw_inp` and their dependent subroutines, each of them recycled from `FLEUR`. The former is a simplified version of the already mentioned `Fleur_init` subroutine. It is called in the regular mode of `juPhon` and provides the complete input data, likewise required for a `FLEUR` calculation. As soon as `Fleur_init` finishes, the mixing parameters read from the `inp` file are overwritten by their equivalents from `JuPhon.inp`. Moreover, in order to initiate

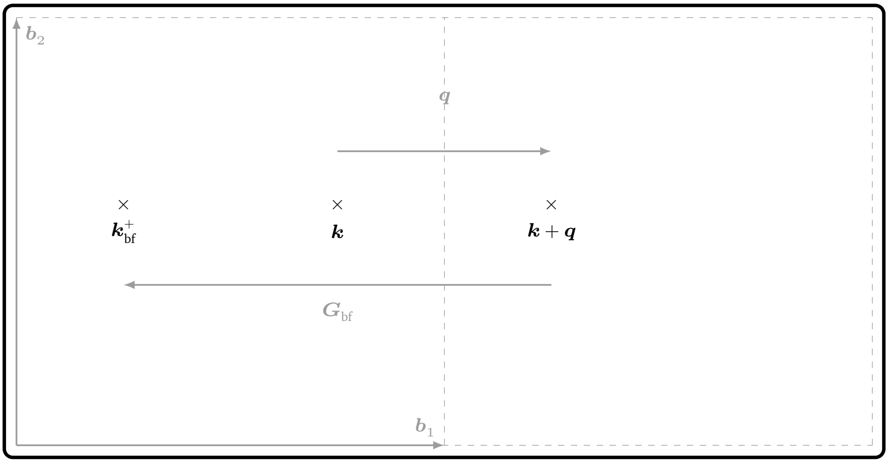

Figure 7.2: Schematic visualization of the relation between $\boldsymbol{k}+\boldsymbol{q}$, that is in a second Brillouin zone, and a (translation-)symmetry related $\boldsymbol{k}^{+}_{\text{bf}}$, that is in the first Brillouin zone and connected to the second Brillouin zone by a back-folding vector $\boldsymbol{G}_{\text{bf}}$. The reciprocal unit-cell vectors b_i are chosen such as in `juPhon`, i.e., $b_i \in [0, 1[$ in internal units.

the back-rotation of the local coordinate systems in the MT spheres, the original orthogonal rotation matrices are substituted by their transposed version. This is equivalent to their inversion. Now, the `eig` file, containing the Kohn–Sham wave-function expansion coefficients and the Kohn–Sham energies, is read in by the subroutine `Read_eig`. The algorithm is guided by the I/O of `eig` in `FLEUR`. Furthermore, within `Read_eig` the number of eigenvalues and of the basis functions per $\boldsymbol{k}$-point are parsed (not listed in table 7.3). Since the reciprocal basis vectors in the sphere of radius k_{max} are partially redundantly stored for every $\boldsymbol{k}$-point, we decided to only store each of the vectors once and generate a mapping array [251]. This is to optimize the storage requirements, which can grow immensely as a function of the $\boldsymbol{k}$-set size. Afterwards, the subroutine `ReadPotFleur` makes the unperturbed potentials from table 7.3 available, by using the `Loddop` subroutine from `FLEUR` and its depending subroutines. The aforementioned `FLEUR` subroutine is likewise utilized for reading the unperturbed charge density. Moreover, the required xc potentials and energy densities are read in by the subroutine `ReadXCquantities`. In contrast, the radial solutions $u^{\mathring{\gamma}}_{lp}$ are calculated within `GenRadSolnInt`, using the subroutine `Radfun` from `FLEUR` and its dependencies. It must be stressed that the result of this subroutine is not the pure quantity $u^{\mathring{\gamma}}_{lp}(r_{\nu\mathring{\gamma}})$, but it is multiplied by the radial mesh points $r_{\nu\mathring{\gamma}}u^{\mathring{\gamma}}_{lp}(r_{\nu\mathring{\gamma}})$ in order to anticipate Jacobi determinants. As a post-processing step, they are sorted for a better computational performance [251]. The set of reciprocal lattice vectors with the cutoff G_{max} is still missing. Its generator is guided by the `FLEUR` equivalent `Strgn`, but the G_{max} from `inp` is not corrected in `juPhon` [127, 278]. Finally, the cardinality

$$N^{\text{occ}}_{\boldsymbol{k}} = \left|\left\{ f^{(0)}_{\boldsymbol{k},n} \,\middle|\, \left|f^{(0)}_{\boldsymbol{k},n}\right| > 10^{-8} \right\}\right|. \tag{7.2}$$

is determined by `juPhon` to find the number of occupied bands per $\boldsymbol{k}$-point. It must be stressed that the $f^{(0)}_{\boldsymbol{k},n}$ are subsequently multiplied by the norm $1/N_{\boldsymbol{k}}$ of the $\boldsymbol{k}$ sums, where $N_{\boldsymbol{k}}$ is the number of employed $\boldsymbol{k}$-points for a calculation [127, 251].

Purification of input data

Due to historical or practical reasons, some information from `FLEUR` is still biased by undesired operations [127, 251]. We decided to use the pure quantities in order to avoid software bugs which are hard to find and generated by confusion. So,

$$\left[V^{(0)\mathring{\gamma}}_{\text{eff}}(r_{\nu\mathring{\gamma}})\right]_{\lambda} = \begin{cases} \left[\dfrac{\sqrt{4\pi}}{r_{\nu\mathring{\gamma}}} V^{(0)\mathring{\gamma}}_{\text{eff, inp}}(r_{\nu\mathring{\gamma}})\right]_{\lambda} & , \lambda = 0 \\ \left[V^{(0)\mathring{\gamma}}_{\text{eff, inp}}(r_{\nu\mathring{\gamma}})\right]_{\lambda} & , \lambda > 0 \end{cases} \tag{7.3}$$

is set up to revert the decorating factor from the $\lambda = 0$ lattice-harmonic coefficient of $V^{(0)\mathring{\gamma}}_{\text{eff, inp}}(\boldsymbol{r})$, which has been parsed from `pottot`. Furthermore, all lattice-harmonic expansion coefficients of the unperturbed charge density in the MT spheres, which are read in from `cdn1`, are multiplied by squared reciprocal mesh points so that

$$\left[\rho^{(0)}_{\mathring{\gamma}}(r_{\nu\mathring{\gamma}})\right]_{\lambda} = \frac{1}{r^2_{\nu\mathring{\gamma}}} \left[\rho^{(0)}_{\mathring{\gamma},\text{inp}}(r_{\nu\mathring{\gamma}})\right]_{\lambda} \tag{7.4}$$

results.

Relaxing symmetry

According to section 7.1.5, the symmetry-optimized expansions of the effective potential and the charge density must be transformed into the original plane-wave and spherical-harmonic expansions of the LAPW basis. For the IR, this is done by multiplying the coefficient $\rho^{(0)}_{\text{IR}}\big(s(\boldsymbol{G}')\big)$ of a star s containing $\boldsymbol{G}'$, by a phase factor $\varphi_{s(\boldsymbol{G}')}$, where $\boldsymbol{G}'$ is an element of the unsymmetrized reciprocal lattice vector set. The latter phase is the complex conjugate summand of equation (5.44c), for which $\underline{\mathfrak{R}}_{\mathbb{m}}\boldsymbol{G} \equiv \boldsymbol{G}'$, so that overall

$$\rho^{(0)}_{\text{IR}}(\boldsymbol{G}') = \rho^{(0)}_{\text{IR}}\big(s(\boldsymbol{G}')\big)\,\varphi_{s(\boldsymbol{G}')} \tag{7.5a}$$

$$V^{(0)\text{IR}}_{\text{eff}}(\boldsymbol{G}') = V^{(0)\text{IR}}_{\text{eff}}\big(s(\boldsymbol{G}')\big)\,\varphi_{s(\boldsymbol{G}')} \tag{7.5b}$$

holds. In the MT spheres, firstly the transformation coefficients

$$c^{\gamma}_{lm} = \sum_{m'} \left[\mathfrak{D}^{\underline{\mathfrak{R}}^{-1}}\right]^{l}_{m,m'} \mathfrak{c}^{\mathring{\gamma}}_{lm'} \tag{7.6a}$$

must be determined, in which the Wigner matrix $\underline{\mathfrak{D}}^{\underline{\mathfrak{R}}^{-1}}$ reverts the rotations of symmetry-related local MT coordinate systems and fulfills [251]

$$\underline{\mathfrak{D}}^{\underline{\mathfrak{R}}}\mathrm{Y}_{lm}(\hat{\boldsymbol{r}}) = \sum_{m'} \mathrm{Y}_{lm'}(\hat{\boldsymbol{r}}) \left\langle \mathrm{Y}^{*}_{lm'}(\hat{\boldsymbol{r}}) \middle| \underline{\mathfrak{D}}^{\underline{\mathfrak{R}}} \middle| \mathrm{Y}^{*}_{lm}(\hat{\boldsymbol{r}}) \right\rangle =: \sum_{m'} \mathfrak{D}^{\underline{\mathfrak{R}},l}_{m,m'} \mathrm{Y}_{lm'}(\hat{\boldsymbol{r}})\,. \tag{7.6b}$$

Actually, the c^{γ}_{lm} from equation (7.6a) are still attributed to lattice harmonics with index λ and members addressed by μ so that relaxing the symmetry of the unperturbed charge density and the unperturbed effective potential formally reads [68]

$$\left[\rho^{(0)}_{\gamma}(r_{\nu\gamma})\right]_{lm} = \left[\rho^{(0)}_{\mathring{\gamma}}(r_{\nu\mathring{\gamma}})\right]_{\lambda(l)} c^{\gamma}_{\lambda(l),\mu(m)} \tag{7.6c}$$

$$\left[V^{(0)\gamma}_{\text{eff}}(r_{\nu\gamma})\right]_{lm} = \left[V^{(0)\mathring{\gamma}}_{\text{eff}}(r_{\nu\mathring{\gamma}})\right]_{\lambda(l)} c^{\gamma}_{\lambda(l),\mu(m)}\,. \tag{7.6d}$$

The orthogonal Wigner matrix $\mathfrak{D}^{\mathfrak{R},l}_{m,m'}$ is generated by the subroutine `D_wigner`, and equation (7.6a) realized by the subroutine `Rotate_clnu` [279] (see also references [68]). Both subroutines are recycled from `FLEUR`. The outcome of `Rotate_clnu` are the arrays `clnu_atom`, `nmem_atom`, `mlh_atom`, and `nmem_atom`. In this order, they contain the c^{γ}_{lm} from equation (7.6a), the number of lattice harmonic members, and their magnetic quantum number for every atom in the back-rotated MT spheres [251]. Moreover, both the charge density and the effective potential are converted from the stars to the plane-wave representation as well as from the lattice-harmonic to the spherical-harmonic representation by the subroutine `UnfoldRhoOnVeff0Symmetry`. This is done utilizing the subroutines `ConvertStar2G` and `ConvertLH2SphHarm`. In algorithm 4 the typical loop structure underlying the conversion conducted in the latter is shown. Although the symmetry optimizations of the expansion coefficients are abandoned, only those expansion coefficients are significant which have a non-vanishing coefficient c^{γ}_{lm}. At the moment this is often not exploited and the loops consider every orbital quantum number l or magnetic quantum number m. This can potentially be optimized in the future [251]. However, it must be analyzed first, whether this leads to a performance gain and does not prevent modern chip architectures from applying optimizations such as vectorization. Using each of the aforesaid subroutines, all variables, arrays, and types are filled with the required information to start a `juPhon` calculation.

Algorithm 4: Loop structure typically employed for converting symmetrized to unsymmetrized expansions (inspired by `FLEUR`).

```
forall $|\boldsymbol{G}| \leq G_{\text{max}}$ do
    Get index of star $s(\boldsymbol{G})$ containing current $\boldsymbol{G}$ (mapping array available);
    Convert star to plane-wave representation (e.g. using equation (7.5a)) ;
end forall
forall $\mathring{\gamma}$ do // atom types
    forall $\gamma$ do // equivalent atoms of an atom type
        forall sym($\mathring{\gamma}$) do // symmetries of an atom type
            forall $\lambda(\text{sym}(\mathring{\gamma}))$ do // lattice harmonics of a symmetry
                Get orbital quantum number $l$ of $\lambda$ (mapping array available);
                forall $\mu(\lambda)$ do // members of a lattice harmonic
                    Get magnetic quantum number $m$ of $\mu$ (mapping array available);
                    Construct combined index lm of $l$ and $m$ ;
                    forall $\nu^{\mathring{\gamma}}$ do // mesh points of a MT
                        Convert lattice-harmonic to spherical-harmonic representation
                          (e.g. using equation (7.6c)) ;
                    end forall
                end forall
            end forall
        end forall
    end forall
end forall
```

Test 1: The k-Point Generator and the `kpts` File

In the regular mode of `juPhon` (the parameter `createKpts` is deactivated in `JuPhon.inp` by a number sign), the $\boldsymbol{k}$-point generator runs in the background. Thus after reading in the $\boldsymbol{k}$-point information from `kpts`, it is compared with the data internally generated for the $\boldsymbol{k}$-point and the $\boldsymbol{q}$-point sets. This identifies possible errors, while converting the data from the `kpts` file. For instance, the k_i are listed as integer and a common divisor is written to the first line of the `kpts` file. But, the internal k_i are real and must be within the interval $[0, 1[$. Detailed information about the `kpts` file can be found in the documentation of `FLEUR`. In a nutshell, `juPhon` only accepts `kpts` files which could have been generated by its own $\boldsymbol{k}$-point generator. Furthermore, the read-in $\boldsymbol{k}$-point information is compared with the $\boldsymbol{k}$-point information written to the `eig` file. There should be no difference.

Finally, a test to check whether the $\boldsymbol{k}$-point generator works correctly is to sum up the weights of the $\boldsymbol{k}$-points

$$\sum_{\boldsymbol{k}} \frac{1}{N_{\boldsymbol{k}}} = 1\,. \tag{7.7}$$

Since symmetry is irrelevant, no irreducible wedge of $\boldsymbol{k}$-points is constructed (see section 5.7.1). Consequently, $\boldsymbol{k}$-points trivally feature the weight ${}^{1}/_{N_{\boldsymbol{k}}}$, where $N_{\boldsymbol{k}}$ is the number of all $\boldsymbol{k}$-points. The sum in the previous equation must therefore yield 1, because it should be normalized.

Test 2: Consistency of the `eig` File Using `Fermie`

The consistency of the `eig` file can be tested by determining the total number of valence electrons $N^{\mathrm{e}^-}_{\mathrm{val}}$. For the relevant systems Ne and Al, the number of valence electrons is 8 and 3, respectively. This test is based on the recycled `FLEUR` subroutine `Fermie` and its depending subroutines. They likewise deliver the unperturbed occupation numbers $f^{(0)}_{\boldsymbol{k},n}$. Evaluating

$$\sum_{\boldsymbol{k},n} \frac{2}{N_{\boldsymbol{k}}} f^{(0)}_{\boldsymbol{k},n} = N^{\mathrm{e}^-}_{\mathrm{v}} \tag{7.8}$$

results in the total number of valence electrons, provided a spin degeneracy factor of 2 is multiplied. The sum runs over all occupied bands n and the $\boldsymbol{k}$-points of the Brillouin zone. By using `Fermie`, the $\boldsymbol{k}$-point weights and the `eig` file is proven to be consistent. The latter covers for example the eigenenergies, the Fermi energy, the number of occupied states, the sum of occupation numbers, the sum of semicore eigenvalues, and the sum of semicore charges.

Test 3: Continuities of the Wave Functions (`eig` file), the Charge Density (`cdn1` file), and the Effective Potential (`pottot_unwarped` file) from `FLEUR`

General idea

The IR and MT expansion coefficients of the charge density, the potential, and the wave functions from `FLEUR` are tested by checking their continuity at random points on the MT surfaces of all atoms. It is important that the potential is not convoluted with a step function in the IR, otherwise the continuity suffers. The continuity data of `juPhon` can be compared to the continuities calculated by the `FLEUR` code, in which the same algorithm (in the `Checkdop` subroutine) is used. I have written an own version of `Checkdop` to get familiar with the read-in quantities.

Sensitivity

The random points from the recycled `FLEUR` routine `Sphpts` are generally different when determined in `FLEUR` or `juPhon`. Furthermore, the discontinuities can be so small that numerical accuracy thwarts an exact comparison. We decided therefore that it is sufficient to ensure the discontinuities written out by `FLEUR` and `juPhon` to be at the same order of magnitude. The former can be found in the file `out` while the latter stands in `juPhon.log`. The continuity information is ended by a statistical evaluation using the `FLEUR` routine `Fitchk`. It yields in particular the root mean square of the differences between the IR and the MT representations on the MT sphere boundary. These values should be similar in `FLEUR` and `juPhon`.

Random generator

The quality of the random generator influences this test, because a well-distributed set of testing points on the MT sphere boundary is most representative to check the continuity. However, the employed generator has proven sufficient. In `juPhon`, a new set of points is generated and then scaled by the MT sphere radii. The number of points can be set behind the label `Pts2ChkCont` in `JuPhon.inp`.

Potential and density

In order to test whether the data related to the stars and the lattice harmonics is correct, the evaluation of the charge density and the potential takes place in these representations. Within `FLEUR` and `juPhon` two scalings, namely the internal (int) and the cartesian (crt) scalings are used. While the former scaling is normalized, i.e., for example the length of each lattice vector is 1, the latter scaling incorporates the material information (real lengths of lattice vectors). The canonical matrices $\underline{A}$ and $\underline{B}$, containing the lattice information of the material in a cartesian basis, communicate between these internal and cartesian representations. Hence, expanding a general function $\mathfrak{g}$ at a random cartesian point $\boldsymbol{r}_{\text{crt}}$ in stars (5.44a) yields

$$\mathfrak{g}(\boldsymbol{r}_{\text{crt}}) = \sum_{s} N_{s}^{\boldsymbol{G}} \mathfrak{g}(s) \phi_{\mathrm{s}}(\boldsymbol{r}_{\text{crt}}) \tag{7.9a}$$

$$= \sum_{s} N_{s}^{\boldsymbol{G}} \mathfrak{g}(s) \frac{1}{N_{\text{op}}} \sum_{\underline{\mathfrak{R}}} \mathrm{e}^{2\pi\mathrm{i}\left(\underline{\mathfrak{R}}\boldsymbol{G}\right)\cdot\left(\frac{1}{2\pi}\underline{B}\boldsymbol{r}_{\text{crt}} - \boldsymbol{t}_{\text{int}}\right)} , \tag{7.9b}$$

where $\boldsymbol{G}$ is the representative reciprocal lattice vector and N_{op} the number of symmetry operations $\left\{\underline{\mathfrak{R}}, \boldsymbol{t}\right\}$. Therefore, the function must be multiplied with $N_{s}^{\boldsymbol{G}}$, the number of plane waves in this star. Furthermore, the position vector in the cartesian scaling is back-transformed to the internal scaling, which is why the argument of the exponential function contains a 2π. In the MT spheres γ, the transformation from the global to the local coordinate system as well as a rotation $\underline{\mathfrak{R}}_{\gamma}$ to the representative MT $\mathring{\gamma}$ is required (cf. equation (5.6) and (5.54)). The function $g_{\gamma}(\boldsymbol{r} - \boldsymbol{\tau}^{\gamma})$ can be expanded in lattice harmonics $\mathfrak{Y}_{\lambda}$ and spherical harmonics Y_{lm}

$$g(\boldsymbol{r} - \boldsymbol{\tau}^{\gamma}) = \sum_{\lambda} g_{\lambda}(|\boldsymbol{r} - \boldsymbol{\tau}^{\gamma}|)\, \mathfrak{Y}_{\lambda}\left(\widehat{\boldsymbol{r} - \boldsymbol{\tau}^{\gamma}}\right) \tag{7.10a}$$

$$= \sum_{lm} g_{l}(|\boldsymbol{r} - \boldsymbol{\tau}^{\gamma}|)\, \mathfrak{c}_{lm}^{\gamma} \mathrm{Y}_{lm}\left(\overline{\underline{A}\, \underline{\mathfrak{R}}^{\gamma} \frac{1}{2\pi} \underline{B}\left(\boldsymbol{r}_{\text{crt}} - \boldsymbol{\tau}_{\text{crt}}^{\gamma}\right)}\right) . \tag{7.10b}$$

For the effective potential, the root mean square of Ne is $0.064\,\%$ and of Al $0.040\,\%$. In comparison, the root mean squares of the charge density are $0.104\,\%$ for Ne and $0.005\,\%$ for Al. This indicates highly continuous quantities.

Wave function

The wave function is expanded in the LAPW basis defined in equation (5.9). With a cartesian vector $\boldsymbol{r}_{\mathrm{crt}\gamma} = \boldsymbol{r}_{\gamma} + \boldsymbol{\tau}_{\gamma}$, pointing to a random point on the MT sphere and $|r|_{\mathring{\gamma}} = R_{\mathring{\gamma}}$ and in the local coordinates of the MT sphere, the IR and the MT wave function read

$$\Psi\Big(\boldsymbol{r}_{\mathrm{crt},\gamma}\Big) = \frac{1}{\sqrt{\Omega}} \sum_{\boldsymbol{k},n,\boldsymbol{G}} z^{(0)}_{\boldsymbol{G}}(\boldsymbol{k},n)\ \mathrm{e}^{\mathrm{i}(\underline{B}(\boldsymbol{k}_{\mathrm{int}}+\boldsymbol{G}_{\mathrm{int}}))\cdot\boldsymbol{r}_{\mathrm{crt},\gamma}} \tag{7.11}$$

and

$$\Psi\Big(R_{\mathring{\gamma}}\hat{\boldsymbol{r}}_{\mathring{\gamma}}\Big) = \sum_{\boldsymbol{k},n}\sum_{lmp} \frac{1}{R_{\mathring{\gamma}}} A^{\boldsymbol{k}\gamma n}_{lmp} R_{\mathring{\gamma}} u^{1\mathring{\gamma}}_{lp}\Big(R_{\mathring{\gamma}}\Big) \mathrm{Y}_{lm}\Big(\hat{\boldsymbol{r}}_{\gamma}\Big)\,, \tag{7.12}$$

respectively. The average absolute mismatch of both systems at the MT sphere boundary is found to be smaller than $7 \cdot 10^{-8}\, e^{0.5}\, a_0^{-1.5}$.

Test 4: Properties of the Radial Functions from the LAPW Basis Set

The idea of this test is to check the overlap (5.57e) of the radial solutions $u^{\mathring{\gamma}}_{lp}(r)$. This can easily be done for the normalization $p = p' = 1$, and if the radial solutions are orthogonal to each other, i.e., $p = 1$ and $p' = 2$ or vice versa. For the case $p = p' = 2$, a constant results that is not known in advance and can thus not be tested in general. When evaluating the radial integrals for all orbital quantum numbers l and representative atoms $\mathring{\gamma}$, the absolute difference to the analytical results 0 and 1 should not be larger than 10^{-7}. This is the case for Ne and Al.

Test 5: Orthogonality of the Kohn–Sham Wave Functions

General concept

The Kohn–Sham wave functions which are expanded in the LAPW basis must be orthonormal, which indirectly also validates the set of Kohn–Sham energies $\epsilon^{(0)}_{\boldsymbol{k},n}$, because both type of quantities stem from the `FLEUR` diagonalization routine [251]. Furthermore, this test covers (i) the wave-function expansion coefficients $z^{(0)}_{\boldsymbol{G}}(\boldsymbol{k},n)$, (ii) the small matching coefficients $a^{\boldsymbol{k}\gamma\boldsymbol{G}}_{lmp}$, determined by the recycled routine `Abcof3`[10], (iii) the $\vec{u}^{\mathring{\gamma}}_{lp}$, and (iv) whether the spherical harmonics are correctly calculated by the recycled routine `Ylm4`. The idea consists in evaluating an analytical overlap of the LAPW basis in the IR and the MT spheres, and numerically contracting it with the wave-function expansion coefficients.

Derivation of the overlap

For the overlap of the LAPW IR wave functions, a transformation to position space is conducted and the LAPW basis functions from equation (5.9) inserted yielding

$$\Big\langle \phi^{(0)}_{\boldsymbol{k},\boldsymbol{G}'} \Big| \phi^{(0)}_{\boldsymbol{k},\boldsymbol{G}} \Big\rangle_{\mathrm{IR}} = \frac{1}{\Omega} \int_{\mathrm{IR}} \mathrm{e}^{-\mathrm{i}\left(\boldsymbol{k}+\boldsymbol{G}'\right)\cdot\boldsymbol{r}} \mathrm{e}^{\mathrm{i}(\boldsymbol{k}+\boldsymbol{G})\cdot\boldsymbol{r}}\, \mathrm{d}^3 r\ . \tag{7.13a}$$

---

[10] This routine was provided by Markus Betzinger and does not consider the factor i^l of the MT matching coefficients (5.55). For polyatomic systems, the array of symmetry-dictated rotations (passed to `Abcof3` for the sake of an optimization) is replaced by a set of unity operations [127].

Then, the IR region can be expressed as the volume of the unit cell Ω without that of the MT spheres γ

$$= \frac{1}{\Omega} \int_{\Omega} \mathrm{e}^{\mathrm{i}(\boldsymbol{G}-\boldsymbol{G}')\cdot\boldsymbol{r}} \, \mathrm{d}^3 r - \sum_{\gamma} \frac{1}{\Omega} \int_{\gamma} \mathrm{e}^{\mathrm{i}(\boldsymbol{G}-\boldsymbol{G}')\cdot\boldsymbol{r}_\gamma} \, \mathrm{d}^3 r_\gamma \ , \tag{7.13b}$$

where $\boldsymbol{r}_\gamma = \boldsymbol{r} - \boldsymbol{\tau}_\gamma$. Defining $\boldsymbol{G}'' := \boldsymbol{G} - \boldsymbol{G}'$ and identifying a Dirac delta distribution

$$= \delta(\boldsymbol{G}'') - \frac{1}{\Omega} \sum_{\gamma} \sum_{lm} \mathrm{e}^{\mathrm{i}\boldsymbol{G}''\cdot\boldsymbol{\tau}_\gamma} 4\pi \mathrm{i}^l \mathrm{Y}^*_{lm}\big(\hat{\boldsymbol{G}}''\big) \int_{\gamma} r_\gamma^2 \mathrm{j}_l\big(G'' r_\gamma\big) \mathrm{Y}_{lm}\big(\hat{\boldsymbol{r}}_\gamma\big) \, \mathrm{d}^3 r_\gamma \tag{7.13c}$$

results, where the Rayleigh decomposition (5.5) is used. Finally, this leads to

$$= \frac{1}{\Omega} \Omega \delta(\boldsymbol{G}'') - \frac{1}{\Omega} 4\pi\sqrt{4\pi} \sum_{\gamma} \mathrm{e}^{\mathrm{i}\boldsymbol{G}''\cdot\boldsymbol{\tau}_\gamma} \mathrm{i}^0 \frac{1}{\sqrt{4\pi}} \int_0^{R_\gamma} r_\gamma^2 \mathrm{j}_0\big(G'' r_\gamma\big) \, \mathrm{d}r_\gamma \tag{7.13d}$$

$$= \delta(\boldsymbol{G}'') - \frac{4\pi}{\Omega} \sum_{\gamma} \mathrm{e}^{\mathrm{i}\boldsymbol{G}''\cdot\boldsymbol{\tau}_\gamma} \frac{\sin\big(G'' R_\gamma\big) - G'' R_\gamma \cos\big(G'' R_\gamma\big)}{|\boldsymbol{G}''|^3} \ . \tag{7.13e}$$

Only the $l = 0$ integral remains due to the symmetry of the spherical harmonics. Inserting the definition of $\mathrm{j}_0(x) = \sin(x) x^{-1}$ enables one to solve the radial integral [280, 281]. The MT overlap is already evaluated in section 5.8.2 and reads

$$\Big\langle \phi^{(0)\gamma}_{\boldsymbol{k},\boldsymbol{G}'} \Big| \phi^{(0)\gamma}_{\boldsymbol{k},\boldsymbol{G}} \Big\rangle_\gamma = \sum_{lm} \sum_{p'p} a^{*\boldsymbol{G}'\boldsymbol{k}\gamma}_{lmp'} a^{\boldsymbol{G}\boldsymbol{k}\gamma}_{lmp} \int_{\mathring{\gamma}} \sum_{s} r_{\nu\mathring{\gamma}} u^{s\mathring{\gamma}}_{lp'}(r_{\nu\mathring{\gamma}}) r_{\nu\mathring{\gamma}} u^{s\mathring{\gamma}}_{lp}(r_{\nu\mathring{\gamma}}) \, \mathrm{d}r_{\nu\mathring{\gamma}} \ ,$$

where the sum over s accounts for the scalar-relativistic character of the MT basis functions and the circles above γ indicate when a loop over atom types is sufficient. Finally, the overlap of the Kohn–Sham wave function can be determined by multiplying the overlaps by the wave-function expansion coefficients

$$\Big\langle \Psi^{(0)}_{\boldsymbol{k},n} \Big| \Psi^{(0)}_{\boldsymbol{k},n} \Big\rangle = \sum_{\boldsymbol{G}'\boldsymbol{G}} z^{*(0)}_{\boldsymbol{G}'}(\boldsymbol{k},n) \left(\Big\langle \phi^{(0)\mathrm{IR}}_{\boldsymbol{k},\boldsymbol{G}'} \Big| \phi^{(0)\mathrm{IR}}_{\boldsymbol{k},\boldsymbol{G}} \Big\rangle_{\mathrm{IR}} + \sum_{\gamma} \Big\langle \phi^{(0)\gamma}_{\boldsymbol{k},\boldsymbol{G}'} \Big| \phi^{(0)\gamma}_{\boldsymbol{k},\boldsymbol{G}} \Big\rangle_\gamma \right) z^{(0)}_{\boldsymbol{G}}(\boldsymbol{k},n) \tag{7.14a}$$

$$\begin{aligned} = \sum_{\boldsymbol{G}'\boldsymbol{G}} \Bigg(& \delta(\boldsymbol{G}'') - \frac{4\pi}{\Omega} \sum_{\gamma} \mathrm{e}^{\mathrm{i}\boldsymbol{G}''\cdot\boldsymbol{\tau}_\gamma} \frac{\sin\big(G'' R_{\mathring{\gamma}}\big) - G'' R_{\mathring{\gamma}} \cos\big(G'' R_{\mathring{\gamma}}\big)}{|\boldsymbol{G}''|^3} \\ & + \sum_{\gamma} \sum_{lm} \sum_{p'p} a^{*\boldsymbol{G}'\boldsymbol{k}\gamma}_{lmp'} a^{\boldsymbol{G}\boldsymbol{k}\gamma}_{lmp} \int_{\mathring{\gamma}} \sum_{s} r_{\nu\mathring{\gamma}} u^{s\mathring{\gamma}}_{lp'}(r_{\nu\mathring{\gamma}}) r_{\nu\mathring{\gamma}} u^{s\mathring{\gamma}}_{lp}(r_{\nu\mathring{\gamma}}) \, \mathrm{d}r_{\nu\mathring{\gamma}} \Bigg) \ . \end{aligned} \tag{7.14b}$$

Test 6: Comparing the Log Files of `FLEUR` and `juPhon`

Exchange-correlation integrals

Apart from the aforementioned tests of the data available after the initialization, the log files of `juPhon` (`juPhon.log`) and `FLEUR` (`out`) can be compared. Basically, the information which can reasonably be written to a file is found there. For the surface-term corrections of the dynamical matrix, it derives benefit to compare the integrals

$$\int_{\Omega} \rho^{(0)}(\boldsymbol{r}) \epsilon^{(0)}_{\mathrm{xc}}(\boldsymbol{r}) \, \mathrm{d}^3 r \tag{7.15a}$$

$$\int_{\Omega} \rho^{(0)}(\boldsymbol{r}) V^{(0)}_{\mathrm{xc}}(\boldsymbol{r}) \, \mathrm{d}^3 r \tag{7.15b}$$

in `juPhon.log` with the ones in `out` [127]. They must be the same within the possible numerical accuracy of the integral routines (cf. section 7.1.2). This test checks the correctness of the routines that calculate IR and MT integrals such as in equation (7.15). The factors of the integrand are either expanded in plane waves $\exp(\mathrm{i}\boldsymbol{G}\cdot\boldsymbol{r})$ or lattice harmonics $\mathrm{Y}(\hat{\boldsymbol{r}})$. Thus also the set of reciprocal $\boldsymbol{G}$ with the cutoff G_{max} and the MT mesh is tested. The detailed algorithm of evaluating such integrals is given at a more prominent place in section 7.6.8.

l-like charge

Another quantity, that can be compared, is the so-called l-like charge in the MT sphere γ [71]

$$Q_l^{\gamma} = \sum_{\boldsymbol{k},n}\sum_{mp} f_{\boldsymbol{k},n}^{(0)} A_{lmp}^{*\boldsymbol{k}\gamma n} A_{lmp}^{\boldsymbol{k}\gamma n} \int_{\mathring{\gamma}} \sum_{s} r_{\nu\mathring{\gamma}} \varphi_{l'm'p'}^{*s\mathring{\gamma}}(r_{\nu\mathring{\gamma}}) r_{\nu\mathring{\gamma}} \varphi_{lmp}^{s\mathring{\gamma}}(r_{\nu\mathring{\gamma}})\,\mathrm{d}r_{\nu\mathring{\gamma}}\ . \tag{7.16}$$

Finally, the total charge is calculated by the recycled `FLEUR` routine `Cdntot`, which essentially sums the previous equation over all orbital quantum numbers l, MT spheres γ, and adds the IR charge.

Test 7: Abandoning the Rotations of the Local Coordinate Systems

The arrays checked by this test are `clnu_atom`, `nmem_atom`, and `mlh_atom` for the back-rotated local coordinate systems of the MT spheres (cf. equation (7.6a)). We decided, without loss of generality, to choose the density here and convert it according to the aforesaid equations.

First the benchmark is obtained from an additional `FLEUR` calculation with the same system in a separate folder. However, the symmetry is deactivated by deleting all symmetry operations in the `sym.out` file except for the unity operation, before executing `FLEUR`. Afterwards, `juPhon` must be executed with only this test activated. It results in the files `radDenslmA`γ`R.ssv` for the real part and `radDenslmA`γ`I.ssv` for the imaginary part of the coefficients. The placeholder γ must be substituted by the index of the atom here[11]. In a system without symmetry, the number of lattice harmonics $(l_{\text{max},\mathring{\gamma}}+1)^2$ corresponds to that of the spherical harmonics. This means every lattice harmonic likewise consists of only one member. The aforesaid files should be renamed and copied to the folder, where the original `juPhon` calculation takes place in. In the original folder, the symmetrization of the charge density is abandoned using the routine `ConvertLH2SphHarm`. The resulting coefficients are written to `radDenslmA`γ`R.ssv` and `radDenslmA`γ`I.ssv`. These files can be compared to those produced before.

7.2 Linear Charge-Density Variations

Outline

Among the linear charge-density variations, the gradient of the unperturbed density provides the toughest challenges regarding its numerics and implementation. These challenges and our way to successfully deal with them are elucidated in section 7.2.1. Moreover, provided core-tails reach out of the MT spheres, terms for correcting them become necessary for the first-order density variation and are introduced in section 7.2.2. Section 7.2.3 then finally presents the details of the complete first-order density variation, also clarifying its relation

---

[11] For polyatomic systems, `FLEUR` can be instructed not to build groups of symmetry equivalent atoms by setting the charge Z of the atom slightly differing from the actual nuclear charge of the atom, i.e., 10^{-3} can be added to $Z_{\mathring{\gamma}}$ for every equivalent atom in the input generator `inpgen.x` [127].

to core-tail corrections and the gradient of the unperturbed density. In order to give an impression of the first-order density variation in real space, I illustrate it in section 7.2.4 for one $\boldsymbol{q}$-value, selecting fcc Ne and fcc Al. Finally, the framework to validate the implementation of the linear density variations is pointed out in section 7.2.5. Apart from the `FLEUR` version 26, specified on page 112, a newer version[12] of `FLEUR` has served as inspiration for the `juPhon` routines.

7.2.1 Gradient of the Unperturbed Charge Density

Interstitial region

After the initialization of `juPhon`, the plane-wave coefficients $\rho_{\mathrm{IR}}^{(0)}(\boldsymbol{G})$ from `FLEUR` are available. By moreover resting on equation (6.16), immediately

$$\left[\boldsymbol{\nabla}\rho_{\mathrm{IR}}^{(0)}\right](\boldsymbol{G}) := \mathrm{i}\boldsymbol{G}\rho_{\mathrm{IR}}^{(0)}(\boldsymbol{G}) \tag{7.17}$$

can be defined and reveals the way of determining the IR unperturbed density-gradient coefficients. Since this approach is based on an analytical derivative of the IR plane-wave basis, numerical inaccuracy can mainly be expected from truncation errors, i.e., a non-converged G_{max}[13]. It implies the usual requirement that the charge density gradient should not change significantly anymore when further raising G_{max}. Apart from that, we established the criterion that the unperturbed charge density gradient must be continuous at the MT sphere boundary [127, 251]. However, this is in principle already ensured by the construction of the LAPW basis, which is continuous to linear order [127, 251].

Motivation of first muffin-tin optimizations

The MT unperturbed density gradient (6.17) requires the coefficients of the unperturbed density which must not be decorated by any additional factor, such as $r_{\nu\gamma}\rho(r_{\nu\gamma})$. Otherwise, either the gradient must be divided by this factor in the end or the latter must possibly be taken into account by using the product rule. After the `juPhon` initialization, these naked coefficients are at hand, both in the lattice-harmonic (7.4) and the spherical-harmonic representation (7.6c). But provided the symmetry of the unperturbed quantities, which remains unaffected by the emergence of phonons, only certain l and m channels have significant contributions [127, 251]. Thus, respectively looping over irrelevant orbital and magnetic quantum numbers in the spherical-harmonic representation is inefficient [251]. These symmetries are partly broken when the gradient is applied, so we decided to use a spherical-harmonic representation of the gradient to reduce complexity in the first implementation [119, 251]. Moreover, a closer inspection of equation (6.17b) displays that the l or m quantum numbers of the input and output quantities differ. For example, a scattering takes place from an input channel l to the output channels $l \pm 1$. Consequently, our first optimization is guided by three aspects: (i) no irrelevant calculation, (ii) an efficient sequential run through the storage of the input coefficients, and (iii) an integration of the transformation (7.6c) [251]. These measures can be characterized as a performance optimization regarding runtime and storage. However, (i) to (iii) cause a non-contiguous storage access of the output-quantity array. Nonetheless,

---

[12] This version can be found in the `FLEUR` repository when searching for the commit indexed by the hash `1138084ca03ddbad5ba178c97d8082234b112988`.

[13] Recollecting that the charge density (5.23) yields from a product of two wave functions featuring a cutoff k_{max}, the unperturbed charge-density should be converged for $G_{\text{max}} \geq 2k_{\text{max}}$ [251]. But due to overlapping core-tails, in general it has proven necessary to increase the lower limit and use the same $G_{\text{max}} > 2k_{\text{max}}$ as for the unperturbed potential, which is larger than $2k_{\text{max}}$ due to the xc part. [127].

we deem this to be the better solution, because an array is available, storing the l and m of the lattice harmonic members characterized by λ and μ [251]. Additionally, in this way no l or m contributions of the lattice harmonic representation are requested, which are not available due to symmetry. Catching these exceptions would necessitate conditional clauses in the inner scope of the loops, which oppose runtime optimizations by the compiler.

First muffin-tin optimization

Realizing the aforesaid optimizations, firstly in equation (6.17b) the l'' sum is evaluated

$$\begin{aligned}
\boldsymbol{\nabla}\rho_{\gamma}^{(0)}\left(\boldsymbol{r}_{\nu\mathring{\gamma}}\right) &= \underline{T}\sum_{m''=-1}^{1}\hat{\boldsymbol{e}}_{m''}(-1)^{m''}\sqrt{\frac{4\pi}{3}}\sum_{lm}\mathrm{Y}_{lm}\left(\hat{\boldsymbol{r}}_{\gamma}\right)G_{l,\ l-1,\ \ 1}^{m,m+m'',-m''} \\
&\qquad\times\left(\frac{\partial\left[\rho_{\gamma}^{(0)}\left(r_{\nu\mathring{\gamma}}\right)\right]_{l-1,m+m''}}{\partial r_{\nu\mathring{\gamma}}}-(l-1)\frac{\left[\rho_{\gamma}^{(0)}\left(r_{\nu\mathring{\gamma}}\right)\right]_{l-1,m+m''}}{r_{\nu\mathring{\gamma}}}\right) \\
&\quad+\underline{T}\sum_{m''=-1}^{1}\hat{\boldsymbol{e}}_{m''}(-1)^{m''}\sqrt{\frac{4\pi}{3}}\sum_{lm}\mathrm{Y}_{lm}\left(\hat{\boldsymbol{r}}_{\gamma}\right)G_{l,\ l+1,\ \ 1}^{m,m+m'',-m''} \\
&\qquad\times\left(\frac{\partial\left[\rho_{\gamma}^{(0)}\left(r_{\nu\mathring{\gamma}}\right)\right]_{l+1,m+m''}}{\partial r_{\nu\mathring{\gamma}}}+(l+2)\frac{\left[\rho_{\gamma}^{(0)}\left(r_{\nu\mathring{\gamma}}\right)\right]_{l+1,m+m''}}{r_{\nu\mathring{\gamma}}}\right) \qquad (7.18a) \\
&:= \underline{T}\sum_{m''=-1}^{1}\hat{\boldsymbol{e}}_{m''}\sum_{lm}\left(\left[\boldsymbol{\nabla}\rho_{\gamma}^{(0)}\left(r_{\nu\mathring{\gamma}}\right)\right]_{lm}^{-1m''}+\left[\boldsymbol{\nabla}\rho_{\gamma}^{(0)}\left(r_{\nu\mathring{\gamma}}\right)\right]_{lm}^{+1m''}\right)\mathrm{Y}_{lm}\left(\hat{\boldsymbol{r}}_{\gamma}\right) \qquad (7.18b)
\end{aligned}$$

which essentially yields two summands, corresponding to the two aforementioned scattering channels $l \pm 1$. In the first summand of (7.18a), now the index shifts $\tilde{l} := l-1 \Leftrightarrow l = \tilde{l}+1$ and $\tilde{m} := m+m'' \Leftrightarrow m = \tilde{m}-m''$ are applied so that

$$\begin{aligned}
\left[\boldsymbol{\nabla}\rho_{\gamma}^{(0)}\left(r_{\nu\mathring{\gamma}}\right)\right]_{\tilde{l}+1,\tilde{m}-m''}^{-1m''} &= (-1)^{m''}\sqrt{\frac{4\pi}{3}}\,G_{\tilde{l}+1,\ \ \tilde{l},\ \ 1}^{\tilde{m}-m'',\tilde{m},-m''} \qquad (7.18c) \\
&\quad\times\left(\frac{\partial\left[\rho_{\gamma}^{(0)}\left(r_{\nu\mathring{\gamma}}\right)\right]_{\tilde{l}\tilde{m}}}{\partial r_{\nu\mathring{\gamma}}}-\frac{\tilde{l}}{r_{\nu\mathring{\gamma}}}\left[\rho_{\gamma}^{(0)}\left(r_{\nu\mathring{\gamma}}\right)\right]_{\tilde{l}\tilde{m}}\right).
\end{aligned}$$

Including the transformation (7.6c) results in

$$\begin{aligned}
\left[\boldsymbol{\nabla}\rho_{\gamma}^{(0)}\left(r_{\nu\mathring{\gamma}}\right)\right]_{\tilde{l}+1,\tilde{m}-m''}^{-1m''} &= (-1)^{m''}\sqrt{\frac{4\pi}{3}}\,G_{\tilde{l}+1,\ \ \tilde{l},\ \ 1}^{\tilde{m}-m'',\tilde{m},-m''} \qquad (7.18d) \\
&\quad\times\left(\frac{\partial\left[\rho_{\mathring{\gamma}}^{(0)}\left(r_{\nu\mathring{\gamma}}\right)\right]_{\lambda\left(\tilde{l}\right)}}{\partial r_{\mathring{\gamma}}}c_{\lambda\left(\tilde{l}\right),\mu(\tilde{m})}^{\gamma}-\frac{\tilde{l}}{r_{\nu\gamma}}\left[\rho_{\mathring{\gamma}}^{(0)}\left(r_{\nu\mathring{\gamma}}\right)\right]_{\lambda\left(\tilde{l}\right)}c_{\lambda\left(\tilde{l}\right),\mu(\tilde{m})}^{\gamma}\right).
\end{aligned}$$

In contrast, the second summand of (7.18a) undergoes the index shift $\tilde{l} := l + 1 \leftrightarrow l = \tilde{l} - 1$ and $\tilde{m} := m + m'' \leftrightarrow m = \tilde{m} - m''$, leading to

$$\left[\boldsymbol{\nabla}\rho_{\gamma}^{(0)}\left(r_{\nu\mathring{\gamma}}\right)\right]_{\tilde{l}-1,\tilde{m}-m''}^{+1m''} = (-1)^{m''}\sqrt{\frac{4\pi}{3}}\,G_{\tilde{l}-1,\quad\tilde{l},\quad 1}^{\tilde{m}-m'',\tilde{m},-m''} \times \left(\frac{\partial\left[\rho_{\gamma}^{(0)}\left(r_{\nu\mathring{\gamma}}\right)\right]_{\tilde{l}\tilde{m}}}{\partial r_{\nu\mathring{\gamma}}} + \frac{\left(\tilde{l}+1\right)}{r_{\nu\mathring{\gamma}}}\left[\rho_{\gamma}^{(0)}\left(r_{\nu\mathring{\gamma}}\right)\right]_{\tilde{l}\tilde{m}}\right) \tag{7.18e}$$

or

$$\left[\boldsymbol{\nabla}\rho_{\gamma}^{(0)}\left(r_{\nu\mathring{\gamma}}\right)\right]_{\tilde{l}-1,\tilde{m}-m''}^{+1m''} = (-1)^{m''}\sqrt{\frac{4\pi}{3}}\,G_{\tilde{l}-1,\quad\tilde{l},\quad 1}^{\tilde{m}-m'',\tilde{m},-m''} \times \left(\frac{\partial\left[\rho_{\mathring{\gamma}}^{(0)}\left(r_{\nu\mathring{\gamma}}\right)\right]_{\lambda\left(\tilde{l}\right)}}{\partial r_{\nu\mathring{\gamma}}}c_{\lambda\left(\tilde{l}\right),\mu(\tilde{m})}^{\gamma} + \frac{\left(\tilde{l}+1\right)}{r_{\nu\mathring{\gamma}}}\left[\rho_{\mathring{\gamma}}^{(0)}\left(r_{\nu\mathring{\gamma}}\right)\right]_{\lambda\left(\tilde{l}\right)}c_{\lambda\left(\tilde{l}\right),\mu(\tilde{m})}^{\gamma}\right). \tag{7.18f}$$

Motivation of second optimization

Apart from the concepts presented in section 7.2.5, one test [127, 251] is prominent in the sense that it has driven further development. Basically, it compares the numerical (n) MT gradient of the test function[14] $\mathfrak{g}(r_{\nu}) = r_{\nu}^{-1}\mathrm{Y}_{00}$ with the analytical (a) result

$$\boldsymbol{\nabla}_{\mathrm{a}}\frac{1}{r_{\nu}} = -\frac{\boldsymbol{r}_{\nu}}{r_{\nu}^{2}}, \tag{7.19a}$$

projected onto the respective cartesian displacement directions $\hat{\boldsymbol{e}}_i$, respectively. Figure 7.3 illustrates the absolute error

$$\left|\delta\left(\hat{\boldsymbol{e}}_x\cdot\boldsymbol{\nabla}_{\mathrm{n}}r_{\nu}^{-1}\mathrm{Y}_{00}\right)\right| := \left|\hat{\boldsymbol{e}}_x\cdot\left(\boldsymbol{\nabla}_{\mathrm{n}}r_{\nu}^{-1}\mathrm{Y}_{00} - \boldsymbol{\nabla}_{\mathrm{a}}r_{\nu}^{-1}\right)\right| \tag{7.19b}$$

and the relative error of the numerical MT gradient with respect to the analytical gradient on doubly logarithmic scales (the y- and z-directions are analogous and do not contain new information). The input file can be found in appendix B. It manifests itself that the error becomes larger the closer the logarithmic mesh points are to the MT sphere center. Still, the relative error is overall smaller than $0.01\,\%$ for the implementation of equation (7.18), which is denoted as the naive implementation in this figure. In my opinion, the increase of inaccuracy towards the MT sphere center can be ascribed to the fact that approximately equal numbers, which become relatively large in this region, are summed in this MT gradient approach (cf. section 7.1.2). Nevertheless, the absolute value can be large relative to typical phonon-frequencies, although the relative error is small. Therefore in practice, the effects of this drawback should be minimized. Furthermore, it becomes obvious that the accuracy of the naive approach is limited and the error grows again at the MT sphere boundary. Reasons could be the thinned-out logarithmic mesh or a non-optimal boundary mesh-points algorithm of the radial derivative subroutine `Derivative`.

---

[14] This test function has been stimulated by the divergence behavior of the external potential variations, because they normally feature the largest values relative to other quantities used here. In particular this holds true for the mesh points in the close vicinity of the MT sphere center.

Second muffin-tin optimization

In order to mitigate the error, we decided to multiply the input coefficients by a damping factor $r^2_{\nu\mathring{\gamma}}$, approaching zero for small $\nu^{\mathring{\gamma}}$ [127, 251]. However, the introduction of such a damping factor entails considering the product rule. I found a way to reformulate the concept (7.18) without damping, such that the implemented subroutine expects an input function multiplied by $r^2_{\nu\mathring{\gamma}}$ and outputs the MT gradient of the original input function multiplied by $r^2_{\nu\mathring{\gamma}}$. Hence, the final result must be divided by the auxiliary $r^2_{\nu\mathring{\gamma}}$ and one gains the desired MT gradient of the original input function. For this reformulation, the charge density in equation (7.18c) is generalized to a function $\tilde{\mathfrak{g}}(\boldsymbol{r}) := r^2\mathfrak{g}(\boldsymbol{r})$. This is because the following derivation also underlies when evaluating the gradient of the unperturbed effective potential or its constituents. So, the generalized version of equation (7.18c) reads

$$\left[\boldsymbol{\nabla}\left(r^2\mathfrak{g}\right)(r)\right]^{-1m''}_{l+1,m-m''} := [\boldsymbol{\nabla}\tilde{\mathfrak{g}}(r)]^{-1m''}_{l+1,m-m''} \tag{7.20a}$$

$$= (-1)^{m''}\sqrt{\frac{4\pi}{3}}G^{m-m'',m,-m''}_{l+1,\;\;l,\;\;1}\left(\frac{\partial\tilde{\mathfrak{g}}_{lm}(r)}{\partial r} - \frac{l}{r}\tilde{\mathfrak{g}}_{lm}(r)\right) . \tag{7.20b}$$

Applying the product rule to the general function leads to

$$= (-1)^{m''}\sqrt{\frac{4\pi}{3}}G^{m-m'',m,-m''}_{l+1,\;\;l,\;\;1}\left(2r\mathfrak{g}_{lm}(r) + r^2\frac{\partial\mathfrak{g}_{lm}(r)}{\partial r} - \frac{l}{r}\tilde{\mathfrak{g}}_{lm}(r)\right) \tag{7,20c}$$

in which the concept (7.18c) can be identified

$$= r^2[\boldsymbol{\nabla}\mathfrak{g}(r)]^{-1m''}_{l+1,m-m''} + (-1)^{m''}\sqrt{\frac{4\pi}{3}}G^{m-m'',m,-m''}_{l+1,\;\;l,\;\;1}2r\mathfrak{g}_{lm}(r) , \tag{7.20d}$$

provided $\mathfrak{g}(\boldsymbol{r})$ is the charge density. Analogously employing equation (7.18e), results in

$$[\boldsymbol{\nabla}\tilde{\mathfrak{g}}(r)]^{+1m''}_{l-1,m-m''} = r^2[\boldsymbol{\nabla}\mathfrak{g}(r)]^{+1m''}_{l-1,m-m''} + (-1)^{m''}\sqrt{\frac{4\pi}{3}}G^{m-m'',m,-m''}_{l-1,\;\;l,\;\;1}2r\mathfrak{g}_{lm}(r) . \tag{7.20e}$$

In practice, it is beneficial to shift the respective remaining terms to the left-hand side:

$$r^2[\boldsymbol{\nabla}\mathfrak{g}(r)]^{-1m''}_{l+1,m-m''} = (-1)^{m''}\sqrt{\frac{4\pi}{3}}G^{m-m'',m,-m''}_{l+1,\;\;l,\;\;1}\left(\frac{\partial\tilde{\mathfrak{g}}_{lm}(r)}{\partial r} - \frac{(l+2)}{r}\tilde{\mathfrak{g}}_{lm}(r)\right) , \tag{7.20f}$$

$$r^2[\boldsymbol{\nabla}\mathfrak{g}(r)]^{+1m''}_{l-1,m-m''} = (-1)^{m''}\sqrt{\frac{4\pi}{3}}G^{m-m'',m,-m''}_{l-1,\;\;l,\;\;1}\left(\frac{\partial\tilde{\mathfrak{g}}_{lm}(r)}{\partial r} + \frac{(l-1)}{r}\tilde{\mathfrak{g}}_{lm}(r)\right) . \tag{7.20g}$$

Finally employing this for the MT gradient of the unperturbed charge density, the implemented expression reads

$$\boldsymbol{\nabla}\rho^{(0)}_{\gamma}(\boldsymbol{r}_{\nu\mathring{\gamma}}) = \sum_{lm}\left[\boldsymbol{\nabla}\rho^{(0)}_{\gamma}(r_{\nu\mathring{\gamma}})\right]_{lm}\mathrm{Y}_{lm}\left(\boldsymbol{r}_{\gamma}\right) \tag{7.21a}$$

$$:= \underline{T}\sum_{m''=-1}^{1}\hat{\boldsymbol{e}}_{m''}\sum_{\tilde{l}\tilde{m}}\left(\left[\boldsymbol{\nabla}\rho^{(0)}_{\gamma}(r_{\nu\mathring{\gamma}})\right]^{\mathrm{opt}^{+}1m''}_{\tilde{l}+1,\tilde{m}-m''}\mathrm{Y}_{\tilde{l}+1,\tilde{m}-m''}\left(\hat{\boldsymbol{r}}_{\gamma}\right)\right. \tag{7.21b}$$

$$\left. +\left[\boldsymbol{\nabla}\rho^{(0)}_{\gamma}(r_{\nu\gamma})\right]^{\mathrm{opt}^{-}1m''}_{\tilde{l}-1,\tilde{m}-m''}\mathrm{Y}_{\tilde{l}-1,\tilde{m}-m''}\left(\hat{\boldsymbol{r}}_{\gamma}\right)\right)$$

with

$$\left[\boldsymbol{\nabla}\rho_{\gamma}^{(0)}\left(r_{\nu\mathring{\gamma}}\right)\right]^{\mathrm{opt}^{-}1m''}_{\tilde{l}+1,\tilde{m}-m''} =: \frac{1}{r_{\nu\mathring{\gamma}}^{2}}\hat{\boldsymbol{e}}_{m''}(-1)^{m''}\sqrt{\frac{4\pi}{3}}\,G^{\tilde{m}-m'',\tilde{m},-m''}_{\tilde{l}+1,\quad\tilde{l},\quad 1} \times\left(\frac{\partial\left[\tilde{\rho}_{\mathring{\gamma}}^{(0)}\left(r_{\nu\mathring{\gamma}}\right)\right]_{\lambda\left(\tilde{l}\right)}}{\partial r_{\mathring{\gamma}}}c^{\gamma}_{\lambda\left(\tilde{l}\right),\mu(\tilde{m})} - \frac{\left(\tilde{l}+2\right)}{r_{\nu\gamma}}\left[\tilde{\rho}_{\mathring{\gamma}}^{(0)}\left(r_{\nu\mathring{\gamma}}\right)\right]_{\lambda\left(\tilde{l}\right)}c^{\gamma}_{\lambda\left(\tilde{l}\right),\mu(\tilde{m})}\right) \tag{7.21c}$$

and

$$\left[\boldsymbol{\nabla}\rho_{\gamma}^{(0)}\left(r_{\nu\mathring{\gamma}}\right)\right]^{\mathrm{opt}^{+}1m''}_{\tilde{l}-1,\tilde{m}-m''} =: \frac{1}{r_{\nu\mathring{\gamma}}^{2}}\hat{\boldsymbol{e}}_{m''}(-1)^{m''}\sqrt{\frac{4\pi}{3}}\,G^{\tilde{m}-m'',\tilde{m},-m''}_{\tilde{l}-1,\quad\tilde{l},\quad 1} \times\left(\frac{\partial\left[\tilde{\rho}_{\mathring{\gamma}}^{(0)}\left(r_{\nu\mathring{\gamma}}\right)\right]_{\lambda\left(\tilde{l}\right)}}{\partial r_{\nu\mathring{\gamma}}}c^{\gamma}_{\lambda\left(\tilde{l}\right),\mu(\tilde{m})} + \frac{\left(\tilde{l}-1\right)}{r_{\nu\mathring{\gamma}}}\left[\tilde{\rho}_{\mathring{\gamma}}^{(0)}\left(r_{\nu\mathring{\gamma}}\right)\right]_{\lambda\left(\tilde{l}\right)}c^{\gamma}_{\lambda\left(\tilde{l}\right),\mu(\tilde{m})}\right). \tag{7.21d}$$

Analysis of second optimization

When analyzing the impact of this optimization (7.21) in figure 7.3 relative to the naive approach (7.18), the desired reduction of the error close to the MT sphere center is essentially not achieved. However, the accuracy at the MT sphere boundary has been increased and seems not to be limited anymore. This will lead to an improved continuity in this region. But, it must be stressed at this point that these results hold particularly true for the discussed test function. Since this optimization has still enhanced the accuracy, we decided to implement this approach (7.21), estimating it to be the better choice for each of the real input coefficients to the MT-gradient routine [127, 251]. Furthermore, both approaches show a similar error for all cartesian displacement directions (not shown), although each direction requires an individual spherical-harmonic expansion of the MT gradient coefficients.

Numerical cutoff

Ultimately, both approaches make obvious that contributions in a channel $l = l_{\max,\mathring{\gamma}}$ are scattered to $l_{\max,\mathring{\gamma}} + 1$ [251]. In the following sections, it shall be discussed that this leads to inconsistencies in the cutoffs, when the gradient coefficients are used within other quantities. Therefore, we decided to cut this quantity at $l_{\max,\mathring{\gamma}}$, i.e., omit the aforesaid $l_{\max,\mathring{\gamma}} + 1$ contribution on condition that $l_{\max,\mathring{\gamma}}$ is converged [127]. Apart from that, the contribution scattering from $l = 0$ to $l = -1$ is caught because it is unphysical. The Gaunt coefficients (5.32d) are determined with the recycled `FLEUR` routine `Gaunt1` and the radial derivative routine is taken from `SpeX` [230], essentially utilizing Lagrange interpolation of 3rd order.

7.2.2 Core-Tail Corrections

Motivation and concept

If core tails exist, a displacement of the MT spheres causes their change. For $\boldsymbol{q} = \boldsymbol{0}$, this correction can be determined from applying the gradient to the core-tail expressions in section 5.5.1. But for a non-vanishing $\boldsymbol{q}$, they must be multiplied by a factor of $\exp(\mathrm{i}\boldsymbol{q}\cdot\boldsymbol{r})$ in advance, mirroring the phonon displacement pattern [127]. According to the frozen-core approximation, the core density is fixed and not dependent on $\boldsymbol{q}$. Hence, the only dependence on $\boldsymbol{q}$ comes from the aforesaid phase factor. Furthermore, the pseudo core-density underlying the Fourier transform

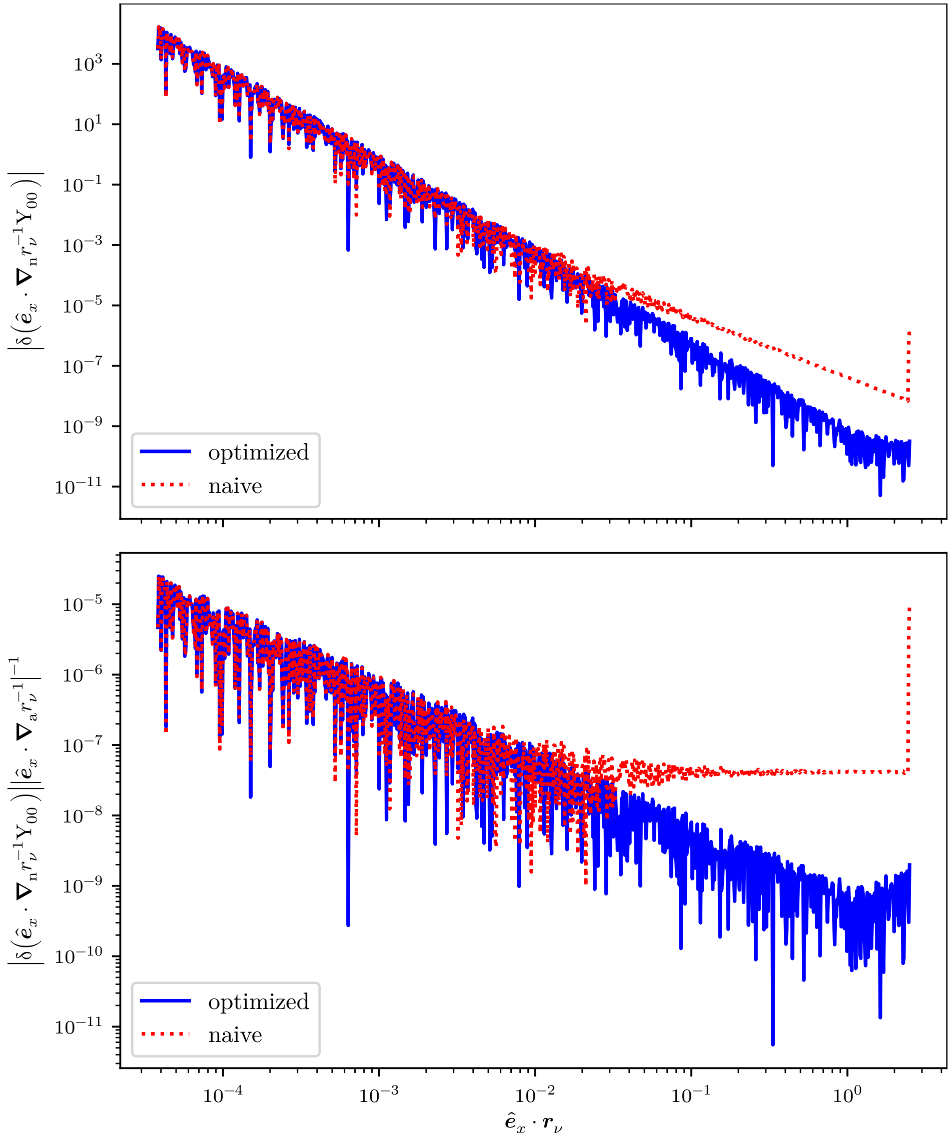

Figure 7.3: Benchmark of the MT gradient subroutine utilized in the `juPhon` code by differentiating the toy function $r_\nu^{-1}\mathrm{Y}_{00}$. The analytical derivative $-{}^{r}/_{r^2}$ is compared with the output of two different numerical approaches: the naive (7.18) and the optimized one (7.21), with the input-density coefficients substituted by the aforementioned test function. The optimized concept exploits a damping factor of $r^2_{\nu\hat{\gamma}}$ relative to the naive method. Since the absolute (above) and the relative (below) error show a similar behavior for all displacement directions, only the x-direction is presented here. The employed input-generator input file can be found in appendix B.

of the core tails (5.26b) is represented by a Gaussian $\rho_{\mathrm{c},\alpha}^{(0),\mathrm{ps}}(r_{\nu\mathring{\alpha}}) = A_\alpha \exp\bigl(-a_\alpha r_{\nu\mathring{\alpha}}^2\bigr)$ with

$$A_\alpha = \rho_{\mathrm{c},\alpha}^{(0),\mathrm{ps}}(R_\alpha) \exp\Bigl(a_\alpha r_{\nu\mathring{\alpha}}^2\Bigr)\,, \quad a_\alpha = -\frac{1}{2R_\alpha} \frac{\frac{\partial \rho_{\mathrm{c},\alpha}^{(0),\mathrm{ps}}(r_{\nu\mathring{\alpha}})}{\partial r_{\nu\mathring{\alpha}}}\Big|_{r_{\nu\mathring{\alpha}}=R_{\mathring{\alpha}}}}{\rho_{\mathrm{c},\alpha}^{(0),\mathrm{ps}}(R_\alpha)} \tag{7.22}$$

in `FLEUR`. In contrast to the core-tails, which in general arise from several MT spheres, the core-tail corrections only originate from the displaced MT sphere (and its periodic images). Therefore, the latter need not be overlapped with those of the non-displaced atoms. Despite the gradient, the core-tail corrections must be continuous at the MT sphere boundary. This is ensured by the requirement on the Gaussian parameters (7.22), which in analogy to the LAPW basis set are determined such that a linear derivative is still continuous. [88]

Interstitial region

In the IR, the first-order core-tail correction reads [88]

$$\begin{aligned} \boldsymbol{\rho}_{\text{IR, ctC}}^{(1)}(\boldsymbol{r}, \boldsymbol{q}^+\alpha) &= -\nabla\left(\sum_{\boldsymbol{G}} \rho_{\mathrm{c},\alpha}^{(0),\mathrm{ps}}(\boldsymbol{G}) \mathrm{e}^{\mathrm{i}\boldsymbol{G}\cdot\boldsymbol{r}} \mathrm{e}^{\mathrm{i}\boldsymbol{q}\cdot\boldsymbol{r}}\right) &\text{(7.23a)}\\ &= -\sum_{\boldsymbol{G}} \mathrm{i}(\boldsymbol{G}+\boldsymbol{q}) \rho_{\alpha,\mathrm{c}}^{(0),\mathrm{ps}}(\boldsymbol{G}) \mathrm{e}^{\mathrm{i}(\boldsymbol{G}+\boldsymbol{q})\cdot\boldsymbol{r}} &\text{(7.23b)}\\ &:= \sum_{\boldsymbol{G}} \boldsymbol{\rho}_{\text{IR, ctC}}^{(1)}(\boldsymbol{G}, \boldsymbol{q}^+\alpha) \mathrm{e}^{\mathrm{i}(\boldsymbol{G}+\boldsymbol{q})\cdot\boldsymbol{r}}\,, &\text{(7.23c)} \end{aligned}$$

where the matrix elements are defined in equation (6.27c). The set of reciprocal lattice vectors for the expansion coefficients $\rho_{\alpha,\mathrm{c}}^{(0),\mathrm{ps}}(\boldsymbol{G})$ lives up to the condition $|\boldsymbol{G}| \leq G_{\text{max}}$, and the same holds true for its gradient, i.e., given the case $\boldsymbol{q} = \boldsymbol{0}$. But for a finite $\boldsymbol{q}$, the basis functions $\exp(\mathrm{i}(\boldsymbol{G}+\boldsymbol{q}) \cdot \boldsymbol{r})$ suggest using the reciprocal lattice vectors within the sphere given by $|\boldsymbol{G}+\boldsymbol{q}| < G_{\text{max}}$. This is a contradiction and cannot be implemented. Two options are at hand: the first one is to ignore the core-tail corrections, and the second one is to ignore the shift of the aforesaid ball by $\boldsymbol{q}$. In order that the latter is a good approximation, G_{max} must be converged. Nevertheless, this entails disadvantages that shall be clarified within the following sections.

Muffin-tin spheres

The first-order core-tail corrections in the MT spheres are given by

$$\begin{aligned} \left[\boldsymbol{\rho}_{\gamma,\mathrm{ctC}}^{(1)}\Bigl(\boldsymbol{r}_{\nu_{\mathring{\gamma}}}, \boldsymbol{q}^+\alpha\Bigr)\right]_{lm} = &-\delta_{\gamma\alpha} 2 r_{\nu_{\mathring{\alpha}}} a_\alpha A_\alpha \exp\bigl(-a_\alpha r_{\nu_{\mathring{\alpha}}}^2\bigr) \sum_{i=1}^{3} \hat{\boldsymbol{e}}_i \zeta_{i,m} \delta_{1l} \\ &- 4\pi \mathrm{i}^l \sum_{\boldsymbol{G}} \mathrm{i}(\boldsymbol{G}+\boldsymbol{q}) \mathrm{e}^{\mathrm{i}(\boldsymbol{G}+\boldsymbol{q})\cdot\boldsymbol{\tau}_\alpha} \mathrm{Y}_{lm}^*\Bigl(\widehat{\boldsymbol{G}+\boldsymbol{q}}\Bigr) \mathrm{j}_l\Bigl(|\boldsymbol{G}+\boldsymbol{q}| r_{\nu_\beta}\Bigr) \rho_{\alpha,\mathrm{c}}^{(0),\mathrm{ps}}(\boldsymbol{G})\,. \end{aligned} \tag{7.24}$$

Their second summand describes the Rayleigh decomposition (5.5) of the core-tail corrections in the IR (7.23c), which are augmented to all MT spheres. But since the source of the core-tail correction is only in the displaced MT sphere, no core-tails that permeate this sphere need to be corrected. Thus, the aforementioned Rayleigh decomposition must be eliminated there. This is done in analogy to `FLEUR` [127]. Instead of subtracting the second term of equation (7.24) again or ignoring it in the displaced MT sphere, the first term in equation (7.24) is added to compensate with the second term. The second term results from the gradient of the pseudo core-density. Due to the fact that it is represented by a Gaussian, the application of the gradient is significantly facilitated. For the implementation of the characterizing Gaussian coefficients (7.22), I recycled the subroutine `Cdnovlp` and its dependencies from `FLEUR`. [88]

7.2.3 First-Order Charge Density Variation

Back-folding

Both the IR and the MT first-order density variation (6.21) contain a contribution in which the wave-function expansion coefficients are varied. Restricting to the $\boldsymbol{q}^{+}$ part (without loss of generality), the resulting Bloch character $\boldsymbol{k}+\boldsymbol{q}$ manifests itself in the aforesaid coefficients and particularly likewise in the basis functions. However for some instances of $\boldsymbol{k}$ and $\boldsymbol{q}$, their sum $\boldsymbol{k}+\boldsymbol{q}$ can leave the first Brillouin zone. One case is for example shown in figure 7.2. This is problematic, because the $\boldsymbol{z}_{\boldsymbol{G}}^{(1)}(\boldsymbol{k}, n; \pm\boldsymbol{q}\alpha)$ in `juPhon` are only determined within the first Brillouin zone. We thus decided to exploit

$$\boldsymbol{k}+\boldsymbol{q}=\boldsymbol{k}_{\mathrm{bf}}^{+}-\boldsymbol{G}_{\mathrm{bf}} \tag{7.25}$$

whenever such a scenario occurs and set $\boldsymbol{G}_{\mathrm{bf}}=\mathbf{0}$ otherwise [127, 251]. So, the reciprocal lattice vector $\boldsymbol{G}_{\mathrm{bf}}$ folds back to the first Brillouin zone if required, thereby assuming the periodicity of the reciprocal space. In our opinion invoking here this periodicity is legitimate, because

$$\varPsi_{\boldsymbol{k}+\boldsymbol{q},n}^{(0)}=\sum_{\boldsymbol{G}} z_{\boldsymbol{G}}^{(0)}(\boldsymbol{k}, n; \boldsymbol{q}) \phi_{\boldsymbol{k}+\boldsymbol{q},\boldsymbol{G}}^{(0)}(\boldsymbol{r}) \equiv \sum_{\boldsymbol{G}} z_{\boldsymbol{G}-\boldsymbol{G}_{\mathrm{bf}}}^{(0)}\left(\boldsymbol{k}_{\mathrm{bf}}^{+}, n\right) \phi_{\boldsymbol{k}_{\mathrm{bf}}^{+}, \boldsymbol{G}-\boldsymbol{G}_{\mathrm{bf}}}^{(0)}(\boldsymbol{r})=\varPsi_{\boldsymbol{k}_{\mathrm{bf}}^{+}, n}^{(0)} \tag{7.26}$$

is beyond dispute [127, 251, 282]. Furthermore, it is assumed that substituting the unperturbed wave-function expansion coefficients by its first-order variation in the previous equation does not break the aforementioned periodicity. By introducing auxiliary first-order variations of the wave-function expansion coefficients, which depend on two bands n and n' instead of being indexed by a band n and a reciprocal lattice vector $\boldsymbol{G}$, the preceding assumptions can be deduced from [251]

$$\sum_{\boldsymbol{G}} \boldsymbol{z}_{\boldsymbol{G}}^{(1)}(\boldsymbol{k}, n; \boldsymbol{q}\alpha) \phi_{\boldsymbol{k}+\boldsymbol{q},\boldsymbol{G}}^{(0)}(\boldsymbol{r})=\sum_{\boldsymbol{G}} \sum_{n'} \boldsymbol{z}_{n'}^{(1)}(\boldsymbol{k}, n; \boldsymbol{q}\alpha) \boldsymbol{z}_{\boldsymbol{G}}^{(0)}(\boldsymbol{k}, n'; \boldsymbol{q}) \phi_{\boldsymbol{k}+\boldsymbol{q},\boldsymbol{G}}^{(0)}(\boldsymbol{r}) \tag{7.27a}$$

$$=\sum_{n'} \boldsymbol{z}_{n'}^{(1)}(\boldsymbol{k}, n; \boldsymbol{q}\alpha) \varPsi_{\boldsymbol{k}+\boldsymbol{q},n'}^{(0)} \,. \tag{7.27b}$$

Basically, it is possible to identify the unperturbed wave function and refer to the relation (7.26) again. For the Sternheimer equation, the same line of arguments can be applied. Consequently, adequate $\boldsymbol{z}_{\boldsymbol{G}-\boldsymbol{G}_{\mathrm{bf}}}^{(1)}\left(\boldsymbol{k}_{\mathrm{bf}}^{+}, n; \alpha\right)$ result so that

$$\boldsymbol{\varPsi}_{\boldsymbol{k},n}^{(1)+}(\boldsymbol{r}; \alpha)=\sum_{\boldsymbol{G}}\left(\boldsymbol{z}_{\boldsymbol{G}}^{(1)}(\boldsymbol{k}, n; \boldsymbol{q}\alpha) \phi_{\boldsymbol{k}+\boldsymbol{q},\boldsymbol{G}}^{(0)}(\boldsymbol{r})+z_{\boldsymbol{G}}^{(0)}(\boldsymbol{k}, n) \boldsymbol{\phi}_{\boldsymbol{k},\boldsymbol{G}}^{(1)\alpha+}(\boldsymbol{r})\right) \tag{7.28a}$$

$$=\sum_{\boldsymbol{G}}\left(\boldsymbol{z}_{\boldsymbol{G}-\boldsymbol{G}_{\mathrm{bf}}}^{(1)}\left(\boldsymbol{k}_{\mathrm{bf}}^{+}, n; \alpha\right) \phi_{\boldsymbol{k}_{\mathrm{bf}}^{+}, \boldsymbol{G}-\boldsymbol{G}_{\mathrm{bf}}}^{(0)}(\boldsymbol{r})+z_{\boldsymbol{G}}^{(0)}(\boldsymbol{k}, n) \boldsymbol{\phi}_{\boldsymbol{k},\boldsymbol{G}}^{(1)\alpha+}(\boldsymbol{r})\right) \tag{7.28b}$$

holds, while equations (6.7) and (6.8) serve as starting point. Moreover, it allows for reformulating the $\boldsymbol{q}^{+}$ part of equation (6.21) into

$$\begin{aligned}
\boldsymbol{\rho}^{(1)}\left(\boldsymbol{r}; \boldsymbol{q}^{+}\alpha\right)= & -2 \sum_{\boldsymbol{R}} \mathrm{e}^{+\mathrm{i}\boldsymbol{q}\cdot\boldsymbol{R}} \boldsymbol{\nabla} \rho_{\alpha}^{(0)}(\boldsymbol{r}) \\
& +4 \sum_{\boldsymbol{k},n} f_{\boldsymbol{k},n}^{(0)} \sum_{\boldsymbol{G}'\boldsymbol{G}}\Big(z_{\boldsymbol{G}'}^{*(0)}(\boldsymbol{k}, n) \boldsymbol{z}_{\boldsymbol{G}-\boldsymbol{G}_{\mathrm{bf}}}^{(1)}\left(\boldsymbol{k}_{\mathrm{bf}}^{+}, n; \alpha\right) \phi_{\boldsymbol{k},\boldsymbol{G}'}^{(0)*}(\boldsymbol{r}) \phi_{\boldsymbol{k}_{\mathrm{bf}}^{+}, \boldsymbol{G}-\boldsymbol{G}_{\mathrm{bf}}}^{(0)}(\boldsymbol{r}) \\
& \qquad +\sum_{\boldsymbol{R}} \Theta\left(R_{\alpha}^{\mathrm{MT}}-\left|\boldsymbol{r}-\boldsymbol{\tau}_{\alpha}-\boldsymbol{R}\right|\right) \mathrm{e}^{+\mathrm{i}\boldsymbol{q}\cdot\boldsymbol{R}} \\
& \qquad \times z_{\boldsymbol{G}'}^{*(0)}(\boldsymbol{k}, n) z_{\boldsymbol{G}}^{(0)}(\boldsymbol{k}, n) \phi_{\boldsymbol{k},\boldsymbol{G}'}^{*(0)}(\boldsymbol{r})(\mathrm{i}(\boldsymbol{k}+\boldsymbol{G})-\boldsymbol{\nabla}) \phi_{\boldsymbol{k},\boldsymbol{G}}^{(0)}(\boldsymbol{r})\Big)
\end{aligned} \tag{7.29}$$

for a non-vanishing $\boldsymbol{q}$. These statements are confirmed by numerical tests [127, 251].

Analytical solution for $\boldsymbol{q} = \boldsymbol{0}$

Evidently in the case of the Goldstone modes, selecting [251]

$$\boldsymbol{z}^{(1)}_{\boldsymbol{G}}(\boldsymbol{k}, n; \boldsymbol{0}\alpha) \equiv -\mathrm{i}(\boldsymbol{k} + \boldsymbol{G})\boldsymbol{z}^{(0)}_{\boldsymbol{G}}(\boldsymbol{k}, n; \boldsymbol{0}\alpha) \tag{7.30}$$

and inserting it into equation (7.29) implies

$$\boldsymbol{\rho}^{(1)}(\boldsymbol{r}; \boldsymbol{0}^{+}\alpha) = -\boldsymbol{\nabla}\rho^{(0)}(\boldsymbol{r}) \tag{7.31}$$

for monoatomic systems[15]. This is due to the fact that the third and fourth line of equation (7.29) vanish for the IR part, and its second line is conform with the gradient of the unperturbed charge density. In most systems, the first line of equation (7.29) involves IR core-tail corrections and is irrelevant otherwise. Within the displaced MT sphere, the second line cancels the term within the third and fourth line which is not proportional to the gradient of the basis function. Thus exactly this term proportional to the gradient of the basis function remains, and forms the valence contribution of minus the density gradient. Combining it with the core-electron part from the first line results in minus the full unperturbed density gradient. All in all given the Goldstone modes, this reflects an infinitesimal shift of the complete crystal, which is specified by the polarization vectors. For polyatomic systems, the IR and the displaced MT sphere behave in the same way, but the non-displaced MT spheres feature a distinct charge-density variation. It is composed of the second line as well as the core-tail corrections from the first line and reflects the scenario that atoms within one unit cell still can move independently. Nevertheless, the center-of-mass movement must still correspond to the infinitesimal displacement described before. However, it is feasible to find polarization vectors for which all atoms of systems with a polyatomic lattice basis are uniformly displaced [251].

Interstitial Region

Final valence-electron form

Focussing on the valence first-order charge-density variation in the IR

$$\boldsymbol{\rho}^{(1)}_{\mathrm{IR,v}}(\boldsymbol{r}, \boldsymbol{q}^{+}\alpha) = 4\sum_{\boldsymbol{k},n} f^{(0)}_{\boldsymbol{k},n}\Psi^{*(0)}_{\boldsymbol{k},n}(\boldsymbol{r})\Psi^{(1)\alpha}_{\boldsymbol{k},n}(\boldsymbol{r}) \tag{7.31a}$$

and expanding it according to equation (7.29) leads to

$$= \frac{4}{\Omega}\sum_{\boldsymbol{k},n} f^{(0)}_{\boldsymbol{k},n}\sum_{\boldsymbol{G}'} z^{*(0)}_{\boldsymbol{G}'}(\boldsymbol{k}, n)\mathrm{e}^{-\mathrm{i}\left(\boldsymbol{k}+\boldsymbol{G}'\right)\cdot\boldsymbol{r}}\sum_{\boldsymbol{G}}\boldsymbol{z}^{(1)}_{\boldsymbol{G}-\boldsymbol{G}_{\mathrm{bf}}}\left(\boldsymbol{k}^{+}_{\mathrm{bf}}, n; \alpha\right)\mathrm{e}^{\mathrm{i}\left(\boldsymbol{k}^{+}_{\mathrm{bf}}-\boldsymbol{G}_{\mathrm{bf}}+\boldsymbol{G}\right)\cdot\boldsymbol{r}} \tag{7.31b}$$

$$= \frac{4}{\Omega}\sum_{\boldsymbol{k},n} f^{(0)}_{\boldsymbol{k},n}\sum_{\boldsymbol{G}'\boldsymbol{G}} z^{*(0)}_{\boldsymbol{G}'}(\boldsymbol{k}, n)\boldsymbol{z}^{(1)}_{\boldsymbol{G}-\boldsymbol{G}_{\mathrm{bf}}}\left(\boldsymbol{k}^{+}_{\mathrm{bf}}, n; \alpha\right)\mathrm{e}^{\mathrm{i}\left(-\boldsymbol{k}-\boldsymbol{G}'+\boldsymbol{k}+\boldsymbol{q}+\boldsymbol{G}\right)\cdot\boldsymbol{r}} . \tag{7.31c}$$

By introducing $\boldsymbol{G}'' = \boldsymbol{G} - \boldsymbol{G}'$

$$= \frac{4}{\Omega}\sum_{\boldsymbol{k},n} f^{(0)}_{\boldsymbol{k},n}\sum_{\boldsymbol{G}''+\boldsymbol{G}'}\sum_{\boldsymbol{G}'} z^{*(0)}_{\boldsymbol{G}'}(\boldsymbol{k}, n)\boldsymbol{z}^{(1)}_{\boldsymbol{G}''+\boldsymbol{G}'-\boldsymbol{G}_{\mathrm{bf}}}\left(\boldsymbol{k}^{+}_{\mathrm{bf}}, n; \alpha\right)\mathrm{e}^{\mathrm{i}\left(\boldsymbol{G}''+\boldsymbol{q}\right)\cdot\boldsymbol{r}} \tag{7.31d}$$

---

[15] The information about the displaced atom is normally suppressed in $\boldsymbol{z}^{(0)}_{\boldsymbol{G}}(\boldsymbol{k}, n; \boldsymbol{0}\alpha)$. Furthermore, the spin degeneracy factor is included implicitly.

and $\boldsymbol{G}''' = \boldsymbol{G}'' + \boldsymbol{G}' - \boldsymbol{G}_{\text{bf}} \Leftrightarrow \boldsymbol{G}'' = \boldsymbol{G}''' - \boldsymbol{G}' + \boldsymbol{G}_{\text{bf}}$ [251]

$$= \frac{4}{\Omega} \sum_{\boldsymbol{k},n} f^{(0)}_{\boldsymbol{k},n} \sum_{\boldsymbol{G}'''|^{+}\boldsymbol{G}_{\text{bf}}} \sum_{\boldsymbol{G}'} z^{*(0)}_{\boldsymbol{G}'}(\boldsymbol{k},n) \boldsymbol{z}^{(1)}_{\boldsymbol{G}'''}\left(\boldsymbol{k}^{+}_{\text{bf}}, n; \alpha\right) \mathrm{e}^{\mathrm{i}\left(\boldsymbol{G}'''-\boldsymbol{G}'+\boldsymbol{G}_{\text{bf}}+\boldsymbol{q}\right)\cdot\boldsymbol{r}} \tag{7.31e}$$

its expansion coefficients

$$\boldsymbol{\rho}^{(1)}_{\text{IR,v}}(\boldsymbol{r}, \boldsymbol{q}^{+}\alpha) =: \sum_{\boldsymbol{G}'} \sum_{\boldsymbol{G}'''|^{+}\boldsymbol{G}_{\text{bf}}} \boldsymbol{\rho}^{(1)}_{\text{IR,v}}(\boldsymbol{G}''' - \boldsymbol{G}' + \boldsymbol{G}_{\text{bf}}, \boldsymbol{q}^{+}\alpha) \mathrm{e}^{\mathrm{i}\left(\boldsymbol{G}'''-\boldsymbol{G}'+\boldsymbol{G}_{\text{bf}}+\boldsymbol{q}\right)\cdot\boldsymbol{r}} \tag{7.31f}$$

$$= \sum_{\boldsymbol{G}''} \boldsymbol{\rho}^{(1)}_{\text{IR,v}}(\boldsymbol{G}'', \boldsymbol{q}^{+}\alpha) \mathrm{e}^{\mathrm{i}\left(\boldsymbol{G}''+\boldsymbol{q}\right)\cdot\boldsymbol{r}} \tag{7.31g}$$

can be defined.

Algorithm

This expression guides the way of the implementation. Having conducted the index shifts in equations (7.31d) and (7.31e), enables us a linear run through the reciprocal lattice-vector indices of the unperturbed and the first-order wave-function expansion coefficients [251]. But this is at the expense of not sequentially addressing the $\boldsymbol{\rho}^{(1)}_{\text{IR,v}}(\boldsymbol{G}'', \boldsymbol{q}^{+}\alpha)$, because $\boldsymbol{G}'' = \boldsymbol{G}''' - \boldsymbol{G}' + \boldsymbol{G}_{\text{bf}}$. Furthermore, despite the index shift indicated at the sum over $\boldsymbol{G}'''$, the addressed index of the first-order wave-function expansion coefficient is not shifted [127]. The shift intrinsically expresses in the set of $\boldsymbol{G}'$ and $\boldsymbol{G}'''$ which is attributed to a certain wave-function expansion coefficient or its first-variation, respectively [127]. This reflects in the cutoff condition $|\boldsymbol{k} + \boldsymbol{q} + \boldsymbol{G}| \leq k_{\text{max}}$, which governs the shift of the ball the $\boldsymbol{G}$ are chosen from as a function of $\boldsymbol{k} + \boldsymbol{q}$ [127]. The two sums in equation (7.31e) can formally be united to one sum in equation (7.31g) so that the unperturbed and the first-order wave function are convoluted with each other. Since this "double sum" method is easy to implement, it is used within this thesis. As part of future work however, the convolution shall be realized by a FFT, performing better in particular for large systems. This FFT subroutine is programmed but not sufficiently tested at the moment.

Cutoff condition

The first-order charge-density cutoff deduces from the cutoffs of the wave functions it is composed of, as visualized in equation (7.31a). While the unperturbed wave function at $\boldsymbol{k}$ is expanded in a set of reciprocal lattice vectors fulfilling $|\boldsymbol{k} + \boldsymbol{G}| < k_{\text{max}}$, the first-order variation must strictly-speaking employ the aforementioned shifted set of reciprocal lattice vectors. The condition $|\boldsymbol{k} + \boldsymbol{q} + \boldsymbol{G}| < k_{\text{max}}$ the latter lives up to mirrors the shift of the Bloch character by $\boldsymbol{q}$. Due to the back-folding mentioned in the beginning of this section, the first-order wave function is actually expanded in a set of reciprocal lattice vectors fulfilling $|\boldsymbol{k} + \boldsymbol{q} + \boldsymbol{G}| = \left|\boldsymbol{k}^{+}_{\text{bf}} - \boldsymbol{G}_{\text{bf}} + \boldsymbol{G}\right| < k_{\text{max}}$, which are at hand [251]. Consequently, the idea of displacing the ball of reciprocal lattice vectors for the product of the aforementioned wave functions must coincide, implying the condition $|\boldsymbol{q} + \boldsymbol{G}| < 2k_{\text{max}}$ for the first-order density variation. As the complete charge-density variation can contain core-tail corrections (7.23c)

$$\boldsymbol{\rho}^{(1)}_{\text{IR}}(\boldsymbol{r}, \boldsymbol{q}^{+}\alpha) = \sum_{\boldsymbol{G}} \left(\boldsymbol{\rho}^{(1)}_{\text{IR,v}}(\boldsymbol{G}, \boldsymbol{q}^{+}\alpha) + \boldsymbol{\rho}^{(1)}_{\text{IR,ctC}}(\boldsymbol{G}, \boldsymbol{q}^{+}\alpha)\right) \mathrm{e}^{\mathrm{i}(\boldsymbol{G}+\boldsymbol{q})\cdot\boldsymbol{r}}\,, \tag{7.32}$$

we decided to extend the upper limit of $2k_{\text{max}}$ to $G_{\text{max}} > 2k_{\text{max}}$ [127]. This is in line with the cutoff of the unperturbed charge density in `FLEUR`, relating to all other unperturbed quantities used in `juPhon`.

Symmetry breaking

Apart from that, for the vector sum $\boldsymbol{G}'' = \boldsymbol{G}''' - \boldsymbol{G}' + \boldsymbol{G}_{\text{bf}}$ in equation (7.31f) generally $G_{\text{max}} > \left|\boldsymbol{q} + \boldsymbol{G}''\right| > 2k_{\text{max}}$ holds. But obviously, this contradicts with the set of reciprocal lattice vectors necessary for the core-tail corrections, on which I already elaborate in section 7.2.2. It must be clear that deciding for the option to ignore this shift technically breaks a symmetry in reciprocal space. This can be learned from inserting the Bloch vector $-\boldsymbol{q}^{+}$ into equation (7.31g) and rearranging it so that $\boldsymbol{\rho}_{\mathrm{IR}}^{*(1)}(\boldsymbol{r};\boldsymbol{q}^{+}\alpha)$ results [251]. But $-\boldsymbol{q}^{+}$ is currently not in the set of $q_i^{+} \in [0, 1[$ implemented in `juPhon`, as it would have been, if $q_i^{+} \in [-0.5, 0.5[$ had held. Therefore, a $-\boldsymbol{q}^{+}$ located outside the current definition of the Brillouin zone is back-folded in a similar fashion as illustrated in figure 7.2

$$\boldsymbol{q}_{\mathrm{f}}^{+} = -\boldsymbol{q}^{+} + \boldsymbol{G}_{\mathrm{f}}\,. \tag{7.33}$$

Using this relation and that the complete linear combination of the first-order variation is real, the reciprocal symmetry actually demands [251]

$$\begin{aligned}
\boldsymbol{\rho}_{\mathrm{IR}}^{(1)}\big(\boldsymbol{r};\boldsymbol{q}_{\mathrm{f}}^{+}\alpha\big) &= \sum_{\boldsymbol{G}} \boldsymbol{\rho}_{\mathrm{IR}}^{(1)}\big(\boldsymbol{G};\boldsymbol{q}_{\mathrm{f}}^{+}\alpha\big)\mathrm{e}^{\mathrm{i}(\boldsymbol{G}-\boldsymbol{q}^{+}+\boldsymbol{G}_{\mathrm{f}})\cdot\boldsymbol{r}} && \text{(7.34a)}\\
&= \sum_{\boldsymbol{G}} \boldsymbol{\rho}_{\mathrm{IR}}^{(1)}\big(\boldsymbol{G};\boldsymbol{q}_{\mathrm{f}}^{+}\alpha\big)\mathrm{e}^{-\mathrm{i}(-\boldsymbol{G}-\boldsymbol{G}_{\mathrm{f}}+\boldsymbol{q}^{+})\cdot\boldsymbol{r}} && \text{(7.34b)}\\
&\overset{!}{=} \sum_{\boldsymbol{G}} \boldsymbol{\rho}_{\mathrm{IR}}^{*(1)}\big(-\boldsymbol{G}-\boldsymbol{G}_{\mathrm{f}};\boldsymbol{q}^{+}\alpha\big)\mathrm{e}^{-\mathrm{i}(-\boldsymbol{G}-\boldsymbol{G}_{\mathrm{f}}+\boldsymbol{q}^{+})\cdot\boldsymbol{r}} && \text{(7.34c)}\\
&= \sum_{\boldsymbol{G}'|^{+}\boldsymbol{G}_{\mathrm{f}}} \boldsymbol{\rho}_{\mathrm{IR}}^{*(1)}\big(\boldsymbol{G}';\boldsymbol{q}^{+}\alpha\big)\mathrm{e}^{-\mathrm{i}\left(\boldsymbol{G}'+\boldsymbol{q}^{+}\right)\cdot\boldsymbol{r}} && \text{(7.34d)}\\
&= \boldsymbol{\rho}_{\mathrm{IR}}^{*(1)}\big(\boldsymbol{r};\boldsymbol{q}^{+}\alpha\big)\,. && \text{(7.34e)}
\end{aligned}$$

I programmed this test, which in essence checks whether

$$\boldsymbol{\rho}_{\mathrm{IR}}^{(1)}\big(\boldsymbol{G};\boldsymbol{q}_{\mathrm{f}}^{+}\alpha\big) = \boldsymbol{\rho}_{\mathrm{IR}}^{*(1)}\big(-\boldsymbol{G}-\boldsymbol{G}_{\mathrm{f}};\boldsymbol{q}^{+}\alpha\big) \tag{7.35}$$

is fulfilled. In the end, I found that the set of employed reciprocal lattice vectors must be shifted according to the currently investigated $\boldsymbol{q}$ for this test to work, i.e., $|\boldsymbol{G} \pm \boldsymbol{q}| < G_{\mathrm{max}}$ must be chosen[16]. In practice, we ignore this at the moment and resort to a large enough G_{max}. This lets the first-order variation coefficients with reciprocal lattice vectors at the boundary of $|\boldsymbol{q} + \boldsymbol{G}| < G_{\mathrm{max}}$ become insignificant, thereby concealing the described symmetry breaking.

Muffin-tin Spheres

Setting the stage

In contrast to the IR, the third and fourth lines of equation (7.29) become additionally relevant for the displaced atoms. As a consequence, the gradient of the core-electron charge density (first line) and the valence-electron charge density (third and fourth lines) can be condensed into the all-electron charge-density gradient. It should be emphasized at this point that this contribution then also effectively involves the core-tail corrections.

Vectorial large matching coefficients

Before inserting the LAPW basis of the MT spheres (5.9) into equation (7.29), the vectorial large matching coefficients

$$\boldsymbol{A}_{lmp}^{\boldsymbol{k}\gamma n} = \sum_{\boldsymbol{G}} \boldsymbol{G} z_{\boldsymbol{G}}^{(0)}(\boldsymbol{k}, n) a_{lmp}^{\boldsymbol{G}\boldsymbol{k}\gamma} \tag{7.36a}$$

---

[16] Since this test does not involve core-tails or their corrections, G_{max} can be substituted by $2k_{\mathrm{max}}$ in principle. But we decided to adhere to the usually employed cutoff G_{max}.

$$\boldsymbol{A}^{\boldsymbol{k}\gamma n}_{lmp}(\boldsymbol{q}^{+}\alpha) := \sum_{\boldsymbol{G}} \boldsymbol{z}^{(1)}_{\boldsymbol{G}}(\boldsymbol{k}, n; \boldsymbol{q}^{+}\alpha) a^{\boldsymbol{G}\boldsymbol{k}\gamma}_{lmp}(\boldsymbol{q}) \tag{7.36b}$$

$$= \sum_{\boldsymbol{G}} \boldsymbol{z}^{(1)}_{\boldsymbol{G}-\boldsymbol{G}_{\text{bf}}}\left(\boldsymbol{k}^{+}_{\text{bf}}, n; \alpha\right) a^{\boldsymbol{G}-\boldsymbol{G}_{\text{bf}}\boldsymbol{k}^{+}_{\text{bf}}\gamma}_{lmp} \tag{7.36c}$$

$$=: \sum_{\boldsymbol{G}'|^{+}\boldsymbol{G}_{\text{bf}}} \boldsymbol{z}^{(1)}_{\boldsymbol{G}'}\left(\boldsymbol{k}^{+}_{\text{bf}}, n; \alpha\right) a^{\boldsymbol{G}'\boldsymbol{k}^{+}_{\text{bf}}\gamma}_{lmp} \tag{7.36d}$$

$$\tilde{\boldsymbol{A}}^{\boldsymbol{k}\gamma n}_{lmp} := \mathrm{i}\left(A^{\boldsymbol{k}n\gamma}_{lmp}\boldsymbol{k} + \boldsymbol{A}^{\boldsymbol{k}n\gamma}_{lmp}\right) \tag{7.36e}$$

$$\bar{\boldsymbol{A}}^{\boldsymbol{k}\gamma n}_{lmp}(\boldsymbol{q}^{+}\alpha) := \boldsymbol{A}^{\boldsymbol{k}n\gamma}_{lmp}(\boldsymbol{q}^{+}\alpha) + \delta_{\gamma\alpha}\tilde{\boldsymbol{A}}^{\boldsymbol{k}n\gamma}_{lmp} \tag{7.36f}$$

are defined. Equations (7.36a) and (7.36b) are borrowed from Klüppelberg [88]. Using equation (7.25) in the latter, a index shift $\boldsymbol{G}' = \boldsymbol{G} - \boldsymbol{G}_{\text{bf}}$ can be conducted. In contrast to the IR, it does not have a persistent impact such as in equation (7.31f). This is due to the fact that the reciprocal lattice-vector indices are equally shifted both in the first-order wave-function expansion coefficients and the small matching coefficients [127, 282]. But again strictly-speaking, the shifted set of reciprocal lattice vectors inheres in the first-order variation of the wave-function expansion coefficients (Bloch-character change $\boldsymbol{q}$). Finally, this leads to the respective formulation of the matching coefficients in equation (7.36d), only containing quantities at hand. Together with the scalar large matching coefficient (5.30), the MT sphere projection of the valence part in equation (7.29) to $\mathrm{Y}_{lm}(\hat{\boldsymbol{r}})$ reads

Final valence-electron form

$$\left[\boldsymbol{\rho}^{(1)}_{\gamma,\text{v}}(\boldsymbol{r}_{\nu\mathring{\gamma}}, \boldsymbol{q}^{+}\alpha)\right]_{lm} \tag{7.37a}$$

$$\begin{aligned}
&= \sum_{l'p'l''p''}\sum_{s} u^{s\mathring{\gamma}}_{l'p'}(r_{\nu\mathring{\gamma}}) u^{s\mathring{\gamma}}_{l''p''}(r_{\nu\mathring{\gamma}}) \sum_{m'm''} G^{m'',m,m'}_{l'',\ \ l,\ \ l'}\, 2 \sum_{\boldsymbol{k}n_{\text{v}}} f^{(0)}_{\boldsymbol{k},n} A^{*\boldsymbol{k}\gamma n}_{l'm'p'} \boldsymbol{A}^{\boldsymbol{k}\gamma n}_{l''m''p''}(\boldsymbol{q}^{+}\alpha) \\
&\quad + \delta_{\gamma\alpha} \sum_{lm} 2\mathrm{i} \sum_{l'p'l''p''}\sum_{s} u^{s\mathring{\gamma}}_{l'p'}(r_{\nu\mathring{\gamma}}) u^{s\mathring{\gamma}}_{l''p''}(r_{\nu\mathring{\gamma}}) \sum_{m'm''} G^{m'',m,m'}_{l'',\ \ l,\ \ l'} \\
&\qquad\qquad \times \sum_{\boldsymbol{k}n} f^{(0)}_{\boldsymbol{k},n} A^{*\boldsymbol{k}\gamma n}_{l',m',p'}\left(\boldsymbol{k}A^{\boldsymbol{k}\gamma n}_{l'm'p'} + \boldsymbol{A}^{\boldsymbol{k}\gamma n}_{l''m''p''}\right)\mathrm{Y}_{lm}\left(\hat{\boldsymbol{r}}_{\gamma}\right) \\
&\quad - \left[\boldsymbol{\nabla}\rho^{(0)}_{\gamma}(r_{\nu\mathring{\gamma}})\right]_{lm}.
\end{aligned}$$

Using equation (7.36f) then leads to

$$\begin{aligned}
&= \sum_{l'p'l''p''}\sum_{s} u^{s\mathring{\gamma}}_{l'p'}(r_{\nu\mathring{\gamma}}) u^{s\mathring{\gamma}}_{l''p''}(r_{\nu\mathring{\gamma}}) \sum_{m'm''} G^{m'',m,m'}_{l'',\ \ l,\ \ l'}\, 4 \sum_{\boldsymbol{k}n} f^{(0)}_{\boldsymbol{k},n} A^{*\boldsymbol{k}\gamma n}_{l'm'p'} \bar{\boldsymbol{A}}^{\boldsymbol{k}\gamma n}_{l''m''p''}(\boldsymbol{q}^{+}\alpha) \\
&\quad - \left[\boldsymbol{\nabla}\rho^{(0)}_{\gamma}(r_{\nu\mathring{\gamma}})\right]_{lm}.
\end{aligned} \tag{7.37b}$$

Finally, the valence-electron part must be combined with the core-tail corrections for the MT spheres (7.24)

$$\left[\boldsymbol{\rho}^{(1)}_{\gamma}(\boldsymbol{r}_{\nu\mathring{\gamma}}, \boldsymbol{q}^{+}\alpha)\right]_{lm} = \left[\boldsymbol{\rho}^{(1)}_{\gamma,\text{v}}(\boldsymbol{r}_{\nu\mathring{\gamma}}, \boldsymbol{q}^{+}\alpha)\right]_{lm} + \left[\boldsymbol{\rho}^{(1)}_{\gamma,\text{ctC}}\left(\boldsymbol{r}_{\nu_{\mathring{\gamma}}}, \boldsymbol{q}^{+}\alpha\right)\right]_{lm}. \tag{7.38}$$

Cutoff

According to section 7.2.1 however, a contradiction occurs since the gradient of the charge density must strictly-speaking be expanded until $l_{\text{max},\mathring{\gamma}} + 1$, while there is no obvious mathematical reason why this should be done for the remaining part of the first-order density variation. We decided therefore to converge $l_{\text{max},\mathring{\gamma}}$ such that the contributions at $l_{\text{max},\mathring{\gamma}}$ and particularly $l_{\text{max},\mathring{\gamma}} + 1$ become too small to be significant [127].

Algorithm

Consistent with our first approach to recycle as much as possible [119, 127, 251], the implementation of the first-order density variation is likewise based on various `FLEUR` subroutines. Doing this, it has essentially been necessary to remove the symmetry optimizations concerning the lattice harmonics. If the documentation of the `FLEUR` routines was poor, I was supported by my advisors [127, 251]. In principle, the `Abcof` subroutine can be employed in its original form, when looping over the displacement directions [127, 251]. However, it must be considered that the term i^{l} in equation (5.55) is *not* part of this subroutine [251]. According to the vectorial matching coefficients (7.36), the coefficients $z_{\boldsymbol{G}}^{(0)}(\boldsymbol{k}, n)$ must for instance be decorated with a $\boldsymbol{G}$ before passing it to `Abcof`. By introducing summarizing matching coefficients such as in equation (7.36f), the $a_{lmp}^{\boldsymbol{G}\boldsymbol{k}\gamma}(\boldsymbol{q})$ can be factored out [251]. This minimizes the number of `Abcof` calls [251]. For a later extension to polyatomic systems, the set of symmetry-guided rotations, which is passed to `Abcof` for the sake of an optimization, is substituted by a set of unity operations [127]. Although `Abcof` does not cause a bottleneck in `FLEUR`, I have found that performance decreases significantly if it is called too often. In contrast to `FLEUR`, this is possible in `juPhon` given a naive implementation. It suggests itself that the `FLEUR` subroutines are essentially taken from the part which calculates the unperturbed charge density (see section 5.5). As a consequence, the spherical part ($l = 0$) of the MT charge density is calculated separately from the non-spherical part. Although this can be designed more efficiently on modern hardware architectures, various combinations of p and p' are furthermore individually dealt with and attributed to respective arrays, which are listed in table 7.7. The indices p' and p'' in the Kronecker deltas are either 1 or 2. The corresponding combinations of Kronecker deltas can be derived from equation (7.37b) in the following way

$$\left[\boldsymbol{\rho}_{\gamma,\mathrm{v}}^{(1)}(r_{\nu\mathring{\gamma}}, \boldsymbol{q}^{+}\alpha)\right]_{lm} \tag{7.39a}$$

$$= \sum_{s} \sum_{l'p'l''p''} u_{l'p'}^{s\mathring{\gamma}}(r_{\nu\mathring{\gamma}}) u_{l''p''}^{s\mathring{\gamma}}(r_{\nu\mathring{\gamma}}) \sum_{mm'} G_{l'',\ l,\ l'}^{m'',m,m'} 4 \sum_{\boldsymbol{k}n_{\mathrm{v}}} f_{\boldsymbol{k},n}^{(0)} A_{l',m',p'}^{*\boldsymbol{k}\gamma n} \bar{\boldsymbol{A}}_{l'',m'',p''}^{\boldsymbol{k}'\gamma n}(\boldsymbol{q}\alpha)$$

$$= \sum_{l'm'p'} \sum_{l''m''p''} \left(1 - \delta_{l0}\delta_{m0}\right)\left(\delta_{p'1}\delta_{p''1} + \delta_{p'1}\delta_{p''2} + \delta_{p'2}\delta_{p''1} + \delta_{p'2}\delta_{p''2}\right) \tag{7.39b}$$

$$\times \sum_{s} u_{l'p'}^{s\mathring{\gamma}}(r_{\nu\mathring{\gamma}}) u_{l''p''}^{s\mathring{\gamma}}(r_{\nu\mathring{\gamma}}) G_{l'',\ l,\ l'}^{m'',m,m'} 4 \sum_{\boldsymbol{k}n_{\mathrm{v}}} f_{\boldsymbol{k},n}^{(0)} A_{l',m',p'}^{*\boldsymbol{k}\gamma n} \bar{\boldsymbol{A}}_{l'',m'',p''}^{\boldsymbol{k}'\gamma n}(\boldsymbol{q}\alpha)$$

$$+ \delta_{l0}\delta_{m0} \sum_{l'm'p'p''} \frac{1}{\sqrt{4\pi}}\left(\delta_{p'1}\delta_{p''1} + \delta_{p'1}\delta_{p''2} + \delta_{p'2}\delta_{p''1} + \delta_{p'2}\delta_{p''2}\right)$$

$$\times \sum_{s} u_{l'p'}^{s\mathring{\gamma}}(r_{\nu\mathring{\gamma}}) u_{l'p''}^{s\mathring{\gamma}}(r_{\nu\mathring{\gamma}})\, 4 \sum_{\boldsymbol{k}n_{\mathrm{v}}} f_{\boldsymbol{k},n}^{(0)} A_{l',m',p'}^{*\boldsymbol{k}\gamma n} \bar{\boldsymbol{A}}_{l',m',p''}^{\boldsymbol{k}'\gamma n}(\boldsymbol{q}\alpha)\,.$$

The implementation of the $\boldsymbol{k}$-dependent matching coefficients is based on the recycled subroutines `Abcof`, `Rhomt`, and `Rhonmt`. However, the radial solutions $u_{l'p'}^{s\mathring{\gamma}}(r_{\nu\mathring{\gamma}})$ are efficiently multiplied outside the $\boldsymbol{k}$ loop based on the recycled `Cdnmt` subroutine (taken from the `FLEUR` version specified on page 133). The separation of the spherical coefficient $l = 0$ from the remaining non-spherical contributions $l \neq 0$ in this subroutine saves one call of the subroutine `Gaunt1`, which calculates the Gaunt coefficients. This originates from the fact that for $l = 0$, the surface integral (5.32d) simplifies to the orthogonality relation of the spherical harmonics

$$\delta_{l0}\delta_{m0} G_{l'',\ 0,\ l'}^{m'',0,m'} = \delta_{l0}\delta_{m0}\frac{1}{\sqrt{4\pi}} \oint \mathrm{Y}_{l''m''}(\hat{\boldsymbol{r}})\mathrm{Y}_{l'm'}^{*}(\hat{\boldsymbol{r}})\,\mathrm{d}\Omega = \frac{1}{\sqrt{4\pi}}\delta_{l0}\delta_{m0}\delta_{l''l'}\delta_{m''m'}\,. \tag{7.40}$$

which can be directly integrated into the formalism. As moreover the $u^{s\mathring{\gamma}}_{l'p'}(r_{\nu\mathring{\gamma}})$ are stored with an additional $r_{\nu\mathring{\gamma}}$, the valence contribution of the density variation accumulates a factor $r^2_{\nu\mathring{\gamma}}$. Therefore, the final first-order density-variation coefficients are divided by this factor in the end at the moment, in order to avoid errors in the first implementation.

Table 7.7: Relating Kronecker deltas in equation (7.39b) and variable names in `juPhon`.

`uu`	$\delta_{l0}\delta_{m0}\delta_{p'1}\delta_{p''1}$	`uunmt`	$\left(1-\delta_{l0}\delta_{m0}\right)\delta_{p'1}\delta_{p''1}$
`ud`	$\delta_{l0}\delta_{m0}\delta_{p'1}\delta_{p''2}$	`dunmt`	$\left(1-\delta_{l0}\delta_{m0}\right)\delta_{p'2}\delta_{p''1}$
`du`	$\delta_{l0}\delta_{m0}\delta_{p'2}\delta_{p''1}$	`udnmt`	$\left(1-\delta_{l0}\delta_{m0}\right)\delta_{p'1}\delta_{p''2}$
`dd`	$\delta_{l0}\delta_{m0}\delta_{p'2}\delta_{p''2}$	`ddnmt`	$\left(1-\delta_{l0}\delta_{m0}\right)\delta_{p'2}\delta_{p''2}$

7.2.4 Visualization

Formalism

In order to illustrate the first-order variation of the density in real space, equation (6.20) must be used. However due to the TRS, `juPhon` only calculates the $\boldsymbol{q}^+$ part of the first-order density variation. But, the IR representation can be reformulated so that

$$\begin{aligned}
&\rho^{(1)}_{\text{IR}}(\boldsymbol{r}_\nu;\boldsymbol{q}^+\alpha) && (7.41\text{a})\\
&\quad=\sum_{\alpha}\boldsymbol{Q}^{\top}_{\alpha}\cdot\boldsymbol{\rho}^{(1)}_{\text{IR}}(\boldsymbol{r}_\nu;\boldsymbol{q}^+\alpha)+\sum_{\alpha}\boldsymbol{Q}^{\dagger}_{\alpha}\cdot\boldsymbol{\rho}^{(1)}_{\text{IR}}(\boldsymbol{r}_\nu;\boldsymbol{q}^-\alpha)\\
&\quad=\sum_{\alpha\boldsymbol{G}}\left(\boldsymbol{Q}^{\top}_{\alpha}\cdot\boldsymbol{\rho}^{(1)}_{\text{IR}}(\boldsymbol{G};\boldsymbol{q}^+\alpha)\right)\mathrm{e}^{\mathrm{i}(\boldsymbol{G}+\boldsymbol{q})\cdot\boldsymbol{r}_\nu}+\sum_{\alpha\boldsymbol{G}}\left(\boldsymbol{Q}^{\dagger}_{\alpha}\cdot\boldsymbol{\rho}^{(1)}_{\text{IR}}(\boldsymbol{G};\boldsymbol{q}^-\alpha)\right)\mathrm{e}^{\mathrm{i}(\boldsymbol{G}-\boldsymbol{q})\cdot\boldsymbol{r}_\nu} && (7.41\text{b})\\
&\quad=\sum_{\alpha\boldsymbol{G}}\left(\boldsymbol{Q}^{\top}_{\alpha}\cdot\boldsymbol{\rho}^{(1)}_{\text{IR}}(\boldsymbol{G};\boldsymbol{q}^+\alpha)\right)\mathrm{e}^{\mathrm{i}(\boldsymbol{G}+\boldsymbol{q})\cdot\boldsymbol{r}_\nu}+\sum_{\alpha\boldsymbol{G}}\left(\boldsymbol{Q}^{\dagger}_{\alpha}\cdot\boldsymbol{\rho}^{*(1)}_{\text{IR}}(-\boldsymbol{G};\boldsymbol{q}^+\alpha)\right)\mathrm{e}^{\mathrm{i}(\boldsymbol{G}-\boldsymbol{q})\cdot\boldsymbol{r}_\nu} && (7.41\text{c})\\
&\quad=\sum_{\alpha\boldsymbol{G}}\left(\boldsymbol{Q}^{\top}_{\alpha}\cdot\boldsymbol{\rho}^{(1)}_{\text{IR}}(\boldsymbol{G};\boldsymbol{q}^+\alpha)\right)\mathrm{e}^{\mathrm{i}(\boldsymbol{G}+\boldsymbol{q})\cdot\boldsymbol{r}_\nu}+\sum_{\alpha,-\boldsymbol{G}}\left(\boldsymbol{Q}^{\dagger}_{\alpha}\cdot\boldsymbol{\rho}^{*(1)}_{\text{IR}}(\boldsymbol{G};\boldsymbol{q}^+\alpha)\right)\mathrm{e}^{-\mathrm{i}(\boldsymbol{G}+\boldsymbol{q})\cdot\boldsymbol{r}_\nu} && (7.41\text{d})\\
&\quad=2\,\mathrm{Re}\left(\sum_{\alpha\boldsymbol{G}}\left(\boldsymbol{Q}^{\top}_{\alpha}\cdot\boldsymbol{\rho}^{(1)}_{\text{IR}}(\boldsymbol{G};\boldsymbol{q}^+\alpha)\right)\mathrm{e}^{\mathrm{i}(\boldsymbol{G}+\boldsymbol{q})\cdot\boldsymbol{r}_\nu}\right) && (7.41\text{e})
\end{aligned}$$

results and thus everything is available. Analogously, the MT part can be rearranged, leading to

$$\begin{aligned}
&\rho^{(1)}_{\gamma}(\boldsymbol{r}_\nu;\boldsymbol{q}^+\alpha) && (7.42\text{a})\\
&\quad=\sum_{\alpha}\boldsymbol{Q}^{\top}_{\alpha}\cdot\boldsymbol{\rho}^{(1)}_{\gamma}(\boldsymbol{r}_\nu;\boldsymbol{q}^+\alpha)+\sum_{\alpha}\boldsymbol{Q}^{\dagger}_{\alpha}\cdot\boldsymbol{\rho}^{(1)}_{\gamma}(\boldsymbol{r}_\nu;\boldsymbol{q}^-\alpha)\\
&\quad=\sum_{\alpha}\boldsymbol{Q}^{\top}_{\alpha}\cdot\boldsymbol{\rho}^{(1)}_{\gamma}(\boldsymbol{r}_\nu;\boldsymbol{q}^+\alpha)+\sum_{\alpha}\boldsymbol{Q}^{\dagger}_{\alpha}\cdot\boldsymbol{\rho}^{*(1)}_{\gamma}(\boldsymbol{r}_\nu;\boldsymbol{q}^+\alpha) && (7.42\text{b})\\
&\quad=\sum_{lm}\left(\sum_{\alpha}\boldsymbol{Q}^{\top}_{\alpha}\cdot\left[\boldsymbol{\rho}^{(1)}_{\gamma}(\boldsymbol{r}_\nu;\boldsymbol{q}^+\alpha)\right]_{lm}\right)\mathrm{Y}_{lm}(\hat{\boldsymbol{r}}_\nu) && (7.42\text{c})\\
&\qquad+\sum_{lm}\left(\sum_{\alpha}\boldsymbol{Q}^{\dagger}_{\alpha}\cdot\left[\boldsymbol{\rho}^{*(1)}_{\gamma}(\boldsymbol{r}_\nu;\boldsymbol{q}^+\alpha)\right]_{lm}\right)\mathrm{Y}^{*}_{lm}(\hat{\boldsymbol{r}}_\nu)\\
&\quad=\sum_{lm}\left(\sum_{\alpha}\boldsymbol{Q}^{\top}_{\alpha}\cdot\left(\left[\boldsymbol{\rho}^{(1)}_{\gamma}(\boldsymbol{r}_\nu;\boldsymbol{q}^+\alpha)\right]_{lm}+(-1)^{-m}\left[\boldsymbol{\rho}^{*(1)}_{\gamma}(\boldsymbol{r}_\nu;\boldsymbol{q}^+\alpha)\right]_{l,-m}\right)\right)\mathrm{Y}_{lm}(\hat{\boldsymbol{r}}_\nu)\,, && (7.42\text{d})
\end{aligned}$$

thereby exploiting (see e.g. references [172, 283])

$$\mathrm{Y}^*_{lm}(\hat{\boldsymbol{r}}) = (-1)^m \mathrm{Y}_{l,-m}(\hat{\boldsymbol{r}})\,. \tag{7.43}$$

Algorithm

When plotting the real-space representation of a quantity given in the LAPW basis, it must be clear which part of the unit cell can be attributed to the IR or lies within any MT sphere. The adequate algorithm can be found in the `FLEUR` subroutine `Plotdop`, although it only accepts quantities given in stars and lattice harmonics. I removed these symmetry optimizations and substituted the existing real-space evaluations by equations (7.41) and (7.42) so that first-order variation quantities can be properly plotted. As an example, the phonon vector $\boldsymbol{q} = (0.25, 0.25, 0)^\top$ (internal units) is chosen for fcc Ne and fcc Al systems, in which the atoms are displaced along the cartesian z-direction. Since `juPhon` provides the plot data for each of the cartesian directions, a linear combination of them is required to achieve the aforementioned displacement along the aforementioned fcc lattice vector. Basically, the data of the y- and z-displacement direction must be added and divided by the factor 2.

Results

Figure 7.4 shows the first-order density variation in a 2D heat map[17] for the fcc Ne system, while the fcc Al example can be found in figure 7.5. In these figures, within the lower plots the gradient term in equation (7.37b) is *not* subtracted. This leads to discontinuities at the MT sphere boundaries. So, these plots impressively substantiate the relevance of the complete MT basis correction. Furthermore, it can be seen that an essential part of the first-order density variation is given by the gradient of the unperturbed full charge density. Since it is mainly governed by the $l = 1$ channel, the shape of the spherical harmonics Y_{1m} can clearly be identified within the MT spheres. Due to the symmetry given by the cubic lattice and the monoatomic lattice basis, all displacement directions must show the same behavior [127, 251]. Therefore, showing only one displacement direction is sufficient here.

7.2.5 Tests

Test coverage

The first-order charge density variation for finite $\boldsymbol{q}$ does actually not differ significantly from its result for $\boldsymbol{q} = \boldsymbol{0}$, since the $\boldsymbol{q}$-character is essentially determined by the first-order wave-function expansion coefficients. Within the displaced MT spheres, this contribution is much smaller relative to the gradient of the full unperturbed density. Additionally, it has proven much easier to find tests for the boundary case of the Goldstone modes. Therefore, the majority of the following tests are devoted to the gradient of the unperturbed density. Still, the few tests for finite $\boldsymbol{q}$ are hard to pass and thus represent a good indicator of whether the first-order variation density variation is correctly programmed.

Outline

While test 8, test 9, and test 10 are supposed to check the gradient of the unperturbed density gradient, test 11, test 12, and test 14 test the routines for the first-order density variation. Test 13 describes the way in which the continuity of both the gradient and the first-order variation of the density is checked.

---

[17] All heat maps within this thesis are generated with `XCrySDen` (see e.g. references [284, 285]), while the 1D plots employ `Matplotlib` [286] and `NumPy` [287].

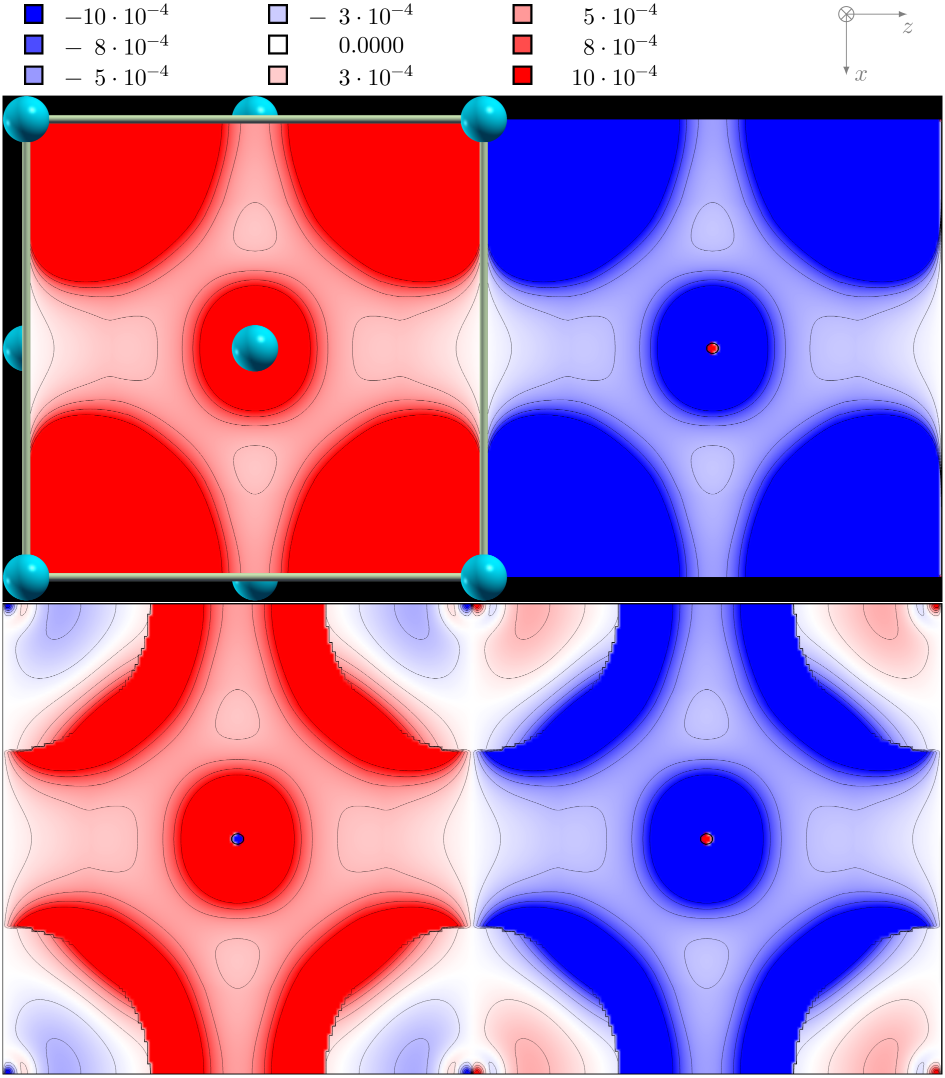

Figure 7.4: Real-space plot of the first-order density variation for fcc Ne. The atoms are displaced along the cartesian z-direction for a phonon with $\boldsymbol{q} = (0.25, 0.25, 0)^\top$ (longitudinal mode). While the upper plot shows the complete first-order density variation, the lower plot omits the gradient of the full unperturbed density. Since this part is central to the LAPW basis-set correction, its relevance is indicated here. The charge density, i.e., particularly the values in the color legend above, are given in the unit $e\, a_0^{-4}$. The input files for the `FLEUR` input generator are given in appendix B.

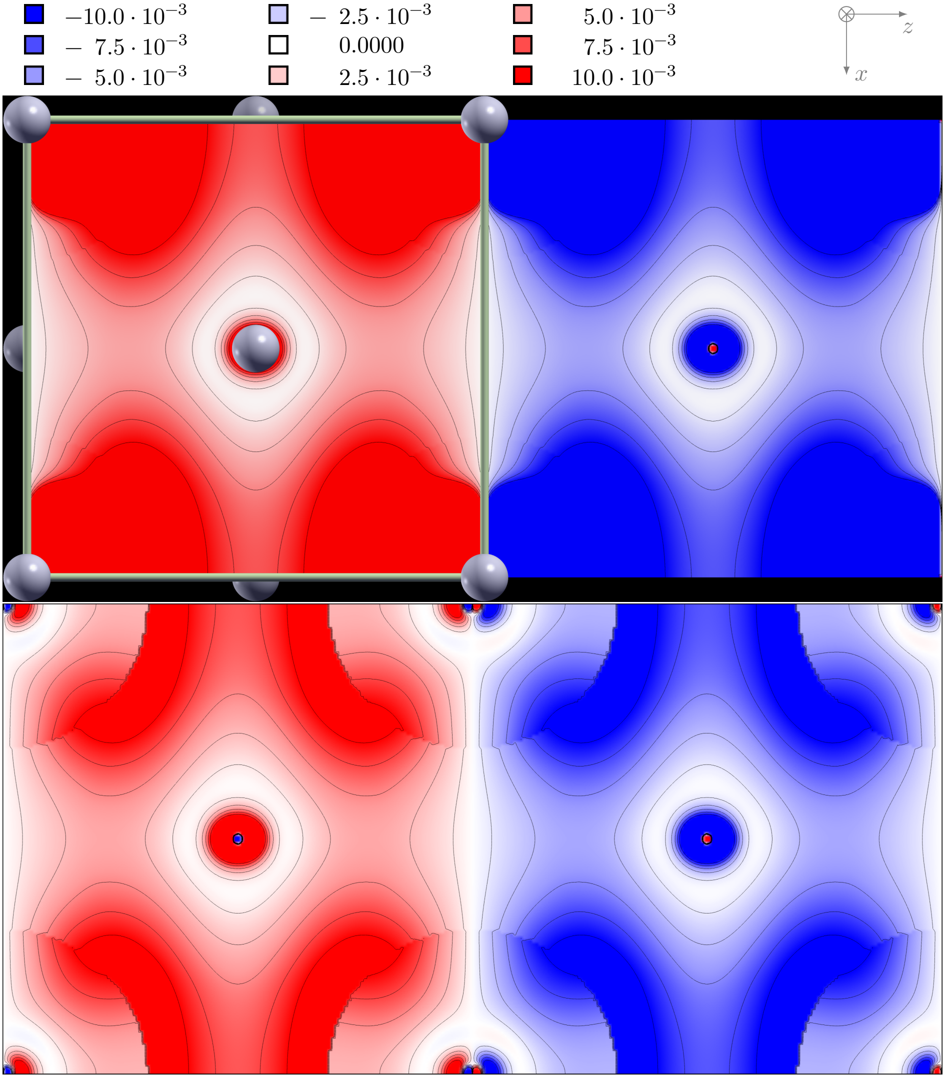

Figure 7.5: Real-space plot of the first-order density variation for fcc Al. The setup and the units are the same as for the Ne plot in figure 7.4. Relative to it, the Al system shows different features in the central MT sphere and at the MT sphere boundaries. Furthermore, the values in the color legend are one order of magnitude larger than for the Ne system.

Test 8: Radial Derivatives

Equation (7.21) requires employing a numerical differentiation routine. It is checked by differentiating the test functions

$$\mathfrak{g}_1(r_{\nu\mathring{\gamma}}) = -r_{\nu\mathring{\gamma}}^{-1}, \quad \mathfrak{g}_2(r_{\nu\mathring{\gamma}}) = \exp(-r_{\nu\mathring{\gamma}}), \tag{7.44}$$

and analyzing the difference to their analytical derivatives. The relative error is shown in figure 7.6 on the logarithmic MT mesh $r_{\nu\mathring{\gamma}}$. Both derivatives feature a small relative error. While for $\mathfrak{g}_1$ it is essentially about 10^{-7}, the relative error of $\mathfrak{g}_2$ basically lies between 10^{-7} and 10^{-15}. Nevertheless, the latter shows a more interesting behavior. It increases towards the MT sphere center, because $\mathfrak{g}_1$ varies there more rapidly, which is numerically more challenging. Furthermore, it increases towards the MT sphere boundary. This is due to the logarithmic mesh. It is dense close to the MT sphere center and less dense near the MT sphere boundary. However, numerical differentiation routines perform better the denser the mesh is chosen. Both functions show a different relative error for the boundary points, for which a different differentiation algorithm is selected by the subroutine.

Test 9: Gaunt coefficients

The recycled subroutine `Gaunt1` can be tested by evaluating the closed forms[18]

$$G^{m+1,m,1}_{l+1,\ \ l,\ 1} = \sqrt{\frac{3}{4\pi}}\sqrt{\frac{(l+m+1)(l+m+2)}{2(2l+1)(2l+3)}} \tag{7.45a}$$

$$G^{m+1,1,m}_{l-1,\ 1,l} = -\sqrt{\frac{3}{4\pi}}\sqrt{\frac{(l-m)(l-m-1)}{2(2l-1)(2l+1)}} \tag{7.45b}$$

$$G^{m,\ m,\,0}_{l+1,\,l,\ 1} = \sqrt{\frac{3}{4\pi}}\sqrt{\frac{(l-m+1)(l+m+1)}{(2l+1)(2l+3)}} \tag{7.45c}$$

$$G^{m,\ m,0}_{l-1,\,l,\,1} = \sqrt{\frac{3}{4\pi}}\sqrt{\frac{(l-m)(l+m)}{(2l-1)(2l+1)}} \tag{7.45d}$$

$$G^{m-1,m,-1}_{l+1,\ \ l,\ \ \ 1} = \sqrt{\frac{3}{4\pi}}\sqrt{\frac{(l-m+1)(l-m+2)}{2(2l+1)(2l+3)}} \tag{7.45e}$$

$$G^{m-1,m,-1}_{l-1,\ \ l,\ \ \ 1} = -\sqrt{\frac{3}{4\pi}}\sqrt{\frac{(l+m)(l+m-1)}{2(2l-1)(2l+1)}} \tag{7.45f}$$

of the Gaunt coefficients for $l \in [0, 30]$ (30 is arbitrarily chosen as an upper bound of the test). They result from applying the gradient to a spherical harmonic. The accuracy of `Gaunt1` proves to be better than 10^{-9}.

---

[18] These forms have been verified employing Wolfram Mathematica [281] by Fabian Lux.

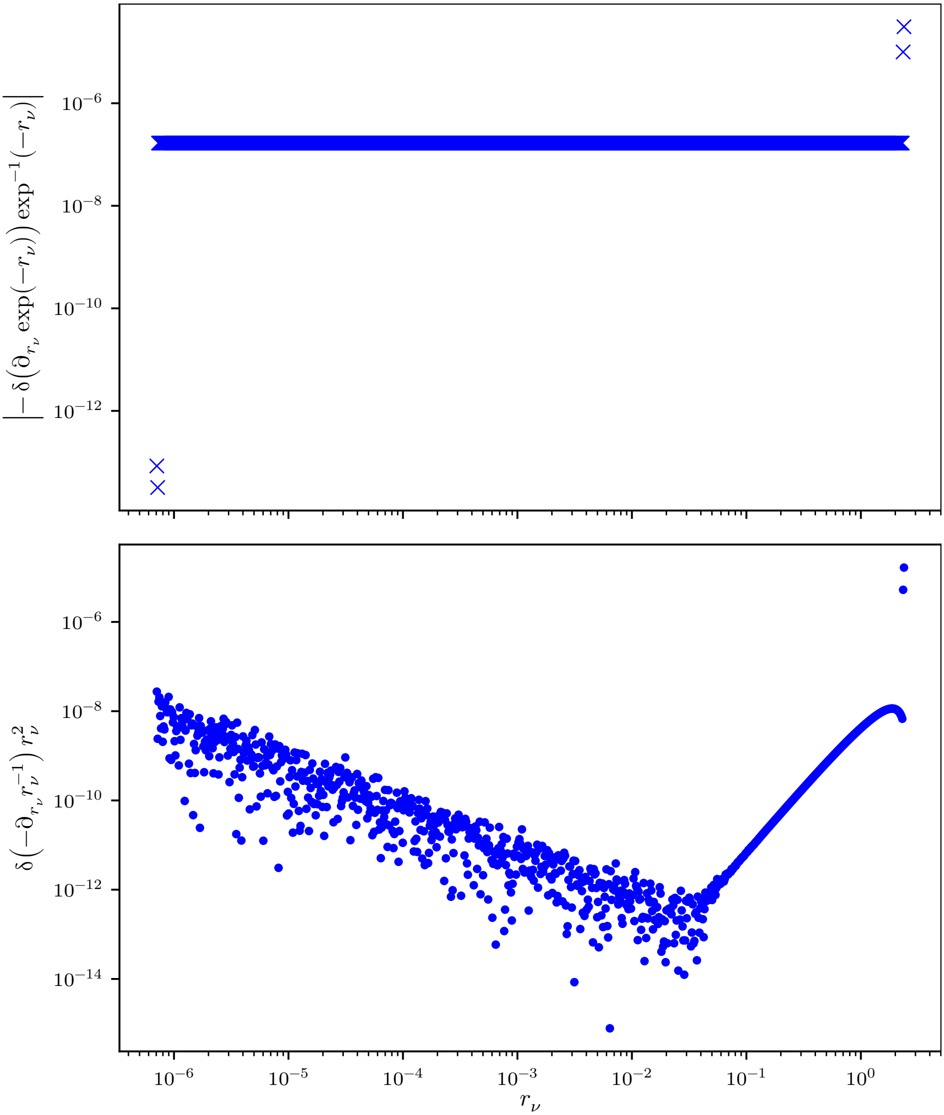

Figure 7.6: Check of the radial derivative subroutine employed in `juPhon`. The relative numerical errors of the functions $\exp(-r_\nu)$ (above) and $-r_\nu^{-1}$ (below) with respect to their analytical derivatives are plotted as a function of a typical MT mesh with the mesh points r_ν on a doubly-logarithmic scale. Apart from boundary effects, the functions are accurately differentiated up to a threshold of about $1 \cdot 10^{-7}$. As boundary points are differentiated with a special method, the accuracy of their differentiation differs from that of the remaining points. As a consequence of the logarithmic mesh, the preciseness towards the MT sphere boundary worsens. The employed input file can be found in appendix B.

Test 10: Trivial Muffin-tin Gradient

In order to check equation (7.21c), the test function $\mathfrak{g}(r_{\nu\mathring{\gamma}}) = r_{\nu\mathring{\gamma}}\mathrm{Y}_{00} = {}^{r_{\nu\mathring{\gamma}}}/\sqrt{4\pi}$ is chosen [251]. An analytical evaluation results in

$$\left[\boldsymbol{\nabla}^{\top}\mathfrak{g}(r_{\nu\mathring{\gamma}})\right]_{1,\mp 1} \cdot \hat{\boldsymbol{e}}_x = \pm\frac{1}{\sqrt{6}}\,, \tag{7.46a}$$

$$\left[\boldsymbol{\nabla}^{\top}\mathfrak{g}(r_{\nu\mathring{\gamma}})\right]_{1,\mp 1} \cdot \hat{\boldsymbol{e}}_y = \mathrm{i}\frac{1}{\sqrt{6}}\,, \tag{7.46b}$$

$$\left[\boldsymbol{\nabla}^{\top}\mathfrak{g}(r_{\nu\mathring{\gamma}})\right]_{1,0} \cdot \hat{\boldsymbol{e}}_z = \frac{1}{\sqrt{3}}\,, \tag{7.46c}$$

which is in line with the numerical results at an accuracy better than 10^{-6}. Since the test function only features a $l = 0$ contribution, the other part of the MT gradient (7.21d) is not covered by this test. An appropriate test function must have expansion coefficients for $l > 0$. As this takes more effort and the gradient subroutine has worked already, we decided to postpone adding it [127, 251].

Test 11: Reproducing the Unperturbed Charge Density

Interstitial region

The subroutines to calculate the first-order density variation can be cross-checked by manipulating their input such that the valence part of the unperturbed density results [127, 251]. In the IR, it requires substituting the first-order variation of the wave-function expansion coefficients with their unperturbed version so that equation (7.31b) is reformulated to

$$2\rho^{(0)}_{\mathrm{IR,v}}(\boldsymbol{r}) = \frac{4}{\Omega}\sum_{\boldsymbol{k},n} f^{(0)}_{\boldsymbol{k},n} \sum_{\boldsymbol{G}''+\boldsymbol{G}'}\sum_{\boldsymbol{G}'} z^{*(0)}_{\boldsymbol{G}'}(\boldsymbol{k},n)\, z^{(0)}_{\boldsymbol{G}''+\boldsymbol{G}'}(\boldsymbol{k}',n)\,\mathrm{e}^{\mathrm{i}\boldsymbol{G}''\cdot\boldsymbol{r}} \tag{7.47a}$$

$$= \frac{4}{\Omega}\sum_{\boldsymbol{k},n} f^{(0)}_{\boldsymbol{k},n} \sum_{\boldsymbol{G}'''}\sum_{\boldsymbol{G}'} z^{*(0)}_{\boldsymbol{G}'}(\boldsymbol{k},n)\, z^{(0)}_{\boldsymbol{G}'''}(\boldsymbol{k}',n)\,\mathrm{e}^{\mathrm{i}\left(\boldsymbol{G}'''-\boldsymbol{G}'\right)\cdot\boldsymbol{r}} \tag{7.47b}$$

$$= \sum_{\boldsymbol{G}''} \rho^{(0)}_{\mathrm{IR,v}}(\boldsymbol{G}'')\,\mathrm{e}^{\mathrm{i}\boldsymbol{G}''\cdot\boldsymbol{r}}\,. \tag{7.47c}$$

In this derivation $\boldsymbol{G}'' = \boldsymbol{G} - \boldsymbol{G}'$ and $\boldsymbol{G}''' = \boldsymbol{G}'' + \boldsymbol{G}'$ are used.

Muffin-tin

The same can be done for the MT spheres, although this involves a more sophisticated manipulation of the `juPhon` subroutines. On the one hand, the first-order variation of the wave-function expansion coefficients in equation (7.29) are analogously replaced. On the other hand, the remaining lines of this equation must be deactivated, because they stem from the basis-set correction or relate to core electrons. All in all, this leads to

$$\left[\boldsymbol{\rho}^{(0)}_{\mathrm{v},\gamma}(\boldsymbol{r}_{\nu\mathring{\gamma}})\right]_{lm} = \sum_{l'p'l''p''s} u^{s\mathring{\gamma}}_{l'p'}(r_{\nu\mathring{\gamma}})\, u^{s\mathring{\gamma}}_{l''p''}(r_{\nu\mathring{\gamma}}) \sum_{m'm''} G^{m'',m,m'}_{l'',\;l,\;l'}\, 2\sum_{\boldsymbol{k},n} f^{(0)}_{\boldsymbol{k},n} A^{*\boldsymbol{k}\gamma n}_{l'm'p'} A^{\boldsymbol{k}\gamma n}_{l''m''p''}\,. \tag{7.48}$$

Aspects to consider

It is important to consider that the first-order density variation is a vector and the unperturbed density a scalar quantity. Despite the possible solution to fill up every vector component with the unperturbed wave-function expansion coefficients, only one component contributes and the others are set to zero. This worsens the test coverage, but the displacement directions are independent from each other and the respective loops are located in a very outer scope. In the long term, parallelization might supplant these direction loops within the tested routines by a parameter, because the loop is shifted to a more outer scope. Furthermore, for core-tail systems this test delivers unsatisfying results, when using the unperturbed charge density from the initialization routine. Therefore, the employed version of `FLEUR` writes out the files `fort.7800` for the IR and `fort.1040` for the MT spheres in `cdnval`, containing the IR and the MT charge density *before* core-tail contributions are added. Additionally, in systems fulfilling TRS `FLEUR` only calculates half of the Brillouin zone ($\boldsymbol{k}$-point set) [127]. The implying factor 2 compensates with the factor 2 inhering in the `juPhon` routines and stemming from the product rule, which is irrelevant in the unperturbed case. Finally, the initialization procedure described in appendix A must be followed in order to ensure that the densities are not taken from different iterations.

Test 12: First-Order Density Variation for the Goldstone Modes

As pointed out in the introduction of section 7.2.3, the first-order density variation becomes the negative unperturbed density gradient, provided relation (7.30) holds. In order to check this, the test exactly sets the first-order variation of the wave-function expansion coefficients as in equation (7.30). The raison d'être of this procedure originates from the circumstance that numerical errors can accumulate while the Sternheimer equation is solved self-consistently. This implies that the resulting first-order wave-function expansion coefficients differ from the aforesaid perfect analytical solution. By conducting the test, the correctness of the implementation is decoupled from numerical issues that might still inhere. Especially, the test aims to check the Pulay basis correction in the MT first-order density variation.

Extended to a polyatomic basis, the first-order wave-function expansion coefficients must be

$$\boldsymbol{z}^{(1)}_{\boldsymbol{G}}(\boldsymbol{k}, n; \boldsymbol{0}\alpha) \equiv -\frac{1}{N_\gamma}\mathrm{i}(\boldsymbol{k}+\boldsymbol{G})\boldsymbol{z}^{(0)}_{\boldsymbol{G}}(\boldsymbol{k}, n; \boldsymbol{0}\alpha)\,. \tag{7.49}$$

The factor ${}^{1}\!/_{N_\gamma}$ accounts for the second line of equation (7.29) which now implicitly contains a sum over all MT spheres. Additionally, a sum over the displaced atoms α is required, which must be normed by the factor ${}^{1}\!/_{N_\gamma}$ again. [251]

Test 13: Continuity of the Density Gradient and First-Order Density Variation

The continuity of the linear density variations is essentially governed by the LAPW basis they are expanded in [251]. Since the LAPW basis (5.6) and the Gaussian parameters (7.22) are constructed such that the energy derivative is also continuous on the MT sphere boundary, the aforementioned variations must likewise be continuous [251]. This check follows the same procedure as in test 3. However, the first-order density variation is represented by its $\boldsymbol{q}^{+}$ part in `juPhon`, which in general is complex-valued. Thus, the continuity of both the real and the imaginary part are investigated. All in all,

$$\begin{aligned}
\boldsymbol{\rho}^{(1)}_{\mathrm{IR}}\left(\boldsymbol{r}_{\mathrm{crt}};\boldsymbol{q}^{+}\alpha\right) &= \sum_{\boldsymbol{G}|\boldsymbol{G}+\boldsymbol{q}\neq\boldsymbol{0}} \boldsymbol{\rho}^{(1)}_{\mathrm{IR}}\left(\boldsymbol{G};\boldsymbol{q}^{+}\alpha\right)\mathrm{e}^{\mathrm{i}(\boldsymbol{G}+\boldsymbol{q})\cdot\underline{B}\boldsymbol{r}_{\mathrm{crt}}}\,, && (7.50\mathrm{a})\\
\boldsymbol{\rho}^{(1)}_{\gamma}\left(\boldsymbol{r}_{\nu\mathring{\gamma}};\boldsymbol{q}^{+}\alpha\right) &= \left[\boldsymbol{\rho}^{(1)}_{\gamma}\left(r_{\nu\mathring{\gamma}};\boldsymbol{q}^{+}\alpha\right)\right]_{lm}\mathrm{Y}_{lm}\left(\hat{\boldsymbol{r}}_{\gamma}-\hat{\boldsymbol{\tau}}_{\gamma}\right)\,, && (7.50\mathrm{b})\\
\boldsymbol{\nabla}\rho^{(0)}_{\mathrm{IR}}\left(\boldsymbol{r}_{\mathrm{crt}}\right) &= \sum_{\boldsymbol{G}|\boldsymbol{G}+\boldsymbol{q}\neq\boldsymbol{0}} \boldsymbol{\nabla}\rho^{(0)}_{\mathrm{IR}}\left(\boldsymbol{G}\right)\mathrm{e}^{\mathrm{i}\boldsymbol{G}\cdot\underline{B}\boldsymbol{r}_{\mathrm{crt}}}\,, && (7.51\mathrm{a})\\
\left[\boldsymbol{\nabla}\rho^{(0)}_{\gamma}\left(\boldsymbol{r}_{\nu\mathring{\gamma}}\right)\right]_{lm} &= \sum_{\gamma}\left[\boldsymbol{\nabla}\rho^{(0)}_{\gamma}\left(r_{\nu\mathring{\gamma}}\right)\right]_{lm}\mathrm{Y}\left(\hat{\boldsymbol{r}}_{\gamma}-\hat{\boldsymbol{\tau}}_{\gamma}\right) && (7.51\mathrm{b})
\end{aligned}$$

are evaluated. The results should roughly be comparable to the continuities of the unperturbed charge densities.

Test 14: First-Order Charge-Density Variation from Difference Quotients

Concept

The strongest and most general test of an arbitrary DFPT first-order density variation is to cross-check it with results from other methods or programs. A fair consistency for the comparison can be expected when the first-order charge-density variation is generated from a finite-difference method, based on the unperturbed charge density of `FLEUR` [127]

$$\boldsymbol{Q}_{\alpha}\cdot\Delta\boldsymbol{\rho}^{(1)}\left(\boldsymbol{r},\boldsymbol{q}^{+}\alpha\right) = \left|\boldsymbol{Q}_{\alpha}\cdot\boldsymbol{\rho}^{(1)\Delta}\left(\boldsymbol{r},\boldsymbol{q}^{+}\alpha\right)-\boldsymbol{Q}_{\alpha}\cdot\boldsymbol{\rho}^{(1)}\left(\boldsymbol{r},\boldsymbol{q}^{+}\alpha\right)\right| \qquad (7.52\mathrm{a})$$

with

$$\boldsymbol{Q}_{\alpha}\cdot\boldsymbol{\rho}^{(1)\Delta}\left(\boldsymbol{r},\boldsymbol{q}^{+}\alpha\right) =: \frac{\rho^{(0)}\left(\boldsymbol{r}+\delta^{\alpha}_{\boldsymbol{q}^{+}}\right)-\rho^{(0)}\left(\boldsymbol{r}\right)}{\left|\delta^{\alpha}_{\boldsymbol{q}^{+}}\right|}\mathrm{e}^{\mathrm{i}\boldsymbol{q}\cdot\boldsymbol{R}}\,. \qquad (7.52\mathrm{b})$$

In this method the displacement $|\delta^{\alpha}_{\boldsymbol{q}^{+}}|$ is to be set so small that the differential quotient converges, i.e., it does not change significantly anymore when further lowering $|\delta^{\alpha}_{\boldsymbol{q}^{+}}|$. We decided this to be the case as soon as equation (7.52a) is on average $1.0\cdot10^{-3}\,e\,a_0^{-4}$, from an inspection of the evaluated values, and $|\delta^{\alpha}_{\boldsymbol{q}^{+}}| = 1\cdot10^{-5}\,a_0$. Based on a perturbation expansion (4.1) of the charge density, a theoretical upper limit $\mathcal{O}(|\delta^{\alpha}_{\boldsymbol{q}^{+}}|^2)$ can be assumed here [251]. Since the real-space first-order density variation is evaluated according to equations (7.41) and (7.42), equation (7.52a) must be multiplied by a factor of 2.

Test systems

In order to avoid superfluous complexity, a sc Ne system is chosen, featuring the phonon vectors $\boldsymbol{q}_1 = (0,0,0.25)^{\top}$ and $\boldsymbol{q}_2 = (0,0.25,0.5)^{\top}$ in internal units (cf. figure 3.1 for $\boldsymbol{q}_2$). The `FLEUR` calculation must be set up in a supercell that contains the complete period of these phonons. Its input parameters can be found in appendix B. This leads in the former case to the dimension $1\times1\times4$ and in the latter case to a $1\times4\times2$ supercell. So, relative to the original unit cell, the lattice constant is doubled or quadruplicated in the respective directions. Furthermore, the $\boldsymbol{k}$ sets must be adjusted because an increase in real space leads to a decrease in reciprocal space. Consequently, $\boldsymbol{q}_1$ necessitates an $8\times8\times2$ and $\boldsymbol{q}_2$ an $8\times4\times2$ set, provided the single unit cell is calculated with an $8\times8\times8$ set. For $\boldsymbol{q}_1$, the `inp` file for `FLEUR` should be checked after the input-file generator has been executed, because the latter does not consistently set the parameters for all neon atoms of the supercell.

Results

Figure 7.7 contrasts 2D heat maps of the `juPhon` calculation with the finite difference method based on `FLEUR`. For $\boldsymbol{q}_1$ a plotting resolution of 150×600 is set in the x and z directions, respectively. The same is done in figure 7.8 for $\boldsymbol{q}_2$ and a resolution of 600×300 in the y and z directions, respectively. In both figures, the origins can be found in the upper left corners. `XcrySDen` cuts all values larger or smaller than the maxima or minima in the legends of the aforementioned figures. For the sake of quantifying the difference between the two methods, the absolute error is evaluated on the complete aforementioned meshes and along horizontal 1D lines between the extrema. The results are shown in figure 7.9 for $\boldsymbol{q}_1$ and for $\boldsymbol{q}_2$. Significant differences manifest in particular at the boundaries of the unit cell. These boundary effects stem for instance from deciding for a naive numerical differentiation method. Moreover, close to the MT sphere centers the values are large, implying a larger absolute error. Still we assume there a sufficiently small relative error [127]. Overall, both methods are very well in line with each other, although the features in the non-displaced atoms differ a little.

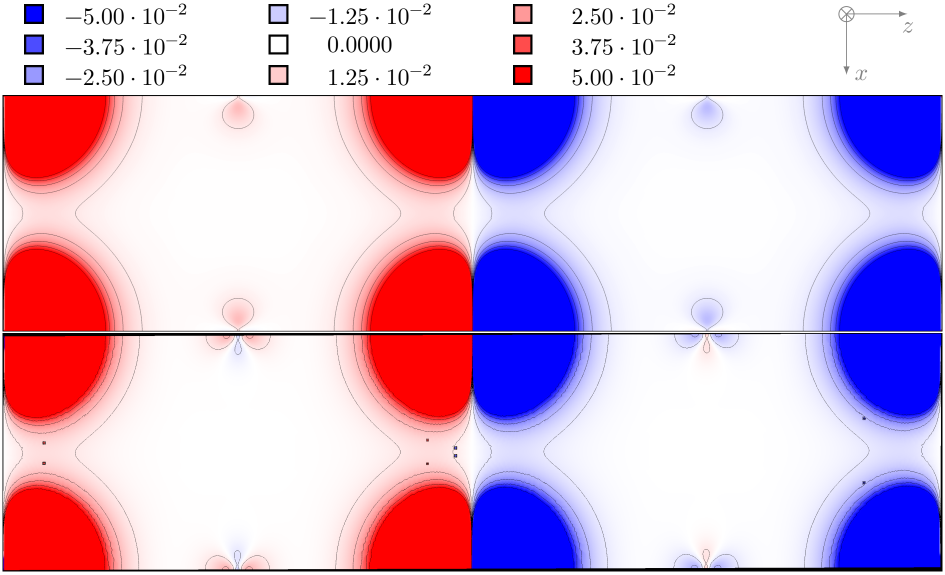

Figure 7.7: Heat maps contrasting the first-order density variation from the `juPhon` code with a benchmark using a difference quotient method (7.52a) based on the `FLEUR` program, for a sc Ne system and a longitudinal phonon with $\boldsymbol{q} = (0, 0, 0.25)^\top$ (internal units). The variable a is the lattice constant. Furthermore, the first-order density variations are given in the unit $e\, a_0^{-4}$, and the input-generator input files are given in appendix B. Although the tiny features in the non-displaced atoms (at (001) and (003)) are only poorly reproduced, the overall consistency is very good. The resolution of each plot is 150×600 in x and z direction, respectively. Within the four upper plots of figure 7.9, the absolute error, i.e., the difference between the two methods is analyzed on a horizontal line on the thirty-eighth mesh point of the 150 data points along the x-direction. The origin are located in the upper left corner.

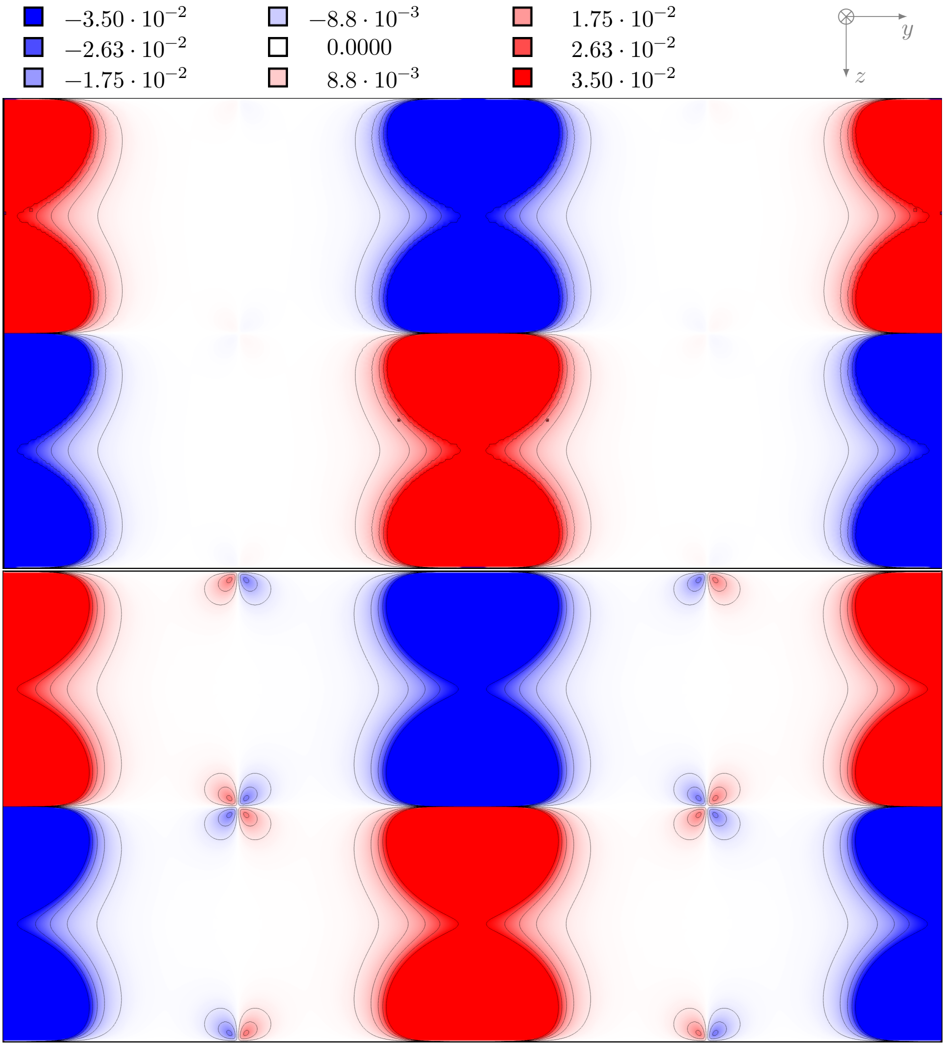

Figure 7.8: Heat maps contrasting the first-order density variation from the `juPhon` code with a benchmark using a difference quotient method (7.52a) based on the `FLEUR` program, for a sc Ne system and a longitudinal phonon with $\boldsymbol{q} = (0, 0.25, 0.5)^\top$ (internal units). The units and involved methods are the same as in figure 7.7. Furthermore, the consistency between the two methods shown here is comparable with the aforementioned figure. Again, the most obvious differences occur in the non-displaced MT spheres. But, the resolution of each plot in this example is 600×300 in y and z direction, respectively. Within the four lower plots of figure 7.9, the absolute error, i.e., the difference between the two methods is likewise analyzed on a horizontal lines at the seventy-fifth, the 161th, and the 150th, mesh points of the 300 data points along the y-direction. The upper left corner is defined as the origin.

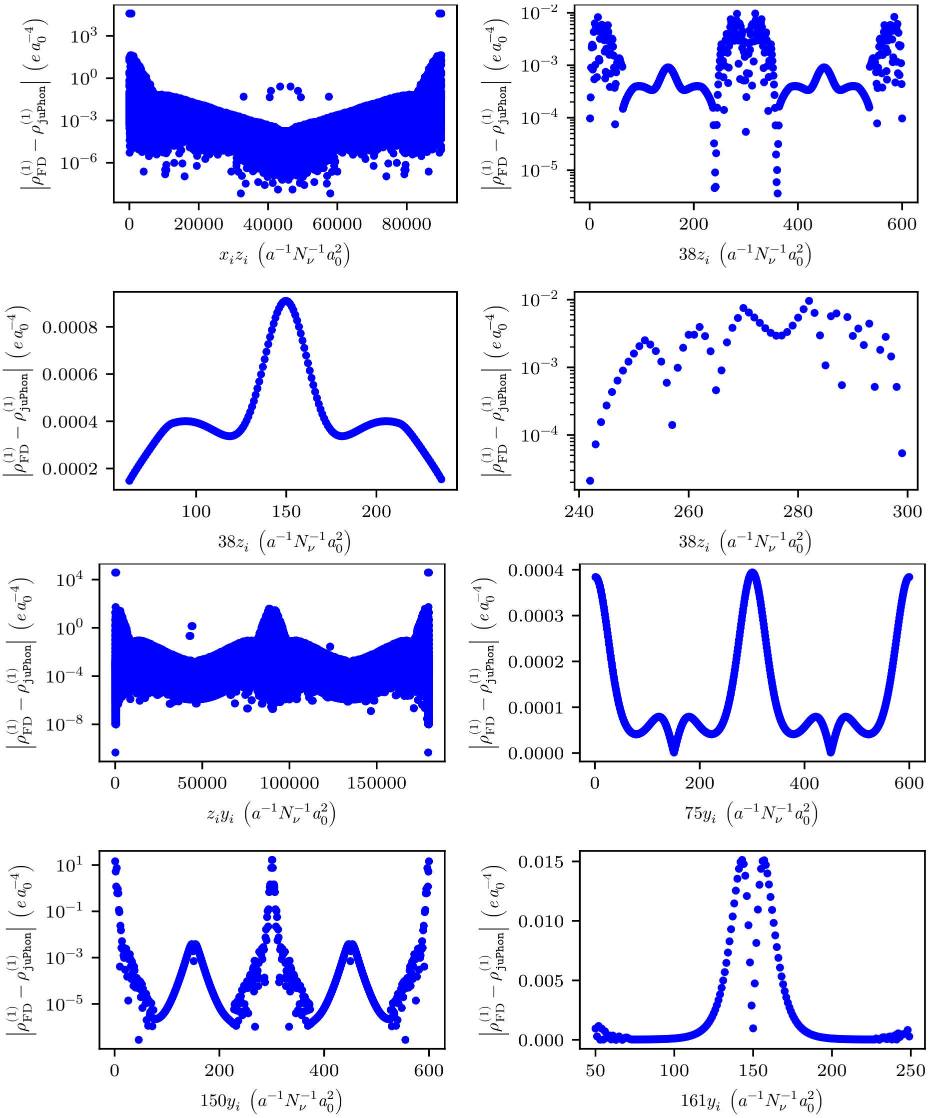

Figure 7.9: Absolute error 1D-analysis of figure 7.7 (four upper plots) and figure 7.8 (four lower plots) on the complete mesh and along horizontal lines between the MT extrema. The locations of the horizontal lines are already explained in the aforementioned figures. Here, N_ν is the number of mesh points and a the lattice constant. In the middle of the MT spheres the absolute error becomes large, but also the values are large there. Furthermore, large differences are caused by boundary effects of the finite-differences method. But, the overall consistency is good. The order of the points in the left plots of the first and third rows is such that all columns (indexed by z_i above and y_i below) are run through before the next row (denoted by x_i above and z_i below) is addressed.

7.3 Linear Potential Variations

Requirements

Chapter 6 clarifies that the linear variations of both the external and the effective potentials form integral parts of the dynamical matrix. Within this framework, the external component of the first-order effective-potential variation expresses the perturbation which acts on the system due to a phonon. Therefore, this contribution is known in advance of the Sternheimer equation and serves as the input for the self-consistency procedure, the outputs of which are the complementary Hartree and xc terms. Moreover, the gradient of the unperturbed effective potential must also be determined before the Sternheimer equation, in which it is incorporated. So overall, the implementation of the linear potential variations must satisfy different requirements that are imposed by the Sternheimer equation, the dynamical matrix, and the test suite. Hence, it must be feasible to flexibly activate and deactivate only certain constituents of the linear effective-potential variations, in order to minimize redundant lines of code and thus the risk of programming errors. This even involves addressing specific compartmentalized terms of the linear Hartree-, external-, or xc-potential variations. Nevertheless, in this section the complete linear effective-potential variations are discussed.

Weinert method for potential gradient

In principle, the unperturbed effective potential (such as the unperturbed charge density) is at hand from a preceding DFT calculation, for which the `FLEUR` code is employed. Consequently, one could naively argue that in order to obtain the gradient of any unperturbed effective-potential part, the numerical gradient procedure is sufficient (as introduced for the unperturbed density in section 6.2.1). But this algorithm in general precipitates numerical issues. They originate from the fact that the aforementioned numerical gradients in the IR and the MT sphere both on their own do not ensure a continuous derivative of the potential at the MT sphere boundary. It constitutes a difference to the gradient of the unperturbed charge density, the continuity of which at the MT sphere boundary is guaranteed by the LAPW basis [251]. In contrast, the formalism of Klüppelberg [88] ensures continuity at the MT sphere boundary for both the linear Hartree- and the linear external-potential variations [251]. This is based on the Weinert [64] construction, and in particular holds true for a converged Rayleigh expansion [127]. As far as the linear variations of the xc potential are concerned, Klüppelberg derives expressions which are functionals of the linear density variations.

Raison d'être of Coulomb potential

It has established itself in the `FLEUR` code to usually deal with the sum of the repulsive Hartree potential and the attractive external potential, which is called the Coulomb potential. This weakens the awkward numerical impact of the $^1/_r$ singularity, lets contributions with large absolute values annihilate each other, and all in all can be handled with the concept of Weinert [64]. Analogously, the Coulomb potential is introduced in the total energy, as described in section 5.9. We decided to follow this approach [127, 251], thereby realizing the linear Hartree- and external-potential variations within the same scope of routines and data structures.

Outline

The implementation details of the linear Coulomb-potential variations are reported in section 7.3.1. Section 7.3.2 then expounds on the implementation of the linear xc-potential variations. In order to give an impression of the linear effective-potential variations, section 7.3.3 is devoted to visualize the shape of the Hartree, the external, or the xc part, utilizing 3D isosurfaces and their 2D cross-sections. The way of verifying the integrity of the resulting linear potential variations is finally discussed in section 7.3.4. Overall, the implementation was guided by subroutines from `FLEUR` version 26 (see page 112), but also from a more modern version[19] of `FLEUR`.

7.3.1 Coulomb Potential

Surface integrals of multipole moments

In this section, the calculation of the unperturbed Coulomb-potential gradient and the first-order Coulomb-potential response to a phonon are explained. Common to both linear Hartree-potential variations is the surface-term contribution to the multipole moments (6.35), which partitions into a MT spheres and an IR term

$$\left[\mathbf{q}^{\gamma\boldsymbol{R}'}_{\text{surf}}\left(\tilde{\boldsymbol{q}}^{\pm}\alpha\right)\right]_{lm} = \left[\mathbf{q}^{\gamma\boldsymbol{R}'}_{\text{surf, MT}}\left(\tilde{\boldsymbol{q}}^{\pm}\alpha\right)\right]_{lm} - \left[\mathbf{q}^{\gamma\boldsymbol{R}'}_{\text{surf, IR}}\left(\tilde{\boldsymbol{q}}^{\pm}\alpha\right)\right]_{lm}. \tag{7.53}$$

Their sign differs, because the normal vectors on the IR boundaries, which encapsulate the MT spheres, are antiparallel to the normal vectors of the MT sphere boundaries. Deciding for the MT normal vector $\hat{\boldsymbol{r}}$, both in the MT term

$$\begin{aligned}
\left[\mathbf{q}^{\gamma\boldsymbol{R}'}_{\text{surf, MT}}\left(\tilde{\boldsymbol{q}}^{\pm}\alpha\right)\right]_{lm} &= \delta_{\gamma\alpha}\mathrm{e}^{\mathrm{i}\boldsymbol{q}^{\pm}\cdot\boldsymbol{R}'}\oint_{\partial\alpha_{\boldsymbol{R}=\boldsymbol{0}}}\hat{\boldsymbol{r}}\mathrm{Y}^{*}_{lm}(\hat{\boldsymbol{r}}_{\alpha})r^{l}_{\mathring{\alpha}}\rho^{(0)}_{\alpha}(\boldsymbol{r}_{\alpha}+\boldsymbol{\tau}_{\alpha})\,\mathrm{d}S & \text{(7.54a)}\\
&= \delta_{\gamma\alpha}\mathrm{e}^{\mathrm{i}\boldsymbol{q}^{\pm}\cdot\boldsymbol{R}'}R^{l+2}_{\mathring{\alpha}}\sum_{l'm'}\left[\rho^{(0)}_{\alpha}(R_{\mathring{\alpha}})\right]_{l'm'}\sum_{m''=-1}^{1}\sum_{i}\hat{\boldsymbol{e}}_{i}\zeta_{i,m''} & \text{(7.54b)}\\
&\quad\times\oint_{\partial\alpha_{\boldsymbol{R}=\boldsymbol{0}}}\mathrm{Y}^{*}_{lm}(\hat{\boldsymbol{r}}_{\alpha})\mathrm{Y}_{l'm'}(\hat{\boldsymbol{r}}_{\alpha})\mathrm{Y}_{1m''}(\hat{\boldsymbol{r}}_{\alpha})\,\mathrm{d}\Omega\\
&= \delta_{\gamma\alpha}\mathrm{e}^{\mathrm{i}\boldsymbol{q}^{\pm}\cdot\boldsymbol{R}'}R^{l+2}_{\mathring{\alpha}}\sum_{l'm'}\left[\rho^{(0)}_{\alpha}(R_{\mathring{\alpha}})\right]_{l'm'}\sum_{m''=-1}^{1}\sum_{i}\hat{\boldsymbol{e}}_{i}\zeta_{i,m''}G^{m,m',m''}_{l,\ l',\ 1} & \text{(7.54c)}
\end{aligned}$$

and the IR term

$$\begin{aligned}
-\left[\mathbf{q}^{\gamma\boldsymbol{R}'}_{\text{surf, IR}}\left(\tilde{\boldsymbol{q}}^{\pm}\alpha\right)\right]_{lm} &= -\delta_{\gamma\alpha}\mathrm{e}^{\mathrm{i}\boldsymbol{q}^{\pm}\cdot\boldsymbol{R}'}\oint_{\partial\alpha_{\boldsymbol{R}=\boldsymbol{0}}}\hat{\boldsymbol{r}}\mathrm{Y}^{*}_{lm}(\hat{\boldsymbol{r}}_{\alpha})r^{l}_{\mathring{\alpha}}\rho^{(0)}_{\text{IR}}(\boldsymbol{r}_{\alpha}+\boldsymbol{\tau}_{\alpha})\,\mathrm{d}S & \text{(7.55a)}\\
&= -\delta_{\gamma\alpha}\mathrm{e}^{\mathrm{i}\boldsymbol{q}^{\pm}\cdot\boldsymbol{R}'}\sum_{l'm'}4\pi\mathrm{i}^{l'}\sum_{\boldsymbol{G}}\mathrm{e}^{\mathrm{i}\boldsymbol{G}\cdot\boldsymbol{\tau}_{\alpha}}\rho^{(0)}_{\text{IR}}(\boldsymbol{G})\mathrm{Y}^{*}_{l'm'}\left(\hat{\boldsymbol{G}}\right)\mathrm{j}_{l'}(|\boldsymbol{G}|R_{\mathring{\alpha}}) & \text{(7.55b)}\\
&\quad\times\sum_{m''=-1}^{1}\sum_{i}\hat{\boldsymbol{e}}_{i}\zeta_{i,m''}\oint_{\partial\alpha_{\boldsymbol{R}=\boldsymbol{0}}}\mathrm{Y}^{*}_{lm}(\hat{\boldsymbol{r}}_{\alpha})\mathrm{Y}_{l'm'}(\hat{\boldsymbol{r}}_{\alpha})\mathrm{Y}_{1m''}(\hat{\boldsymbol{r}}_{\alpha})\,\mathrm{d}\Omega\\
&= -\delta_{\gamma\alpha}\mathrm{e}^{\mathrm{i}\boldsymbol{q}^{\pm}\cdot\boldsymbol{R}'}\sum_{l'm'}4\pi\mathrm{i}^{l'}\sum_{\boldsymbol{G}}\mathrm{e}^{\mathrm{i}\boldsymbol{G}\cdot\boldsymbol{\tau}_{\alpha}}\rho^{(0)}_{\text{IR}}(\boldsymbol{G})\mathrm{Y}^{*}_{l'm'}\left(\hat{\boldsymbol{G}}\right)\mathrm{j}_{l'}(|\boldsymbol{G}|R_{\mathring{\alpha}}) & \text{(7.55c)}\\
&\quad\times\sum_{m''=-1}^{1}\sum_{i}\hat{\boldsymbol{e}}_{i}\zeta_{i,m''}G^{m,m',m''}_{l,\ l',\ 1}
\end{aligned}$$

finally implies a minus sign in the latter. Within equation (7.54b), the spherical-harmonic expansion of the unperturbed charge density (5.18) is used. According to equation (6.27b), the normal vectors $\hat{\boldsymbol{r}}$ are moreover expanded in spherical harmonics in each of the cartesian directions. Furthermore, the surface integral is evaluated at the MT sphere boundary $|\boldsymbol{r}_{\alpha}| \equiv R_{\mathring{\alpha}}$, and the differential $\mathrm{d}S$ is unfolded to $R^{2}_{\mathring{\alpha}}\,\mathrm{d}\Omega$. This enables one to identify the Gaunt coefficients (5.32d) in equation (7.54c). Due to one orbital quantum number of the Gaunt

---

[19] The version referred to is in the `FLEUR` repository and can be found under the commit labeled by the hash `1069634bca0c874f65be440dc9c58c165a968d74`.

coefficients being fixed to 1, only a few Gaunt coefficients remain (fulfilling the selection rules $m = m' + m''$ and $\left|l' - 1\right| < l \leq l + 1$ [88]). I usually avoid implementing these Gaunt selection rules, because if-clauses within loops are required, preventing performance optimizations of modern CPU architectures. Exceptions (in recycled routines) will be eliminated in the future. The approach (7.55) for the multipole moments in the IR is similar to the aforementioned one in the MT spheres. However for the former, the IR plane-wave expansion of the charge density (5.18) is used and the subject of a Rayleigh decomposition (5.5). Evaluating the surface terms (7.53), (7.54), and (7.55) is already partly and less precisely described in reference [88].

Their relevance

Since equation (7.53) is proportional to the discontinuity of the charge density, it suggests itself that this contribution is small relative to the remaining multipole-moment parts (6.33) and (6.34). I can confirm this for the systems relevant within this dissertation. Still, one could possibly imagine more problematic systems, in which converging the LAPW parameter k_{max} and $l_{\text{max},\mathring{\gamma}}$ significantly increases the computation time. Surface terms then allow smaller cutoffs and thus a better computational performance [88]. Again it must be stressed that only the $\boldsymbol{q}^{+}$ parts in the relevant equations of the first-order Coulomb-potential variation are programmed and discussed in the following (TRS).

Optimal Weinert parameter

Aspiring for a correct implementation of the Coulomb potential, the question arises how the Weinert convergence parameter N in the pseudo-densities (6.28b), (6.38), and (6.40) should be set. This parameter is actually supposed to optimize the Fourier expansion of the pseudo-charge [64, 251]. But, the resulting Coulomb potential should *not* be dependent on the choice of N [251], provided it is converged with respect to the LAPW parameters and the aforesaid Fourier expansion behaves well. Checking this for a linear external potential variation, I found that the choice of a sufficiently small G_{max} implied the potential to become a function of the Weinert parameter N. Ultimately, it has turned out to be adequate if the parameter N is chosen such as in the construction of the unperturbed Coulomb potential $V_{\text{C}}^{(0)}(\boldsymbol{r})$.

Gradient of the Unperturbed Interstitial Part

External potential multipole moment

The exact numerical realization of the multipole moments (6.26) is impossible, because the expression undergoing the application of the gradient must afterwards be evaluated at $\boldsymbol{r} = \boldsymbol{0}$. Both `juPhon` and `FLEUR` employ a logarithmic MT mesh to achieve the required accuracy in the close vicinity of the MT sphere center, therefore $\boldsymbol{r} = 0$ can only be approached. But deciding for this approximate solution, numerical errors must possibly be handled in a MT gradient expression, as it is depicted in figure 7.3. Furthermore, pathological functions which rapidly vary close to the MT sphere center cause knotty problems. These issues are circumvented in the reformulation (6.27b) and therefore

$$\mathbf{q}^{\gamma\boldsymbol{R}'}_{lm}(\mathbf{0},\alpha) = -Z_{\mathring{\alpha}}\delta_{\gamma\alpha}\boldsymbol{\nabla}\left[r^{l}\mathrm{Y}^{*}_{lm}(\hat{\boldsymbol{r}})\right]_{\boldsymbol{r}=0} \tag{7.56a}$$

$$= -Z_{\mathring{\alpha}}\delta_{\gamma\alpha}\sum_{i=1}^{3}\hat{\boldsymbol{e}}_{i}\sum_{m=-1}^{1}\frac{3}{4\pi}\zeta_{i,m} \tag{7.56b}$$

is implemented in `juPhon`.

Coulomb pseudo-density

As in FLEUR, the multipole moments of the Hartree-potential gradient (6.39) and the external-potential gradient (7.56) are combined to those of the Coulomb-potential gradient. This results in the pseudo-charge Fourier coefficients

$$\boldsymbol{n}_{\mathrm{Cou}}^{\mathrm{ps},\boldsymbol{\nabla}}(\boldsymbol{G}) = \boldsymbol{\nabla}\rho_{\mathrm{IR}}^{(0)}(\boldsymbol{G}) + \frac{4\pi}{\Omega}\sum_{\gamma}\sum_{lm}\frac{(-\mathrm{i})^{l}\left(2N_{\mathring{\gamma}}^{\mathrm{opt}}+3\right)!!}{(2l+1)!!R_{\mathring{\gamma}}^{l}}\frac{\mathrm{j}_{l+N+1}\left(|\boldsymbol{G}|R_{\mathring{\gamma}}\right)}{\left(|\boldsymbol{G}|R_{\mathring{\gamma}}\right)^{N+1}} \\ \times \mathrm{e}^{-\mathrm{i}\boldsymbol{G}\cdot\boldsymbol{\tau}_{\gamma}}\mathrm{Y}_{lm}\left(\hat{\boldsymbol{G}}\right)\left(\left[\mathfrak{q}_{\boldsymbol{\nabla}\rho,\mathrm{tot}}^{\gamma\boldsymbol{R}'}\right]_{lm} - \delta_{l1}\sum_{\alpha}\mathfrak{q}_{lm}^{\gamma\boldsymbol{R}'}(\alpha)\right) \tag{7.57}$$

(the minus from equation (6.30a) is taken into account here). In cases which only require the gradient of the unperturbed Hartree or external potential, the respective complementary contribution of the Coulomb potential gradient is omitted. Moreover, it must be considered that within FLEUR the convergence parameter N is optimized for each atom type $\mathring{\gamma}$ [64]. Overall, this results in the optimized

$$N_{\mathring{\gamma}}^{\mathrm{opt}} := N + l\,, \tag{7.58}$$

Final form

which are constant with respect to the quantum number l. With equation, the IR Coulomb potential finally reads

$$\boldsymbol{\nabla}V_{\mathrm{Cou}}^{(0)}(\boldsymbol{r}) = \sum_{\boldsymbol{G}|\boldsymbol{G}\neq\boldsymbol{0}} 4\pi\frac{\boldsymbol{n}_{\mathrm{Cou}}^{\mathrm{ps},\boldsymbol{\nabla}}(\boldsymbol{G})}{|\boldsymbol{G}|^{2}}\mathrm{e}^{\mathrm{i}\boldsymbol{G}\cdot\boldsymbol{r}} \tag{7.59a}$$

$$=: \sum_{\boldsymbol{G}|\boldsymbol{G}\neq\boldsymbol{0}}\left[\boldsymbol{\nabla}V_{\mathrm{Cou}}^{(0)}\right](\boldsymbol{G})\mathrm{e}^{\mathrm{i}\boldsymbol{G}\cdot\boldsymbol{r}}\,. \tag{7.59b}$$

The sum over $\boldsymbol{G}$ features the property that $\boldsymbol{G} = \boldsymbol{0}$ is explicitly excluded. Overall, the IR algorithm is inspired by the recycled FLEUR routines Vgen and Psqpw.

Gradient of the Unperturbed Muffin-tin Part

Original expression

For the Coulomb-potential gradient in the MT spheres, the previous equation is used in the surface-integral term of equation (5.43). The volume-integral contributions of the Dirichlet boundary-value problem for the unperturbed Coulomb-potential gradient are taken from the second lines in the respective external (6.32) and Hartree expressions (6.44)

$$\left[\boldsymbol{\nabla}V_{\mathrm{Cou}}^{(0)}\left(\boldsymbol{r}_{\gamma}+\boldsymbol{\tau}_{\gamma}\right)\right]_{lm} = \left(\frac{r_{\gamma}}{R_{\gamma}}\right)^{l}\sum_{\boldsymbol{G}|\boldsymbol{G}\neq\boldsymbol{0}}\mathrm{e}^{\mathrm{i}\boldsymbol{G}\cdot\boldsymbol{\tau}_{\gamma}}\left[\boldsymbol{\nabla}V_{\mathrm{Cou}}^{(0)}\right](\boldsymbol{G})4\pi\sum_{lm}\mathrm{i}^{l}\mathrm{Y}_{lm}^{*}\left(\hat{\boldsymbol{G}}\right)\mathrm{j}_{l}\left(|\boldsymbol{G}|R_{\gamma}\right) \\ + Z_{\alpha}\delta_{\gamma\alpha}\frac{4\pi}{3}\frac{1}{r_{\alpha}^{2}}\left(1-\left(\frac{r_{\alpha}}{R_{\alpha}}\right)^{3}\right)\sum_{m=-1}^{1}\frac{3}{4\pi}\sum_{i}\hat{\boldsymbol{e}}_{i}\zeta_{i,m} \\ + \frac{4\pi}{2l+1}\int_{0}^{R_{\gamma}} s_{\gamma}^{2}\left[\boldsymbol{\nabla}\rho_{\gamma}^{(0)}\left(s_{\gamma}\right)\right]_{lm}\frac{r_{<}^{l}}{r_{>}^{l+1}}\left(1-\left(\frac{r_{>}}{R_{\gamma}}\right)^{2l+1}\right)\mathrm{d}s_{\gamma}\,. \tag{7.60}$$

Rearrangement due to recycling

Since the subroutine Vmts from FLEUR is recycled, the implemented Hartree volume-integral differs from equation (7.60). It must be rearranged to

$$\left[\boldsymbol{\nabla}V_{\mathrm{Htr,\,vol}}^{(0)}\left(r_{\gamma}\right)\right]_{lm} = \frac{4\pi}{2l+1}\int_{0}^{R_{\gamma}} s_{\gamma}^{2}\left[\boldsymbol{\nabla}\rho_{\gamma}^{(0)}\left(s_{\gamma}\right)\right]_{lm}\frac{r_{<}^{l}}{r_{>}^{l+1}}\left(1-\left(\frac{r_{\gamma}}{R_{\gamma}}\right)^{2l+1}\right)\mathrm{d}s_{\gamma} \tag{7.61a}$$

$$
\begin{aligned}
&= \frac{4\pi}{2l+1}\int_0^{r_\gamma} s_\gamma^2\Big[\boldsymbol{\nabla}\rho_\gamma^{(0)}\big(s_\gamma\big)\Big]_{lm}\frac{s_\gamma^l}{r_\gamma^{l+1}}\left(1-\left(\frac{r_\gamma}{R_\gamma}\right)^{2l+1}\right)\mathrm{d}s_\gamma && (7.61\text{b})\\
&\quad+\frac{4\pi}{2l+1}\int_{r_\gamma}^{R_\gamma} s_\gamma^2\Big[\boldsymbol{\nabla}\rho_\gamma^{(0)}\big(s_\gamma\big)\Big]_{lm}\frac{r_\gamma^l}{s_\gamma^{l+1}}\left(1-\left(\frac{r_\gamma}{R_\gamma}\right)^{2l+1}\right)\mathrm{d}s_\gamma\\
&= \frac{4\pi}{2l+1}\left(\frac{1}{r_\gamma^{l+1}}-\frac{r_\gamma^l}{R_\gamma^{2l+1}}\right)\int_0^{r_\gamma} s_\gamma^{l+2}\Big[\boldsymbol{\nabla}\rho_\gamma^{(0)}\big(s_\gamma\big)\Big]_{lm}\mathrm{d}s_\gamma && (7.61\text{c})\\
&\quad+\frac{4\pi}{2l+1}r_\gamma^l\int_{r_\gamma}^{R_\gamma}\Big[\boldsymbol{\nabla}\rho_\gamma^{(0)}\big(s_\gamma\big)\Big]_{lm}\frac{1}{s^{l-1}}\mathrm{d}s_\gamma\\
&\quad-\frac{4\pi}{2l+1}\frac{r_\gamma^l}{R_\gamma^{2l+1}}\int_{r_\gamma}^{R_\gamma}\Big[\boldsymbol{\nabla}\rho_\gamma^{(0)}\big(s_\gamma\big)\Big]_{lm}s_\gamma^{l+2}\,\mathrm{d}s_\gamma\\
&= -\frac{4\pi}{2l+1}\frac{r_\gamma^l}{R_\gamma^{2l+1}}\int_0^{R_\gamma} s_\gamma^{l+2}\Big[\boldsymbol{\nabla}\rho_\gamma^{(0)}\big(s_\gamma\big)\Big]_{lm}\mathrm{d}s_\gamma && (7.61\text{d})\\
&\quad+\frac{4\pi}{2l+1}\frac{1}{r_\gamma^{l+1}}\int_0^{r_\gamma} s_\gamma^{l+2}\Big[\boldsymbol{\nabla}\rho_\gamma^{(0)}\big(s_\gamma\big)\Big]_{lm}\mathrm{d}s_\gamma\\
&\quad+\frac{4\pi}{2l+1}r_\gamma^l\left(\int_0^{R_\gamma}\frac{1}{s_\gamma^{l-1}}\Big[\boldsymbol{\nabla}\rho_\gamma^{(0)}\big(s_\gamma\big)\Big]_{lm}\mathrm{d}s_\gamma-\int_0^{r_\gamma}\frac{1}{s_\gamma^{l-1}}\Big[\boldsymbol{\nabla}\rho_\gamma^{(0)}\big(s_\gamma\big)\Big]_{lm}\right)\mathrm{d}s_\gamma\;.
\end{aligned}
$$

Final form

Ultimately, the realized MT Coulomb-potential gradient ($\boldsymbol{R}'=\boldsymbol{0}$) can be presented

$$
\begin{aligned}
&\Big[\boldsymbol{\nabla}V_{\text{Cou}}^{(0)}\big(\boldsymbol{r}_{\nu\mathring{\gamma}}+\boldsymbol{\tau}_\gamma\big)\Big]_{lm} && (7.62)\\
&\quad=\left(\frac{r_{\nu\mathring{\gamma}}}{R_{\mathring{\gamma}}}\right)^l\sum_{\boldsymbol{G}|\boldsymbol{G}\neq\boldsymbol{0}}\mathrm{e}^{\mathrm{i}\boldsymbol{G}\cdot\boldsymbol{\tau}_\gamma}\Big[\boldsymbol{\nabla}V_{\text{Cou}}^{(0)}\Big](\boldsymbol{G})4\pi\sum_{lm}\mathrm{i}^l\mathrm{Y}_{lm}^*\Big(\hat{\boldsymbol{G}}\Big)\mathrm{j}_l\Big(|\boldsymbol{G}|R_{\mathring{\gamma}}\Big)\\
&\qquad+Z_{\mathring{\alpha}}\delta_{\gamma\alpha}\frac{4\pi}{3}\frac{1}{r_{\nu\mathring{\alpha}}^2}\left(1-\left(\frac{r_{\nu\mathring{\alpha}}}{R_{\mathring{\alpha}}}\right)^3\right)\sum_{m=-1}^{1}\frac{3}{4\pi}\sum_i\hat{\boldsymbol{e}}_i\zeta_{i,m}\\
&\qquad-\frac{4\pi}{2l+1}\frac{r_{\nu\mathring{\gamma}}^l}{R_{\mathring{\gamma}}^{2l+1}}\int_0^{R_{\mathring{\gamma}}}s_{\nu\mathring{\gamma}}^{l+2}\Big[\boldsymbol{\nabla}\rho_\gamma^{(0)}(s_{\nu\mathring{\gamma}})\Big]_{lm}\mathrm{d}s_{\nu\mathring{\gamma}}\\
&\qquad+\frac{4\pi}{2l+1}\frac{1}{r_{\nu\mathring{\gamma}}^{l+1}}\int_0^{r_{\nu\mathring{\gamma}}}s_{\nu\mathring{\gamma}}^{l+2}\Big[\boldsymbol{\nabla}\rho_\gamma^{(0)}(s_{\nu\mathring{\gamma}})\Big]_{lm}\mathrm{d}s_{\nu\mathring{\gamma}}\\
&\qquad+\frac{4\pi}{2l+1}r_{\nu\mathring{\gamma}}^l\left(\int_0^{R_{\mathring{\gamma}}}\frac{1}{s_{\nu\mathring{\gamma}}^{l-1}}\Big[\boldsymbol{\nabla}\rho_\gamma^{(0)}(s_{\nu\mathring{\gamma}})\Big]_{lm}\mathrm{d}s_{\nu\mathring{\gamma}}-\int_0^{r_{\nu\mathring{\gamma}}}\frac{1}{s_{\nu\mathring{\gamma}}^{l-1}}\Big[\boldsymbol{\nabla}\rho_\gamma^{(0)}(s_{\nu\mathring{\gamma}})\Big]_{lm}\mathrm{d}s_{\nu\mathring{\gamma}}\right)\;.
\end{aligned}
$$

Algorithm

In summary, the procedure for calculating the gradient of the unperturbed Coulomb potential in a Weinert [64, 88] fashion is described in algorithm 5. Utilizing conditional clauses, it is feasible to select whether only the Hartree-, only the external-, or the complete Coulomb-potential gradient is evaluated. Furthermore, it is possible to deactivate the volume integral terms in equation (7.61), the motivation of which shall be pointed out in the subsequent sections.

Algorithm 5: Calculating $\boldsymbol{\nabla} V^{(0)\mathrm{IR}}_{\subseteq\mathrm{C}}(\boldsymbol{r})$ (7.59b) and $\boldsymbol{\nabla} V^{(0)\gamma}_{\subseteq\mathrm{C}}(\boldsymbol{r})$ (7.62).

```
if Hartree then
    qlmGrVhar0Vol ← Eval. Eq. (6.34) ;
    qlmGrVhar0Surf ← Eval. Eq. (7.53) ;
    qlmGrVc0 ← Eval. Eq. (6.39) ;
end if
if extern then
    qlmGrVext0 ← Eval. Eq. (7.56b) ;
    qlmGrVc0 ← qlmGrVc0 + qlmGrVext0 only for l = 1;
end if
nPsGrVc ← Eval. Eq. (7.57) using qlmGrVc0;
grVIR ← Eval. Eq. (7.59b) using nPsGrVc;
grVMT ← Eval. Eq. (7.62) second line using grVIR;
if fullMT then
    if Hartree then
        grVMT ← (7.62) except for first three lines;
    end if
    if extern then
        grVMT ← only third line of (7.62) ;
    end if
end if
```

First-Order Variation of the Interstitial Part

Pseudo-density

Analogously to the gradient of the unperturbed Coulomb potential, the pseudo-density Fourier coefficients for the first-order variation of the Coulomb potential read

$$\begin{aligned} \boldsymbol{n}^{\mathrm{ps},\delta\rho}_{\mathrm{Cou}}(\boldsymbol{G};\boldsymbol{q}^{+}\alpha) = \boldsymbol{\rho}^{(1)}_{\mathrm{IR}}(\boldsymbol{G},\boldsymbol{q}^{+}\alpha) + \frac{4\pi}{\Omega}\sum_{\gamma}\sum_{lm}\frac{(-\mathrm{i})^{l}\left(2N^{\mathrm{opt}}_{\mathring{\gamma}}+3\right)!!}{(2l+1)!!R^{l}_{\mathring{\gamma}}}\frac{\mathrm{j}_{l+N+1}\left(|\boldsymbol{G}+\boldsymbol{q}|R_{\mathring{\gamma}}\right)}{\left(|\boldsymbol{G}+\boldsymbol{q}|R_{\mathring{\gamma}}\right)^{N+1}} \quad (7.63) \\ \times\, \mathrm{e}^{-\mathrm{i}(\boldsymbol{G}+\boldsymbol{q})\cdot\boldsymbol{\tau}_{\gamma}}\mathrm{Y}_{lm}\left(\widehat{\boldsymbol{G}+\boldsymbol{q}}\right)\left(\left[\boldsymbol{q}^{\gamma\boldsymbol{0}}_{\delta\rho,\mathrm{tot}}(\mathbf{q}^{+}\alpha)\right]_{lm} + \delta_{l1}\sum_{\alpha}\mathbf{q}^{\gamma\boldsymbol{0}}_{lm}(\boldsymbol{q}^{+}\alpha)\right). \end{aligned}$$

Final form

In this equation, the multipole moments of the external potential gradient (7.56b) are utilized. This is legitimate, because the dependency of equation (6.26) on $\boldsymbol{q}$ is only given by $\exp(\pm\mathrm{i}\boldsymbol{q}\cdot\boldsymbol{R})$, and DFPT enables us to restrict ourselves to $\boldsymbol{R}=\boldsymbol{0}$. Moreover, the $\boldsymbol{q}^{+}$ part of the first-order Hartree-potential multipole moments (6.33) is employed. So, the IR first-order Coulomb-potential variation reads

$$\boldsymbol{V}^{(1)}_{\mathrm{Cou}}(\boldsymbol{r};\boldsymbol{q}^{+}\alpha) = \sum_{\boldsymbol{G}|\boldsymbol{G}+\boldsymbol{q}\neq\boldsymbol{0}} 4\pi\frac{\boldsymbol{n}^{\mathrm{ps},\delta\rho}_{\mathrm{Cou}}(\boldsymbol{G};\boldsymbol{q}^{+}\alpha)}{|\boldsymbol{G}+\boldsymbol{q}|^{2}}\mathrm{e}^{\mathrm{i}(\boldsymbol{G}+\boldsymbol{q})\cdot\boldsymbol{r}} \quad (7.64a)$$

$$=: \sum_{\boldsymbol{G}|\boldsymbol{G}+\boldsymbol{q}\neq\boldsymbol{0}} \boldsymbol{V}^{(1)}_{\mathrm{Cou}}(\boldsymbol{G};\boldsymbol{q}^{+}\alpha)\mathrm{e}^{\mathrm{i}(\boldsymbol{G}+\boldsymbol{q})\cdot\boldsymbol{r}}\,. \quad (7.64b)$$

Case $\boldsymbol{q} = \mathbf{0}$

In section 7.2.3, the behavior of the first-order density variation for the Goldstone modes is pointed out. For this special modes, it turns into the negative gradient of the unperturbed charge density. Given polyatomic systems, in particular a sum over all displaced atoms α must be considered. Making a mental note about this, and comparing the pseudo-density Fourier coefficients (7.57) with (7.63), a similar relation for the IR linear potential variation is deducible: Equation (7.64b) yields the negative equivalent of (7.59b), provided it is summed over the displaced atoms α and $\boldsymbol{q} = \mathbf{0}$.

First-Order Variation of the Muffin-tin Part

Original form

Following a procedure similar to the gradient of the unperturbed Coulomb potential, the MT expansion coefficients of the first-order Coulomb-potential variation read

$$\begin{aligned}
&\Big[\boldsymbol{V}^{(1)}_{\text{Cou}}\big(\boldsymbol{r}_\gamma + \boldsymbol{\tau}_\gamma; \boldsymbol{q}^+\alpha\big)\Big]_{lm} \\
&\quad= \left(\frac{r_\gamma}{R_\gamma}\right)^l \sum_{\boldsymbol{G}|\boldsymbol{G}+\boldsymbol{q}\neq\mathbf{0}} \mathrm{e}^{\mathrm{i}(\boldsymbol{G}+\boldsymbol{q})\cdot\boldsymbol{\tau}_\gamma} \boldsymbol{V}^{(1)}_{\text{Cou}}(\boldsymbol{G}; \boldsymbol{q}^+\alpha) 4\pi \sum_{lm} \mathrm{i}^l \mathrm{Y}^*_{lm}\Big(\widehat{\boldsymbol{G}+\boldsymbol{q}}\Big) \mathrm{j}_l\big(|\boldsymbol{G}+\boldsymbol{q}| R_\gamma\big) \\
&\qquad - Z_\alpha \delta_{\gamma\alpha} \frac{4\pi}{3} \frac{1}{r_\alpha^2} \left(1 - \left(\frac{r_\alpha}{R_\alpha}\right)^3\right) \sum_{m=-1}^{1} \frac{3}{4\pi} \sum_i \hat{\boldsymbol{e}}_i \zeta_{i,m} \\
&\qquad + \frac{4\pi}{2l+1} \int_0^{R_\gamma} \mathrm{d}s_\gamma\, s_\gamma^2 \Big[\boldsymbol{\rho}^{(1)}_{\gamma,\text{full}}\big(\boldsymbol{r}_\gamma; \boldsymbol{q}^\pm\alpha\big)\Big]_{lm} \frac{r_<^l}{r_>^{l+1}} \left(1 - \left(\frac{r_>}{R_\gamma}\right)^{2l+1}\right).
\end{aligned} \tag{7.65}$$

Within this expression, the Fourier coefficients from equation (7.64b) are used. In the third line of equation (7.65), the volume term in equation (6.31) is copied, and the fourth line is equal to the volume integral in equation (6.43).

Case $\boldsymbol{q} = \mathbf{0}$

The discussion about the Goldstone-condition consequences for the IR first-order Coulomb potential variation can be continued. Applying it to equation (7.65), it can likewise be stated that the MT first-order Coulomb variation becomes the negative gradient of the unperturbed Coulomb potential. For the second line of (7.65), this follows from the aforesaid IR discussion. When moreover comparing the third line of equation (7.65) with the third line of equation (7.60), the desired minus sign manifests immediately. Finally, the fourth line of equation (7.65) becomes minus the last line of (7.60), remembering the discussion of section 7.2.3. Each of the statements in this paragraph presumes that a sum over α is simultaneously performed for polyatomic systems.

Algorithm due to recycling

Again, the last line in equation (7.65) must be reformulated so that

$$\begin{aligned}
&\Big[\boldsymbol{V}^{(1)}_{\text{Cou}}\big(\boldsymbol{r}_{\nu\mathring{\gamma}} + \boldsymbol{\tau}_\gamma; \boldsymbol{q}^+\alpha\big)\Big]_{lm} \\
&= \left(\frac{r_{\nu\mathring{\gamma}}}{R_{\mathring{\gamma}}}\right)^l \sum_{\boldsymbol{G}|\boldsymbol{G}+\boldsymbol{q}\neq\mathbf{0}} \mathrm{e}^{\mathrm{i}(\boldsymbol{G}+\boldsymbol{q})\cdot\boldsymbol{\tau}_\gamma} \boldsymbol{V}^{(1)}_{\text{Cou}}(\boldsymbol{G}; \boldsymbol{q}^+\alpha) 4\pi \sum_{lm} \mathrm{i}^l \mathrm{Y}^*_{lm}\Big(\widehat{\boldsymbol{G}+\boldsymbol{q}}\Big) \mathrm{j}_l\big(|\boldsymbol{G}+\boldsymbol{q}| R_{\mathring{\gamma}}\big) \\
&\quad - Z_{\mathring{\alpha}} \delta_{\gamma\alpha} \frac{4\pi}{3} \frac{1}{r_{\nu\mathring{\alpha}}^2} \left(1 - \left(\frac{r_{\nu\mathring{\alpha}}}{R_{\mathring{\alpha}}}\right)^3\right) \sum_{m=-1}^{1} \frac{3}{4\pi} \sum_i \hat{\boldsymbol{e}}_i \zeta_{im} \\
&\quad - \frac{4\pi}{2l+1} \frac{r_{\nu\mathring{\gamma}}^l}{R_{\mathring{\gamma}}^{2l+1}} \int_0^{R_{\mathring{\gamma}}} s_{\nu\mathring{\gamma}}^{l+2} \Big[\boldsymbol{\rho}^{(1)}_{\gamma,\text{full}}\big(s_{\nu\mathring{\gamma}}; \boldsymbol{q}^\pm\alpha\big)\Big]_{lm} \mathrm{d}s_{\nu\mathring{\gamma}}
\end{aligned} \tag{7.66}$$

$$+\frac{4\pi}{2l+1}\frac{1}{r_{\nu\mathring{\gamma}}^{l+1}}\int_0^{r_{\nu\mathring{\gamma}}} s_{\nu\mathring{\gamma}}^{l+2}\Big[\boldsymbol{\rho}^{(1)}_{\gamma,\mathrm{full}}\big(s_{\nu\mathring{\gamma}};\boldsymbol{q}^{\pm}\alpha\big)\Big]_{lm}\mathrm{d}s_{\nu\mathring{\gamma}}$$
$$+\frac{4\pi}{2l+1}r^{l}_{\nu\mathring{\gamma}}\left(\int_0^{R_{\mathring{\gamma}}}\frac{1}{s^{l-1}_{\nu\mathring{\gamma}}}\Big[\boldsymbol{\rho}^{(1)}_{\gamma,\mathrm{full}}\big(s_{\nu\mathring{\gamma}};\boldsymbol{q}^{\pm}\alpha\big)\Big]_{lm}\mathrm{d}s_{\nu\mathring{\gamma}}-\int_0^{r_{\nu\mathring{\gamma}}}\frac{1}{s^{l-1}_{\nu\mathring{\gamma}}}\Big[\boldsymbol{\rho}^{(1)}_{\gamma,\mathrm{full}}\big(s_{\nu\mathring{\gamma}};\boldsymbol{q}^{\pm}\alpha\big)\Big]_{lm}\mathrm{d}s_{\nu\mathring{\gamma}}\right)$$

implies and represents the implemented version in `juPhon`. Deducing this expression is analogous to equation (7.61), since only the gradient of the unperturbed density must be substituted by the first-order variation of the density. The procedure for the complete first-order Coulomb potential is sketched in algorithm 6, in which likewise the methods for either only calculating the first-order Hartree or external potential inhere and the volume terms can be deactivated.

Algorithm 6: Calculating $\boldsymbol{V}^{(1)\mathrm{IR}}_{\subseteq\mathrm{Cou}}(\boldsymbol{r})$ (7.64b) and $\boldsymbol{V}^{(1)\gamma}_{\subseteq\mathrm{Cou}}(\boldsymbol{r})$ (7.66)

```
if Hartree then
    qlmVhar1Vol ← Eval. Eq. (6.33);
    qlmVhar1Surf ← Eval. Eq. (7.53);
    qlmVc1 ← Eval. Eq. (6.37);
end if
if extern then
    qlmVext1 ← Eval. Eq. (7.56b) ;
    qlmVc1 ← qlmVc1 + qlmVext1 only for l = 1;
end if
nPsVc1 ← Eval. Eq. (7.63) using qlmVc1;
v1IR ← Eval. Eq. (7.64b) using nPsVc1;
v1MT ← Eval. Eq. (7.66) second line using v1IR;
if fullMT then
    if Hartree then
        v1MT ← (7.66) except for first three lines;
    end if
    if extern then
        v1MT ← only third line of (7.66);
    end if
end if
```

7.3.2 Exchange-Correlation Potential

Concept

Determining the linear xc-potential variations differs from the Weinert-like method, employed for the linear Coulomb-potential variations. Basically, the Fourier coefficients of equations (6.47) and (6.48) must be determined in the IR. Within the MT spheres, it is imperative to find the spherical-harmonic expansion coefficients of equations (6.49) and (6.50). Each equation contains a functional derivative of the unperturbed xc-potential with respect to the unperturbed density.

Xα xc-potential

In order to reduce complexity in the first implementation we decided to resort to the Xα xc-potential [119, 127, 251]

$$V_{\mathrm{xc}}^{(0)}[\rho(\boldsymbol{r})] = -\frac{1}{2}2\alpha\left(\frac{3}{2\pi}\right)^{\frac{2}{3}}\left(\frac{4\pi}{3}\right)^{\frac{1}{3}}\left(\rho^{(0)}(\boldsymbol{r})\right)^{\frac{1}{3}}\,. \tag{7.67}$$

In this definition, the factor 1/2 is due to the conversion from Rydberg into Hartree energy units, and the factor 2 accounts for the spin degeneracy. The advantage of the Xα potential is that the functional derivative with respect to $\rho^{(0)}$ is uncomplicated relative to other instances in the plethora of xc potentials (cf. section 2.2.2, section 2.3 and Klüppelberg [88])

$$\frac{\delta V_{\mathrm{xc}}^{(0)}[\rho(\boldsymbol{r})]}{\delta\rho(\boldsymbol{r})} := \mathfrak{f}_{\mathrm{xc}}^{(0)}[\rho](\boldsymbol{r}) = -\frac{1}{2}2\alpha\left(\frac{3}{2\pi}\right)^{\frac{2}{3}}\left(\frac{4\pi}{3}\right)^{\frac{1}{3}}\frac{\delta}{\delta\rho(\boldsymbol{r})}\left(\rho^{(0)}(\boldsymbol{r})\right)^{\frac{1}{3}} \tag{7.68a}$$

$$= -\left(\frac{1}{9\pi}\right)^{\frac{1}{3}}\alpha\left(\rho^{(0)}(r_{\nu})\right)^{-\frac{2}{3}}\,. \tag{7.68b}$$

Future extension with `libxc`

However, I prepared the current implementation for a straight-forward extension with any further xc types. This is realized by separating the functional derivative of the xc potential from generating the complete linear xc-potential variation. In this regard, integrating the well-established library `libxc` [288] suggests itself, because it allows for accessing a wide selection of various xc-potential kernels and their functional derivatives [251].

Recycling

The algorithms of the linear xc-potential variations are based on the `FLEUR` routines `Visxc`, `Vmtxc`, `Vxcall`, and their dependencies. Apart from that, the concepts of these routines are already described by Singh and Nordström [68] as well as Blügel and Bihlmayer [71]. They shall be applied to the linear xc-potential variations.

Gradient of the Unperturbed Interstitial Part

Final Form

By defining $\boldsymbol{G}'' := \boldsymbol{G} + \boldsymbol{G}' \Leftrightarrow \boldsymbol{G}' = \boldsymbol{G}'' - \boldsymbol{G} \Leftrightarrow \boldsymbol{G} = \boldsymbol{G}'' - \boldsymbol{G}'$, equation (6.45) becomes

$$\boldsymbol{\nabla}V_{\mathrm{xc}}^{(0)\mathrm{IR}}(\boldsymbol{r}) = \sum_{\boldsymbol{G}''|\boldsymbol{G}''-\boldsymbol{G}}\left(\sum_{\boldsymbol{G}}\left[\boldsymbol{\nabla}\rho_{\mathrm{IR}}^{(0)}\right](\boldsymbol{G})\left[\mathfrak{f}_{\mathrm{xc}}^{(0)}[\rho]\right](\boldsymbol{G}''-\boldsymbol{G})\right)\mathrm{e}^{\mathrm{i}\boldsymbol{G}''\cdot\boldsymbol{r}}\,. \tag{7.69a}$$

The shift in the sum over $\boldsymbol{G}''$ can be omitted due to the underlying periodicity in the reciprocal space. While furthermore the Fourier coefficients of the unperturbed density gradient are already given in equation (7.17), the plane-wave expansion coefficients of the functional derivative are unknown. But according to equation (7.68b), the real-space representation of the latter is not. However, it incorporates the real-space unperturbed charge density in the IR, of which only the Fourier coefficients (7.5a) are at hand after the `juPhon` initialization. Essentially, this stimulates to exploit the convolution theorem including several FFTs in order to calculate

$$\boldsymbol{\nabla}V_{\mathrm{xc}}^{(0)\mathrm{IR}}(\boldsymbol{r};\boldsymbol{q}^{+}\alpha) = \sum_{\boldsymbol{G}''}\left[\left(\boldsymbol{\nabla}\rho_{\mathrm{IR}}^{(0)}\right) * \mathfrak{f}_{\mathrm{xc}}^{(0)}[\rho]\right](\boldsymbol{G}'')\mathrm{e}^{\mathrm{i}\boldsymbol{G}''\cdot\boldsymbol{r}} \tag{7.69b}$$

$$=: \sum_{\boldsymbol{G}''}\left[\boldsymbol{\nabla}V_{\mathrm{xc}}^{(0),\mathrm{IR}}\right](\boldsymbol{G}'')\mathrm{e}^{\mathrm{i}\boldsymbol{G}''\cdot\boldsymbol{r}}\,. \tag{7.69c}$$

Aliasing

The implemented procedure for this task is sketched in algorithm 7. First a linear FFT

Algorithm 7: Calculating the convolution of $\boldsymbol{\nabla} V_{\mathrm{xc}}^{(0),\mathrm{IR}}(\boldsymbol{r}; \boldsymbol{q}^{+}\alpha)$ (7.69)

```
1  nfft[1] = $3 \times$ k1d, nfft[2] = $3 \times$ k2d, nfft[3] = $3 \times$ k3d ;
2  forall $|\boldsymbol{G}| <$ Gmax do
3      if $\boldsymbol{G}_i >= 0$ then
4          Gpos[$i$] = $G_i$ ;
5      else
6          Gpos[$i$] = $G_i$ + nfft[$i$] ;
7      end if
8  end forall
9  mapFFTmesh[$G$] = Gpos[1] + Gpos[2] $\times$ nfft[1] + Gpos[3] $\times$ nfft[1] $\times$ nfft[2] ;
10 Setup grRho0IR on FFT mesh grRho0IRFFT and kernelDerivIR on FFT mesh
     kernelDerivFFT using mapFFTmesh;
11 Perform FFT on grRho0IRFFT and kernelDerivFFT using Cfft from FLEUR ;
12 grVxc0IR ← Multiply grRho0IRFFT and kernelDerivFFT;
13 Perform FFT on grVxc0IR using Cfft from FLEUR ;
14 /* Next line performs cut-off to Gmax                                  */
15 Back-Transform from Fourier mesh grVxc0IR to grVxc0IR using mapFFTmesh;
```

mesh with $27 \times \mathtt{k1d} \times \mathtt{k2d} \times \mathtt{k3d}$ points is created. The variables `k1d`, `k2d`, and `k3d` define a box with the volume

$$\Omega_{\mathrm{FFT}} = (\mathtt{k1d} - (-\mathtt{k1d})) \times (\mathtt{k2d} - (-\mathtt{k2d})) \times (\mathtt{k3d} - (-\mathtt{k3d})) \,, \tag{7.70}$$

which must surround the ball $|\boldsymbol{G}| < G_{\mathrm{max}}$ in the middle of this box. Thus, $G_i \in [-\mathtt{k}i\mathtt{d}, \mathtt{k}i\mathtt{d}]$ holds, so a mesh with $8 \times \mathtt{k1d} \times \mathtt{k2d} \times \mathtt{k3d}$ points naively suffices. But in practice, aliasing errors must be faced [289], which corrupt the FFTs. These drawbacks originate from overlapping effects caused by FFT meshes which are not generously dimensioned [127, 278]. Particularly, this subtlety must be considered for plane-wave expansion coefficients [127]. In contrast, the star construction averages such errors out, because plane-wave coefficients with equivalent absolute values of their labelling $\boldsymbol{G}$ are summarized [127]. As a long-term solution in `FLEUR`, a factor of 3 precedes every `k`i`d` and implies the aforementioned size of the linear FFT mesh.

Mesh size

However, we found that the proposed size of the `FLEUR` mesh is still not sufficient for a `juPhon` calculation [127]. The most organic way to overcome this problem is to already increase the G_{max} proposed by the `FLEUR` input generator. In order to find a minimal G_{max} for the `juPhon` calculation, we designed a benchmark test [127, 251]. This test compares the `juPhon` convolution of the IR unperturbed effective potential and the IR Heaviside function with its equivalent outcome of `FLEUR` (see appendix A).

Algorithm

The convolution described in algorithm 7 is straight-forward, apart from a mapping array constructed from line 2 to 9. This array communicates between the plane-wave coefficients and the aforesaid FFT mesh. So, both the unperturbed IR density and its gradient are determined on the aforesaid FFT mesh, before the FFT is applied to obtain their real-space representation. Then, the product in equation (6.45) can trivally be formed in real-space, based on equation (7.68b). It is attributed to a FFT mesh, which is back-transformed to reciprocal space. Reversely utilizing the aforementioned mapping array results in the desired

Fourier coefficients of the xc-potential gradient (7.69c). However, it must be clear that this back-mapping restricts the accuracy of the xc-potential gradient to the cutoff $\boldsymbol{G}_{\text{max}}$. This cutoff is applied, although the product of two IR quantities actually must be expanded on condition that $|\boldsymbol{G}| < 2G_{\text{max}}$. Finally, a factor conform to the size of the FFT mesh accumulates from the convolution procedure. At the end of the numerical convolution, the coefficients must be divided by this factor, because FFTs should not change the physics.

First-Order Variation of the Interstitial Part

Final form

The algorithm for the IR first-order variation of the xc potential is similar to that of the unperturbed xc-potential gradient. Instead of the unperturbed density gradient however, the first-order variation of the density for a finite $\boldsymbol{q}$ is employed. So, the $\boldsymbol{q}^+$ part of equation (6.48) can analogously be transformed into

$$\boldsymbol{V}_{\text{xc}}^{(1)}(\boldsymbol{r};\boldsymbol{q}^+\alpha) = \sum_{\boldsymbol{G}''}\left[\boldsymbol{\rho}_{\text{IR}}^{(1)} * \mathfrak{f}_{\text{xc}}^{(0)}[\rho]\right](\boldsymbol{G}'';\boldsymbol{q}^+\alpha)\mathrm{e}^{\mathrm{i}(\boldsymbol{G}''+\boldsymbol{q})\cdot\boldsymbol{r}} \tag{7.70a}$$

$$=: \sum_{\boldsymbol{G}''}\boldsymbol{V}_{\text{xc}}^{(1)}(\boldsymbol{G}'';\boldsymbol{q}^+\alpha)\mathrm{e}^{\mathrm{i}(\boldsymbol{G}''+\boldsymbol{q})\cdot\boldsymbol{r}}\,. \tag{7.70b}$$

Algorithm

In comparison to equation (7.69), a phase factor $\exp(\mathrm{i}\boldsymbol{q}\cdot\boldsymbol{r})$ inheres to account for the Bloch character $\boldsymbol{q}$ of the resulting first-order xc-potential variation. But, this phase can be factored out so that it is irrelevant in the convolution [127]. Strictly-speaking and as already discussed in section 6.2.2, the Bloch character $\boldsymbol{q}$ entails a shift of the ball $|\boldsymbol{G}+\boldsymbol{q}| < G_{\text{max}}$ that defines the set of the utilized reciprocal lattice vectors. Due to this effect, the mapping array for distributing the Fourier coefficients of the first-order density variation on the FFT mesh differs from that of the unperturbed charge density. In addition, the same new mapping array must be used to collect the Fourier coefficients of the first-order xc-potential variation from the Fourier mesh again. Since $\exp(\mathrm{i}\boldsymbol{q}\cdot\boldsymbol{r})$ can be factored out and despite the special mapping array, the numerical results showed that the FFT mesh of the unperturbed xc-potential gradient is sufficient. Moreover, if a shifted set of reciprocal lattice vectors is employed, we estimate that $2\left|\boldsymbol{G}_i+\boldsymbol{q}\right| \ll 3\times\texttt{k}i\texttt{d}$ must hold to avoid aliasing effects. It must be clear that ignoring the shift of the reciprocal lattice vectors (for a large enough G_{max}) strictly-speaking also neglects the Bloch character of the IR xc-potential to a certain extent. Furthermore, the aforementioned special mapping arrays become obsolete. Finally, it must be considered that the real-space representation of $\boldsymbol{\rho}_{\text{IR}}^{(1)}\left(\boldsymbol{G};\boldsymbol{q}^+\alpha\right)$ can possibly be complex-valued. But this is legitimate, because it forms only a part of the complete first-order density variation (6.20), which must be real as an observable.

Gradient of the Unperturbed Muffin-tin Part

Challenge

Within the MT spheres, the left-hand spherical-harmonic coefficients of

$$\boldsymbol{\nabla} V_{\text{xc}}^{(0)\gamma}(\boldsymbol{r}) = \sum_{l'm'}\left[\boldsymbol{\nabla}\rho_{\gamma}^{(0)}(r)\right]_{l'm'}\mathrm{Y}_{l'm'}(\hat{\boldsymbol{r}})\sum_{l''m''}\left[\mathfrak{f}_{\text{xc}}^{(0)}[\rho](r)\right]_{l''m''}\mathrm{Y}_{l''m''}(\hat{\boldsymbol{r}}) \tag{7.71a}$$

must be found (cf. equations (6.49) and (7.68b)). Essentially, this can be done by projecting both sides onto an arbitrary lattice harmonic so that

$$\begin{aligned}&\Big[\boldsymbol{\nabla} V_{\mathrm{xc}}^{(0)\gamma}(r_{\nu\mathring{\gamma}})\Big]_{lm} \qquad\qquad (7.71\mathrm{b})\\ &\quad= \oint_{\partial\gamma} \mathrm{Y}^{*}_{lm}\big(\hat{\boldsymbol{r}}_{\gamma}\big) \sum_{l'm'} \Big[\boldsymbol{\nabla}\rho_{\gamma}^{(0)}(r_{\nu\mathring{\gamma}})\Big]_{l'm'} \mathrm{Y}_{l'm'}\big(\hat{\boldsymbol{r}}_{\gamma}\big) \sum_{l''m''} \Big[\mathfrak{f}_{\mathrm{xc}}^{(0)}[\rho](r_{\nu\mathring{\gamma}})\Big]_{l''m''} \mathrm{Y}_{l''m''}\big(\hat{\boldsymbol{r}}_{\gamma}\big)\, \mathrm{d}\Omega\end{aligned}$$

results. But its computation features a poor performance, since a surface integral such as in equation (7.54) must be evaluated for *each* mesh point ν.

Final form and algorithm

An approximation to this problem consists in the Gauss–Legendre integration [71]

$$\begin{aligned}\Big[\boldsymbol{\nabla} V_{\mathrm{xc}}^{(0)\gamma}(r_{\nu\mathring{\gamma}})\Big]_{lm} &\approx \sum_{\boldsymbol{\xi}^{\mathrm{g}}_{\mu}} w\big(\boldsymbol{\xi}^{\mathrm{g}}_{\mu}\big) \mathrm{Y}^{*}_{lm}\big(\hat{\boldsymbol{\xi}}^{\mathrm{g}}_{\mu}\big) \sum_{l'm'} \Big[\boldsymbol{\nabla}\rho_{\gamma}^{(0)}\big(\xi^{\mathrm{g}}_{\mu}; r_{\nu\mathring{\gamma}}\big)\Big]_{l'm'} \mathrm{Y}_{l'm'}\big(\hat{\boldsymbol{\xi}}^{\mathrm{g}}_{\mu}\big) && (7.71\mathrm{c})\\ &\quad\times \sum_{l''m''} \Big[\mathfrak{f}_{\mathrm{xc}}^{(0)}[\rho]\big(\xi^{\mathrm{g}}_{\mu}; r_{\nu\mathring{\gamma}}\big)\Big]_{l''m''} \mathrm{Y}_{l''m''}\big(\hat{\boldsymbol{\xi}}^{\mathrm{g}}_{\mu}\big)\\ &:= \sum_{\boldsymbol{\xi}^{\mathrm{g}}_{\mu}} \mathrm{Y}^{*}_{lm}\big(\hat{\boldsymbol{\xi}}^{\mathrm{g}}_{\mu}\big) \Big[\boldsymbol{\nabla} V_{\mathrm{xc}}^{(0)\gamma}\big(\xi^{\mathrm{g}}_{\mu}; r_{\nu\mathring{\gamma}}\big)\Big]_{lm} . && (7.71\mathrm{d})\end{aligned}$$

In this method, the surface integral in equation (7.71b) is reformulated to a weighted sum over all points of so-called real-space Gauss meshes. A Gauss mesh ξ^{g}_{μ} with according Gauss weights $w(\xi^{\mathrm{g}}_{\mu})$ is generated on the surface of a unit ball by the recycled `FLEUR` routine `Gaussp`. With the set of $\hat{\boldsymbol{\xi}}^{\mathrm{g}}_{\mu}$ pointing to the respective Gauss mesh points, spherical harmonics up to a cutoff $l_{\mathrm{max},\mathring{\gamma}}$ can be set up, using the `FLEUR` routine `Ylm4`. Although the gradient of the unperturbed density must actually be expanded until $l_{\mathrm{max},\mathring{\gamma}} + 1$, we again decided to choose the cutoff $l_{\mathrm{max},\mathring{\gamma}}$ on condition that it is converged [127]. By expanding both the unperturbed density and its gradient on the Gauss mesh, their angular-distributed real-space representation on the sphere surface results. The mesh of the latter is then multiplied by equation (7.68b), employing the mesh of the former. After evaluating all sums in equation (7.71d), the MT coefficients of the first-order xc-potential variation are known for a specific MT mesh point $r_{\nu\mathring{\gamma}}$. Hence, the aforementioned procedure must be repeated for each shell of the MT sphere, according to the logarithmic MT mesh.

First-Order Variation of the Muffin-tin Part

Final form and algorithm

For obtaining the spherical-harmonic coefficients of the first-order xc-potential variation, the gradient of the charge density must be replaced by the first-order density variation, so that analogously

$$\boldsymbol{V}_{\mathrm{xc}}^{(1)\gamma}(\boldsymbol{r};\boldsymbol{q}\alpha) = \sum_{l'm'} \Big[\boldsymbol{\rho}_{\gamma}^{(1)}(r;\boldsymbol{q}\alpha)\Big]_{l'm'} \mathrm{Y}_{l'm'}(\hat{\boldsymbol{r}}) \sum_{l''m''} \Big[\mathfrak{f}_{\mathrm{xc}}^{(0)}[\rho](r)\Big]_{l''m''} \mathrm{Y}_{l''m''}(\hat{\boldsymbol{r}}) \qquad (7.71\mathrm{e})$$

can be deduced from equations (6.50) and (7.68b). Applying again the Gauss quadrature,

$$\begin{aligned}&\Big[\boldsymbol{V}_{\mathrm{xc}}^{(1)\gamma}(r_{\nu\mathring{\gamma}};\boldsymbol{q}\alpha)\Big]_{lm} \qquad\qquad (7.72\mathrm{a})\\ &\quad= \oint_{\partial\gamma} \mathrm{d}\Omega\, \mathrm{Y}^{*}_{lm}\big(\hat{\boldsymbol{r}}_{\gamma}\big) \sum_{l'm'} \Big[\boldsymbol{\rho}_{\gamma}^{(1)}(r_{\nu\mathring{\gamma}};\boldsymbol{q}\alpha)\Big]_{l'm'} \mathrm{Y}_{l'm'}\big(\hat{\boldsymbol{r}}_{\gamma}\big) \sum_{l''m''} \Big[\mathfrak{f}_{\mathrm{xc}}^{(0)}[\rho](r_{\nu\mathring{\gamma}})\Big]_{l''m''} \mathrm{Y}_{l''m''}\big(\hat{\boldsymbol{r}}_{\gamma}\big)\end{aligned}$$

$$\approx \sum_{\boldsymbol{\xi}^{\mathrm{g}}_{\mu}} \mathrm{Y}^{*}_{lm}\left(\hat{\boldsymbol{\xi}}^{\mathrm{g}}_{\mu}\right) w\left(\xi^{\mathrm{g}}_{\mu}\right) \sum_{l'm'} \left[\boldsymbol{\rho}^{(1)}_{\gamma}\left(\xi^{\mathrm{g}}_{\mu}; r_{\nu\mathring{\gamma}}; \boldsymbol{q}\alpha\right)\right]_{l'm'} \mathrm{Y}_{l'm'}\left(\hat{\boldsymbol{\xi}}^{\mathrm{g}}_{\mu}\right) \tag{7.72b}$$

$$\times \sum_{l''m''} \left[\mathfrak{f}^{(0)}_{\mathrm{xc}}[\rho]\left(\xi^{\mathrm{g}}_{\mu}; r_{\nu\mathring{\gamma}}\right)\right]_{l''m''} \mathrm{Y}_{l''m''}\left(\hat{\boldsymbol{\xi}}^{\mathrm{g}}_{\mu}\right)$$

$$= \sum_{\boldsymbol{\xi}^{\mathrm{g}}_{\mu}} \mathrm{Y}^{*}_{lm}\left(\hat{\boldsymbol{\xi}}^{\mathrm{g}}_{\mu}\right) \left[\boldsymbol{V}^{(1)\gamma}_{\mathrm{xc}}\left(r_{\nu\mathring{\gamma}}; \xi^{\mathrm{g}}_{\mu}; \boldsymbol{q}\alpha\right)\right]_{lm} \tag{7.72c}$$

finally results for the implementation.

7.3.3 Visualization

Formalism

The real-space visualization of the first-order effective-potential variations or its constituents (all combinations summarized by the index "⊆ eff") requires the approach which is already discussed in section 7.2.4. All relevant equations from the aforesaid section can simply be translated into expressions which are required here. So in the IR, the evaluation must live up to

$$V^{(1)\mathrm{IR}}_{\subseteq\mathrm{eff}}(\boldsymbol{r}_{\nu}; \boldsymbol{q}\alpha) = \sum_{\alpha} \boldsymbol{Q}^{\top}_{\alpha} \cdot \boldsymbol{V}^{(1)\mathrm{IR}}_{\subseteq\mathrm{eff}}(\boldsymbol{r}_{\nu}; \boldsymbol{q}^{+}\alpha) + \sum_{\alpha} \boldsymbol{Q}^{\dagger}_{\alpha} \cdot \boldsymbol{V}^{(1)\mathrm{IR}}_{\subseteq\mathrm{eff}}(\boldsymbol{r}_{\nu}; \boldsymbol{q}^{-}\alpha) \tag{7.73a}$$

$$= 2\,\mathrm{Re}\left(\sum_{\alpha\boldsymbol{G}} \left(\boldsymbol{Q}^{\top}_{\alpha} \cdot \boldsymbol{V}^{(1)\mathrm{IR}}_{\subseteq\mathrm{eff}}(\boldsymbol{G}, \boldsymbol{q}^{+}\alpha)\right) \mathrm{e}^{\mathrm{i}(\boldsymbol{G}+\boldsymbol{q})\cdot\boldsymbol{r}_{\nu}}\right) \tag{7.73b}$$

and in the MT spheres to

$$V^{(1)\gamma}_{\subseteq\mathrm{eff}}(\boldsymbol{r}_{\nu}; \boldsymbol{q}\alpha) \tag{7.74a}$$

$$= \sum_{\alpha} \boldsymbol{Q}^{\top}_{\alpha} \cdot \boldsymbol{V}^{(1)\gamma}_{\subseteq\mathrm{eff}}(\boldsymbol{r}_{\nu}; \boldsymbol{q}^{+}\alpha) + \sum_{\alpha} \boldsymbol{Q}^{\dagger}_{\alpha} \cdot \boldsymbol{V}^{(1)\gamma}_{\subseteq\mathrm{eff}}(\boldsymbol{r}_{\nu}; \boldsymbol{q}^{-}\alpha)$$

$$= \sum_{lm} \sum_{\alpha} \boldsymbol{Q}^{\top}_{\alpha} \cdot \left(\left[\boldsymbol{V}^{(1)\gamma}_{\subseteq\mathrm{eff}}(\boldsymbol{r}_{\nu}; \boldsymbol{q}^{+}\alpha)\right]_{lm} + (-1)^{-m}\left[\boldsymbol{V}^{*(1)\gamma}_{\subseteq\mathrm{eff}}(\boldsymbol{r}_{\nu}; \boldsymbol{q}^{+}\alpha)\right]_{l-m}\right) \mathrm{Y}_{lm}(\hat{\boldsymbol{r}}_{\nu})\,. \tag{7.74b}$$

In contrast, the gradient of the effective potential (or parts of it) is simpler to construct. Basically, it is equal to the FLAPW expansion of the unperturbed quantities so that

$$\boldsymbol{\nabla} V^{(0)\mathrm{IR}}_{\subseteq\mathrm{eff}}(\boldsymbol{r}_{\nu}) = \sum_{\boldsymbol{G}} \left(\boldsymbol{Q}^{\top} \cdot \boldsymbol{\nabla} V^{(0)\mathrm{IR}}_{\subseteq\mathrm{eff}}(\boldsymbol{G})\right) \mathrm{e}^{\mathrm{i}\boldsymbol{G}\cdot\boldsymbol{r}_{\nu}} \tag{7.75}$$

and

$$\boldsymbol{\nabla} V^{(0)\gamma}_{\subseteq\mathrm{eff}}(\boldsymbol{r}_{\nu}) = \sum_{lm} \left(\boldsymbol{Q}^{\top} \cdot \left[\boldsymbol{\nabla} V^{(0)\gamma}_{\subseteq\mathrm{eff}}(\boldsymbol{r}_{\nu})\right]_{lm}\right) \mathrm{Y}_{lm}(\hat{\boldsymbol{r}}_{\nu}) \tag{7.76}$$

hold.

Plot types and shown systems

This section contains two types of plots for fcc Ne and fcc Al, respectively. The first-order variations of the effective potential or its constituents for $\boldsymbol{q} = (0.25, 0.25, 0)^{\top} a a_0^{-1}$ are plotted in 2D, parallel to the x-z area. In a second group of plots, the gradients of the unperturbed aforementioned potentials are plotted as 3D isosurfaces. The units are composed of the lattice constant a, the Bohr radius a_0, the Hartree energy E_{h}, and the elementary charge e. In all plots, the phonon displaces the atoms in z-direction.

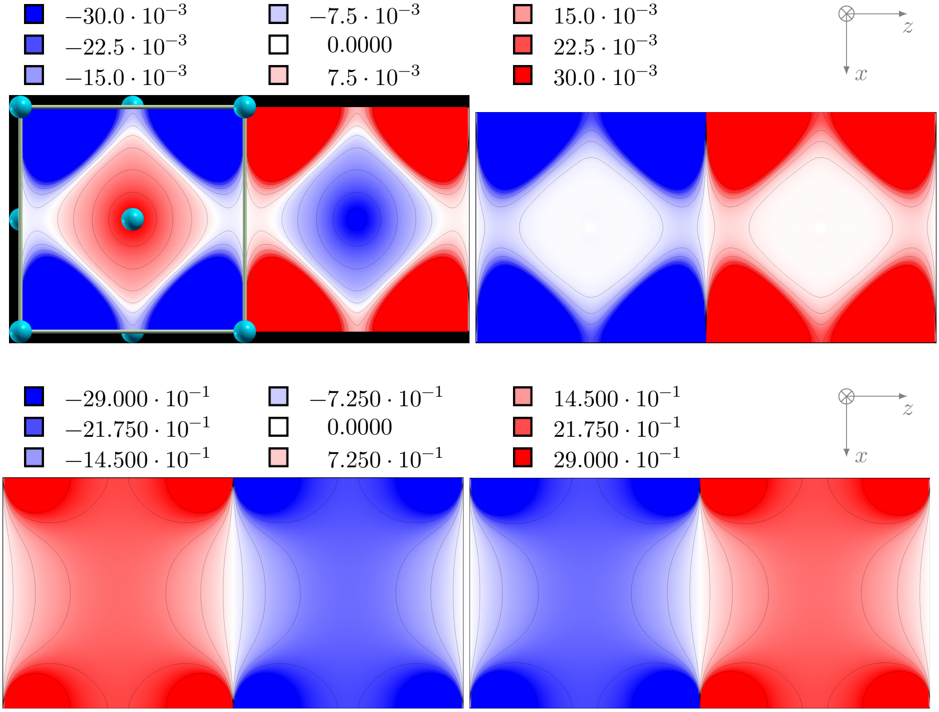

Figure 7.10: 2D-slices of first-order effective (upper left), xc (upper right), Hartree (lower left), and external (lower right) potential variations for fcc Ne and $\boldsymbol{q} = (1/4, 1/4, 0)^{\top}$ (internal units). The features of the upper left and right plots show similarities, except for the central region which stems from the two lower plots. Due to the opposite sign the contributions shown in the lower plots partially cancel each other. The first-order potentials are in the unit $E_{\mathrm{h}}\, e^{-1}\, a_0^{-1}$. The input-generator input file is given in appendix B.

Ne 2D

Figure 7.10 contains the first-order variations of the effective potential and its constituents for fcc Ne. Comparing the effective with the xc potential variation, it can be seen that the shape of the colored areas in the four corners is similar. However, the central region of the former cannot be found in the latter. It is essentially shaped by the sum of the Hartree and the external potentials in the lower plots. Their absolute values look equal at the order of magnitude 10^0, but the sign of their values is opposite to each other, leading to an annihilation at the aforesaid order of magnitude. The remainder of this sum can in particular be identified in the center of the upper left plot in figure 7.10.

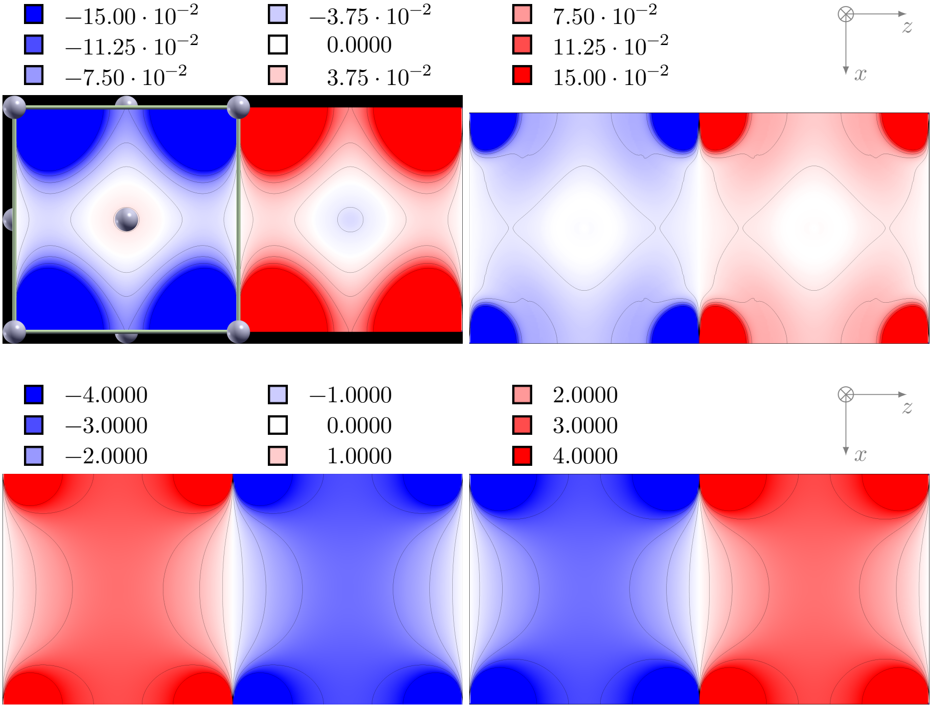

Figure 7.11: 2D-slices of first-order effective (upper left), xc (upper right), Hartree (lower left), and external (lower right) potential variations for fcc Al and $\boldsymbol{q} = ({}^{1}\!/{}_{4}, {}^{1}\!/{}_{4}, 0)^{\top}$. The units and the location of the input-generator input file are the same as in figure 7.10. Likewise, the Hartree and external potential partially cancel each other. However, relative to fcc Ne the features of the xc potential in the MT spheres at the corners as well as of the effective potential in the central MT sphere are different.

Al 2D

For fcc Al, the same first-order potential variations can be found in figure 7.11. While the Hartree and the external potentials cancel each other again, as they have the same order of magnitude but an opposite sign, the xc potential differs slightly relative to fcc Ne. I think, compared to neon, this leads to different features for the central atom in the effective potential.

Ne 3D

Isosurfaces of the effective-potential gradient and its constituents for fcc Ne are plotted in figure 7.12. The isosurfaces of the external- and Hartree-potential gradients have the

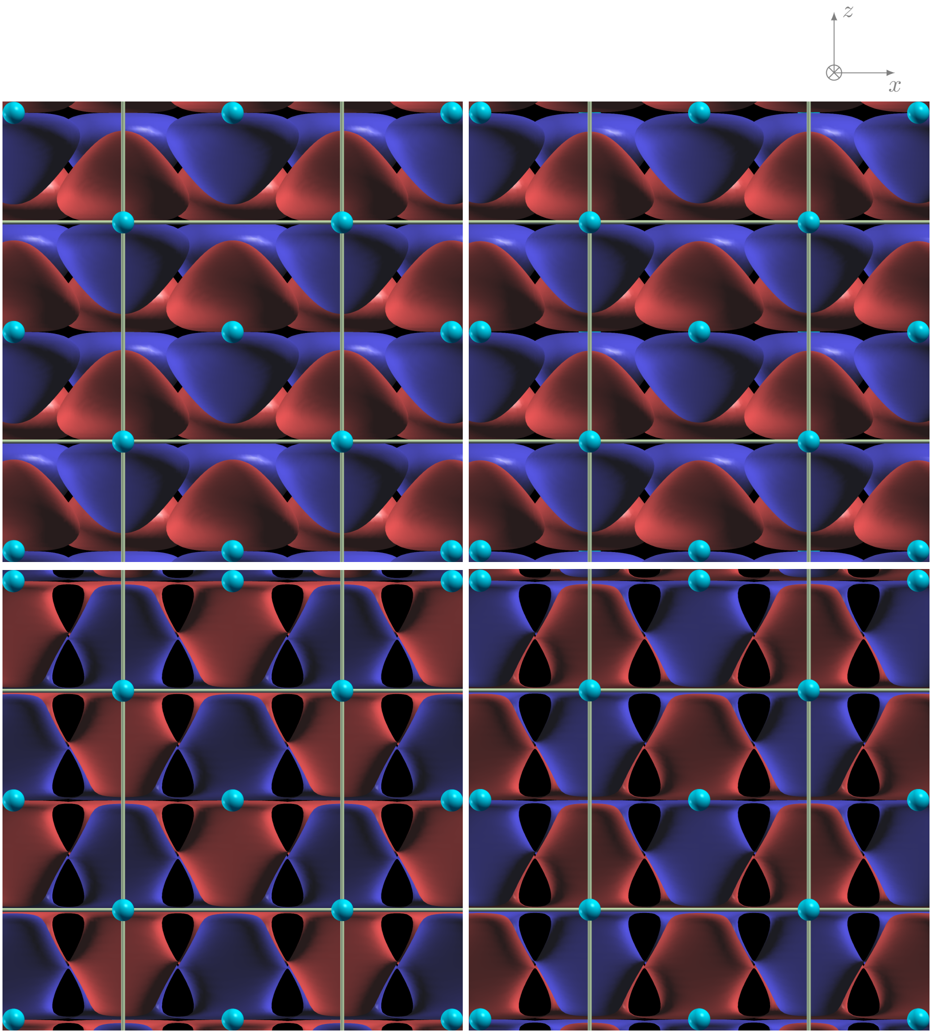

Figure 7.12: 3D isosurfaces of unperturbed effective- (upper left), exchange-correlation- (upper right), Hartree- (lower left), and external-potential (lower right) gradients for fcc Ne. All isosurfaces are shown at $4 \cdot 10^{-2}\,E_\mathrm{h}\,e^{-1}\,a_0^{-1}$. Furthermore, the input files are provided in appendix B. It can be seen that the features of the effective and the xc potential look almost similar. Moreover, the Hartree potential features a different sign than the external potential so that they partially annihilate each other, substantiating the use of the Coulomb potential gradient. As a consequence of the annihilation, there is a close resemblance between the effective and the xc-potential gradients.

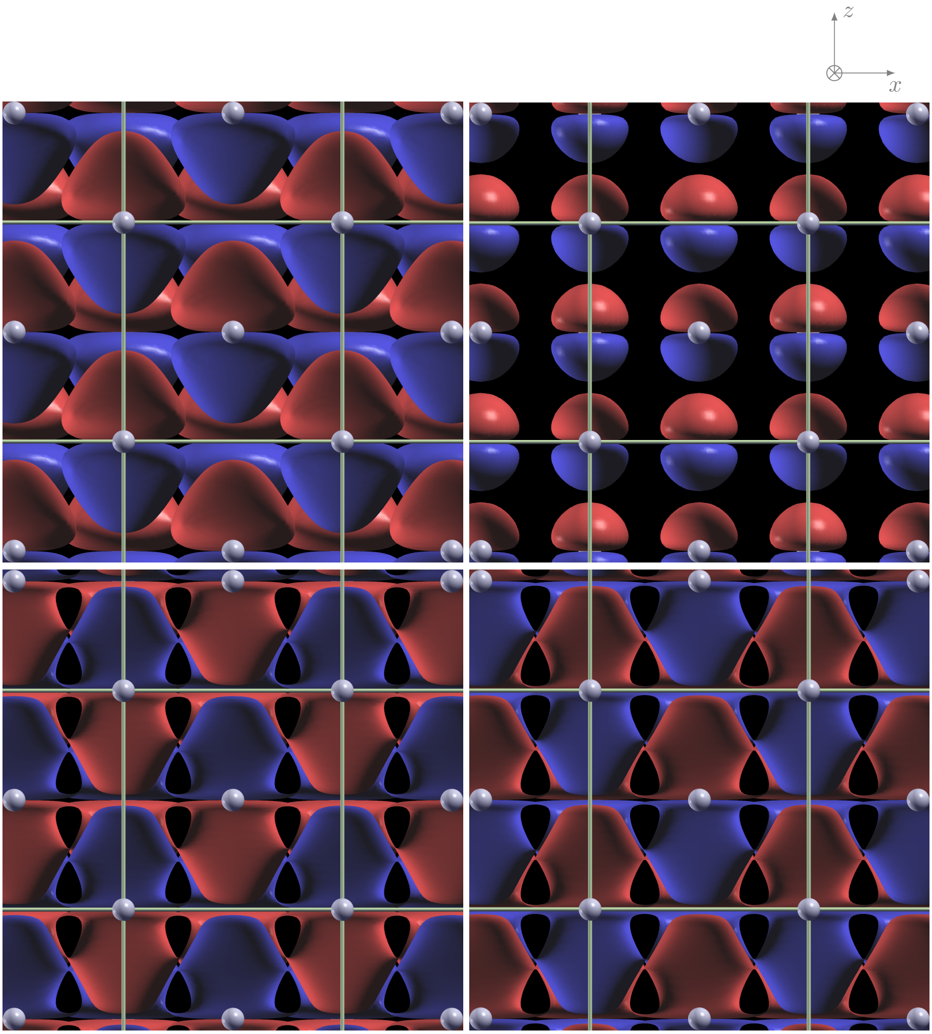

Figure 7.13: 3D isosurfaces of unperturbed effective- (upper left), exchange-correlation- (upper right), Hartree- (lower left), and external-potential (lower right) gradients for fcc Al. All isosurfaces are shown at $8 \cdot 10^{-2}\,E_\mathrm{h}\,e^{-1}\,a_0^{-1}$. The units and the reference to the input-generator input file have already be defined in figure 7.12. Relative to Ne the shape of the effective potential gradient for fcc Al is similar but only at a larger value. In particular, the shapes and values of the xc-potential gradient are significantly different, whereas the Hartree and external potential gradients appear practically equal compared to figure 7.12. Nevertheless, the Hartree and the external isosurfaces are shown at a larger value than for neon.

same shape but an opposite sign so they partially cancel each other, which is why the xc potential essentially governs the shape of the effective potential. It must be emphasized, that I manipulated all instances of the largest value in the data files of the effective- and the external-potential gradients for fcc Ne and Al so that they feature a similar order of magnitude than the instances of the second-largest value [127]. This does not have an effect on the shape of the isosurfaces but allows for a correct coloring (fixing a bug of `XcrySDen`) [127].

Al 3D

The same isosurfaces for fcc Al are depicted in figure 7.13. Relative to fcc Ne, the isosurfaces of the xc-potential gradients have a different more localized shape. However, the isosurfaces are shown at larger value relative to neon in order to reproduce the shapes of the remaining neon isosurfaces.

7.3.4 Tests

Test coverage

Analogously to section 7.2.4, again there are more tests that check the case of a vanishing than of a finite $\boldsymbol{q}$. However, the checks for the Goldstone modes form already an essential part of what can be tested. The differences emerging as far as a finite $\boldsymbol{q}$ is concerned can be handled with fewer tests. In addition, it is simpler to find tests for $\boldsymbol{q} = \boldsymbol{0}$.

Overview

First in test 15, the gradient of the effective potential is cross-checked with the input from `FLEUR`. Based on this, test 19 compares the first-order effective potential with the gradient of the unperturbed effective potential, given the boundary case $\boldsymbol{q} = \boldsymbol{0}$. The contribution of the former, which stems from a finite $\boldsymbol{q}$, is then checked in test 20. Finally, the continuity of all linear potential variations is monitored within test 17. So, the aforementioned tests basically cover the complete linear potential variations, whereas the remaining tests are devoted to check intermediate steps.

Test 15: Alternative for the Gradient of the Unperturbed Coulomb Potential

Concept

Basically, `juPhon` provides two methods to calculate the gradient of the effective potential. The first one is being employed in the `juPhon` production. It is the Weinert-like method elaborated in section 7.3.1, and the calculation of the xc-potential gradient as in section 7.3.2. But, it is also possible to apply the numerical gradient to equations (7.5b) and (7.6d), respectively. The procedure to be followed is very similar to that introduced for the unperturbed charge density (cf. section 7.2.1). Again, for the MT spheres it is beneficial to employ the original MT potential $V^{(0)\mathring{\gamma}}_{\text{eff, inp}}(r_{\nu\mathring{\gamma}})$ on the right-hand side of equation (7.3) instead of that from equation (7.6d). Hence in the IR,

$$\boldsymbol{\nabla} V^{(0)}_{\text{eff}}(\boldsymbol{r}) = \mathrm{i}\boldsymbol{G}\boldsymbol{\nabla} V^{(0)}_{\text{eff}}(\boldsymbol{G})\mathrm{e}^{\mathrm{i}\boldsymbol{G}\cdot\boldsymbol{r}} \tag{7.77}$$

holds and the MT sphere gradient reads

$$\begin{aligned}\boldsymbol{\nabla} V^{(0)\gamma}_{\text{Cou}}(\boldsymbol{r}_{\nu\mathring{\gamma}}) &= \sum_{lm}\Big[\boldsymbol{\nabla} V^{(0)\gamma}_{\text{Cou}}(r_{\nu\mathring{\gamma}})\Big]_{lm}\mathrm{Y}_{lm}\big(\boldsymbol{r}_{\gamma}\big) &\text{(7.78a)}\\ &:= \underline{T}\sum_{m''=-1}^{1}\hat{\boldsymbol{e}}_{m''}\sum_{\tilde{l}\tilde{m}}\Bigg(\Big[\boldsymbol{\nabla} V^{(0)\gamma}_{\text{Cou}}(r_{\nu\mathring{\gamma}})\Big]^{\text{opt}^{+}1m''}_{\tilde{l}+1,\tilde{m}-m''}\mathrm{Y}_{\tilde{l}+1,\tilde{m}-m''}\big(\hat{\boldsymbol{r}}_{\gamma}\big) &\text{(7.78b)}\\ &\qquad + \Big[\boldsymbol{\nabla} V^{(0)\gamma}_{\text{Cou}}(r_{\nu\gamma})\Big]^{\text{opt}^{-}1m''}_{\tilde{l}-1,\tilde{m}-m''}\mathrm{Y}_{\tilde{l}-1,\tilde{m}-m''}\big(\hat{\boldsymbol{r}}_{\gamma}\big)\Bigg)\,. &\end{aligned}$$

Its two required channels are given by

$$\left[\boldsymbol{\nabla} V_{\mathrm{C}}^{(0)\gamma}(r_{\nu\mathring{\gamma}})\right]^{\mathrm{opt}^{+}1m''}_{\tilde{l}-1,\tilde{m}-m''} =: \frac{1}{r^{2}_{\nu\mathring{\gamma}}}\hat{\boldsymbol{e}}_{m''}(-1)^{m''}\sqrt{\frac{4\pi}{3}}G^{\tilde{m}-m'',\tilde{m},-m''}_{\tilde{l}-1,\quad \tilde{l},\quad 1} \times \left(\frac{\partial\left[\tilde{V}_{\mathrm{C}}^{(0)\mathring{\gamma}}(r_{\nu\mathring{\gamma}})\right]_{\lambda\left(\tilde{l}\right)}}{\partial r_{\nu\mathring{\gamma}}}c^{\gamma}_{\lambda\left(\tilde{l}\right),\mu(\tilde{m})} + \frac{\left(\tilde{l}-1\right)}{r_{\nu\mathring{\gamma}}}\left[\tilde{V}_{\mathrm{C}}^{(0)\mathring{\gamma}}(r_{\nu\mathring{\gamma}})\right]_{\lambda\left(\tilde{l}\right)}c^{\gamma}_{\lambda\left(\tilde{l}\right),\mu(\tilde{m})}\right) \tag{7.78c}$$

and

$$\left[\boldsymbol{\nabla} V_{\mathrm{C}}^{(0)\gamma}(r_{\nu\mathring{\gamma}})\right]^{\mathrm{opt}^{-}1m''}_{\tilde{l}+1,\tilde{m}-m''} =: \frac{1}{r^{2}_{\nu\mathring{\gamma}}}\hat{\boldsymbol{e}}_{m''}(-1)^{m''}\sqrt{\frac{4\pi}{3}}G^{\tilde{m}-m'',\tilde{m},-m''}_{\tilde{l}+1,\quad \tilde{l},\quad 1} \times \left(\frac{\partial\left[\tilde{V}_{\mathrm{C}}^{(0)\mathring{\gamma}}(r_{\nu\mathring{\gamma}})\right]_{\lambda\left(\tilde{l}\right)}}{\partial r_{\mathring{\gamma}}}c^{\gamma}_{\lambda\left(\tilde{l}\right),\mu(\tilde{m})} - \frac{\left(\tilde{l}+2\right)}{r_{\nu\gamma}}\left[\tilde{V}_{\mathrm{C}}^{(0)\mathring{\gamma}}(r_{\nu\mathring{\gamma}})\right]_{\lambda\left(\tilde{l}\right)}c^{\gamma}_{\lambda\left(\tilde{l}\right),\mu(\tilde{m})}\right). \tag{7.78d}$$

Continuity

The essential difference manifesting in a comparison between the two aforesaid methods is the continuity at the MT sphere boundary. While the Coulomb-potential gradient from the Weinert-like method is per construction urged to be continuous there, there is no reason why this must be fulfilled for the numerical gradient. In contrast to the numerical gradient of the charge density variation, the LAPW basis with its matching coefficients is not utilized for the unperturbed potential gradients. Nevertheless, the latter are also expanded in plane waves and spherical harmonics within the FLAPW method (see equation (5.19)).

Results

The aforesaid comparison is illustrated in figure 7.14 for the x-z area and a displacement in the z-direction. Close to the core, the absolute error of the numerical gradient compared to the production method is large, although the relative error is small. To mitigate this effect, I have multiplied the MT sphere coefficients with a factor of $r^{2}_{\nu\gamma}$. As a consequence, both for fcc Ne and for fcc Al, the error in the MT sphere is of the order 10^{-3}. Still, the absolute error of the former system is a little smaller than that of the latter. But in both cases, the largest error displays close to the MT sphere boundary in the MT spheres, as expected. The IR region is nearly identical for both methods. In particular, the Hartree potential Fourier coefficients are different at an order of about 10^{-6}, which might be correlated with the accuracy of the integral in the first line of equation (6.34). This is substantiated by the fact that the errors of the xc and the external potential gradients are at least two or three orders of magnitude smaller. Still this cannot be recognized well in figure 7.14, because the error originating from the discrepancy in the continuity is of the order $1.0 \cdot 10^{-3}\,E_{\mathrm{h}}\,e^{-1}\,a_{0}^{-1}$.

Test 16: Alternative of Pseudo-Density for the External-Potential Variations

For the sake of being as close as possible to the recycled `FLEUR` routines, the pseudo-density for the external potential is evaluated as in equation (6.28a). But, using equation (7.56b), the pseudo-density can further be rearranged and results in equation (6.28b). In the end, both methods should deliver the same outcome. Indeed, this is the case. It indicates that the numerical benefit of using the analytically facilitated version (6.28b) is negligible. Hence, it

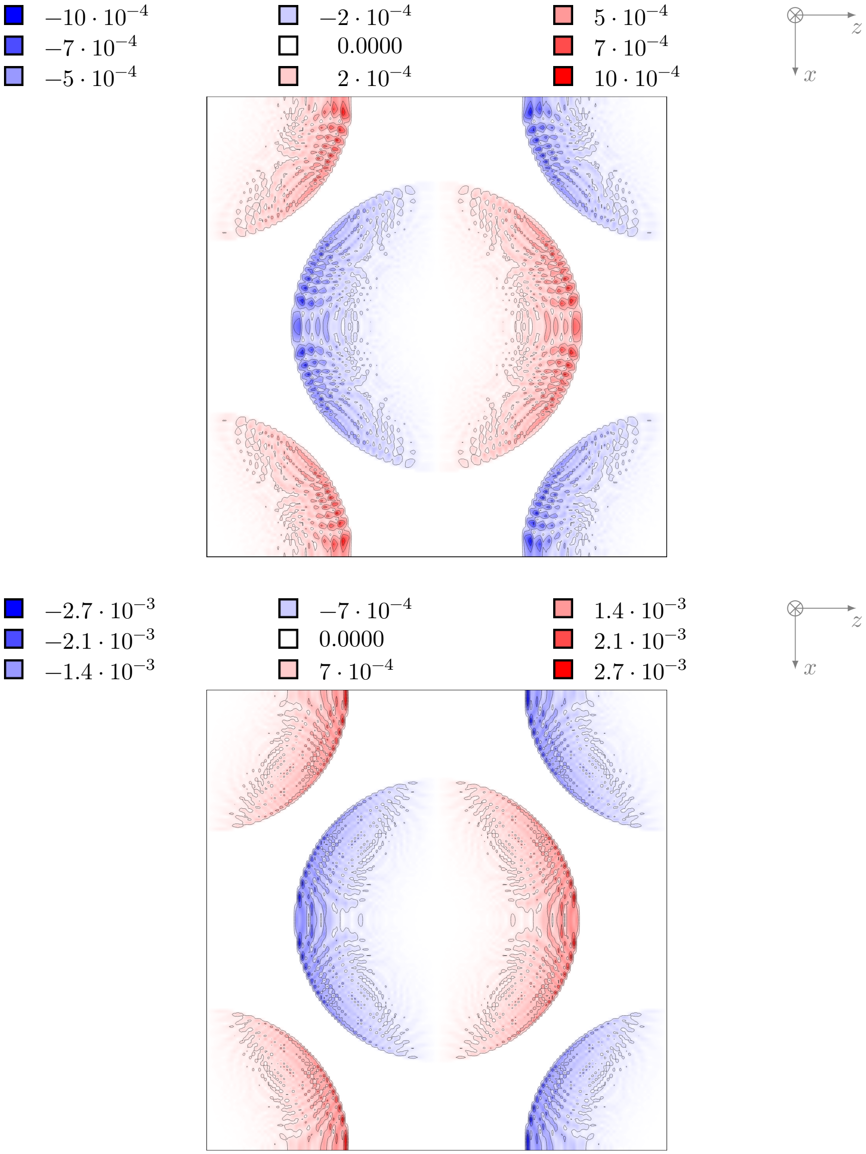

Figure 7.14: Difference between the Weinert and the numerical gradient method, using the example of the effective potential gradient ($\boldsymbol{q} = \mathbf{0}$) for fcc Ne (above) and fcc Al (below). On the MT mesh, the values are mitigated with a factor $r^2_{\nu\hat{\gamma}}$. The differences are in particular well-marked at the MT sphere boundary, because the Weinert method urges continuity at the MT sphere, whereas the numerical gradient does not. Comparing fcc Ne with fcc Al, the differences of the former are little smaller. The units are $E_\mathrm{h}\, e^{-1}\, a_0^{-1}$ and the input file can be found in appendix B.

is acceptable to add the multipole moments for the complete pseudo-density of the Coulomb potential as done in equation (7.57).

Test 17: Continuity of the Linear Potential Variations

Concept

The continuities of the linear effective potential variations are similarly checked as in test 13. Thus,

$$\boldsymbol{\nabla} V_{\text{eff}}^{(0)\text{IR}}(\boldsymbol{r}_{\text{crt}}) = \left(\sum_{\boldsymbol{G}|\boldsymbol{G}\neq\boldsymbol{0}} \left[\boldsymbol{\nabla} V_{\text{Cou}}^{(0)}\right](\boldsymbol{G}) + \sum_{\boldsymbol{G}} \left[\boldsymbol{\nabla} V_{\text{xc}}^{(0)}\right](\boldsymbol{G}) \right) \mathrm{e}^{2\pi\mathrm{i}\boldsymbol{G}\cdot\frac{1}{2\pi}\underline{B}\boldsymbol{r}_{\text{crt}}}\,, \tag{7.79a}$$

$$\boldsymbol{\nabla} V_{\text{eff}}^{(0)\gamma}(\boldsymbol{r}_{\text{crt}}) = \sum_{lm} \left(\left[\boldsymbol{\nabla} V_{\text{Cou}}^{(0)}\left(R_{\mathring{\gamma}}\right)\right]_{lm} + \left[\boldsymbol{\nabla} V_{\text{xc}}^{(0)\gamma}\left(R_{\mathring{\gamma}}\right)\right]_{lm} \right) \mathrm{Y}_{lm}\left(\hat{\boldsymbol{r}}_{\text{crt}} - \hat{\boldsymbol{\tau}}_{\gamma}\right)\,, \tag{7.79b}$$

$$\boldsymbol{V}_{\text{eff}}^{(1)}\left(\boldsymbol{r}_{\text{crt}}; \boldsymbol{q}^{+}\alpha\right) = \left(\sum_{\boldsymbol{G}|\boldsymbol{G}+\boldsymbol{q}\neq\boldsymbol{0}} \boldsymbol{V}_{\text{Cou}}^{(1)}(\boldsymbol{G}; \boldsymbol{q}^{+}\alpha) + \sum_{\boldsymbol{G}} \boldsymbol{V}_{\text{xc}}^{(1)}(\boldsymbol{G}; \boldsymbol{q}^{+}\alpha) \right) \mathrm{e}^{2\pi\mathrm{i}(\boldsymbol{G}+\boldsymbol{q})\cdot\frac{1}{2\pi}\underline{B}\boldsymbol{r}_{\text{crt}}}\,, \tag{7.80a}$$

and

$$\boldsymbol{V}_{\text{eff}}^{(1)\gamma}\left(\boldsymbol{r}_{\text{crt}}; \boldsymbol{q}^{+}\alpha\right) = \sum_{lm} \left(\left[\boldsymbol{V}_{\text{Cou}}^{(1)}\left(R_{\mathring{\gamma}}; \boldsymbol{q}^{+}\alpha\right)\right]_{lm} + \left[\boldsymbol{V}_{\text{xc}}^{(1)\gamma}\left(R_{\mathring{\gamma}}; \boldsymbol{q}\alpha\right)\right]_{lm} \right) \mathrm{Y}_{lm}\left(\hat{\boldsymbol{r}}_{\text{crt}} - \hat{\boldsymbol{\tau}}_{\gamma}\right) \tag{7.80b}$$

hold. As mentioned in the previous sections, the continuity of the linear Coulomb-potential variations is mainly governed by the Weinert construction. It is excellent, provided the Rayleigh expansion is converged. However, the continuity of the linear xc-potential variations is a little poorer, because there is no comparable requirement to the continuity. Still, it is based on the continuity of the linear density variations which are unified with the functional derivative of the unperturbed xc potentials, again dependent on the charge density.

Realization

Before the Sternheimer cycle, actually only the gradient of the effective potential and the first-order variation of the external potential is at hand. Therefore, only those are suitable for the test suite, which is executed in advance of the `juPhon` calculation. But, the continuity of the complete first-order variation can be checked after the Sternheimer equation is converged. It is possible to write the results to the log file `juPhon.log`. Finally, also in this case the coefficients of the first-order effective potential attributed to $\boldsymbol{q}^{+}$ can be complex in general. Therefore, both the real and the imaginary parts are checked.

Test 18: Reproducing the Unperturbed `FLEUR` Potentials

Concept

A comprehensive test of the subroutines to calculate the first-order variation of the Coulomb potential is to manipulate their input such that they generate the unperturbed Coulomb potential. This can be cross-checked with the outcome of `FLEUR` and is in this sense analogous to test 11.

Interstitial adjustments

Comparing equation (5.39) (including (5.36) and (5.40)) with equation (6.37), $\boldsymbol{q}$ must be set to zero and the first-order density variation must be substituted by the unperturbed charge density[20]. Furthermore, the multipole moments of the first-order external potential variation (6.26) must be replaced by

$$\mathfrak{q}_{lm}^{\gamma,\text{ext,IR}} = \frac{\sqrt{4\pi}}{3} R_{\gamma}^{3} \rho_{\text{IR}}^{(0)}(\boldsymbol{G} = \boldsymbol{0}) \delta_{l0} \delta_{m0} \,, \tag{7.81}$$

which is proportional to the average charge density in the IR. If (i) these multipole moments are employed in the subroutine to calculate equation (7.63) for $\boldsymbol{G} \neq \boldsymbol{0}$ and (ii) the first-order variation of the charge density is again substituted by the unperturbed charge density, the desired pseudo-charge Fourier coefficients (5.42) are almost reproduced. It remains to add the term

$$n_{\text{diff}}^{\text{ps}}(\boldsymbol{G}) = \delta_{\boldsymbol{G}\boldsymbol{0}} \delta_{l0} \delta_{m0} \frac{\sqrt{4\pi}}{\Omega} \sum_{\gamma} \mathfrak{q}_{lm}^{\gamma,\text{ps}} \,. \tag{7.82}$$

Now for the Goldstone modes, the IR Coulomb potential (5.42) must be reproducible with the subroutines thought for equation (7.64b).

Muffin-tin adjustments

In the MT spheres, the third line of equation (7.66) must be left away. In addition, the aforementioned IR potential must be passed to the subroutine in order to substitute the first-order variation of the Coulomb potential in equation (7.66). Finally, in the volume integrals of the aforementioned equation, the unperturbed charge density minus ZY_{00} replaces the first-order density variation in the MT sphere γ. In this way equations (5.43) should be reproducible.

Realization

The reference arrays are determined from the files `rho0pwFLEUR` (pseudo-density IR) and `v0MTFLEUR_coul` (MT unperturbed effective potential) which are written out after `Vmts` has been executed in `Vgen`. I have implemented in `FLEUR` that these files contain the Coulomb potential after the call of the `FLEUR` routine `Vmts`, i.e., the IR part is not convoluted with the step function. Furthermore, the unperturbed charge density must stem from the plane-wave (7.5a) and spherical-harmonic expansion (7.6c), respectively.

Test 19: The First-Order Effective-Potential Variations for $q = 0$

Analogously to test 12, the first-order variation of the effective potential can be evaluated for the Goldstone modes and summed over all displaced atoms α. As already discussed in the previous sections, the first-order effective-potential variation should then be the negative gradient of the effective potential.

Test 20: Time Reversal Symmetry

For a finite $\boldsymbol{q}$, the quantities which depend on reciprocal lattice vectors must fulfill certain relations [251]. This aspect is already elucidated at the end of section 7.2.3 and shall be applied to the first-order variation of the external potential, because it is available without a

---

[20] Since a scalar quantity is put into a vectorial variable, we deem it sufficient to only check one component of the first-order variation vector and set the other components to zero.

converged Sternheimer equation. So, using $\boldsymbol{q}_{\mathrm{f}}^{+} = -\boldsymbol{q}^{+} + \boldsymbol{G}_{\mathrm{f}}$ in equation (6.28b) leads to

$$
\begin{aligned}
&\boldsymbol{n}_{\text{ext}}^{\text{ps}}\left(\boldsymbol{G}; \boldsymbol{q}_{\mathrm{f}}^{+}\alpha\right) && (7.83\text{a})\\
&= \mathrm{i}\frac{Z_\alpha}{\Omega}(2N+5)!!\frac{\left(\boldsymbol{G}-\boldsymbol{q}^{+}+\boldsymbol{G}_{\mathrm{f}}\right)\mathrm{e}^{-\mathrm{i}\left(\boldsymbol{G}-\boldsymbol{q}^{+}+\boldsymbol{G}_{\mathrm{f}}\right)\cdot\boldsymbol{\tau}_\alpha}}{\left(\left|\boldsymbol{G}-\boldsymbol{q}^{+}+\boldsymbol{G}_{\mathrm{f}}\right|R_\alpha\right)^{N+2}}\mathrm{j}_{N+2}\left(\left|\boldsymbol{G}-\boldsymbol{q}^{+}+\boldsymbol{G}_{\mathrm{f}}\right|R_\alpha\right)\\
&= -\mathrm{i}\frac{Z_\alpha}{\Omega}(2N+5)!!\frac{\left(-\boldsymbol{G}-\boldsymbol{G}_{\mathrm{f}}+\boldsymbol{q}^{+}\right)\mathrm{e}^{\mathrm{i}\left(-\boldsymbol{G}-\boldsymbol{G}_{\mathrm{f}}+\boldsymbol{q}^{+}\right)\cdot\boldsymbol{\tau}_\alpha}}{\left(\left|-\boldsymbol{G}-\boldsymbol{G}_{\mathrm{f}}+\boldsymbol{q}^{+}\right|R_\alpha\right)^{N+2}}\mathrm{j}_{N+2}\left(\left|-\boldsymbol{G}-\boldsymbol{G}_{\mathrm{f}}+\boldsymbol{q}^{+}\right|R_\alpha\right) && (7.83\text{b})\\
&= \boldsymbol{n}_{\text{ext}}^{*\text{ps}}\left(-\boldsymbol{G}-\boldsymbol{G}_{\mathrm{f}}; \boldsymbol{q}^{+}\alpha\right) && (7.83\text{c})
\end{aligned}
$$

for the Fourier coefficients of the pseudo-density.

This implies for the IR external potential

$$
\begin{aligned}
\boldsymbol{V}_{\text{ext}}^{(1)}\left(\boldsymbol{r}; \boldsymbol{q}_{\mathrm{f}}^{+}\alpha\right) &= \sum_{\boldsymbol{G}|\boldsymbol{G}\pm\boldsymbol{q}\neq\boldsymbol{0}} 4\pi\frac{\boldsymbol{n}_{\text{ext}}^{\text{ps}}\left(\boldsymbol{G}; \boldsymbol{q}_{\mathrm{f}}^{+}\alpha\right)}{\left|\boldsymbol{G}+\boldsymbol{q}_{\mathrm{f}}\right|^2}\mathrm{e}^{\mathrm{i}\left(\boldsymbol{G}+\boldsymbol{q}_{\mathrm{f}}\right)\cdot\boldsymbol{r}} && (7.84\text{a})\\
&= \sum_{\boldsymbol{G}|\boldsymbol{G}\pm\boldsymbol{q}\neq\boldsymbol{0}} 4\pi\frac{\boldsymbol{n}_{\text{ext}}^{*\text{ps}}\left(-\boldsymbol{G}-\boldsymbol{G}_{\mathrm{f}}; \boldsymbol{q}^{+}\alpha\right)}{\left|-\boldsymbol{G}-\boldsymbol{G}_{\mathrm{f}}+\boldsymbol{q}^{+}\right|^2}\mathrm{e}^{-\mathrm{i}\left(-\boldsymbol{G}-\boldsymbol{G}_{\mathrm{f}}+\boldsymbol{q}^{+}\right)\cdot\boldsymbol{r}} && (7.84\text{b})\\
&= \sum_{\boldsymbol{G}'|\boldsymbol{G}'\pm\boldsymbol{q}\neq\boldsymbol{0},{}^{+}\boldsymbol{G}_{\mathrm{f}}} 4\pi\frac{\boldsymbol{n}_{\text{ext}}^{*\text{ps}}\left(\boldsymbol{G}'; \boldsymbol{q}^{+}\alpha\right)}{\left|\boldsymbol{G}'+\boldsymbol{q}^{+}\right|^2}\mathrm{e}^{-\mathrm{i}\left(\boldsymbol{G}'+\boldsymbol{q}^{+}\right)\cdot\boldsymbol{r}} && (7.84\text{c})\\
&= \boldsymbol{V}_{\text{ext}}^{*(1)}\left(\boldsymbol{r}; \boldsymbol{q}^{+}\alpha\right). && (7.84\text{d})
\end{aligned}
$$

Hence, basically

$$
\boldsymbol{V}_{\subseteq\text{ext}}^{(1)}\left(\boldsymbol{G}; \boldsymbol{q}_{\mathrm{f}}^{+}\alpha\right) = \boldsymbol{V}_{\subseteq\text{ext}}^{*(1)}\left(-\boldsymbol{G}-\boldsymbol{G}_{\mathrm{f}}; \boldsymbol{q}^{+}\alpha\right) \tag{7.85}
$$

must be checked.

This concept can also be applied to the second line of equation (7.66) and to the coefficients of the first-order xc-potential variation (7.70a). However, this must be done after the Sternheimer equation is converged. The remaining terms of the MT first-order effective-potential variation incorporate the first-order variation of the density, the correct behavior of which for a finite and exemplary $\boldsymbol{q}$ is proven on test 14.

7.4 Solving the Sternheimer Equation

Setting the stage

The linear response of the electronic system to a specific phonon perturbation is governed by the self-consistent Sternheimer equation, which contains the interdependent first-order variations of the charge density and the effective potential. They are determined in an iterative procedure up to a predefined threshold of accuracy, thereby solving the Sternheimer equation with the same precision. It stands to reason that correct implementations of this process can be ranked according to their efficiency, their numerical stability and their versatility regarding the plethora of material systems. This chapter introduces the approach of `juPhon` to this challenge. The ultimate organization of the principal loop structure in the Sternheimer module results from a discussion [127, 251, 260]. For the Goldstone modes, the analytical solution of the Sternheimer equation is already anticipated in equation (7.30) and proven in appendix D.

Outline

The form (6.61e) of the Sternheimer equation features several deficiencies in its numerics, hampering its effective implementation in the sense of the aforesaid criteria. These drawbacks, our strategy to circumvent them, and the finally implemented representation of the Sternheimer equation are elucidated in section 7.4.1. As anticipated in section 6.4.1, the terms of the Sternheimer equation fall into three categories: the HF, the Pulay and the surface contributions. In the aforementioned order, section 7.4.2, section 7.4.3, and section 7.4.4 present the intricacies of and challenges faced in their realization. Furthermore, mixing is essential in order to reach self-consistency. The way of doing it in `juPhon` is dealt with in section 7.4.5. Section 7.4.6 is devoted to give an overview of the self-consistency cycle (SCC), including its optimizations. Finally, section 7.4.7 presents the tests that verify the integrity of the Sternheimer SCC. Some subroutines of `juPhon` are inspired by subroutines of `FLEUR` version 26 and newer versions[21] of `FLEUR`.

7.4.1 Facilitating the Numerics

Avoiding basis-function gradients

There are manifold compelling reasons stimulating a rearrangement of the Sternheimer equation (6.61e) before its implementation. As far as the two Pulay terms (in its third line) are concerned, they feature one first-order variation of the LAPW basis function per braket. These brakets are evaluated in the unit cell with the volume Ω. But according to equations (5.71) and (6.7), the first-order LAPW basis variation only delivers a contribution in the displaced MT spheres α. Furthermore, this variation contains a gradient that is applied to the unperturbed LAPW basis functions, inducing undesired contributions outside their Hilbert space. However, these potentially hinder us from building on the success of DFT codes that employ the FLAPW method (cf. chapter 5). Thus, Klüppelberg [88] proposes introducing two lacking terms, enabling a backward application of the product rule for the gradient. If focussing on the $\boldsymbol{q}^+$ part of the Sternheimer equation, overall this reads

$$\begin{aligned}
&\sum_{\boldsymbol{G}} \left\langle \phi^{(0)}_{\boldsymbol{k}+\boldsymbol{q},\boldsymbol{G}'} \middle| \mathscr{H}^{(0)} - \varepsilon^{(0)}_{\boldsymbol{k},n} \middle| \phi^{(0)}_{\boldsymbol{k}+\boldsymbol{q},\boldsymbol{G}} \right\rangle_{\Omega} \boldsymbol{z}^{(1)}_{\boldsymbol{G}}(\boldsymbol{k}, n; \boldsymbol{q}^+\alpha) \qquad (7.86a)\\
&= -\sum_{\boldsymbol{G}} \Bigg\{ \left\langle \phi^{(0)}_{\boldsymbol{k}+\boldsymbol{q},\boldsymbol{G}'} \middle| \boldsymbol{\mathscr{V}}^{(1)}_{\text{eff}}(\boldsymbol{q}^+\alpha) - \delta_{\boldsymbol{q}\boldsymbol{0}} \epsilon^{(1)}_{\boldsymbol{k},n}(\boldsymbol{q}^+\alpha) \middle| \phi^{(0)}_{\boldsymbol{k},\boldsymbol{G}} \right\rangle_{\Omega} \\
&\quad + \left\langle \vec{\phi}^{(0)}_{\boldsymbol{k}+\boldsymbol{q},\boldsymbol{G}'} \middle| \boldsymbol{\nabla} \mathscr{V}^{(0)}_{\text{eff}} \middle| \vec{\phi}^{(0)}_{\boldsymbol{k},\boldsymbol{G}} \right\rangle_{\alpha} - \boldsymbol{\nabla} \left\langle \vec{\phi}^{(0)}_{\boldsymbol{k}+\boldsymbol{q},\boldsymbol{G}'} \middle| \mathscr{H}^{(0)} - \varepsilon^{(0)}_{\boldsymbol{k},n} \middle| \vec{\phi}^{(0)}_{\boldsymbol{k},\boldsymbol{G}} \right\rangle_{\alpha} \\
&\quad + \mathrm{i}(\boldsymbol{k} + \boldsymbol{G} - \boldsymbol{k} - \boldsymbol{G}' - \boldsymbol{q}) \left\langle \vec{\phi}^{(0)}_{\boldsymbol{k}+\boldsymbol{q},\boldsymbol{G}'} \middle| \mathscr{H}^{(0)} - \varepsilon^{(0)}_{\boldsymbol{k},n} \middle| \vec{\phi}^{(0)}_{\boldsymbol{k},\boldsymbol{G}} \right\rangle_{\alpha} \\
&\quad + \oint_{\partial\alpha} \vec{\phi}^{*(0)\alpha}_{\boldsymbol{k}+\boldsymbol{q},\boldsymbol{G}'}(\boldsymbol{r}) \left(\mathscr{H}^{(0)} - \varepsilon^{(0)}_{\boldsymbol{k},n} \right) \vec{\phi}^{(0)\alpha}_{\boldsymbol{k},\boldsymbol{G}}(\boldsymbol{r})\, \mathrm{d}\boldsymbol{S} \\
&\quad - \oint_{\partial\alpha} \phi^{*(0)\mathrm{IR}}_{\boldsymbol{k}+\boldsymbol{q},\boldsymbol{G}'} \left(\mathscr{H}^{(0)} - \varepsilon^{(0)}_{\boldsymbol{k},n} \right) \phi^{(0)\mathrm{IR}}_{\boldsymbol{k},\boldsymbol{G}}\, \mathrm{d}\boldsymbol{S} \Bigg\} z^{(0)}_{\boldsymbol{G}}(\boldsymbol{k}, n)\,.
\end{aligned}$$

Exploiting then the divergence theorem

$$-\boldsymbol{\nabla} \left\langle \vec{\phi}^{(0)}_{\boldsymbol{k}+\boldsymbol{q},\boldsymbol{G}'} \middle| \mathscr{H}^{(0)} - \varepsilon^{(0)}_{\boldsymbol{k},n} \middle| \vec{\phi}^{(0)}_{\boldsymbol{k},\boldsymbol{G}} \right\rangle_{\alpha} = -\oint_{\partial\alpha} \vec{\phi}^{*(0)\alpha}_{\boldsymbol{k}+\boldsymbol{q},\boldsymbol{G}'}(\boldsymbol{r}) \left(\mathscr{H}^{(0)} - \varepsilon^{(0)}_{\boldsymbol{k},n} \right) \vec{\phi}^{(0)\alpha}_{\boldsymbol{k},\boldsymbol{G}}(\boldsymbol{r})\, \mathrm{d}\boldsymbol{S} \qquad (7.86b)$$

---

[21] For section 7.4, the version defined on page 159 is referred to. Especially for section 7.4, the version is stored in the `FLEUR` repository and can be addressed by the hash `acb2166b19a55a6b2891ac9244f5ca8b7db63cde`.

in equation (7.86a)

$$\begin{aligned}
&\sum_{\boldsymbol{G}} \left\langle \phi^{(0)}_{\boldsymbol{k}+\boldsymbol{q},\boldsymbol{G}'} \middle| \mathscr{H}^{(0)} - \varepsilon^{(0)}_{\boldsymbol{k},n} \middle| \phi^{(0)}_{\boldsymbol{k}+\boldsymbol{q},\boldsymbol{G}} \right\rangle_{\Omega} \boldsymbol{z}^{(1)}_{\boldsymbol{G}}(\boldsymbol{k}, n; \boldsymbol{q}^{+}\alpha) \qquad (7.86c)\\
&= -\sum_{\boldsymbol{G}} \Bigg\{ \left\langle \phi^{(0)}_{\boldsymbol{k}+\boldsymbol{q},\boldsymbol{G}'} \middle| \boldsymbol{\mathscr{V}}^{(1)}_{\text{eff}}(\boldsymbol{q}^{+}\alpha) - \delta_{\boldsymbol{q}\boldsymbol{0}} \epsilon^{(1)}_{\boldsymbol{k},n}(\boldsymbol{q}^{+}\alpha) \middle| \phi^{(0)}_{\boldsymbol{k},\boldsymbol{G}} \right\rangle_{\Omega} \\
&\qquad + \left\langle \vec{\phi}^{(0)}_{\boldsymbol{k}+\boldsymbol{q},\boldsymbol{G}'} \middle| \boldsymbol{\nabla} \mathscr{V}^{(0)}_{\text{eff}} \middle| \vec{\phi}^{(0)}_{\boldsymbol{k},\boldsymbol{G}} \right\rangle_{\alpha} \\
&\qquad + \mathrm{i}(\boldsymbol{k} + \boldsymbol{G} - \boldsymbol{k} - \boldsymbol{G}' - \boldsymbol{q}) \left\langle \vec{\phi}^{(0)}_{\boldsymbol{k}+\boldsymbol{q},\boldsymbol{G}'} \middle| \mathscr{H}^{(0)} - \varepsilon^{(0)}_{\boldsymbol{k},n} \middle| \vec{\phi}^{(0)}_{\boldsymbol{k},\boldsymbol{G}} \right\rangle_{\alpha} \\
&\qquad - \oint_{\partial\alpha} \hat{\boldsymbol{r}} \phi^{*(0)\mathrm{IR}}_{\boldsymbol{k}+\boldsymbol{q},\boldsymbol{G}'} \left(\mathscr{H}^{(0)} - \varepsilon^{(0)}_{\boldsymbol{k},n} \right) \phi^{(0)\mathrm{IR}}_{\boldsymbol{k},\boldsymbol{G}} \, \mathrm{d}S \Bigg\} z^{(0)}_{\boldsymbol{G}}(\boldsymbol{k}, n)
\end{aligned}$$

results. In this reformulated Sternheimer equation[22], Klüppelberg [88] has eliminated the brakets with LAPW basis function gradients, thereby canceling the MT surface integral in the last line of equation (7.86a).

Avoiding numerical (matrix) inversion

Drawing an analogy to the mixing of the charge density in FLEUR [119, 127, 251] precedes the next step. Ultimately, the aforesaid procedure translates into mixing the first-order charge-density variation. Hence, it is imperative to solve equation (7.86c) for $\boldsymbol{z}^{(1)}_{\boldsymbol{G}}(\boldsymbol{k}, n; \boldsymbol{q}^{+}\alpha)$. Consequently, the $N_{\boldsymbol{G}} \times N_{\boldsymbol{G}'}$ braket on the left-hand side of equation (7.86c) must be inverted ($N_{\boldsymbol{G}'}$ denotes the number of reciprocal lattice vectors $\boldsymbol{G}'$). Given the number of $N_{\boldsymbol{k}}$ $\boldsymbol{k}$- and of $N_{\boldsymbol{q}}$ $\boldsymbol{q}$-vectors, numerically inverting the aforementioned quadratic matrix roughly scales with $\mathcal{O}\left(N^3_{\boldsymbol{q}} N^3_{\boldsymbol{k}} N^3_{\boldsymbol{G}'}\right)$ per iteration (LUP-decomposition algorithm) [272]. Moreover, additional numerical inaccuracies might emerge, making an adverse impact upon reaching self-consistency. But, these drawbacks could be avoided when renouncing to operate in the representation of LAPW basis functions [260]. As soon as the latter are substituted by Kohn–Sham wave functions[23] on the left-hand side of equation (7.86c), tremendous effort is taken out of the numerical inversion [260]. This originates from the fact that the Kohn–Sham equations can now be exploited. So, the Hamiltonian can now either act on the right or on the left, leading to Kohn–Sham energies at bands p or m, respectively. However, the Kronecker delta resulting from the overlap of the Kohn–Sham wave functions in

$$\begin{aligned}
&\sum_{n''} \left\langle \Psi^{(0)}_{\boldsymbol{k}+\boldsymbol{q},n'} \middle| \mathscr{H}^{(0)} - \varepsilon^{(0)}_{\boldsymbol{k},n} \middle| \Psi^{(0)}_{\boldsymbol{k}+\boldsymbol{q},n''} \right\rangle_{\Omega} \boldsymbol{z}^{(1)}_{n''}(\boldsymbol{k}, n; \boldsymbol{q}^{+}\alpha) \qquad (7.87a)\\
&\quad = \sum_{n''} \delta_{n'n''} \left(\varepsilon^{(0)}_{\boldsymbol{k}+\boldsymbol{q},n''} - \varepsilon^{(0)}_{\boldsymbol{k},n} \right) \boldsymbol{z}^{(1)}_{n''}(\boldsymbol{k}, n; \boldsymbol{q}^{+}\alpha) \\
&\quad = \left(\varepsilon^{(0)}_{\boldsymbol{k}+\boldsymbol{q},n'} - \varepsilon^{(0)}_{\boldsymbol{k},n} \right) \boldsymbol{z}^{(1)}_{n'}(\boldsymbol{k}, n; \boldsymbol{q}^{+}\alpha) \qquad (7.87b)
\end{aligned}$$

makes both options equivalent in the end. Finally in equation (7.87b), the difference of Kohn–Sham energies simplifies the original braket matrix-elements. A systematic application of this concept requires multiplying both sides of equation (7.86c) from the left by unperturbed wave-function coefficients $z^{(0)}_{\boldsymbol{G}'}(\boldsymbol{k}, \boldsymbol{n})$, and summing over all reciprocal lattice vectors $\boldsymbol{G}'$. Moreover, we introduce an auxiliary first-order wave-function expansion-coefficients variation, which is a matrix dimensioned by the bands n and n' [251]. The vector of n' unperturbed wave-function

---

[22] This form has firstly been suggested by Kouba et al. [93] based on a numerical experiment.

[23] This idea of using the Kohn–Sham wave functions instead of the LAPW basis functions is also realized in FLEUR in the subroutines that calculate SOC from second variation [260].

coefficients is multiplied by this matrix in [251]

$$\begin{aligned}\boldsymbol{z}^{(1)}_{\boldsymbol{G}}(\boldsymbol{k},n;\boldsymbol{q}^{+}\alpha) &=: \sum_{n'} z^{(0)}_{\boldsymbol{G}}(\boldsymbol{k},n';\boldsymbol{q})\boldsymbol{z}^{(1)}_{n'}(\boldsymbol{k},n;\boldsymbol{q}^{+}\alpha) && \text{(7.87c)}\\ &= \boldsymbol{z}^{(1)}_{\boldsymbol{G}}\left(\boldsymbol{k}^{+}_{\text{bf}},n;\alpha\right)\,. && \text{(7.87d)}\end{aligned}$$

Defining furthermore

$$\left\langle\widetilde{\vec{\boldsymbol{\Psi}}}^{(0)}_{\boldsymbol{k}+\boldsymbol{q},n'}\right| := \left\langle \mathrm{i}\sum_{\boldsymbol{G}'}(\boldsymbol{k}+\boldsymbol{q}+\boldsymbol{G}')z^{(0)}_{\boldsymbol{G}'}(\boldsymbol{k},n';\boldsymbol{q})\vec{\phi}^{(0)}_{\boldsymbol{k}+\boldsymbol{q},\boldsymbol{G}'}\right|\,, \tag{7.87e}$$

from which the expression $\left|\widetilde{\vec{\boldsymbol{\Psi}}}^{(0)}_{\boldsymbol{k},n}\right\rangle$ can trivally be deduced, leads all in all to

$$\begin{aligned}&\sum_{n''}\left\langle\Psi^{(0)}_{\boldsymbol{k}+\boldsymbol{q},n'}\middle|\mathscr{H}^{(0)}-\varepsilon^{(0)}_{\boldsymbol{k},n}\middle|\Psi^{(0)}_{\boldsymbol{k}+\boldsymbol{q},n''}\right\rangle_{\Omega}\boldsymbol{z}^{(1)}_{n''}(\boldsymbol{k},n;\boldsymbol{q}^{+}\alpha) && \text{(7.87f)}\\ &= -\left\langle\Psi^{(0)}_{\boldsymbol{k}+\boldsymbol{q},n'}\middle|\boldsymbol{\mathscr{V}}^{(1)}_{\text{eff}}(\boldsymbol{q}^{+}\alpha)-\delta_{\boldsymbol{q}\boldsymbol{0}}\epsilon^{(1)}_{\boldsymbol{k},n}(\boldsymbol{q}^{+}\alpha)\middle|\Psi^{(0)}_{\boldsymbol{k},n}\right\rangle_{\Omega}\\ &\quad-\left\langle\vec{\Psi}^{(0)}_{\boldsymbol{k}+\boldsymbol{q},n'}\middle|\boldsymbol{\nabla}\mathscr{V}^{(0)}_{\text{eff}}\middle|\vec{\Psi}^{(0)}_{\boldsymbol{k},n}\right\rangle_{\alpha}\\ &\quad-\left\langle\widetilde{\vec{\boldsymbol{\Psi}}}^{(0)}_{\boldsymbol{k}+\boldsymbol{q},n'}\middle|\mathscr{H}^{(0)}-\varepsilon^{(0)}_{\boldsymbol{k},n}\middle|\vec{\Psi}^{(0)}_{\boldsymbol{k},n}\right\rangle_{\alpha}-\left\langle\vec{\Psi}^{(0)}_{\boldsymbol{k}+\boldsymbol{q},n'}\middle|\mathscr{H}^{(0)}-\varepsilon^{(0)}_{\boldsymbol{k},n}\middle|\widetilde{\vec{\boldsymbol{\Psi}}}^{(0)}_{\boldsymbol{k},n}\right\rangle_{\alpha}\\ &\quad+\oint_{\partial\alpha}\hat{\boldsymbol{r}}\,\Psi^{*(0)\text{IR}}_{\boldsymbol{k}+\boldsymbol{q},n'}\left(\mathscr{H}^{(0)}-\varepsilon^{(0)}_{\boldsymbol{k},n}\right)\Psi^{(0)\text{IR}}_{\boldsymbol{k},n}\,\mathrm{d}S\;.\end{aligned}$$

Using equation (7.87b), the difference of Kohn–Sham energies can be brought to the right-hand side yielding

$$\begin{aligned}\boldsymbol{z}^{(1)}_{n'}(\boldsymbol{k},n;\boldsymbol{q}^{+}\alpha) = -&\frac{1}{\varepsilon^{(0)}_{\boldsymbol{k}+\boldsymbol{q},n'}-\varepsilon^{(0)}_{\boldsymbol{k},n}} && \text{(7.87g)}\\ &\times\left\{\left\langle\Psi^{(0)}_{\boldsymbol{k}+\boldsymbol{q},n'}\middle|\boldsymbol{\mathscr{V}}^{(1)}_{\text{eff}}(\boldsymbol{q}^{+}\alpha)-\delta_{\boldsymbol{q}\boldsymbol{0}}\epsilon^{(1)}_{\boldsymbol{k},n}(\boldsymbol{q}^{+}\alpha)\middle|\Psi^{(0)}_{\boldsymbol{k},n}\right\rangle_{\Omega}\right.\\ &\quad+\left\langle\vec{\Psi}^{(0)}_{\boldsymbol{k}+\boldsymbol{q},n'}\middle|\boldsymbol{\nabla}\mathscr{V}^{(0)}_{\text{eff}}\middle|\vec{\Psi}^{(0)}_{\boldsymbol{k},n}\right\rangle_{\alpha}\\ &\quad+\left\langle\widetilde{\vec{\boldsymbol{\Psi}}}^{(0)}_{\boldsymbol{k}+\boldsymbol{q},n'}\middle|\mathscr{H}^{(0)}-\varepsilon^{(0)}_{\boldsymbol{k},n}\middle|\vec{\Psi}^{(0)}_{\boldsymbol{k},n}\right\rangle_{\alpha}+\left\langle\vec{\Psi}^{(0)}_{\boldsymbol{k}+\boldsymbol{q},n'}\middle|\mathscr{H}^{(0)}-\varepsilon^{(0)}_{\boldsymbol{k},n}\middle|\widetilde{\vec{\boldsymbol{\Psi}}}^{(0)}_{\boldsymbol{k},n}\right\rangle_{\alpha}\\ &\quad\left.-\oint_{\partial\text{IR}_{\alpha}}\hat{\boldsymbol{r}}\,\Psi^{*(0)\text{IR}}_{\boldsymbol{k}+\boldsymbol{q},n'}\left(\mathscr{H}^{(0)}-\varepsilon^{(0)}_{\boldsymbol{k},n}\right)\Psi^{(0)\text{IR}}_{\boldsymbol{k},n}\,\mathrm{d}S\right\}\,,\end{aligned}$$

which is a rectangular matrix concerning the bands n and n'.

Numerical benefit

Klüppelberg [88] additionally states that in equation (7.87g), the brakets of the displaced atoms α containing the linear variations of the effective potential can be unified to one braket. Thus

$$\begin{aligned}\boldsymbol{z}^{(1)}_{n'}(\boldsymbol{k},n;\boldsymbol{q}^{+}\alpha) &= -\frac{1}{\varepsilon^{(0)}_{\boldsymbol{k}+\boldsymbol{q},n'}-\varepsilon^{(0)}_{\boldsymbol{k},n}} && \text{(7.87h)}\\ \times&\left\{\left\langle\Psi^{(0)}_{\boldsymbol{k}+\boldsymbol{q},n'}\middle|\boldsymbol{\mathscr{V}}^{(1)}_{\text{eff}}(\boldsymbol{q}^{+}\alpha)\middle|\Psi^{(0)}_{\boldsymbol{k},n}\right\rangle_{\text{IR}}+\sum_{\gamma}\left\langle\vec{\Psi}^{(0)}_{\boldsymbol{k}+\boldsymbol{q},n'}\middle|\boldsymbol{\mathscr{V}}^{(1)}_{\text{eff}}(\boldsymbol{q}^{+}\alpha)+\boldsymbol{\nabla}\mathscr{V}^{(0)}_{\text{eff}}\delta_{\gamma\alpha}\middle|\vec{\Psi}^{(0)}_{\boldsymbol{k},n}\right\rangle_{\gamma}\right.\end{aligned}$$

$$+ \left\langle \widetilde{\vec{\boldsymbol{\Psi}}}^{(0)}_{\boldsymbol{k}+\boldsymbol{q},n'} \middle| \mathscr{H}^{(0)} - \varepsilon^{(0)}_{\boldsymbol{k},n} \middle| \vec{\Psi}^{(0)}_{\boldsymbol{k},n} \right\rangle_{\alpha} + \left\langle \vec{\Psi}^{(0)}_{\boldsymbol{k}+\boldsymbol{q},n'} \middle| \mathscr{H}^{(0)} - \varepsilon^{(0)}_{\boldsymbol{k},n} \middle| \widetilde{\vec{\boldsymbol{\Psi}}}^{(0)}_{\boldsymbol{k},n} \right\rangle_{\alpha}$$

$$- \oint_{\partial \mathrm{IR}_{\alpha}} \hat{\boldsymbol{r}} \Psi^{*(0)\mathrm{IR}}_{\boldsymbol{k}+\boldsymbol{q},n'} \left(\mathscr{H}^{(0)} - \varepsilon^{(0)}_{\boldsymbol{k},n} \right) \Psi^{(0)\mathrm{IR}}_{\boldsymbol{k},n} \, \mathrm{d}S \Bigg\}$$

results. The sum of the linear potential variations in the last braket of the second line leads to further simplifications in the implementation [88]. Analyzing equations (7.62) and (7.66) for the displaced MT sphere α, it becomes obvious that their third lines cancel in the case of the Goldstone modes. Furthermore, the gradient of the unperturbed charge density is subtracted in the first-order density variation (7.37b). Therefore also the last three lines of equations (7.62) cancel in general, because they compensate with respective parts of the last three lines in equation (7.37b). In a similar way, the sum of equations (7.71d) and (7.72c) can be simplified. As a consequence, the $^1/_r$ and the $^1/_{r^2}$ behavior as well as the large potentially inaccurate numbers of the MT gradients at the core are not calculated anymore. This alleviates the MT braket in the second line of equation (7.87h) and is beneficial for the convergence behavior of the self-consistency cycle, the overall accuracy as well as the performance.

Back-folding and final form

Another problem we face in the implementation is that the unperturbed wave-function expansion coefficients are not available outside the first Brillouin zone. But if

$$\boldsymbol{z}^{(1)}_{n'}(\boldsymbol{k}^{+}_{\mathrm{bf}}, n; \alpha) = -\frac{1}{\epsilon^{(0)}_{\boldsymbol{k}^{+}_{\mathrm{bf}},n'} - \epsilon^{(0)}_{\boldsymbol{k},n}} \tag{7.88}$$

$$\times \Bigg\{ \left\langle \Psi^{(0)}_{\boldsymbol{k}^{+}_{\mathrm{bf}},n'} \middle| \boldsymbol{\mathscr{V}}^{(1)}_{\text{eff}}(\boldsymbol{q}^{+}\alpha) \middle| \Psi^{(0)}_{\boldsymbol{k},n} \right\rangle_{\mathrm{IR}} + \sum_{\gamma} \left\langle \vec{\Psi}^{(0)}_{\boldsymbol{k}^{+}_{\mathrm{bf}},n'} \middle| \boldsymbol{\mathscr{V}}^{(1)}_{\text{eff}}(\boldsymbol{q}^{+}\alpha) + \boldsymbol{\nabla}\mathscr{V}^{(0)}_{\text{eff}} \delta_{\gamma\alpha} \middle| \vec{\Psi}^{(0)}_{\boldsymbol{k},n} \right\rangle_{\gamma}$$

$$+ \left\langle \widetilde{\vec{\boldsymbol{\Psi}}}^{(0)}_{\boldsymbol{k}^{+}_{\mathrm{bf}},n'} \middle| \mathscr{H}^{(0)} - \varepsilon^{(0)}_{\boldsymbol{k},n} \middle| \vec{\Psi}^{(0)}_{\boldsymbol{k},n} \right\rangle_{\alpha} + \left\langle \vec{\Psi}^{(0)}_{\boldsymbol{k}^{+}_{\mathrm{bf}},n'} \middle| \mathscr{H}^{(0)} - \varepsilon^{(0)}_{\boldsymbol{k},n} \middle| \widetilde{\vec{\boldsymbol{\Psi}}}^{(0)}_{\boldsymbol{k},n} \right\rangle_{\alpha}$$

$$- \oint_{\partial \mathrm{IR}_{\alpha}} \hat{\boldsymbol{e}}_{\mathrm{IR}} \Psi^{*(0)\mathrm{IR}}_{\boldsymbol{k}^{+}_{\mathrm{bf}},n'} \left(\mathscr{H}^{(0)} - \varepsilon^{(0)}_{\boldsymbol{k},n} \right) \Psi^{(0)\mathrm{IR}}_{\boldsymbol{k},n} \, \mathrm{d}S \Bigg\} .$$

was implemented according to equation (7.25), they and the set of reciprocal lattice vectors $\left|\boldsymbol{k}^{+}_{\mathrm{bf}} + \boldsymbol{G}\right| < k_{\mathrm{max}}$ from the `eig` file would always be at hand [127, 251].

Singularities

For the Goldstone modes, equation (7.88) features a singularity for $n' = n$. However according to equation (4.20b), only combinations of occupied and unoccupied states contribute to the first-order density variation [3, 87]. Thus, the division by zero is ruled out [3, 87]. Degenerate Kohn–Sham energies in the Sternheimer equation are an additional case in which the first-order wave-function expansion coefficients vanish [251]. This can be understood from multiplying the reciprocal difference of Kohn–Sham energies back to the left-hand side of equation (7.87g). Provided a configuration of bands and Bloch vectors featuring degeneracy, the remaining right-hand side then equals zero. Moreover in practice, two general energies for any distinct bands and arbitrary Bloch vectors $\boldsymbol{k}$ and $\boldsymbol{q}$ can lie very close to each other. It can cause pseudo-singularities with a severe impact on the numerics, therefore this “numerical degeneracy” is caught by a threshold[24] [251]. When dealing with the aforesaid singularities

---

[24] Alexander Neukirchen has analyzed the differences of various Sternheimer quantities from `juPhon` with the `Elk` program for fcc Ne and fcc Al. The best results have been achieved if the threshold was $5 \cdot 10^{-3}\,E_{\mathrm{h}}$ and thus identical to `Elk` (with E_{h} being the Hartree energy). However, Neukirchen has likewise found for the

of the Sternheimer equation, the orthogonality of (i) two unperturbed Kohn–Sham wave functions (see equation (7.14)) and (ii) an unperturbed Kohn–Sham wave function and a first-order Kohn–Sham wave function (cf. equation (6.11)) are decisive [3, 251]. However, the variational ansatz underlying the DFT and the DFPT method intrinsically guarantees it for both cases. Orthogonality forms a constraint in these variational approaches. On these facts the respective previous chapters already elaborate in detail.

Future projects

Stimulated by the reformulations of the dynamical matrix, which shall be discussed in section 7.6, the effect of transforming the surface integral in the last line of equation (7.88) should be investigated in a future project. This reformulation, which underlies the divergence theorem as in equation (7.86b), might lead to a better error cancelation, because each IR quantity would then be evaluated by a FFT. Thereby, the numerical errors committed might be more similar. But, it must be examined if a potentially deteriorating performance is acceptable, because one surface integral is replaced by three FFT volume integrals. Nevertheless, this reformulation would make the discussion about the best form of the IR kinetic energy in section 7.4.4 obsolete. Apart from that, it is at the moment not exploited that a Sternheimer equation with n and n' only addressing occupied bands leads to a vanishing first-order density variation [251]. However, I tested it successfully for the Goldstone modes and fcc Ne during the development. Nonetheless, including this analytical assumption could further improve the numerical accuracy. Due to numeric errors in more challenging systems, the aforesaid band combinations could still wrongly contribute to the first-order density variation. However, in the first implementation we decided to investigate to which extent the Pulay and the surface terms cause well-behaving numerics.

7.4.2 Optimized Hellmann–Feynman Contribution

Subdivision

Having provided the complete optimized Sternheimer equation (7.88), the implementation of its second line is now described. These HF contributions fall into an IR integral and MT matrix elements of all atoms γ, i.e., including the displaced atom α.

Interstitial Part

Concept and final form

The HF contribution in the IR is similar to the potential component of the central DFT Hamiltonian matrix element (5.49). This suggests analogously employing a FFT in order to evaluate the former. Furthermore, implementing the latter has already been optimized by Michalicek [290, Section 5.2] on which the `juPhon` implementation is based. But, it is important to consider some additional subtleties [127, 251, 282], which manifest themselves when reformulating the respective braket in equation (7.88). Expressing it in position space and letting the potential operator act on the ket implies

$$\begin{aligned}&\left\langle \mathit{\Psi}^{(0)}_{\boldsymbol{k}^{+}_{\mathrm{bf}},n'} \middle| \boldsymbol{\mathscr{V}}^{(1)}_{\text{eff}}(\boldsymbol{q}^{+}\alpha) \middle| \mathit{\Psi}^{(0)}_{\boldsymbol{k},n} \right\rangle_{\mathrm{IR}} \qquad (7.89\mathrm{a})\\ &\qquad = \int_{\Omega} \mathit{\Psi}^{*(0)\mathrm{IR}}_{\boldsymbol{k}^{+}_{\mathrm{bf}},n'}(\boldsymbol{r}) \Theta^{\mathrm{IR}}(\boldsymbol{r}) \boldsymbol{V}^{(1)}_{\text{eff}}(\boldsymbol{r};\boldsymbol{q}^{+}\alpha) \mathit{\Psi}^{(0)\mathrm{IR}}_{\boldsymbol{k},n}(\boldsymbol{r})\,\mathrm{d}^{3}r \ .\end{aligned}$$

---

discussed systems in this thesis that the best dispersion relations result if the cutoff is set to $1 \cdot 10^{-12}\,E_{\mathrm{h}}$. Thus, I use this value for all calculations presented in this dissertation, except for those in section 7.7.1.

Inserting equation (7.26), but substituting $\boldsymbol{k}_{\mathrm{bf}}^{+}$ according to equation (7.25) in the argument of the complex-conjugated basis-function yields

$$= \sum_{\boldsymbol{G}'} z^{*(0)}_{\boldsymbol{G}'-\boldsymbol{G}_{\mathrm{bf}}}\left(\boldsymbol{k}_{\mathrm{bf}}^{+}, n'\right) \int_{\Omega} \frac{1}{\sqrt{\Omega}} \mathrm{e}^{-\mathrm{i}\left(\boldsymbol{k}+\boldsymbol{q}+\boldsymbol{G}'\right)\cdot\boldsymbol{r}} \Theta^{\mathrm{IR}}(\boldsymbol{r}) \boldsymbol{V}_{\mathrm{eff}}^{(1)}\left(\boldsymbol{r}; \boldsymbol{q}^{+}\alpha\right) \Psi_{\boldsymbol{k},n}^{(0)\mathrm{IR}}(\boldsymbol{r})\, \mathrm{d}^3 r \tag{7.89b}$$

This reveals the necessity of employing a FFT, the result of which is represented by the convoluted quantity $\boldsymbol{\xi}_{\boldsymbol{q}^{+}\alpha}^{[\Theta V \Psi]}(\boldsymbol{r})$ (see equation (7.90)) so that

$$=: \sum_{\boldsymbol{G}'\boldsymbol{G}} z^{*(0)}_{\boldsymbol{G}'-\boldsymbol{G}_{\mathrm{bf}}}\left(\boldsymbol{k}_{\mathrm{bf}}^{+}, n'\right) \frac{1}{\Omega} \int_{\Omega} \mathrm{e}^{-\mathrm{i}\left(\boldsymbol{k}+\boldsymbol{q}+\boldsymbol{G}'\right)\cdot\boldsymbol{r}} \boldsymbol{\xi}_{\boldsymbol{q}^{+}\alpha}^{[\Theta V \Psi]}(\boldsymbol{G}) \mathrm{e}^{\mathrm{i}(\boldsymbol{k}+\boldsymbol{q}+\boldsymbol{G})\cdot\boldsymbol{r}}\, \mathrm{d}^3 r \tag{7.89c}$$

$$=: \sum_{\boldsymbol{G}'\boldsymbol{G}} z^{*(0)}_{\boldsymbol{G}'-\boldsymbol{G}_{\mathrm{bf}}}\left(\boldsymbol{k}_{\mathrm{bf}}^{+}, n'\right) \boldsymbol{\xi}_{\boldsymbol{q}^{+}\alpha}^{[\Theta V \Psi]}(\boldsymbol{G}) \frac{1}{\Omega} \int_{\Omega} \mathrm{e}^{\mathrm{i}\left(\boldsymbol{G}-\boldsymbol{G}'\right)\cdot\boldsymbol{r}}\, \mathrm{d}^3 r \tag{7.89d}$$

$$= \sum_{\boldsymbol{G}'\boldsymbol{G}} z^{*(0)}_{\boldsymbol{G}'-\boldsymbol{G}_{\mathrm{bf}}}\left(\boldsymbol{k}_{\mathrm{bf}}^{+}, n'\right) \boldsymbol{\xi}_{\boldsymbol{q}^{+}\alpha}^{[\Theta V \Psi]}(\boldsymbol{G}) \delta_{\boldsymbol{G}\boldsymbol{G}'} \tag{7.89e}$$

$$= \sum_{\boldsymbol{G}'} z^{*(0)}_{\boldsymbol{G}'-\boldsymbol{G}_{\mathrm{bf}}}\left(\boldsymbol{k}_{\mathrm{bf}}^{+}, n'\right) \boldsymbol{\xi}_{\boldsymbol{q}^{+}\alpha}^{[\Theta V \Psi]}(\boldsymbol{G}') \tag{7.89f}$$

$$= \sum_{\boldsymbol{G}}^{+\boldsymbol{G}_{\mathrm{bf}}} z^{*(0)}_{\boldsymbol{G}}\left(\boldsymbol{k}_{\mathrm{bf}}^{+}, n'\right) \boldsymbol{\xi}_{\boldsymbol{q}^{+}\alpha}^{[\Theta V \Psi]}(\boldsymbol{G}+\boldsymbol{G}_{\mathrm{bf}}) \tag{7.89g}$$

results. The quantity

$$\boldsymbol{\xi}_{\boldsymbol{q}^{+}\alpha}^{[\Theta V \Psi]}(\boldsymbol{r}) := \Theta^{\mathrm{IR}}(\boldsymbol{r}) \boldsymbol{V}_{\mathrm{eff}}^{(1)}\left(\boldsymbol{r}; \boldsymbol{q}^{+}\alpha\right) \Psi_{\boldsymbol{k},n}^{(0)\mathrm{IR}}(\boldsymbol{r}) \tag{7.90a}$$

can be expanded in plane waves, if defining $\boldsymbol{G}''' := \boldsymbol{G} + \boldsymbol{G}' + \boldsymbol{G}''$

$$= \sum_{\boldsymbol{G}\boldsymbol{G}'\boldsymbol{G}''} \Theta^{\mathrm{IR}}(\boldsymbol{G}) \boldsymbol{V}_{\mathrm{eff}}^{(1)}\left(\boldsymbol{G}'; \boldsymbol{q}^{+}\alpha\right) \frac{1}{\sqrt{\Omega}} z^{(0)}_{\boldsymbol{G}''}(\boldsymbol{k}, n) \mathrm{e}^{\mathrm{i}\left(\boldsymbol{G}+\boldsymbol{G}'+\boldsymbol{q}+\boldsymbol{k}+\boldsymbol{G}''\right)\cdot\boldsymbol{r}}\,, \tag{7.90b}$$

$$:= \sum_{\boldsymbol{G}'''} \frac{1}{\sqrt{\Omega}} \boldsymbol{\xi}_{\boldsymbol{q}^{+}\alpha}^{[\Theta V \Psi]}(\boldsymbol{G}''') \mathrm{e}^{\mathrm{i}\left(\boldsymbol{k}+\boldsymbol{q}+\boldsymbol{G}'''\right)\cdot\boldsymbol{r}}\,. \tag{7.90c}$$

When furthermore identifying the integral in equation (7.89d) as a representation of the delta-distribution, it is important to consider that the periodicity of the lattice is exploited, because the integration volume should actually be the complete crystal. Since moreover the reciprocal lattice vectors are discrete, a Kronecker delta is chosen. As can be seen from equation (7.89g), the Fourier coefficients of $\boldsymbol{\xi}_{\boldsymbol{q}^{+}\alpha}^{[\Theta V \Psi]}(\boldsymbol{r})$ and the unperturbed wave-function expansion coefficients are shifted relative to each other by the reciprocal back-folding vector $\boldsymbol{G}_{\mathrm{bf}}$.

Implementation

The recycled subroutine of Michalicek is named `Hsint_wu`. It differs from the normal `FLEUR` FFT subroutine `Fft3d` by utilizing the faster external FFT library `fftw` [291]. Furthermore, the wave-function expansion coefficients feature the cutoff $|\boldsymbol{k}+\boldsymbol{G}| \leq k_{\mathrm{max}}$, the Fourier coefficients of the potential variation $|\boldsymbol{G}+\boldsymbol{q}| \leq G_{\mathrm{max}}$, and those of the step function $|\boldsymbol{G}| \leq G_{\mathrm{max}}$. Hence, all Fourier coefficients of $\boldsymbol{\xi}_{\boldsymbol{q}^{+}\alpha}^{[\Theta V \Psi]}(\boldsymbol{r})$ fulfilling $|\boldsymbol{G}+\boldsymbol{q}| \leq 2G_{\mathrm{max}} + k_{\mathrm{max}}$ must be taken into account. In order to be consistent with the FFT necessary for the xc-potential variation in section 7.3.2, the size of the mesh is the same and given by $3^3 \times$ `k1d` $\times$ `k2d` $\times$ `k3d`. This is sufficient to embed each Fourier coefficient of $\boldsymbol{\xi}_{\boldsymbol{q}^{+}\alpha}^{[\Theta V \Psi]}(\boldsymbol{r})$ without aliasing effects. Analogously to section 7.3.2, the G_{max} we assume to be adequate for this matrix element is determined in the prearrangements of the `juPhon` calculation, according to appendix A [127, 278].

Algorithm

The procedure to calculate the matrix element (7.89) is sketched in algorithm 8. A simpler but similar method is provided in algorithm 7, given the context of the unperturbed xc-potential gradient. For the matrix element (7.89), different mapping arrays must be constructed for (i) the ket wave-function expansion coefficients, (ii) the first-order potential variation, and (iii) the auxiliary quantity $\boldsymbol{\xi}^{[\Theta V \Psi]}_{\boldsymbol{q}^{+}\alpha}(\boldsymbol{r})$ [251]. The mapping array (iii) must be shifted by the reciprocal lattice vector $\boldsymbol{G}_{\mathrm{bf}}$ relative to mapping array (i) (see equation (7.89g)). Considering this already in the mapping array (iii), the reciprocal lattice vectors in equation (7.89g) need not to be shifted anymore. All Fourier coefficients fulfilling $\left|\boldsymbol{k}^{+}_{\mathrm{bf}} + \boldsymbol{G}\right| \leq k_{\mathrm{max}}$ can be multiplied now in a straight-forward way. Moreover, our decision to ignore the Bloch vector shift in the set of reciprocal lattice vectors $|\boldsymbol{G} + \boldsymbol{q}| \leq G_{\mathrm{max}}$ for the first-order effective potential leads also here to a small inconsistency. But until now, it can be kept under control by a sufficiently large G_{max}. Furthermore, the step function is taken from the `ufft` array, generated during the `juPhon` initialization in `Fleur_init`. It contains the real-space representation of a step function, the Fourier coefficients of which must be expanded until $|\boldsymbol{G}| \leq 2G_{\mathrm{max}}$ [68, 127]. This is due to the fact that a step function, which is once truncated by the cutoff G_{max}, severely looses accuracy in real space and should therefore not be transformed back [68, 127]. Finally, it must be clear that the $\boldsymbol{q}^{+}$ component of the effective potential can generally be complex-valued in real space, i.e., after one FFT.

Muffin-tin Part

Setting the stage

In order to elucidate the implementation, the last braket in the second line of equation (7.88) must be simplified first. So, the potential operators act on the ket, the sum of the linear potential variations is denoted as $\tilde{\boldsymbol{V}}^{\mathrm{stbl},\gamma}_{\mathrm{eff}}(\boldsymbol{q}^{+}\alpha)$, and the large matching coefficients are separated from the braket reading

$$
\begin{aligned}
&\sum_{\gamma}\left\langle \vec{\Psi}^{(0)}_{\boldsymbol{k}^{+}_{\mathrm{bf}},n'} \middle| \boldsymbol{\mathscr{V}}^{(1)}_{\mathrm{eff}}(\boldsymbol{q}^{+}\alpha) + \boldsymbol{\nabla}\mathscr{V}^{(0)}_{\mathrm{eff}}\delta_{\gamma\alpha} \middle| \vec{\Psi}^{(0)}_{\boldsymbol{k},n} \right\rangle_{\gamma} && (7.91\mathrm{a})\\
={}& \sum_{\gamma}\left\langle \vec{\Psi}^{(0)}_{\boldsymbol{k}^{+}_{\mathrm{bf}},n'} \middle| \boldsymbol{V}^{(1)\gamma}_{\mathrm{eff}}(\boldsymbol{q}^{+}\alpha) + \boldsymbol{\nabla}V^{(0)\gamma}_{\mathrm{eff}}\delta_{\gamma\alpha} \middle| \vec{\Psi}^{(0)}_{\boldsymbol{k},n} \right\rangle_{\gamma} \\
:={}& \sum_{\gamma}\left\langle \vec{\Psi}^{(0)}_{\boldsymbol{k}^{+}_{\mathrm{bf}},n'} \middle| \tilde{\boldsymbol{V}}^{\mathrm{stbl},\gamma}_{\mathrm{eff}}(\boldsymbol{q}^{+}\alpha) \middle| \vec{\Psi}^{(0)}_{\boldsymbol{k},n} \right\rangle_{\gamma} && (7.91\mathrm{b})\\
={}& \sum_{\gamma}\sum_{l'm'p'}\sum_{lmp} A^{*\boldsymbol{k}^{+}_{\mathrm{bf}}\alpha n'}_{l'm'p'} \left\langle \vec{\varphi}^{\mathring{\alpha}}_{l'm'p'} \middle| \tilde{\boldsymbol{V}}^{\mathrm{stbl},\gamma}_{\mathrm{eff}}(\boldsymbol{q}^{+}\alpha) \middle| \vec{\varphi}^{\mathring{\alpha}}_{lmp} \right\rangle_{\gamma} A^{\boldsymbol{k}\alpha n}_{lmp}\,. && (7.91\mathrm{c})
\end{aligned}
$$

In the last step (7.91c), the reduced MT basis functions $\vec{\varphi}^{\mathring{\alpha}}_{lmp}$ are already defined in equation (5.17b) and the large matching coefficients are introduced in equation (5.30). Furthermore, the reciprocal lattice vectors at $\boldsymbol{k}^{+}_{\mathrm{bf}}$ are at hand and no shift of them is required [127, 282]. Finally, the $l_{\mathrm{max},\mathring{\gamma}} + 1$ cutoff of the effective potential gradient is reduced to $l_{\mathrm{max},\mathring{\gamma}}$, provided $l_{\mathrm{max},\mathring{\gamma}}$ is converged, in order to simplify the complexity in the first implementation (see section 7.2.1)

Recycling subroutines

It is obvious to make an analogy between equation (7.91c) and the MT non-spherical potential part of the Hamiltonian matrix element (5.53). However, the linear potential varia-

Algorithm 8: Calculation of the matrix element in equations (7.89), based on the subroutine in Michalicek [290].

```
shiftFFT[$i$] =3×GboxDim[$i$] ;   // GboxDim contains dimensions of box incorporating ball of used $\boldsymbol{G}$ for potential and density ($\boldsymbol{q} = \mathbf{0}$)
fftMeshDim $= \prod_{i=1}^{3}$ shiftFFT[$i$] ;
forall $|\boldsymbol{G} + \boldsymbol{q}| <$ Gmax do
    if $G_i < 0$ then
        Gpositive[$i$] $= G_i +$ shiftFFT[$i$]
    else
        Gpositive[$i$] $= G_i$
    end if
    indexFFTMeshV[$\boldsymbol{G}$] = Gpositive (1) + shiftFFT[1] $\times$ Gpositive (2) + shiftFFT[1] $\times$ shiftFFT[2] $\times$ Gpositive (3) ;   // Mapping array between plane-wave and FFT mesh representation for linear potential variation.
end forall
init VFFTmesh with size fftMeshDim;
VFFTmesh[indexFFTMeshV[$\boldsymbol{G}$]] $= \boldsymbol{V}_{\text{eff}}^{(1)\text{IR}}(\boldsymbol{G}; \boldsymbol{q}^{+}\alpha)$ ;
FFTr2d(VFFTmesh[.]) ;   // FFT from reciprocal to direct space.
forall $|\boldsymbol{G} + \boldsymbol{k}| <$ kmax do
    if $G_i < 0$ then
        Gpositive[$i$] $= G_i +$ shiftFFT[$i$]
    else
        Gpositive[$i$] $= G_i$
    end if
    indexFFTMeshKet[$\boldsymbol{G}$] = Gpositive (1) + shiftFFT[1] $\times$ Gpositive (2) + shiftFFT[1] $\times$ shiftFFT[2] $\times$ Gpositive (3) ;   // Mapping array ket wave function.
end forall
forall $\left|\boldsymbol{G} + \boldsymbol{k}_{\text{bf}}^{+}\right| <$ kmax do
    if $G_i < 0$ then
        Gpositive[$i$] $= G_i +$ shiftFFT[$i$] $+ [\boldsymbol{G}_{\text{bf}}]_i$
    else
        Gpositive[$i$] $= G_i + [\boldsymbol{G}_{\text{f}}]_i$
    end if
    indexFFTMeshBra[$\boldsymbol{G}$] = Gpositive (1) + shiftFFT[1] $\times$ Gpositive (2) + shiftFFT[1] $\times$ shiftFFT[2] $\times$ Gpositive (3) ;   // Mapping array bra wave function.
end forall
ketFFTMesh[indexFFTMeshKet[$\boldsymbol{G}$]] $\leftarrow z_{\boldsymbol{G}}^{(0)}(\boldsymbol{k}, n)$ ;
xiFFTMesh[.] $\leftarrow$ thetaMesh[.] $\times$ VFFTmesh[.] $\times$ ketFFTMesh[.] ;   // thetaMesh is direct-space step function $\Theta(\boldsymbol{r})$ evaluated on FFT mesh.
FFTd2r(xiFFTMesh[.]) ;   // FFT from direct to reciprocal space.
xiG[$\boldsymbol{G}$] $\leftarrow$ xiFFTMesh[indexFFTMeshBra[$\boldsymbol{G}$]];
xiG[$\boldsymbol{G}$] = xiG[$\boldsymbol{G}$] / fftMeshDim ;   // Remove FFT-overhead factor.
Evaluate (7.89g) using xiG[.] and $z_{\boldsymbol{G}'}^{*(0)}\left(\boldsymbol{k}_{\text{bf}}^{+}, n\right)$ ;
```

tion in the former equation features three coordinates instead of having a scalar character. Moreover, the matrix element (7.91c) is set up in the the Kohn–Sham wave-function representation instead of the LAPW basis-function one. Ultimately, there exist enough similarities so that the `FLEUR` subroutines `Tlmplm` and `Hsssr_wu` are recycled for the first implementation. But due to their optimizations to former hardware architectures, their algorithm is highly sophisticated and often self-defeating as far as modern compiler optimizations are concerned. A simplified version of calculating the MT potential part of the Hamiltonian matrix element shall be introduced in section 7.6.6, and is meanwhile partially realized in the latest `FLEUR` version. In a future project, it will substitute the current algorithm for determining equation (7.91c). Having done this, in particular LOs can be included in an organic way later, in contrast to their separate calculation in `FLEUR`. But the LO implementation is outside the scope of this dissertation, implying p and p' to equal either 1 or 2.

Reformulation due to `Tlmplm` and final form

For the sake of using snippets of `Tlmplm`, the matrix element with the reduced MT basis functions is extracted from equation (7.91c), i.e., the large matching coefficients are ignored for a moment. This remaining part must be reformulated to reveal the way the aforesaid subroutine can be employed:

$$
\begin{aligned}
&\left\langle \vec{\varphi}^{\mathring{\gamma}}_{l'm'p'} \middle| \tilde{\boldsymbol{V}}^{\text{stbl},\gamma}_{\text{eff}}(\boldsymbol{q}^{+}\alpha) \middle| \vec{\varphi}^{\mathring{\gamma}}_{lmp} \right\rangle_{\gamma} && (7.92\text{a})\\
&\quad = \int_{\gamma} \sum_{s} \varphi^{*s\mathring{\gamma}}_{l'm'p'}(\boldsymbol{r}_{\nu\mathring{\gamma}}) \tilde{\boldsymbol{V}}^{\text{stbl},\gamma}_{\text{eff}}(\boldsymbol{r}_{\nu\mathring{\gamma}}; \boldsymbol{q}^{+}\alpha) \varphi^{s\mathring{\gamma}}_{lmp}(\boldsymbol{r}_{\nu\mathring{\gamma}}) \,\mathrm{d}^3 r_{\nu\mathring{\gamma}}\\
&\quad = \int_{0}^{R_{\mathring{\gamma}}} r^2_{\nu\mathring{\gamma}} \sum_{s} u^{s\mathring{\gamma}}_{l'p'}(r_{\nu\mathring{\gamma}}) \sum_{l''m''} \left[\tilde{\boldsymbol{V}}^{\text{stbl},\gamma}_{\text{eff}}(r_{\nu\mathring{\gamma}}; \boldsymbol{q}^{+}\alpha) \right]_{l''m''} u^{s\mathring{\gamma}}_{lp}(r_{\nu\mathring{\gamma}}) \,\mathrm{d}r_{\nu\mathring{\gamma}} && (7.92\text{b})\\
&\qquad\qquad \times \oint_{\partial\gamma} \mathrm{Y}^{*}_{l'm'}\big(\hat{\boldsymbol{r}}_{\gamma}\big) \mathrm{Y}_{l''m''}\big(\hat{\boldsymbol{r}}_{\gamma}\big) \mathrm{Y}_{lm}\big(\hat{\boldsymbol{r}}_{\gamma}\big) \,\mathrm{d}\Omega\\
&\quad = \sum_{l''m''} G^{m',m'',m}_{l',\ l'',\ l} \int_{0}^{R_{\mathring{\gamma}}} r^2_{\nu\mathring{\gamma}} \left[\tilde{\boldsymbol{V}}^{\text{stbl},\gamma}_{\text{eff}}(r_{\nu\mathring{\gamma}}; \boldsymbol{q}^{+}\alpha) \right]_{l''m''} \sum_{s} u^{s\mathring{\gamma}}_{l'p'}(r_{\nu\mathring{\gamma}}) u^{s\mathring{\gamma}}_{lp}(r_{\nu\mathring{\gamma}}) \,\mathrm{d}r_{\nu\mathring{\gamma}} && (7.92\text{c})\\
&\quad = \sum_{l''m''} G^{m',m'',m}_{l',\ l'',\ l} \boldsymbol{\Sigma}^{pp'\gamma}_{ll'l''m''}(\boldsymbol{q}^{+}\alpha) && (7.92\text{d})\\
&\quad := \boldsymbol{t}^{\text{full},pp'\gamma}_{\eta(l'm'lm)}(\boldsymbol{q}^{+}\alpha) = \boldsymbol{t}^{\text{L},pp'\gamma}_{\eta(l'm'lm)}(\boldsymbol{q}^{+}\alpha) + \boldsymbol{t}^{\text{U},pp'\gamma}_{\eta(l'm'lm)}(\boldsymbol{q}^{+}\alpha)\,. && (7.92\text{e})
\end{aligned}
$$

It is important to know that due to the hermiticity of the matrix element (5.62), only the lower (L) $l \leq l'$ matrix is evaluated. Therefore, in equation (7.92e), I subdivide the complete matrix into a lower and an upper (U) $l > l'$ part. This is illustrated in figure 7.15. If $\boldsymbol{t}^{\text{full},pp'\gamma}_{\eta(l'm'lm)}(\boldsymbol{q}^{+}\alpha)$ had been a Hermitian matrix, it would have been easily feasible to deduce the U matrix from adjoining the L one (the diagonal must additionally be omitted). However, $\tilde{\boldsymbol{V}}^{\text{stbl},\gamma}_{\text{eff}}(\boldsymbol{r}; \boldsymbol{q}^{+}\alpha)$ can generally be complex, since only its superposition with the $\boldsymbol{q}^{-}$ complement is an observable. Therefore, the recycled `Tlmplm` routine needs the input

$$
\left[\tilde{\boldsymbol{V}}^{\text{stbl},\gamma}_{\text{eff, U}}(\boldsymbol{r}_{\nu\mathring{\gamma}}; \boldsymbol{q}^{+}\alpha) \right]_{l''m''} \equiv (-1)^{-m''} \left[\tilde{\boldsymbol{V}}^{*\,\text{stbl},\gamma}_{\text{eff}}(\boldsymbol{r}_{\nu\mathring{\gamma}}; \boldsymbol{q}^{+}\alpha) \right]_{l''-m''} \tag{7.93}
$$

so that $\boldsymbol{t}^{\text{U},pp'\gamma}_{\eta(l'm'lm)}(\boldsymbol{q}^{+}\alpha)$ can be determined from a complex conjugation of the subroutine output. In order to prove this, the derivation starts with the aforesaid upper part of $\boldsymbol{t}$ and reformulates it to a form of $\boldsymbol{t}^{\text{L},pp'\gamma}_{\eta(l'm'lm)}(\boldsymbol{q}^{+}\alpha)$, in which equation (7.93) can be identified. So by exploiting equation (7.43), the relation

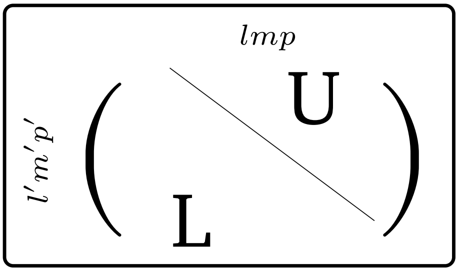

Figure 7.15: Defining the lower (L) and upper (U) parts of the matrix elements $\boldsymbol{t}^{\text{full},pp'\gamma}_{\eta(l'm'lm)}(\boldsymbol{q}^{+}\alpha)$. The former lives up to $l \leq l'$, i.e., including the diagonal and the latter to $l > l'$.

$$\begin{align}
&\boldsymbol{t}^{pp'\gamma,\mathrm{U}}_{\eta(lm,l'm')}\left[\tilde{\boldsymbol{V}}^{\text{stbl},\gamma}_{\text{eff}}(\boldsymbol{r};\boldsymbol{q}^{+}\alpha)\right] \tag{7.94a}\\
&\quad= \left\langle \vec{\varphi}^{\mathring{\gamma}}_{lmp}\middle|\tilde{\boldsymbol{V}}^{\text{stbl},\gamma}_{\text{eff}}(\boldsymbol{q}^{+}\alpha)\middle|\vec{\varphi}^{\mathring{\gamma}}_{l'm'p'}\right\rangle \nonumber\\
&\quad= \left\langle \vec{\varphi}^{\mathring{\gamma}}_{l'm'p'}\middle|\tilde{\boldsymbol{V}}^{*\text{stbl},\gamma}_{\text{eff}}(\boldsymbol{q}^{+}\alpha)\middle|\vec{\varphi}^{\mathring{\gamma}}_{lmp}\right\rangle^{*} \tag{7.94b}\\
&\quad= \Bigg(\int_{0^{+}}^{R_{\mathring{\gamma}}} r^{2}_{\mathring{\gamma}}\sum_{s} u^{s\mathring{\gamma}}_{l'p'}\left(r_{\mathring{\gamma}}\right)\sum_{l''m''}\left[\tilde{\boldsymbol{V}}^{*\text{stbl},\gamma}_{\text{eff}}\left(\boldsymbol{r}_{\mathring{\gamma}};\boldsymbol{q}^{+}\alpha\right)\right]_{l''m''} u^{s\mathring{\gamma}}_{lp}\left(r_{\mathring{\gamma}}\right)\mathrm{d}r_{\mathring{\gamma}} \tag{7.94c}\\
&\qquad\qquad\times\oint_{\partial\gamma}\mathrm{Y}^{*}_{l'm'}\left(\hat{\boldsymbol{r}}_{\gamma}\right)\mathrm{Y}^{*}_{l''m''}\left(\hat{\boldsymbol{r}}_{\gamma}\right)\mathrm{Y}_{lm}\left(\hat{\boldsymbol{r}}_{\gamma}\right)\mathrm{d}\Omega\Bigg)^{*} \nonumber\\
&\quad= \Bigg(\int_{0^{+}}^{R_{\mathring{\gamma}}} r^{2}_{\mathring{\gamma}}\sum_{s} u^{s\mathring{\gamma}}_{l'p'}\left(r_{\mathring{\gamma}}\right)\sum_{l''m''}\left[\tilde{\boldsymbol{V}}^{*\text{stbl},\gamma}_{\text{eff}}\left(r_{\mathring{\gamma}};\boldsymbol{q}^{+}\alpha\right)\right]_{l''m''} u^{s\mathring{\gamma}}_{lp}\left(r_{\mathring{\gamma}}\right)\mathrm{d}r_{\mathring{\gamma}} \tag{7.94d}\\
&\qquad\qquad\times\oint_{\partial\gamma}\mathrm{Y}^{*}_{l'm'}\left(\hat{\boldsymbol{r}}_{\gamma}\right)(-1)^{m''}\mathrm{Y}_{l''-m''}\left(\hat{\boldsymbol{r}}_{\gamma}\right)\mathrm{Y}_{lm}\left(\hat{\boldsymbol{r}}_{\gamma}\right)\mathrm{d}\Omega\Bigg)^{*} \nonumber\\
&\quad= \Bigg(\int_{0^{+}}^{R_{\mathring{\gamma}}}\sum_{s} r_{\mathring{\gamma}} u^{s\mathring{\gamma}}_{l'p'}(r)\sum_{l''m''}(-1)^{-m''}\left[\tilde{\boldsymbol{V}}^{*\text{stbl},\gamma}_{\text{eff}}\left(r_{\mathring{\gamma}};\boldsymbol{q}^{+}\alpha\right)\right]_{l''-m''} r_{\mathring{\gamma}} u^{s\mathring{\gamma}}_{lp}\left(r_{\mathring{\gamma}}\right)\mathrm{d}r_{\mathring{\gamma}} \tag{7.94e}\\
&\qquad\qquad\times\oint_{\partial\gamma}\mathrm{Y}^{*}_{l'm'}\left(\hat{\boldsymbol{r}}_{\gamma}\right)\mathrm{Y}_{l''m''}\left(\hat{\boldsymbol{r}}_{\gamma}\right)\mathrm{Y}_{lm}\left(\hat{\boldsymbol{r}}_{\gamma}\right)\mathrm{d}\Omega\Bigg)^{*} \nonumber\\
&\quad= \left\langle \vec{\varphi}^{\mathring{\gamma}}_{l'm'p'}\middle|\tilde{\boldsymbol{V}}^{\text{stbl},\gamma}_{\text{eff, U}}(\boldsymbol{q}^{+}\alpha)\middle|\vec{\varphi}^{\mathring{\gamma}}_{lmp}\right\rangle^{*} \tag{7.94f}\\
&\quad= \boldsymbol{t}^{*p'p\gamma,\mathrm{L}}_{\eta(l'm'lm)}\left[\tilde{\boldsymbol{V}}^{\text{stbl},\gamma}_{\text{eff, U}}(\boldsymbol{r};\boldsymbol{q}^{+}\alpha)\right] \tag{7.94g}
\end{align}$$

can be deduced. If the input potential had been real, it would have been an equivalent operation to just complex conjugate its starred expansion coefficients and the attributed starred spherical harmonics in equation (7.94c).

Adjusting `Tlmplm`

While recycling the `Tlmplm` subroutine from `FLEUR`, it is important to find all optimizations that only hold for lattice harmonics. One example is that the integrands of the radial integrals are not generally real anymore, because lattice-harmonic coefficients are real and spherical-harmonic coefficients may not be. Thus integrals for the imaginary part must be added. During the development, we decided moreover to change the interpolation in the FLEUR integration routine `Intgr3`. The integral between the first mesh point and the MT sphere center is interpolated by a triangle, since all integrands become zero at the MT sphere center [127]. But due to the Jacobi determinant and the sum of linear potential variations, the form of the interpolation (at least for the monoatomic systems) proved to be irrelevant.

Reformulations due to `Hsssr_wu` and final form

The large matching coefficients are multiplied in a routine which is based on `Hsssr_wu`. Therefore, there is no sum over p or p', but each of their four possible permutations is separately dealt with. As soon as the sums over p and p' are introduced, it should be easier for the compiler to optimize, e.g. employing vectorization (especially when LOs are involved). To prepare this, the three large matching-coefficients arrays from the recycled FLEUR subroutine `Abcof` are summarized to one array and already reordered. Hence for the implementation, equation (7.91c) transforms into

$$\begin{aligned}
&\sum_{\gamma}\sum_{l'm'p'}\sum_{lmp} A^{*\boldsymbol{k}_{\text{bf}}^{+}\alpha n'}_{l'm'p'} \left\langle \vec{\varphi}^{\mathring{\alpha}}_{l'm'p'} \middle| \tilde{\boldsymbol{V}}^{\text{stbl},\gamma}_{\text{eff}}(\boldsymbol{q}^{+}\alpha) \middle| \vec{\varphi}^{\mathring{\alpha}}_{lmp} \right\rangle_{\gamma} A^{\boldsymbol{k}\alpha n}_{lmp} \qquad (7.95)\\
&= \sum_{\gamma}\sum_{l'm'}\sum_{lm} A^{*\boldsymbol{k}_{\text{bf}}^{+}\alpha n'}_{l'm'1'} \left(A^{\boldsymbol{k}\alpha n}_{lm1} t^{\text{full},11\alpha}_{\eta(l'm'lm)} \left[\tilde{\boldsymbol{V}}^{\text{stbl},\gamma}_{\text{eff}}(\boldsymbol{q}^{+}\alpha)\right] + A^{\boldsymbol{k}\alpha n}_{lm2} t^{\text{full},12\alpha}_{\eta(l'm'lm)} \left[\tilde{\boldsymbol{V}}^{\text{stbl},\gamma}_{\text{eff}}(\boldsymbol{q}^{+}\alpha)\right]\right)\\
&\quad + \sum_{\gamma}\sum_{l'm'}\sum_{lm} A^{*\boldsymbol{k}_{\text{bf}}^{+}\alpha n'}_{l'm'2} \left(A^{\boldsymbol{k}\alpha n}_{lm1} t^{\text{full},21\alpha}_{\eta(l'm'lm)} \left[\tilde{\boldsymbol{V}}^{\text{stbl},\gamma}_{\text{eff}}(\boldsymbol{q}^{+}\alpha)\right] + A^{\boldsymbol{k}\alpha n}_{lm2} t^{\text{full},22\alpha}_{\eta(l'm'lm)} \left[\tilde{\boldsymbol{V}}^{\text{stbl},\gamma}_{\text{eff}}(\boldsymbol{q}^{+}\alpha)\right]\right) .
\end{aligned}$$

Algorithm

Since furthermore `Abcof` is programmed for systems in which symmetry can be exploited, its output may be rotated in polyatomic system [127]. This is based on an array addressing the types of symmetry operations, so this parameter array must only contain the index of the unit matrix in `juPhon` [127]. Moreover, in this routine the factors i^{l} are multiplied and the diagonal of $\boldsymbol{t}^{\text{full},pp'\gamma}_{\eta(l'm'lm)}(\boldsymbol{q}^{+}\alpha)$ is only considered once. Although the speed of light within `juPhon` is increased by three orders of magnitude and suppresses the $p = 2$ components, the scalar-relativistic character of the LAPW basis is already programmed. Finally, the complete procedure of calculating equation (7.91c) is sketched in algorithm 9, which includes algorithm 10 as well as algorithm 11, and in algorithm 12.

7.4.3 Optimized Pulay Corrections

Varied-bra braket: subdivision and inventory

Within the third line of the Sternheimer equation (7.88), there are two Pulay terms owing to the fact that it is possible to vary the basis function both in the bra and in the ket. First, the former is reformulated, aiming to identify already discussed expressions, or those in principle available from FLEUR:

$$\begin{aligned}
&\left\langle \tilde{\vec{\boldsymbol{\varPsi}}}^{(0)}_{\boldsymbol{k}_{\text{bf}}^{+},n'} \middle| \mathscr{H}^{(0)} - \varepsilon^{(0)}_{\boldsymbol{k},n} \middle| \vec{\varPsi}^{(0)}_{\boldsymbol{k},n} \right\rangle_{\alpha} \qquad (7.96\text{a})\\
&= \sum_{\boldsymbol{G}'} \left(\mathrm{i}\left(\boldsymbol{k}_{\text{bf}}^{+} + \boldsymbol{G}'\right) z^{(0)}_{\boldsymbol{G}'}\left(\boldsymbol{k}_{\text{bf}}^{+}, n'\right)\right)^{*} \left\langle \vec{\phi}^{(0)}_{\boldsymbol{k}_{\text{bf}}^{+},\boldsymbol{G}'} \middle| \mathscr{H}^{(0)} - \varepsilon^{(0)}_{\boldsymbol{k},n} \middle| \vec{\varPsi}^{(0)}_{\boldsymbol{k},n} \right\rangle_{\alpha}\\
&= \sum_{l'm'p'}\sum_{lmp}\sum_{\boldsymbol{G}'} \left(\mathrm{i}\left(\boldsymbol{k}_{\text{bf}}^{+} + \boldsymbol{G}'\right) z^{(0)}_{\boldsymbol{G}'}\left(\boldsymbol{k}_{\text{bf}}^{+}, n'\right) a^{\boldsymbol{k}_{\text{bf}}^{+}\alpha\boldsymbol{G}'}_{lmp}\right)^{*} \left\langle \vec{\varphi}^{\mathring{\alpha}}_{l'm'p'} \middle| \mathscr{H}^{(0)} - \epsilon^{(0)}_{\boldsymbol{k},n} \middle| \vec{\varphi}^{\mathring{\alpha}}_{lmp} \right\rangle_{\alpha} A^{\boldsymbol{k}\alpha n}_{lmp} \qquad (7.96\text{b})\\
&= \sum_{l'm'p'}\sum_{lmp} \tilde{\boldsymbol{A}}^{*\boldsymbol{k}_{\text{bf}}^{+}\alpha n'}_{l'm'p'} \left\langle \vec{\varphi}^{\mathring{\alpha}}_{l'm'p'} \middle| \mathscr{H}^{(0)} - \epsilon^{(0)}_{\boldsymbol{k},n} \middle| \vec{\varphi}^{\mathring{\alpha}}_{lmp} \right\rangle_{\alpha} A^{\boldsymbol{k}\alpha n}_{lmp} \qquad (7.96\text{c})
\end{aligned}$$

Algorithm 9: Main algorithm to calculate $\boldsymbol{t}^{\mathrm{L},pp'\gamma}_{\eta(l'm'lm)}(\boldsymbol{q}^{+}\alpha)$ from equation (7.92e). This routine is also used to calculate $\boldsymbol{t}^{\mathrm{U},pp'\gamma}_{\eta(l'm'lm)}(\boldsymbol{q}^{+}\alpha)$ using equation (7.93).

```
forall atoms $\gamma$ in unit cell do
    for $l' = 0$ to $l_{\mathrm{max},\mathring{\alpha}}$ do
        $l'_{\triangle} = 0.5 \times l' \times (l' + 1)$ ;                     // Triangular numbers
        for $l = 0$ to $l'$ do
            $ɭ = l + l'_{\triangle}$ ;                               // Packed storage for $l', l$
            for $l'' = 0$ to $l_{\mathrm{max},\mathring{\alpha}}$ do
                if $l + l' + l''$ even $\wedge \left|l - l'\right| < l'' < \left|l + l'\right|$ then //   $G^{m', m'', m}_{l', l'', l}$ finite
                    for $m'' <= \left|l''\right|$ do
                        $L'' = l'' \times (l'' + 1) + 1 + m''$ ;   // Packed storage for $l'', m''$
                        uvu[ɭ, $L''$] = $\boldsymbol{\Sigma}^{11'\gamma}_{ll'l''m''}(\boldsymbol{q}^{+}\alpha)$;
                        dvu[ɭ, $L''$] = $\boldsymbol{\Sigma}^{21\gamma}_{ll'l''m''}(\boldsymbol{q}^{+}\alpha)$;
                        uvd[ɭ, $L''$] = $\boldsymbol{\Sigma}^{12\gamma}_{ll'l''m''}(\boldsymbol{q}^{+}\alpha)$;
                        dvd[ɭ, $L''$] = $\boldsymbol{\Sigma}^{22\gamma}_{ll'l''m''}(\boldsymbol{q}^{+}\alpha)$;
                    end for
                end if
            end for
        end for
    end for
    Include algorithm 10 ;
    Include algorithm 11 ;
end forall
```

Algorithm 10: Outsourced part of algorithm 9 covering the multiplication of the matrices $\boldsymbol{\Sigma}^{pp'\gamma}_{ll'l''m''}(\boldsymbol{q}^{+}\alpha)$ with the Gaunt coefficients as described in equation (7.92d) using the Gaunt selection and only $l \leq l'$ (see figure 7.15).

```
for $l' = 0$ to $l_{\text{max},\mathring{\alpha}}$ do
    $l'_{\triangle} = 0.5 \times l' \times (l' + 1)$ ;
    for $m' <= |l'|$ do
        $L' = l' \times (l' + 1) + m'$ ;
        $L'_{\triangle} = 0.5 \times L' \times (L' + 1)$ ;
        for $l'' = 0$ to $\min\big(l_{\text{max},\mathring{\alpha}}, 2l'\big)$ do
            $\tilde{l}_{\text{min}} = |l' - l''|$ ;    // $|l' - l''| \leq l \leq l' + l''$
            $l_{\text{max}} = l' - (l'' \mod 2)$ ;    // $(l \leq l' + l'') \wedge l <= l' \Rightarrow l \leq l'$; latter
             condition not violated as modulo result subtracted.
             Subtracting ensures $l'' \mod 2 = 0$ in $(l_{\text{max}} + l' + l'')$, while $l_{\text{max}}$
             $\mod 2 = l' \mod 2$ holds.
            for $|m''| \leq l''$ do
                $L'' = l'' \times (l'' + 1) + m''$ ;    // Packed storage for $l'', m''$
                $m = m' - m''$ ;    // Gaunt selection rule for $m, m', m''$
                $l_{\text{min}} = \max(\tilde{l}_{\text{min}}, |m|)$ ;    // $|m| < l$ must hold, either way.
                $l_{\text{min}} = l_{\text{min}} + (l_{\text{max}} - l_{\text{min}})$ ;    // Ensure that $l_{\text{min}} \mod 2$ equals $l_{\text{max}}$
                 $\mod 2$ so that $(l'' + l' + l) \mod 2 = 0$ holds provided $l$ is
                 incremented by steps of size 2.
                for $l \in [l_{\text{min}}, l_{\text{min}} + 2, \ldots, l_{\text{max}} - 2, l_{\text{max}}] \cap l_{\text{min}} \leq l \leq l_{\text{max}}$ do
                    $L = l \times (l + 1) + m$ ;
                    if $L \leq L'$ then
                        $\mathfrak{l} = l'_{\triangle} + l$ ;    // Packed storage for $l', l$
                        $\mathfrak{L} = L'_{\triangle} + L$ ;    // Packed storage for $L', L$
                        $\text{tuu}[\mathfrak{L}, \gamma] = \boldsymbol{t}^{*11\gamma,\text{L}}_{\eta(l'm'lm)}\Big[\tilde{\boldsymbol{V}}^{\text{stbl},\gamma}_{\text{eff, U}}(\boldsymbol{r}; \boldsymbol{q}^{+}\alpha)\Big]$ ;    // Using uvu.
                        $\text{tud}[\mathfrak{L}, \gamma] = \boldsymbol{t}^{*12\gamma,\text{L}}_{\eta(l'm'lm)}\Big[\tilde{\boldsymbol{V}}^{\text{stbl},\gamma}_{\text{eff, U}}(\boldsymbol{r}; \boldsymbol{q}^{+}\alpha)\Big]$ ;    // Using uvd.
                        $\text{tdu}[\mathfrak{L}, \gamma] = \boldsymbol{t}^{*21\gamma,\text{L}}_{\eta(l'm'lm)}\Big[\tilde{\boldsymbol{V}}^{\text{stbl},\gamma}_{\text{eff, U}}(\boldsymbol{r}; \boldsymbol{q}^{+}\alpha)\Big]$ ;    // Using dvu.
                        $\text{tdd}[\mathfrak{L}, \gamma] = \boldsymbol{t}^{*22\gamma,\text{L}}_{\eta(l'm'lm)}\Big[\tilde{\boldsymbol{V}}^{\text{stbl},\gamma}_{\text{eff, U}}(\boldsymbol{r}; \boldsymbol{q}^{+}\alpha)\Big]$ ;    // Using dvd.
                        $\text{isSet}[\mathfrak{L}] = \text{True}$ ;
                    end if
                end for
            end for
        end for
    end for
end for
```

Algorithm 11: Outsourced part of algorithm 9 setting up an index and logical matrix to provide all matrix elements $\boldsymbol{t}^{\text{full},pp'\gamma}_{\eta(l'm'lm)}(\boldsymbol{q}^{+}\alpha)$ from the calculated matrix elements $\boldsymbol{t}^{\text{L},pp'\gamma}_{\eta(l'm'lm)}(\boldsymbol{q}^{+}\alpha)$ from equation (7.92e) (see figure 7.15).

```
for $l' = 0$ to $l_{\text{max},\mathring{\alpha}}$ do
    for $m' <= |l'|$ do
        $L' = l' \times (l' + 1) + m'$ ;
        for $l = 0$ to $l_{\text{max},\mathring{\alpha}}$ do
            for $m <= |l|$ do
                $L = l \times (l + 1) + m$ ;
                if $L' \geq L$ then
                    $\mathfrak{L} = 0.5 \times L' \times (L' + 1) + L$ ;
                    if isSet[$\mathfrak{L}$] then
                        eta($L'$, $L$, $\gamma$) = $\mathfrak{L}$
                    else
                        eta($L'$, $L$, $\gamma$) = $-9999$ ;            // $\mathfrak{L}$ is never $-9999$
                    end if
                else
                    $\mathfrak{L} = 0.5 \times L \times (L + 1) + L'$ ; // Transpose means interchanging
                        $L$ and $L'$
                    if isSet[$\mathfrak{L}$] then
                        eta2($L'$, $L$, $\gamma$) = -$\mathfrak{L}$
                    else
                        eta2($L'$, $L$, $\gamma$) = $-9999$ ;    // $-\mathfrak{L}$ is very unlikely $-9999$
                    end if
                end if
            end for
        end for
    end for
end for
```

Algorithm 12: Implements equation (7.95), provided with the input of algorithm algorithm 9 which includes algorithm 10 and algorithm 11 for generating the tuu1, tud1, tdu1 and tdd1. For eta2, tuu2, tud2, tdu2 and tdd2 equation (7.93) is used.

```
forall atoms $\gamma$ in unit cell do
    $L' = -1$ ; $\mathcal{L}' = 1$ ;
    for $l' = 0$ to $l_{\max,\mathring{\alpha}}$ do
        for $|m'| <= |l'|$ do
            $L' = L' + 1$ ; $L = -1$ ; $\mathcal{L} = 1$;
            for $l = 0$ to $l_{\max,\mathring{\alpha}}$ do
                for $m <= |l|$ do
                    $L = L + 1$ ;
                    if $L \leq L'$ then
                        $\mathfrak{L}$ = eta($L'$, $L$, $\gamma$)
                    else
                        $\mathfrak{L}$ = eta2($L'$, $L$, $\gamma$)
                    end if
                    if $\mathfrak{L} \neq -9999$ then
                        if $\mathfrak{L} > 0$ then
                            utu = $i^{l-l'}$ × tuu1[$\mathfrak{L}$, $\gamma$] ; utd = $i^{l-l'}$ × tud1[$\mathfrak{L}$, $\gamma$] ; dtu = $i^{l-l'}$ ×
                              tdu1[$\mathfrak{L}$, $\gamma$] ; dtd = $i^{l-l'}$ × tdd1[$\mathfrak{L}$, $\gamma$] ;
                        else
                            utu = $i^{l-l'}$ × (tuu2[-$\mathfrak{L}$, $\gamma$])$^*$ ; utd = $i^{l-l'}$ × (tud2[-$\mathfrak{L}$, $\gamma$])$^*$ ; dtu
                              = $i^{l-l'}$ × (tdu2[-$\mathfrak{L}$, $\gamma$])$^*$ ; dtd = $i^{l-l'}$ × (tdd2[-$\mathfrak{L}$, $\gamma$])$^*$ ;
                        end if
                        forall $n$ do occupied bands
                            ax[$n$] = ax[$n$] + utu × mCoeffK[$n$,$\mathcal{L}$,$\gamma$] + utd ×
                              mCoeffK[$n$,$\mathcal{L}+1$,$\gamma$] ;
                            bx[$n$] = bx[$n$] + dtu × mCoeffK[$n$,$\mathcal{L}$,$\gamma$] + dtd ×
                              mCoeffK[$n$,$\mathcal{L}+1$,$\gamma$] ;
                        end forall
                    end if
                    $\mathcal{L} = \mathcal{L} + 2$
                end for
            end for
            forall occupied $n$ at $\boldsymbol{k}$ do
                forall occupied and unoccupied $n'$ at $\boldsymbol{k}+\boldsymbol{q}$ do
                    matElem[$n'$, $n$] = matElem[$n'$, $n$] + (mCoeffB[$n'$,$\mathcal{L}'$,$\gamma$])$^*$ × ax[$n$] +
                      (mCoeffB[$n'$,$\mathcal{L}'$,$\gamma$])$^*$ × bx[$n$]
                end forall
            end forall
        end for
    end for
    $\mathcal{L}' = \mathcal{L}' + 2$
end forall
```

$$
\begin{aligned}
&= \sum_{l'm'p'} \sum_{lmp} \tilde{\boldsymbol{A}}^{*\boldsymbol{k}^{+}_{\mathrm{bf}}\alpha n'}_{l'm'p'} A^{\boldsymbol{k}\alpha n}_{lmp} \left(\int_{\alpha} \sum_{s} \varphi^{*s\mathring{\alpha}}_{l'm'p'}(\boldsymbol{r}_{\nu\mathring{\alpha}}) \left(\left(\mathscr{H}^{(0)}_{\mathrm{sph}} + V^{(0)\alpha}_{\mathrm{eff,nsph}}(\boldsymbol{r}_{\nu\mathring{\alpha}}) \right) \varphi^{s\mathring{\alpha}}_{lmp}(\boldsymbol{r}_{\nu\mathring{\alpha}}) \right) \mathrm{d}^3 r_{\nu\mathring{\alpha}} \right. \\
&\qquad \left. - \epsilon^{(0)}_{\boldsymbol{k},n} \int_{\mathring{\alpha}} \sum_{s} \varphi^{*s\mathring{\alpha}}_{l'm'p'}(\boldsymbol{r}_{\nu\mathring{\alpha}}) \varphi^{s\mathring{\alpha}}_{lmp}(\boldsymbol{r}_{\nu\mathring{\alpha}}) \, \mathrm{d}^3 r_{\nu\mathring{\alpha}} \right) . \qquad (7.96\mathrm{d})
\end{aligned}
$$

In fact, it turns out that the overlap integral in the second line of equation (7.96d) is with equation (5.57). Moreover, the Hamiltonian integral (excluding the matching coefficients) in the first line of the former equation shows strong similarities to the integrals within the parentheses of equation (5.59). The only difference consists in the fact that the left- and right-directed action of the Hamiltonian is averaged in equation (5.59), but this does not manifest itself in equation (7.96d). The scalar matching coefficient occurring in equation (7.96) is already defined in equation (5.30) and the vectorial one is introduced in equations (7.36b) to (7.36e). Since therefore analogous derivations are already described in section 5.8.2 and the MT part of section 7.2.3, the following discussion is focussed on the final results. Although furthermore the recycled subroutines `Tlmplm` and `Hssr_wu` could be left untouched, we still decided to remove the symmetry optimizations for the sake of consistency in the first implementation [127, 251]. This, for instance, requires again handling complex-valued MT integrals or calculating some of them for all atoms instead of only the representative one.

Varied-bra braket: final form

All in all, the overlap term of Equation (7.96d) is condensed to

$$
\begin{aligned}
&-\epsilon^{(0)}_{\boldsymbol{k},n} \sum_{l'm'p'} \sum_{lmp} \tilde{\boldsymbol{A}}^{*\boldsymbol{k}^{+}_{\mathrm{bf}}\alpha n'}_{l'm'p'} A^{\boldsymbol{k}\alpha n}_{lmp} \int_{\mathring{\alpha}} \sum_{s} \varphi^{*s\mathring{\alpha}}_{l'm'p'}(\boldsymbol{r}_{\nu\mathring{\alpha}}) \varphi^{s\mathring{\alpha}}_{lmp}(\boldsymbol{r}_{\nu\mathring{\alpha}}) \, \mathrm{d}^3 r_{\nu\mathring{\alpha}} && (7.97\mathrm{a}) \\
&\quad = -\epsilon^{(0)}_{\boldsymbol{k},n} \sum_{lm} \left(\tilde{\boldsymbol{A}}^{*\boldsymbol{k}^{+}_{\mathrm{bf}}\alpha n'}_{lm1} A^{\boldsymbol{k}\alpha n}_{lm1} + \tilde{\boldsymbol{A}}^{*\boldsymbol{k}^{+}_{\mathrm{bf}}\alpha n'}_{lm2} A^{\boldsymbol{k}\alpha n}_{lm2} N^{\mathring{\alpha}}_{ll} \right) .
\end{aligned}
$$

Moreover, the spherical Hamiltonian part in equation (7.96d) finally results in

$$
\begin{aligned}
&\sum_{l'm'p'} \sum_{lmp} \tilde{\boldsymbol{A}}^{*\boldsymbol{k}^{+}_{\mathrm{bf}}\alpha n'}_{l'm'p'} A^{\boldsymbol{k}\alpha n}_{lmp} \int_{\alpha} \sum_{s} \varphi^{*s\mathring{\alpha}}_{l'm'p'}(\boldsymbol{r}_{\nu\mathring{\alpha}}) \left[\mathscr{H}^{(0)}_{\mathrm{sph}} \varphi^{s\mathring{\alpha}}_{lmp}(\boldsymbol{r}_{\nu\mathring{\alpha}}) \right] \mathrm{d}^3 r_{\nu\mathring{\alpha}} && (7.98\mathrm{a}) \\
&\quad = \sum_{lm} \left(E^{\mathring{\alpha}}_{l} \tilde{\boldsymbol{A}}^{*\boldsymbol{k}^{+}_{\mathrm{bf}}\alpha n'}_{lm1} A^{\boldsymbol{k}\alpha n}_{lm1} + \tilde{\boldsymbol{A}}^{*\boldsymbol{k}^{+}_{\mathrm{bf}}\alpha n'}_{lm1} A^{\boldsymbol{k}\alpha n}_{lm2} + N_{ll} \tilde{\boldsymbol{A}}^{*\boldsymbol{k}^{+}_{\mathrm{bf}}\alpha n'}_{lm2} A^{\boldsymbol{k}\alpha n}_{lm2} E^{\mathring{\alpha}}_{l} \right) \\
&\quad = \sum_{lm} E^{\mathring{\alpha}}_{l} \left(\tilde{\boldsymbol{A}}^{*\boldsymbol{k}^{+}_{\mathrm{bf}}\alpha n'}_{lm1} A^{\boldsymbol{k}\alpha n}_{lm1} + N_{ll} \tilde{\boldsymbol{A}}^{*\boldsymbol{k}^{+}_{\mathrm{bf}}\alpha n'}_{lm2} A^{\boldsymbol{k}\alpha n}_{lm2} \right) + \sum_{lm} \tilde{\boldsymbol{A}}^{*\boldsymbol{k}^{+}_{\mathrm{bf}}\alpha n'}_{lm1} A^{\boldsymbol{k}\alpha n}_{lm2} \, . && (7.98\mathrm{b})
\end{aligned}
$$

As the Hamiltonian only acts on the ket, in general no Hermitian matrix results. However at least for the Goldstone modes, effectively a hermitization takes place if the second Pulay matrix element (7.100) is added in the Sternheimer equation. Although this does not hold anymore given a finite $\boldsymbol{q}$, the dynamical matrix in the end is hermitized. Furthermore, this discussion only focuses on the $\boldsymbol{q}^{+}$ part of the complete Sternheimer equation (6.61d). Since finally the Hamiltonian matrix is not diagonalized as in a DFT calculation, the presented implementation is uncritical [127]. The non-spherical potential term in equation (7.96d) remains to be reformulated into

$$
\begin{aligned}
&\sum_{l'm'p'} \sum_{lmp} \tilde{\boldsymbol{A}}^{*\boldsymbol{k}^{+}_{\mathrm{bf}}\alpha n'}_{l'm'p'} A^{\boldsymbol{k}\alpha n}_{lmp} \int_{\alpha} \sum_{s} \varphi^{*s\mathring{\alpha}}_{l'm'p'}(\boldsymbol{r}_{\nu\mathring{\alpha}}) V^{(0)\alpha}_{\mathrm{eff,nsph}}(\boldsymbol{r}_{\nu\mathring{\alpha}}) \varphi^{s\mathring{\alpha}}_{lmp}(\boldsymbol{r}_{\nu\mathring{\alpha}}) \, \mathrm{d}^3 r_{\nu\mathring{\alpha}} && (7.99\mathrm{a}) \\
&\quad = \sum_{l'm'} \sum_{lm} \tilde{\boldsymbol{A}}^{*\boldsymbol{k}^{+}_{\mathrm{bf}}\alpha n'}_{l'm'1} A^{\boldsymbol{k}\alpha n}_{lm1} t^{\mathrm{full},11\alpha}_{\eta(l'm'lm)} \left[V^{(0)\alpha}_{\mathrm{eff,nsph}}(\boldsymbol{r}_{\nu\mathring{\alpha}}) \right]
\end{aligned}
$$

$$
\begin{aligned}
&+\sum_{l'm'}\sum_{lm}\tilde{\boldsymbol{A}}^{*\boldsymbol{k}_{\mathrm{bf}}^{+}\alpha n'}_{l'm'1}A^{\boldsymbol{k}\alpha n}_{lm2}t^{\mathrm{full},21\alpha}_{\eta(l'm'lm)}\left[V^{(0)\alpha}_{\mathrm{eff,nsph}}(\boldsymbol{r}_{\nu\mathring{\alpha}})\right]\\
&+\sum_{l'm'}\sum_{lm}\tilde{\boldsymbol{A}}^{*\boldsymbol{k}_{\mathrm{bf}}^{+}\alpha n'}_{l'm'2}A^{\boldsymbol{k}\alpha n}_{lm1}t^{\mathrm{full},12\alpha}_{\eta(l'm'lm)}\left[V^{(0)\alpha}_{\mathrm{eff,nsph}}(\boldsymbol{r}_{\nu\mathring{\alpha}})\right]\\
&+\sum_{l'm'}\sum_{lm}\tilde{\boldsymbol{A}}^{*\boldsymbol{k}_{\mathrm{bf}}^{+}\alpha n'}_{l'm'2}A^{\boldsymbol{k}\alpha n}_{lm2}t^{\mathrm{full},22\alpha}_{\eta(l'm'lm)}\left[V^{(0)\alpha}_{\mathrm{eff,nsph}}(\boldsymbol{r}_{\nu\mathring{\alpha}})\right].
\end{aligned}
$$

It is straight-forward to apply the recent considerations to the the second Pulay matrix element in the Sternheimer equation

Ket-varied braket: final form

$$
\left\langle\vec{\mathit{\Psi}}^{(0)}_{\boldsymbol{k}_{\mathrm{bf}}^{+},n}\middle|\mathscr{H}^{(0)}-\varepsilon^{(0)}_{\boldsymbol{k},n}\middle|\widetilde{\vec{\boldsymbol{\Psi}}}^{(0)}_{\boldsymbol{k},n'}\right\rangle_{\alpha} \tag{7.100a}
$$

$$
\begin{aligned}
&=\sum_{\boldsymbol{G}}\left\langle\vec{\mathit{\Psi}}^{(0)}_{\boldsymbol{k}_{\mathrm{bf}}^{+},n}\middle|\mathscr{H}^{(0)}-\varepsilon^{(0)}_{\boldsymbol{k},n}\middle|\vec{\phi}^{(0)}_{\boldsymbol{k},\boldsymbol{G}}\right\rangle_{\alpha}\mathrm{i}\big(\boldsymbol{k}_{\mathrm{bf}}^{+}+\boldsymbol{G}\big)z^{(0)}_{\boldsymbol{G}}\left(\boldsymbol{k}_{\mathrm{bf}}^{+},n'\right)\\
&=\sum_{l'm'p'}\sum_{lmp}A^{*\boldsymbol{k}_{\mathrm{bf}}^{+}\alpha n}_{lmp}\tilde{\boldsymbol{A}}^{\boldsymbol{k}\alpha n'}_{l'm'p'}\Bigg(\int_{\alpha}\sum_{s}\varphi^{*s\mathring{\alpha}}_{l'm'p'}(\boldsymbol{r}_{\nu\mathring{\alpha}})\Big[\Big(\mathscr{H}^{(0)}_{\mathrm{sph}}+V^{(0)\alpha}_{\mathrm{eff,nsph}}(\boldsymbol{r}_{\nu\mathring{\alpha}})\Big)\varphi^{s\mathring{\alpha}}_{lmp}(\boldsymbol{r}_{\nu\mathring{\alpha}})\Big]\,\mathrm{d}^3r_{\nu\mathring{\alpha}}\\
&\qquad\qquad-\epsilon^{(0)}_{\boldsymbol{k}n}\int_{\mathring{\alpha}}\sum_{s}\varphi^{*s\mathring{\alpha}}_{l'm'p'}(\boldsymbol{r}_{\nu\mathring{\alpha}})\varphi^{s\mathring{\alpha}}_{lmp}(\boldsymbol{r}_{\nu\mathring{\alpha}})\,\mathrm{d}^3r_{\nu\mathring{\alpha}}\Bigg)
\end{aligned}
\tag{7.100b}
$$

The overlap part is given by

$$
\begin{aligned}
&-\epsilon^{(0)}_{\boldsymbol{k},n}\sum_{l'm'p'}\sum_{lmp}A^{*\boldsymbol{k}_{\mathrm{bf}}^{+}\alpha n'}_{l'm'p'}\tilde{\boldsymbol{A}}^{\boldsymbol{k}\alpha n}_{lmp}\int_{\mathring{\alpha}}\sum_{s}\varphi^{*s\mathring{\alpha}}_{l'm'p'}(\boldsymbol{r}_{\nu\mathring{\alpha}})\varphi^{s\mathring{\alpha}}_{lmp}(\boldsymbol{r}_{\nu\mathring{\alpha}})\,\mathrm{d}^3r_{\nu\mathring{\alpha}} \qquad (7.101)\\
&\qquad=-\epsilon^{(0)}_{\boldsymbol{k},n}\sum_{lm}\left(A^{*\boldsymbol{k}_{\mathrm{bf}}^{+}\alpha n'}_{lm1}\tilde{\boldsymbol{A}}^{\boldsymbol{k}\alpha n}_{lm1}+A^{*\boldsymbol{k}_{\mathrm{bf}}^{+}\alpha n'}_{lm2}\tilde{\boldsymbol{A}}^{\boldsymbol{k}\alpha n}_{lm2}N^{\mathring{\alpha}}_{ll}\right),
\end{aligned}
$$

the spherical Hamiltonian part by

$$
\sum_{l'm'p'}\sum_{lmp}A^{*\boldsymbol{k}_{\mathrm{bf}}^{+}\alpha n'}_{l'm'p'}\tilde{\boldsymbol{A}}^{\boldsymbol{k}\alpha n}_{lmp}\int_{\alpha}\sum_{s}\varphi^{*s\mathring{\alpha}}_{l'm'p'}(\boldsymbol{r}_{\nu\mathring{\alpha}})\left[\mathscr{H}^{(0)}_{\mathrm{sph}}\varphi^{s\mathring{\alpha}}_{lmp}(\boldsymbol{r}_{\nu\mathring{\alpha}})\right]\mathrm{d}^3r_{\nu\mathring{\alpha}} \tag{7.102a}
$$

$$
\begin{aligned}
&=\sum_{lm}\left(E^{\mathring{\alpha}}_{l}A^{*\boldsymbol{k}_{\mathrm{bf}}^{+}\alpha n'}_{lm1}\tilde{\boldsymbol{A}}^{\boldsymbol{k}\alpha n}_{lm1}+A^{*\boldsymbol{k}_{\mathrm{bf}}^{+}\alpha n'}_{lm1}\tilde{\boldsymbol{A}}^{\boldsymbol{k}\alpha n}_{lm2}+N_{ll}A^{*\boldsymbol{k}_{\mathrm{bf}}^{+}\alpha n'}_{lm2}\tilde{\boldsymbol{A}}^{\boldsymbol{k}\alpha n}_{lm2}E^{\mathring{\alpha}}_{l}\right)\\
&=\sum_{lm}E^{\mathring{\alpha}}_{l}\left(A^{*\boldsymbol{k}_{\mathrm{bf}}^{+}\alpha n'}_{lm1}\tilde{\boldsymbol{A}}^{\boldsymbol{k}\alpha n}_{lm1}+N_{ll}A^{*\boldsymbol{k}_{\mathrm{bf}}^{+}\alpha n'}_{lm2}\tilde{\boldsymbol{A}}^{\boldsymbol{k}\alpha n}_{lm2}\right)+\sum_{lm}A^{*\boldsymbol{k}_{\mathrm{bf}}^{+}\alpha n'}_{lm1}\tilde{\boldsymbol{A}}^{\boldsymbol{k}\alpha n}_{lm2},
\end{aligned}
\tag{7.102b}
$$

and the non-spherical Hamiltonian contribution by

$$
\begin{aligned}
&\sum_{l'm'p'}\sum_{lmp}A^{*\boldsymbol{k}_{\mathrm{bf}}^{+}\alpha n'}_{l'm'p'}\tilde{\boldsymbol{A}}^{\boldsymbol{k}\alpha n}_{lmp}\int_{\alpha}\sum_{s}\varphi^{*s\mathring{\alpha}}_{l'm'p'}(\boldsymbol{r}_{\nu\mathring{\alpha}})V^{(0)\alpha}_{\mathrm{eff,nsph}}(\boldsymbol{r}_{\nu\mathring{\alpha}})\varphi^{s\mathring{\alpha}}_{lmp}(\boldsymbol{r}_{\nu\mathring{\alpha}})\,\mathrm{d}^3r_{\nu\mathring{\alpha}} \qquad (7.103)\\
&=\sum_{l'm'}\sum_{lm}A^{*\boldsymbol{k}_{\mathrm{bf}}^{+}\alpha n'}_{l'm'1}\left(\tilde{\boldsymbol{A}}^{\boldsymbol{k}\alpha n}_{lm1}t^{\mathrm{full},11\alpha}_{\eta(l'm'lm)}\left[V^{(0)\alpha}_{\mathrm{eff,nsph}}(\boldsymbol{r}_{\nu\mathring{\alpha}})\right]+\tilde{\boldsymbol{A}}^{\boldsymbol{k}\alpha n}_{lm2}t^{\mathrm{full},12\alpha}_{\eta(l'm'lm)}\left[V^{(0)\alpha}_{\mathrm{eff,nsph}}(\boldsymbol{r}_{\nu\mathring{\alpha}})\right]\right)\\
&\quad+\sum_{l'm'}\sum_{lm}A^{*\boldsymbol{k}_{\mathrm{bf}}^{+}\alpha n'}_{l'm'2}\left(\tilde{\boldsymbol{A}}^{\boldsymbol{k}\alpha n}_{lm1}t^{\mathrm{full},21\alpha}_{\eta(l'm'lm)}\left[V^{(0)\alpha}_{\mathrm{eff,nsph}}(\boldsymbol{r}_{\nu\mathring{\alpha}})\right]+\tilde{\boldsymbol{A}}^{\boldsymbol{k}\alpha n}_{lm2}t^{\mathrm{full},22\alpha}_{\eta(l'm'lm)}\left[V^{(0)\alpha}_{\mathrm{eff,nsph}}(\boldsymbol{r}_{\nu\mathring{\alpha}})\right]\right).
\end{aligned}
$$

It must be considered that these two matrix elements must both be calculated because a complex conjugation is not necessarily the same. Surface integrals such as described by

Algorithm

Klüppelberg [88, equation (A.52)] might entail. The implemented procedure of the non-spherical part is analogous to the already referenced algorithm 9, algorithm 10, algorithm 11 and algorithm 12. However, there is no distinct treatment of triangular parts because the effective potential is real. Finally, analogous to the MT part of section 7.4.2, the triangle interpolation of `Intgr3` is applied, but it has shown no significant effect.

7.4.4 Optimized Surface-Integral Correction

Subdivision

The IR surface integral in the last line of the Sternheimer equation (7.88)

$$\begin{aligned}&\oint_{\partial\mathrm{IR}_\alpha} \hat{\boldsymbol{e}}_{\mathrm{IR}}\varPsi^{*(0)\mathrm{IR}}_{\boldsymbol{k}+\boldsymbol{q},n'}(\boldsymbol{r})\Big(\mathscr{H}^{(0)}-\varepsilon^{(0)}_{\boldsymbol{k},n}\Big)\varPsi^{(0)\mathrm{IR}}_{\boldsymbol{k},n}(\boldsymbol{r})\,\mathrm{d}S \\ &= -\oint_{\partial\alpha}\hat{\boldsymbol{r}}\varPsi^{*(0)\mathrm{IR}}_{\boldsymbol{k}^+_{\mathrm{bf}},n'}(\boldsymbol{r})\Big(\mathscr{T}+V^{(0)\mathrm{IR}}_{\mathrm{eff}}(\boldsymbol{r})-\varepsilon^{(0)}_{\boldsymbol{k},n}\Big)\varPsi^{(0)\mathrm{IR}}_{\boldsymbol{k},n}(\boldsymbol{r})\,\mathrm{d}S\end{aligned} \tag{7.104}$$

subdivides into a kinetic-energy part, an overlap part multiplied by the Kohn–Sham energy, and a part containing the full effective potential. This partitioning is typical for the IR Hamiltonian matrix-element, as already discussed in section 5.8.1. Furthermore, some concepts of equation (7.55) can here likewise be adapted.

Overlap

Focussing on the overlap integral, the LAPW basis functions (5.17b) can be inserted and summarized by using equation (7.25):

$$\oint_{\partial\alpha}\hat{\boldsymbol{r}}\,\varPsi^{*(0)\mathrm{IR}}_{\boldsymbol{k}^+_{\mathrm{bf}},n'}(\boldsymbol{r})\varPsi^{(0)\mathrm{IR}}_{\boldsymbol{k},n}(\boldsymbol{r})\,\mathrm{d}S \tag{7.105a}$$

$$= \frac{R^2_{\mathring{\alpha}}}{\varOmega}\oint_{\partial\alpha}\hat{\boldsymbol{r}}\sum_{\boldsymbol{G}'\boldsymbol{G}} z^{*(0)}_{\boldsymbol{G}'}\Big(\boldsymbol{k}^+_{\mathrm{bf}},n'\Big)\mathrm{e}^{-\mathrm{i}\left(\boldsymbol{k}^+_{\mathrm{bf}}+\boldsymbol{G}'\right)\cdot\boldsymbol{r}}z^{(0)}_{\boldsymbol{G}}(\boldsymbol{k},n)\mathrm{e}^{\mathrm{i}(\boldsymbol{k}+\boldsymbol{G})\cdot\boldsymbol{r}}\,\mathrm{d}\varOmega$$

$$= \frac{R^2_{\mathring{\alpha}}}{\varOmega}\sum_{\boldsymbol{G}'\boldsymbol{G}} z^{*(0)}_{\boldsymbol{G}'}\Big(\boldsymbol{k}^+_{\mathrm{bf}},n'\Big)z^{(0)}_{\boldsymbol{G}}(\boldsymbol{k},n)\oint_{\partial\alpha}\hat{\boldsymbol{r}}\sum_{\boldsymbol{G}\boldsymbol{G}'}\mathrm{e}^{-\mathrm{i}\left(\boldsymbol{k}+\boldsymbol{q}+\boldsymbol{G}_{\mathrm{f}}+\boldsymbol{G}'\right)\cdot\boldsymbol{r}}\mathrm{e}^{\mathrm{i}(\boldsymbol{k}+\boldsymbol{G})\cdot\boldsymbol{r}}\,\mathrm{d}\varOmega \tag{7.105b}$$

$$= \frac{R^2_{\mathring{\alpha}}}{\varOmega}\sum_{\boldsymbol{G}'\boldsymbol{G}} z^{*(0)}_{\boldsymbol{G}'}\Big(\boldsymbol{k}^+_{\mathrm{bf}},n'\Big)z^{(0)}_{\boldsymbol{G}}(\boldsymbol{k},n)\oint_{\partial\alpha}\hat{\boldsymbol{r}}^*\mathrm{e}^{\mathrm{i}\left(\boldsymbol{G}-\boldsymbol{q}-\boldsymbol{G}_{\mathrm{f}}-\boldsymbol{G}'\right)\cdot(\boldsymbol{r}_\alpha+\boldsymbol{\tau}_\alpha)}\,\mathrm{d}\varOmega\ . \tag{7.105c}$$

Having changed into the local coordinate system $\boldsymbol{r}_\gamma = \boldsymbol{r}-\boldsymbol{\tau}_\gamma$, a Rayleigh decomposition (5.5), the definition $\boldsymbol{G}'' := \boldsymbol{G}-\boldsymbol{G}_{\mathrm{bf}}-\boldsymbol{G}'$, and the orthogonality of the spherical harmonics can be applied. The latter selects $l = 1$ as only relevant channel

$$\oint_{\partial\alpha}\hat{\boldsymbol{r}}\,\varPsi^{*(0)\mathrm{IR}}_{\boldsymbol{k}^+_{\mathrm{bf}},n'}(\boldsymbol{r})\varPsi^{(0)\mathrm{IR}}_{\boldsymbol{k},n}(\boldsymbol{r})\,\mathrm{d}S \tag{7.105d}$$

$$= \frac{R^2_{\mathring{\alpha}}}{\varOmega}\sum_{\boldsymbol{G}'\boldsymbol{G}} z^{*(0)}_{\boldsymbol{G}'}\Big(\boldsymbol{k}^+_{\mathrm{bf}},n'\Big)z^{(0)}_{\boldsymbol{G}}(\boldsymbol{k},n)\oint_{\partial\alpha}\hat{\boldsymbol{r}}^*\mathrm{e}^{\mathrm{i}\left(\boldsymbol{G}''-\boldsymbol{q}\right)\cdot(\boldsymbol{r}_\alpha+\boldsymbol{\tau}_\alpha)}\,\mathrm{d}\varOmega$$

$$\begin{aligned}&= \frac{R^2_{\mathring{\alpha}}}{\varOmega}\sum_{\boldsymbol{G}'\boldsymbol{G}} z^{*(0)}_{\boldsymbol{G}'}\Big(\boldsymbol{k}^+_{\mathrm{bf}},n'\Big)z^{(0)}_{\boldsymbol{G}}(\boldsymbol{k},n)\sum_{im'}\zeta^*_{i,m'}\hat{\boldsymbol{e}}_i\sum_{lm}4\pi\mathrm{i}^l\mathrm{j}_l\Big(\big|\boldsymbol{G}''-\boldsymbol{q}\big|R_{\mathring{\alpha}}\Big)\mathrm{e}^{\mathrm{i}\left(\boldsymbol{G}''-\boldsymbol{q}\right)\cdot\boldsymbol{\tau}_\alpha} \\ &\qquad\times\mathrm{Y}^*_{lm}\Big(\widehat{\boldsymbol{G}''-\boldsymbol{q}}\Big)\oint_{\partial\alpha}\mathrm{Y}^*_{1m'}(\hat{\boldsymbol{r}}_\alpha)\mathrm{Y}_{lm}(\boldsymbol{r}_\alpha)\,\mathrm{d}\varOmega\end{aligned} \tag{7.105e}$$

$$= \mathrm{i}\frac{4\pi R^2_{\mathring{\alpha}}}{\varOmega}\sum_{\boldsymbol{G}'\boldsymbol{G}} z^{*(0)}_{\boldsymbol{G}'}\Big(\boldsymbol{k}^+_{\mathrm{bf}},n'\Big)z^{(0)}_{\boldsymbol{G}}(\boldsymbol{k},n)\mathrm{j}_1\Big(\big|\boldsymbol{G}''-\boldsymbol{q}\big|R_{\mathring{\alpha}}\Big)\mathrm{e}^{\mathrm{i}\left(\boldsymbol{G}''-\boldsymbol{q}\right)\cdot\boldsymbol{\tau}_\alpha} \tag{7.105f}$$

$$\times \sum_{im} \zeta^{*}_{i,m} \hat{\boldsymbol{e}}_i \mathrm{Y}^{*}_{1m}\left(\widehat{\boldsymbol{G}'' - \boldsymbol{q}}\right) .$$

Kinetic-energy

For the kinetic energy, the Laplace operator only acts on the ket in the first implementation:

$$\oint_{\partial\alpha} \hat{\boldsymbol{r}}\, \Psi^{*(0)\mathrm{IR}}_{\boldsymbol{k}^{+}_{\mathrm{bf}},n'}(\boldsymbol{r})\, \mathscr{T} \Psi^{(0)\mathrm{IR}}_{\boldsymbol{k},n}(\boldsymbol{r})\, \mathrm{d}S \tag{7.106a}$$

$$= -\frac{R^2_{\mathrm{MT}}}{\Omega} \oint_{\partial\alpha} \hat{\boldsymbol{r}} \sum_{\boldsymbol{G}'\boldsymbol{G}} z^{*(0)}_{\boldsymbol{G}'}\left(\boldsymbol{k}^{+}_{\mathrm{bf}}, n'\right) \mathrm{e}^{-\mathrm{i}\left(\boldsymbol{k}^{+}_{\mathrm{bf}}+\boldsymbol{G}'\right)\cdot\boldsymbol{r}} z^{(0)}_{\boldsymbol{G}}(\boldsymbol{k}, n) \frac{\Delta}{2} \mathrm{e}^{\mathrm{i}(\boldsymbol{k}+\boldsymbol{G})\cdot\boldsymbol{r}}\, \mathrm{d}\Omega \tag{7.106b}$$

$$= \mathrm{i}\frac{4\pi R^2_{\mathring{\alpha}}}{\Omega} \sum_{\boldsymbol{G}'\boldsymbol{G}} z^{*(0)}_{\boldsymbol{G}'}\left(\boldsymbol{k}^{+}_{\mathrm{bf}}, n'\right) z^{(0)}_{\boldsymbol{G}}(\boldsymbol{k}, n) \frac{|\boldsymbol{k}+\boldsymbol{G}|^2}{2} \mathrm{j}_1\left(\left|\boldsymbol{G}'' - \boldsymbol{q}\right| R_{\mathring{\alpha}}\right) \mathrm{e}^{\mathrm{i}\left(\boldsymbol{G}''-\boldsymbol{q}\right)\cdot\boldsymbol{\tau}_{\alpha}} \tag{7.106c}$$

$$\times \sum_{im} \zeta^{*}_{i,m} \hat{\boldsymbol{e}}_i \mathrm{Y}^{*}_{1m}\left(\widehat{\boldsymbol{G}'' - \boldsymbol{q}}\right) .$$

But as anticipated in section 5.11, this can lead to numerical problems, because the LAPW basis is only continuous up to the first-order energy derivative. A symmetric application of the kinetic energy, as on the left-hand side of equation (5.77), appears to be more stable from a numeric point of view[25] [119, 127, 278]. When choosing the type of the kinetic energy operator, consistency is decisive [251]. For the Pulay matrix elements in section 7.4.3 the numerics are controllable with the Laplace operator, since the eigenvalue equations (5.4) and (5.10) can be exploited. Therefore, one must also start from a Laplace operator in the IR, which however can be reformulated causing additional terms similar to those in equation section 5.11.

Potential

For the surface integral containing the potential in equation (7.104), an auxiliary quantity

$$\boldsymbol{\xi}_{l''m''} := \oint_{\partial\alpha} \mathrm{Y}^{*}_{l''m''}(\hat{\boldsymbol{r}}_{\alpha}) \hat{\boldsymbol{r}} V^{(0)\mathrm{IR}}_{\mathrm{eff}}(\boldsymbol{r})\, \mathrm{d}S \tag{7.107a}$$

$$= \oint_{\partial\alpha} \mathrm{Y}^{*}_{l''m''}(\hat{\boldsymbol{r}}_{\alpha}) \sum_{i}\sum_{m'} \zeta_{i,m'} \hat{\boldsymbol{e}}_i \mathrm{Y}_{1m'}(\hat{\boldsymbol{r}}_{\alpha}) \sum_{\boldsymbol{G}} V^{(0)\mathrm{IR}}_{\mathrm{eff}}(\boldsymbol{G}) \mathrm{e}^{\mathrm{i}\boldsymbol{G}\cdot\boldsymbol{r}}\, \mathrm{d}S \tag{7.107b}$$

$$= \oint_{\partial\alpha} \mathrm{Y}^{*}_{l''m''}(\hat{\boldsymbol{r}}_{\alpha}) \sum_{i}\sum_{m'} \zeta_{i,m'} \hat{\boldsymbol{e}}_i \mathrm{Y}_{1m'}(\hat{\boldsymbol{r}}_{\alpha}) \sum_{\boldsymbol{G}} V^{(0)\mathrm{IR}}_{\mathrm{eff}}(\boldsymbol{G}) \mathrm{e}^{\mathrm{i}\boldsymbol{G}\cdot(\boldsymbol{r}_{\alpha}+\boldsymbol{\tau}_{\alpha})}\, \mathrm{d}S \tag{7.107c}$$

$$= \oint_{\partial\alpha} \mathrm{Y}^{*}_{l''m''}(\hat{\boldsymbol{r}}_{\alpha}) \sum_{i}\sum_{m'} \zeta_{i,m'} \hat{\boldsymbol{e}}_i \mathrm{Y}_{1m'}(\hat{\boldsymbol{r}}_{\alpha}) \sum_{\boldsymbol{G}} V^{(0)\mathrm{IR}}_{\mathrm{eff}}(\boldsymbol{G}) \mathrm{e}^{\mathrm{i}\boldsymbol{G}\cdot\boldsymbol{\tau}_{\alpha}} \tag{7.107d}$$

$$\times \sum_{lm} 4\pi \mathrm{i}^{l} \mathrm{Y}^{*}_{lm}\left(\hat{\boldsymbol{G}}\right) \mathrm{j}_l(Gr) \mathrm{Y}^{*}_{lm}(\hat{\boldsymbol{r}}_{\alpha})\, \mathrm{d}S$$

$$= \sum_{i}\sum_{m'} \zeta_{i,m'} \hat{\boldsymbol{e}}_i \sum_{\boldsymbol{G}} V^{(0)\mathrm{IR}}_{\mathrm{eff}}(\boldsymbol{G}) \sum_{lm} 4\pi \mathrm{i}^{l} \mathrm{Y}^{*}_{lm}\left(\hat{\boldsymbol{G}}\right) \mathrm{j}_l(GR_{\mathring{\alpha}}) \mathrm{e}^{\mathrm{i}\boldsymbol{G}\cdot\boldsymbol{\tau}_{\alpha}} \tag{7.107e}$$

$$\times \oint_{\partial\alpha} \mathrm{Y}^{*}_{l''m''}(\hat{\boldsymbol{r}}_{\alpha}) \mathrm{Y}_{1m'}(\hat{\boldsymbol{r}}_{\alpha}) \mathrm{Y}_{lm}(\boldsymbol{r})\, \mathrm{d}S$$

$$= 4\pi \sum_{\boldsymbol{G}} V^{(0)\mathrm{IR}}_{\mathrm{eff}}(\boldsymbol{G}) \mathrm{e}^{\mathrm{i}\boldsymbol{G}\cdot\boldsymbol{\tau}_{\alpha}} \sum_{lm} \mathrm{i}^{l} \mathrm{j}_l(GR_{\mathring{\alpha}}) \mathrm{Y}^{*}_{lm}\left(\hat{\boldsymbol{G}}\right) \sum_{m'i} \zeta_{i,m'} \hat{\boldsymbol{e}}_i G^{m'',m',m}_{l'',\ 1,\ l} \tag{7.107f}$$

is introduced. This is because the number of four expandable quantities (two wave functions, the potential and the normal vector) must be reduced, because one Gaunt coefficient is

---

[25] Alexander Neukirchen has found that this has only a marginal effect on the phonon dispersion relation of fcc Al. However he has programmed it as a potential backup solution for more complicated systems.

composed of only three spherical harmonics. Using this $\boldsymbol{\xi}_{l''m''}$, the potential part of the surface integral finally yields

$$\begin{aligned}
&\oint_{\partial\alpha} \hat{\boldsymbol{r}}\,\Psi^{*(0)}_{\boldsymbol{k}^{+}_{\text{bf}},n'}(\boldsymbol{r}) V^{(0)\text{IR}}_{\text{eff}}(\boldsymbol{r}) \Psi^{(0)}_{\boldsymbol{k},n}(\boldsymbol{r})\,\mathrm{d}S && \text{(7.108a)}\\
&= \frac{1}{\Omega} \oint_{\partial\alpha} \sum_{\boldsymbol{G}\boldsymbol{G}'} z^{*(0)}_{\boldsymbol{G}'}\left(\boldsymbol{k}^{+}_{\text{bf}}, n'\right) \mathrm{e}^{-\mathrm{i}\left(\boldsymbol{k}^{+}_{\text{bf}}+\boldsymbol{G}'\right)\cdot\boldsymbol{r}} z^{(0)}_{\boldsymbol{G}}(\boldsymbol{k}, n) \mathrm{e}^{\mathrm{i}(\boldsymbol{k}+\boldsymbol{G})\cdot\boldsymbol{r}} \sum_{l''m''} \boldsymbol{\xi}_{l''m''} \mathrm{Y}_{l''m''}(\boldsymbol{r}_{\alpha})\,\mathrm{d}S && \text{(7.108b)}\\
&= \frac{(4\pi R_{\mathring{\alpha}})^2}{\Omega} \sum_{\boldsymbol{G}'} z^{*(0)}_{\boldsymbol{G}'}\left(\boldsymbol{k}^{+}_{\text{bf}}, n'\right) \sum_{l'm'} (-\mathrm{i})^{l'} \mathrm{j}_{l'}\left(\left|\boldsymbol{k}^{+}_{\text{bf}} + \boldsymbol{G}\right| R_{\mathring{\alpha}}\right) \mathrm{Y}_{l'm'}\left(\widehat{\boldsymbol{k}^{+}_{\text{bf}} + \boldsymbol{G}}\right) \mathrm{e}^{\mathrm{i}\left(\boldsymbol{k}^{+}_{\text{bf}}+\boldsymbol{G}'\right)\cdot\boldsymbol{\tau}_{\alpha}} \\
&\quad \times \sum_{\boldsymbol{G}} z^{(0)}_{\boldsymbol{G}}(\boldsymbol{k}, n) \sum_{lm} \mathrm{i}^{l} \mathrm{j}_{l}(|\boldsymbol{k} + \boldsymbol{G}| R_{\mathring{\alpha}}) \mathrm{Y}^{*}_{lm}\left(\widehat{\boldsymbol{k} + \boldsymbol{G}}\right) \mathrm{e}^{\mathrm{i}(\boldsymbol{k}+\boldsymbol{G})\cdot\boldsymbol{\tau}_{\alpha}} \sum_{l''m''} \boldsymbol{\xi}_{l''m''} && \text{(7.108c)}\\
&\quad \times \oint_{\partial\alpha} \mathrm{Y}^{*}_{l'm'}(\boldsymbol{r}_{\alpha}) \mathrm{Y}_{lm}(\boldsymbol{r}_{\alpha}) \mathrm{Y}_{l''m''}(\boldsymbol{r}_{\alpha})\,\mathrm{d}\Omega \\
&= \frac{(4\pi R_{\mathring{\alpha}})^2}{\Omega} \sum_{l'm'} && \text{(7.108d)}\\
&\quad \times \left(\sum_{\boldsymbol{G}'} z^{*(0)}_{\boldsymbol{G}'}\left(\boldsymbol{k}^{+}_{\text{bf}}, n'\right) \left((-\mathrm{i})^{l'} \mathrm{j}_{l'}\left(\left|\boldsymbol{k}^{+}_{\text{bf}} + \boldsymbol{G}\right| R_{\mathring{\alpha}}\right) \mathrm{Y}_{l'm'}\left(\widehat{\boldsymbol{k}^{+}_{\text{bf}} + \boldsymbol{G}}\right) \mathrm{e}^{-\mathrm{i}\left(\boldsymbol{k}^{+}_{\text{bf}}+\boldsymbol{G}'\right)\cdot\boldsymbol{\tau}_{\alpha}} \right) \right) \\
&\quad \times \sum_{lm} \left(\sum_{\boldsymbol{G}} z^{(0)}_{\boldsymbol{G}}(\boldsymbol{k}, n) \left(\mathrm{i}^{l} \mathrm{j}_{l}(|\boldsymbol{k} + \boldsymbol{G}| R_{\mathring{\alpha}}) \mathrm{Y}^{*}_{lm}\left(\widehat{\boldsymbol{k} + \boldsymbol{G}}\right) \mathrm{e}^{\mathrm{i}(\boldsymbol{k}+\boldsymbol{G})\cdot\boldsymbol{\tau}_{\alpha}} \right) \right) \sum_{l''m''} \boldsymbol{\xi}_{l''m''} G^{m',m,m''}_{l',\,l,\,l''} \\
&= \frac{(4\pi R_{\mathring{\alpha}})^2}{\Omega} \sum_{l'=|l-l''|}^{|l+l''|} && \text{(7.108e)}\\
&\quad \times \left(\sum_{\boldsymbol{G}'} z^{*(0)}_{\boldsymbol{G}'}\left(\boldsymbol{k}^{+}_{\text{bf}}, n'\right) \left((-\mathrm{i})^{l'} \mathrm{j}_{l'}\left(\left|\boldsymbol{k}^{+}_{\text{bf}} + \boldsymbol{G}\right| R_{\mathring{\alpha}}\right) \mathrm{Y}_{l',m+m''}\left(\widehat{\boldsymbol{k}^{+}_{\text{bf}} + \boldsymbol{G}}\right) \mathrm{e}^{-\mathrm{i}\left(\boldsymbol{k}^{+}_{\text{bf}}+\boldsymbol{G}'\right)\cdot\boldsymbol{\tau}_{\alpha}} \right) \right) \\
&\quad \times \sum_{lm} \left(\sum_{\boldsymbol{G}} z^{(0)}_{\boldsymbol{G}}(\boldsymbol{k}, n) \left(\mathrm{i}^{l} \mathrm{j}_{l}(|\boldsymbol{k} + \boldsymbol{G}| R_{\mathring{\alpha}}) \mathrm{Y}^{*}_{lm}\left(\widehat{\boldsymbol{k} + \boldsymbol{G}}\right) \mathrm{e}^{\mathrm{i}(\boldsymbol{k}+\boldsymbol{G})\cdot\boldsymbol{\tau}_{\alpha}} \right) \right) \sum_{l''m''} \boldsymbol{\xi}_{l''m''} G^{m+m'',m'',m}_{l',\qquad l'',\,l}\,.
\end{aligned}$$

Algorithm

It is important to use the unwarped potential, i.e., lacking the convolution with the IR Heaviside step function [251]. The algorithm which has been presented for the surface integral (7.104) is inspired by the strategy which has been developed by Klüppelberg [88] for similar surface integrals in his force formalism. Finally, I programmed a factor to increase the $l_{\text{max},\mathring{\gamma}}$ of the Rayleigh decomposition as discussed by Klüppelberg [88], who proposes a factor of 2 [251]. Although for fcc Ne and fcc Al a factor of 1 is sufficient, it might be necessary to increase it for more sophisticated materials. It must be considered that expanding IR quantities by a Rayleigh decomposition until $l_{\text{max},\mathring{\gamma}}$ introduces to some extent a new cutoff, which should be well-converged [251].

7.4.5 Mixing

Concept

As already touched in section 7.4.1, the output first-order density variation $\boldsymbol{\rho}^{(1)}_{\text{out}}(\boldsymbol{r}, \boldsymbol{q}^{+}\alpha)$ must be mixed with the input one $\boldsymbol{\rho}^{(1)}_{\text{in}}(\boldsymbol{r}, \boldsymbol{q}^{+}\alpha)$ for the Sternheimer equation to reach self-consistency. Following section 2.2.3, the mixing of the first-order density variation translates into finding the minimum of

$$\min\left\|\boldsymbol{\rho}^{(1)}_{\text{out}}(\boldsymbol{r},\boldsymbol{q}^{+}\alpha)-\boldsymbol{\rho}^{(1)}_{\text{in}}(\boldsymbol{r},\boldsymbol{q}^{+}\alpha)\right\| =: \min\left\|\Delta\boldsymbol{\rho}^{(1)}\left(\boldsymbol{r},\boldsymbol{q}^{+}\alpha\right)\right\| . \tag{7.109a}$$

In `FLEUR`, i.e., in the FLAPW method (see in chapter 5), the norm reads

$$\begin{aligned}\min\left\|\Delta\boldsymbol{\rho}^{(1)}\left(\boldsymbol{r},\boldsymbol{q}^{+}\alpha\right)\right\| &= \int_{\Omega}\Delta\boldsymbol{\rho}^{*(1)}\left(\boldsymbol{r},\boldsymbol{q}^{+}\alpha\right)w(\boldsymbol{r})\,\Delta\boldsymbol{\rho}^{(1)}\left(\boldsymbol{r},\boldsymbol{q}^{+}\alpha\right)\mathrm{d}^3r && (7.109\text{b})\\ &= \int_{\text{IR}}\Delta\boldsymbol{\rho}^{*(1)}\left(\boldsymbol{r},\boldsymbol{q}^{+}\alpha\right)w(\boldsymbol{r})\,\Delta\boldsymbol{\rho}^{(1)}\left(\boldsymbol{r},\boldsymbol{q}^{+}\alpha\right)\mathrm{d}^3r && (7.109\text{c})\\ &\quad+\sum_{\gamma}\int_{\gamma}\Delta\boldsymbol{\rho}^{*(1)}\left(\boldsymbol{r},\boldsymbol{q}^{+}\alpha\right)w(\boldsymbol{r})\,\Delta\boldsymbol{\rho}^{(1)}\left(\boldsymbol{r},\boldsymbol{q}^{+}\alpha\right)\mathrm{d}^3r\end{aligned}$$

where the metric w is utilized [292]. By analogy with equation (5.18), the plane-wave and spherical-harmonic basis set is now inserted. Furthermore, the IR integral volume is extended to the complete unit cell by introducing the IR step function (5.48b). This allows for revealing the definition of the metric w [292] in the IR

$$\begin{aligned}&\int_{\text{IR}}\Delta\boldsymbol{\rho}^{*(1)}(\boldsymbol{r},\boldsymbol{q}^{+}\alpha)w(\boldsymbol{r})\,\Delta\boldsymbol{\rho}^{(1)}(\boldsymbol{r},\boldsymbol{q}^{+}\alpha)\,\mathrm{d}^3r && (7.110\text{a})\\ &\quad:=\sum_{\boldsymbol{G}}\Delta\boldsymbol{\rho}^{*(1)}(\boldsymbol{G};\boldsymbol{q}^{+}\alpha)\sum_{\boldsymbol{G}'}\Delta\boldsymbol{\rho}^{(1)}(\boldsymbol{G}';\boldsymbol{q}^{+}\alpha)\frac{1}{\Omega}\int_{\Omega}\mathrm{e}^{-\mathrm{i}\boldsymbol{G}\cdot\boldsymbol{r}}\Theta(\boldsymbol{r})\mathrm{e}^{\mathrm{i}\boldsymbol{G}'\cdot\boldsymbol{r}}\,\mathrm{d}^3r\\ &\quad=\sum_{\boldsymbol{G}}\Delta\boldsymbol{\rho}^{*(1)}(\boldsymbol{G};\boldsymbol{q}^{+}\alpha)\left[\Delta\boldsymbol{\rho}^{(1)}\,\Theta\right](\boldsymbol{G};\boldsymbol{q}^{+}\alpha)\,, && (7.110\text{b})\end{aligned}$$

and for the MT integral with a logarithmic mesh

$$\begin{aligned}&\sum_{\gamma}\int_{\gamma}\Delta\boldsymbol{\rho}^{*(1)}_{\gamma}\left(\boldsymbol{r},\boldsymbol{q}^{+}\alpha\right)w(\boldsymbol{r})\,\Delta\boldsymbol{\rho}^{(1)}_{\gamma}\left(\boldsymbol{r},\boldsymbol{q}^{+}\alpha\right)\mathrm{d}^3r && (7.111\text{a})\\ &\quad:=\sum_{\gamma}\sum_{lm}\sum_{\nu}\left[\boldsymbol{\rho}^{*(1)}_{\gamma}(r_\nu,\boldsymbol{q}^{+}\alpha)\right]_{lm}\frac{1}{\Omega}r^2_{\nu\mathring{\gamma}}\frac{\mathrm{d}r_{\nu\mathring{\gamma}}}{\mathrm{d}\nu\mathring{\gamma}}\left[\boldsymbol{\rho}^{(1)}_{\gamma}(r_\nu,\boldsymbol{q}^{+}\alpha)\right]_{lm}\\ &\quad=\sum_{\gamma}\sum_{lm}\sum_{\nu\mathring{\gamma}}\frac{1}{\Omega}r^3_{\nu\mathring{\gamma}}\,\delta r_{\nu\mathring{\gamma}}\left[\boldsymbol{\rho}^{*(1)\gamma}_{\mathring{\gamma}}(r_\nu,\boldsymbol{q}^{+}\alpha)\right]_{lm}\left[\boldsymbol{\rho}^{(1)\gamma}_{\mathring{\gamma}}(r_\nu,\boldsymbol{q}^{+}\alpha)\right]_{lm}. && (7.111\text{b})\end{aligned}$$

The integral in equation (7.110a) including Ω^{-1} and the prefactor $\Omega^{-1}r^3_{\nu\mathring{\gamma}}\,\delta r_{\nu\mathring{\gamma}}$ in equation (7.111a) are denoted as elements of the so-called Gram matrix [127, 293]. Furthermore, the latter expression shows that predominantly the mesh points close to the boundary contribute to the mixing because of the factor $r^3_{\nu\mathring{\gamma}}$ in equation (7.111b). However as an additional security measure for the convergence of the mixing, we do not involve the second line of equation (7.37b) into the mixing, since it does not change during the self-consistency procedure. Equations (7.110b) and (7.111b) contain the coefficients which are strung together into a mixing vector, subject to a mixing algorithm. In the current version of `juPhon`, one can choose between simple mixing and general Anderson mixing (cf. section 2.2.3).

Algorithm

Finally, it must be considered that coefficients of the charge-density variation are (i) complex-valued and (ii) have a vectorial character. Case (i) does not present a challenge, because likewise the star coefficients are complex [119, 127, 278]. Therefore, for each single IR coefficient (7.110b) its real and imaginary parts are placed subsequently into the aforementioned mixing vector. This can analogously be applied to the complex-valued spherical harmonic coefficients (7.111b) which replace the real lattice harmonic coefficients in the recycled routines. These `FLEUR` routines are `Mix.F` and their dependencies [127]. As far as case (ii) is concerned, I implemented that the displacement directions are separately dealt with. This enables us to stop the mixing in one direction while the other directions are not converged yet. In order to allow for a close inspection of the mixing distance (2.10), the real and imaginary part as well as each displacement direction are printed for every iteration step.

Evolution of mixing distances

The aforementioned distances for fcc Ne and bcc Al are plotted in figure 7.16 as a function of iteration steps for various real and imaginary parts, displacement directions and $\boldsymbol{q}$-vectors. Some distances are very large in the first two iterations but rapidly collapse then. This originates from the fact that the general Anderson mixing requires two iteration to store a history, before it unlocks its true potential. In general the distances of fcc Al are a little larger relative to fcc Ne. This might be due to their different orders of magnitude for their phonon frequencies or the different importance of the Hartree potential, since fcc Al features stronger bondings (covalent for the former vs. Van der Waals for the latter) [127]. For both materials, $\boldsymbol{q} = \mathbf{0}$ converges fastest relative to finite $\boldsymbol{q}$-vectors. The calculation in `juPhon` is assumed to be converged below $4 \cdot 10^{-5}\, e\, a_0^{-4}$ and mixing parameter α reads 0.05.

7.4.6 Self-Consistency Cycle

Setting the stage

The self-consistency cycle (SCC) serves the purpose of iteratively achieving a self-consistent solution of the Sternheimer equation, i.e., self-consistent first-order potential and density variations. Both quantities (ideally) increase their accuracy as a function of the iteration steps. The efficiency and the numerical stability of this minimization procedure is governed by its strategy. In the following the approach of `juPhon` is described.

Initial density variations

As already discussed in section 6.4.3, the first-order external-potential variation is known before the first iteration. It describes the perturbation the system undergoes, inducing a response. Therefore, the density variation as well as the Hartree- and xc-potential variations cannot be generated before the second iteration. Apart from those quantities, all gradients of the unperturbed density or the unperturbed effective potential are at hand from the beginning. Hence, two options for the HF contributions to the Sternheimer equation (7.88) in the displaced MT α are available for the first iteration. The first one (i) is to switch off the gradient of the unperturbed Hartree and xc potentials and activate them again for the second iteration in the second matrix element of the second line in equation (7.88), as soon as an approximation to the first-order *effective* potential is available. In contrast, the second option (ii) is to include the gradient of the complete effective potential from the beginning of the SCC. On the one hand, the HF contributions are optimized to avoid inaccuracies due to the summation of large numbers. In this sense, option (i) should be preferred and is consistent with the proposal of Klüppelberg [88]. Given this choice, inaccuracies from the gradients of the Hartree and the xc potentials need not to be dealt with in the first iteration. On the other hand, one could argue that omitting the gradient of the Hartree- and the xc potentials in the first iteration could hinder the SCC from converging to the correct minimum [256]. But, the volume integrals in the MT Hartree-potential gradient (6.44) and the xc-potential gradient (7.71d) only give a contribution in the first iteration. Furthermore, they are large relative to the contributions of the remaining iterations. Still, in all iterations

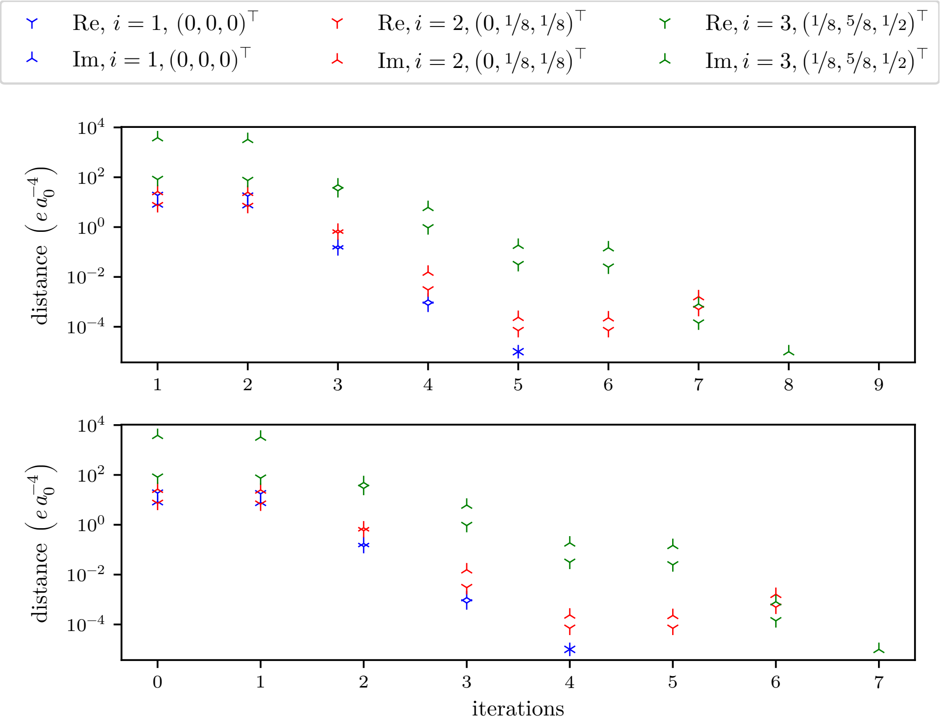

Figure 7.16: Mixing distances of first-order density variation as a function of iteration steps for fcc Ne (above) and fcc Al (below). Shown are its real and imaginary parts for various displacement directions i and $\boldsymbol{q}$-vectors. As soon as the mixing distances are below the threshold $4 \cdot 10^{-5}\,e\,a_0^{-4}$, the calculation is assumed to be converged. Finally, the `FLEUR` input-generator input files this calculations are based on can be found in appendix B.

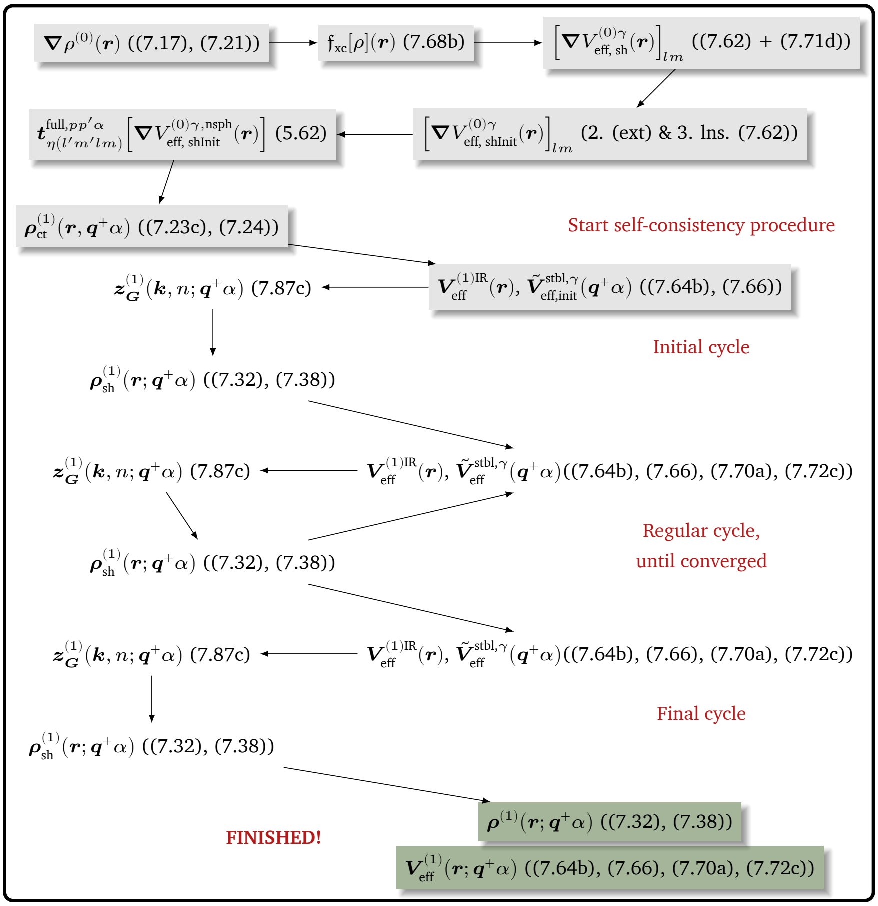

Figure 7.17: Flow chart of the implemented Sternheimer self-consistency cycle. Various quantities (grayish background) are generated before the actual self-consistency procedure starts with the first cycle, in order to avoid calculating them redundantly. For the initial cycle only the external part of the unperturbed effective potential gradient and the first-order effective-potential variation are utilized. After the regular cycle has converged, the final cycle serves to calculate all resulting quantities (greenish background) without any adjustments for the Sternheimer equation. This ensures to have a complete result when the Sternheimer self-consistency cycle is finished.

they are sufficiently mitigated by the radial Jacobi determinant $r^2_{\nu\hat{\gamma}}$. In the end, a numerical analysis of the final results by Alexander Neukirchen has shown for fcc Ne and fcc Al that no difference between options (i) and (ii) can be observed. Although this must be tested for further systems in the future, this discussion proceeds with option (i), because it is more consistent with the overall optimization concept.

Start of mixing

A further decision we reached is to start the mixing, i.e., to store a mixing history after the third iteration (the second one of the regular cycle in figure 7.17). The first-order density variations known after the second and third iterations serve as an input for the mixing routine. Its output first-order density variation is inserted into the first-order effective potential variations for the fourth iteration. This gives lower starting distances than if the mixing would have been started after the second iteration.

Further optimizations and algorithm

According to the frozen-core and the frozen-augmentation approximations, only the first-order variations of the wave-function expansion coefficients are the subjects of the SCC. Furthermore, the MT gradient is assumed to cause severe numerical challenges disadvantageous for the mixing, i.e., the convergence of the Sternheimer equation. Therefore, the gradient of the density is separated from the mixing process, i.e., only the part of the density variation that lies fully in the LAPW Hilbert space is varied by the mixing. However, the generation of the first-order Hartree-potential variation multipole-moments (6.37) requires the full charge-density variation. This in particular includes the gradient of the unperturbed charge density. Since moreover the complete first-order density variation is required for the dynamical matrix, the gradient is added after the SCC has converged. The same holds true for the linear first-order effective potential variation, which is optimized for the Sternheimer equation. All terms that have been deactivated for the sake of optimizing the Sternheimer equation must be enabled in the final iteration. Otherwise, continuity checks fail. Before starting a new mixing sequence, all files with “`broyden`” in their name must be deleted, on condition that the general Anderson mixing is activated. The complete SCC is sketched in figure 7.17.

7.4.7 Tests

Outline

The tests of the Sternheimer equation fall into different categories. While test 21, test 22, as well as test 23 deal with the HF contributions, test 24 is devoted to the Pulay part, and test 25 checks the IR surface integral. The ultimate test of the mixing subroutines is that the converged results are correct. Still, the small consistency check in test 26 makes sense in this context. Finally, test 27, test 28, and test 29 check the outcome of the Sternheimer equation.

Test 21: Hellmann–Feynman Sternheimer Equation

Ignoring the Pulay and surface corrections in the Sternheimer equation (7.86) and setting $\boldsymbol{q} = \boldsymbol{0}$ leads to

$$\boldsymbol{z}^{(1)}_{n'}(\boldsymbol{k}, n; \boldsymbol{0}^+\alpha) = -\frac{\left\langle \Psi^{(0)}_{\boldsymbol{k},n'} \middle| \mathscr{V}^{(1)}_{\text{eff}}(\boldsymbol{0}^+\alpha) \middle| \Psi^{(0)}_{\boldsymbol{k},n} \right\rangle_{\Omega}}{\varepsilon^{(0)}_{\boldsymbol{k},n'} - \varepsilon^{(0)}_{\boldsymbol{k},n}} \tag{7.112a}$$

results. This equation features close analogies to the expression for the first-order wave function in Rayleigh–Schrödinger perturbation theory (4.8c). The background details are already pointed out in chapter 4. When choosing now a constant potential with value 1, so

$$\left[\boldsymbol{\mathscr{V}}_{\text{eff}}^{(1)\text{IR}}(\boldsymbol{G}=\boldsymbol{0};\boldsymbol{0}^{+}\alpha)\right]=1 \tag{7.112b}$$

and

$$\left[\boldsymbol{\mathscr{V}}_{\text{eff}}^{(1)\gamma}(r_{\nu\hat{\gamma}};\boldsymbol{0}^{+}\alpha)\right]_{00}=\sqrt{4\pi}\,, \tag{7.112c}$$

the overlap in the nominator of equation (7.112) remains. For every $\boldsymbol{k}$-vector it equals $\delta_{nn'}$ and is already checked in test 5. But if $n = n'$, the Kohn–Sham energies are degenerate. Thus, this band configuration gives no contribution to the first-order wave-function expansion coefficients (see section 7.4.1). According to the implementation, this test passes provided $\left[\boldsymbol{z}_{n'}^{(1)}(\boldsymbol{k},n;\boldsymbol{q}\alpha)\right]_i < 9{\cdot}10^{-8}\,e^{\frac{1}{2}}\,a_0^{-2}$, where i denotes the displacement directions. [251]

Test 22: Hellmann–Feynman Matrix Element for $q = 0$

For the Goldstone modes, the IR first-order effective-potential variation equals minus the gradient of the unperturbed potential (for polyatomic system a sum over all displaced atoms is required). As a consequence, the first matrix element in the second line of the Sternheimer equation (7.88) turns into the summands of

$$-\sum_{\boldsymbol{k},n}\left\langle\Psi_{\boldsymbol{k},n}^{(0)}\middle|\boldsymbol{\nabla}V_{\text{eff}}^{(0)}\middle|\Psi_{\boldsymbol{k},n}^{(0)}\right\rangle_{\text{IR}}=-\Omega\sum_{\boldsymbol{k},n}\frac{1}{\Omega}\int_{\Omega}\Psi_{\boldsymbol{k},n}^{*(0)}\boldsymbol{\nabla}V_{\text{eff}}^{(0)}\Theta_{\text{IR}}(\boldsymbol{r})\Psi_{\boldsymbol{k},n}^{(0)}\,\mathrm{d}^3r\,. \tag{7.113}$$

The test passes if the difference of the left and the right sides for every $\boldsymbol{k}$-vector and band n is less than $1\cdot10^{-6}\,E_{\text{h}}\,a_0^{-1}$, where E_{h} is the Hartree energy and a_0 the Bohr radius.

Test 23: Vanishing of the First-Order Kohn–Sham Energy

Concept

According to the theory in section 6.1, the first-order variation of the Kohn–Sham energy vanishes for non-metallic systems and for metals with a monoatomic lattice basis. So, this test passes if $\boldsymbol{\epsilon}_{\boldsymbol{k}n}^{(1)}(\alpha\boldsymbol{0}^{+})\leq 9\cdot10^{-6}\,E_{\text{h}}\,a_0^{-1}$, which is fulfilled for each system relevant in this dissertation. For polyatomic metals, this test must be deactivated, because $\boldsymbol{\epsilon}_{\boldsymbol{k}n}^{(1)}(\alpha\boldsymbol{0}^{+})$ can have a finite value for the Goldstone modes.

Formalism and algorithm

Starting from Equation (6.62), $\boldsymbol{\epsilon}_{\boldsymbol{k}n}^{(1)}(\alpha\boldsymbol{0}^{+})$ can be reformulated with an ansatz very similar to section 7.4.1. This yields

$$\begin{aligned}\boldsymbol{\epsilon}_{\boldsymbol{k},n}^{(1)}(\alpha\boldsymbol{0}^{+}) &= \left\langle\Psi_{\boldsymbol{k},n}^{(0)}\middle|\boldsymbol{\mathscr{V}}_{\text{eff}}^{(1)}(\boldsymbol{0}^{+}\alpha)\middle|\Psi_{\boldsymbol{k},n}^{(0)}\right\rangle_{\text{IR}} \\ &\quad+\sum_{\gamma}\left\langle\vec{\Psi}_{\boldsymbol{k},n}^{(0)}\middle|\boldsymbol{\mathscr{V}}_{\text{eff}}^{(1)}(\boldsymbol{0}^{+}\alpha)+\boldsymbol{\nabla}\mathscr{V}_{\text{eff}}^{(0)}\delta_{\gamma\alpha}\middle|\vec{\Psi}_{\boldsymbol{k},n}^{(0)}\right\rangle_{\gamma}+\left\langle\widetilde{\vec{\boldsymbol{\Psi}}}_{\boldsymbol{k},n}^{(0)}\middle|\mathscr{H}^{(0)}-\varepsilon_{\boldsymbol{k},n}^{(0)}\middle|\vec{\Psi}_{\boldsymbol{k},n}^{(0)}\right\rangle_{\alpha} \\ &\quad+\left\langle\vec{\Psi}_{\boldsymbol{k},n}^{(0)}\middle|\mathscr{H}^{(0)}-\varepsilon_{\boldsymbol{k},n}^{(0)}\middle|\widetilde{\vec{\boldsymbol{\Psi}}}_{\boldsymbol{k},n}^{(0)}\right\rangle_{\alpha}+\oint_{\partial\text{IR}_{\alpha}}\hat{\boldsymbol{e}}_{\text{IR}}\Psi_{\boldsymbol{k},n}^{*(0)\text{IR}}\left(\mathscr{H}^{(0)}-\varepsilon_{\boldsymbol{k},n}^{(0)}\right)\Psi_{\boldsymbol{k},n}^{(0)\text{IR}}\,\mathrm{d}\boldsymbol{S}\,.\end{aligned} \tag{7.114}$$

For being able to conduct this test before the first-order variation of the effective potential is at hand, the negative gradient of the unperturbed effective potential is inserted. Furthermore, by testing whether the right-hand side of equation (7.114) vanishes, also the complete Sternheimer equation is checked, because the former and latter are identical for $\boldsymbol{q} = \mathbf{0}$ and $n = n'$.

Optimizing Sternheimer implementation

Thus, when inserting equation (7.114) into the Sternheimer equation (7.87g) on condition that $\boldsymbol{q} = \mathbf{0}$, the right-hand side of the latter becomes zero for equal bands. Hence, for equal bands in the bras and kets, the right hand-side of the Sternheimer equation can be set to zero to improve numerics. This can be seen in

$$\begin{aligned}
&-\boldsymbol{z}_{n}^{(1)}(\boldsymbol{k}, n; \alpha\mathbf{0}^{+})\left(\varepsilon_{\boldsymbol{k},n}^{(0)} - \varepsilon_{\boldsymbol{k},n}^{(0)}\right) \qquad (7.115)\\
&\quad= \left\langle \Psi_{\boldsymbol{k},n}^{(0)} \middle| \boldsymbol{\mathscr{V}}_{\text{eff}}^{(1)}(\mathbf{0}^{+}\alpha) \middle| \Psi_{\boldsymbol{k},n}^{(0)} \right\rangle_{\text{IR}} + \sum_{\gamma} \left\langle \vec{\Psi}_{\boldsymbol{k},n}^{(0)} \middle| \boldsymbol{\mathscr{V}}_{\text{eff}}^{(1)}(\mathbf{0}^{+}\alpha) + \boldsymbol{\nabla}\mathscr{V}_{\text{eff}}^{(0)}\delta_{\gamma\alpha} \middle| \vec{\Psi}_{\boldsymbol{k},n}^{(0)} \right\rangle_{\gamma} - \boldsymbol{\epsilon}_{\boldsymbol{k},n}^{(1)}(\mathbf{0}^{+}\alpha)\\
&\qquad+ \left\langle \widetilde{\vec{\boldsymbol{\Psi}}}_{\boldsymbol{k},n}^{(0)} \middle| \mathscr{H}^{(0)} - \varepsilon_{\boldsymbol{k},n}^{(0)} \middle| \vec{\Psi}_{\boldsymbol{k},n}^{(0)} \right\rangle_{\alpha} + \left\langle \vec{\Psi}_{\boldsymbol{k},n}^{(0)} \middle| \mathscr{H}^{(0)} - \varepsilon_{\boldsymbol{k},n}^{(0)} \middle| \widetilde{\vec{\boldsymbol{\Psi}}}_{\boldsymbol{k},n}^{(0)} \right\rangle_{\alpha}\\
&\qquad+ \oint_{\partial\text{IR}_{\alpha}} \hat{\boldsymbol{e}}_{\text{IR}} \Psi_{\boldsymbol{k},n}^{*(0)\text{IR}} \left(\mathscr{H}^{(0)} - \varepsilon_{\boldsymbol{k},n}^{(0)}\right) \Psi_{\boldsymbol{k},n}^{(0)\text{IR}} \, \mathrm{d}\boldsymbol{S} \; .
\end{aligned}$$

Test 24: Cross-Checking the Pulay Contributions

Concept

Since large implementation parts of both Pulay contributions in the third line of the Sternheimer equation (7.88) can be borrowed from FLEUR, a cross-checking suggests itself. Although the algorithms of FLEUR (see section 5.8.2) and juPhon (see section 7.4.3) differ regarding a few subtleties, these matrix elements can in principle easily be compared. It must be considered however, that the regular mode in FLEUR is to set up the Hamiltonian in the representation of the LAPW basis functions, while juPhon utilizes Kohn–Sham wave functions. Therefore, the matrix element from FLEUR must be contracted with two wave-function expansion coefficients.

Algorithm

The prerequisite for running this test is to generate the files `hmatTest` and `smatTest`, containing the FLEUR Hamiltonian matrix elements and the overlap of the LAPW basis functions, respectively. These files are written out in the FLEUR subroutine `Eigen` after `Hssphn`. It is best to make a new folder, copy at least the FLEUR calculation into it, and change the directory into this folder. Within this folder, the `inp` file of FLEUR must be manipulated. It is important to set the number of iterations to 1 and to set the mixing parameter `alpha` to 0.00. This is due to an anew mixing would probably impede the aforesaid comparison of the matrix elements, unless an extremely good convergence of the FLEUR calculation was given. The contraction of the Hamiltonian matrix elements is done in FLEUR before the files are written out, both happening in the `eigen` subroutine of FLEUR. In order to configure FLEUR to generate the aforementioned files, an empty file `writeoutHS` must be created. It is also beneficial to delete the files `wkf2`, `stars`, `broyden`, and `broyden.7`, then FLEUR can be executed. The last step is to copy the desired files `hmatTest` and `smatTest` to the original folder.

Challenges

Since there is a difference in the action of the spherical Hamiltonian between the FLEUR method in equation (5.59) and the procedure of juPhon in equation (7.98b), this must be corrected by a respective subtraction and addition of terms. Apart from that, in juPhon the wave function $\tilde{\Psi}$ must be substituted by the canonical unperturbed wave function $\Psi^{(0)}_{\boldsymbol{k},n}$. For polyatomic systems, the rotation of the small matching coefficients must not be removed in `juPhon`, because in `FLEUR` symmetry is still exploited. Moreover, at the moment this test is only executed for one arbitrary $\boldsymbol{k}$-point (currently the $\boldsymbol{k}$-vector with index 28). In principle, this test could be extended to check all $\boldsymbol{k}$-points.

Test 25: Muffin-Tin Sphere Complement of IR Surface integral

Concept As seen in the last two lines of equation (7.86a), the IR and MT surface integrals differ by a global sign, among other things. This is because the normal vector of the former is antiparallel to that used in the latter. Another difference originates from the discontinuity at the MT sphere boundary. If however this difference is small enough, the IR surface integral can in principle be tested by calculating the MT surface integral.

Formalism This can be applied to the last line of the Sternheimer equation (7.88) [251]. For computing the MT complement of the IR surface integral in the aforesaid Sternheimer equation

$$\begin{aligned}
&\oint_{\partial\alpha} \hat{\boldsymbol{r}}\, \vec{\Psi}^{*(0)\alpha}_{\boldsymbol{k}^{+}_{\text{bf}},n'}(\boldsymbol{r}) \Big(\mathscr{H}^{(0)} - \varepsilon^{(0)}_{\boldsymbol{k},n} \Big) \vec{\Psi}^{(0)\alpha}_{\boldsymbol{k},n}(\boldsymbol{r}) \,\mathrm{d}S && \text{(7.116a)}\\
&= \oint_{\partial\alpha} \hat{\boldsymbol{r}}\, \vec{\Psi}^{*(0)\alpha}_{\boldsymbol{k}^{+}_{\text{bf}},n'}(\boldsymbol{r}) \Big(\mathscr{H}^{(0)}_{\text{sph}} - \varepsilon^{(0)}_{\boldsymbol{k},n} + V^{(0)\alpha}_{\text{eff,nsph}}(\boldsymbol{r}) \Big) \vec{\Psi}^{(0)\alpha}_{\boldsymbol{k},n}(\boldsymbol{r}) \,\mathrm{d}S
\end{aligned}$$

must be evaluated. In the MT spheres, the Hamiltonian is differently subdivided relative to the IR, as already seen for volume integrals. Before presenting the final result, first two quantities are defined. They describe the action of the spherical Hamiltonian on the ket wave function

$$\begin{aligned}
&\sum_{lmp} A^{\boldsymbol{k}\alpha n}_{lmp} \bigg(\Big(\mathscr{H}^{(0)}_{\text{sph}} - \varepsilon^{(0)}_{\boldsymbol{k},n} \Big) \vec{\varphi}^{\mathring{\alpha}}_{lmp}(\boldsymbol{r}) \bigg) && \text{(7.116b)}\\
&= \sum_{lm} \bigg(A^{\boldsymbol{k}\alpha n}_{lm1} \Big(E^{\mathring{\alpha}}_{l} - \varepsilon^{(0)}_{\boldsymbol{k},n} \Big) \vec{u}^{\mathring{\alpha}}_{l1}(r) + A^{\boldsymbol{k}\alpha n}_{lm2} \Big(\vec{u}^{\mathring{\alpha}}_{l1}(r) + \Big(E^{\mathring{\alpha}}_{l} - \varepsilon^{(0)}_{\boldsymbol{k},n} \Big) \vec{u}^{\mathring{\alpha}}_{l2}(r) \Big) \bigg) \mathrm{Y}_{lm}(\hat{\boldsymbol{r}}) \\
&:= \vec{\mathfrak{h}}^{\boldsymbol{k}\alpha n}_{lm}(r) \mathrm{Y}_{lm}(\hat{\boldsymbol{r}}) && \text{(7.116c)}
\end{aligned}$$

and a projection of the unit vector as well as the non-spherical potential to a general lattice harmonic

$$\mathfrak{v}^{(0)\alpha}_{l''m''}(r) := \sum_{l'''m'''} \sum_{m^{\text{iv}}=-1}^{1} \sum_{i} \zeta_{i,m^{\text{iv}}} \Big[V^{(0)\alpha}_{\text{eff,nsph}}(\boldsymbol{r}) \Big)\Big]_{l'''m'''} \hat{\boldsymbol{e}}_i G^{m'', \, m''', \, m^{\text{iv}}}_{l'', \;\; l''', \;\; 1} \,. \tag{7.116d}$$

Hence ultimately,

$$\begin{aligned}
&\oint_{\partial\alpha} \hat{\boldsymbol{r}}\, \vec{\Psi}^{*(0)\alpha}_{\boldsymbol{k}^{+}_{\text{bf}},n'}(\boldsymbol{r}) \Big(\mathscr{H}^{(0)}_{\text{sph}} - \varepsilon^{(0)}_{\boldsymbol{k},n} \Big) \vec{\Psi}^{(0)\alpha}_{\boldsymbol{k},n}(\boldsymbol{r}) \,\mathrm{d}S && \text{(7.116e)}\\
&= \sum_{l'm'p'} A^{*\boldsymbol{k}^{+}_{\text{bf}}\alpha n}_{l'm'p'} \sum_{s} u^{\mathring{\alpha}s}_{l'p'}(R_{\mathring{\alpha}}) \sum_{lm} \mathfrak{h}^{\boldsymbol{k}\alpha n}_{lms}(R_{\mathring{\alpha}}) \sum_{m''=-1}^{1} \sum_{i} \hat{\boldsymbol{e}}_i \zeta_{i,m''} R^2_{\mathring{\alpha}} G^{m',m,m''}_{l', \; l, \; 1}
\end{aligned}$$

and

$$\oint_{\partial\alpha} \hat{\boldsymbol{r}}\, \vec{\Psi}^{*(0)\alpha}_{\boldsymbol{k}^{+}_{\text{bf}},n'}(\boldsymbol{r}) V^{(0)\alpha}_{\text{eff,nsph}}(\boldsymbol{r}) \vec{\Psi}^{(0)\alpha}_{\boldsymbol{k},n}(\boldsymbol{r}) \,\mathrm{d}S \tag{7.116f}$$

$$= \sum_{s} \sum_{l''m''} \mathfrak{v}^{(0)\alpha}_{l''m''}(R_{\mathring{\alpha}}) \sum_{l'm'p'} A^{*\boldsymbol{k}^{+}_{\text{bf}}\alpha n}_{l'm'p'} u^{\mathring{\alpha}s}_{l'p'}(R_{\mathring{\alpha}}) \sum_{lmp} A^{\boldsymbol{k}\alpha n}_{lmp} u^{\mathring{\alpha}s}_{lp}(R_{\mathring{\alpha}}) \sum_{m''=-1}^{1} \sum_{i} \hat{\boldsymbol{e}}_i \zeta_{i,m''} R^2_{\mathring{\alpha}} G^{m',m'',m}_{l',\ l'',\ l}$$

must be implemented (see also the discussion around equation (7.54)).

Continuity of kinetic-energy part

However, in practice only the potential and overlap parts are compared, because the effective potential and the LAPW basis are fairly continuous. The kinetic energy is known to be discontinuous in the LAPW basis, if essentially a Laplace operator is applied (cf. section 5.11). Therefore, given a single Bloch vector $\boldsymbol{k}$ and band n, the kinetic energies of the IR and the MT surface integrals cannot convincingly be compared. However, summed over all Bloch vectors and bands, I found that this discrepancy disappears again, at least for fcc Ne. When contrasting the potential part of the IR and MT surface integrals, in the latter the spherical Hamiltonian must be omitted. Instead the routines for the non-spherical potential must be manipulated to also consider the $l = 0$ component.

Test 26: Converge Sternheimer Equation from Analytical Goldstone-Modes Solution

For being able to assess whether the mixing subroutines in `juPhon` are broken, the Sternheimer self-consistency cycle can be started with the analytical solution of the Goldstone modes. Essentially, I already elaborate on this outcome around equation (7.30) and in appendix D. So, in this test the Sternheimer SCC is started with minus the gradient of the unperturbed density, being the initial first-order density variation. A first-order effective potential variation can be generated, and theoretically the Sternheimer equation should be immediately converged. In practice, the number of iterations significantly decreases. But depending on the threshold that defines at which point the Sternheimer equation is converged, still a few iterations must be processed. This is due to the numerical noise which impedes an absolutely precise numerical solution of the Sternheimer equation for the Goldstone modes. The fact that the SCC in this test does not significantly diverge from the correct solution shows that the Sternheimer equation for $\boldsymbol{q} = \boldsymbol{0}$ is correctly implemented.

Test 27: Comparing Converged Result to Analytical Solution for $\boldsymbol{q} = 0$

Concept

This check can be interpreted as an intensification of the last test. The outcome of the Sternheimer equation should be converged to the analytical solution (7.30), after the Sternheimer SCC is finished (see section 7.4.6). Thus in the IR, the Fourier coefficients of the first-order density variation can be cross-checked with minus the Fourier coefficients of the unperturbed density gradient. However in the MT spheres, it is disadvantageous from a numerical point of view to compare the coefficients of minus the unperturbed density gradient with those of the first-order density variation. A better solution consists in conducting test 12 with the results of the Sternheimer equation, i.e., the first line in equation (7.37b) must vanish. This is excellently fulfilled for fcc Ne and fairly well for fcc Al. In the former case, the difference from the analytical result is of the order $10^{-6} e\, a_0^{-4}$, and in the latter case of the order $10^{-3} e\, a_0^{-4}$. Due to performance optimizations in the general version of `FLEUR`[26], its diagonalization routines for the DFT Hamiltonian do not completely converge out the wave-function expansion coefficients [127]. These errors actually cancel when calculating the charge density later. But

---

[26] There is one version of `FLEUR` for materials featuring inversion symmetry, such as fcc Ne and fcc Al.

focussing on the wave functions, this expresses in small imaginary values in the wave-function expansion coefficients, although they should have been real in the case of inversion symmetry. Hence, we think that the quality of the `FLEUR` calculation has amongst others an impact on the accuracy of the Sternheimer results [251].

Alternative concept

An alternative, which is harder and takes significantly more effort to be realized, is to compare the resulting first-order wave-function expansion coefficients directly to equation (7.30). However, real challenges must be faced. For example unitary transformations can make degenerate subspaces more difficult to compare [251]. Furthermore, numerical errors of the wave functions must be brought under control, because `FLEUR` is designed for an optimal charge density, in which errors of the wave functions cancel away. Investigating selected $\boldsymbol{k}$-vectors and fcc Ne with this approach, I found fair consistency. But, the band–band representation in equation (7.87c) delivers slightly better results than the band-reciprocal lattice vectors representation of the first-order wave-function expansion coefficients. If comparing the former and starting from the latter, equation (7.87c) must be inverted by multiplying the inverse[27] of $z^{(0)}_{\boldsymbol{G}}(\boldsymbol{G})$ from the left on both sides, provided it can be inverted. But, this should be the case, unless k_{max} is chosen too large (the basis set becomes increasingly linearly dependent) [251].

Test 28: First-Order Density Variation from Occupied-Occupied Band Combinations

As stated in section 4.2, the Sternheimer equation delivers only contributions for occupied–unoccupied band combinations (see also reference [87]). In this test, the loop over all bands in the `juPhon` subroutine `SolveSternheimerEq` is restricted such that only occupied–occupied band combinations are evaluated [251]. For the case of fcc Ne, the resulting first-order density variation vanishes in the first iteration.

Test 29: Time Reversal Symmetry of Converged Quantities

This test idea is actually already presented around equations (7.33), (7.34), and (7.35) for the first-order density variation. However, this quantity represents an outcome of the Sternheimer equation, so this test is mentioned at this point again. Analogously, test 20 describes the same approach for the first-order external-potential variation, which is known before or without the Sternheimer SCC. But, this does not hold true for the Hartree- and xc-potential variations, which are converged given a self-consistent Sternheimer equation. Hence all in all and provided a finished SCC, checking the TRS of the first-order density and effective-potential variation defines this test. For fcc Ne and fcc Al, it passes.

7.5 Second-Order Variation of the Ion–Ion Interaction

Outline

In section 6.3.4, the second-order ion–ion interaction is introduced according to the dissertation of Klüppelberg [88]. However, a correct implementation involving the expressions

---

[27] The matrix dimensions of these wave-function expansion coefficients are the reciprocal lattice vectors and all bands n'.

from the aforesaid section is impossible. Therefore, section 7.5.1 deals with my employed optimizations and corrections. The results of the `juPhon` subroutines are then presented in section 7.5.2 for an exemplary fcc Al and bcc Na structure. Justifying my ultimate form of the implementation is realized by strict tests to which section 7.5.3 is devoted.

7.5.1 Algorithm

Final form

For the relevant part of the dynamical matrix, essentially equation (6.54) must be evaluated, which incorporates equation (6.55) for both $\boldsymbol{q} = \boldsymbol{0}$ and $\boldsymbol{q} \neq \boldsymbol{0}$. In monoatomic systems, it is sufficient to reformulate equation (6.60) further, in order to obtain an expression suitable for the implementation. This has already been done by Klüppelberg [88], by using the Rayleigh decomposition (5.5) of equation (6.59a) and the Legendre polynomials (e.g. reference [3])

$$\mathrm{P}_l(x) = \frac{1}{2^l l!} \frac{\mathrm{d}^l \left(x^2 - 1\right)^l}{\mathrm{d}x^l} \, . \tag{7.117}$$

Finally,

$$\begin{aligned} \underline{E}_{\mathrm{ii}}^{(2)\beta\alpha}\left(\boldsymbol{q}^{-+}\right) = {} & -Z_\alpha \sum_{\boldsymbol{G}|\boldsymbol{G}-\boldsymbol{q}\neq\boldsymbol{0}} \frac{4\pi \underline{n}_{\mathrm{ps}}^{\beta}\left(\boldsymbol{G};\boldsymbol{q}^{-+}\right) \mathrm{e}^{\mathrm{i}(\boldsymbol{G}-\boldsymbol{q})\cdot\boldsymbol{\tau}_\beta}}{|\boldsymbol{G}-\boldsymbol{q}|^2} \mathrm{j}_0\Big(|\boldsymbol{G}-\boldsymbol{q}|R_\beta\Big) \\ & + Z_\alpha \frac{Z_\beta}{R_\beta^3} \sum_{t=-1}^{1} \sum_{ij} \left(\frac{3}{4\pi} c_{i,t} c_{j,-t} (-1)^t - \delta_{ij} \right) . \end{aligned} \tag{7.118}$$

results. However, this expression differs by a global minus sign from the outcome of Klüppelberg [88], because his derivation is in this sense a little inconsistent or the reader could at least be misdirected. For polyatomic systems, the previous equation is only valid for $\alpha = \beta$, i.e., in the 3×3 submatrices located on the diagonal of the complete $3N_{\mathrm{at}} \times 3N_{\mathrm{at}}$ dynamical matrix. The submatrices off the large matrix diagonal must be filled according to equation (6.59b).

Algorithm

In my implementation, I leave out the second line of equation (7.118). This can be done, because in equation (6.54) the integrals (6.55) for $\boldsymbol{q} = \boldsymbol{0}$ and $\boldsymbol{q} \neq \boldsymbol{0}$ are subtracted from each other. As a consequence, the second line in equation (7.118) is incorporated both in its original form and multiplied by -1. These contributions therefore annihilate each other for every $\boldsymbol{q}$, because they are constant with respect to $\boldsymbol{q}$. Ultimately, this leads to the implementation of

$$\begin{aligned} & \underline{E}_{\mathrm{ii}}^{(2)\beta\alpha}\left(\boldsymbol{q}^{-+}\right) \\ & = 4\pi Z_\alpha \left[\sum_{\boldsymbol{G}|\boldsymbol{G}\neq\boldsymbol{0}} \frac{\underline{n}_{\mathrm{ps}}^{\beta}\left(\boldsymbol{G};\boldsymbol{0}^{-+}\right)}{|\boldsymbol{G}|^2} \mathrm{j}_0\Big(|\boldsymbol{G}|R_\beta\Big) - \sum_{\boldsymbol{G}|\boldsymbol{G}-\boldsymbol{q}\neq\boldsymbol{0}} \frac{\underline{n}_{\mathrm{ps}}^{\beta}\left(\boldsymbol{G};\boldsymbol{q}^{-+}\right)}{|\boldsymbol{G}-\boldsymbol{q}|^2} \mathrm{j}_0\Big(|\boldsymbol{G}-\boldsymbol{q}|R_\beta\Big) \right] . \end{aligned} \tag{7.119}$$

So basically, the question how to properly consider the exclusion of self-interaction becomes obsolete now, because this term effectively cancels.

Not subtracting the trace

But it must be emphasized at this point that calculating the second-order ion–ion interaction in the described way implies wrong results. The last term in the parentheses of equation (6.58) induces a vanishing diagonal of the second-order ion–ion-interaction matrix, because its trace is subtracted. My idea to ignore the trace has finally led to correct numerical results, as can be seen from test 35. Hence, the employed pseudo-density Fourier coefficients read

$$\underline{n}^{\beta}_{\text{ps}}(\boldsymbol{G};\boldsymbol{q}^{-+}) = \frac{Z_\beta}{\Omega}(2N+7)!!\frac{\mathrm{j}_{N+3}\big(|\boldsymbol{G}-\boldsymbol{q}|R_\beta\big)}{\big(|\boldsymbol{G}-\boldsymbol{q}|R_\beta\big)^{N+3}}\mathrm{e}^{-\mathrm{i}(\boldsymbol{G}-\boldsymbol{q})\cdot\boldsymbol{\tau}_\beta}(\boldsymbol{G}-\boldsymbol{q})(\boldsymbol{G}-\boldsymbol{q})^\top\,. \tag{7.120}$$

Up to now however, we were not able to analytically reason it [127, 251, 256]. Furthermore, according to our understanding the term we ignore in the following actually excludes self-interaction, appearing to be a contradiction to the excellent consistency with benchmark data [127, 251].

7.5.2 Visualization

High-symmetry points

In this section, the second-order ion–ion interaction for a fcc and a bcc lattice structure with a monoatomic lattice basis are presented. This is done for a $\boldsymbol{q}$ along the common path of high-symmetry points (HSPs), which is also used in respective phonon-dispersion relations. As usual in the literature, given a fcc structure the HSP sequence Γ - X - K - Γ - L is employed, and for bcc Γ - H - P - Γ - N - H is used [127]. Table 7.8 lists which $\boldsymbol{q}$ vectors correspond to the aforesaid HSPs.

Table 7.8: Legend of high-symmetry points (HSP) for fcc and bcc lattice structures. The $\boldsymbol{q}$-vectors are given in internal units.

HSP	$\boldsymbol{q}^\top$
Γ	$(0, 0, 0)$
X	$(0, 0.5, 0.5)$
K	$(0.375, 0.75, 0.375)$
L	$(0.5, 0.5, 0.5)$
H	$(-0.5, 0.5, 0.5)$
P	$(0, 0, 0)$
N	$(0.25, 0.25, 0.25)$

Results

Since the only information required about the material is concerned with the lattice geometry and the atomic numbers, the shape of the second-order ion–ion interaction remains equal among materials of the same lattice structure. The difference between them is basically a global scaling of the curves. Therefore, only fcc Al and bcc Na are shown as examples in figure 7.18 and figure 7.19, respectively. Due to the hermiticity of the dynamical matrix, of which $E^{(2)}_{\text{ii}}$ is a constituent, overall six different curves manifest themselves in each of the figures, i.e., for both lattice structures.

Performance

In test 35, the second-order ion–ion interaction is calculated with an `ABINIT` subroutine [55–57, 255]. This allows for benchmarking the performance of `juPhon`. The Weinert-like `juPhon` implementation proves to be superior to the Ewald-summation method, at least as implemented in `ABINIT`. This in particular becomes obvious for bcc structures.

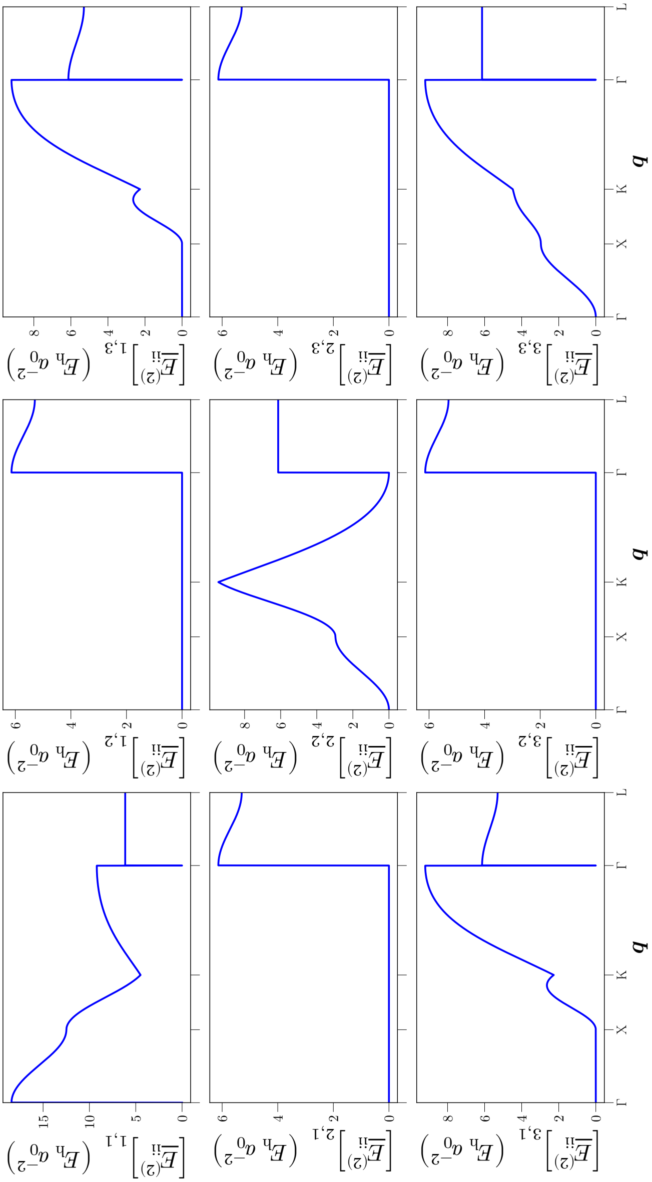

Figure 7.18: Behavior of the second-order ion–ion interaction $\underline{E}_{\text{ii}}^{(2)}$ from `juPhon` for fcc Al on a typical path, incorporating fcc high-symmetry points. The unit is $E_\text{h}\,a_0^{-2}$. Moreover, the 3×3 grid of plots represents the entries of the 3×3 matrix $\underline{E}_{\text{ii}}^{(2)}$. The input file can be found in appendix B.

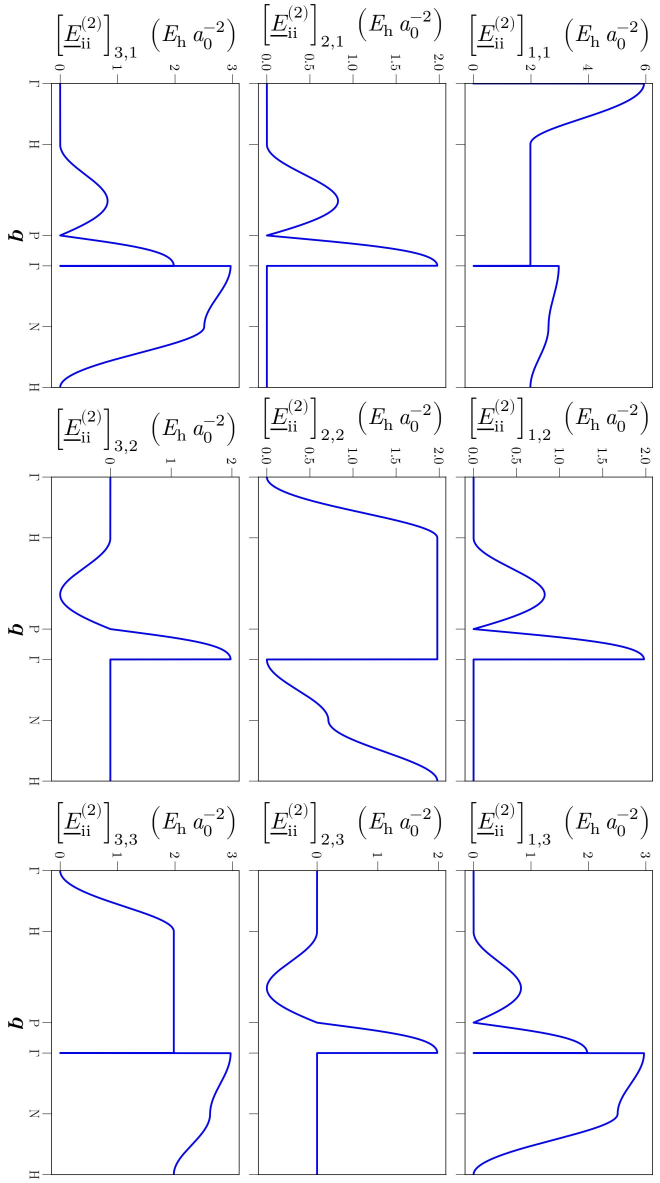

Figure 7.19: Behavior of the second-order ion–ion interaction $\underline{E}_{\mathrm{ii}}^{(2)}$ from `juPhon` for bcc Na on a typical path, incorporating bcc high-symmetry points. The unit, the arrangement of the plots for this matrix quantity, and the location of the input file are the same as in figure 7.18.

7.5.3 Tests

Outline

Since the second-order ion–ion interaction vanishes by construction for the Goldstone modes, foremost of interest are tests that check the behavior for $\boldsymbol{q} \neq \mathbf{0}$. While test 33 and test 34 focus on the intermediate Fourier coefficients of the pseudo-density (7.120), test 35 is devoted to cross-check the complete second-order ion–ion interaction for an arbitrary $\boldsymbol{q}$. The latter is a strict test and clearly shows the correctness of this quantity from `juPhon`.

Test 30: Alternative Method for Pseudo-Density Fourier Coefficients

Klüppelberg [88] points out the close relation between the second-order variation of the external potential and the second-order ion–ion interaction. Essentially, the integral in equation (6.55c) for $\boldsymbol{q} = \mathbf{0}$ shows analogies to the integral underlying the second-order variation of the external potential. Although the second-order external-potential variation is not further specified in this dissertation, the last statement becomes plausible from a close inspection of equation (6.55c). In this expression, the external potential for $\boldsymbol{q} = \mathbf{0}$ can be identified, provided the gradients are ignored. It stimulated me to compare the analytical derivative of the first-order external potential-variation Fourier coefficients (6.28b) with the Fourier coefficients required for the second-order ion–ion interaction (7.120). So, in a nutshell this test checks whether the relation

$$\mathrm{i}(\boldsymbol{G} - \boldsymbol{q})\boldsymbol{n}_{\mathrm{ext}}^{\top\mathrm{ps}}(\boldsymbol{G}; -\boldsymbol{q}^{+}\alpha) = \underline{n}_{\mathrm{ps}}^{\beta}(\boldsymbol{G}; \boldsymbol{q}^{-+}) \tag{7.121}$$

holds. It must be stressed that this can only be ensured if the pseudo-density from equation (7.120), instead of that from equation (6.58) is utilized. The analytical equivalence, assumed in equation (7.121), is not derived analytically. Still, I found that it is numerically fulfilled up to an accuracy of $1 \cdot 10^{-8}\, E_{\mathrm{h}}\, a_0^{-2}$, where E_{h} is the Hartree energy and a_0 the Bohr radius. The presented test can be performed for an arbitrary $\boldsymbol{q}$, i.e., likewise for $\boldsymbol{q} = \mathbf{0}$. In practice, all $\boldsymbol{q}$ from the set available in a `juPhon` calculation are checked.

Test 31: Time Reversal Symmetry

In analogy to equation (7.34), the relation

$$E_{\mathrm{ii}}^{(2)}(\boldsymbol{q}_{\mathrm{f}}) = E_{\mathrm{ii}}^{(2)}(\boldsymbol{q}) \tag{7.122}$$

is checked within the $\boldsymbol{q}$-set at hand in `juPhon` [251]. The test passes if the equality is fulfilled up to an accuracy of $1 \cdot 10^{-9}\, E_{\mathrm{h}}\, a_0^{-2}$.

Test 32: Cross-Checking of Weinert Method (`juPhon`) with Ewald Method (`ABINIT`)

Algorithm

For this test, we have chosen the subroutine `Ewald9` of the `ABINIT` package [55–57, 127, 256]. This subroutine calculates the second-order ion–ion interaction, using an Ewald-summation method [3, 255]. I have written a small program, which calls `Ewald9` and employs the `FLEUR` subroutine `Dotset`[28]. This allows for flexibly manipulating the parameters of the former,

---

[28] This program is located within a subfolder of the `juPhon` repository under the commit with the hash `e7c50ff83e44aeb32a63741e1bb5ae4ac2e8aaaa`.

independent of how it is originally embedded in `ABINIT`. Basically, the information necessary for the parameters can be extracted from the `FLEUR` `out` file (for instance lattice geometry and atomic numbers). It is pivotal that `Ewald9` is *not* called with an activated performance optimization flag [127]. In this case, the calculation of `ABINIT` runs faster but delivers the wrong results.

Result

This test has been conducted for fcc Ne, fcc Al, and bcc Na and delivered similar results in all scenarios. Consistent with section 7.5.2, figure 7.20 shows the absolute error for the second aforesaid system and figure 7.21 for the third one. Although the second-order variation of the ion–ion interaction has been calculated with two different methods, the maximal absolute error is $1 \cdot 10^{-6}\, E_\mathrm{h}\, a_0^{-2}$.

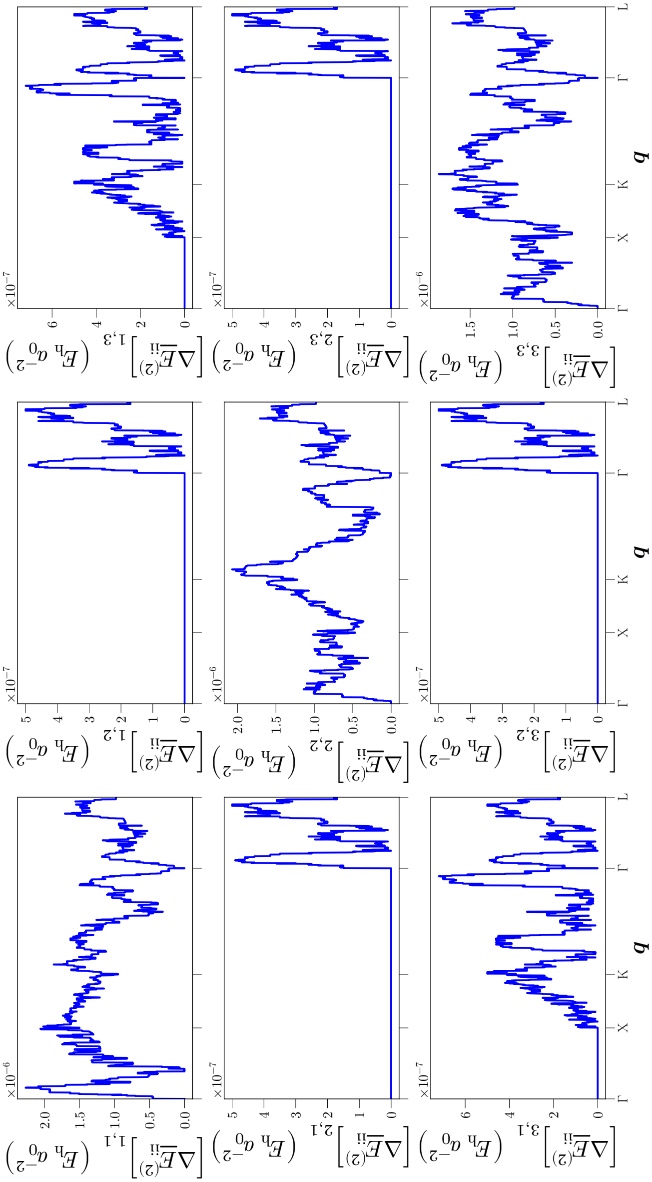

Figure 7.20: Absolute error of second-order ion–ion interaction $\underline{E}_{\mathrm{ii}}^{(2)}$ for fcc Al on a typical path, incorporating fcc high-symmetry points. Results from `juPhon` are cross-checked with an extracted subroutine of `ABINIT`. The unit is $E_\mathrm{h}\, a_0^{-2}$. Moreover, the 3×3 grid of plots represents the entries of the 3×3 matrix $\underline{E}_{\mathrm{ii}}^{(2)}$. Overall, the error is at the same order of magnitude as for the employed integration and differentiation subroutines. The input file is given in appendix B.

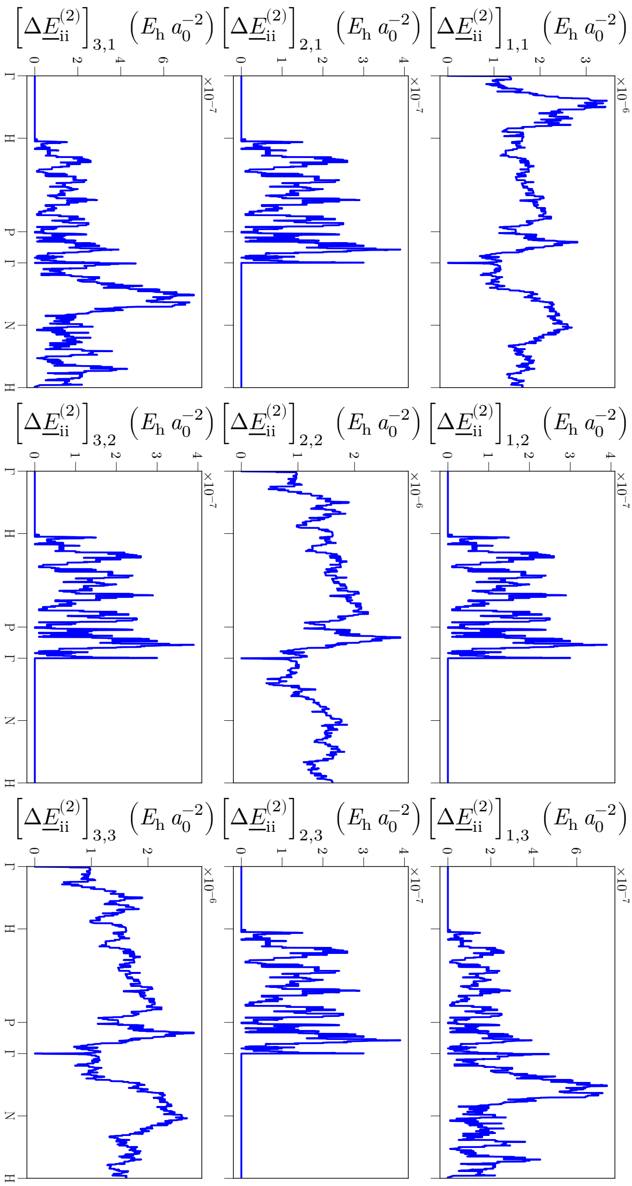

Figure 7.21: Absolute error of second-order ion–ion interaction $\underline{E}_{\mathrm{ii}}^{(2)}$ for bcc Na on a typical path, incorporating bcc high-symmetry points. The method, the unit, the arrangement of the plots, and the location of the input file are the same as for neon in figure 7.20. The consistency of the bcc test is comparable with the fcc test in the aforementioned figure.

7.6 Dynamical matrix

Translation into numerics

Conceptual tests and ultimately dispersion relations reveal that the involved dynamical matrix approach of Klüppelberg [88] is absolutely inapplicable to numerics. Consequently, the successful realization of accurate phonon frequencies proved to be a tough challenge. Still it must be emphasized: from an analytical standpoint, the expressions of Klüppelberg are in principle correct (apart from typos).

Challenges

Delicate subjects are in particular MT terms with gradients or Hessian matrices (see also reference [3]). If such (numerical) derivatives of Kohn–Sham wave functions are incorporated in MT matrix-elements or MT surface-integrals, selecting the correct indices for the evaluation turns out to be a complex task (cf. section 7.2). For instance, focussing only on the orbital quantum number l, two applications of the numerical gradient connect contributions of the original channel l to five resulting channels, namely from $l-2$ to $l+2$. When programming such terms, the aforementioned channel relations are required, and must be stored [251]. Further obstacles are presented by relevant integral contributions beyond logarithmic integration meshes, e.g. between the radial integral boundary $r_\gamma = 0$ and the first mesh point $\nu = 1$. Overall, numerical inaccuracies have a massive impact and must be circumvented or surmounted as well as possible, when dealing with such small energy scales as in phonon dispersion-relations.

Outline

In this section, the dynamical matrix equations given in reference [88] are radically reformulated, aiming for a numerically-optimized condensed framework, which we found to be well-performing [127, 256]. Given the specific context, I shall point out in more detail (i) the underlying numerical problems and (ii) the way of alleviating their influence on the final results. But at first, the explicit way of obtaining the phonon frequencies in `juPhon` is elucidated in section 7.6.1. Based on this approach and on TRS, relations can be implied which are exploited in the subsequent discussion. Then in section 7.6.2, the dynamical matrix shown in section 6.5 is further evaluated to conform for the most part with the equations suggested by Klüppelberg [88]. However, I already re-express some terms by exploiting TRS so that every quantity is available from the Sternheimer self-consistency cycle in `juPhon`. In section 7.6.3, I describe my reformulation of this dynamical-matrix approach for the purpose of avoiding terms which incorporate an outer product of gradients. It is based on a generalized divergence theorem, a proof of which by Fabian Lux is given in appendix E [294]. Moreover, section 7.6.4 deals with my rearrangement of the terms, encouraging numerically vanishing phonon frequencies for $\boldsymbol{q} = \mathbf{0}$. For monoatomic systems and ignoring small surface terms, I additionally show there that the rewritten formalism theoretically leads to these desired frequencies. Although computations of fcc Ne in fact confirm this, the numerical accuracy for finite $\boldsymbol{q}$-vectors is still insufficient. Hence, unphysical results are produced, i.e., instabilities of experimentally stable structures such as fcc Al are forecasted (imaginary frequencies in the dispersion relations). But, a derivation of the second-order total energy by Neukirchen [256], which is more general and most widely independent from Klüppelberg, does not feature terms incorporating MT gradients of wave functions. Therefore, section 7.6.5 is devoted to further reformulations, eliminating all gradients of MT wave functions and starting with the expressions presented in section 7.6.4. Apart from that, I have experienced that some radial integrands are extremely large close to the MT sphere center, despite the Jacobi determinant. Hence, the interpolation between the first integration-mesh point and the center of the MT sphere becomes very relevant. In order to avoid developing versatile and accurate interpolations, we further rearrange the equations so that interpolations become insignificant, which is the subject of section 7.6.6 [256]. The basic idea employed is borrowed from an optimization that has already been suggested by Klüppelberg [88] for the Sternheimer equation. Still, he does not consistently apply it to the dynamical matrix. The last step is grounded on the aforementioned derivation of Neukirchen, in which already terms of the first-order total-energy variation are canceled, in contrast to Klüppelberg. Therefore, these expressions are identified in section 7.6.7 and ignored in the implementation. All described optimizations are summarized in section 7.6.8 so that an overview of the currently programmed equations is provided. Finally, I elaborate on consistency tests in section 7.6.9 related to the dynamical matrix.

7.6.1 Determining the Phonon Frequencies

Extracting the dynamical matrix

According to equation (6.12), both $\underline{D}^{\beta\alpha}(\boldsymbol{q}^{+-})$ and $\underline{D}^{\beta\alpha}(\boldsymbol{q}^{-+})$ contribute to the linear combination, which is equal to the second-order total energy variation. This expression can be reformulated to [127, 251]

$$
\begin{aligned}
E^{(2)}_{\text{tot}}(\boldsymbol{q}) &= \sum_{\beta\alpha}\Big(\boldsymbol{Q}^{\dagger}_{\beta}\,\underline{D}^{\beta\alpha}(\boldsymbol{q}^{+-})\,\boldsymbol{Q}_{\alpha} + \boldsymbol{Q}^{\top}_{\beta}\,\underline{D}^{\beta\alpha}(\boldsymbol{q}^{-+})\,\boldsymbol{Q}^{*}_{\alpha}\Big) && (7.123a)\\
&= \sum_{\beta\alpha}\sum_{ij}\Big(\big[Q^{*}_{\beta}\big]_{i}\big[\underline{D}^{\beta\alpha}(\boldsymbol{q}^{+-})\big]_{ij}[Q_{\alpha}]_{j} + \big[Q_{\beta}\big]_{i}\big[\underline{D}^{\beta\alpha}(\boldsymbol{q}^{-+})\big]_{ij}[Q^{*}_{\alpha}]_{j}\Big) && (7.123b)\\
&= \sum_{\beta\alpha}\sum_{ij}\Big(\big[Q^{*}_{\beta}\big]_{i}\big[\underline{D}^{\beta\alpha}(\boldsymbol{q}^{+-})\big]_{ij}[Q_{\alpha}]_{j} + [Q_{\alpha}]_{j}\big[\underline{D}^{\alpha\beta}(\boldsymbol{q}^{-+})\big]_{ji}\big[Q^{*}_{\beta}\big]_{i}\Big) && (7.123c)\\
&= \sum_{\beta\alpha}\sum_{ij}\big[Q^{*}_{\beta}\big]_{i}\Big(\big[\underline{D}^{\beta\alpha}(\boldsymbol{q}^{+-})\big]_{ij} + \big[\underline{D}^{\alpha\beta}(\boldsymbol{q}^{-+})\big]_{ji}\Big)[Q_{\alpha}]_{j} && (7.123d)\\
&= \sum_{\beta\alpha}\boldsymbol{Q}^{\dagger}_{\beta}\Big(\underline{D}^{\beta\alpha}(\boldsymbol{q}^{+-}) + \big[\underline{D}^{\alpha\beta}(\boldsymbol{q}^{-+})\big]^{\top}\Big)\boldsymbol{Q}_{\alpha}\,, && (7.123e)
\end{aligned}
$$

and provided TRS holds to

$$
\begin{aligned}
&= \sum_{\beta\alpha}\boldsymbol{Q}^{\dagger}_{\beta}\Big(\underline{D}^{\beta\alpha}(\boldsymbol{q}^{+-}) + \big[\underline{D}^{\alpha\beta}(\boldsymbol{q}^{+-})\big]^{\dagger}\Big)\boldsymbol{Q}_{\alpha} && (7.123f)\\
&=: 2\sum_{\beta\alpha}\boldsymbol{Q}^{\dagger}_{\beta}\big(\underline{D}^{\beta\alpha}(\boldsymbol{q})\big)\boldsymbol{Q}_{\alpha} && (7.123g)\\
&= 2\boldsymbol{Q}^{\dagger}\,\underline{D}(\boldsymbol{q})\,\boldsymbol{Q}\,. && (7.123h)
\end{aligned}
$$

In these equations, the indices i and j address components of the polarization vectors as well as the matrix entries of the 3×3 submatrices $\underline{D}^{\beta\alpha}$, in which α and β indicate the displaced atoms. The complete $3N_{\gamma}\times3N_{\gamma}$ dynamical matrix $\underline{D}$ is composed of these submatrices, where N_{γ} is the number of atoms per unit cell. Furthermore, in the second summand of equation (7.123c) i is renamed to j and vice versa, which also holds true for the atom indices α and β. Since `juPhon` currently assumes TRS, only $\underline{D}^{\beta\alpha}(\boldsymbol{q}^{+-})$ is set up and discussed in the following. Moreover, it is important to know that in `juPhon` the dynamical matrix $\underline{D}^{\beta\alpha}$ is summed with $[\underline{D}^{\alpha\beta}]^{\dagger}$ (as in equation (7.123f)) and divided by 2 to ensure real eigenvalues [127, 251, 256].

Preparing substitutions

Due to the commutativity of summation, it is legitimate to substitute components of $\underline{D}^{\beta\alpha}(\boldsymbol{q}^{+-})$ with their complements in $[\underline{D}^{\alpha\beta}(\boldsymbol{q}^{+-})]^{\dagger}$ or $[\underline{D}^{\alpha\beta}(\boldsymbol{q}^{-+})]^{\top}$ (for the latter see equation (7.123e)). This becomes necessary if terms are not at hand in `juPhon` or when it turns out to be beneficial in the following subsections. One example is the Pulay term

$$\begin{aligned}
&\left(\boldsymbol{Q}^{\dagger}_{\beta}\,\boldsymbol{z}^{(1)}_{\boldsymbol{G}}(\boldsymbol{k},n;-\boldsymbol{q}\beta)\left[\vec{\phi}^{(1)\alpha+}_{\boldsymbol{k}-\boldsymbol{q},\boldsymbol{G}}\right]^{\top}\boldsymbol{Q}_{\alpha}+\boldsymbol{Q}^{\top}_{\beta}\,\boldsymbol{z}^{(1)}_{\boldsymbol{G}}(\boldsymbol{k},n;\boldsymbol{q}\beta)\left[\vec{\phi}^{(1)\alpha-}_{\boldsymbol{k}+\boldsymbol{q},\boldsymbol{G}}\right]^{\top}\boldsymbol{Q}^{*}_{\alpha}\right) \qquad (7.124a)\\
&=\boldsymbol{Q}^{\dagger}_{\beta}\left(\boldsymbol{z}^{(1)}_{\boldsymbol{G}}(\boldsymbol{k},n;-\boldsymbol{q}\beta)\left[\vec{\phi}^{(1)\alpha+}_{\boldsymbol{k}-\boldsymbol{q},\boldsymbol{G}}\right]^{\top}+\vec{\phi}^{(1)\beta-}_{\boldsymbol{k}+\boldsymbol{q},\boldsymbol{G}}\left[\boldsymbol{z}^{(1)}_{\boldsymbol{G}}(\boldsymbol{k},n;\boldsymbol{q}\alpha)\right]^{\top}\right)\boldsymbol{Q}_{\alpha}
\end{aligned}$$

in which the second summand on the right-hand side is replaced by the first summand, since `juPhon` only calculates $\boldsymbol{z}^{(1)}_{\boldsymbol{G}}(\boldsymbol{k},n;\boldsymbol{q}\alpha)$. In addition, I substitute the first two lines by the last two lines on the right-hand side of the two relations

$$\begin{aligned}
&\boldsymbol{Q}^{\dagger}_{\beta}\,2\oint_{\partial\beta}\hat{\boldsymbol{r}}\Bigg(\left[\boldsymbol{\varPsi}^{(1)\beta-}_{\boldsymbol{k},n}(\boldsymbol{r};\alpha)\right]^{\dagger}\left(\mathscr{H}^{(0)}-\epsilon^{(0)}_{\boldsymbol{k},n}\right)\varPsi^{(0)\beta}_{\boldsymbol{k},n}(\boldsymbol{r}) \qquad (7.124b)\\
&\qquad-\left[\boldsymbol{\varPsi}^{(1)\mathrm{IR}-}_{\boldsymbol{k},n}(\boldsymbol{r};\alpha)\right]^{\dagger}\left(\mathscr{H}^{(0)}-\epsilon^{(0)}_{\boldsymbol{k},n}\right)\varPsi^{(0)\mathrm{IR}}_{\boldsymbol{k},n}(\boldsymbol{r})\Bigg)\,\mathrm{d}S\;\boldsymbol{Q}_{\alpha}\\
&+\boldsymbol{Q}^{\top}_{\beta}\,2\oint_{\partial\beta}\hat{\boldsymbol{r}}\Bigg(\left[\boldsymbol{\varPsi}^{(1)\beta+}_{\boldsymbol{k},n}(\boldsymbol{r};\alpha)\right]^{\dagger}\left(\mathscr{H}^{(0)}-\epsilon^{(0)}_{\boldsymbol{k},n}\right)\varPsi^{(0)\beta}_{\boldsymbol{k},n}(\boldsymbol{r})\\
&\qquad-\left[\boldsymbol{\varPsi}^{(1)\mathrm{IR}+}_{\boldsymbol{k},n}(\boldsymbol{r};\alpha)\right]^{\dagger}\left(\mathscr{H}^{(0)}-\epsilon^{(0)}_{\boldsymbol{k},n}\right)\varPsi^{(0)\mathrm{IR}}_{\boldsymbol{k},n}(\boldsymbol{r})\Bigg)\,\mathrm{d}S\;\boldsymbol{Q}^{*}_{\alpha}\\
&=\boldsymbol{Q}^{\dagger}_{\beta}\,2\Bigg\{\oint_{\partial\beta}\hat{\boldsymbol{r}}\Bigg(\left[\boldsymbol{\varPsi}^{(1)\beta-}_{\boldsymbol{k},n}(\boldsymbol{r};\alpha)\right]^{\dagger}\left(\mathscr{H}^{(0)}-\epsilon^{(0)}_{\boldsymbol{k},n}\right)\varPsi^{(0)\beta}_{\boldsymbol{k},n}(\boldsymbol{r})\\
&\qquad-\left[\boldsymbol{\varPsi}^{(1)\mathrm{IR}-}_{\boldsymbol{k},n}(\boldsymbol{r};\alpha)\right]^{\dagger}\left(\mathscr{H}^{(0)}-\epsilon^{(0)}_{\boldsymbol{k},n}\right)\varPsi^{(0)\mathrm{IR}}_{\boldsymbol{k},n}(\boldsymbol{r})\Bigg)\,\mathrm{d}S\\
&\quad+\oint_{\partial\alpha}\Bigg(\boldsymbol{\varPsi}^{*(1)\alpha+}_{\boldsymbol{k},n}(\boldsymbol{r};\beta)\left(\mathscr{H}^{(0)}-\epsilon^{(0)}_{\boldsymbol{k},n}\right)\varPsi^{(0)\alpha}_{\boldsymbol{k},n}(\boldsymbol{r})\\
&\qquad-\boldsymbol{\varPsi}^{*(1)\mathrm{IR}+}_{\boldsymbol{k},n}(\boldsymbol{r};\beta)\left(\mathscr{H}^{(0)}-\epsilon^{(0)}_{\boldsymbol{k},n}\right)\varPsi^{(0)\mathrm{IR}}_{\boldsymbol{k},n}(\boldsymbol{r})\Bigg)\hat{\boldsymbol{r}}^{\top}\,\mathrm{d}S\Bigg\}\boldsymbol{Q}_{\alpha}\,,
\end{aligned}$$

$$\begin{aligned}
&\boldsymbol{Q}^{\dagger}_{\beta}\,\delta_{\beta\alpha}\oint_{\partial\beta}\Bigg(\vec{\varPsi}^{*(0)\beta}_{\boldsymbol{k},n}(\boldsymbol{r})\left(\mathscr{H}^{(0)}-\epsilon^{(0)}_{\boldsymbol{k},n}\right)\boldsymbol{\nabla}\vec{\varPsi}^{(0)\beta}_{\boldsymbol{k},n}(\boldsymbol{r}) \qquad (7.124c)\\
&\qquad-\varPsi^{*(0)\mathrm{IR}}_{\boldsymbol{k},n}(\boldsymbol{r})\left(\mathscr{H}^{(0)}-\epsilon^{(0)}_{\boldsymbol{k},n}\right)\boldsymbol{\nabla}\varPsi^{(0)\mathrm{IR}}_{\boldsymbol{k},n}(\boldsymbol{r})\Bigg)\hat{\boldsymbol{r}}^{\top}\,\mathrm{d}S\;\boldsymbol{Q}_{\alpha}\\
&+\boldsymbol{Q}^{\top}_{\beta}\,\delta_{\beta\alpha}\oint_{\partial\beta}\Bigg(\vec{\varPsi}^{*(0)\beta}_{\boldsymbol{k},n}(\boldsymbol{r})\left(\mathscr{H}^{(0)}-\epsilon^{(0)}_{\boldsymbol{k},n}\right)\boldsymbol{\nabla}\vec{\varPsi}^{(0)\beta}_{\boldsymbol{k},n}(\boldsymbol{r})\\
&\qquad-\varPsi^{*(0)\mathrm{IR}}_{\boldsymbol{k},n}(\boldsymbol{r})\left(\mathscr{H}^{(0)}-\epsilon^{(0)}_{\boldsymbol{k},n}\right)\boldsymbol{\nabla}\varPsi^{(0)\mathrm{IR}}_{\boldsymbol{k},n}(\boldsymbol{r})\Bigg)\hat{\boldsymbol{r}}^{\top}\,\mathrm{d}S\;\boldsymbol{Q}^{*}_{\alpha}\\
&=\boldsymbol{Q}^{\dagger}_{\beta}\Bigg\{\delta_{\beta\alpha}\oint_{\partial\beta}\Bigg(\vec{\varPsi}^{*(0)\beta}_{\boldsymbol{k},n}(\boldsymbol{r})\left(\mathscr{H}^{(0)}-\epsilon^{(0)}_{\boldsymbol{k},n}\right)\boldsymbol{\nabla}\vec{\varPsi}^{(0)\beta}_{\boldsymbol{k},n}(\boldsymbol{r})\\
&\qquad-\varPsi^{*(0)\mathrm{IR}}_{\boldsymbol{k},n}(\boldsymbol{r})\left(\mathscr{H}^{(0)}-\epsilon^{(0)}_{\boldsymbol{k},n}\right)\boldsymbol{\nabla}\varPsi^{(0)\mathrm{IR}}_{\boldsymbol{k},n}(\boldsymbol{r})\Bigg)\hat{\boldsymbol{r}}^{\top}\,\mathrm{d}S\\
&\quad+\delta_{\alpha\beta}\oint_{\partial\alpha}\hat{\boldsymbol{r}}\Bigg(\vec{\varPsi}^{*(0)\alpha}_{\boldsymbol{k},n}(\boldsymbol{r})\left(\mathscr{H}^{(0)}-\epsilon^{(0)}_{\boldsymbol{k},n}\right)\boldsymbol{\nabla}^{\top}\vec{\varPsi}^{(0)\alpha}_{\boldsymbol{k},n}(\boldsymbol{r})\\
&\qquad-\varPsi^{*(0)\mathrm{IR}}_{\boldsymbol{k},n}(\boldsymbol{r})\left(\mathscr{H}^{(0)}-\epsilon^{(0)}_{\boldsymbol{k},n}\right)\boldsymbol{\nabla}^{\top}\varPsi^{(0)\mathrm{IR}}_{\boldsymbol{k},n}(\boldsymbol{r})\Bigg)\,\mathrm{d}S\Bigg\}\boldsymbol{Q}_{\alpha}\,.
\end{aligned}$$

They only contribute if $\alpha = \beta$, and one can show that they are real. Thus, interchanging α and β is formally correct, but effectively not necessary, and adjoining translates into transposing. So, either the last two lines or the first two lines on the right-hand side of equation (7.124c) can be used.

Determining the phonon frequencies

If the dynamical matrix is completely set up and self-adjoint, the eigenvalues λ_ι are determined by a numerical diagonalization, employing the `LAPACK` routine `Zheev` [295] (Intel(R) Math Kernel Library Version 2020.0.0 Product Build 20191122 [296]). According to equations (3.7b) and (3.8a), the modes ω_ι are then given by

$$\begin{aligned}\omega_\iota &= \sqrt{\frac{\lambda_\iota}{M_\gamma}} && (7.125a)\\ &\approx \sqrt{\frac{\lambda_\iota E_\mathrm{h}^{-1}\, a_0^2}{A_\mathrm{r}(\gamma)}} \sqrt{\frac{4.3597 \cdot 10^{-18}\,\mathrm{J}}{(5.2918 \cdot 10^{-11}\,\mathrm{m})^2\, 1.836\,15 \cdot 10^3\, m_\mathrm{e}}} && (7.125b)\\ &\approx \sqrt{\frac{\lambda_\iota E_\mathrm{h}^{-1}\, a_0^2}{A_\mathrm{r}(\gamma)}}\, \frac{1}{33} \sqrt{\frac{4.3597 \cdot 10^{-18}}{(5.2918 \cdot 10^{-11})^2\, 1.836\,15 \cdot 10^3\, 9.1094 \cdot 10^{-31}}}\mathrm{cm}^{-1}\,. && (7.125c)\end{aligned}$$

The atomic weights $A_\mathrm{r}(\gamma)$ are provided by table 7.9.

Table 7.9: Atomic weights utilized in this thesis according to Meija et al. [297].

element	A_r
Ne	20.180
Al	26.982
Cu	63.546
Ar	39.948
Mo	95.951
Au	196.967

7.6.2 Expanding under Time Reversal Symmetry

Intention

As shown in equation (7.123), systems with TRS allow for calculating only a part of the dynamical matrix, and adding its adjoint in the end. So firstly, these expressions in section 6.5 are identified, further evaluated, and reformulated on condition that TRS holds. As a consequence, they essentially conform with the terms that are finally suggested by Klüppelberg [88]. But, the ultimate aim shall be that they only contain quantities at hand, which leads to differences. Altogether, these equations are composed of Sternheimer-equation solutions and the outcome of the second-order ion–ion interaction. Thereby, the categorization of the aforesaid section into HF, PI unit-cell integral, PI matrix-elements, and sf contributions predetermines the following discussion.

Hellmann–Feynman Contributions

It is only necessary to further elaborate on the first term in the linear combination of equation (6.64c), the matrix part of which is

$$
\begin{aligned}
&\underline{D}^{\beta\alpha}_{\mathrm{HF}}(\boldsymbol{q}^{-+}) && (7.126\mathrm{a})\\
&\quad= \int_\Omega \boldsymbol{\rho}^{(1)}(\boldsymbol{r};\boldsymbol{q}^-\beta)\left[\boldsymbol{V}^{(1)}_{\mathrm{ext}}(\boldsymbol{r};\boldsymbol{q}^+\alpha)\right]^\top \mathrm{d}^3r\\
&\qquad+ \delta_{\beta\alpha}\int_\Omega \rho^{(0)}(\boldsymbol{r})\boldsymbol{\nabla}\boldsymbol{\nabla}^\top V^{(0)}_{\mathrm{ext}}(\boldsymbol{r})\,\mathrm{d}^3r\\
&\qquad+ \underline{E}^{(2)\beta\alpha}_{\mathrm{ii}}(\boldsymbol{q}^{-+}) + \delta_{\boldsymbol{Q}_\beta\boldsymbol{Q}_\alpha}\underline{E}^{(2)\beta\alpha}_{\mathrm{ii}}(\boldsymbol{0}^{-+})\\
&\quad= \int_{\mathrm{IR}} \boldsymbol{\rho}^{*(1)}_{\mathrm{IR}}(\boldsymbol{r};\boldsymbol{q}^+\beta)\left[\boldsymbol{V}^{(1)\mathrm{IR}}_{\mathrm{ext}}(\boldsymbol{r};\boldsymbol{q}^+\alpha)\right]^\top \mathrm{d}^3r + \sum_\gamma\int_\gamma \boldsymbol{\rho}^{*(1)}_{\gamma}(\boldsymbol{r};\boldsymbol{q}^+\beta)\left[\boldsymbol{V}^{(1)\gamma}_{\mathrm{ext}}(\boldsymbol{r};\boldsymbol{q}^+\alpha)\right]^\top \mathrm{d}^3r\\
&\qquad+ \delta_{\beta\alpha}\int_{\mathrm{IR}} \rho^{(0)}_{\mathrm{IR}}(\boldsymbol{r})\boldsymbol{\nabla}\boldsymbol{\nabla}^\top V^{(0)\mathrm{IR}}_{\mathrm{ext}}(\boldsymbol{r})\,\mathrm{d}^3r + \delta_{\beta\alpha}\sum_\gamma\int_\gamma \rho^{(0)}_{\gamma}(\boldsymbol{r})\boldsymbol{\nabla}\boldsymbol{\nabla}^\top V^{(0)\gamma}_{\mathrm{ext}}(\boldsymbol{r})\,\mathrm{d}^3r\\
&\qquad+ \underline{E}^{(2)\beta\alpha}_{\mathrm{ii}}(\boldsymbol{q}^{-+}) + \delta_{\boldsymbol{Q}_\beta\boldsymbol{Q}_\alpha}\underline{E}^{(2)\beta\alpha}_{\mathrm{ii}}(\boldsymbol{0}^{-+})\,. && (7.126\mathrm{b})
\end{aligned}
$$

In equation (7.126b), the first-order density with Bloch character $\boldsymbol{q}^-$ is transformed by a complex conjugation to the result of the Sternheimer equation with Bloch character $\boldsymbol{q}^+$. Furthermore, the integral volume is subdivided into the IR and the MT spheres, because they are differently evaluated, due to the partitioning of the LAPW basis. Explaining in which way to compute these integrals in detail is postponed to section 7.6.8. These HF contributions in equation (7.126b) are essentially consistent with the respective expressions by Klüppelberg [88].

Pulay Unit-Cell Integral Correction

Since the Pulay integral

$$
\begin{aligned}
&\underline{D}^{\beta\alpha}_{\mathrm{Pl,dp}}(\boldsymbol{q}^{-+}) && (7.127\mathrm{a})\\
&= \sum_\gamma\int_\gamma \boldsymbol{\rho}^{(1)}_{\gamma}(\boldsymbol{r};\boldsymbol{q}^-\beta)\left[\boldsymbol{V}^{(1)\gamma}_{\mathrm{eff}}(\boldsymbol{r};\boldsymbol{q}^+\alpha)\right]^\top \mathrm{d}^3r + \int_{\mathrm{IR}} \boldsymbol{\rho}^{(1)}_{\mathrm{IR}}(\boldsymbol{r};\boldsymbol{q}^-\beta)\left[\boldsymbol{V}^{(1)\mathrm{IR}}_{\mathrm{eff}}(\boldsymbol{r};\boldsymbol{q}^+\alpha)\right]^\top \mathrm{d}^3r\\
&= \sum_\gamma\int_\gamma \boldsymbol{\rho}^{*(1)}_{\gamma}(\boldsymbol{r};\boldsymbol{q}^+\beta)\left[\boldsymbol{V}^{(1)\gamma}_{\mathrm{eff}}(\boldsymbol{r};\boldsymbol{q}^+\alpha)\right]^\top \mathrm{d}^3r + \int_{\mathrm{IR}} \boldsymbol{\rho}^{*(1)}_{\mathrm{IR}}(\boldsymbol{r};\boldsymbol{q}^+\beta)\left[\boldsymbol{V}^{(1)\mathrm{IR}}_{\mathrm{eff}}(\boldsymbol{r};\boldsymbol{q}^+\alpha)\right]^\top \mathrm{d}^3r && (7.127\mathrm{b})
\end{aligned}
$$

from the first line of equation (6.66b) is similar to the first term in equation (7.126b), the procedure is analogous. This means the first-order density is complex conjugated so that the integral is expressed by available quantities. Furthermore, the integral volume is subdivided into the IR and the MT spheres. The form as given in (7.127a) is equivalent to the proposal of Klüppelberg [88].

Exploiting TRS, equation (6.67) reduces to

$$D^{\beta\alpha}_{\mathrm{Pl,bk}}(\boldsymbol{q}) := \boldsymbol{Q}^{\dagger}_{\beta} \sum_{\boldsymbol{k},n} 2 f^{(0)}_{\boldsymbol{k},n} \Big(\underline{D}^{\boldsymbol{k}n\beta\alpha}_{\mathrm{Pu2b}}(\boldsymbol{q}^{+-}) + \underline{D}^{\boldsymbol{k}n\beta\alpha}_{\mathrm{Pu2kO}}(\boldsymbol{q}^{-+}) + 2\underline{D}^{\boldsymbol{k}n\beta\alpha}_{\mathrm{Pu1bk}}(\boldsymbol{q}^{++}) \Big) \boldsymbol{Q}_{\alpha} \,. \tag{7.128a}$$

From equation (6.67b), only

$$\begin{aligned}
&\underline{D}^{\boldsymbol{k}n\beta\alpha}_{\mathrm{Pu2b}}(\boldsymbol{q}^{+-}) \\
&\quad = \sum_{l'm'p'} \sum_{lmp} \sum_{\boldsymbol{G}'\boldsymbol{G}} \Big\{ \\
&\qquad 2\Big(\boldsymbol{z}^{(1)}_{\boldsymbol{G}'}(\boldsymbol{k},n;\boldsymbol{q}\beta) a^{\boldsymbol{G}'\boldsymbol{k}\alpha}_{l'm'p'}(\boldsymbol{q}) \mathrm{i}[\boldsymbol{k}+\boldsymbol{q}+\boldsymbol{G}']^{\top} \Big)^{*} \Big\langle \vec{\varphi}^{\mathring{\alpha}}_{l'm'p'} \Big| \mathscr{H}^{(0)} - \epsilon^{(0)}_{\boldsymbol{k},n} \Big| \vec{\varphi}^{\mathring{\alpha}}_{lmp} \Big\rangle_{\alpha} z^{(0)}_{\boldsymbol{G}}(\boldsymbol{k},n) a^{\boldsymbol{G}\boldsymbol{k}\alpha}_{lmp} \\
&\quad - 2\Big(\boldsymbol{z}^{(1)}_{\boldsymbol{G}'}(\boldsymbol{k},n;\boldsymbol{q}\beta) a^{\boldsymbol{G}'\boldsymbol{k}\alpha}_{l'm'p'}(\boldsymbol{q}) \Big)^{*} \Big\langle \boldsymbol{\nabla}^{\top} \vec{\varphi}^{\mathring{\alpha}}_{l'm'p'} \Big| \mathscr{H}^{(0)} - \epsilon^{(0)}_{\boldsymbol{k},n} \Big| \vec{\varphi}^{\mathring{\alpha}}_{lmp} \Big\rangle_{\alpha} z^{(0)}_{\boldsymbol{G}}(\boldsymbol{k},n) a^{\boldsymbol{G}\boldsymbol{k}\alpha}_{lmp} \\
&\quad - \delta_{\beta\alpha} \Big(z^{(0)}_{\boldsymbol{G}'}(\boldsymbol{k},n) a^{\boldsymbol{G}'\boldsymbol{k}\alpha}_{l'm'p'} \Big)^{*} [\boldsymbol{k}+\boldsymbol{G}'] [\boldsymbol{k}+\boldsymbol{G}']^{\top} \Big\langle \vec{\varphi}^{\mathring{\alpha}}_{l'm'p'} \Big| \mathscr{H}^{(0)} - \epsilon^{(0)}_{\boldsymbol{k},n} \Big| \vec{\varphi}^{\mathring{\alpha}}_{lmp} \Big\rangle_{\alpha} z^{(0)}_{\boldsymbol{G}}(\boldsymbol{k},n) a^{\boldsymbol{G}\boldsymbol{k}\alpha}_{lmp} \\
&\quad - \delta_{\beta\alpha} \Big(z^{(0)}_{\boldsymbol{G}'}(\boldsymbol{k},n) a^{\boldsymbol{G}'\boldsymbol{k}\alpha}_{l'm'p'} \mathrm{i}[\boldsymbol{k}+\boldsymbol{G}'] \Big)^{*} \Big\langle \boldsymbol{\nabla}^{\top} \vec{\varphi}^{\mathring{\alpha}}_{l'm'p'} \Big| \mathscr{H}^{(0)} - \epsilon^{(0)}_{\boldsymbol{k},n} \Big| \vec{\varphi}^{\mathring{\alpha}}_{lmp} \Big\rangle_{\alpha} z^{(0)}_{\boldsymbol{G}}(\boldsymbol{k},n) a^{\boldsymbol{G}\boldsymbol{k}\alpha}_{lmp} \\
&\quad - \delta_{\beta\alpha} \Big\langle \boldsymbol{\nabla} \vec{\varphi}^{\mathring{\alpha}}_{l'm'p'} \Big| \mathscr{H}^{(0)} - \epsilon^{(0)}_{\boldsymbol{k},n} \Big| \vec{\varphi}^{\mathring{\alpha}}_{lmp} \Big\rangle_{\alpha} \Big[z^{(0)}_{\boldsymbol{G}'}(\boldsymbol{k},n) a^{\boldsymbol{G}'\boldsymbol{k}\alpha}_{l'm'p'} \mathrm{i}[\boldsymbol{k}+\boldsymbol{G}'] \Big]^{\dagger} z^{(0)}_{\boldsymbol{G}}(\boldsymbol{k},n) a^{\boldsymbol{G}\boldsymbol{k}\alpha}_{lmp} \\
&\quad + \delta_{\beta\alpha} \Big(z^{(0)}_{\boldsymbol{G}}(\boldsymbol{k},n) a^{\boldsymbol{G}'\boldsymbol{k}\alpha}_{l'm'p'} \Big)^{*} \Big\langle \boldsymbol{\nabla}\boldsymbol{\nabla}^{\top} \vec{\varphi}^{\mathring{\alpha}}_{l'm'p'} \Big| \mathscr{H}^{(0)} - \epsilon^{(0)}_{\boldsymbol{k},n} \Big| \vec{\varphi}^{\mathring{\alpha}}_{lmp} \Big\rangle_{\alpha} z^{(0)}_{\boldsymbol{G}}(\boldsymbol{k},n) a^{\boldsymbol{G}\boldsymbol{k}\alpha}_{lmp} \Big\}
\end{aligned} \tag{7.128b}$$

is required, where the definitions of the respective basis functions and their variations from equations (5.17b), (6.7), and (5.72) are now inserted. Doing this, only the "—"-part of equation (6.7) and only the Bloch character **0** of equation (6.9) are necessary, respectively. In the latter, additionally equation (6.5) is employed. Analogously, equation (6.67c) can be rewritten into

$$\begin{aligned}
&\underline{D}^{\boldsymbol{k}n\beta\alpha}_{\mathrm{Pu2kO}}(\boldsymbol{q}^{-+}) \\
&= \sum_{l'm'p'} \sum_{lmp} \sum_{\boldsymbol{G}'\boldsymbol{G}} \Big\{ \\
&\quad 2\Big(z^{(0)}_{\boldsymbol{G}'}(\boldsymbol{k},n) a^{\boldsymbol{G}'\boldsymbol{k}\beta}_{l'm'p'} \Big)^{*} \Big\langle \vec{\varphi}^{\mathring{\beta}}_{l'm'p'} \Big| \mathscr{H}^{(0)} - \epsilon^{(0)}_{\boldsymbol{k},n} \Big| \vec{\varphi}^{\mathring{\beta}}_{lmp} \Big\rangle_{\beta} a^{\boldsymbol{G}\boldsymbol{k}\beta}_{lmp}(\boldsymbol{q}) \mathrm{i}[\boldsymbol{k}+\boldsymbol{q}+\boldsymbol{G}] \Big[\boldsymbol{z}^{(1)}_{\boldsymbol{G}}(\boldsymbol{k},n;\boldsymbol{q}\alpha) \Big]^{\top} \\
&- 2\Big(z^{(0)}_{\boldsymbol{G}'}(\boldsymbol{k},n) a^{\boldsymbol{G}'\boldsymbol{k}\beta}_{l'm'p'} \Big)^{*} \Big\langle \vec{\varphi}^{\mathring{\beta}}_{l'm'p'} \Big| \mathscr{H}^{(0)} - \epsilon^{(0)}_{\boldsymbol{k},n} \Big| \boldsymbol{\nabla} \vec{\varphi}^{\mathring{\beta}}_{lmp} \Big\rangle_{\beta} a^{\boldsymbol{G}\boldsymbol{k}\beta}_{lmp}(\boldsymbol{q}) \Big[\boldsymbol{z}^{(1)}_{\boldsymbol{G}}(\boldsymbol{k},n;\boldsymbol{q}\alpha) \Big]^{\top} \\
&- \delta_{\beta\alpha} \Big(z^{(0)}_{\boldsymbol{G}'}(\boldsymbol{k},n) a^{\boldsymbol{G}'\boldsymbol{k}\alpha}_{l'm'p'} \Big)^{*} [\boldsymbol{k}+\boldsymbol{G}] [\boldsymbol{k}+\boldsymbol{G}]^{\top} \Big\langle \vec{\varphi}^{\mathring{\alpha}}_{l'm'p'} \Big| \mathscr{H}^{(0)} - \epsilon^{(0)}_{\boldsymbol{k},n} \Big| \vec{\varphi}^{\mathring{\alpha}}_{lmp} \Big\rangle_{\alpha} z^{(0)}_{\boldsymbol{G}}(\boldsymbol{k},n) a^{\boldsymbol{G}\boldsymbol{k}\alpha}_{lmp} \\
&- \delta_{\beta\alpha} \Big(z^{(0)}_{\boldsymbol{G}'}(\boldsymbol{k},n) a^{\boldsymbol{G}'\boldsymbol{k}\alpha}_{l'm'p'} \Big)^{*} z^{(0)}_{\boldsymbol{G}}(\boldsymbol{k},n) a^{\boldsymbol{G}\boldsymbol{k}\alpha}_{lmp} \mathrm{i}[\boldsymbol{k}+\boldsymbol{G}] \Big\langle \vec{\varphi}^{\mathring{\alpha}}_{l'm'p'} \Big| \mathscr{H}^{(0)} - \epsilon^{(0)}_{\boldsymbol{k},n} \Big| \boldsymbol{\nabla}^{\top} \vec{\varphi}^{\mathring{\alpha}}_{lmp} \Big\rangle_{\alpha} \\
&- \delta_{\beta\alpha} \Big\langle \vec{\varphi}^{\mathring{\alpha}}_{l'm'p'} \Big| \mathscr{H}^{(0)} - \epsilon^{(0)}_{\boldsymbol{k},n} \Big| \boldsymbol{\nabla} \vec{\varphi}^{\mathring{\alpha}}_{lmp} \Big\rangle_{\alpha} \Big(z^{(0)}_{\boldsymbol{G}'}(\boldsymbol{k},n) a^{\boldsymbol{G}'\boldsymbol{k}\alpha}_{l'm'p'} \Big)^{*} \Big[z^{(0)}_{\boldsymbol{G}}(\boldsymbol{k},n) a^{\boldsymbol{G}\boldsymbol{k}\alpha}_{lmp} \mathrm{i}[\boldsymbol{k}+\boldsymbol{G}] \Big]^{\top} \\
&+ \delta_{\beta\alpha} \Big(z^{(0)}_{\boldsymbol{G}}(\boldsymbol{k},n) a^{\boldsymbol{G}'\boldsymbol{k}\alpha}_{l'm'p'} \Big)^{*} \Big\langle \vec{\varphi}^{\mathring{\alpha}}_{l'm'p'} \Big| \mathscr{H}^{(0)} - \epsilon^{(0)}_{\boldsymbol{k},n} \Big| \boldsymbol{\nabla}\boldsymbol{\nabla}^{\top} \vec{\varphi}^{\mathring{\alpha}}_{lmp} \Big\rangle_{\alpha} z^{(0)}_{\boldsymbol{G}}(\boldsymbol{k},n) a^{\boldsymbol{G}\boldsymbol{k}\alpha}_{lmp} \Big\} \,.
\end{aligned} \tag{7.128c}$$

But in equation (6.67c), the demanded first-order variations of the expansion coefficients stem from the Sternheimer equation, in which the bra wave-functions are evaluated at $\boldsymbol{k}-\boldsymbol{q}$. Therefore, I exploit that in the end a Hermitian matrix is ensured so that it is legitimate to substitute the first term in (7.124a) with its second term. As a consequence, equation (7.128c) only contains quantities at hand. Finally with the aforementioned strategies, equation (6.67d) is rewritten into

$$\begin{aligned}
&\underline{D}^{\boldsymbol{k}n\beta\alpha}_{\text{Pu1bk}}(\boldsymbol{q}^{++})\\
&= \sum_{\boldsymbol{G}'\boldsymbol{G}}\Bigg(\boldsymbol{z}^{*(1)}_{\boldsymbol{G}'}(\boldsymbol{k},n;\boldsymbol{q}\beta)\Big\langle \phi^{(0)\text{IR}}_{\boldsymbol{k}+\boldsymbol{q},\boldsymbol{G}'}\Big|\mathscr{H}^{(0)}-\epsilon^{(0)}_{\boldsymbol{k},n}\Big|\phi^{(0)\text{IR}}_{\boldsymbol{k}+\boldsymbol{q},\boldsymbol{G}}\Big\rangle_{\text{IR}}\Big[\boldsymbol{z}^{(1)}_{\boldsymbol{G}}(\boldsymbol{k},n;\boldsymbol{q}\alpha)\Big]^{\top}\\
&\quad+\sum_{l'm'p'}\sum_{lmp}\Bigg\{\\
&\qquad\sum_{\gamma}\Big(\boldsymbol{z}^{(1)}_{\boldsymbol{G}'}(\boldsymbol{k},n;\boldsymbol{q}\beta)a^{\boldsymbol{G}'\boldsymbol{k}\gamma}_{l'm'p'}(\boldsymbol{q})\Big)^{*}\Big\langle\vec{\varphi}^{\mathring{\gamma}}_{l'm'p'}\Big|\mathscr{H}^{(0)}-\epsilon^{(0)}_{\boldsymbol{k},n}\Big|\vec{\varphi}^{\mathring{\gamma}}_{lmp}\Big\rangle_{\gamma}\Big[\boldsymbol{z}^{(1)}_{\boldsymbol{G}}(\boldsymbol{k},n;\boldsymbol{q}\alpha)\Big]^{\top}a^{\boldsymbol{G}\boldsymbol{k}\gamma}_{lmp}(\boldsymbol{q})\\
&\quad+\Big(\boldsymbol{z}^{(1)}_{\boldsymbol{G}'}(\boldsymbol{k},n;\boldsymbol{q}\beta)a^{\boldsymbol{G}'\boldsymbol{k}\alpha}_{l'm'p'}(\boldsymbol{q})\Big)^{*}\Big\langle\vec{\varphi}^{\mathring{\alpha}}_{l'm'p'}\Big|\mathscr{H}^{(0)}-\epsilon^{(0)}_{\boldsymbol{k},n}\Big|\vec{\varphi}^{\mathring{\alpha}}_{lmp}\Big\rangle_{\alpha}\mathrm{i}[\boldsymbol{k}+\boldsymbol{G}]^{\top}z^{(0)}_{\boldsymbol{G}}(\boldsymbol{k},n)a^{\boldsymbol{G}\boldsymbol{k}\alpha}_{lmp}\\
&\quad-\Big(\boldsymbol{z}^{(1)}_{\boldsymbol{G}'}(\boldsymbol{k},n;\boldsymbol{q}\beta)a^{\boldsymbol{G}'\boldsymbol{k}\alpha}_{l'm'p'}(\boldsymbol{q})\Big)^{*}\Big\langle\vec{\varphi}^{\mathring{\alpha}}_{l'm'p'}\Big|\mathscr{H}^{(0)}-\epsilon^{(0)}_{\boldsymbol{k},n}\Big|\boldsymbol{\nabla}^{\top}\vec{\varphi}^{\mathring{\alpha}}_{lmp}\Big\rangle_{\alpha}z^{(0)}_{\boldsymbol{G}}(\boldsymbol{k},n)a^{\boldsymbol{G}\boldsymbol{k}\alpha}_{lmp}\\
&\quad+\Big(z^{(0)}_{\boldsymbol{G}'}(\boldsymbol{k},n)a^{\boldsymbol{G}'\boldsymbol{k}\beta}_{l'm'p'}\mathrm{i}[\boldsymbol{k}+\boldsymbol{G}']\Big)^{*}\Big\langle\vec{\varphi}^{\mathring{\beta}}_{l'm'p'}\Big|\mathscr{H}^{(0)}-\epsilon^{(0)}_{\boldsymbol{k},n}\Big|\vec{\varphi}^{\mathring{\beta}}_{lmp}\Big\rangle_{\beta}\Big[\boldsymbol{z}^{(1)}_{\boldsymbol{G}}(\boldsymbol{k},n;\boldsymbol{q}\alpha)\Big]^{\top}a^{\boldsymbol{G}\boldsymbol{k}\beta}_{lmp}(\boldsymbol{q})\\
&\quad-\Big(z^{(0)}_{\boldsymbol{G}'}(\boldsymbol{k},n)a^{\boldsymbol{G}'\boldsymbol{k}\beta}_{l'm'p'}\Big)^{*}\Big\langle\boldsymbol{\nabla}\vec{\varphi}^{\mathring{\beta}}_{l'm'p'}\Big|\mathscr{H}^{(0)}-\epsilon^{(0)}_{\boldsymbol{k},n}\Big|\vec{\varphi}^{\mathring{\beta}}_{lmp}\Big\rangle_{\beta}\Big[\boldsymbol{z}^{(1)}_{\boldsymbol{G}}(\boldsymbol{k},n;\boldsymbol{q}\alpha)\Big]^{\top}a^{\boldsymbol{G}\boldsymbol{k}\beta}_{lmp}(\boldsymbol{q})\\
&\quad+\delta_{\beta\alpha}\Big(z^{(0)}_{\boldsymbol{G}'}(\boldsymbol{k},n)a^{\boldsymbol{G}'\boldsymbol{k}\alpha}_{l'm'p'}\mathrm{i}[\boldsymbol{k}+\boldsymbol{G}']\Big)^{*}\Big\langle\vec{\varphi}^{\mathring{\alpha}}_{l'm'p'}\Big|\mathscr{H}^{(0)}-\epsilon^{(0)}_{\boldsymbol{k},n}\Big|\vec{\varphi}^{\mathring{\alpha}}_{lmp}\Big\rangle_{\alpha}z^{(0)}_{\boldsymbol{G}}(\boldsymbol{k},n)a^{\boldsymbol{G}\boldsymbol{k}\alpha}_{lmp}\mathrm{i}[\boldsymbol{k}+\boldsymbol{G}]^{\top}\\
&\quad-\delta_{\beta\alpha}\Big(z^{(0)}_{\boldsymbol{G}'}(\boldsymbol{k},n)a^{\boldsymbol{G}'\boldsymbol{k}\alpha}_{l'm'p'}\Big)^{*}\Big\langle\boldsymbol{\nabla}\vec{\varphi}^{\mathring{\alpha}}_{l'm'p'}\Big|\mathscr{H}^{(0)}-\epsilon^{(0)}_{\boldsymbol{k},n}\Big|\vec{\varphi}^{\mathring{\alpha}}_{lmp}\Big\rangle_{\alpha}z^{(0)}_{\boldsymbol{G}}(\boldsymbol{k},n)a^{\boldsymbol{G}\boldsymbol{k}\alpha}_{lmp}\mathrm{i}[\boldsymbol{k}+\boldsymbol{G}]^{\top}\\
&\quad-\delta_{\beta\alpha}\Big(z^{(0)}_{\boldsymbol{G}'}(\boldsymbol{k},n)a^{\boldsymbol{G}'\boldsymbol{k}\alpha}_{l'm'p'}\mathrm{i}[\boldsymbol{k}+\boldsymbol{G}']\Big)^{*}\Big\langle\vec{\varphi}^{\mathring{\alpha}}_{l'm'p'}\Big|\mathscr{H}^{(0)}-\epsilon^{(0)}_{\boldsymbol{k},n}\Big|\boldsymbol{\nabla}^{\top}\vec{\varphi}^{\mathring{\alpha}}_{lmp}\Big\rangle_{\alpha}z^{(0)}_{\boldsymbol{G}}(\boldsymbol{k},n)a^{\boldsymbol{G}\boldsymbol{k}\alpha}_{lmp}\\
&\quad+\delta_{\beta\alpha}\Big(z^{(0)}_{\boldsymbol{G}'}(\boldsymbol{k},n)a^{\boldsymbol{G}'\boldsymbol{k}\alpha}_{l'm'p'}\Big)^{*}\Big\langle\boldsymbol{\nabla}\vec{\varphi}^{\mathring{\alpha}}_{l'm'p'}\Big|\mathscr{H}^{(0)}-\epsilon^{(0)}_{\boldsymbol{k},n}\Big|\boldsymbol{\nabla}^{\top}\vec{\varphi}^{\mathring{\alpha}}_{lmp}\Big\rangle_{\alpha}z^{(0)}_{\boldsymbol{G}}(\boldsymbol{k},n)a^{\boldsymbol{G}\boldsymbol{k}\alpha}_{lmp}\Bigg\}\Bigg)\,.
\end{aligned}\tag{7.128d}$$

These three $\boldsymbol{k}$- and band-dependent Pulay contributions are essentially already published in the appendix of Klüppelberg [88]. However, Klüppelberg does *not* reformulate them such that only the first-order expansion coefficients with Bloch character $\boldsymbol{q}^{+}$ are necessitated and has a typo in a relative minus. Furthermore, relative to him I regroup the terms in order to set the stage for the following discussion.

Surface-Terms Correction

In the $\boldsymbol{q}^{+}$ part of equation (6.68c), those terms incorporating wave functions or their variations can further be evaluated so that

$$
\begin{aligned}
&\underline{D}^{\beta\alpha}_{\text{sfO}}(\boldsymbol{q}^{+}) \qquad\qquad (7.129)\\
&\quad = \sum_{\boldsymbol{k},n} f^{(0)}_{\boldsymbol{k},n} \sum_{\boldsymbol{G}'\boldsymbol{G}} \Bigg\{ \\
&\qquad\quad 2 \oint_{\partial\alpha} \Bigg(\Big(\boldsymbol{z}^{(1)}_{\boldsymbol{G}'}(\boldsymbol{k}, n; \boldsymbol{q}\beta) \vec{\phi}^{(0)\alpha}_{\boldsymbol{k}+\boldsymbol{q},\boldsymbol{G}'}(\boldsymbol{r}) \Big)^{*} \Big(\mathscr{H}^{(0)} - \epsilon^{(0)}_{\boldsymbol{k},n} \Big) z^{(0)}_{\boldsymbol{G}}(\boldsymbol{k}, n) \vec{\phi}^{(0)\alpha}_{\boldsymbol{k},\boldsymbol{G}}(\boldsymbol{r}) \\
&\qquad\qquad\quad + \delta_{\beta\alpha} \Big(z^{(0)}_{\boldsymbol{G}'}(\boldsymbol{k}, n) \mathrm{i}(\boldsymbol{k} + \boldsymbol{G}') \vec{\phi}^{(0)\beta}_{\boldsymbol{k},\boldsymbol{G}'}(\boldsymbol{r}) \Big)^{*} \Big(\mathscr{H}^{(0)} - \epsilon^{(0)}_{\boldsymbol{k},n} \Big) z^{(0)}_{\boldsymbol{G}}(\boldsymbol{k}, n) \vec{\phi}^{(0)\beta}_{\boldsymbol{k},\boldsymbol{G}}(\boldsymbol{r}) \\
&\qquad\qquad\quad - \delta_{\beta\alpha} \Big(z^{(0)}_{\boldsymbol{G}'}(\boldsymbol{k}, n) \boldsymbol{\nabla} \vec{\phi}^{(0)\beta}_{\boldsymbol{k},\boldsymbol{G}'}(\boldsymbol{r}) \Big)^{*} \Big(\mathscr{H}^{(0)} - \epsilon^{(0)}_{\boldsymbol{k},n} \Big) z^{(0)}_{\boldsymbol{G}}(\boldsymbol{k}, n) \vec{\phi}^{(0)\beta}_{\boldsymbol{k},\boldsymbol{G}}(\boldsymbol{r}) \\
&\qquad\qquad\quad - \Big(\boldsymbol{z}^{(1)}_{\boldsymbol{G}'}(\boldsymbol{k}, n; \boldsymbol{q}\beta) \phi^{(0)\mathrm{IR}}_{\boldsymbol{k}+\boldsymbol{q},\boldsymbol{G}'}(\boldsymbol{r}) \Big)^{*} \Big(\mathscr{H}^{(0)} - \epsilon^{(0)}_{\boldsymbol{k},n} \Big) z^{(0)}_{\boldsymbol{G}}(\boldsymbol{k}, n) \phi^{(0)\mathrm{IR}}_{\boldsymbol{k},\boldsymbol{G}}(\boldsymbol{r}) \Bigg) \hat{\boldsymbol{r}}^{\top} \,\mathrm{d}S \\
&\qquad\quad + 2 \oint_{\partial\beta} \hat{\boldsymbol{r}} \Bigg(z^{*(0)}_{\boldsymbol{G}'}(\boldsymbol{k}, n) \vec{\phi}^{*(0)\beta}_{\boldsymbol{k},\boldsymbol{G}'}(\boldsymbol{r}) \Big(\mathscr{H}^{(0)} - \epsilon^{(0)}_{\boldsymbol{k},n} \Big) \Big[\boldsymbol{z}^{(1)}_{\boldsymbol{G}}(\boldsymbol{k}, n; \boldsymbol{q}\alpha) \Big]^{\top} \vec{\phi}^{(0)\beta}_{\boldsymbol{k}+\boldsymbol{q},\boldsymbol{G}}(\boldsymbol{r}) \\
&\qquad\qquad\quad + \delta_{\beta\alpha} z^{*(0)}_{\boldsymbol{G}'}(\boldsymbol{k}, n) \vec{\phi}^{*(0)\beta}_{\boldsymbol{k},\boldsymbol{G}'}(\boldsymbol{r}) \Big(\mathscr{H}^{(0)} - \epsilon^{(0)}_{\boldsymbol{k},n} \Big) z^{(0)}_{\boldsymbol{G}}(\boldsymbol{k}, n) \mathrm{i}[\boldsymbol{k} + \boldsymbol{G}]^{\top} \vec{\phi}^{(0)\beta}_{\boldsymbol{k},\boldsymbol{G}}(\boldsymbol{r}) \\
&\qquad\qquad\quad - \delta_{\beta\alpha} z^{*(0)}_{\boldsymbol{G}'}(\boldsymbol{k}, n) \vec{\phi}^{*(0)\beta}_{\boldsymbol{k},\boldsymbol{G}'}(\boldsymbol{r}) \Big(\mathscr{H}^{(0)} - \epsilon^{(0)}_{\boldsymbol{k},n} \Big) z^{(0)}_{\boldsymbol{G}}(\boldsymbol{k}, n) \Big(\boldsymbol{\nabla}^{\top} \vec{\phi}^{(0)\beta}_{\boldsymbol{k},\boldsymbol{G}}(\boldsymbol{r}) \Big) \\
&\qquad\qquad\quad - z^{*(0)}_{\boldsymbol{G}'}(\boldsymbol{k}, n) \phi^{*(0)\mathrm{IR}}_{\boldsymbol{k},\boldsymbol{G}'}(\boldsymbol{r}) \Big(\mathscr{H}^{(0)} - \epsilon^{(0)}_{\boldsymbol{k},n} \Big) \Big[\boldsymbol{z}^{(1)}_{\boldsymbol{G}}(\boldsymbol{k}, n; \boldsymbol{q}\alpha) \Big]^{\top} \phi^{(0)\mathrm{IR}}_{\boldsymbol{k}+\boldsymbol{q},\boldsymbol{G}}(\boldsymbol{r}) \Bigg) \,\mathrm{d}S \\
&\qquad\quad + \delta_{\beta\alpha} \oint_{\partial\beta} \Bigg(z^{*(0)}_{\boldsymbol{G}'}(\boldsymbol{k}, n) \Big(\boldsymbol{\nabla} \vec{\phi}^{*(0)\beta}_{\boldsymbol{k},\boldsymbol{G}'}(\boldsymbol{r}) \Big) \Big(\mathscr{H}^{(0)} - \epsilon^{(0)}_{\boldsymbol{k},n} \Big) z^{(0)}_{\boldsymbol{G}}(\boldsymbol{k}, n) \vec{\phi}^{(0)\beta}_{\boldsymbol{k},\boldsymbol{G}}(\boldsymbol{r}) \\
&\qquad\qquad\quad - z^{*(0)}_{\boldsymbol{G}'}(\boldsymbol{k}, n) \Big(\boldsymbol{\nabla} \phi^{*(0)\mathrm{IR}}_{\boldsymbol{k},\boldsymbol{G}'}(\boldsymbol{r}) \Big) \Big(\mathscr{H}^{(0)} - \epsilon^{(0)}_{\boldsymbol{k},n} \Big) z^{(0)}_{\boldsymbol{G}}(\boldsymbol{k}, n) \phi^{(0)\mathrm{IR}}_{\boldsymbol{k},\boldsymbol{G}}(\boldsymbol{r}) \\
&\qquad\qquad\quad + z^{*(0)}_{\boldsymbol{G}'}(\boldsymbol{k}, n) \vec{\phi}^{*(0)\beta}_{\boldsymbol{k},\boldsymbol{G}'}(\boldsymbol{r}) \Big(\boldsymbol{\nabla} V^{(0)\beta}_{\text{eff}}(\boldsymbol{r}) \Big) z^{(0)}_{\boldsymbol{G}}(\boldsymbol{k}, n) \vec{\phi}^{(0)\beta}_{\boldsymbol{k},\boldsymbol{G}}(\boldsymbol{r}) \\
&\qquad\qquad\quad - z^{*(0)}_{\boldsymbol{G}'}(\boldsymbol{k}, n) \phi^{*(0)\mathrm{IR}}_{\boldsymbol{k},\boldsymbol{G}'}(\boldsymbol{r}) \Big(\boldsymbol{\nabla} V^{(0)\mathrm{IR}}_{\text{eff}}(\boldsymbol{r}) \Big) z^{(0)}_{\boldsymbol{G}}(\boldsymbol{k}, n) \phi^{(0)\mathrm{IR}}_{\boldsymbol{k},\boldsymbol{G}}(\boldsymbol{r}) \Bigg) \hat{\boldsymbol{r}}^{\top} \,\mathrm{d}S \\
&\qquad\quad + \delta_{\beta\alpha} \oint_{\partial\beta} \hat{\boldsymbol{r}} \Bigg(z^{*(0)}_{\boldsymbol{G}'}(\boldsymbol{k}, n) \vec{\phi}^{*(0)\beta}_{\boldsymbol{k},\boldsymbol{G}'}(\boldsymbol{r}) \Big(\mathscr{H}^{(0)} - \epsilon^{(0)}_{\boldsymbol{k},n} \Big) z^{(0)}_{\boldsymbol{G}}(\boldsymbol{k}, n) \Big(\boldsymbol{\nabla}^{\top} \vec{\phi}^{(0)\beta}_{\boldsymbol{k},\boldsymbol{G}}(\boldsymbol{r}) \Big) \\
&\qquad\qquad\quad - z^{*(0)}_{\boldsymbol{G}'}(\boldsymbol{k}, n) \phi^{*(0)\mathrm{IR}}_{\boldsymbol{k},\boldsymbol{G}'}(\boldsymbol{r}) \Big(\mathscr{H}^{(0)} - \epsilon^{(0)}_{\boldsymbol{k},n} \Big) z^{(0)}_{\boldsymbol{G}}(\boldsymbol{k}, n) \Big(\boldsymbol{\nabla}^{\top} \phi^{(0)\mathrm{IR}}_{\boldsymbol{k},\boldsymbol{G}}(\boldsymbol{r}) \Big) \Bigg) \,\mathrm{d}S \Bigg\} \\
&\qquad\quad + \delta_{\beta\alpha} \oint_{\partial\beta} \Bigg[\boldsymbol{\nabla} \Big(\rho^{(0)}_{\beta}(\boldsymbol{r}) \Big(\epsilon^{(0)\beta}_{\text{xc}}(\boldsymbol{r}) - V^{(0)\beta}_{\text{xc}}(\boldsymbol{r}) \Big) \Big) \\
&\qquad\qquad\quad - \boldsymbol{\nabla} \Big(\rho^{(0)}_{\text{IR}}(\boldsymbol{r}) \Big(\epsilon^{(0)\mathrm{IR}}_{\text{xc}}(\boldsymbol{r}) - V^{(0)\mathrm{IR}}_{\text{xc}}(\boldsymbol{r}) \Big) \Big) \Bigg] \hat{\boldsymbol{r}}^{\top} \,\mathrm{d}S \\
&\qquad\quad + \delta_{\beta\alpha} \oint_{\partial\beta} \hat{\boldsymbol{r}} \Bigg[\rho^{(0)}_{\beta}(\boldsymbol{r}) \Big(2 \Big[\boldsymbol{V}^{(1)\beta}_{\text{ext}}(\boldsymbol{r}; \boldsymbol{q}^{+}\alpha) \Big]^{\top} + \Big[\boldsymbol{V}^{(1)\beta}_{\text{Htr}}(\boldsymbol{r}; \boldsymbol{q}^{+}\alpha) \Big]^{\top} \Big) \\
&\qquad\qquad\quad - \rho^{(0)}_{\text{IR}}(\boldsymbol{r}) \Big(2 \Big[\boldsymbol{V}^{(1)\mathrm{IR}}_{\text{ext}}(\boldsymbol{r}; \boldsymbol{q}^{+}\alpha) \Big]^{\top} + \Big[\boldsymbol{V}^{(1)\mathrm{IR}}_{\text{Htr}}(\boldsymbol{r}; \boldsymbol{q}^{+}\alpha) \Big]^{\top} \Big) \Bigg] \,\mathrm{d}S
\end{aligned}
$$

results. Basically, the wave functions are expanded in the LAPW basis (5.17b) and the respective parts in the definition of the first-order wave-function variation (cf. equations (6.8) and (6.7)) are inserted. Again, there are first-order wave-function expansion coefficients with Bloch character $\boldsymbol{q}^{-}$, which are not available. But due to making the dynamical matrix self-adjoint in the end, the first two lines on the right-hand side of equation (7.124b) can be substituted by the last two lines. Furthermore, the first two lines of equation (7.124c) are replaced by the last two lines to prepare the following derivation. Mainly, this is consistent with Klüppelberg [88], but certain terms of his thesis are not at hand after the `juPhon` computation. Furthermore, he describes how to calculate his surface-integral expressions in detail. However, in my opinion this is highly inefficient, because many terms can and should be summarized first.

7.6.3 Circumventing Hessian Contributions

Motivation

Having implemented the dynamical matrix approach of Klüppelberg [88] as described in section 7.6.2 [251], the numerics turn out to be absolutely *not* satisfying. From our conceptual tests [127, 251] that I have programmed, in particular those have permanently failed which check fundamental relations based on the divergence theorem or the product rule of derivation. Localizing most of the numerical problems in those terms which incorporate outer products of two gradients stimulated me to develop a reformulation that circumvents them. It is based on a generalized outer-product divergence theorem [294] which is provided first, as well as its implications (a proof by Fabian Lux can be found in appendix E). Then, the HF part of the dynamical matrix is separately discussed from its valence Pulay and surface correction terms. Finally, the Pulay core-electron corrections are elucidated and rectified.

Outer-Product Divergence Theorem

Required relation

The divergence theorem with a vectorial integrand only incorporates one gradient in the volume integral and none in the surface integral. However, it is possible to generalize it so that the surface integral contains an outer product of the gradient and the normal vector, while the volume integral comprises an outer product of two gradients [294]

$$\begin{aligned}
\int_{\partial\mathfrak{D}} \mathfrak{k}^*(\boldsymbol{r})\hat{\boldsymbol{n}}\boldsymbol{\nabla}^\top\mathfrak{g}(\boldsymbol{r})\,\mathrm{d}S &= \int_{\mathfrak{D}} \boldsymbol{\nabla}\Big(\mathfrak{k}^*(\boldsymbol{r})\boldsymbol{\nabla}^\top\mathfrak{g}(\boldsymbol{r})\Big)\,\mathrm{d}^3r && (7.130a)\\
&= \int_{\mathfrak{D}} (\boldsymbol{\nabla}\mathfrak{k}^*(\boldsymbol{r}))\Big(\boldsymbol{\nabla}^\top\mathfrak{g}(\boldsymbol{r})\Big)\,\mathrm{d}^3r + \int_{\mathfrak{D}} \mathfrak{k}^*(\boldsymbol{r})\boldsymbol{\nabla}\boldsymbol{\nabla}^\top\mathfrak{g}(\boldsymbol{r})\,\mathrm{d}^3r && (7.130b)\\
&= \int_{\mathfrak{D}} \langle\boldsymbol{\nabla}\mathfrak{k}|\boldsymbol{r}\rangle\Big\langle\boldsymbol{r}\Big|\boldsymbol{\nabla}^\top\mathfrak{g}\Big\rangle\,\mathrm{d}^3r + \int_{\mathfrak{D}} \langle\mathfrak{k}|\boldsymbol{r}\rangle\Big\langle\boldsymbol{r}\Big|\boldsymbol{\nabla}\boldsymbol{\nabla}^\top\mathfrak{g}\Big\rangle\,\mathrm{d}^3r && (7.130c)\\
&= \Big\langle\boldsymbol{\nabla}\mathfrak{k}\Big|\boldsymbol{\nabla}^\top\mathfrak{g}\Big\rangle_{\mathfrak{D}} + \Big\langle\mathfrak{k}\Big|\boldsymbol{\nabla}\boldsymbol{\nabla}^\top\mathfrak{g}\Big\rangle_{\mathfrak{D}}\,, && (7.130d)
\end{aligned}$$

where $\mathfrak{D}$ is a domain and $\partial\mathfrak{D}$ its surface. Furthermore, by interchanging $\mathfrak{k}^*$ and $\mathfrak{g}$

$$\Big\langle\boldsymbol{\nabla}\mathfrak{k}\Big|\boldsymbol{\nabla}^\top\mathfrak{g}\Big\rangle_{\mathfrak{D}}^\top + \Big\langle\boldsymbol{\nabla}\boldsymbol{\nabla}^\top\mathfrak{k}\Big|\mathfrak{g}\Big\rangle_{\mathfrak{D}} = \int_{\partial\mathfrak{D}} \Big[(\boldsymbol{\nabla}\mathfrak{k}^*(\boldsymbol{r}))\hat{\boldsymbol{n}}^\top\Big]^\top\mathfrak{g}(\boldsymbol{r})\,\mathrm{d}S \qquad (7.131)$$

can be implied [294].

Hellmann–Feynman Terms

Second-order external potential variation

Within the HF contributions (6.64b), only that part of the second-order external-potential variation must be calculated which features a Bloch character of $\mathbf{0}$. Essentially, this is the

Hessian matrix of the external potential. Klüppelberg [88] suggests an algorithm for this quantity, based on the Weinert [64] method for computing the Coulomb potential. Although it enables us to generate a continuous quantity, this non-linear variation is still unemployable.

No subtraction of trace

After I have programmed it, we are able to give two reasons why the numerical results are inadequate and conceptual tests fail. The first one concerns the pseudo-density, which is utilized for the second-order external-potential variation. Basically, it is given by setting $\boldsymbol{q}$ equal to zero in equation (6.58). But, comparing this pseudo-density with that of the external potential gradient in equation (6.28), which is transposed and undergoes an outer product with $\mathrm{i}\boldsymbol{G}$, fails. I found in a numerical experiment that this can be overcome with omitting the subtraction of the trace, by analogy with the discussion around the optimized pseudo-density (7.120) of the second-order ion–ion-interaction variation. Likewise, for this external-potential variation we have not been able yet to analytically explain this numerical finding [127, 251, 256, 261].

Decisive drawback stimulating the reformulation

While the aforementioned error can in principle be numerically rectified, another one in the MT spheres cannot, representing the second and main reason for the reformulation hereinafter. In a test, the Hessian matrix of the external potential in the MT spheres has been calculated in two ways. On the one hand with the Weinert-based approach of Klüppelberg, and on the other hand by employing the numerical gradient of a MT function [127, 251]. This is analogous to test 15, in which the gradient instead of the Hessian matrix is used. Both applying the numerical gradient once to the transposed version of equation (6.32), and an outer product of two numerical gradients applied to the unperturbed external potential from `FLEUR` essentially lead to the same result. Comparing it moreover with the outcome of the Weinert method for the second-order external-potential variation, it is consistent within the expected preciseness [127]. This means considering the aforesaid first reason and regarding to which extent both methods can be compared (continuity at the MT sphere boundary) [127]. However, reviewing the Hessian matrix of the external potential, it becomes obvious that its trace equals the application of the Laplacian operator Δ to the unperturbed external potential. Moreover, from the Poisson equation it is known that $\boldsymbol{r} = \boldsymbol{0}$ (conform with the center of the MT sphere) is absolutely relevant. But, due to the discrete *logarithmic* MT mesh points employed, $r_{\nu\gamma} = 0$ is never included[29]. Hence, the main contribution of $\underline{V}^{(2)}_{\text{ext}}$ cannot be exactly calculated [127]. This motivated me to search for a relation allowing for reformulating the integrals such that the Hessian matrix of the external potential is avoided (as anticipated in chapter 6). In fact, this requires a variation of the divergence theorem which is suited for integrals incorporating outer products. It is given by the right-hand side of equation (7.130b) equaling the left-hand side in equation (7.130a). Applying it to the next to last line of equation (7.126b), while the IR and the respective MT spheres are separate connected domains, reads

$$\begin{aligned}&\int_{\text{IR}} \rho^{(0)}_{\text{IR}}(\boldsymbol{r})\boldsymbol{\nabla}\boldsymbol{\nabla}^{\top}V^{(0)\text{IR}}_{\text{ext}}(\boldsymbol{r})\,\mathrm{d}^3r + \sum_{\gamma}\int_{\gamma}\rho^{(0)}_{\gamma}(\boldsymbol{r})\boldsymbol{\nabla}\boldsymbol{\nabla}^{\top}V^{(0)\gamma}_{\text{ext}}(\boldsymbol{r})\,\mathrm{d}^3r \\ &= -\int_{\text{IR}}\Big(\boldsymbol{\nabla}\rho^{(0)}_{\text{IR}}(\boldsymbol{r})\Big)\boldsymbol{\nabla}^{\top}V^{(0)\text{IR}}_{\text{ext}}(\boldsymbol{r})\,\mathrm{d}^3r - \sum_{\gamma}\int_{\gamma}\Big(\boldsymbol{\nabla}\rho^{(0)}_{\gamma}(\boldsymbol{r})\Big)\boldsymbol{\nabla}^{\top}V^{(0)\gamma}_{\text{ext}}(\boldsymbol{r})\,\mathrm{d}^3r\end{aligned} \tag{7.132}$$

---

[29] In reality, the core electrons screen the core and lead to a non-diverging Yukawa potential for distances smaller than about $1 \cdot 10^{-5}\,a_0$ [119, 127]. In the DFT, the $^1/_r$ potential is assumed, which must be coped with, because it and its variations diverge at the core [119, 127, 251].

$$+\sum_{\gamma}\oint_{\gamma}\hat{\boldsymbol{r}}\rho_{\gamma}^{(0)}(\boldsymbol{r})\boldsymbol{\nabla}^{\top}V_{\text{ext}}^{(0)\gamma}(\boldsymbol{r})\,\mathrm{d}S-\oint_{\text{IR}}\hat{\boldsymbol{r}}\rho_{\text{IR}}^{(0)}(\boldsymbol{r})\boldsymbol{\nabla}^{\top}V_{\text{ext}}^{(0)\text{IR}}(\boldsymbol{r})\,\mathrm{d}S\ .$$

Valence-Electron Pulay and Surface Correction Terms

Reasons why reformulation urges

The last lines of equations (7.128b), (7.128c), and (7.128d) comprise outer products of two gradients. Although gradients or Hessian matrices of Kohn–Sham wave functions do not regularly feature a very large absolute value at the core, they can still be numerically imprecise. Furthermore, implementing them is a tremendous challenge, since test scenarios are hard to find, and the MT basis functions are differentiated with a numerical MT gradient subroutine, similar to that in section 7.2.1. It must be emphasized that the gradient connects contributions from the orbital quantum number l with the neighboring channels $l \pm 1$. For a Hessian matrix, a channel l influences all channels from $l-2$ to $l+2$. Additionally, there are the magnetic quantum numbers and the three displacement directions to be considered. But, as can be deduced for instance from section 7.4.3, evaluating matrix elements requires summing the right combinations of orbital and magnetic quantum numbers. If gradients or Hessian matrices are involved, both the information from which channel one contribution stems and to which channels it is distributed must be stored [251]. I have programmed our implementation [251] of these matrix elements and we have developed tests based on the product rule [127, 251]. For example, the numerically calculated Hessian matrix of the charge density has been compared to a sum of differentiated wave-function overlaps, incorporating amongst others Hessian matrices of wave functions [127]. The numerical performance of these tests has not been satisfying. Apart from that, this test only covers a simple scenario. In the worst case, the kinetic energy operator applied to a Hessian matrix of a wave function implies fourfold derivatives of Kohn–Sham wave functions, which are only continuous up to linear order. All in all, handling the outer product of two gradients is at least numerically demanding. This stimulated me to rearrange the terms so that the Hessian matrices of Kohn–Sham wave functions are circumvented.

Auxiliary relation

For preparing the main derivation, the auxiliary relation

$$\sum_{\boldsymbol{k},n} f_{\boldsymbol{k},n}^{(0)}\Bigg(\left\langle\vec{\Psi}_{\boldsymbol{k},n}^{(0)\alpha}\middle|\boldsymbol{\nabla}\boldsymbol{\nabla}^{\top}\mathscr{V}_{\text{eff}}^{(0)}\middle|\vec{\Psi}_{\boldsymbol{k},n}^{(0)\alpha}\right\rangle_{\alpha}+\left\langle\vec{\Psi}_{\boldsymbol{k},n}^{(0)\alpha}\middle|\boldsymbol{\nabla}\mathscr{V}_{\text{eff}}^{(0)}\middle|\boldsymbol{\nabla}^{\top}\vec{\Psi}_{\boldsymbol{k},n}^{(0)\alpha}\right\rangle_{\alpha} \tag{7.133a}$$

$$+\left\langle\vec{\Psi}_{\boldsymbol{k},n}^{(0)\alpha}\middle|\boldsymbol{\nabla}\mathscr{V}_{\text{eff}}^{(0)}\middle|\boldsymbol{\nabla}^{\top}\vec{\Psi}_{\boldsymbol{k},n}^{(0)\alpha}\right\rangle_{\alpha}^{\top}\Bigg)$$

$$=\int_{\alpha}\rho_{\alpha,\text{v}}^{(0)}(\boldsymbol{r})\boldsymbol{\nabla}\boldsymbol{\nabla}^{\top}V_{\text{eff}}^{(0)\alpha}(\boldsymbol{r})\,\mathrm{d}^{3}r+\frac{1}{2}\int_{\alpha}\Big(\boldsymbol{\nabla}V_{\text{eff}}^{(0)\alpha}(\boldsymbol{r})\boldsymbol{\nabla}^{\top}\rho_{\alpha,\text{v}}^{(0)}(\boldsymbol{r})+\boldsymbol{\nabla}\rho_{\alpha,\text{v}}^{(0)}(\boldsymbol{r})\boldsymbol{\nabla}^{\top}V_{\text{eff}}^{(0)\alpha}(\boldsymbol{r})\Big)\,\mathrm{d}^{3}r$$

$$=\int_{\alpha}\rho_{\alpha,\text{v}}^{(0)}(\boldsymbol{r})\boldsymbol{\nabla}\boldsymbol{\nabla}^{\top}V_{\text{eff}}^{(0)\alpha}(\boldsymbol{r})\,\mathrm{d}^{3}r+\int_{\alpha}\boldsymbol{\nabla}\rho_{\alpha,\text{v}}^{(0)}(\boldsymbol{r})\boldsymbol{\nabla}^{\top}V_{\text{eff}}^{(0)\alpha}(\boldsymbol{r})\,\mathrm{d}^{3}r \tag{7.133b}$$

$$=\oint_{\partial\alpha}\hat{\boldsymbol{r}}\rho_{\alpha,\text{v}}^{(0)}(\boldsymbol{r})\boldsymbol{\nabla}^{\top}V_{\text{eff}}^{(0)\alpha}(\boldsymbol{r})\,\mathrm{d}S \tag{7.133c}$$

is necessary. Evaluating the sums on the left-hand side of equation (7.133a), the valence-electron density and its gradient (regular and transposed) can be identified. According to equation (7.123f) furthermore, terms within the dynamical matrix can always be substituted by their adjoint version with interchanged indices α and β. Assuming $\alpha = \beta$ here, interchanging these atom indices is not required. Moreover, it suffices to replace by a transposed version instead of an adjoint one, provided only real quantities are involved (e.g. the charge density and the effective potential). Hence, the second integral on the right-hand side of equation (7.133a) can be substituted by its transposed version and summarized with its succeeding term. In the last step (7.133c), the equivalence of equations (7.130a) and (7.130b) is utilized, by analogy with equation (7.132).

Reformulation

For the main part, the left-hand side of equation (7.130a) and the right-hand side of equation (7.130d) are necessary, while

$$\mathfrak{k} = \vec{\varPsi}^{(0)\alpha}_{\boldsymbol{k},n} \;, \qquad \mathfrak{g} = \Big(\mathscr{H}^{(0)} - \epsilon^{(0)}_{\boldsymbol{k},n}\Big)\vec{\varPsi}^{(0)\alpha}_{\boldsymbol{k},n} \;. \tag{7.134}$$

This yields

$$\begin{aligned}&\sum_{\boldsymbol{k},n} f^{(0)}_{\boldsymbol{k},n}\Bigg(\Big\langle \boldsymbol{\nabla}\vec{\varPsi}^{(0)\alpha}_{\boldsymbol{k},n}\Big|\boldsymbol{\nabla}^{\top}\Big(\mathscr{H}^{(0)} - \epsilon^{(0)}_{\boldsymbol{k},n}\Big)\vec{\varPsi}^{(0)\alpha}_{\boldsymbol{k},n}\Big\rangle_{\alpha} + \Big\langle \vec{\varPsi}^{(0)\alpha}_{\boldsymbol{k},n}\Big|\boldsymbol{\nabla}\boldsymbol{\nabla}^{\top}\Big(\mathscr{H}^{(0)} - \epsilon^{(0)}_{\boldsymbol{k},n}\Big)\vec{\varPsi}^{(0)}_{\boldsymbol{k},n}\Big\rangle_{\alpha}\Bigg) \\ &= \sum_{\boldsymbol{k}n} f^{(0)}_{\boldsymbol{k},n}\oint_{\partial\alpha}\hat{\boldsymbol{r}}\,\vec{\varPsi}^{*(0)\alpha}_{\boldsymbol{k},n}(\boldsymbol{r})\boldsymbol{\nabla}^{\top}\Big(\mathscr{H}^{(0)} - \epsilon^{(0)}_{\boldsymbol{k},n}\Big)\vec{\varPsi}^{(0)\alpha}_{\boldsymbol{k},n}(\boldsymbol{r})\,\mathrm{d}S \;.\end{aligned} \tag{7.135a}$$

Applying then the product rule and exploiting the Schwarz theorem reads

$$\begin{aligned}&\sum_{\boldsymbol{k},n} f^{(0)}_{\boldsymbol{k},n}\Bigg(\Big\langle \boldsymbol{\nabla}\vec{\varPsi}^{(0)\alpha}_{\boldsymbol{k},n}\Big|\boldsymbol{\nabla}^{\top}\mathscr{V}^{(0)}_{\text{eff}}\Big|\vec{\varPsi}^{(0)\alpha}_{\boldsymbol{k},n}\Big\rangle_{\alpha} + \Big\langle \boldsymbol{\nabla}\vec{\varPsi}^{(0)\alpha}_{\boldsymbol{k},n}\Big|\mathscr{H}^{(0)} - \epsilon^{(0)}_{\boldsymbol{k},n}\Big|\boldsymbol{\nabla}^{\top}\vec{\varPsi}^{(0)\alpha}_{\boldsymbol{k},n}\Big\rangle_{\alpha} \\ &\qquad + \Big\langle \vec{\varPsi}^{(0)\alpha}_{\boldsymbol{k},n}\Big|\boldsymbol{\nabla}\boldsymbol{\nabla}^{\top}\mathscr{V}^{(0)}_{\text{eff}}\Big|\vec{\varPsi}^{(0)\alpha}_{\boldsymbol{k},n}\Big\rangle_{\alpha} + \Big\langle \vec{\varPsi}^{(0)\alpha}_{\boldsymbol{k},n}\Big|\boldsymbol{\nabla}\mathscr{V}^{(0)}_{\text{eff}}\Big|\boldsymbol{\nabla}^{\top}\vec{\varPsi}^{(0)\alpha}_{\boldsymbol{k},n}\Big\rangle_{\alpha} \\ &\qquad + \Big\langle \vec{\varPsi}^{(0)\alpha}_{\boldsymbol{k},n}\Big|\boldsymbol{\nabla}\mathscr{V}^{(0)}_{\text{eff}}\Big|\boldsymbol{\nabla}^{\top}\vec{\varPsi}^{(0)\alpha}_{\boldsymbol{k},n}\Big\rangle^{\top}_{\alpha} + \Big\langle \vec{\varPsi}^{(0)\alpha}_{\boldsymbol{k},n}\Big|\Big(\mathscr{H}^{(0)} - \epsilon^{(0)}_{\boldsymbol{k},n}\Big)\Big|\boldsymbol{\nabla}\boldsymbol{\nabla}^{\top}\vec{\varPsi}^{(0)\alpha}_{\boldsymbol{k},n}\Big\rangle_{\alpha}\Bigg) \\ &= \sum_{\boldsymbol{k},n} f^{(0)}_{\boldsymbol{k},n}\Bigg(\oint_{\partial\alpha}\hat{\boldsymbol{r}}\,\vec{\varPsi}^{*(0)\alpha}_{\boldsymbol{k},n}(\boldsymbol{r})\Big(\boldsymbol{\nabla}^{\top}\mathscr{V}^{(0)}_{\text{eff}}\Big)\vec{\varPsi}^{(0)\alpha}_{\boldsymbol{k},n}(\boldsymbol{r})\,\mathrm{d}S \\ &\qquad + \oint_{\partial\alpha}\hat{\boldsymbol{r}}\,\vec{\varPsi}^{*(0)\alpha}_{\boldsymbol{k},n}(\boldsymbol{r})\Big(\mathscr{H}^{(0)} - \epsilon^{(0)}_{\boldsymbol{k},n}\Big)\boldsymbol{\nabla}^{\top}\vec{\varPsi}^{(0)\alpha}_{\boldsymbol{k},n}(\boldsymbol{r})\,\mathrm{d}S\Bigg) \;.\end{aligned} \tag{7.135b}$$

By using the relation (7.133), the previous step can be simplified to

$$\begin{aligned}&\frac{1}{2}\int \boldsymbol{\nabla}\rho^{(0)}_{\alpha,\mathrm{v}}(\boldsymbol{r})\boldsymbol{\nabla}^{\top}V^{(0)\alpha}_{\text{eff}}(\boldsymbol{r})\,\mathrm{d}^3 r + \oint_{\partial\alpha}\hat{\boldsymbol{r}}\rho^{(0)}_{\alpha,\mathrm{v}}(\boldsymbol{r})\boldsymbol{\nabla}^{\top}V^{(0)\alpha}_{\text{eff}}(\boldsymbol{r})\,\mathrm{d}S \\ &\quad + \sum_{\boldsymbol{k},n} f^{(0)}_{\boldsymbol{k},n}\Bigg(\Big\langle \boldsymbol{\nabla}\vec{\varPsi}^{(0)\alpha}_{\boldsymbol{k},n}\Big|\mathscr{H}^{(0)} - \epsilon^{(0)}_{\boldsymbol{k},n}\Big|\boldsymbol{\nabla}^{\top}\vec{\varPsi}^{(0)\alpha}_{\boldsymbol{k},n}\Big\rangle_{\alpha} + \Big\langle \vec{\varPsi}^{(0)\alpha}_{\boldsymbol{k},n}\Big|\Big(\mathscr{H}^{(0)} - \epsilon^{(0)}_{\boldsymbol{k},n}\Big)\Big|\boldsymbol{\nabla}\boldsymbol{\nabla}^{\top}\vec{\varPsi}^{(0)\alpha}_{\boldsymbol{k},n}\Big\rangle_{\alpha}\Bigg) \\ &= \oint_{\partial\alpha}\hat{\boldsymbol{r}}\rho^{(0)}_{\alpha,\mathrm{v}}(\boldsymbol{r})\boldsymbol{\nabla}^{\top}V^{(0)\alpha}_{\text{eff}}(\boldsymbol{r})\,\mathrm{d}S + \sum_{\boldsymbol{k},n} f^{(0)}_{\boldsymbol{k},n}\oint_{\partial\alpha}\hat{\boldsymbol{r}}\,\vec{\varPsi}^{*(0)\alpha}_{\boldsymbol{k},n}(\boldsymbol{r})\Big(\mathscr{H}^{(0)} - \epsilon^{(0)}_{\boldsymbol{k},n}\Big)\boldsymbol{\nabla}^{\top}\vec{\varPsi}^{(0)\alpha}_{\boldsymbol{k},n}(\boldsymbol{r})\,\mathrm{d}S \;,\end{aligned} \tag{7.135c}$$

a rearrangement of which finally leads to

$$\begin{aligned}&\sum_{\boldsymbol{k},n} f^{(0)}_{\boldsymbol{k},n}\Big\langle \vec{\varPsi}^{(0)\alpha}_{\boldsymbol{k},n}\Big|\Big(\mathscr{H}^{(0)} - \epsilon^{(0)}_{\boldsymbol{k},n}\Big)\Big|\boldsymbol{\nabla}\boldsymbol{\nabla}^{\top}\vec{\varPsi}^{(0)\alpha}_{\boldsymbol{k},n}\Big\rangle_{\alpha} \\ &= -\frac{1}{2}\int \boldsymbol{\nabla}\rho^{(0)}_{\alpha,\mathrm{v}}(\boldsymbol{r})\boldsymbol{\nabla}^{\top}V^{(0)\alpha}_{\text{eff}}(\boldsymbol{r})\,\mathrm{d}^3 r - \sum_{\boldsymbol{k},n} f^{(0)}_{\boldsymbol{k},n}\Big\langle \boldsymbol{\nabla}\vec{\varPsi}^{(0)\alpha}_{\boldsymbol{k},n}\Big|\mathscr{H}^{(0)} - \epsilon^{(0)}_{\boldsymbol{k},n}\Big|\boldsymbol{\nabla}^{\top}\vec{\varPsi}^{(0)\alpha}_{\boldsymbol{k},n}\Big\rangle_{\alpha} \\ &\quad + \sum_{\boldsymbol{k},n} f^{(0)}_{\boldsymbol{k},n}\oint_{\partial\alpha}\hat{\boldsymbol{r}}\,\vec{\varPsi}^{*(0)\alpha}_{\boldsymbol{k},n}(\boldsymbol{r})\Big(\mathscr{H}^{(0)} - \epsilon^{(0)}_{\boldsymbol{k},n}\Big)\boldsymbol{\nabla}^{\top}\vec{\varPsi}^{(0)\alpha}_{\boldsymbol{k},n}(\boldsymbol{r})\,\mathrm{d}S \;.\end{aligned} \tag{7.135d}$$

Inserting analogously the definitions (7.134) into (7.131) implies

$$\begin{aligned}
&\sum_{\boldsymbol{k}n} f^{(0)}_{\boldsymbol{k},n}\left(\left\langle \boldsymbol{\nabla}\vec{\varPsi}^{(0)\alpha}_{\boldsymbol{k},n}\middle|\boldsymbol{\nabla}^{\top}\left(\mathscr{H}^{(0)}-\epsilon^{(0)}_{\boldsymbol{k},n}\right)\vec{\varPsi}^{(0)\alpha}_{\boldsymbol{k},n}\right\rangle_{\alpha}^{\top}+\left\langle \boldsymbol{\nabla}\boldsymbol{\nabla}^{\top}\vec{\varPsi}^{(0)\alpha}_{\boldsymbol{k},n}\middle|\left(\mathscr{H}^{(0)}-\epsilon^{(0)}_{\boldsymbol{k},n}\right)\vec{\varPsi}^{(0)\alpha}_{\boldsymbol{k},n}\right\rangle_{\alpha}\right)\\
&=\sum_{\boldsymbol{k},n} f^{(0)}_{\boldsymbol{k},n}\oint_{\partial\alpha}\hat{\boldsymbol{r}}\left(\boldsymbol{\nabla}^{\top}\vec{\varPsi}^{*(0)\alpha}_{\boldsymbol{k},n}(\boldsymbol{r})\right)\left(\mathscr{H}^{(0)}-\epsilon^{(0)}_{\boldsymbol{k},n}\right)\vec{\varPsi}^{(0)\alpha}_{\boldsymbol{k},n}(\boldsymbol{r})\,\mathrm{d}S\ . \qquad (7.136\text{a})
\end{aligned}$$

Applying then the product rule reads

$$\begin{aligned}
&\sum_{\boldsymbol{k},n} f^{(0)}_{\boldsymbol{k},n}\left(\left\langle \boldsymbol{\nabla}\vec{\varPsi}^{(0)\alpha}_{\boldsymbol{k},n}\middle|\boldsymbol{\nabla}^{\top}\mathscr{V}^{(0)}_{\text{eff}}\middle|\vec{\varPsi}^{(0)\alpha}_{\boldsymbol{k},n}\right\rangle_{\alpha}^{\top}+\left\langle \boldsymbol{\nabla}\vec{\varPsi}^{(0)\alpha}_{\boldsymbol{k},n}\middle|\mathscr{H}^{(0)}-\epsilon^{(0)}_{\boldsymbol{k},n}\middle|\boldsymbol{\nabla}^{\top}\vec{\varPsi}^{(0)\alpha}_{\boldsymbol{k},n}\right\rangle_{\alpha}^{\top}\right. \qquad (7.136\text{b})\\
&\left.+\left\langle \boldsymbol{\nabla}\boldsymbol{\nabla}^{\top}\vec{\varPsi}^{(0)\alpha}_{\boldsymbol{k},n}\middle|\left(\mathscr{H}^{(0)}-\epsilon^{(0)}_{\boldsymbol{k},n}\right)\middle|\vec{\varPsi}^{(0)\alpha}_{\boldsymbol{k},n}\right\rangle_{\alpha}\right)\\
&=\sum_{\boldsymbol{k},n} f^{(0)}_{\boldsymbol{k},n}\oint_{\partial\alpha}\hat{\boldsymbol{r}}\left(\boldsymbol{\nabla}^{\top}\vec{\varPsi}^{*(0)\alpha}_{\boldsymbol{k},n}(\boldsymbol{r})\right)\left(\mathscr{H}^{(0)}-\epsilon^{(0)}_{\boldsymbol{k},n}\right)\vec{\varPsi}^{(0)\alpha}_{\boldsymbol{k},n}(\boldsymbol{r})\,\mathrm{d}S\ .
\end{aligned}$$

Now, only the first term is summed over the $\boldsymbol{k}$-points and bands n so that

$$\begin{aligned}
&\frac{1}{2}\int_{\alpha}\boldsymbol{\nabla}V^{(0)\alpha}_{\text{eff}}(\boldsymbol{r})\boldsymbol{\nabla}^{\top}\rho^{(0)}_{\alpha,\text{v}}(\boldsymbol{r})\,\mathrm{d}^3r \qquad (7.136\text{c})\\
&+\sum_{\boldsymbol{k},n} f^{(0)}_{\boldsymbol{k},n}\left(\left\langle \boldsymbol{\nabla}\vec{\varPsi}^{(0)\alpha}_{\boldsymbol{k},n}\middle|\mathscr{H}^{(0)}-\epsilon^{(0)}_{\boldsymbol{k},n}\middle|\boldsymbol{\nabla}^{\top}\vec{\varPsi}^{(0)\alpha}_{\boldsymbol{k},n}\right\rangle_{\alpha}^{\top}+\left\langle \boldsymbol{\nabla}\boldsymbol{\nabla}^{\top}\vec{\varPsi}^{(0)\alpha}_{\boldsymbol{k},n}\middle|\left(\mathscr{H}^{(0)}-\epsilon^{(0)}_{\boldsymbol{k},n}\right)\middle|\vec{\varPsi}^{(0)\alpha}_{\boldsymbol{k},n}\right\rangle_{\alpha}\right)\\
&=\sum_{\boldsymbol{k},n} f^{(0)}_{\boldsymbol{k},n}\oint_{\partial\alpha}\hat{\boldsymbol{r}}\left(\boldsymbol{\nabla}^{\top}\vec{\varPsi}^{*(0)\alpha}_{\boldsymbol{k},n}(\boldsymbol{r})\right)\left(\mathscr{H}^{(0)}-\epsilon^{(0)}_{\boldsymbol{k},n}\right)\vec{\varPsi}^{(0)\alpha}_{\boldsymbol{k},n}(\boldsymbol{r})\,\mathrm{d}S\ .
\end{aligned}$$

Substituting the first and second term by their adjoint complement and rewriting leads to

$$\begin{aligned}
&\sum_{\boldsymbol{k},n} f^{(0)}_{\boldsymbol{k},n}\left\langle \boldsymbol{\nabla}\boldsymbol{\nabla}^{\top}\vec{\varPsi}^{(0)\alpha}_{\boldsymbol{k},n}\middle|\left(\mathscr{H}^{(0)}-\epsilon^{(0)}_{\boldsymbol{k},n}\right)\middle|\vec{\varPsi}^{(0)\alpha}_{\boldsymbol{k},n}\right\rangle_{\alpha} \qquad (7.136\text{d})\\
&=-\frac{1}{2}\int\boldsymbol{\nabla}\rho^{(0)}_{\alpha,\text{v}}(\boldsymbol{r})\boldsymbol{\nabla}^{\top}V^{(0)\alpha}_{\text{eff}}(\boldsymbol{r})\,\mathrm{d}^3r-\sum_{\boldsymbol{k},n} f^{(0)}_{\boldsymbol{k},n}\left\langle \boldsymbol{\nabla}\vec{\varPsi}^{(0)\alpha}_{\boldsymbol{k},n}\middle|\mathscr{H}^{(0)}-\epsilon^{(0)}_{\boldsymbol{k},n}\middle|\boldsymbol{\nabla}^{\top}\vec{\varPsi}^{(0)\alpha}_{\boldsymbol{k},n}\right\rangle_{\alpha}\\
&+\sum_{\boldsymbol{k}n} f^{(0)}_{\boldsymbol{k},n}\oint_{\partial\alpha}\hat{\boldsymbol{r}}\left(\boldsymbol{\nabla}^{\top}\vec{\varPsi}^{*(0)\alpha}_{\boldsymbol{k},n}(\boldsymbol{r})\right)\left(\mathscr{H}^{(0)}-\epsilon^{(0)}_{\boldsymbol{k},n}\right)\vec{\varPsi}^{(0)\alpha}_{\boldsymbol{k},n}(\boldsymbol{r})\,\mathrm{d}S\ .
\end{aligned}$$

Adding (7.135d) and (7.136d) then implies

$$\begin{aligned}
&\sum_{\boldsymbol{k},n} f^{(0)}_{\boldsymbol{k},n}\left\langle \vec{\varPsi}^{(0)\alpha}_{\boldsymbol{k},n}\middle|\left(\mathscr{H}^{(0)}-\epsilon^{(0)}_{\boldsymbol{k},n}\right)\middle|\boldsymbol{\nabla}\boldsymbol{\nabla}^{\top}\vec{\varPsi}^{(0)\alpha}_{\boldsymbol{k},n}\right\rangle_{\alpha}+\sum_{\boldsymbol{k},n} f^{(0)}_{\boldsymbol{k},n}\left\langle \boldsymbol{\nabla}\boldsymbol{\nabla}^{\top}\vec{\varPsi}^{(0)\alpha}_{\boldsymbol{k},n}\middle|\left(\mathscr{H}^{(0)}-\epsilon^{(0)}_{\boldsymbol{k},n}\right)\middle|\vec{\varPsi}^{(0)\alpha}_{\boldsymbol{k},n}\right\rangle_{\alpha}\\
&=-\int_{\alpha}\boldsymbol{\nabla}\rho^{(0)}_{\alpha,\text{v}}(\boldsymbol{r})\boldsymbol{\nabla}^{\top}V^{(0)\alpha}_{\text{eff}}(\boldsymbol{r})\,\mathrm{d}^3r-2\sum_{\boldsymbol{k},n} f^{(0)}_{\boldsymbol{k},n}\left\langle \boldsymbol{\nabla}\vec{\varPsi}^{(0)\alpha}_{\boldsymbol{k},n}\middle|\mathscr{H}^{(0)}-\epsilon^{(0)}_{\boldsymbol{k},n}\middle|\boldsymbol{\nabla}^{\top}\vec{\varPsi}^{(0)\alpha}_{\boldsymbol{k},n}\right\rangle_{\alpha}\\
&+\sum_{\boldsymbol{k},n} f^{(0)}_{\boldsymbol{k},n}\oint_{\partial\alpha}\left(\boldsymbol{\nabla}\vec{\varPsi}^{*(0)\alpha}_{\boldsymbol{k},n}(\boldsymbol{r})\right)\left(\mathscr{H}^{(0)}-\epsilon^{(0)}_{\boldsymbol{k},n}\right)\vec{\varPsi}^{(0)\alpha}_{\boldsymbol{k},n}(\boldsymbol{r})\hat{\boldsymbol{r}}^{\top}\,\mathrm{d}S\\
&+\sum_{\boldsymbol{k},n} f^{(0)}_{\boldsymbol{k},n}\oint_{\partial\alpha}\hat{\boldsymbol{r}}\,\vec{\varPsi}^{*(0)\alpha}_{\boldsymbol{k},n}(\boldsymbol{r})\left(\mathscr{H}^{(0)}-\epsilon^{(0)}_{\boldsymbol{k},n}\right)\boldsymbol{\nabla}^{\top}\vec{\varPsi}^{(0)\alpha}_{\boldsymbol{k},n}(\boldsymbol{r})\,\mathrm{d}S\ . \qquad (7.137)
\end{aligned}$$

In a nutshell, equation (7.137) means that we can neglect the terms with tensor gradients in the last line of equations (7.128b), (7.128c), and (7.128d). But we must add the two surface integrals from equations (7.137) to (7.129). Moreover, the volume integral in equation (7.137), incorporating the gradients of the valence density and the unperturbed effective potential, must be summed with equation (7.127b).

Core-Electron Pulay Correction Terms

Neglecting relativism

Core-electron wave functions are normally pointwise solutions of the Dirac equation in `FLEUR` [127]. However, in our opinion, it seems that the Pulay corrections for the core-electrons by Klüppelberg [88]

$$\begin{aligned}&\underline{D}^{\beta\alpha}_{\text{Pl,c}} \\ &= \delta_{\beta\alpha}\sum_{\mathfrak{p}}\left(2\left\langle\Psi^{(1)}_{\mathfrak{p}}\middle|\mathscr{H}^{(0)}-\epsilon^{(0)}_{\mathfrak{p}}\middle|\Psi^{(1)}_{\mathfrak{p}}\right\rangle_{\alpha}+\left\langle\Psi^{(0)}_{\mathfrak{p}}\middle|\mathscr{H}^{(0)}-\epsilon^{(0)}_{\mathfrak{p}}\middle|\Psi^{(2)}_{\mathfrak{p}}\right\rangle_{\alpha}+\left\langle\Psi^{(2)}_{\mathfrak{p}}\middle|\mathscr{H}^{(0)}-\epsilon^{(0)}_{\mathfrak{p}}\middle|\Psi^{(0)}_{\mathfrak{p}}\right\rangle_{\alpha}\right)\end{aligned} \tag{7.138}$$

are based on the non-relativistic Schrödinger equation. For light elements, it is legitimate to neglect relativistic corrections. So in a first implementation, we decided to postpone their thorough analysis and increase the variable, storing the speed of light, both in `juPhon` and `FLEUR` by a factor of 10^3 [119, 127, 251]. Consequently, relativistic corrections become less relevant. Furthermore, this dissertation focusses on systems with a monoatomic lattice basis. Thus, there is one MT sphere per unit cell, and it is displaced.

Correction of Klüppelberg [88]

In my opinion, the further reformulation of equation (7.138) by Klüppelberg contains errors. So, I suggest rearranging this equation in the following way: since the core-electron wave functions are pointwise solutions, their variation, in particular within the frozen-core approximation, is simply [251]

$$\left|\Psi^{(1)}_{\mathfrak{p}}\right\rangle \equiv \left|\boldsymbol{\nabla}\Psi^{(0)}_{\mathfrak{p}}\right\rangle, \qquad \left|\Psi^{(2)}_{\mathfrak{p}}\right\rangle \equiv \left|\boldsymbol{\nabla}\boldsymbol{\nabla}^{\top}\Psi^{(0)}_{\mathfrak{p}}\right\rangle. \tag{7.139}$$

As a consequence, the Hamiltonian is self-adjoint [88]. Then, equation (7.138) reads

$$\begin{aligned}\underline{D}^{\beta\alpha}_{\text{Pl,c}} = \delta_{\beta\alpha}\sum_{\mathfrak{p}}\Bigg[2\left\langle\boldsymbol{\nabla}\Psi^{(0)}_{\mathfrak{p}}\middle|\mathscr{H}^{(0)}-\epsilon^{(0)}_{\mathfrak{p}}\middle|\boldsymbol{\nabla}^{\top}\Psi^{(0)}_{\mathfrak{p}}\right\rangle_{\alpha}&+\left\langle\Psi^{(0)}_{\mathfrak{p}}\middle|\mathscr{H}^{(0)}-\epsilon^{(0)}_{\mathfrak{p}}\middle|\boldsymbol{\nabla}\boldsymbol{\nabla}^{\top}\Psi^{(0)}_{\mathfrak{p}}\right\rangle_{\alpha} \\ &+\left\langle\boldsymbol{\nabla}\boldsymbol{\nabla}^{\top}\Psi^{(0)}_{\mathfrak{p}}\middle|\mathscr{H}^{(0)}-\epsilon^{(0)}_{\mathfrak{p}}\middle|\Psi^{(0)}_{\mathfrak{p}}\right\rangle_{\alpha}\Bigg].\end{aligned} \tag{7.140a}$$

If the Hamiltonian acts on the bra in the second term or on the ket in the third term, only the non-spherical part of the potential remains

$$\left\langle\Psi^{(0)}_{\mathfrak{p}}\right|\left(\mathscr{H}^{(0)}_{\text{sph}}-\epsilon^{(0)}_{\mathfrak{p}}\right)=0=\left(\mathscr{H}^{(0)}_{\text{sph}}-\epsilon^{(0)}_{\mathfrak{p}}\right)\left|\Psi^{(0)}_{\mathfrak{p}}\right\rangle \tag{7.140b}$$

because the spherical part of the Hamiltonian results in the eigenenergy so that

$$\begin{aligned}\underline{D}^{\beta\alpha}_{\text{Pl,c}} = \delta_{\beta\alpha}\sum_{\mathfrak{p}}\Bigg[2\left\langle\boldsymbol{\nabla}\Psi^{(0)}_{\mathfrak{p}}\middle|\mathscr{H}^{(0)}-\epsilon^{(0)}_{\mathfrak{p}}\middle|\boldsymbol{\nabla}^{\top}\Psi^{(0)}_{\mathfrak{p}}\right\rangle_{\alpha}&+\left\langle\Psi^{(0)}_{\mathfrak{p}}\middle|\mathscr{V}^{(0)}_{\text{eff, nsph}}\middle|\boldsymbol{\nabla}\boldsymbol{\nabla}^{\top}\Psi^{(0)}_{\mathfrak{p}}\right\rangle_{\alpha} \\ &+\left\langle\boldsymbol{\nabla}\boldsymbol{\nabla}^{\top}\Psi^{(0)}_{\mathfrak{p}}\middle|\mathscr{V}^{(0)}_{\text{eff, nsph}}\middle|\Psi^{(0)}_{\mathfrak{p}}\right\rangle_{\alpha}\Bigg].\end{aligned} \tag{7.140c}$$

By analogy with a procedure suggested by Klüppelberg [88] for valence electrons, a gradient is applied to the Schrödinger equation of the core-electrons reading

$$\left\langle\boldsymbol{\nabla}\Psi^{(0)}_{\mathfrak{p}}\right|\mathscr{H}^{(0)}_{\text{sph}}=\left\langle\boldsymbol{\nabla}\Psi^{(0)}_{\mathfrak{p}}\right|\epsilon^{(0)}_{\mathfrak{p}}-\left\langle\Psi^{(0)}_{\mathfrak{p}}\right|\boldsymbol{\nabla}\mathscr{V}^{(0)}_{\text{eff, sph}} \tag{7.141a}$$

$$\mathscr{H}^{(0)}_{\text{sph}}\Big|\boldsymbol{\nabla}^{\top}\varPsi^{(0)}_{\mathfrak{p}}\Big\rangle = \epsilon^{(0)}_{\mathfrak{p}}\Big|\boldsymbol{\nabla}^{\top}\varPsi^{(0)}_{\mathfrak{p}}\Big\rangle - \Big(\boldsymbol{\nabla}^{\top}\mathscr{V}^{(0)}_{\text{eff, sph}}\Big)\Big|\varPsi^{(0)}_{\mathfrak{p}}\Big\rangle\,. \tag{7.141b}$$

Therefore, we can rewrite the matrix element with one gradient per ket and bra as

$$\begin{aligned}
&\Big\langle\boldsymbol{\nabla}\varPsi^{(0)}_{\mathfrak{p}}\Big|\mathscr{H}^{(0)}_{\text{sph}} + \mathscr{V}^{(0)}_{\text{eff, nsph}} - \epsilon^{(0)}_{\mathfrak{p}}\Big|\boldsymbol{\nabla}^{\top}\varPsi^{(0)}_{\mathfrak{p}}\Big\rangle_{\alpha} && (7.141\text{c})\\
&= -\Big\langle\varPsi^{(0)}_{\mathfrak{p}}\Big|\boldsymbol{\nabla}\mathscr{V}^{(0)}_{\text{eff, sph}}\Big|\boldsymbol{\nabla}^{\top}\varPsi^{(0)}_{\mathfrak{p}}\Big\rangle_{\alpha} + \Big\langle\boldsymbol{\nabla}\varPsi^{(0)}_{\mathfrak{p}}\Big|\mathscr{V}^{(0)}_{\text{eff, nsph}}\Big|\boldsymbol{\nabla}^{\top}\varPsi^{(0)}_{\mathfrak{p}}\Big\rangle_{\alpha}\\
&= -\Big\langle\boldsymbol{\nabla}\varPsi^{(0)}_{\mathfrak{p}}\Big|\boldsymbol{\nabla}^{\top}\mathscr{V}^{(0)}_{\text{eff, sph}}\Big|\varPsi^{(0)}_{\mathfrak{p}}\Big\rangle_{\alpha} + \Big\langle\boldsymbol{\nabla}\varPsi^{(0)}_{\mathfrak{p}}\Big|\mathscr{V}^{(0)}_{\text{eff, nsph}}\Big|\boldsymbol{\nabla}^{\top}\varPsi^{(0)}_{\mathfrak{p}}\Big\rangle_{\alpha}\,, && (7.141\text{d})
\end{aligned}$$

and thus

$$\begin{aligned}
&2\Big\langle\boldsymbol{\nabla}\varPsi^{(0)}_{\mathfrak{p}}\Big|\mathscr{H}^{(0)}_{\text{sph}} + \mathscr{V}^{(0)}_{\text{eff, nsph}} - \epsilon^{(0)}_{\mathfrak{p}}\Big|\boldsymbol{\nabla}^{\top}\varPsi^{(0)}_{\mathfrak{p}}\Big\rangle_{\alpha} && (7.141\text{e})\\
&= -\Big\langle\varPsi^{(0)}_{\mathfrak{p}}\Big|\boldsymbol{\nabla}\mathscr{V}^{(0)}_{\text{eff, sph}}\Big|\boldsymbol{\nabla}^{\top}\varPsi^{(0)}_{\mathfrak{p}}\Big\rangle_{\alpha} + \Big\langle\boldsymbol{\nabla}\varPsi^{(0)}_{\mathfrak{p}}\Big|\mathscr{V}^{(0)}_{\text{eff, nsph}}\Big|\boldsymbol{\nabla}^{\top}\varPsi^{(0)}_{\mathfrak{p}}\Big\rangle^{\top}_{\alpha}\\
&\quad -\Big\langle\boldsymbol{\nabla}\varPsi^{(0)}_{\mathfrak{p}}\Big|\boldsymbol{\nabla}^{\top}\mathscr{V}^{(0)}_{\text{eff, sph}}\Big|\varPsi^{(0)}_{\mathfrak{p}}\Big\rangle_{\alpha} + \Big\langle\boldsymbol{\nabla}\varPsi^{(0)}_{\mathfrak{p}}\Big|\mathscr{V}^{(0)}_{\text{eff, nsph}}\Big|\boldsymbol{\nabla}^{\top}\varPsi^{(0)}_{\mathfrak{p}}\Big\rangle_{\alpha}
\end{aligned}$$

holds, where the second term on the right-hand side of the equation can be substituted by its transposed complement (the dynamical matrix is made self-adjoint in the end).

Utilizing equation (7.131) for the third term in (7.140c) implies

$$\begin{aligned}
&\int_{\alpha}\Big(\boldsymbol{\nabla}\boldsymbol{\nabla}^{\top}\varPsi^{*(0)}_{\mathfrak{p}}(\boldsymbol{r})\Big)V^{(0)\alpha}_{\text{eff, nsph}}(\boldsymbol{r})\varPsi^{(0)}_{\mathfrak{p}}(\boldsymbol{r})\,\mathrm{d}^3r && (7.142\text{a})\\
&= -\bigg(\int_{\alpha}\Big(\boldsymbol{\nabla}\varPsi^{*(0)}_{\mathfrak{p}}(\boldsymbol{r})\Big)\boldsymbol{\nabla}^{\top}\Big(V^{(0)\alpha}_{\text{eff, nsph}}(\boldsymbol{r})\varPsi^{(0)}_{\mathfrak{p}}(\boldsymbol{r})\Big)\,\mathrm{d}^3r\bigg)^{\top}\\
&\quad + \oint_{\partial\alpha}\hat{\boldsymbol{r}}\Big(\boldsymbol{\nabla}^{\top}\varPsi^{*(0)}_{\mathfrak{p}}(\boldsymbol{r})\Big)V^{(0)\alpha}_{\text{eff, nsph}}(\boldsymbol{r})\varPsi^{(0)}_{\mathfrak{p}}(\boldsymbol{r})\,\mathrm{d}S\\
&= -\Big\langle\boldsymbol{\nabla}\varPsi^{(0)}_{\mathfrak{p}}\Big|\boldsymbol{\nabla}^{\top}\mathscr{V}^{(0)}_{\text{eff, nsph}}\Big|\varPsi^{(0)}_{\mathfrak{p}}\Big\rangle^{\top}_{\alpha} - \Big\langle\boldsymbol{\nabla}\varPsi^{(0)}_{\mathfrak{p}}\Big|\mathscr{V}^{(0)}_{\text{eff, nsph}}\Big|\boldsymbol{\nabla}^{\top}\varPsi^{(0)}_{\mathfrak{p}}\Big\rangle^{\top}_{\alpha}\,. && (7.142\text{b})
\end{aligned}$$

Assuming now that the core-electron wave functions vanish at the MT sphere boundary, the surface integral in equation (7.142a) is zero and can be omitted. For the materials relevant in this dissertation, we think that this is fulfilled in good approximation [127]. This is because a product of core-wave wave functions and non-spherical potential should not deliver significant contributions at the MT sphere boundary. Therefore, we decided to postpone the implementation of these integrals. Furthermore, the second term in (7.142b) is substituted by its transposed version in the following (legitimate because the dynamical matrix is ensured to be Hermitian). An analogous calculation can be conducted, exploiting the relation (7.130d):

$$\begin{aligned}
&\int_{\alpha}\varPsi^{*(0)}_{\mathfrak{p}}(\boldsymbol{r})V^{(0)\alpha}_{\text{eff, nsph}}(\boldsymbol{r})\Big(\boldsymbol{\nabla}\boldsymbol{\nabla}^{\top}\varPsi^{(0)}_{\mathfrak{p}}(\boldsymbol{r})\Big)\,\mathrm{d}^3r && (7.143\text{a})\\
&= -\int_{\alpha}\Big(\boldsymbol{\nabla}\varPsi^{*(0)}_{\mathfrak{p}}(\boldsymbol{r})\Big)\boldsymbol{\nabla}^{\top}\Big(V^{(0)\alpha}_{\text{eff, nsph}}(\boldsymbol{r})\varPsi^{(0)}_{\mathfrak{p}}(\boldsymbol{r})\Big)\,\mathrm{d}^3r + \oint_{\partial\alpha}\hat{\boldsymbol{r}}\,\varPsi^{*(0)}_{\mathfrak{p}}(\boldsymbol{r})\boldsymbol{\nabla}^{\top}\Big(V^{(0)\alpha}_{\text{eff, nsph}}(\boldsymbol{r})\varPsi^{(0)}_{\mathfrak{p}}(\boldsymbol{r})\Big)\,\mathrm{d}S\\
&= -\Big\langle\boldsymbol{\nabla}\varPsi^{(0)}_{\mathfrak{p}}\Big|\boldsymbol{\nabla}^{\top}\mathscr{V}^{(0)}_{\text{eff, nsph}}\Big|\varPsi^{(0)}_{\mathfrak{p}}\Big\rangle_{\alpha} - \Big\langle\boldsymbol{\nabla}\varPsi^{*(0)}_{\mathfrak{p}}\Big|\mathscr{V}^{(0)}_{\text{eff, nsph}}\Big|\boldsymbol{\nabla}^{\top}\varPsi^{(0)}_{\mathfrak{p}}\Big\rangle_{\alpha}\,. && (7.143\text{b})
\end{aligned}$$

Resume All in all, this leads to

$$\underline{D}^{\beta\alpha}_{\text{Pl,c}} = -\delta_{\beta\alpha}\sum_{\mathfrak{p}}\Bigg(\Big\langle \Psi^{(0)}_{\mathfrak{p}}\Big|\boldsymbol{\nabla}\mathscr{V}^{(0)}_{\text{eff, sph}}\Big|\boldsymbol{\nabla}^{\top}\Psi^{(0)}_{\mathfrak{p}}\Big\rangle_{\alpha} + \Big\langle \boldsymbol{\nabla}\Psi^{(0)}_{\mathfrak{p}}\Big|\boldsymbol{\nabla}^{\top}\mathscr{V}^{(0)}_{\text{eff, sph}}\Big|\Psi^{(0)}_{\mathfrak{p}}\Big\rangle_{\alpha} + \Big\langle \boldsymbol{\nabla}\Psi^{(0)}_{\mathfrak{p}}\Big|\boldsymbol{\nabla}^{\top}\mathscr{V}^{(0)}_{\text{eff, nsph}}\Big|\Psi^{(0)}_{\mathfrak{p}}\Big\rangle^{\top}_{\alpha} + \Big\langle \boldsymbol{\nabla}\Psi^{(0)}_{\mathfrak{p}}\Big|\boldsymbol{\nabla}^{\top}\mathscr{V}^{(0)}_{\text{eff, nsph}}\Big|\Psi^{(0)}_{\mathfrak{p}}\Big\rangle_{\alpha}\Bigg)\,. \tag{7.144a}$$

Substituting its first and third braket by their transposed version, and complex conjugating the fourth braket, we can re-express the previous expression as

$$\underline{D}^{\beta\alpha}_{\text{Pl,c}} = -\delta_{\beta\alpha}\int_{\alpha}\Big(\boldsymbol{\nabla}\rho^{(0)}_{\alpha,\text{c}}(\boldsymbol{r})\Big)\Big(\boldsymbol{\nabla}^{\top}V^{(0)\alpha}_{\text{eff}}(\boldsymbol{r})\Big)\,\mathrm{d}^3r\,. \tag{7.144b}$$

In practice, the mesh of the core density is the logarithmic MT mesh for the valence electrons, since contributions of the core-density within the IR are attributed to the IR valence-density (core-tails). Furthermore the complex conjugation is an equivalent operation, since the gradients of both the charge density and the potential are observables, and therefore the braket ist real. Finally, in my derivation the gradient is applied to the full effective potential, instead of only its non-spherical part as proposed by Klüppelberg [88].

7.6.4 Goldstone Condition

Outline For the Goldstone modes and monoatomic systems, the solution of the Sternheimer equation is given by equation (7.30) [251]. As a consequence, many terms of the dynamical-matrix expressions cancel each other. Hereinafter, I discuss this separately for the HF terms, the Pulay integral, the Pulay matrix elements, and the surface terms. Each of them shall be shown without outer products of gradients (see section 7.6.3). Moreover, I prove that the remaining terms must likewise vanish in monoatomic systems for $\boldsymbol{q} = \boldsymbol{0}$. A dynamical matrix equalling zero leads to phonon frequencies with energy zero, which is consistent with the fact that for infinite wavelengths only the complete crystal is rigidly shifted, not requiring any energy. In this section, I explain how I have rearranged the dynamical-matrix expressions so that the numerics is optimized for these Goldstone modes.

Hellmann–Feynman Terms

Inserting equation (7.132) into (7.126b), the HF contribution to the dynamical matrix reads

$$\begin{aligned}
&\underline{D}^{\beta\alpha}_{\text{HF}}(\boldsymbol{q}^{-+}) \\
&\quad= \int_{\text{IR}}\boldsymbol{\rho}^{*(1)}_{\text{IR}}(\boldsymbol{r};\boldsymbol{q}^{+}\beta)\Big[\boldsymbol{V}^{(1)\text{IR}}_{\text{ext}}(\boldsymbol{r};\boldsymbol{q}^{+}\alpha)\Big]^{\top}\mathrm{d}^3r - \delta_{\beta\alpha}\int_{\text{IR}}\Big(\boldsymbol{\nabla}\rho^{(0)}_{\text{IR}}(\boldsymbol{r})\Big)\boldsymbol{\nabla}^{\top}V^{(0)\text{IR}}_{\text{ext}}(\boldsymbol{r})\,\mathrm{d}^3r \\
&\qquad+ \sum_{\gamma}\int_{\gamma}\boldsymbol{\rho}^{*(1)}_{\gamma}(\boldsymbol{r};\boldsymbol{q}^{+}\beta)\Big[\boldsymbol{V}^{(1)\gamma}_{\text{ext}}(\boldsymbol{r};\boldsymbol{q}^{+}\alpha)\Big]^{\top}\mathrm{d}^3r - \sum_{\gamma}\delta_{\beta\alpha}\int_{\gamma}\Big(\boldsymbol{\nabla}\rho^{(0)}_{\gamma}(\boldsymbol{r})\Big)\boldsymbol{\nabla}^{\top}V^{(0)\gamma}_{\text{ext}}(\boldsymbol{r})\,\mathrm{d}^3r \\
&\qquad+ \delta_{\beta\alpha}\sum_{\gamma}\oint_{\gamma}\hat{\boldsymbol{r}}\rho^{(0)}_{\gamma}(\boldsymbol{r})\boldsymbol{\nabla}^{\top}V^{(0)\gamma}_{\text{ext}}(\boldsymbol{r})\,\mathrm{d}S - \delta_{\beta\alpha}\oint_{\text{IR}}\hat{\boldsymbol{r}}\rho^{(0)}_{\text{IR}}(\boldsymbol{r})\boldsymbol{\nabla}^{\top}V^{(0)\text{IR}}_{\text{ext}}(\boldsymbol{r})\,\mathrm{d}S \\
&\qquad+ \underline{E}^{(2)\beta\alpha}_{\text{ii}}(\boldsymbol{q}^{-+}) + \delta_{\boldsymbol{Q}_{\beta}\boldsymbol{Q}_{\alpha}}\underline{E}^{(2)\beta\alpha}_{\text{ii}}(\boldsymbol{0}^{-+})\,.
\end{aligned} \tag{7.145}$$

For $\boldsymbol{q} = \boldsymbol{0}$ and monoatomic systems, the first-order density variation is given by equation (7.31). Furthermore,

$$\left[\boldsymbol{V}_{\text{ext}}^{(1)}(\boldsymbol{r}; \boldsymbol{0}^{+}\alpha)\right]^{\top} = -\boldsymbol{\nabla}^{\top}\boldsymbol{V}_{\text{ext}}^{(1)}(\boldsymbol{r}; \boldsymbol{q}^{+}\alpha) \tag{7.146}$$

holds, which is discussed in section 7.3.1. As a consequence, the second and third lines in equation (7.145) analytically cancel each other. Likewise, these expressions exactly annihilate in the numerics, since the integrals containing the linear variations of the density and the external potential are successively arranged. The integrands in principle become equivalent for $\boldsymbol{q} = \boldsymbol{0}$ and the same numerical errors are made, implying an effective error cancelation. Moreover, the sum of the surface integrals in the fourth line of the aforementioned equation should be smaller than $1 \cdot 10^{-5}\, E_{\text{h}}\, a_0^{-2}$. This originates from the fact that both the charge density and the gradient of the external potential are rather continuous at the MT sphere boundary, due to the construction of the LAPW basis and the Weinert method. Thus effectively, this sum of surface integrals does not significantly contribute to the phonon frequencies in the end. Finally, it manifests itself in equation (6.54) that the second-order variation of the ion–ion interaction vanishes for the Goldstone modes. So overall, the HF contribution should vanish completely. If it does not, this draws from the fact that the outcome of the Sternheimer equation is not perfectly consistent with the analytical solution for $\boldsymbol{q} = \boldsymbol{0}$ given by equation (7.30).

Pulay Integral Terms

If combining equation (7.127b) with the first term in equation (7.137) and equation (7.144b),

$$\begin{aligned}\underline{D}_{\text{Pl,dp}}^{\beta\alpha}(\boldsymbol{q}^{-+}) &= \int_{\text{IR}} \boldsymbol{\rho}_{\text{IR}}^{*(1)}(\boldsymbol{r}; \boldsymbol{q}^{+}\beta)\left[\boldsymbol{V}_{\text{eff}}^{(1)\text{IR}}(\boldsymbol{r}; \boldsymbol{q}^{+}\alpha)\right]^{\top} \mathrm{d}^3 r \\ &\quad + \sum_{\gamma}\int_{\gamma} \boldsymbol{\rho}_{\gamma}^{*(1)}(\boldsymbol{r}; \boldsymbol{q}^{+}\beta)\left[\boldsymbol{V}_{\text{eff}}^{(1)\gamma}(\boldsymbol{r}; \boldsymbol{q}^{+}\alpha)\right]^{\top} - \delta_{\gamma\alpha}\delta_{\beta\alpha}\boldsymbol{\nabla}\rho_{\alpha}^{(0)}(\boldsymbol{r})\boldsymbol{\nabla}^{\top}V_{\text{eff}}^{(0)\alpha}(\boldsymbol{r})\, \mathrm{d}^3 r\end{aligned} \tag{7.147}$$

results. In contrast to the HF contribution (7.145), this expression only contains one IR integral with first-order variations, but none with gradients. Hence, this term does not obviously vanish for $\boldsymbol{q} = \boldsymbol{0}$. For the MT sphere γ in monoatomic systems, the integrals are arranged such that they annihilate each other again, analogously to the aforementioned HF contributions. Since moreover equation (7.31) holds for the first-order charge density variation,

$$\left[\boldsymbol{V}_{\text{eff}}^{(1)\gamma}(\boldsymbol{r}; \boldsymbol{0}^{+}\alpha)\right]^{\top} = -\boldsymbol{\nabla}^{\top}\boldsymbol{V}_{\text{eff}}^{(0)\gamma}(\boldsymbol{r}) \tag{7.148}$$

is implied. This is discussed in section 7.3.1 for the Coulomb potential. However, regarding the xc potential, it becomes immediately obvious when inserting equation (7.31) into equation (7.71e) and comparing it with (7.71) in the MT sphere γ.

Pulay Matrix-Element Terms

According to equation (7.137), the terms with outer products of gradients cancel in equations (7.128b), (7.128c), and (7.128d). This yields

$$\begin{aligned}
&\underline{D}^{\boldsymbol{k}n\beta\alpha}_{\text{Pu2b}}(\boldsymbol{q}^{+-})\\
&= \sum_{l'm'p'}\sum_{lmp}\sum_{\boldsymbol{G}'\boldsymbol{G}}\Bigg\{\\
&\quad 2\Big(\boldsymbol{z}^{(1)}_{\boldsymbol{G}'}(\boldsymbol{k},n;\boldsymbol{q}\beta)a^{\boldsymbol{G}'\boldsymbol{k}\alpha}_{l'm'p'}(\boldsymbol{q})\mathrm{i}[\boldsymbol{k}+\boldsymbol{q}+\boldsymbol{G}']^{\top}\Big)^{*}\Big\langle\vec{\varphi}^{\mathring{\alpha}}_{l'm'p'}\Big|\mathscr{H}^{(0)}-\epsilon^{(0)}_{\boldsymbol{k},n}\Big|\vec{\varphi}^{\mathring{\alpha}}_{lmp}\Big\rangle_{\alpha}z^{(0)}_{\boldsymbol{G}}(\boldsymbol{k},n)a^{\boldsymbol{G}\boldsymbol{k}\alpha}_{lmp}\\
&\quad-\delta_{\beta\alpha}\Big(z^{(0)}_{\boldsymbol{G}'}(\boldsymbol{k},n)a^{\boldsymbol{G}'\boldsymbol{k}\alpha}_{l'm'p'}\Big)^{*}[\boldsymbol{k}+\boldsymbol{G}'][\boldsymbol{k}+\boldsymbol{G}']^{\top}\Big\langle\vec{\varphi}^{\mathring{\alpha}}_{l'm'p'}\Big|\mathscr{H}^{(0)}-\epsilon^{(0)}_{\boldsymbol{k},n}\Big|\vec{\varphi}^{\mathring{\alpha}}_{lmp}\Big\rangle_{\alpha}z^{(0)}_{\boldsymbol{G}}(\boldsymbol{k},n)a^{\boldsymbol{G}\boldsymbol{k}\alpha}_{lmp}\\
&\quad-2\Big(\boldsymbol{z}^{(1)}_{\boldsymbol{G}'}(\boldsymbol{k},n;\boldsymbol{q}\beta)a^{\boldsymbol{G}'\boldsymbol{k}\alpha}_{l'm'p'}(\boldsymbol{q})\Big)^{*}\Big\langle\boldsymbol{\nabla}^{\top}\vec{\varphi}^{\mathring{\alpha}}_{l'm'p'}\Big|\mathscr{H}^{(0)}-\epsilon^{(0)}_{\boldsymbol{k},n}\Big|\vec{\varphi}^{\mathring{\alpha}}_{lmp}\Big\rangle_{\alpha}z^{(0)}_{\boldsymbol{G}}(\boldsymbol{k},n)a^{\boldsymbol{G}\boldsymbol{k}\alpha}_{lmp}\\
&\quad-\delta_{\beta\alpha}\Big(z^{(0)}_{\boldsymbol{G}'}(\boldsymbol{k},n)a^{\boldsymbol{G}'\boldsymbol{k}\alpha}_{l'm'p'}\mathrm{i}[\boldsymbol{k}+\boldsymbol{G}']\Big)^{*}\Big\langle\boldsymbol{\nabla}^{\top}\vec{\varphi}^{\mathring{\alpha}}_{l'm'p'}\Big|\mathscr{H}^{(0)}-\epsilon^{(0)}_{\boldsymbol{k},n}\Big|\vec{\varphi}^{\mathring{\alpha}}_{lmp}\Big\rangle_{\alpha}z^{(0)}_{\boldsymbol{G}}(\boldsymbol{k},n)a^{\boldsymbol{G}\boldsymbol{k}\alpha}_{lmp}\\
&\quad-\delta_{\beta\alpha}\Big\langle\boldsymbol{\nabla}\vec{\varphi}^{\mathring{\alpha}}_{l'm'p'}\Big|\mathscr{H}^{(0)}-\epsilon^{(0)}_{\boldsymbol{k},n}\Big|\vec{\varphi}^{\mathring{\alpha}}_{lmp}\Big\rangle_{\alpha}\Big[z^{(0)}_{\boldsymbol{G}'}(\boldsymbol{k},n)a^{\boldsymbol{G}'\boldsymbol{k}\alpha}_{l'm'p'}\mathrm{i}[\boldsymbol{k}+\boldsymbol{G}']\Big]^{\dagger}z^{(0)}_{\boldsymbol{G}}(\boldsymbol{k},n)a^{\boldsymbol{G}\boldsymbol{k}\alpha}_{lmp}\Bigg\},
\end{aligned}\tag{7.149a}$$

$$\begin{aligned}
&\underline{D}^{\boldsymbol{k}n\beta\alpha}_{\text{Pu2kO}}(\boldsymbol{q}^{-+})\\
&= \sum_{l'm'p'}\sum_{lmp}\sum_{\boldsymbol{G}'\boldsymbol{G}}\Bigg\{\\
&\quad 2\Big(z^{(0)}_{\boldsymbol{G}'}(\boldsymbol{k},n)a^{\boldsymbol{G}'\boldsymbol{k}\beta}_{l'm'p'}\Big)^{*}\Big\langle\vec{\varphi}^{\mathring{\beta}}_{l'm'p'}\Big|\mathscr{H}^{(0)}-\epsilon^{(0)}_{\boldsymbol{k},n}\Big|\vec{\varphi}^{\mathring{\beta}}_{lmp}\Big\rangle_{\beta}a^{\boldsymbol{G}\boldsymbol{k}\beta}_{lmp}(\boldsymbol{q})\mathrm{i}[\boldsymbol{k}+\boldsymbol{q}+\boldsymbol{G}]\Big[\boldsymbol{z}^{(1)}_{\boldsymbol{G}}(\boldsymbol{k},n;\boldsymbol{q}\alpha)\Big]^{\top}\\
&\quad-\delta_{\beta\alpha}\Big(z^{(0)}_{\boldsymbol{G}'}(\boldsymbol{k},n)a^{\boldsymbol{G}'\boldsymbol{k}\alpha}_{l'm'p'}\Big)^{*}[\boldsymbol{k}+\boldsymbol{G}][\boldsymbol{k}+\boldsymbol{G}]^{\top}\Big\langle\vec{\varphi}^{\mathring{\alpha}}_{l'm'p'}\Big|\mathscr{H}^{(0)}-\epsilon^{(0)}_{\boldsymbol{k},n}\Big|\vec{\varphi}^{\mathring{\alpha}}_{lmp}\Big\rangle_{\alpha}z^{(0)}_{\boldsymbol{G}}(\boldsymbol{k},n)a^{\boldsymbol{G}\boldsymbol{k}\alpha}_{lmp}\\
&\quad-2\Big(z^{(0)}_{\boldsymbol{G}'}(\boldsymbol{k},n)a^{\boldsymbol{G}'\boldsymbol{k}\beta}_{l'm'p'}\Big)^{*}\Big\langle\vec{\varphi}^{\mathring{\beta}}_{l'm'p'}\Big|\mathscr{H}^{(0)}-\epsilon^{(0)}_{\boldsymbol{k},n}\Big|\boldsymbol{\nabla}\vec{\varphi}^{\mathring{\beta}}_{lmp}\Big\rangle_{\beta}a^{\boldsymbol{G}\boldsymbol{k}\beta}_{lmp}(\boldsymbol{q})\Big[\boldsymbol{z}^{(1)}_{\boldsymbol{G}}(\boldsymbol{k},n;\boldsymbol{q}\alpha)\Big]^{\top}\\
&\quad-\delta_{\beta\alpha}\Big(z^{(0)}_{\boldsymbol{G}'}(\boldsymbol{k},n)a^{\boldsymbol{G}'\boldsymbol{k}\alpha}_{l'm'p'}\Big)^{*}z^{(0)}_{\boldsymbol{G}}(\boldsymbol{k},n)a^{\boldsymbol{G}\boldsymbol{k}\alpha}_{lmp}\mathrm{i}[\boldsymbol{k}+\boldsymbol{G}]\Big\langle\vec{\varphi}^{\mathring{\alpha}}_{l'm'p'}\Big|\mathscr{H}^{(0)}-\epsilon^{(0)}_{\boldsymbol{k},n}\Big|\boldsymbol{\nabla}^{\top}\vec{\varphi}^{\mathring{\alpha}}_{lmp}\Big\rangle_{\alpha}\\
&\quad-\delta_{\beta\alpha}\Big\langle\vec{\varphi}^{\mathring{\alpha}}_{l'm'p'}\Big|\mathscr{H}^{(0)}-\epsilon^{(0)}_{\boldsymbol{k},n}\Big|\boldsymbol{\nabla}\vec{\varphi}^{\mathring{\alpha}}_{lmp}\Big\rangle_{\alpha}\Big(z^{(0)}_{\boldsymbol{G}'}(\boldsymbol{k},n)a^{\boldsymbol{G}'\boldsymbol{k}\alpha}_{l'm'p'}\Big)^{*}\Big[z^{(0)}_{\boldsymbol{G}}(\boldsymbol{k},n)a^{\boldsymbol{G}\boldsymbol{k}\alpha}_{lmp}\mathrm{i}[\boldsymbol{k}+\boldsymbol{G}]\Big]^{\top}\Bigg\},
\end{aligned}\tag{7.149b}$$

and

$$\begin{aligned}
&\underline{D}^{\boldsymbol{k}n\beta\alpha}_{\text{Pu1bk}}(\boldsymbol{q}^{++})\\
&= \sum_{\boldsymbol{G}'\boldsymbol{G}}\Bigg\{\boldsymbol{z}^{*(1)}_{\boldsymbol{G}'}(\boldsymbol{k},n;\boldsymbol{q}\beta)\Big\langle\phi^{(0)\mathrm{IR}}_{\boldsymbol{k}+\boldsymbol{q},\boldsymbol{G}'}\Big|\mathscr{H}^{(0)}-\epsilon^{(0)}_{\boldsymbol{k},n}\Big|\phi^{(0)\mathrm{IR}}_{\boldsymbol{k}+\boldsymbol{q},\boldsymbol{G}}\Big\rangle_{\mathrm{IR}}\Big[\boldsymbol{z}^{(1)}_{\boldsymbol{G}}(\boldsymbol{k},n;\boldsymbol{q}\alpha)\Big]^{\top}\\
&\quad+\sum_{l'm'p'}\sum_{lmp}\Bigg\{\\
&\quad\sum_{\gamma}\Big(\boldsymbol{z}^{(1)}_{\boldsymbol{G}'}(\boldsymbol{k},n;\boldsymbol{q}\beta)a^{\boldsymbol{G}'\boldsymbol{k}\gamma}_{l'm'p'}(\boldsymbol{q})\Big)^{*}\Big\langle\vec{\varphi}^{\mathring{\gamma}}_{l'm'p'}\Big|\mathscr{H}^{(0)}-\epsilon^{(0)}_{\boldsymbol{k},n}\Big|\vec{\varphi}^{\mathring{\gamma}}_{lmp}\Big\rangle_{\gamma}\Big[\boldsymbol{z}^{(1)}_{\boldsymbol{G}}(\boldsymbol{k},n;\boldsymbol{q}\alpha)\Big]^{\top}a^{\boldsymbol{G}\boldsymbol{k}\gamma}_{lmp}(\boldsymbol{q})\\
&\quad+\delta_{\beta\alpha}\Big(z^{(0)}_{\boldsymbol{G}'}(\boldsymbol{k},n)a^{\boldsymbol{G}'\boldsymbol{k}\alpha}_{l'm'p'}\mathrm{i}[\boldsymbol{k}+\boldsymbol{G}']\Big)^{*}\Big\langle\vec{\varphi}^{\mathring{\alpha}}_{l'm'p'}\Big|\mathscr{H}^{(0)}-\epsilon^{(0)}_{\boldsymbol{k},n}\Big|\vec{\varphi}^{\mathring{\alpha}}_{lmp}\Big\rangle_{\alpha}z^{(0)}_{\boldsymbol{G}}(\boldsymbol{k},n)a^{\boldsymbol{G}\boldsymbol{k}\alpha}_{lmp}\mathrm{i}[\boldsymbol{k}+\boldsymbol{G}]^{\top}\\
&\quad+\Big(\boldsymbol{z}^{(1)}_{\boldsymbol{G}'}(\boldsymbol{k},n;\boldsymbol{q}\beta)a^{\boldsymbol{G}'\boldsymbol{k}\alpha}_{l'm'p'}(\boldsymbol{q})\Big)^{*}\Big\langle\vec{\varphi}^{\mathring{\alpha}}_{l'm'p'}\Big|\mathscr{H}^{(0)}-\epsilon^{(0)}_{\boldsymbol{k},n}\Big|\vec{\varphi}^{\mathring{\alpha}}_{lmp}\Big\rangle_{\alpha}\mathrm{i}[\boldsymbol{k}+\boldsymbol{G}]^{\top}z^{(0)}_{\boldsymbol{G}}(\boldsymbol{k},n)a^{\boldsymbol{G}\boldsymbol{k}\alpha}_{lmp}
\end{aligned}\tag{7.149c}$$

$$
\begin{aligned}
&+\Big(z^{(0)}_{\boldsymbol{G}'}(\boldsymbol{k},n)a^{\boldsymbol{G}'\boldsymbol{k}\beta}_{l'm'p'}\mathrm{i}[\boldsymbol{k}+\boldsymbol{G}']\Big)^{*}\Big\langle\vec{\varphi}^{\mathring{\beta}}_{l'm'p'}\Big|\mathscr{H}^{(0)}-\epsilon^{(0)}_{\boldsymbol{k},n}\Big|\vec{\varphi}^{\mathring{\beta}}_{lmp}\Big\rangle_{\beta}\Big[\boldsymbol{z}^{(1)}_{\boldsymbol{G}}(\boldsymbol{k},n;\boldsymbol{q}\alpha)\Big]^{\top}a^{\boldsymbol{G}\boldsymbol{k}\beta}_{lmp}(\boldsymbol{q})\\
&-\Big(z^{(0)}_{\boldsymbol{G}'}(\boldsymbol{k},n)a^{\boldsymbol{G}'\boldsymbol{k}\beta}_{l'm'p'}\Big)^{*}\Big\langle\boldsymbol{\nabla}\vec{\varphi}^{\mathring{\beta}}_{l'm'p'}\Big|\mathscr{H}^{(0)}-\epsilon^{(0)}_{\boldsymbol{k},n}\Big|\vec{\varphi}^{\mathring{\beta}}_{lmp}\Big\rangle_{\beta}\Big[\boldsymbol{z}^{(1)}_{\boldsymbol{G}}(\boldsymbol{k},n;\boldsymbol{q}\alpha)\Big]^{\top}a^{\boldsymbol{G}\boldsymbol{k}\beta}_{lmp}(\boldsymbol{q})\\
&-\delta_{\beta\alpha}\Big(z^{(0)}_{\boldsymbol{G}'}(\boldsymbol{k},n)a^{\boldsymbol{G}'\boldsymbol{k}\alpha}_{l'm'p'}\Big)^{*}\Big\langle\boldsymbol{\nabla}\vec{\varphi}^{\mathring{\alpha}}_{l'm'p'}\Big|\mathscr{H}^{(0)}-\epsilon^{(0)}_{\boldsymbol{k},n}\Big|\vec{\varphi}^{\mathring{\alpha}}_{lmp}\Big\rangle_{\alpha}z^{(0)}_{\boldsymbol{G}}(\boldsymbol{k},n)a^{\boldsymbol{G}\boldsymbol{k}\alpha}_{lmp}\mathrm{i}[\boldsymbol{k}+\boldsymbol{G}]^{\top}\\
&-\Big(\boldsymbol{z}^{(1)}_{\boldsymbol{G}'}(\boldsymbol{k},n;\boldsymbol{q}\beta)a^{\boldsymbol{G}'\boldsymbol{k}\alpha}_{l'm'p'}(\boldsymbol{q})\Big)^{*}\Big\langle\vec{\varphi}^{\mathring{\alpha}}_{l'm'p'}\Big|\mathscr{H}^{(0)}-\epsilon^{(0)}_{\boldsymbol{k},n}\Big|\boldsymbol{\nabla}^{\top}\vec{\varphi}^{\mathring{\alpha}}_{lmp}\Big\rangle_{\alpha}z^{(0)}_{\boldsymbol{G}}(\boldsymbol{k},n)a^{\boldsymbol{G}\boldsymbol{k}\alpha}_{lmp}\\
&-\delta_{\beta\alpha}\Big(z^{(0)}_{\boldsymbol{G}'}(\boldsymbol{k},n)a^{\boldsymbol{G}'\boldsymbol{k}\alpha}_{l'm'p'}\mathrm{i}[\boldsymbol{k}+\boldsymbol{G}']\Big)^{*}\Big\langle\vec{\varphi}^{\mathring{\alpha}}_{l'm'p'}\Big|\mathscr{H}^{(0)}-\epsilon^{(0)}_{\boldsymbol{k},n}\Big|\boldsymbol{\nabla}^{\top}\vec{\varphi}^{\mathring{\alpha}}_{lmp}\Big\rangle_{\alpha}z^{(0)}_{\boldsymbol{G}}(\boldsymbol{k},n)a^{\boldsymbol{G}\boldsymbol{k}\alpha}_{lmp}\Bigg\}\Bigg\}\,.
\end{aligned}
$$

In these expressions, similar terms are arranged in groups, based on equation (7.30). Given Goldstone modes in monoatomic systems, the last three lines of equation (7.149a) cancel each other (provided the last one is substituted by its transposed version, which is valid according to section 7.6.1). In contrast, the third line is multiplied by a factor of two and so does not completely cancel with the fourth line in equation (7.149a). Equation (7.149b) behaves analogously for $\boldsymbol{q}=\boldsymbol{0}$. Thus, also its third line without the factor of two remains. As far as equation (7.149c) is concerned, all lines from the fourth to the eleventh cancel each other, i.e., the fourth with the fifth, the sixth with the seventh, the eighth with the ninth, and the tenth with the eleventh. What persists, is the IR matrix element in the second line.

Surface Terms

If the two surface terms from equation (7.137) are omitted in equation (7.129),

$$
\begin{aligned}
&\underline{D}^{\beta\alpha}_{\mathrm{sfO}}(\boldsymbol{q}^{+}) \qquad\qquad (7.150\mathrm{a})\\
&\quad=\sum_{\boldsymbol{k},n}f^{(0)}_{\boldsymbol{k},n}\sum_{\boldsymbol{G}'\boldsymbol{G}}\Bigg\{\\
&\qquad 2\oint_{\partial\alpha}\Bigg(\Big(\boldsymbol{z}^{(1)}_{\boldsymbol{G}'}(\boldsymbol{k},n;\boldsymbol{q}\beta)\vec{\phi}^{(0)\alpha}_{\boldsymbol{k}+\boldsymbol{q},\boldsymbol{G}'}(\boldsymbol{r})\Big)^{*}\Big(\mathscr{H}^{(0)}-\epsilon^{(0)}_{\boldsymbol{k},n}\Big)z^{(0)}_{\boldsymbol{G}}(\boldsymbol{k},n)\vec{\phi}^{(0)\alpha}_{\boldsymbol{k},\boldsymbol{G}}(\boldsymbol{r})\\
&\qquad\quad+\delta_{\beta\alpha}\Big(z^{(0)}_{\boldsymbol{G}'}(\boldsymbol{k},n)\mathrm{i}(\boldsymbol{k}+\boldsymbol{G}')\vec{\phi}^{(0)\beta}_{\boldsymbol{k},\boldsymbol{G}'}(\boldsymbol{r})\Big)^{*}\Big(\mathscr{H}^{(0)}-\epsilon^{(0)}_{\boldsymbol{k},n}\Big)z^{(0)}_{\boldsymbol{G}}(\boldsymbol{k},n)\vec{\phi}^{(0)\beta}_{\boldsymbol{k},\boldsymbol{G}}(\boldsymbol{r})\\
&\qquad\quad-\delta_{\beta\alpha}\Big(z^{(0)}_{\boldsymbol{G}'}(\boldsymbol{k},n)\boldsymbol{\nabla}\vec{\phi}^{(0)\beta}_{\boldsymbol{k},\boldsymbol{G}'}(\boldsymbol{r})\Big)^{*}\Big(\mathscr{H}^{(0)}-\epsilon^{(0)}_{\boldsymbol{k},n}\Big)z^{(0)}_{\boldsymbol{G}}(\boldsymbol{k},n)\vec{\phi}^{(0)\beta}_{\boldsymbol{k},\boldsymbol{G}}(\boldsymbol{r})\\
&\qquad\quad-\Big(\boldsymbol{z}^{(1)}_{\boldsymbol{G}'}(\boldsymbol{k},n;\boldsymbol{q}\beta)\phi^{(0)\mathrm{IR}}_{\boldsymbol{k}+\boldsymbol{q},\boldsymbol{G}'}(\boldsymbol{r})\Big)^{*}\Big(\mathscr{H}^{(0)}-\epsilon^{(0)}_{\boldsymbol{k},n}\Big)z^{(0)}_{\boldsymbol{G}}(\boldsymbol{k},n)\phi^{(0)\mathrm{IR}}_{\boldsymbol{k},\boldsymbol{G}}(\boldsymbol{r})\Bigg)\hat{\boldsymbol{r}}^{\top}\,\mathrm{d}S\\
&\qquad+2\oint_{\partial\beta}\hat{\boldsymbol{r}}\Bigg(z^{*(0)}_{\boldsymbol{G}'}(\boldsymbol{k},n)\vec{\phi}^{*(0)\beta}_{\boldsymbol{k},\boldsymbol{G}'}(\boldsymbol{r})\Big(\mathscr{H}^{(0)}-\epsilon^{(0)}_{\boldsymbol{k},n}\Big)\Big[\boldsymbol{z}^{(1)}_{\boldsymbol{G}}(\boldsymbol{k},n;\boldsymbol{q}\alpha)\Big]^{\top}\vec{\phi}^{(0)\beta}_{\boldsymbol{k}+\boldsymbol{q},\boldsymbol{G}}(\boldsymbol{r})\\
&\qquad\quad+\delta_{\beta\alpha}z^{*(0)}_{\boldsymbol{G}'}(\boldsymbol{k},n)\vec{\phi}^{*(0)\beta}_{\boldsymbol{k},\boldsymbol{G}'}(\boldsymbol{r})\Big(\mathscr{H}^{(0)}-\epsilon^{(0)}_{\boldsymbol{k},n}\Big)z^{(0)}_{\boldsymbol{G}}(\boldsymbol{k},n)\mathrm{i}[\boldsymbol{k}+\boldsymbol{G}]^{\top}\vec{\phi}^{(0)\beta}_{\boldsymbol{k},\boldsymbol{G}}(\boldsymbol{r})\\
&\qquad\quad-\delta_{\beta\alpha}z^{*(0)}_{\boldsymbol{G}'}(\boldsymbol{k},n)\vec{\phi}^{*(0)\beta}_{\boldsymbol{k},\boldsymbol{G}'}(\boldsymbol{r})\Big(\mathscr{H}^{(0)}-\epsilon^{(0)}_{\boldsymbol{k},n}\Big)z^{(0)}_{\boldsymbol{G}}(\boldsymbol{k},n)\Big(\boldsymbol{\nabla}^{\top}\vec{\phi}^{(0)\beta}_{\boldsymbol{k},\boldsymbol{G}}(\boldsymbol{r})\Big)\\
&\qquad\quad-z^{*(0)}_{\boldsymbol{G}'}(\boldsymbol{k},n)\phi^{*(0)\mathrm{IR}}_{\boldsymbol{k},\boldsymbol{G}'}(\boldsymbol{r})\Big(\mathscr{H}^{(0)}-\epsilon^{(0)}_{\boldsymbol{k},n}\Big)\Big[\boldsymbol{z}^{(1)}_{\boldsymbol{G}}(\boldsymbol{k},n;\boldsymbol{q}\alpha)\Big]^{\top}\phi^{(0)\mathrm{IR}}_{\boldsymbol{k}+\boldsymbol{q},\boldsymbol{G}}(\boldsymbol{r})\Bigg)\,\mathrm{d}S\\
&\qquad+\delta_{\beta\alpha}\oint_{\partial\beta}\Bigg(2z^{*(0)}_{\boldsymbol{G}'}(\boldsymbol{k},n)\Big(\boldsymbol{\nabla}\vec{\phi}^{*(0)\beta}_{\boldsymbol{k},\boldsymbol{G}'}(\boldsymbol{r})\Big)\Big(\mathscr{H}^{(0)}-\epsilon^{(0)}_{\boldsymbol{k},n}\Big)z^{(0)}_{\boldsymbol{G}}(\boldsymbol{k},n)\vec{\phi}^{(0)\beta}_{\boldsymbol{k},\boldsymbol{G}}(\boldsymbol{r})\\
&\qquad\quad-z^{*(0)}_{\boldsymbol{G}'}(\boldsymbol{k},n)\Big(\boldsymbol{\nabla}\phi^{*(0)\mathrm{IR}}_{\boldsymbol{k},\boldsymbol{G}'}(\boldsymbol{r})\Big)\Big(\mathscr{H}^{(0)}-\epsilon^{(0)}_{\boldsymbol{k},n}\Big)z^{(0)}_{\boldsymbol{G}}(\boldsymbol{k},n)\phi^{(0)\mathrm{IR}}_{\boldsymbol{k},\boldsymbol{G}}(\boldsymbol{r})
\end{aligned}
$$

$$
\begin{aligned}
&\quad + z^{*(0)}_{\boldsymbol{G}'}(\boldsymbol{k},n)\vec{\phi}^{*(0)\beta}_{\boldsymbol{k},\boldsymbol{G}'}(\boldsymbol{r})\Big(\boldsymbol{\nabla} V^{(0)\beta}_{\text{eff}}(\boldsymbol{r})\Big) z^{(0)}_{\boldsymbol{G}}(\boldsymbol{k},n)\vec{\phi}^{(0)\beta}_{\boldsymbol{k},\boldsymbol{G}}(\boldsymbol{r}) \\
&\quad - z^{*(0)}_{\boldsymbol{G}'}(\boldsymbol{k},n)\phi^{*(0)\text{IR}}_{\boldsymbol{k},\boldsymbol{G}'}(\boldsymbol{r})\Big(\boldsymbol{\nabla} V^{(0)\text{IR}}_{\text{eff}}(\boldsymbol{r})\Big) z^{(0)}_{\boldsymbol{G}}(\boldsymbol{k},n)\phi^{(0)\text{IR}}_{\boldsymbol{k},\boldsymbol{G}}(\boldsymbol{r})\ \Big)\hat{\boldsymbol{r}}^{\top}\,\mathrm{d}S \\
&+ \delta_{\beta\alpha}\oint_{\partial\beta}\hat{\boldsymbol{r}}\Big(2z^{*(0)}_{\boldsymbol{G}'}(\boldsymbol{k},n)\vec{\phi}^{*(0)\beta}_{\boldsymbol{k},\boldsymbol{G}'}(\boldsymbol{r})\Big(\mathscr{H}^{(0)} - \epsilon^{(0)}_{\boldsymbol{k},n}\Big) z^{(0)}_{\boldsymbol{G}}(\boldsymbol{k},n)\Big(\boldsymbol{\nabla}^{\top}\vec{\phi}^{(0)\beta}_{\boldsymbol{k},\boldsymbol{G}}(\boldsymbol{r})\Big) \\
&\quad - z^{*(0)}_{\boldsymbol{G}'}(\boldsymbol{k},n)\phi^{*(0)\text{IR}}_{\boldsymbol{k},\boldsymbol{G}'}(\boldsymbol{r})\Big(\mathscr{H}^{(0)} - \epsilon^{(0)}_{\boldsymbol{k},n}\Big) z^{(0)}_{\boldsymbol{G}}(\boldsymbol{k},n)\Big(\boldsymbol{\nabla}^{\top}\phi^{(0)\text{IR}}_{\boldsymbol{k},\boldsymbol{G}}(\boldsymbol{r})\Big)\Big)\,\mathrm{d}S\ \Big\} \\
&+ \delta_{\beta\alpha}\oint_{\partial\beta}\Big[\boldsymbol{\nabla}\Big(\rho^{(0)}_{\beta}(\boldsymbol{r})\Big(\epsilon^{(0)\beta}_{\text{xc}}(\boldsymbol{r}) - V^{(0)\beta}_{\text{xc}}(\boldsymbol{r})\Big)\Big) \\
&\quad - \boldsymbol{\nabla}\Big(\rho^{(0)}_{\text{IR}}(\boldsymbol{r})\Big(\epsilon^{(0)\text{IR}}_{\text{xc}}(\boldsymbol{r}) - V^{(0)\text{IR}}_{\text{xc}}(\boldsymbol{r})\Big)\Big)\Big]\hat{\boldsymbol{r}}^{\top}\,\mathrm{d}S \\
&+ \delta_{\beta\alpha}\oint_{\partial\beta}\hat{\boldsymbol{r}}\Big[\rho^{(0)}_{\beta}(\boldsymbol{r})\Big(2\Big[\boldsymbol{V}^{(1)\beta}_{\text{ext}}(\boldsymbol{r};\boldsymbol{q}^{+}\alpha)\Big]^{\top} + \Big[\boldsymbol{V}^{(1)\beta}_{\text{Htr}}(\boldsymbol{r};\boldsymbol{q}^{+}\alpha)\Big]^{\top}\Big) \\
&\quad - \rho^{(0)}_{\text{IR}}(\boldsymbol{r})\Big(2\Big[\boldsymbol{V}^{(1)\text{IR}}_{\text{ext}}(\boldsymbol{r};\boldsymbol{q}^{+}\alpha)\Big]^{\top} + \Big[\boldsymbol{V}^{(1)\text{IR}}_{\text{Htr}}(\boldsymbol{r};\boldsymbol{q}^{+}\alpha)\Big]^{\top}\Big)\Big]\,\mathrm{d}S
\end{aligned}
$$

results and can be simplifed and rewritten as

$$
\begin{aligned}
&\underline{D}^{\beta\alpha}_{\text{sfO}}(\boldsymbol{q}^{+}) \qquad\qquad (7.150\text{b}) \\
&\quad = \sum_{\boldsymbol{k},n} f^{(0)}_{\boldsymbol{k},n}\sum_{\boldsymbol{G}'\boldsymbol{G}}\Big\{ \\
&\qquad 2\oint_{\partial\alpha}\Big(\Big(\boldsymbol{z}^{(1)}_{\boldsymbol{G}'}(\boldsymbol{k},n;\boldsymbol{q}\beta)\vec{\phi}^{(0)\alpha}_{\boldsymbol{k}+\boldsymbol{q},\boldsymbol{G}'}(\boldsymbol{r})\Big)^{*}\Big(\mathscr{H}^{(0)} - \epsilon^{(0)}_{\boldsymbol{k},n}\Big) z^{(0)}_{\boldsymbol{G}}(\boldsymbol{k},n)\vec{\phi}^{(0)\alpha}_{\boldsymbol{k},\boldsymbol{G}}(\boldsymbol{r}) \\
&\qquad\quad + \delta_{\beta\alpha}\Big(z^{(0)}_{\boldsymbol{G}'}(\boldsymbol{k},n)\mathrm{i}(\boldsymbol{k}+\boldsymbol{G}')\vec{\phi}^{(0)\beta}_{\boldsymbol{k},\boldsymbol{G}'}(\boldsymbol{r})\Big)^{*}\Big(\mathscr{H}^{(0)} - \epsilon^{(0)}_{\boldsymbol{k},n}\Big) z^{(0)}_{\boldsymbol{G}}(\boldsymbol{k},n)\vec{\phi}^{(0)\beta}_{\boldsymbol{k},\boldsymbol{G}}(\boldsymbol{r}) \\
&\qquad\quad - \Big(\boldsymbol{z}^{(1)}_{\boldsymbol{G}'}(\boldsymbol{k},n;\boldsymbol{q}\beta)\phi^{(0)\text{IR}}_{\boldsymbol{k}+\boldsymbol{q},\boldsymbol{G}'}(\boldsymbol{r})\Big)^{*}\Big(\mathscr{H}^{(0)} - \epsilon^{(0)}_{\boldsymbol{k},n}\Big) z^{(0)}_{\boldsymbol{G}}(\boldsymbol{k},n)\phi^{(0)\text{IR}}_{\boldsymbol{k},\boldsymbol{G}}(\boldsymbol{r}) \\
&\qquad\quad - \frac{1}{2}\delta_{\beta\alpha} z^{*(0)}_{\boldsymbol{G}'}(\boldsymbol{k},n)\Big(\boldsymbol{\nabla}\phi^{*(0)\text{IR}}_{\boldsymbol{k},\boldsymbol{G}'}(\boldsymbol{r})\Big)\Big(\mathscr{H}^{(0)} - \epsilon^{(0)}_{\boldsymbol{k},n}\Big) z^{(0)}_{\boldsymbol{G}}(\boldsymbol{k},n)\phi^{(0)\text{IR}}_{\boldsymbol{k},\boldsymbol{G}}(\boldsymbol{r})\Big)\hat{\boldsymbol{r}}^{\top}\,\mathrm{d}S \\
&\qquad + 2\oint_{\partial\beta}\hat{\boldsymbol{r}}\Big(z^{*(0)}_{\boldsymbol{G}'}(\boldsymbol{k},n)\vec{\phi}^{*(0)\beta}_{\boldsymbol{k},\boldsymbol{G}'}(\boldsymbol{r})\Big(\mathscr{H}^{(0)} - \epsilon^{(0)}_{\boldsymbol{k},n}\Big)\Big[\boldsymbol{z}^{(1)}_{\boldsymbol{G}}(\boldsymbol{k},n;\boldsymbol{q}\alpha)\Big]^{\top}\vec{\phi}^{(0)\beta}_{\boldsymbol{k}+\boldsymbol{q},\boldsymbol{G}}(\boldsymbol{r}) \\
&\qquad\quad + \delta_{\beta\alpha} z^{*(0)}_{\boldsymbol{G}'}(\boldsymbol{k},n)\vec{\phi}^{*(0)\beta}_{\boldsymbol{k},\boldsymbol{G}'}(\boldsymbol{r})\Big(\mathscr{H}^{(0)} - \epsilon^{(0)}_{\boldsymbol{k},n}\Big) z^{(0)}_{\boldsymbol{G}}(\boldsymbol{k},n)\mathrm{i}[\boldsymbol{k}+\boldsymbol{G}]^{\top}\vec{\phi}^{(0)\beta}_{\boldsymbol{k},\boldsymbol{G}}(\boldsymbol{r}) \\
&\qquad\quad - z^{*(0)}_{\boldsymbol{G}'}(\boldsymbol{k},n)\phi^{*(0)\text{IR}}_{\boldsymbol{k},\boldsymbol{G}'}(\boldsymbol{r})\Big(\mathscr{H}^{(0)} - \epsilon^{(0)}_{\boldsymbol{k},n}\Big)\Big[\boldsymbol{z}^{(1)}_{\boldsymbol{G}}(\boldsymbol{k},n;\boldsymbol{q}\alpha)\Big]^{\top}\phi^{(0)\text{IR}}_{\boldsymbol{k}+\boldsymbol{q},\boldsymbol{G}}(\boldsymbol{r}) \\
&\qquad\quad - \frac{1}{2}\delta_{\beta\alpha}\ z^{*(0)}_{\boldsymbol{G}'}(\boldsymbol{k},n)\phi^{*(0)\text{IR}}_{\boldsymbol{k},\boldsymbol{G}'}(\boldsymbol{r})\Big(\mathscr{H}^{(0)} - \epsilon^{(0)}_{\boldsymbol{k},n}\Big) z^{(0)}_{\boldsymbol{G}}(\boldsymbol{k},n)\Big(\boldsymbol{\nabla}^{\top}\phi^{(0)\text{IR}}_{\boldsymbol{k},\boldsymbol{G}}(\boldsymbol{r})\Big)\Big)\,\mathrm{d}S\ \Big\} \\
&\qquad + \delta_{\beta\alpha}\oint_{\partial\beta}\Big(\rho^{(0)}_{\beta}\Big(\boldsymbol{\nabla} V^{(0)\beta}_{\text{eff}}(\boldsymbol{r})\Big) - \rho^{(0)}_{\text{IR}}(\boldsymbol{r})\Big(\boldsymbol{\nabla} V^{(0)\text{IR}}_{\text{eff}}(\boldsymbol{r})\Big)\Big)\hat{\boldsymbol{r}}^{\top}\,\mathrm{d}S \\
&\qquad + \delta_{\beta\alpha}\oint_{\partial\beta}\Big[\boldsymbol{\nabla}\Big(\rho^{(0)}_{\beta}(\boldsymbol{r})\Big(\epsilon^{(0)\beta}_{\text{xc}}(\boldsymbol{r}) - V^{(0)\beta}_{\text{xc}}(\boldsymbol{r})\Big)\Big) \\
&\qquad\quad - \boldsymbol{\nabla}\Big(\rho^{(0)}_{\text{IR}}(\boldsymbol{r})\Big(\epsilon^{(0)\text{IR}}_{\text{xc}}(\boldsymbol{r}) - V^{(0)\text{IR}}_{\text{xc}}(\boldsymbol{r})\Big)\Big)\Big]\hat{\boldsymbol{r}}^{\top}\,\mathrm{d}S \\
&\qquad + \delta_{\beta\alpha}\oint_{\partial\beta}\hat{\boldsymbol{r}}\Big[\rho^{(0)}_{\beta}(\boldsymbol{r})\Big(2\Big[\boldsymbol{V}^{(1)\beta}_{\text{ext}}(\boldsymbol{r};\boldsymbol{q}^{+}\alpha)\Big]^{\top} + \Big[\boldsymbol{V}^{(1)\beta}_{\text{Htr}}(\boldsymbol{r};\boldsymbol{q}^{+}\alpha)\Big]^{\top}\Big)
\end{aligned}
$$

$$- \rho_{\mathrm{IR}}^{(0)}(\boldsymbol{r})\Big(2\Big[\boldsymbol{V}_{\mathrm{ext}}^{(1)\mathrm{IR}}(\boldsymbol{r};\boldsymbol{q}^{+}\alpha)\Big]^{\top} + \Big[\boldsymbol{V}_{\mathrm{Htr}}^{(1)\mathrm{IR}}(\boldsymbol{r};\boldsymbol{q}^{+}\alpha)\Big]^{\top}\Big)\Big]\,\mathrm{d}S\,.$$

Restricting to monoatomic systems and inserting equation (7.30) for $\boldsymbol{q} = \boldsymbol{0}$, the third and fourth, as well as the seventh and eighth lines in equation (7.150b) cancel each other. However, the sixth and the tenth lines are multiplied by a factor of one half, which is why they do not completely cancel the fifth and the ninth lines, respectively. Finally, the last five lines in equation (7.150b) contain sums of surface integrals which are small, analogously to the sum of surface integrals in equation (7.145). The largest of these surface term contributions are normally those incorporating either the xc energy density or the xc potential. However, it has turned out later that the last five lines in equation (7.150b) can be further simplified. As a consequence, the aforementioned xc surface terms vanish (cf. section 7.6.8).

Leftover Terms

Intention

Those terms of the dynamical matrix which do not directly cancel are displayed in equation (7.152f). In the following, I show that they vanish given monoatomic systems and $\boldsymbol{q} = \boldsymbol{0}$, because the Schrödinger equation

$$\begin{aligned}
0 &= \Big(\mathscr{H}^{(0)} - \epsilon_{\boldsymbol{k},n}^{(0)}\Big)\Big|\Psi_{\boldsymbol{k},n}^{(0)}\Big\rangle && (7.151\mathrm{a})\\
&= \sum_{\boldsymbol{G}'\boldsymbol{G}}\sum_{\boldsymbol{k},n} f_{\boldsymbol{k},n}^{(0)} z_{\boldsymbol{G}'}^{*(0)}(\boldsymbol{k},n) z_{\boldsymbol{G}}^{(0)}(\boldsymbol{k},n) && (7.151\mathrm{b})\\
&\quad\times\Big(\Big\langle\phi_{\boldsymbol{k},\boldsymbol{G}'}^{(0)\mathrm{IR}}\Big|\mathscr{H}^{(0)} - \epsilon_{\boldsymbol{k},n}^{(0)}\Big|\phi_{\boldsymbol{k},\boldsymbol{G}}^{(0)\mathrm{IR}}\Big\rangle_{\mathrm{IR}} + \Big\langle\vec{\phi}_{\boldsymbol{k},\boldsymbol{G}'}^{(0)\alpha}\Big|\mathscr{H}^{(0)} - \epsilon_{\boldsymbol{k},n}^{(0)}\Big|\vec{\phi}_{\boldsymbol{k},\boldsymbol{G}}^{(0)\alpha}\Big\rangle_{\alpha}\Big)
\end{aligned}$$

must hold.

Proof

I start with the assumption that the right-hand side of

$$\begin{aligned}
0 = \sum_{\boldsymbol{G}'\boldsymbol{G}}\sum_{\boldsymbol{k},n} f_{\boldsymbol{k},n}^{(0)}\Big\{&\Big(-\mathrm{i}^2[\boldsymbol{k}+\boldsymbol{G}'][\boldsymbol{k}+\boldsymbol{G}']^{\top} - \mathrm{i}^2[\boldsymbol{k}+\boldsymbol{G}][\boldsymbol{k}+\boldsymbol{G}]^{\top}\Big) z_{\boldsymbol{G}'}^{*(0)}(\boldsymbol{k},n) z_{\boldsymbol{G}}^{(0)}(\boldsymbol{k},n) \quad (7.152\mathrm{a})\\
&\times\Big(\Big\langle\phi_{\boldsymbol{k},\boldsymbol{G}'}^{(0)\mathrm{IR}}\Big|\mathscr{H}^{(0)} - \epsilon_{\boldsymbol{k},n}^{(0)}\Big|\phi_{\boldsymbol{k},\boldsymbol{G}}^{(0)\mathrm{IR}}\Big\rangle_{\mathrm{IR}} + \sum_{\alpha}\Big\langle\vec{\phi}_{\boldsymbol{k},\boldsymbol{G}'}^{(0)\alpha}\Big|\mathscr{H}^{(0)} - \epsilon_{\boldsymbol{k},n}^{(0)}\Big|\vec{\phi}_{\boldsymbol{k},\boldsymbol{G}}^{(0)\alpha}\Big\rangle_{\alpha}\Big)\Big\}
\end{aligned}$$

still is equal to zero if it is expanded in this manner relative to the right-hand side of equation (7.151b) [251]. Exploiting

$$\sum_{\boldsymbol{G}} z_{\boldsymbol{G}}^{(0)}(\boldsymbol{k},n)\mathrm{i}[\boldsymbol{k}+\boldsymbol{G}]\phi_{\boldsymbol{k},\boldsymbol{G}}^{(0)\mathrm{IR}}(\boldsymbol{r}) = \sum_{\boldsymbol{G}} z_{\boldsymbol{G}}^{(0)}(\boldsymbol{k},n)\boldsymbol{\nabla}\phi_{\boldsymbol{k},\boldsymbol{G}}^{(0)\mathrm{IR}}(\boldsymbol{r}) = \boldsymbol{\nabla}\Psi_{\boldsymbol{k},n}^{(0)\mathrm{IR}}(\boldsymbol{r}) \quad (7.152\mathrm{b})$$

for the IR then leads to

$$\begin{aligned}
0 = &-\sum_{\boldsymbol{k},n} f_{\boldsymbol{k},n}^{(0)}\Big(\Big\langle\boldsymbol{\nabla}\boldsymbol{\nabla}^{\top}\Psi_{\boldsymbol{k},n}^{(0)\mathrm{IR}}\Big|\mathscr{H}^{(0)} - \epsilon_{\boldsymbol{k},n}^{(0)}\Big|\Psi_{\boldsymbol{k},n}^{(0)\mathrm{IR}}\Big\rangle_{\mathrm{IR}} + \Big\langle\Psi_{\boldsymbol{k},n}^{(0)\mathrm{IR}}\Big|\mathscr{H}^{(0)} - \epsilon_{\boldsymbol{k},n}^{(0)}\Big|\boldsymbol{\nabla}\boldsymbol{\nabla}^{\top}\Psi_{\boldsymbol{k},n}^{(0)\mathrm{IR}}\Big\rangle_{\mathrm{IR}}\Big)\\
&+\sum_{\alpha}\sum_{\boldsymbol{k},n} f_{\boldsymbol{k},n}^{(0)}\sum_{\boldsymbol{G}'\boldsymbol{G}}\Big\{\Big(-\mathrm{i}^2[\boldsymbol{k}+\boldsymbol{G}'][\boldsymbol{k}+\boldsymbol{G}']^{\top} - \mathrm{i}^2[\boldsymbol{k}+\boldsymbol{G}][\boldsymbol{k}+\boldsymbol{G}]^{\top}\Big) && (7.152\mathrm{c})\\
&\quad\times\sum_{l'm'p'}\sum_{lmp}\Big(z_{\boldsymbol{G}'}^{(0)}(\boldsymbol{k},n)a_{l'm'p'}^{\boldsymbol{G}'\boldsymbol{k}\alpha}\Big)^{*}\Big\langle\vec{\varphi}_{l'm'p'}^{\mathring{\alpha}}\Big|\mathscr{H}^{(0)} - \epsilon_{\boldsymbol{k},n}^{(0)}\Big|\vec{\varphi}_{lmp}^{\mathring{\alpha}}\Big\rangle_{\alpha} z_{\boldsymbol{G}}^{(0)}(\boldsymbol{k},n)a_{lmp}^{\boldsymbol{G}\boldsymbol{k}\alpha}\Big\}\,.
\end{aligned}$$

Now, the IR matrix elements incorporating an outer product of gradients can be replaced by using an IR version of equations (7.136d) and (7.135d), in which the gradient acts on the IR basis functions. This yields

$$
\begin{aligned}
0 = {} & \int_{\mathrm{IR}} \left(\boldsymbol{\nabla}\rho_{\mathrm{IR}}^{(0)}(\boldsymbol{r})\right)\left(\boldsymbol{\nabla}^{\top}V_{\mathrm{eff}}^{(0)\mathrm{IR}}(\boldsymbol{r})\right)\mathrm{d}^3r \\
& + 2\sum_{\boldsymbol{k},n} f_{\boldsymbol{k},n}^{(0)} \sum_{\boldsymbol{G}'\boldsymbol{G}'} \left\langle -\mathrm{i}[\boldsymbol{k}+\boldsymbol{G}'] z_{\boldsymbol{G}'}^{(0)}(\boldsymbol{k},n)\phi_{\boldsymbol{k},\boldsymbol{G}'}^{(0)\mathrm{IR}} \middle| \mathscr{H}^{(0)} - \epsilon_{\boldsymbol{k},n}^{(0)} \middle| -\mathrm{i}[\boldsymbol{k}+\boldsymbol{G}]^{\top} z_{\boldsymbol{G}}^{(0)}(\boldsymbol{k},n)\phi_{\boldsymbol{k},\boldsymbol{G}}^{(0)\mathrm{IR}} \right\rangle_{\mathrm{IR}} \\
& - \sum_{\alpha}\sum_{\boldsymbol{k},n} f_{\boldsymbol{k},n}^{(0)} \Bigg\{ \oint_{\partial\alpha} \hat{\boldsymbol{r}} \left(\sum_{\boldsymbol{G}'} -\mathrm{i}[\boldsymbol{k}+\boldsymbol{G}']^{\top} z_{\boldsymbol{G}'}^{(0)}(\boldsymbol{k},n)\phi_{\boldsymbol{k},\boldsymbol{G}'}^{(0)\mathrm{IR}}(\boldsymbol{r}) \right)^{*} \left(\mathscr{H}^{(0)} - \epsilon_{\boldsymbol{k},n}^{(0)}\right) \varPsi_{\boldsymbol{k},n}^{(0)}(\boldsymbol{r})\,\mathrm{d}S \\
& \qquad + \oint_{\partial\alpha} \hat{\boldsymbol{r}}\,\varPsi_{\boldsymbol{k},n}^{(0)*}(\boldsymbol{r}) \left(\mathscr{H}^{(0)} - \epsilon_{\boldsymbol{k},n}^{(0)}\right) \sum_{\boldsymbol{G}} (-\mathrm{i})[\boldsymbol{k}+\boldsymbol{G}]^{\top} z_{\boldsymbol{G}}^{(0)}(\boldsymbol{k},n)\phi_{\boldsymbol{k},\boldsymbol{G}}^{(0)\mathrm{IR}}(\boldsymbol{r})\,\mathrm{d}S \Bigg\} \\
& - \sum_{\alpha}\sum_{\boldsymbol{k},n} f_{\boldsymbol{k},n}^{(0)} \sum_{\boldsymbol{G}'\boldsymbol{G}} \sum_{l'm'p'} \sum_{lmp} \left(\mathrm{i}^2 [\boldsymbol{k}+\boldsymbol{G}'][\boldsymbol{k}+\boldsymbol{G}']^{\top} z_{\boldsymbol{G}'}^{(0)}(\boldsymbol{k},n) a_{l'm'p'}^{\boldsymbol{G}'\boldsymbol{k}\alpha} \right)^{*} z_{\boldsymbol{G}}^{(0)}(\boldsymbol{k},n) a_{lmp}^{\boldsymbol{G}\boldsymbol{k}\alpha} \\
& \qquad \times \left\langle \vec{\varphi}_{l'm'p'}^{\mathring{\alpha}} \middle| \mathscr{H}^{(0)} - \epsilon_{\boldsymbol{k},n}^{(0)} \middle| \vec{\varphi}_{lmp}^{\mathring{\alpha}} \right\rangle_{\alpha} \\
& - \sum_{\alpha}\sum_{\boldsymbol{k},n} f_{\boldsymbol{k},n}^{(0)} \sum_{\boldsymbol{G}'\boldsymbol{G}} \sum_{l'm'p'} \sum_{lmp} \left(z_{\boldsymbol{G}'}^{(0)}(\boldsymbol{k},n) a_{lmp}^{\boldsymbol{G}'\boldsymbol{k}\alpha} \right)^{*} \mathrm{i}^2 [\boldsymbol{k}+\boldsymbol{G}][\boldsymbol{k}+\boldsymbol{G}]^{\top} z_{\boldsymbol{G}}^{(0)}(\boldsymbol{k},n) a_{l'm'p'}^{\boldsymbol{G}\boldsymbol{k}\alpha} \\
& \qquad \times \left\langle \vec{\varphi}_{l'm'p'}^{\mathring{\alpha}} \middle| \mathscr{H}^{(0)} - \epsilon_{\boldsymbol{k},n}^{(0)} \middle| \vec{\varphi}_{lmp}^{\mathring{\alpha}} \right\rangle_{\alpha} ,
\end{aligned}
\tag{7.152d}
$$

where in the second line a product of two minus signs is inserted. For the surface integrals in the third and fourth lines of equation (7.152d), an additional minus sign results from the fact that the normal vector on the outside of the IR surface is antiparallel to the normal vector on the MT sphere. Furthermore, the MT terms in equation (7.152c) have been further evaluated. Identifying $\boldsymbol{z}_{\boldsymbol{G}'}^{(1)}(\boldsymbol{k},n;\boldsymbol{0}\alpha) = -\mathrm{i}[\boldsymbol{k}+\boldsymbol{G}] z_{\boldsymbol{G}}^{(0)}(\boldsymbol{k},n)$ leads to

$$
\begin{aligned}
0 = {} & \int_{\mathrm{IR}} \left(\boldsymbol{\nabla}\rho_{\mathrm{IR}}^{(0)}(\boldsymbol{r})\right)\left(\boldsymbol{\nabla}^{\top}V_{\mathrm{eff}}^{(0)\mathrm{IR}}(\boldsymbol{r})\right)\mathrm{d}^3r \\
& + 2\sum_{\boldsymbol{k},n} f_{\boldsymbol{k},n}^{(0)} \left\langle \sum_{\boldsymbol{G}'} \boldsymbol{z}_{\boldsymbol{G}'}^{(1)}(\boldsymbol{k},n;\boldsymbol{0}\alpha)\phi_{\boldsymbol{k},\boldsymbol{G}'}^{(0)\mathrm{IR}} \middle| \mathscr{H}^{(0)} - \epsilon_{\boldsymbol{k},n}^{(0)} \middle| \sum_{\boldsymbol{G}} \boldsymbol{z}_{\boldsymbol{G}}^{(1)}(\boldsymbol{k},n;\boldsymbol{0}\alpha)\phi_{\boldsymbol{k},\boldsymbol{G}}^{(0)\mathrm{IR}} \right\rangle_{\mathrm{IR}} \\
& - \sum_{\boldsymbol{k},n} f_{\boldsymbol{k},n}^{(0)} \Bigg\{ \oint_{\partial\alpha} \hat{\boldsymbol{r}} \left(\sum_{\boldsymbol{G}'} \boldsymbol{z}_{\boldsymbol{G}'}^{(1)}(\boldsymbol{k},n;\boldsymbol{0}\alpha)\phi_{\boldsymbol{k},\boldsymbol{G}'}^{(0)\mathrm{IR}} \right)^{*} \left(\mathscr{H}^{(0)} - \epsilon_{\boldsymbol{k},n}^{(0)}\right) \varPsi_{\boldsymbol{k},n}^{(0)}\,\mathrm{d}S \\
& \qquad + \oint_{\partial\alpha} \hat{\boldsymbol{r}}\,\varPsi^{*(0)}(\boldsymbol{r}) \left(\mathscr{H}^{(0)} - \epsilon_{\boldsymbol{k},n}^{(0)}\right) \sum_{\boldsymbol{G}} \boldsymbol{z}_{\boldsymbol{G}}^{(1)}(\boldsymbol{k},n;\boldsymbol{0}\alpha)\phi_{\boldsymbol{k},\boldsymbol{G}}^{(0)\mathrm{IR}}\,\mathrm{d}S \Bigg\} \\
& + \sum_{\boldsymbol{k},n} f_{\boldsymbol{k},n}^{(0)} \sum_{\boldsymbol{G}'\boldsymbol{G}} \sum_{l'm'p'} \sum_{lmp} \left(\boldsymbol{z}_{\boldsymbol{G}'}^{(1)}(\boldsymbol{k},n;\boldsymbol{0}\alpha)\mathrm{i}[\boldsymbol{k}+\boldsymbol{G}']^{\top} a_{l'm'p'}^{\boldsymbol{G}'\boldsymbol{k}\alpha} \right)^{*} z_{\boldsymbol{G}}^{(0)}(\boldsymbol{k},n) a_{lmp}^{\boldsymbol{G}\boldsymbol{k}\alpha} \\
& \qquad \times \left\langle \vec{\varphi}_{l'm'p'}^{\mathring{\alpha}} \middle| \mathscr{H}^{(0)} - \epsilon_{\boldsymbol{k},n}^{(0)} \middle| \vec{\varphi}_{lmp}^{\mathring{\alpha}} \right\rangle_{\alpha} \\
& + \sum_{\boldsymbol{k},n} f_{\boldsymbol{k},n}^{(0)} \sum_{\boldsymbol{G}'\boldsymbol{G}} \sum_{l'm'p'} \sum_{lmp} \left(z_{\boldsymbol{G}'}^{(0)}(\boldsymbol{k},n) a_{lmp}^{\boldsymbol{G}'\boldsymbol{k}\alpha} \right)^{*} \boldsymbol{z}_{\boldsymbol{G}'}^{(1)}(\boldsymbol{k},n;\boldsymbol{0}\alpha)\mathrm{i}[\boldsymbol{k}+\boldsymbol{G}]^{\top} a_{l'm'p'}^{\boldsymbol{G}\boldsymbol{k}\alpha} \\
& \qquad \times \left\langle \vec{\varphi}_{l'm'p'}^{\mathring{\alpha}} \middle| \mathscr{H}^{(0)} - \epsilon_{\boldsymbol{k},n}^{(0)} \middle| \vec{\varphi}_{lmp}^{\mathring{\alpha}} \right\rangle_{\alpha} .
\end{aligned}
\tag{7.152e}
$$

Finally, this is reformulated to the desired terms that do not obviously cancel:

$$
\begin{aligned}
0 = {} & \int_{\mathrm{IR}} \boldsymbol{\nabla}\rho_{\mathrm{IR}}^{(0)}(\boldsymbol{r})\boldsymbol{\nabla}^{\top}V_{\mathrm{eff}}^{(0)\mathrm{IR}}(\boldsymbol{r})\,\mathrm{d}^3r \\
& + 2\sum_{\boldsymbol{k}n} f_{\boldsymbol{k},n}^{(0)} \sum_{\boldsymbol{G}'\boldsymbol{G}} \boldsymbol{z}_{\boldsymbol{G}'}^{*(1)}(\boldsymbol{k},n;\boldsymbol{0}\alpha)\left\langle \phi_{\boldsymbol{k},\boldsymbol{G}'}^{(0)\mathrm{IR}} \middle| \mathscr{H}^{(0)} - \epsilon_{\boldsymbol{k},n}^{(0)} \middle| \phi_{\boldsymbol{k},\boldsymbol{G}}^{(0)\mathrm{IR}} \right\rangle_{\mathrm{IR}} \boldsymbol{z}_{\boldsymbol{G}}^{(1)}(\boldsymbol{k},n;\boldsymbol{0}\alpha) \\
& - \sum_{\boldsymbol{k},n} f_{\boldsymbol{k},n}^{(0)} \left\{ \oint_{\partial\alpha} \boldsymbol{\Psi}_{\boldsymbol{k},n}^{*(1)\mathrm{IR}\boldsymbol{0}}(\boldsymbol{r};\alpha)\left(\mathscr{H}^{(0)} - \epsilon_{\boldsymbol{k},n}^{(0)}\right)\Psi_{\boldsymbol{k},n}^{(0)\mathrm{IR}}\hat{\boldsymbol{r}}^{\top}\,\mathrm{d}S \right. \\
& \qquad\qquad \left. + \oint_{\partial\alpha} \hat{\boldsymbol{r}}\,\Psi_{\boldsymbol{k},n}^{*(0)\mathrm{IR}}(\boldsymbol{r})\left(\mathscr{H}^{(0)} - \epsilon_{\boldsymbol{k},n}^{(0)}\right)\left[\boldsymbol{\Psi}_{\boldsymbol{k},n}^{(1)\mathrm{IR}\boldsymbol{0}}(\boldsymbol{r};\alpha)\right]^{\top}\mathrm{d}S \right\} \\
& + \sum_{\boldsymbol{k},n} f_{\boldsymbol{k},n}^{(0)} \sum_{\boldsymbol{G}'\boldsymbol{G}} \sum_{l'm'p'} \sum_{lmp} \left(\boldsymbol{z}_{\boldsymbol{G}'}^{(1)}(\boldsymbol{k},n;\boldsymbol{0}\alpha)\mathrm{i}[\boldsymbol{k}+\boldsymbol{G}']^{\top}a_{l'm'p'}^{\boldsymbol{G}'\boldsymbol{k}\alpha}\right)^{*} z_{\boldsymbol{G}}^{(0)}(\boldsymbol{k},n)a_{lmp}^{\boldsymbol{G}\boldsymbol{k}\alpha} \\
& \qquad\qquad\qquad\qquad \times \left\langle \vec{\varphi}_{l'm'p'}^{\mathring{\alpha}} \middle| \mathscr{H}^{(0)} - \epsilon_{\boldsymbol{k},n}^{(0)} \middle| \vec{\varphi}_{lmp}^{\mathring{\alpha}} \right\rangle_{\alpha} \\
& + \sum_{\boldsymbol{k},n} f_{\boldsymbol{k},n}^{(0)} \sum_{\boldsymbol{G}'\boldsymbol{G}} \sum_{l'm'p'} \sum_{lmp} \left(z_{\boldsymbol{G}'}^{(0)}(\boldsymbol{k},n)a_{lmp}^{\boldsymbol{G}'\boldsymbol{k}\alpha}\right)^{*} \boldsymbol{z}_{\boldsymbol{G}'}^{(1)}(\boldsymbol{k},n;\boldsymbol{0}\alpha)\mathrm{i}[\boldsymbol{k}+\boldsymbol{G}]^{\top}a_{l'm'p'}^{\boldsymbol{G}\boldsymbol{k}\alpha} \\
& \qquad\qquad\qquad\qquad \times \left\langle \vec{\varphi}_{l'm'p'}^{\mathring{\alpha}} \middle| \mathscr{H}^{(0)} - \epsilon_{\boldsymbol{k},n}^{(0)} \middle| \vec{\varphi}_{lmp}^{\mathring{\alpha}} \right\rangle_{\alpha} .
\end{aligned}
\tag{7.152f}
$$

But as shown, they overall vanish for monoatomic systems and Goldstone modes.

7.6.5 Canceling Gradient Pulay Matrix-Elements with Surface Integrals

Resume and motivating further reformulations

Relative to the dynamical-matrix approach of Klüppelberg [88], thus far (i) the expressions for the Pulay core-electron corrections have been rectified, (ii) terms containing outer products of gradients are avoided, and (iii) only those quantities are demanded that are actually available from `juPhon`. Having programmed these optimizations, each of our developed tests passes. Furthermore, the acoustical frequencies of fcc Ne for $\boldsymbol{q} = \boldsymbol{0}$ vanish, as well as the numerical accuracy of the employed integration routines admits it, whereas computing the Goldstone modes of fcc Al works less well. Although implementing Hessian matrices of Kohn–Sham wave functions in the MT spheres is not required anymore, matrix elements and surface integrals incorporating gradients of Kohn–Sham wave functions are still a challenging part of the formalism. But, the fact that the resulting dispersion relations are absolutely unphysical, i.e., they predict material instabilities not reproducible by the experiment or FD reference calculations, poses the main problem.

Inspiring contradiction

Neukirchen has derived a more general form of the second-order total-energy variation due to a phonon, in particular being valid for arbitrary metals [256]. In contrast to Klüppelberg [88], it takes all terms into account which are proportional to variations of the occupation number. However, omitting these contributions, his formalism seems not consistent with the equations that Klüppelberg has deduced. Especially, it does not comprise terms in which gradients of wave functions are required. Inspired by this outcome, I have found a way to reformulate the formalism of Klüppelberg so that it better conforms with the results of Neukirchen.

Reformulation

Extracting the third, fourth, eighth, and ninth lines of equation (7.129) as well as separating those terms which are independent of the surface integral reads

$$\begin{aligned}
&2\Big(\boldsymbol{z}^{(1)}_{\boldsymbol{G}'}(\boldsymbol{k},n;\boldsymbol{q}\beta)a^{\boldsymbol{G}'\boldsymbol{k}\alpha}_{l'm'p'}(\boldsymbol{q}) + \delta_{\beta\alpha}\mathrm{i}(\boldsymbol{k}+\boldsymbol{G}')z^{(0)}_{\boldsymbol{G}'}(\boldsymbol{k},n)a^{\boldsymbol{G}'\boldsymbol{k}\alpha}_{l'm'p'}\Big)^{*} z^{(0)}_{\boldsymbol{G}}(\boldsymbol{k},n)a^{\boldsymbol{G}\boldsymbol{k}\alpha}_{lmp} \\
&\qquad\qquad\qquad \times \oint_{\partial\alpha} \hat{\boldsymbol{r}}^{\top}\vec{\varphi}^{\,*s\mathring{\alpha}}_{l'm'p'}\Big(\mathscr{H}^{(0)} - \epsilon^{(0)}_{\boldsymbol{k},n}\Big)\vec{\varphi}^{\,*s\mathring{\alpha}}_{lmp}\,\mathrm{d}S \\
&+ 2\oint_{\partial\beta} \hat{\boldsymbol{r}}\vec{\varphi}^{\,*s\mathring{\beta}}_{l'm'p'}\Big(\mathscr{H}^{(0)} - \epsilon^{(0)}_{\boldsymbol{k},n}\Big)\vec{\varphi}^{\,*s\mathring{\beta}}_{lmp}\,\mathrm{d}S \\
&\qquad \times z^{*(0)}_{\boldsymbol{G}'}(\boldsymbol{k},n)a^{*\boldsymbol{G}'\boldsymbol{k}\beta}_{l'm'p'}\Big[\boldsymbol{z}^{(1)}_{\boldsymbol{G}}(\boldsymbol{k},n;\boldsymbol{q}\alpha)a^{\boldsymbol{G}\boldsymbol{k}\beta}_{lmp}(\boldsymbol{q}) + \delta_{\beta\alpha}\mathrm{i}(\boldsymbol{k}+\boldsymbol{G})z^{(0)}_{\boldsymbol{G}}(\boldsymbol{k},n)a^{\boldsymbol{G}\boldsymbol{k}\beta}_{lmp}\Big]^{\top}.
\end{aligned} \tag{7.153a}$$

Now, the divergence theorem

$$\begin{aligned}
&\oint_{\partial\alpha} \hat{\boldsymbol{r}}^{\top}\vec{\varphi}^{\,*s\mathring{\alpha}}_{l'm'p'}\Big(\mathscr{H}^{(0)} - \epsilon^{(0)}_{\boldsymbol{k},n}\Big)\vec{\varphi}^{\,s\mathring{\alpha}}_{lmp}\,\mathrm{d}S \\
&= \Big\langle\vec{\varphi}^{\,\mathring{\alpha}}_{l'm'p'}\Big|\mathscr{H}^{(0)} - \epsilon^{(0)}_{\boldsymbol{k},n}\Big|\boldsymbol{\nabla}^{\top}\vec{\varphi}^{\,\mathring{\alpha}}_{lmp}\Big\rangle_{\alpha} + \Big\langle\boldsymbol{\nabla}^{\top}\vec{\varphi}^{\,\mathring{\alpha}}_{l'm'p'}\Big|\mathscr{H}^{(0)} - \epsilon^{(0)}_{\boldsymbol{k},n}\Big|\vec{\varphi}^{\,\mathring{\alpha}}_{lmp}\Big\rangle_{\alpha} \\
&\quad + \Big\langle\vec{\varphi}^{\,\mathring{\alpha}}_{l'm'p'}\Big|\boldsymbol{\nabla}^{\top}\mathscr{V}^{(0)}_{\text{eff}}\Big|\vec{\varphi}^{\,\mathring{\alpha}}_{lmp}\Big\rangle_{\alpha}
\end{aligned} \tag{7.153b}$$

can be applied, which is likewise valid in its transposed form

$$\begin{aligned}
&\oint_{\partial\beta} \hat{\boldsymbol{r}}\vec{\varphi}^{\,*s\mathring{\beta}}_{l'm'p'}\Big(\mathscr{H}^{(0)} - \epsilon^{(0)}_{\boldsymbol{k},n}\Big)\vec{\varphi}^{\,s\mathring{\beta}}_{lmp}\,\mathrm{d}S \\
&= \Big\langle\vec{\varphi}^{\,\mathring{\beta}}_{l'm'p'}\Big|\mathscr{H}^{(0)} - \epsilon^{(0)}_{\boldsymbol{k},n}\Big|\boldsymbol{\nabla}\vec{\varphi}^{\,\mathring{\beta}}_{lmp}\Big\rangle_{\beta} + \Big\langle\boldsymbol{\nabla}\vec{\varphi}^{\,\mathring{\beta}}_{l'm'p'}\Big|\mathscr{H}^{(0)} - \epsilon^{(0)}_{\boldsymbol{k},n}\Big|\vec{\varphi}^{\,\mathring{\beta}}_{lmp}\Big\rangle_{\beta} \\
&\quad + \Big\langle\vec{\varphi}^{\,\mathring{\beta}}_{l'm'p'}\Big|\boldsymbol{\nabla}\mathscr{V}^{(0)}_{\text{eff}}\Big|\vec{\varphi}^{\,\mathring{\beta}}_{lmp}\Big\rangle_{\beta}.
\end{aligned} \tag{7.153c}$$

Doing this and adding those terms with a gradient in equations (7.128b), (7.128c), as well as (7.128d) results in

$$\begin{aligned}
&2\Big(\boldsymbol{z}^{(1)}_{\boldsymbol{G}'}(\boldsymbol{k},n;\boldsymbol{q}\beta)a^{\boldsymbol{G}'\boldsymbol{k}\alpha}_{l'm'p'}(\boldsymbol{q})\Big)^{*}\Big\langle\vec{\varphi}^{\,\mathring{\alpha}}_{l'm'p'}\Big|\boldsymbol{\nabla}^{\top}\mathscr{V}^{(0)}_{\text{eff}}\Big|\vec{\varphi}^{\,\mathring{\alpha}}_{lmp}\Big\rangle_{\alpha} z^{(0)}_{\boldsymbol{G}}(\boldsymbol{k},n)a^{\boldsymbol{G}\boldsymbol{k}\alpha}_{lmp} \\
&+ 2\delta_{\beta\alpha}\Big(\mathrm{i}(\boldsymbol{k}+\boldsymbol{G}')z^{(0)}_{\boldsymbol{G}'}(\boldsymbol{k},n)a^{\boldsymbol{G}'\boldsymbol{k}\alpha}_{l'm'p'}\Big)^{*}\Big\langle\vec{\varphi}^{\,\mathring{\alpha}}_{l'm'p'}\Big|\boldsymbol{\nabla}^{\top}\mathscr{V}^{(0)}_{\text{eff}}\Big|\vec{\varphi}^{\,\mathring{\beta}}_{lmp}\Big\rangle_{\alpha} z^{(0)}_{\boldsymbol{G}}(\boldsymbol{k},n)a^{\boldsymbol{G}\boldsymbol{k}\alpha}_{lmp} \\
&+ 2\Big\langle\vec{\varphi}^{\,\mathring{\beta}}_{l'm'p'}\Big|\boldsymbol{\nabla}\mathscr{V}^{(0)}_{\text{eff}}\Big|\vec{\varphi}^{\,\mathring{\beta}}_{lmp}\Big\rangle_{\beta} z^{*(0)}_{\boldsymbol{G}'}(\boldsymbol{k},n)a^{*\boldsymbol{G}'\boldsymbol{k}\beta}_{l'm'p'}\Big[\boldsymbol{z}^{(1)}_{\boldsymbol{G}}(\boldsymbol{k},n;\boldsymbol{q}\alpha)a^{\boldsymbol{G}\boldsymbol{k}\beta}_{lmp}(\boldsymbol{q})\Big]^{\top} \\
&+ 2\delta_{\beta\alpha}\Big\langle\vec{\varphi}^{\,\mathring{\beta}}_{l'm'p'}\Big|\boldsymbol{\nabla}\mathscr{V}^{(0)}_{\text{eff}}\Big|\vec{\varphi}^{\,\mathring{\beta}}_{lmp}\Big\rangle_{\beta} z^{*(0)}_{\boldsymbol{G}'}(\boldsymbol{k},n)a^{*\boldsymbol{G}'\boldsymbol{k}\beta}_{l'm'p'}\Big[\mathrm{i}(\boldsymbol{k}+\boldsymbol{G})z^{(0)}_{\boldsymbol{G}}(\boldsymbol{k},n)a^{\boldsymbol{G}\boldsymbol{k}\beta}_{lmp}\Big]^{\top} \\
&+ 2\Big(\boldsymbol{z}^{(1)}_{\boldsymbol{G}'}(\boldsymbol{k},n;\boldsymbol{q}\beta)a^{\boldsymbol{G}'\boldsymbol{k}\alpha}_{l'm'p'}(\boldsymbol{q})\Big)^{*}\Big\langle\boldsymbol{\nabla}^{\top}\vec{\varphi}^{\,\mathring{\alpha}}_{l'm'p'}\Big|\mathscr{H}^{(0)} - \epsilon^{(0)}_{\boldsymbol{k},n}\Big|\vec{\varphi}^{\,\mathring{\alpha}}_{lmp}\Big\rangle_{\alpha} z^{(0)}_{\boldsymbol{G}}(\boldsymbol{k},n)a^{\boldsymbol{G}\boldsymbol{k}\alpha}_{lmp} \\
&- 2\Big(\boldsymbol{z}^{(1)}_{\boldsymbol{G}'}(\boldsymbol{k},n;\boldsymbol{q}\beta)a^{\boldsymbol{G}'\boldsymbol{k}\alpha}_{l'm'p'}(\boldsymbol{q})\Big)^{*}\Big\langle\boldsymbol{\nabla}^{\top}\vec{\varphi}^{\,\mathring{\alpha}}_{l'm'p'}\Big|\mathscr{H}^{(0)} - \epsilon^{(0)}_{\boldsymbol{k},n}\Big|\vec{\varphi}^{\,\mathring{\alpha}}_{lmp}\Big\rangle_{\alpha} z^{(0)}_{\boldsymbol{G}}(\boldsymbol{k},n)a^{\boldsymbol{G}\boldsymbol{k}\alpha}_{lmp} \\
&- \delta_{\beta\alpha}\Big(z^{(0)}_{\boldsymbol{G}'}(\boldsymbol{k},n)a^{\boldsymbol{G}'\boldsymbol{k}\alpha}_{l'm'p'}\mathrm{i}[\boldsymbol{k}+\boldsymbol{G}']\Big)^{*}\Big\langle\boldsymbol{\nabla}^{\top}\vec{\varphi}^{\,\mathring{\alpha}}_{l'm'p'}\Big|\mathscr{H}^{(0)} - \epsilon^{(0)}_{\boldsymbol{k},n}\Big|\vec{\varphi}^{\,\mathring{\alpha}}_{lmp}\Big\rangle_{\alpha} z^{(0)}_{\boldsymbol{G}}(\boldsymbol{k},n)a^{\boldsymbol{G}\boldsymbol{k}\alpha}_{lmp} \\
&+ 2\delta_{\beta\alpha}\Big(z^{(0)}_{\boldsymbol{G}'}(\boldsymbol{k},n)a^{\boldsymbol{G}'\boldsymbol{k}\alpha}_{l'm'p'}\mathrm{i}[\boldsymbol{k}+\boldsymbol{G}']\Big)^{*}\Big\langle\boldsymbol{\nabla}^{\top}\vec{\varphi}^{\,\mathring{\alpha}}_{l'm'p'}\Big|\mathscr{H}^{(0)} - \epsilon^{(0)}_{\boldsymbol{k},n}\Big|\vec{\varphi}^{\,\mathring{\alpha}}_{lmp}\Big\rangle_{\alpha} z^{(0)}_{\boldsymbol{G}}(\boldsymbol{k},n)a^{\boldsymbol{G}\boldsymbol{k}\alpha}_{lmp} \\
&- \delta_{\beta\alpha}\Big(z^{(0)}_{\boldsymbol{G}'}(\boldsymbol{k},n)a^{\boldsymbol{G}'\boldsymbol{k}\alpha}_{l'm'p'}\Big)^{*}z^{(0)}_{\boldsymbol{G}}(\boldsymbol{k},n)a^{\boldsymbol{G}\boldsymbol{k}\alpha}_{lmp}\mathrm{i}[\boldsymbol{k}+\boldsymbol{G}]\Big\langle\vec{\varphi}^{\,\mathring{\alpha}}_{l'm'p'}\Big|\mathscr{H}^{(0)} - \epsilon^{(0)}_{\boldsymbol{k},n}\Big|\boldsymbol{\nabla}^{\top}\vec{\varphi}^{\,\mathring{\alpha}}_{lmp}\Big\rangle_{\alpha} \\
&+ 2\Big(\boldsymbol{z}^{(1)}_{\boldsymbol{G}'}(\boldsymbol{k},n;\boldsymbol{q}\beta)a^{\boldsymbol{G}'\boldsymbol{k}\alpha}_{l'm'p'}(\boldsymbol{q})\Big)^{*}\Big\langle\vec{\varphi}^{\,\mathring{\alpha}}_{l'm'p'}\Big|\mathscr{H}^{(0)} - \epsilon^{(0)}_{\boldsymbol{k},n}\Big|\boldsymbol{\nabla}^{\top}\vec{\varphi}^{\,\mathring{\alpha}}_{lmp}\Big\rangle_{\alpha} z^{(0)}_{\boldsymbol{G}}(\boldsymbol{k},n)a^{\boldsymbol{G}\boldsymbol{k}\alpha}_{lmp}
\end{aligned} \tag{7.153d}$$

$$
\begin{aligned}
&- 2\Big(\boldsymbol{z}^{(1)}_{\boldsymbol{G}'}(\boldsymbol{k},n;\boldsymbol{q}\beta)a^{\boldsymbol{G}'\boldsymbol{k}\alpha}_{l'm'p'}(\boldsymbol{q})\Big)^{*}\Big\langle\vec{\varphi}^{\mathring{\alpha}}_{l'm'p'}\Big|\mathscr{H}^{(0)}-\epsilon^{(0)}_{\boldsymbol{k},n}\Big|\boldsymbol{\nabla}^{\top}\vec{\varphi}^{\mathring{\alpha}}_{lmp}\Big\rangle_{\alpha}z^{(0)}_{\boldsymbol{G}}(\boldsymbol{k},n)a^{\boldsymbol{G}\boldsymbol{k}\alpha}_{lmp}\\
&+ 2\delta_{\beta\alpha}\Big(z^{(0)}_{\boldsymbol{G}'}(\boldsymbol{k},n)a^{\boldsymbol{G}'\boldsymbol{k}\alpha}_{l'm'p'}\mathrm{i}[\boldsymbol{k}+\boldsymbol{G}']\Big)^{*}\Big\langle\vec{\varphi}^{\mathring{\alpha}}_{l'm'p'}\Big|\mathscr{H}^{(0)}-\epsilon^{(0)}_{\boldsymbol{k},n}\Big|\boldsymbol{\nabla}^{\top}\vec{\varphi}^{\mathring{\alpha}}_{lmp}\Big\rangle_{\alpha}z^{(0)}_{\boldsymbol{G}}(\boldsymbol{k},n)a^{\boldsymbol{G}\boldsymbol{k}\alpha}_{lmp}\\
&- 2\delta_{\beta\alpha}\Big(z^{(0)}_{\boldsymbol{G}'}(\boldsymbol{k},n)a^{\boldsymbol{G}'\boldsymbol{k}\alpha}_{l'm'p'}\mathrm{i}[\boldsymbol{k}+\boldsymbol{G}']\Big)^{*}\Big\langle\vec{\varphi}^{\mathring{\alpha}}_{l'm'p'}\Big|\mathscr{H}^{(0)}-\epsilon^{(0)}_{\boldsymbol{k},n}\Big|\boldsymbol{\nabla}^{\top}\vec{\varphi}^{\mathring{\alpha}}_{lmp}\Big\rangle_{\alpha}z^{(0)}_{\boldsymbol{G}}(\boldsymbol{k},n)a^{\boldsymbol{G}\boldsymbol{k}\alpha}_{lmp}\\
&+ 2\Big(z^{(0)}_{\boldsymbol{G}'}(\boldsymbol{k},n)a^{\boldsymbol{G}'\boldsymbol{k}\beta}_{l'm'p'}\Big)^{*}a^{\boldsymbol{G}\boldsymbol{k}\beta}_{lmp}(\boldsymbol{q})\Big\langle\vec{\varphi}^{\mathring{\beta}}_{l'm'p'}\Big|\mathscr{H}^{(0)}-\epsilon^{(0)}_{\boldsymbol{k},n}\Big|\boldsymbol{\nabla}\vec{\varphi}^{\mathring{\beta}}_{lmp}\Big\rangle_{\beta}\Big[\boldsymbol{z}^{(1)}_{\boldsymbol{G}}(\boldsymbol{k},n;\boldsymbol{q}\alpha)\Big]^{\top}\\
&- 2\Big(z^{(0)}_{\boldsymbol{G}'}(\boldsymbol{k},n)a^{\boldsymbol{G}'\boldsymbol{k}\beta}_{l'm'p'}\Big)^{*}a^{\boldsymbol{G}\boldsymbol{k}\beta}_{lmp}(\boldsymbol{q})\Big\langle\vec{\varphi}^{\mathring{\beta}}_{l'm'p'}\Big|\mathscr{H}^{(0)}-\epsilon^{(0)}_{\boldsymbol{k},n}\Big|\boldsymbol{\nabla}\vec{\varphi}^{\mathring{\beta}}_{lmp}\Big\rangle_{\beta}\Big[\boldsymbol{z}^{(1)}_{\boldsymbol{G}}(\boldsymbol{k},n;\boldsymbol{q}\alpha)\Big]^{\top}\\
&- \delta_{\beta\alpha}\Big\langle\vec{\varphi}^{\mathring{\alpha}}_{l'm'p'}\Big|\mathscr{H}^{(0)}-\epsilon^{(0)}_{\boldsymbol{k},n}\Big|\boldsymbol{\nabla}\vec{\varphi}^{\mathring{\alpha}}_{lmp}\Big\rangle_{\alpha}\Big(z^{(0)}_{\boldsymbol{G}'}(\boldsymbol{k},n)a^{\boldsymbol{G}'\boldsymbol{k}\alpha}_{l'm'p'}\Big)^{*}\Big[z^{(0)}_{\boldsymbol{G}}(\boldsymbol{k},n)a^{\boldsymbol{G}\boldsymbol{k}\alpha}_{lmp}\mathrm{i}[\boldsymbol{k}+\boldsymbol{G}]\Big]^{\top}\\
&+ 2\delta_{\beta\alpha}\Big\langle\vec{\varphi}^{\mathring{\alpha}}_{l'm'p'}\Big|\mathscr{H}^{(0)}-\epsilon^{(0)}_{\boldsymbol{k},n}\Big|\boldsymbol{\nabla}\vec{\varphi}^{\mathring{\alpha}}_{lmp}\Big\rangle_{\alpha}\Big(z^{(0)}_{\boldsymbol{G}'}(\boldsymbol{k},n)a^{\boldsymbol{G}'\boldsymbol{k}\alpha}_{lmp}\Big)^{*}\Big[z^{(0)}_{\boldsymbol{G}}(\boldsymbol{k},n)a^{\boldsymbol{G}\boldsymbol{k}\alpha}_{l'm'p'}\mathrm{i}[\boldsymbol{k}+\boldsymbol{G}]\Big]^{\top}\\
&- \delta_{\beta\alpha}\Big\langle\boldsymbol{\nabla}\vec{\varphi}^{\mathring{\alpha}}_{l'm'p'}\Big|\mathscr{H}^{(0)}-\epsilon^{(0)}_{\boldsymbol{k},n}\Big|\vec{\varphi}^{\mathring{\alpha}}_{lmp}\Big\rangle_{\alpha}\Big[z^{(0)}_{\boldsymbol{G}'}(\boldsymbol{k},n)a^{\boldsymbol{G}'\boldsymbol{k}\alpha}_{l'm'p'}\mathrm{i}[\boldsymbol{k}+\boldsymbol{G}']\Big]^{\dagger}z^{(0)}_{\boldsymbol{G}}(\boldsymbol{k},n)a^{\boldsymbol{G}\boldsymbol{k}\alpha}_{lmp}\\
&+ 2\delta_{\beta\alpha}\Big(z^{(0)}_{\boldsymbol{G}'}(\boldsymbol{k},n)a^{\boldsymbol{G}'\boldsymbol{k}\alpha}_{l'm'p'}\Big)^{*}\Big\langle\boldsymbol{\nabla}\vec{\varphi}^{\mathring{\alpha}}_{l'm'p'}\Big|\mathscr{H}^{(0)}-\epsilon^{(0)}_{\boldsymbol{k},n}\Big|\vec{\varphi}^{\mathring{\alpha}}_{lmp}\Big\rangle_{\alpha}z^{(0)}_{\boldsymbol{G}}(\boldsymbol{k},n)a^{\boldsymbol{G}\boldsymbol{k}\alpha}_{lmp}\mathrm{i}[\boldsymbol{k}+\boldsymbol{G}]^{\top}\\
&- 2\delta_{\beta\alpha}\Big(z^{(0)}_{\boldsymbol{G}'}(\boldsymbol{k},n)a^{\boldsymbol{G}'\boldsymbol{k}\alpha}_{l'm'p'}\Big)^{*}\Big\langle\boldsymbol{\nabla}\vec{\varphi}^{\mathring{\alpha}}_{l'm'p'}\Big|\mathscr{H}^{(0)}-\epsilon^{(0)}_{\boldsymbol{k},n}\Big|\vec{\varphi}^{\mathring{\alpha}}_{lmp}\Big\rangle_{\alpha}z^{(0)}_{\boldsymbol{G}}(\boldsymbol{k},n)a^{\boldsymbol{G}\boldsymbol{k}\alpha}_{lmp}\mathrm{i}[\boldsymbol{k}+\boldsymbol{G}]^{\top}\\
&+ 2\Big(z^{(0)}_{\boldsymbol{G}'}(\boldsymbol{k},n)a^{\boldsymbol{G}'\boldsymbol{k}\beta}_{l'm'p'}\Big)^{*}\Big\langle\boldsymbol{\nabla}\vec{\varphi}^{\mathring{\beta}}_{l'm'p'}\Big|\mathscr{H}^{(0)}-\epsilon^{(0)}_{\boldsymbol{k},n}\Big|\vec{\varphi}^{\mathring{\beta}}_{lmp}\Big\rangle_{\beta}\Big[\boldsymbol{z}^{(1)}_{\boldsymbol{G}}(\boldsymbol{k},n;\boldsymbol{q}\alpha)\Big]^{\top}a^{\boldsymbol{G}\boldsymbol{k}\beta}_{lmp}(\boldsymbol{q})\\
&- 2\Big(z^{(0)}_{\boldsymbol{G}'}(\boldsymbol{k},n)a^{\boldsymbol{G}'\boldsymbol{k}\beta}_{l'm'p'}\Big)^{*}\Big\langle\boldsymbol{\nabla}\vec{\varphi}^{\mathring{\beta}}_{l'm'p'}\Big|\mathscr{H}^{(0)}-\epsilon^{(0)}_{\boldsymbol{k},n}\Big|\vec{\varphi}^{\mathring{\beta}}_{lmp}\Big\rangle_{\beta}\Big[\boldsymbol{z}^{(1)}_{\boldsymbol{G}}(\boldsymbol{k},n;\boldsymbol{q}\alpha)\Big]^{\top}a^{\boldsymbol{G}\boldsymbol{k}\beta}_{lmp}(\boldsymbol{q})\,,
\end{aligned}
$$

which can be simplifed to

$$
\begin{aligned}
&= 2\Big(\boldsymbol{z}^{(1)}_{\boldsymbol{G}'}(\boldsymbol{k},n;\boldsymbol{q}\beta)a^{\boldsymbol{G}'\boldsymbol{k}\alpha}_{l'm'p'}(\boldsymbol{q})\Big)^{*}\Big\langle\vec{\varphi}^{\mathring{\alpha}}_{l'm'p'}\Big|\boldsymbol{\nabla}^{\top}\mathscr{V}^{(0)}_{\text{eff}}\Big|\vec{\varphi}^{\mathring{\alpha}}_{lmp}\Big\rangle_{\alpha}z^{(0)}_{\boldsymbol{G}}(\boldsymbol{k},n)a^{\boldsymbol{G}\boldsymbol{k}\alpha}_{lmp} \qquad (7.153\text{e})\\
&+ 2\delta_{\beta\alpha}\Big(\mathrm{i}(\boldsymbol{k}+\boldsymbol{G}')z^{(0)}_{\boldsymbol{G}'}(\boldsymbol{k},n)a^{\boldsymbol{G}'\boldsymbol{k}\alpha}_{l'm'p'}\Big)^{*}\Big\langle\vec{\varphi}^{\mathring{\alpha}}_{l'm'p'}\Big|\boldsymbol{\nabla}^{\top}\mathscr{V}^{(0)}_{\text{eff}}\Big|\vec{\varphi}^{\mathring{\alpha}}_{lmp}\Big\rangle_{\alpha}z^{(0)}_{\boldsymbol{G}}(\boldsymbol{k},n)a^{\boldsymbol{G}\boldsymbol{k}\alpha}_{lmp}\\
&+ 2\Big\langle\vec{\varphi}^{\mathring{\beta}}_{l'm'p'}\Big|\boldsymbol{\nabla}\mathscr{V}^{(0)}_{\text{eff}}\Big|\vec{\varphi}^{\mathring{\beta}}_{lmp}\Big\rangle_{\beta}z^{*(0)}_{\boldsymbol{G}'}(\boldsymbol{k},n)a^{*\boldsymbol{G}'\boldsymbol{k}\beta}_{l'm'p'}\Big[\boldsymbol{z}^{(1)}_{\boldsymbol{G}}(\boldsymbol{k},n;\boldsymbol{q}\alpha)a^{\boldsymbol{G}\boldsymbol{k}\beta}_{lmp}(\boldsymbol{q})\Big]^{\top}\\
&+ 2\delta_{\beta\alpha}\Big\langle\vec{\varphi}^{\mathring{\beta}}_{l'm'p'}\Big|\boldsymbol{\nabla}\mathscr{V}^{(0)}_{\text{eff}}\Big|\vec{\varphi}^{\mathring{\beta}}_{lmp}\Big\rangle_{\beta}z^{*(0)}_{\boldsymbol{G}'}(\boldsymbol{k},n)a^{*\boldsymbol{G}'\boldsymbol{k}\beta}_{l'm'p'}\Big[\mathrm{i}(\boldsymbol{k}+\boldsymbol{G})z^{(0)}_{\boldsymbol{G}}(\boldsymbol{k},n)a^{\boldsymbol{G}\boldsymbol{k}\beta}_{lmp}\Big]^{\top}\\
&+ 2\mathrm{i}\delta_{\beta\alpha}\,\mathrm{Im}\bigg(\Big(z^{(0)}_{\boldsymbol{G}'}(\boldsymbol{k},n)a^{\boldsymbol{G}'\boldsymbol{k}\alpha}_{l'm'p'}\mathrm{i}[\boldsymbol{k}+\boldsymbol{G}']\Big)^{*}\Big\langle\boldsymbol{\nabla}^{\top}\vec{\varphi}^{\mathring{\alpha}}_{l'm'p'}\Big|\mathscr{H}^{(0)}-\epsilon^{(0)}_{\boldsymbol{k},n}\Big|\vec{\varphi}^{\mathring{\alpha}}_{lmp}\Big\rangle_{\alpha}z^{(0)}_{\boldsymbol{G}}(\boldsymbol{k},n)a^{\boldsymbol{G}\boldsymbol{k}\alpha}_{lmp}\bigg)\\
&+ 2\mathrm{i}\delta_{\beta\alpha}\,\mathrm{Im}\bigg(\Big\langle\vec{\varphi}^{\mathring{\alpha}}_{l'm'p'}\Big|\mathscr{H}^{(0)}-\epsilon^{(0)}_{\boldsymbol{k},n}\Big|\boldsymbol{\nabla}\vec{\varphi}^{\mathring{\alpha}}_{lmp}\Big\rangle_{\alpha}\Big(z^{(0)}_{\boldsymbol{G}'}(\boldsymbol{k},n)a^{\boldsymbol{G}'\boldsymbol{k}\alpha}_{lmp}\Big)^{*}\Big[z^{(0)}_{\boldsymbol{G}'}(\boldsymbol{k},n)a^{\boldsymbol{G}'\boldsymbol{k}\alpha}_{l'm'p'}\mathrm{i}[\boldsymbol{k}+\boldsymbol{G}']\Big]^{\top}\bigg)\,.
\end{aligned}
$$

Since the dynamical matrix is made self-adjoint in the end, imaginary parts cancel. As a consequence, the last two lines of the previous equation are ignored in the following. Finally, it must be stressed that a reformulation of equation (7.153a) enormously simplifies the formalism of Klüppelberg [88]. Now, no matrix elements with gradients of the Kohn–Sham wave functions need to be calculated anymore.

7.6.6 Alleviating Muffin-Tin Integrands

Motivation

Through a numerical analysis, I have found that certain MT integrands are extremely large close to the core. The ultimate example is provided by the integrals of the displaced MT sphere in the third line of equation (7.145). Here, linear variations of the external potential and the density are multiplied. At the first mesh points, the integrands are about $10^{15} E_{\mathrm{h}}\, a_0^{-5}$, while average radial Jacobi determinants $r_{\nu\gamma}^2$ are about $10^{-10} a_0^2$ there. So, the Jacobi determinant, which normally leads to an irrelevant integrand close the core, is not efficient enough. As discussed in section 7.6.4, I have optimally arranged the formalism for the vanishing Goldstone modes by exploiting error cancelation. But for finite $\boldsymbol{q}$, this only partially helps, because some of the involved terms are dependent on $\boldsymbol{q}$ and their change worsens the aforementioned error cancelation. As a consequence, the interpolation between $\boldsymbol{r} = \boldsymbol{0}$ and the last mesh point becomes significant, especially against the background of the small energy scales that are usual for phonons.

Idea of Klüppelberg [88]

Since the development of general and accurate interpolations takes considerable effort, we searched for a way to avoid it. Finally, our discussion has come to the decision that it would be most consistent to apply again an optimization that was already suggested by Klüppelberg [88] for the Sternheimer equation [256]. He rewrites it such that a sum of the MT first-order effective potential and the MT gradient of the effective potential results (see section 7.4.1). As a consequence, numerically inaccurate sums analytically cancel and need not to be calculated anymore. Nonetheless, he has not transferred these ideas to the dynamical matrix.

Reformulation

For applying the aforementioned optimization of Klüppelberg [256], I proceed with the remaining terms of section 7.6.5, given by

$$\begin{aligned}
\sum_{l'm'p'} \sum_{lmp} \sum_{\boldsymbol{G}'\boldsymbol{G}} \sum_{\boldsymbol{k},n} f_{\boldsymbol{k},n}^{(0)} \Bigg\{ & 2\Big(\boldsymbol{z}_{\boldsymbol{G}'}^{(1)}(\boldsymbol{k},n;\boldsymbol{q}\beta) a_{l'm'p'}^{\boldsymbol{G}'\boldsymbol{k}\alpha}(\boldsymbol{q})\Big)^{*} \Big\langle \vec{\varphi}_{l'm'p'}^{\mathring{\alpha}} \Big| \boldsymbol{\nabla}^{\top} \mathscr{V}_{\mathrm{eff}}^{(0)} \Big| \vec{\varphi}_{lmp}^{\mathring{\alpha}} \Big\rangle_{\alpha} z_{\boldsymbol{G}}^{(0)}(\boldsymbol{k},n) a_{lmp}^{\boldsymbol{G}\boldsymbol{k}\alpha} \\
&+ 2\delta_{\beta\alpha} \Big(\mathrm{i}(\boldsymbol{k}+\boldsymbol{G}') z_{\boldsymbol{G}'}^{(0)}(\boldsymbol{k},n) a_{l'm'p'}^{\boldsymbol{G}'\boldsymbol{k}\alpha}\Big)^{*} \Big\langle \vec{\varphi}_{l'm'p'}^{\mathring{\alpha}} \Big| \boldsymbol{\nabla}^{\top} \mathscr{V}_{\mathrm{eff}}^{(0)} \Big| \vec{\varphi}_{lmp}^{\mathring{\alpha}} \Big\rangle_{\alpha} z_{\boldsymbol{G}}^{(0)}(\boldsymbol{k},n) a_{lmp}^{\boldsymbol{G}\boldsymbol{k}\alpha} \\
&+ 2\Big\langle \vec{\varphi}_{l'm'p'}^{\mathring{\beta}} \Big| \boldsymbol{\nabla} \mathscr{V}_{\mathrm{eff}}^{(0)} \Big| \vec{\varphi}_{lmp}^{\mathring{\beta}} \Big\rangle_{\beta} z_{\boldsymbol{G}'}^{*(0)}(\boldsymbol{k},n) a_{l'm'p'}^{*\boldsymbol{G}'\boldsymbol{k}\beta} \Big[\boldsymbol{z}_{\boldsymbol{G}}^{(1)}(\boldsymbol{k},n;\boldsymbol{q}\alpha) a_{lmp}^{\boldsymbol{G}\boldsymbol{k}\beta}(\boldsymbol{q})\Big]^{\top} \\
&+ 2\delta_{\beta\alpha} \Big\langle \vec{\varphi}_{l'm'p'}^{\mathring{\beta}} \Big| \boldsymbol{\nabla} \mathscr{V}_{\mathrm{eff}}^{(0)} \Big| \vec{\varphi}_{lmp}^{\mathring{\beta}} \Big\rangle_{\beta} z_{\boldsymbol{G}'}^{*(0)}(\boldsymbol{k},n) a_{l'm'p'}^{*\boldsymbol{G}'\boldsymbol{k}\beta} \Big[\mathrm{i}(\boldsymbol{k}+\boldsymbol{G}) z_{\boldsymbol{G}}^{(0)}(\boldsymbol{k},n) a_{lmp}^{\boldsymbol{G}\boldsymbol{k}\beta}\Big]^{\top} \Bigg\} .
\end{aligned} \tag{7.154a}$$

Adding supplementary zeroes and substituting terms according to equation (7.123f) leads to

$$\begin{aligned}
= \sum_{l'm'p'} \sum_{lmp} \sum_{\boldsymbol{G}'\boldsymbol{G}} \sum_{\boldsymbol{k},n} f_{\boldsymbol{k},n}^{(0)} \Bigg\{ & 2\Big(\boldsymbol{z}_{\boldsymbol{G}'}^{(1)}(\boldsymbol{k},n;\boldsymbol{q}\beta) a_{l'm'p'}^{\boldsymbol{G}'\boldsymbol{k}\alpha}(\boldsymbol{q})\Big)^{*} z_{\boldsymbol{G}}^{(0)}(\boldsymbol{k},n) a_{lmp}^{\boldsymbol{G}\boldsymbol{k}\alpha} \Big\langle \vec{\varphi}_{l'm'p'}^{\mathring{\alpha}} \Big| \boldsymbol{\nabla}^{\top} \mathscr{V}_{\mathrm{eff}}^{(0)} \Big| \vec{\varphi}_{lmp}^{\mathring{\alpha}} \Big\rangle_{\alpha} \\
&+ 2\delta_{\beta\alpha} \Big(\mathrm{i}(\boldsymbol{k}+\boldsymbol{G}') z_{\boldsymbol{G}'}^{(0)}(\boldsymbol{k},n) a_{l'm'p'}^{\boldsymbol{G}'\boldsymbol{k}\alpha}\Big)^{*} z_{\boldsymbol{G}}^{(0)}(\boldsymbol{k},n) a_{lmp}^{\boldsymbol{G}\boldsymbol{k}\alpha} \Big\langle \vec{\varphi}_{l'm'p'}^{\mathring{\alpha}} \Big| \boldsymbol{\nabla}^{\top} \mathscr{V}_{\mathrm{eff}}^{(0)} \Big| \vec{\varphi}_{lmp}^{\mathring{\alpha}} \Big\rangle_{\alpha} \\
&+ 2 z_{\boldsymbol{G}'}^{*(0)}(\boldsymbol{k},n) a_{l'm'p'}^{*\boldsymbol{G}'\boldsymbol{k}\alpha} \boldsymbol{z}_{\boldsymbol{G}}^{(1)}(\boldsymbol{k},n;-\boldsymbol{q}\beta) a_{lmp}^{\boldsymbol{G}\boldsymbol{k}\alpha}(-\boldsymbol{q}) \Big\langle \vec{\varphi}_{l'm'p'}^{\mathring{\alpha}} \Big| \boldsymbol{\nabla}^{\top} \mathscr{V}_{\mathrm{eff}}^{(0)} \Big| \vec{\varphi}_{lmp}^{\mathring{\alpha}} \Big\rangle_{\alpha} \\
&+ 2\delta_{\beta\alpha} z_{\boldsymbol{G}'}^{*(0)}(\boldsymbol{k},n) a_{l'm'p'}^{*\boldsymbol{G}'\boldsymbol{k}\alpha} \mathrm{i}(\boldsymbol{k}+\boldsymbol{G}) z_{\boldsymbol{G}}^{(0)}(\boldsymbol{k},n) a_{lmp}^{\boldsymbol{G}\boldsymbol{k}\alpha} \Big\langle \vec{\varphi}_{l'm'p'}^{\mathring{\alpha}} \Big| \boldsymbol{\nabla}^{\top} \mathscr{V}_{\mathrm{eff}}^{(0)} \Big| \vec{\varphi}_{lmp}^{\mathring{\alpha}} \Big\rangle_{\alpha} \\
&+ 2\delta_{\beta\alpha} z_{\boldsymbol{G}'}^{*(0)}(\boldsymbol{k},n) a_{l'm'p'}^{*\boldsymbol{G}'\boldsymbol{k}\alpha} z_{\boldsymbol{G}}^{(0)}(\boldsymbol{k},n) a_{lmp}^{\boldsymbol{G}\boldsymbol{k}\alpha} \Big\langle \boldsymbol{\nabla} \vec{\varphi}_{l'm'p'}^{\mathring{\alpha}} \Big| \boldsymbol{\nabla}^{\top} \mathscr{V}_{\mathrm{eff}}^{(0)} \Big| \vec{\varphi}_{lmp}^{\mathring{\alpha}} \Big\rangle_{\alpha} \\
&- 2\delta_{\beta\alpha} z_{\boldsymbol{G}'}^{*(0)}(\boldsymbol{k},n) a_{l'm'p'}^{*\boldsymbol{G}'\boldsymbol{k}\alpha} z_{\boldsymbol{G}}^{(0)}(\boldsymbol{k},n) a_{lmp}^{\boldsymbol{G}\boldsymbol{k}\alpha} \Big\langle \boldsymbol{\nabla} \vec{\varphi}_{l'm'p'}^{\mathring{\alpha}} \Big| \boldsymbol{\nabla}^{\top} \mathscr{V}_{\mathrm{eff}}^{(0)} \Big| \vec{\varphi}_{lmp}^{\mathring{\alpha}} \Big\rangle_{\alpha} \\
&+ 2\delta_{\beta\alpha} z_{\boldsymbol{G}'}^{(0)}(\boldsymbol{k},n) a_{l'm'p'}^{\boldsymbol{G}'\boldsymbol{k}\alpha} z_{\boldsymbol{G}}^{*(0)}(\boldsymbol{k},n) a_{lmp}^{*\boldsymbol{G}\boldsymbol{k}\alpha} \Big\langle \boldsymbol{\nabla} \vec{\varphi}_{l'm'p'}^{\mathring{\alpha}} \Big| \boldsymbol{\nabla}^{\top} \mathscr{V}_{\mathrm{eff}}^{(0)} \Big| \vec{\varphi}_{lmp}^{\mathring{\alpha}} \Big\rangle_{\alpha}^{*} \\
&- 2\delta_{\beta\alpha} z_{\boldsymbol{G}'}^{(0)}(\boldsymbol{k},n) a_{l'm'p'}^{\boldsymbol{G}'\boldsymbol{k}\alpha} z_{\boldsymbol{G}}^{*(0)}(\boldsymbol{k},n) a_{lmp}^{*\boldsymbol{G}\boldsymbol{k}\alpha} \Big\langle \boldsymbol{\nabla} \vec{\varphi}_{l'm'p'}^{\mathring{\alpha}} \Big| \boldsymbol{\nabla}^{\top} \mathscr{V}_{\mathrm{eff}}^{(0)} \Big| \vec{\varphi}_{lmp}^{\mathring{\alpha}} \Big\rangle_{\alpha}^{*} \Bigg\} .
\end{aligned} \tag{7.154b}$$

This allows for identifying the first-order variation and the gradient of the Kohn–Sham wave function in the MT, resulting in the matrix elements

$$\begin{aligned}
&= 2\left\langle \Psi_{\boldsymbol{k},n}^{(1)+} \middle| \boldsymbol{\nabla}^{\top} \mathscr{V}_{\text{eff}}^{(0)} \middle| \Psi_{\boldsymbol{k},n}^{(0)} \right\rangle_{\alpha} + 2\left\langle \Psi_{\boldsymbol{k},n}^{(1)-} \middle| \boldsymbol{\nabla}^{\top} \mathscr{V}_{\text{eff}}^{(0)} \middle| \Psi_{\boldsymbol{k},n}^{(0)} \right\rangle_{\alpha}^{*} && (7.154\text{c}) \\
&\quad + 2\delta_{\beta\alpha} \left\langle \boldsymbol{\nabla} \Psi_{\boldsymbol{k},n}^{(0)} \middle| \boldsymbol{\nabla}^{\top} \mathscr{V}_{\text{eff}}^{(0)} \middle| \Psi_{\boldsymbol{k},n}^{(0)} \right\rangle_{\alpha} + 2\delta_{\beta\alpha} \left\langle \boldsymbol{\nabla} \Psi_{\boldsymbol{k},n}^{(0)} \middle| \boldsymbol{\nabla}^{\top} \mathscr{V}_{\text{eff}}^{(0)} \middle| \Psi_{\boldsymbol{k},n}^{(0)} \right\rangle_{\alpha}^{*} ,
\end{aligned}$$

which can be written as the integrals

$$\begin{aligned}
&= \int_{\alpha} \boldsymbol{\rho}_{\alpha,\text{v}}^{*(1)}(\boldsymbol{r}; \boldsymbol{q}^{+}\beta) \boldsymbol{\nabla}^{\top} V_{\text{eff}}^{(0)\alpha}(\boldsymbol{r}) \, \mathrm{d}^3 r + \int_{\alpha} \boldsymbol{\rho}_{\alpha,\text{v}}^{(1)}(\boldsymbol{r}; \boldsymbol{q}^{-}\beta) \boldsymbol{\nabla}^{\top} V_{\text{eff}}^{(0)\alpha}(\boldsymbol{r}) \, \mathrm{d}^3 r && (7.154\text{d}) \\
&\quad + \delta_{\beta\alpha} \int_{\alpha} \boldsymbol{\nabla} \rho_{\alpha,\text{v}}^{(0)}(\boldsymbol{r}) \boldsymbol{\nabla}^{\top} V_{\text{eff}}^{(0)\alpha}(\boldsymbol{r}) \, \mathrm{d}^3 r + \delta_{\beta\alpha} \int_{\alpha} \boldsymbol{\nabla} \rho_{\alpha,\text{v}}^{(0)}(\boldsymbol{r}) \boldsymbol{\nabla}^{\top} V_{\text{eff}}^{(0)\alpha}(\boldsymbol{r}) \, \mathrm{d}^3 r \ ,
\end{aligned}$$

and simplfied due to TRS to

$$= 2 \int_{\alpha} \boldsymbol{\rho}_{\alpha,\text{v}}^{*(1)}(\boldsymbol{r}; \boldsymbol{q}^{+}\beta) \boldsymbol{\nabla}^{\top} V_{\text{eff}}^{(0)\alpha}(\boldsymbol{r}) \, \mathrm{d}^3 r + 2\delta_{\beta\alpha} \int_{\alpha} \boldsymbol{\nabla} \rho_{\alpha,\text{v}}^{(0)}(\boldsymbol{r}) \boldsymbol{\nabla}^{\top} V_{\text{eff}}^{(0)\alpha}(\boldsymbol{r}) \, \mathrm{d}^3 r \ . \tag{7.154e}$$

Finally, these integrals are written as sums over all atoms γ with Kronecker deltas

$$= 2 \sum_{\gamma} \delta_{\gamma\alpha} \int_{\alpha} \boldsymbol{\rho}_{\alpha,\text{v}}^{*(1)}(\boldsymbol{r}; \boldsymbol{q}^{+}\beta) \boldsymbol{\nabla}^{\top} V_{\text{eff}}^{(0)\alpha}(\boldsymbol{r}) \, \mathrm{d}^3 r + 2\delta_{\beta\alpha} \sum_{\gamma} \delta_{\gamma\alpha} \int_{\alpha} \boldsymbol{\nabla} \rho_{\alpha,\text{v}}^{(0)}(\boldsymbol{r}) \boldsymbol{\nabla}^{\top} V_{\text{eff}}^{(0)\alpha}(\boldsymbol{r}) \mathrm{d}^3 r \tag{7.154f}$$

Now, equation (7.145) can be optimized by adding equation (7.154f) divided by two:

$$\begin{aligned}
&\sum_{\gamma} \int_{\gamma} \boldsymbol{\rho}_{\gamma}^{*(1)}(\boldsymbol{r}; \boldsymbol{q}^{+}\beta) \left[\boldsymbol{V}_{\text{ext}}^{(1)\gamma}(\boldsymbol{r}; \boldsymbol{q}^{+}\alpha) \right]^{\top} \mathrm{d}^3 r - \sum_{\gamma} \delta_{\beta\alpha} \int_{\gamma} \left(\boldsymbol{\nabla} \rho_{\gamma}^{(0)}(\boldsymbol{r}) \right) \boldsymbol{\nabla}^{\top} V_{\text{ext}}^{(0)\gamma}(\boldsymbol{r}) \, \mathrm{d}^3 r && (7.155\text{a}) \\
&+ \sum_{\gamma} \delta_{\gamma\alpha} \int_{\alpha} \boldsymbol{\rho}_{\alpha,\text{v}}^{*(1)}(\boldsymbol{r}; \boldsymbol{q}^{+}\beta) \boldsymbol{\nabla}^{\top} V_{\text{eff}}^{(0)\alpha}(\boldsymbol{r}) \, \mathrm{d}^3 r + \delta_{\beta\alpha} \sum_{\gamma} \delta_{\gamma\alpha} \int_{\alpha} \boldsymbol{\nabla} \rho_{\alpha,\text{v}}^{(0)}(\boldsymbol{r}) \boldsymbol{\nabla}^{\top} V_{\text{eff}}^{(0)\alpha}(\boldsymbol{r}) \, \mathrm{d}^3 r \ .
\end{aligned}$$

The first-order density variation (7.38) is subdivided into a part $\boldsymbol{\rho}_{\gamma,\text{Sh}}^{*(1)}(\boldsymbol{r}; \boldsymbol{q}^{+}\beta)$ without the all-electron gradient (omitting the second line in equation (7.37b)) and the gradient contribution in the second line of equation (7.37b). Moreover, the all-electron gradients are rewritten as a sum of the valence contribution $\boldsymbol{\nabla} \rho_{\gamma,\text{v}}^{(0)}(\boldsymbol{r})$ and the core contribution $\boldsymbol{\nabla} \rho_{\gamma,\text{c}}^{(0)}(\boldsymbol{r})$, resulting in

$$\begin{aligned}
&\sum_{\gamma} \int_{\gamma} \left(\boldsymbol{\rho}_{\gamma,\text{Sh}}^{*(1)}(\boldsymbol{r}; \boldsymbol{q}^{+}\beta) - \delta_{\gamma\beta} \boldsymbol{\nabla} \rho_{\gamma,\text{v}}^{(0)}(\boldsymbol{r}) - \delta_{\gamma\beta} \boldsymbol{\nabla} \rho_{\gamma,\text{c}}^{(0)}(\boldsymbol{r}) \right) \left[\boldsymbol{V}_{\text{ext}}^{(1)\gamma}(\boldsymbol{r}; \boldsymbol{q}^{+}\alpha) \right]^{\top} \mathrm{d}^3 r && (7.155\text{b}) \\
&\quad - \sum_{\gamma} \delta_{\beta\alpha} \int_{\gamma} \left(\boldsymbol{\nabla} \rho_{\gamma,\text{v}}^{(0)}(\boldsymbol{r}) + \boldsymbol{\nabla} \rho_{\gamma,\text{c}}^{(0)}(\boldsymbol{r}) \right) \boldsymbol{\nabla}^{\top} V_{\text{ext}}^{(0)\gamma}(\boldsymbol{r}) \, \mathrm{d}^3 r \\
&\quad + \sum_{\gamma} \int_{\gamma} \left(\boldsymbol{\rho}_{\gamma,\text{Sh}}^{*(1)}(\boldsymbol{r}; \boldsymbol{q}^{+}\beta) - \delta_{\beta\alpha} \delta_{\gamma\beta} \boldsymbol{\nabla} \rho_{\gamma,\text{v}}^{(0)}(\boldsymbol{r}) \right) \delta_{\gamma\alpha} \boldsymbol{\nabla}^{\top} V_{\text{ext}}^{(0)\gamma}(\boldsymbol{r}) \, \mathrm{d}^3 r \\
&\quad + \delta_{\beta\alpha} \sum_{\gamma} \delta_{\gamma\alpha} \int_{\gamma} \boldsymbol{\nabla} \rho_{\gamma,\text{v}}^{(0)}(\boldsymbol{r}) \boldsymbol{\nabla}^{\top} V_{\text{ext}}^{(0)\gamma}(\boldsymbol{r}) \, \mathrm{d}^3 r \\
&\quad + \sum_{\gamma} \delta_{\gamma\alpha} \int_{\alpha} \boldsymbol{\rho}_{\alpha,\text{val}}^{*(1)}(\boldsymbol{r}; \boldsymbol{q}^{+}\beta) \boldsymbol{\nabla}^{\top} V_{\text{Hxc}}^{(0)\alpha}(\boldsymbol{r}) \, \mathrm{d}^3 r + \delta_{\beta\alpha} \sum_{\gamma} \delta_{\gamma\alpha} \int_{\alpha} \boldsymbol{\nabla} \rho_{\alpha,\text{val}}^{(0)}(\boldsymbol{r}) \boldsymbol{\nabla}^{\top} V_{\text{Hxc}}^{(0)\alpha}(\boldsymbol{r}) \, \mathrm{d}^3 r \\
&= \sum_{\gamma} \int_{\gamma} \boldsymbol{\rho}_{\gamma,\text{Sh}}^{*(1)}(\boldsymbol{r}; \boldsymbol{q}^{+}\beta) \left[\boldsymbol{V}_{\text{ext}}^{(1)\gamma}(\boldsymbol{r}; \boldsymbol{q}^{+}\alpha) + \delta_{\gamma\alpha} \boldsymbol{\nabla} V_{\text{ext}}^{(0)\gamma}(\boldsymbol{r}) \right]^{\top} \mathrm{d}^3 r && (7.155\text{c})
\end{aligned}$$

$$
\begin{aligned}
&-\sum_{\gamma}\int_{\gamma}\delta_{\gamma\beta}\boldsymbol{\nabla}\rho^{(0)}_{\gamma,\mathrm{v}}(\boldsymbol{r})\Big[\boldsymbol{V}^{(1)\gamma}_{\text{ext}}(\boldsymbol{r};\boldsymbol{q}^{+}\alpha)+\delta_{\beta\alpha}\delta_{\gamma\alpha}\boldsymbol{\nabla}V^{(0)\gamma}_{\text{ext}}(\boldsymbol{r})\Big]^{\top}\,\mathrm{d}^3r\\
&-\sum_{\gamma}\int_{\gamma}\delta_{\gamma\beta}\boldsymbol{\nabla}\rho^{(0)}_{\gamma,\mathrm{c}}(\boldsymbol{r})\Big[\boldsymbol{V}^{(1)\gamma}_{\text{ext}}(\boldsymbol{r};\boldsymbol{q}^{+}\alpha)+\delta_{\beta\alpha}\delta_{\gamma\alpha}\boldsymbol{\nabla}V^{(0)\gamma}_{\text{ext}}(\boldsymbol{r})\Big]^{\top}\,\mathrm{d}^3r\\
&+\delta_{\beta\alpha}\sum_{\gamma}\big(\delta_{\gamma\alpha}-1\big)\int_{\gamma}\boldsymbol{\nabla}\rho^{(0)}_{\gamma,\mathrm{v}}(\boldsymbol{r})\boldsymbol{\nabla}^{\top}V^{(0)\gamma}_{\text{ext}}(\boldsymbol{r})\,\mathrm{d}^3r+\int_{\alpha}\boldsymbol{\rho}^{*(1)}_{\alpha,\mathrm{Sh}}(\boldsymbol{r};\boldsymbol{q}^{+}\beta)\boldsymbol{\nabla}^{\top}V^{(0)\alpha}_{\text{Hxc}}(\boldsymbol{r})\,\mathrm{d}^3r\\
=&\sum_{\gamma}\int_{\gamma}\boldsymbol{\rho}^{*(1)}_{\gamma}(\boldsymbol{r};\boldsymbol{q}^{+}\beta)\Big[\boldsymbol{V}^{(1)\gamma}_{\text{ext}}(\boldsymbol{r};\boldsymbol{q}^{+}\alpha)+\delta_{\gamma\alpha}\boldsymbol{\nabla}V^{(0)\gamma}_{\text{ext}}(\boldsymbol{r})\Big]^{\top}\,\mathrm{d}^3r \qquad (7.155\text{d})\\
&+\int_{\alpha}\boldsymbol{\rho}^{*(1)}_{\alpha,\mathrm{Sh}}(\boldsymbol{r};\boldsymbol{q}^{+}\beta)\boldsymbol{\nabla}^{\top}V^{(0)\alpha}_{\text{Hxc}}(\boldsymbol{r})\,\mathrm{d}^3r+\delta_{\beta\alpha}\sum_{\gamma}\big(\delta_{\gamma\alpha}-1\big)\int_{\gamma}\boldsymbol{\nabla}\rho^{(0)}_{\gamma,\mathrm{v}}(\boldsymbol{r})\boldsymbol{\nabla}^{\top}V^{(0)\gamma}_{\text{ext}}(\boldsymbol{r})\,\mathrm{d}^3r\ ,
\end{aligned}
$$

where $V^{(0)\alpha}_{\text{Hxc}}(\boldsymbol{r})$ is the sum of the Hartree and the xc potentials.

The same can be done with the Pulay integral in equation (7.147), yielding

$$
\begin{aligned}
&\sum_{\gamma}\int_{\gamma}\Big(\boldsymbol{\rho}^{*(1)}_{\gamma,\mathrm{Sh}}(\boldsymbol{r};\boldsymbol{q}^{+}\beta)-\delta_{\gamma\beta}\boldsymbol{\nabla}\rho^{(0)}_{\gamma,\mathrm{v}}(\boldsymbol{r})-\delta_{\gamma\beta}\boldsymbol{\nabla}\rho^{(0)}_{\gamma,\mathrm{c}}(\boldsymbol{r})\Big)\Big[\boldsymbol{V}^{(1)\gamma}_{\text{eff}}(\boldsymbol{r};\boldsymbol{q}^{+}\alpha)\Big]^{\top}\,\mathrm{d}^3r \qquad (7.156\text{a})\\
&\quad-\delta_{\beta\alpha}\int_{\alpha}\boldsymbol{\nabla}\rho^{*(0)}_{\alpha,\mathrm{v}}(\boldsymbol{r})\boldsymbol{\nabla}^{\top}V^{(0)\alpha}_{\text{eff}}(\boldsymbol{r})\,\mathrm{d}^3r-\delta_{\beta\alpha}\int_{\alpha}\boldsymbol{\nabla}\rho^{*(0)}_{\alpha,\mathrm{c}}(\boldsymbol{r})\boldsymbol{\nabla}^{\top}V^{(0)\alpha}_{\text{eff}}(\boldsymbol{r})\,\mathrm{d}^3r\\
&\quad+\sum_{\gamma}\int_{\gamma}\Big(\boldsymbol{\rho}^{*(1)}_{\gamma,\mathrm{Sh}}(\boldsymbol{r};\boldsymbol{q}^{+}\beta)-\delta_{\beta\alpha}\delta_{\gamma\beta}\boldsymbol{\nabla}\rho^{(0)}_{\gamma,\mathrm{v}}(\boldsymbol{r})\Big)\delta_{\gamma\alpha}\boldsymbol{\nabla}^{\top}V^{(0)\gamma}_{\text{ext}}(\boldsymbol{r})\,\mathrm{d}^3r\\
&\quad+\delta_{\beta\alpha}\int_{\alpha}\boldsymbol{\nabla}\rho^{(0)}_{\alpha,\mathrm{v}}(\boldsymbol{r})\boldsymbol{\nabla}^{\top}V^{(0)\alpha}_{\text{eff}}(\boldsymbol{r})\,\mathrm{d}^3r\\
&=\sum_{\gamma}\int_{\gamma}\Big(\boldsymbol{\rho}^{*(1)}_{\gamma,\mathrm{Sh}}(\boldsymbol{r};\boldsymbol{q}^{+}\beta)-\delta_{\gamma\beta}\boldsymbol{\nabla}\rho^{(0)}_{\gamma,\mathrm{v}}(\boldsymbol{r})-\delta_{\gamma\beta}\boldsymbol{\nabla}\rho^{(0)}_{\gamma,\mathrm{c}}(\boldsymbol{r})\Big)\Big[\boldsymbol{V}^{(1)\gamma}_{\text{eff}}(\boldsymbol{r};\boldsymbol{q}^{+}\alpha)\Big]^{\top}\,\mathrm{d}^3r\\
&\quad-\sum_{\gamma}\delta_{\gamma\beta}\delta_{\gamma\alpha}\delta_{\beta\alpha}\int_{\gamma}\boldsymbol{\nabla}\rho^{*(0)}_{\gamma,\mathrm{c}}(\boldsymbol{r})\boldsymbol{\nabla}^{\top}V^{(0)\gamma}_{\text{eff}}(\boldsymbol{r})\,\mathrm{d}^3r\\
&\quad+\sum_{\gamma}\int_{\gamma}\Big(\boldsymbol{\rho}^{*(1)}_{\gamma,\mathrm{Sh}}(\boldsymbol{r};\boldsymbol{q}^{+}\beta)-\delta_{\beta\alpha}\delta_{\gamma\beta}\boldsymbol{\nabla}\rho^{(0)}_{\gamma,\mathrm{v}}(\boldsymbol{r})\Big)\delta_{\gamma\alpha}\boldsymbol{\nabla}^{\top}V^{(0)\gamma}_{\text{ext}}(\boldsymbol{r})\,\mathrm{d}^3r\\
&=\sum_{\gamma}\int_{\gamma}\boldsymbol{\rho}^{*(1)}_{\gamma}(\boldsymbol{r};\boldsymbol{q}^{+}\beta)\Big[\boldsymbol{V}^{(1)\gamma}_{\text{eff}}(\boldsymbol{r};\boldsymbol{q}^{+}\alpha)+\delta_{\gamma\alpha}\boldsymbol{\nabla}V^{(0)\gamma}_{\text{eff}}(\boldsymbol{r})\Big]^{\top}\,\mathrm{d}^3r\ . \qquad (7.156\text{b})
\end{aligned}
$$

Utilizing these mitigated integrals makes the interpolations practically irrelevant.

7.6.7 Avoiding Second-Order Terms Already Vanishing in First Order

Motivation

Neukirchen has found in his derivation that

$$
\begin{aligned}
0&=\left\langle\sum_{\boldsymbol{G}'}\boldsymbol{z}^{(1)}_{\boldsymbol{G}'}(\boldsymbol{k},n;\boldsymbol{q}\beta)\vec{\phi}^{(0)}_{\boldsymbol{k}+\boldsymbol{q},\boldsymbol{G}}\middle|\mathscr{H}^{(0)}-\epsilon^{(0)}_{\boldsymbol{k},n}\middle|\varPsi^{(0)}_{\boldsymbol{k},n}\right\rangle_{\varOmega} \qquad (7.157\text{a})\\
&=\sum_{n}\boldsymbol{z}^{(1)}_{n}(\boldsymbol{k},n';\boldsymbol{q}\beta)\Big\langle\varPsi^{(0)}_{\boldsymbol{k}+\boldsymbol{q},n}\Big|\mathscr{H}^{(0)}-\epsilon^{(0)}_{\boldsymbol{k},n}\Big|\varPsi^{(0)}_{\boldsymbol{k},n}\Big\rangle_{\varOmega}
\end{aligned}
$$

and

$$
0=\left\langle\varPsi^{(0)}_{\boldsymbol{k},n}\middle|\mathscr{H}^{(0)}-\epsilon^{(0)}_{\boldsymbol{k},n}\middle|\sum_{\boldsymbol{G}}\boldsymbol{z}^{(1)}_{\boldsymbol{G}}(\boldsymbol{k},n;\boldsymbol{q}\alpha)\vec{\phi}^{(0)}_{\boldsymbol{k}+\boldsymbol{q},\boldsymbol{G}}\right\rangle_{\varOmega} \qquad (7.157\text{b})
$$

are part of the first-order total energy variation and vanish. Therefore, he does not vary them further.

Reformulation

But by nevertheless summing equations (7.157a) and (7.157b) and varying them again, superfluous terms in the formalism of Klüppelberg [88] can be spotted [256]. Applying a variation to the aforementioned sum reads

$$
\begin{aligned}
&\left\langle \sum_{\boldsymbol{G}'} \boldsymbol{z}^{(1)}_{\boldsymbol{G}'}(\boldsymbol{k}, n; \boldsymbol{q}\beta) \left[\vec{\phi}^{(1)\alpha-}_{\boldsymbol{k}+\boldsymbol{q},\boldsymbol{G}'}\right]^{\top} \middle| \mathscr{H}^{(0)} - \epsilon^{(0)}_{\boldsymbol{k},n} \middle| \Psi^{(0)}_{\boldsymbol{k},n} \right\rangle_{\Omega} \\
&+ \left\langle \sum_{\boldsymbol{G}'} \boldsymbol{z}^{(1)}_{\boldsymbol{G}'}(\boldsymbol{k}, n; \boldsymbol{q}\beta) \vec{\phi}^{(0)}_{\boldsymbol{k}+\boldsymbol{q},\boldsymbol{G}'} \middle| \left[\boldsymbol{\mathscr{V}}^{(1)}_{\text{eff}}(\boldsymbol{q}\alpha)\right]^{\top} \middle| \Psi^{(0)}_{\boldsymbol{k},n} \right\rangle_{\Omega} \\
&+ \left\langle \sum_{\boldsymbol{G}'} \boldsymbol{z}^{(1)}_{\boldsymbol{G}'}(\boldsymbol{k}, n; \boldsymbol{q}\beta) \vec{\phi}^{(0)}_{\boldsymbol{k}+\boldsymbol{q},\boldsymbol{G}'} \middle| \mathscr{H}^{(0)} - \epsilon^{(0)}_{\boldsymbol{k},n} \middle| \sum_{\boldsymbol{G}} \left[\boldsymbol{z}^{(1)}_{\boldsymbol{G}}(\boldsymbol{k}, n; \boldsymbol{q}\alpha)\right]^{\top} \vec{\phi}^{(0)}_{\boldsymbol{k}+\boldsymbol{q},\boldsymbol{G}} \right\rangle_{\Omega} \\
&+ \left\langle \sum_{\boldsymbol{G}'} \boldsymbol{z}^{(1)}_{\boldsymbol{G}'}(\boldsymbol{k}, n; \boldsymbol{q}\beta) \vec{\phi}^{(0)}_{\boldsymbol{k}+\boldsymbol{q},\boldsymbol{G}'} \middle| \mathscr{H}^{(0)} - \epsilon^{(0)}_{\boldsymbol{k},n} \middle| \sum_{\boldsymbol{G}} \boldsymbol{z}^{(0)}_{\boldsymbol{G}}(\boldsymbol{k}, n) \left[\vec{\boldsymbol{\phi}}^{(1)\alpha+}_{\boldsymbol{k},\boldsymbol{G}}\right]^{\top} \right\rangle_{\Omega} \\
&+ \left\langle \Psi^{(0)}_{\boldsymbol{k},n} \middle| \mathscr{H}^{(0)} - \epsilon^{(0)}_{\boldsymbol{k},n} \middle| \sum_{\boldsymbol{G}} \vec{\boldsymbol{\phi}}^{(1)\beta-}_{\boldsymbol{k}+\boldsymbol{q},\boldsymbol{G}} \left[\boldsymbol{z}^{(1)}_{\boldsymbol{G}}(\boldsymbol{k}, n; \boldsymbol{q}\alpha)\right]^{\top} \right\rangle_{\Omega} \\
&+ \left\langle \Psi^{(0)}_{\boldsymbol{k},n} \middle| \boldsymbol{\mathscr{V}}^{(1)}_{\text{eff}}(\boldsymbol{q}\beta) \middle| \sum_{\boldsymbol{G}} \left[\boldsymbol{z}^{(1)}_{\boldsymbol{G}}(\boldsymbol{k}, n; \boldsymbol{q}\alpha)\right]^{\top} \vec{\phi}^{(0)}_{\boldsymbol{k}+\boldsymbol{q},\boldsymbol{G}} \right\rangle_{\Omega} \\
&+ \left\langle \sum_{\boldsymbol{G}'} \boldsymbol{z}^{(1)}_{\boldsymbol{G}'}(\boldsymbol{k}, n; \boldsymbol{q}\beta) \vec{\phi}^{(0)}_{\boldsymbol{k}+\boldsymbol{q},\boldsymbol{G}'} \middle| \mathscr{H}^{(0)} - \epsilon^{(0)}_{\boldsymbol{k},n} \middle| \sum_{\boldsymbol{G}} \left[\boldsymbol{z}^{(1)}_{\boldsymbol{G}}(\boldsymbol{k}, n; \boldsymbol{q}\alpha)\right]^{\top} \vec{\phi}^{(0)}_{\boldsymbol{k}+\boldsymbol{q},\boldsymbol{G}} \right\rangle_{\Omega} \\
&+ \left\langle \sum_{\boldsymbol{G}'} \boldsymbol{z}^{(0)}_{\boldsymbol{G}'}(\boldsymbol{k}, n) \vec{\boldsymbol{\phi}}^{(1)\beta+}_{\boldsymbol{k},\boldsymbol{G}'} \middle| \mathscr{H}^{(0)} - \epsilon^{(0)}_{\boldsymbol{k},n} \middle| \sum_{\boldsymbol{G}} \left[\boldsymbol{z}^{(1)}_{\boldsymbol{G}}(\boldsymbol{k}, n; \boldsymbol{q}\alpha)\right]^{\top} \vec{\phi}^{(0)}_{\boldsymbol{k}+\boldsymbol{q},\boldsymbol{G}} \right\rangle_{\Omega} \\
&+ \oint_{\alpha} \sum_{\boldsymbol{G}'} \boldsymbol{z}^{(1)}_{\boldsymbol{G}'}(\boldsymbol{k}, n; \boldsymbol{q}\beta) \vec{\phi}^{(0)\alpha}_{\boldsymbol{k}+\boldsymbol{q},\boldsymbol{G}} \left(\mathscr{H}^{(0)} - \epsilon^{(0)}_{\boldsymbol{k},n}\right) \Psi^{(0)\alpha}_{\boldsymbol{k},n} \hat{\boldsymbol{r}}^{\top} \,\mathrm{d}S \\
&- \oint_{\alpha} \sum_{\boldsymbol{G}'} \boldsymbol{z}^{(1)}_{\boldsymbol{G}'}(\boldsymbol{k}, n; \boldsymbol{q}\beta) \vec{\phi}^{(0)\alpha}_{\boldsymbol{k}+\boldsymbol{q},\boldsymbol{G}} \left(\mathscr{H}^{(0)} - \epsilon^{(0)}_{\boldsymbol{k},n}\right) \Psi^{(0)\alpha}_{\boldsymbol{k},n} \hat{\boldsymbol{r}}^{\top} \,\mathrm{d}S \\
&+ \oint_{\beta} \hat{\boldsymbol{r}} \Psi^{(0)}_{\boldsymbol{k},n} \left(\mathscr{H}^{(0)} - \epsilon^{(0)}_{\boldsymbol{k},n}\right) \sum_{\boldsymbol{G}} \left[\boldsymbol{z}^{(1)}_{\boldsymbol{G}}(\boldsymbol{k}, n; \boldsymbol{q}\alpha)\right]^{\top} \vec{\phi}^{(0)}_{\boldsymbol{k}+\boldsymbol{q},\boldsymbol{G}} \,\mathrm{d}S \\
&+ \oint_{\beta} \hat{\boldsymbol{r}} \Psi^{(0)}_{\boldsymbol{k},n} \left(\mathscr{H}^{(0)} - \epsilon^{(0)}_{\boldsymbol{k},n}\right) \sum_{\boldsymbol{G}} \left[\boldsymbol{z}^{(1)}_{\boldsymbol{G}}(\boldsymbol{k}, n; \boldsymbol{q}\alpha)\right]^{\top} \vec{\phi}^{(0)}_{\boldsymbol{k}+\boldsymbol{q},\boldsymbol{G}} \,\mathrm{d}S \ .
\end{aligned}
\tag{7.158}
$$

From these terms, in my preceding derivation the matrix-element terms

$$
\begin{aligned}
&\left(\boldsymbol{z}^{(1)}_{\boldsymbol{G}'}(\boldsymbol{k}, n; \boldsymbol{q}\beta) a^{\boldsymbol{G}'\boldsymbol{k}\alpha}_{l'm'p'}(\boldsymbol{q})\right)^{*} \left\langle \vec{\varphi}^{\mathring{\alpha}}_{l'm'p'} \middle| \boldsymbol{\nabla}^{\top} \mathscr{V}^{(0)}_{\text{eff}} \middle| \vec{\varphi}^{\mathring{\alpha}}_{lmp} \right\rangle_{\alpha} z^{(0)}_{\boldsymbol{G}}(\boldsymbol{k}, n) a^{\boldsymbol{G}\boldsymbol{k}\alpha}_{lmp} \\
&+ \left\langle \vec{\varphi}^{\mathring{\beta}}_{l'm'p'} \middle| \boldsymbol{\nabla} \mathscr{V}^{(0)}_{\text{eff}} \middle| \vec{\varphi}^{\mathring{\beta}}_{lmp} \right\rangle_{\beta} z^{*(0)}_{\boldsymbol{G}'}(\boldsymbol{k}, n) a^{*\boldsymbol{G}'\boldsymbol{k}\beta}_{l'm'p'} \left[\boldsymbol{z}^{(1)}_{\boldsymbol{G}}(\boldsymbol{k}, n; \boldsymbol{q}\alpha) a^{\boldsymbol{G}\boldsymbol{k}\beta}_{lmp}(\boldsymbol{q})\right]^{\top} \\
&+ \left(\boldsymbol{z}^{(1)}_{\boldsymbol{G}'}(\boldsymbol{k}, n; \boldsymbol{q}\beta) a^{\boldsymbol{G}'\boldsymbol{k}\alpha}_{l'm'p'}(\boldsymbol{q})\right)^{*} \left\langle \vec{\varphi}^{\mathring{\alpha}}_{l'm'p'} \middle| \left[\boldsymbol{\mathscr{V}}^{(1)}_{\text{eff}}(\boldsymbol{q}, \alpha)\right]^{\top} \middle| \vec{\varphi}^{\mathring{\alpha}}_{lmp} \right\rangle_{\Omega} z^{(0)}_{\boldsymbol{G}}(\boldsymbol{k}, n) a^{\boldsymbol{G}\boldsymbol{k}\alpha}_{lmp} \\
&+ \left\langle \vec{\varphi}^{\mathring{\beta}}_{l'm'p'} \middle| \boldsymbol{\mathscr{V}}^{(1)}_{\text{eff}}(\boldsymbol{q}, \beta) \middle| \vec{\varphi}^{\mathring{\beta}}_{lmp} \right\rangle_{\Omega} z^{*(0)}_{\boldsymbol{G}'}(\boldsymbol{k}, n) a^{*\boldsymbol{G}'\boldsymbol{k}\beta}_{l'm'p'} \left[\boldsymbol{z}^{(1)}_{\boldsymbol{G}}(\boldsymbol{k}, n; \boldsymbol{q}\alpha) a^{\boldsymbol{G}\boldsymbol{k}\beta}_{lmp}(\boldsymbol{q})\right]^{\top} \\
&+ \left(\boldsymbol{z}^{(1)}_{\boldsymbol{G}'}(\boldsymbol{k}, n; \boldsymbol{q}\beta) a^{\boldsymbol{G}'\boldsymbol{k}\alpha}_{l'm'p'}(\boldsymbol{q})\right)^{*} \left\langle \boldsymbol{\nabla}^{\top} \vec{\varphi}^{\mathring{\alpha}}_{l'm'p'} \middle| \mathscr{H}^{(0)} - \epsilon^{(0)}_{\boldsymbol{k},n} \middle| \vec{\varphi}^{\mathring{\alpha}}_{lmp} \right\rangle_{\alpha} z^{(0)}_{\boldsymbol{G}}(\boldsymbol{k}, n) a^{\boldsymbol{G}\boldsymbol{k}\alpha}_{lmp}
\end{aligned}
\tag{7.159a}
$$

$$
\begin{aligned}
&-\left(\boldsymbol{z}^{(1)}_{\boldsymbol{G}'}(\boldsymbol{k},n;\boldsymbol{q}\beta)a^{\boldsymbol{G}'\boldsymbol{k}\alpha}_{l'm'p'}(\boldsymbol{q})\right)^{*}\left\langle\boldsymbol{\nabla}^{\top}\vec{\varphi}^{\mathring{\alpha}}_{l'm'p'}\middle|\mathscr{H}^{(0)}-\epsilon^{(0)}_{\boldsymbol{k},n}\middle|\vec{\varphi}^{\mathring{\alpha}}_{lmp}\right\rangle_{\alpha}z^{(0)}_{\boldsymbol{G}}(\boldsymbol{k},n)a^{\boldsymbol{G}\boldsymbol{k}\alpha}_{lmp}\\
&+\left(\boldsymbol{z}^{(1)}_{\boldsymbol{G}'}(\boldsymbol{k},n;\boldsymbol{q}\beta)a^{\boldsymbol{G}'\boldsymbol{k}\alpha}_{l'm'p'}(\boldsymbol{q})\right)^{*}\left\langle\vec{\varphi}^{\mathring{\alpha}}_{l'm'p'}\middle|\mathscr{H}^{(0)}-\epsilon^{(0)}_{\boldsymbol{k},n}\middle|\boldsymbol{\nabla}^{\top}\vec{\varphi}^{\mathring{\alpha}}_{lmp}\right\rangle_{\alpha}z^{(0)}_{\boldsymbol{G}}(\boldsymbol{k},n)a^{\boldsymbol{G}\boldsymbol{k}\alpha}_{lmp}\\
&-\left(\boldsymbol{z}^{(1)}_{\boldsymbol{G}'}(\boldsymbol{k},n;\boldsymbol{q}\beta)a^{\boldsymbol{G}'\boldsymbol{k}\alpha}_{l'm'p'}(\boldsymbol{q})\right)^{*}\left\langle\vec{\varphi}^{\mathring{\alpha}}_{l'm'p'}\middle|\mathscr{H}^{(0)}-\epsilon^{(0)}_{\boldsymbol{k},n}\middle|\boldsymbol{\nabla}^{\top}\vec{\varphi}^{\mathring{\alpha}}_{lmp}\right\rangle_{\alpha}z^{(0)}_{\boldsymbol{G}}(\boldsymbol{k},n)a^{\boldsymbol{G}\boldsymbol{k}\alpha}_{lmp}\\
&+\left(z^{(0)}_{\boldsymbol{G}'}(\boldsymbol{k},n)a^{\boldsymbol{G}'\boldsymbol{k}\beta}_{l'm'p'}\right)^{*}a^{\boldsymbol{G}\boldsymbol{k}\beta}_{lmp}(\boldsymbol{q})\left\langle\vec{\varphi}^{\mathring{\beta}}_{l'm'p'}\middle|\mathscr{H}^{(0)}-\epsilon^{(0)}_{\boldsymbol{k},n}\middle|\boldsymbol{\nabla}\vec{\varphi}^{\mathring{\beta}}_{lmp}\right\rangle_{\beta}\left[\boldsymbol{z}^{(1)}_{\boldsymbol{G}}(\boldsymbol{k},n;\boldsymbol{q}\alpha)\right]^{\top}\\
&-\left(z^{(0)}_{\boldsymbol{G}'}(\boldsymbol{k},n)a^{\boldsymbol{G}'\boldsymbol{k}\beta}_{l'm'p'}\right)^{*}a^{\boldsymbol{G}\boldsymbol{k}\beta}_{lmp}(\boldsymbol{q})\left\langle\vec{\varphi}^{\mathring{\beta}}_{l'm'p'}\middle|\mathscr{H}^{(0)}-\epsilon^{(0)}_{\boldsymbol{k},n}\middle|\boldsymbol{\nabla}\vec{\varphi}^{\mathring{\beta}}_{lmp}\right\rangle_{\beta}\left[\boldsymbol{z}^{(1)}_{\boldsymbol{G}}(\boldsymbol{k},n;\boldsymbol{q}\alpha)\right]^{\top}\\
&+\left(z^{(0)}_{\boldsymbol{G}'}(\boldsymbol{k},n)a^{\boldsymbol{G}'\boldsymbol{k}\beta}_{l'm'p'}\right)^{*}\left\langle\boldsymbol{\nabla}\vec{\varphi}^{\mathring{\beta}}_{l'm'p'}\middle|\mathscr{H}^{(0)}-\epsilon^{(0)}_{\boldsymbol{k},n}\middle|\vec{\varphi}^{\mathring{\beta}}_{lmp}\right\rangle_{\beta}\left[\boldsymbol{z}^{(1)}_{\boldsymbol{G}}(\boldsymbol{k},n;\boldsymbol{q}\alpha)\right]^{\top}a^{\boldsymbol{G}\boldsymbol{k}\beta}_{lmp}(\boldsymbol{q})\\
&-\left(z^{(0)}_{\boldsymbol{G}'}(\boldsymbol{k},n)a^{\boldsymbol{G}'\boldsymbol{k}\beta}_{l'm'p'}\right)^{*}\left\langle\boldsymbol{\nabla}\vec{\varphi}^{\mathring{\beta}}_{l'm'p'}\middle|\mathscr{H}^{(0)}-\epsilon^{(0)}_{\boldsymbol{k},n}\middle|\vec{\varphi}^{\mathring{\beta}}_{lmp}\right\rangle_{\beta}\left[\boldsymbol{z}^{(1)}_{\boldsymbol{G}}(\boldsymbol{k},n;\boldsymbol{q}\alpha)\right]^{\top}a^{\boldsymbol{G}\boldsymbol{k}\beta}_{lmp}(\boldsymbol{q})\\
&+\left(\boldsymbol{z}^{(1)}_{\boldsymbol{G}'}(\boldsymbol{k},n;\boldsymbol{q}\beta)a^{\boldsymbol{G}'\boldsymbol{k}\alpha}_{l'm'p'}(\boldsymbol{q})\mathrm{i}[\boldsymbol{k}+\boldsymbol{q}+\boldsymbol{G}']^{\top}\right)^{*}\left\langle\vec{\varphi}^{\mathring{\alpha}}_{l'm'p'}\middle|\mathscr{H}^{(0)}-\epsilon^{(0)}_{\boldsymbol{k},n}\middle|\vec{\varphi}^{\mathring{\alpha}}_{lmp}\right\rangle_{\alpha}z^{(0)}_{\boldsymbol{G}}(\boldsymbol{k},n)a^{\boldsymbol{G}\boldsymbol{k}\alpha}_{lmp}\\
&+\left(z^{(0)}_{\boldsymbol{G}'}(\boldsymbol{k},n)a^{\boldsymbol{G}'\boldsymbol{k}\beta}_{l'm'p'}\right)^{*}\left\langle\vec{\varphi}^{\mathring{\beta}}_{l'm'p'}\middle|\mathscr{H}^{(0)}-\epsilon^{(0)}_{\boldsymbol{k},n}\middle|\vec{\varphi}^{\mathring{\beta}}_{lmp}\right\rangle_{\beta}a^{\boldsymbol{G}\boldsymbol{k}\beta}_{lmp}(\boldsymbol{q})\mathrm{i}[\boldsymbol{k}+\boldsymbol{q}+\boldsymbol{G}]\left[\boldsymbol{z}^{(1)}_{\boldsymbol{G}}(\boldsymbol{k},n;+\boldsymbol{q}\alpha)\right]^{\top}\\
&+\left(z^{(0)}_{\boldsymbol{G}'}(\boldsymbol{k},n)a^{\boldsymbol{G}'\boldsymbol{k}\beta}_{l'm'p'}\mathrm{i}[\boldsymbol{k}+\boldsymbol{G}']\right)^{*}\left\langle\vec{\varphi}^{\mathring{\beta}}_{l'm'p'}\middle|\mathscr{H}^{(0)}-\epsilon^{(0)}_{\boldsymbol{k},n}\middle|\vec{\varphi}^{\mathring{\beta}}_{lmp}\right\rangle_{\beta}\left[\boldsymbol{z}^{(1)}_{\boldsymbol{G}}(\boldsymbol{k},n;\boldsymbol{q}\alpha)\right]^{\top}a^{\boldsymbol{G}\boldsymbol{k}\beta}_{lmp}(\boldsymbol{q})\\
&+\left(\boldsymbol{z}^{(1)}_{\boldsymbol{G}'}(\boldsymbol{k},n;\boldsymbol{q}\beta)a^{\boldsymbol{G}'\boldsymbol{k}\alpha}_{l'm'p'}(\boldsymbol{q})\right)^{*}\left\langle\vec{\varphi}^{\mathring{\alpha}}_{l'm'p'}\middle|\mathscr{H}^{(0)}-\epsilon^{(0)}_{\boldsymbol{k},n}\middle|\vec{\varphi}^{\mathring{\alpha}}_{lmp}\right\rangle_{\alpha}\mathrm{i}[\boldsymbol{k}+\boldsymbol{G}]^{\top}z^{(0)}_{\boldsymbol{G}}(\boldsymbol{k},n)a^{\boldsymbol{G}\boldsymbol{k}\alpha}_{lmp}\\
&+2\left(\boldsymbol{z}^{(1)}_{\boldsymbol{G}'}(\boldsymbol{k},n;\boldsymbol{q}\beta)a^{\boldsymbol{G}'\boldsymbol{k}\gamma}_{l'm'p'}(\boldsymbol{q})\right)^{*}\left\langle\vec{\varphi}^{\mathring{\gamma}}_{l'm'p'}\middle|\mathscr{H}^{(0)}-\epsilon^{(0)}_{\boldsymbol{k},n}\middle|\vec{\varphi}^{\mathring{\gamma}}_{lmp}\right\rangle_{\Omega}\left[\boldsymbol{z}^{(1)}_{\boldsymbol{G}}(\boldsymbol{k},n;\boldsymbol{q}\alpha)\right]^{\top}a^{\boldsymbol{G}\boldsymbol{k}\gamma}_{lmp}(\boldsymbol{q})
\end{aligned}
$$

can be identified and shall therefore be ignored in the following. Furthermore, the first four lines can be rewritten as

$$
\begin{aligned}
&\left(\boldsymbol{z}^{(1)}_{\boldsymbol{G}'}(\boldsymbol{k},n;\boldsymbol{q}\beta)a^{\boldsymbol{G}'\boldsymbol{k}\alpha}_{l'm'p'}(\boldsymbol{q})\right)^{*}\left\langle\vec{\varphi}^{\mathring{\alpha}}_{l'm'p'}\middle|\boldsymbol{\nabla}^{\top}\mathscr{V}^{(0)}_{\text{eff}}\middle|\vec{\varphi}^{\mathring{\alpha}}_{lmp}\right\rangle_{\alpha}z^{(0)}_{\boldsymbol{G}}(\boldsymbol{k},n)a^{\boldsymbol{G}\boldsymbol{k}\alpha}_{lmp}\\
&+\left\langle\vec{\varphi}^{\mathring{\beta}}_{l'm'p'}\middle|\boldsymbol{\nabla}\mathscr{V}^{(0)}_{\text{eff}}\middle|\vec{\varphi}^{\mathring{\beta}}_{lmp}\right\rangle_{\beta}z^{*(0)}_{\boldsymbol{G}'}(\boldsymbol{k},n)a^{*\boldsymbol{G}'\boldsymbol{k}\beta}_{l'm'p'}\left[\boldsymbol{z}^{(1)}_{\boldsymbol{G}}(\boldsymbol{k},n;\boldsymbol{q}\alpha)a^{\boldsymbol{G}\boldsymbol{k}\beta}_{lmp}(\boldsymbol{q})\right]^{\top}\\
&+\left(\boldsymbol{z}^{(1)}_{\boldsymbol{G}'}(\boldsymbol{k},n;\boldsymbol{q}\beta)a^{\boldsymbol{G}'\boldsymbol{k}\alpha}_{l'm'p'}(\boldsymbol{q})\right)^{*}\left\langle\vec{\varphi}^{\mathring{\alpha}}_{l'm'p'}\middle|\left[\boldsymbol{\mathscr{V}}^{(1)}_{\text{eff}}(\boldsymbol{q},\alpha)\right]^{\top}\middle|\vec{\varphi}^{\mathring{\alpha}}_{lmp}\right\rangle_{\Omega}z^{(0)}_{\boldsymbol{G}}(\boldsymbol{k},n)a^{\boldsymbol{G}\boldsymbol{k}\alpha}_{lmp}\\
&+\left\langle\vec{\varphi}^{\mathring{\beta}}_{l'm'p'}\middle|\boldsymbol{\mathscr{V}}^{(1)}_{\text{eff}}(\boldsymbol{q},\beta)\middle|\vec{\varphi}^{\mathring{\beta}}_{lmp}\right\rangle_{\Omega}z^{*(0)}_{\boldsymbol{G}'}(\boldsymbol{k},n)a^{*\boldsymbol{G}'\boldsymbol{k}\beta}_{l'm'p'}\left[\boldsymbol{z}^{(1)}_{\boldsymbol{G}}(\boldsymbol{k},n;\boldsymbol{q}\alpha)a^{\boldsymbol{G}\boldsymbol{k}\beta}_{lmp}(\boldsymbol{q})\right]^{\top}\\
&=\int_{\text{IR}}\boldsymbol{\rho}^{*(1)}_{\text{IR}}(\boldsymbol{r};\boldsymbol{q}^{+}\beta)\left[\boldsymbol{V}^{(1)\text{IR}}_{\text{eff}}(\boldsymbol{r};\boldsymbol{q}^{+}\alpha)\right]^{\top}\mathrm{d}^{3}r\\
&\quad+\sum_{\gamma}\int_{\gamma}\boldsymbol{\rho}^{*(1)}_{\gamma,\boldsymbol{z}^{(1)}}(\boldsymbol{r};\boldsymbol{q}^{+}\beta)\left[\boldsymbol{V}^{(1)\gamma}_{\text{eff}}(\boldsymbol{r};\boldsymbol{q}^{+}\alpha)+\boldsymbol{\nabla}\boldsymbol{V}^{(0)\gamma}_{\text{eff}}(\boldsymbol{r})\right]^{\top}\mathrm{d}^{3}r\ ,
\end{aligned}
\tag{7.159b}
$$

where $\boldsymbol{\rho}^{*(1)}_{\gamma,\boldsymbol{z}^{(1)}}(\boldsymbol{r};\boldsymbol{q}^{+}\beta)$ is the MT first-order density variation without the Pulay basis-correction, i.e., equation (7.37a) without the third, fourth, and fifth lines. Moreover, the surface-terms

$$
\begin{aligned}
-\sum_{\boldsymbol{G}'\boldsymbol{G}}\Bigg\{&\boldsymbol{z}^{*(1)}_{\boldsymbol{G}'}(\boldsymbol{k},n;\boldsymbol{q}\beta)z^{(0)}_{\boldsymbol{G}}(\boldsymbol{k},n)\oint_{\partial\alpha}\phi^{*(0)\text{IR}}_{\boldsymbol{k}+\boldsymbol{q},\boldsymbol{G}'}(\boldsymbol{r})\left(\mathscr{H}^{(0)}-\epsilon^{(0)}_{\boldsymbol{k},n}\right)\phi^{(0)\text{IR}}_{\boldsymbol{k},\boldsymbol{G}}(\boldsymbol{r})\hat{\boldsymbol{r}}^{\top}\,\mathrm{d}S\\
&+\oint_{\partial\beta}\hat{\boldsymbol{r}}\phi^{*(0)\text{IR}}_{\boldsymbol{k},\boldsymbol{G}'}(\boldsymbol{r})\left(\mathscr{H}^{(0)}-\epsilon^{(0)}_{\boldsymbol{k},n}\right)\phi^{(0)\text{IR}}_{\boldsymbol{k}+\boldsymbol{q},\boldsymbol{G}}(\boldsymbol{r})\,\mathrm{d}S\,z^{*(0)}_{\boldsymbol{G}'}(\boldsymbol{k},n)\left[\boldsymbol{z}^{(1)}_{\boldsymbol{G}}(\boldsymbol{k},n;\boldsymbol{q}\alpha)\right]^{\top}\Bigg\}
\end{aligned}
\tag{7.159c}
$$

vanish. The fact that these terms can be neglected is related to the discussion of the leftover terms for the Goldstone modes in section 7.6.4.

7.6.8 Final Expressions

Resume

Including all discussed reformulations, a final form of the dynamical matrix results. Apart from almost irrelevant surface terms, it is consistent with the outcome of Neukirchen [256]. These surface terms are as small as the discontinuities of the unperturbed charge density, the LAPW basis, or the Coulomb potential (not significantly larger than $1 \cdot 10^{-5}\, E_\mathrm{h}\, a_0^{-2}$ for the investigated materials). However, in his derivation contributions dependent on the variations of the occupation number or the Kohn–Sham energy must be excluded (vanishing for the relevant systems in this thesis) [256].

Assistance, symmetric kinetic energy, and subdivision

All changes that imply from omitting the terms in equation (7.159) have been programmed by Neukirchen. Furthermore, he has implemented the symmetric application of the kinetic energy in the IR. As stated in section 7.4.4, he has also done this for the Sternheimer equation, but there the impact on the results of Al is only marginal. Therefore, we decided to deactivate it now, but to investigate the effect on the results of more complicated systems in the future [127, 256]. Still, within the dynamical matrix it is activated, because a thorough analysis about the relevance on different system has not been done yet. Activating it in the dynamical matrix, but deactivating it in the Sternheimer equation, is an inconsistency. But, we deem it to be small, which is deduced from our experience with the Sternheimer equation [127, 256]. This is legitimate, because the terms referred to in the Sternheimer equation and the dynamical matrix show many analogies. Furthermore, I assume that estimating the inconsistency to be insignificant is supported by the fact that Klüppelberg takes the discontinuities rigorously into account by introducing surface terms. In particular, Klüppelberg [88] states that those surface terms incorporating kinetic energy operators are very relevant for forces. Since the results are convincing for a first implementation, we decided to postpone a thorough analysis of the kinetic-energy form to the future. The final expressions for the dynamical matrix are again subdivided into HF, Pulay integral, Pulay matrix-elements, and surface terms.

Hellmann–Feynman Contributions

Reverting optimization

Applying equations (7.155) to the MT volume integrals in equation (7.145) the HF dynamical-matrix reads

$$\begin{aligned}
\underline{D}_{\mathrm{HF}}^{\beta\alpha}(\boldsymbol{q}^{-+}) = {} & \int_{\mathrm{IR}} \boldsymbol{\rho}_{\mathrm{IR}}^{*(1)}(\boldsymbol{r};\boldsymbol{q}^{+}\beta)\left[\boldsymbol{V}_{\mathrm{ext}}^{(1)\mathrm{IR}}(\boldsymbol{r};\boldsymbol{q}^{+}\alpha)\right]^{\top}\mathrm{d}^3r - \delta_{\beta\alpha}\int_{\mathrm{IR}} \boldsymbol{\nabla}\rho_{\mathrm{IR}}^{(0)}(\boldsymbol{r})\boldsymbol{\nabla}^{\top}V_{\mathrm{ext}}^{(0)\mathrm{IR}}(\boldsymbol{r})\,\mathrm{d}^3r \\
& + \sum_{\gamma}\int_{\gamma} \boldsymbol{\rho}_{\gamma}^{*(1)}(\boldsymbol{r};\boldsymbol{q}^{+}\beta)\left[\boldsymbol{V}_{\mathrm{ext}}^{(1)\gamma}(\boldsymbol{r};\boldsymbol{q}^{+}\alpha) + \delta_{\gamma\alpha}\boldsymbol{\nabla}V_{\mathrm{ext}}^{(0)\gamma}(\boldsymbol{r})\right]^{\top}\mathrm{d}^3r \\
& + \int_{\alpha} \boldsymbol{\rho}_{\alpha,\mathrm{Sh}}^{*(1)}(\boldsymbol{r};\boldsymbol{q}^{+}\beta)\boldsymbol{\nabla}^{\top}V_{\mathrm{Hxc}}^{(0)\alpha}(\boldsymbol{r})\,\mathrm{d}^3r \\
& + \delta_{\beta\alpha}\sum_{\gamma}\oint_{\gamma}\hat{\boldsymbol{r}}\rho_{\gamma}^{(0)}(\boldsymbol{r})\boldsymbol{\nabla}^{\top}V_{\mathrm{ext}}^{(0)\gamma}(\boldsymbol{r})\,\mathrm{d}S - \delta_{\beta\alpha}\oint_{\mathrm{IR}}\hat{\boldsymbol{r}}\rho_{\mathrm{IR}}^{(0)}(\boldsymbol{r})\boldsymbol{\nabla}^{\top}V_{\mathrm{ext}}^{(0)\mathrm{IR}}(\boldsymbol{r})\,\mathrm{d}S \\
& + \underline{E}_{\mathrm{ii}}^{(2)\beta\alpha}(\boldsymbol{q}^{-+}) + \delta_{\boldsymbol{Q}_{\beta}\boldsymbol{Q}_{\alpha}}\underline{E}_{\mathrm{ii}}^{(2)\beta\alpha}(\boldsymbol{0}^{-+}) \\
& + \delta_{\beta\alpha}\sum_{\gamma}\left(\delta_{\gamma\alpha}-1\right)\int_{\gamma}\boldsymbol{\nabla}\rho_{\gamma,\mathrm{v}}^{(0)}(\boldsymbol{r})\boldsymbol{\nabla}^{\top}V_{\mathrm{ext}}^{(0)\gamma}(\boldsymbol{r})\,\mathrm{d}^3r\ , \qquad (7.160\mathrm{a})
\end{aligned}$$

However, Neukirchen has found from numerical experiments that the optimization discussed in equations (7.155) does rather worsens the frequencies for the systems in this thesis. Therefore, equation (7.160a) is simplified in the implementation by Neukirchen, principally reverting the optimization to the form in equation (7.155a) (see also equation (7.154e)):

$$
\begin{aligned}
&\underline{D}_{\mathrm{HF}}^{\beta\alpha}(\boldsymbol{q}^{-+}) && (7.160\mathrm{b})\\
&\quad= \int_{\mathrm{IR}} \boldsymbol{\rho}_{\mathrm{IR}}^{*(1)}(\boldsymbol{r};\boldsymbol{q}^{+}\beta)\Big[\boldsymbol{V}_{\mathrm{ext}}^{(1)\mathrm{IR}}(\boldsymbol{r};\boldsymbol{q}^{+}\alpha)\Big]^{\top}\,\mathrm{d}^3r - \delta_{\beta\alpha}\int_{\mathrm{IR}} \boldsymbol{\nabla}\rho_{\mathrm{IR}}^{(0)}(\boldsymbol{r})\boldsymbol{\nabla}^{\top}V_{\mathrm{ext}}^{(0)\mathrm{IR}}(\boldsymbol{r})\,\mathrm{d}^3r\\
&\qquad \sum_{\gamma}\int_{\gamma} \boldsymbol{\rho}_{\gamma}^{*(1)}(\boldsymbol{r};\boldsymbol{q}^{+}\beta)\Big[\boldsymbol{V}_{\mathrm{ext}}^{(1)\gamma}(\boldsymbol{r};\boldsymbol{q}^{+}\alpha)\Big]^{\top}\,\mathrm{d}^3r - \sum_{\gamma}\delta_{\beta\alpha}\int_{\gamma}\Big(\boldsymbol{\nabla}\rho_{\gamma}^{(0)}(\boldsymbol{r})\Big)\boldsymbol{\nabla}^{\top}V_{\mathrm{ext}}^{(0)\gamma}(\boldsymbol{r})\,\mathrm{d}^3r\\
&\qquad + \int_{\alpha} \boldsymbol{\rho}_{\alpha,\mathrm{Sh}}^{*(1)}(\boldsymbol{r};\boldsymbol{q}^{+}\beta)\boldsymbol{\nabla}^{\top}V_{\mathrm{eff}}^{(0)\alpha}(\boldsymbol{r})\,\mathrm{d}^3r\\
&\qquad + \delta_{\beta\alpha}\sum_{\gamma}\oint_{\gamma}\hat{\boldsymbol{r}}\rho_{\gamma}^{(0)}(\boldsymbol{r})\boldsymbol{\nabla}^{\top}V_{\mathrm{ext}}^{(0)\gamma}(\boldsymbol{r})\,\mathrm{d}S - \delta_{\beta\alpha}\oint_{\mathrm{IR}}\hat{\boldsymbol{r}}\rho_{\mathrm{IR}}^{(0)}(\boldsymbol{r})\boldsymbol{\nabla}^{\top}V_{\mathrm{ext}}^{(0)\mathrm{IR}}(\boldsymbol{r})\,\mathrm{d}S\\
&\qquad + \underline{E}_{\mathrm{ii}}^{(2)\beta\alpha}(\boldsymbol{q}^{-+}) + \delta_{\boldsymbol{Q}_{\beta}\boldsymbol{Q}_{\alpha}}\underline{E}_{\mathrm{ii}}^{(2)\beta\alpha}(\boldsymbol{0}^{-+})\,.
\end{aligned}
$$

Interstitial integral algorithm

For evaluating the IR integrals in equation (7.160b), their integration volume is expanded from the IR to the complete unit cell, requiring the introduction of an IR step function (5.48b). Expanding the linear variations of the density and the external potential as well as the unperturbed step function in plane waves, a convolution of the step function, for example with the first-order external potential variation, becomes obvious (the so-called *warping*). This warping is analogous to combining the IR xc kernel with the linear variation of the density (see section 7.3.2). Ultimately, the IR integral reduces to a multiplication of Fourier coefficients, such as in

$$
\begin{aligned}
&\int_{\mathrm{IR}} \boldsymbol{\rho}_{\mathrm{IR}}^{*(1)}(\boldsymbol{r};\boldsymbol{q}^{+}\beta)\Big[\boldsymbol{V}_{\mathrm{ext}}^{(1)\mathrm{IR}}(\boldsymbol{r};\boldsymbol{q}^{+}\alpha)\Big]^{\top}\,\mathrm{d}^3r && (7.161\mathrm{a})\\
&= \int_{\Omega} \boldsymbol{\rho}_{\mathrm{IR}}^{*(1)}(\boldsymbol{r};\boldsymbol{q}^{+}\beta)\Big[\boldsymbol{V}_{\mathrm{ext}}^{(1)\mathrm{IR}}(\boldsymbol{r};\boldsymbol{q}^{+}\alpha)\Big]^{\top}\Theta_{\mathrm{IR}}(\boldsymbol{r})\,\mathrm{d}^3r\\
&= \Omega\sum_{\boldsymbol{G}} \boldsymbol{\rho}_{\mathrm{IR}}^{*(1)}(\boldsymbol{G};\boldsymbol{q}^{+}\beta)\Big[\Big[\boldsymbol{V}_{\mathrm{ext}}^{(1)\mathrm{IR}}\Theta_{\mathrm{IR}}\Big](\boldsymbol{G};\boldsymbol{q}^{+}\alpha)\Big]^{\top}\,. && (7.161\mathrm{b})
\end{aligned}
$$

Warping the potential can lead to aliasing errors if the FFT grid is not chosen large enough [127, 278]. Therefore, conducting test 34 is vital before investigating a new system (or convergence parameter set). Furthermore, it is known and not critical that warping worsens the continuity of the respective quantity [127, 251].

Muffin-tin integral algorithm

For computing the MT sphere integrals, the orthogonality relation of the spherical harmonics is exploited. This means for an exemplary MT integral in equation (7.160b)

$$
\begin{aligned}
&\int_{\gamma} \boldsymbol{\rho}_{\gamma}^{*(1)}(\boldsymbol{r};\boldsymbol{q}^{+}\beta)\Big[\boldsymbol{V}_{\mathrm{ext}}^{(1)\gamma}(\boldsymbol{r};\boldsymbol{q}^{+}\alpha)\Big]^{\top}\,\mathrm{d}^3r && (7.162\mathrm{a})\\
&= \sum_{l'm'}\sum_{lm}\int_{\gamma} r_{\nu\mathring{\gamma}}^{2}\Big[\boldsymbol{\rho}_{\gamma}^{*(1)}(r_{\nu\mathring{\gamma}};\boldsymbol{q}^{+}\beta)\Big]_{l'm'}\Big[\boldsymbol{V}_{\mathrm{ext}}^{(1)\gamma}(r_{\nu\mathring{\gamma}};\boldsymbol{q}^{+}\alpha)\Big]_{lm}^{\top}\,\mathrm{d}r_{\nu\mathring{\gamma}}\int_{\partial\gamma}\mathrm{Y}_{l'm'}(\hat{\boldsymbol{r}})\mathrm{Y}_{lm}(\hat{\boldsymbol{r}})\,\mathrm{d}\Omega\\
&= \sum_{lm}\int_{\gamma} r_{\nu\mathring{\gamma}}^{2}\Big[\boldsymbol{\rho}_{\gamma}^{*(1)}(r_{\nu\mathring{\gamma}};\boldsymbol{q}^{+}\beta)\Big]_{lm}\Big[\boldsymbol{V}_{\mathrm{ext}}^{(1)\gamma}(r_{\nu\mathring{\gamma}};\boldsymbol{q}^{+}\alpha)\Big]_{lm}^{\top}\,\mathrm{d}r_{\nu\mathring{\gamma}}\,. && (7.162\mathrm{b})
\end{aligned}
$$

So, the volume integral reduces to a sum of radial integrals for every combination of the orbital quantum number l and the magnetic quantum number m. This is done employing the recycled radial integration routine `Intgr3` of `FLEUR`.

Surface-integral algorithm

The IR surface integral in equation (7.160b) is computed as in

$$\oint_{\beta} \hat{\boldsymbol{r}} \rho^{(0)}_{\mathrm{IR}}(\boldsymbol{r}) \boldsymbol{\nabla}^{\top} \boldsymbol{V}^{(0)\mathrm{IR}}_{\mathrm{ext}}(\boldsymbol{r}) \, \mathrm{d}S \tag{7.163a}$$

$$= \sum_{\boldsymbol{G},\boldsymbol{G}'} R^2_{\beta} \oint \hat{\boldsymbol{r}} \mathrm{e}^{\mathrm{i}(\boldsymbol{G}-\boldsymbol{G}'+\boldsymbol{q})\cdot\boldsymbol{r}} \, \mathrm{d}\Omega \, \rho^{(0)}_{\mathrm{IR}}(\boldsymbol{G}') \boldsymbol{\nabla}^{\top} \boldsymbol{V}^{(0)\mathrm{IR}}_{\mathrm{ext}}(\boldsymbol{G})$$

$$= 4\mathrm{i}\pi R^2_{\mathring{\alpha}} \sum_{\boldsymbol{G}'\boldsymbol{G}} \mathrm{j}_1\left(|\boldsymbol{G}-\boldsymbol{G}'+\boldsymbol{q}| R_{\mathring{\alpha}}\right) \mathrm{e}^{\mathrm{i}(\boldsymbol{G}-\boldsymbol{G}'+\boldsymbol{q})\cdot\boldsymbol{\tau}_{\alpha}} \sum_{im} \zeta^{*}_{i,m} \hat{\boldsymbol{e}}_i \mathrm{Y}^{*}_{1m}\left(\widehat{\boldsymbol{G}-\boldsymbol{G}'+\boldsymbol{q}}\right) \tag{7.163b}$$
$$\times \rho^{(0)}_{\mathrm{IR}}(\boldsymbol{G}') \boldsymbol{\nabla}^{\top} \boldsymbol{V}^{(0)\mathrm{IR}}_{\mathrm{ext}}(\boldsymbol{G}) \, ,$$

and the MT surface integral as in

$$\oint_{\beta} \hat{\boldsymbol{r}} \rho^{(0)}_{\beta}(\boldsymbol{r}) \boldsymbol{\nabla}^{\top} V^{(0)\beta}_{\mathrm{ext}}(\boldsymbol{r}) \, \mathrm{d}S \tag{7.164a}$$

$$= \sum_{l''m''} \sum_{lm} R^2_{\beta} \oint_{\beta} \hat{\boldsymbol{r}} \mathrm{Y}^{*}_{l''m''}(\hat{\boldsymbol{r}}) \mathrm{Y}_{lm}(\hat{\boldsymbol{r}}) \, \mathrm{d}\Omega \left[\rho^{(0)}_{\mathring{\beta}}\left(R_{\beta}\right)\right]_{\lambda(l)} c^{\beta}_{\lambda(l)\mu(m)} \left[\boldsymbol{\nabla}^{\top} \boldsymbol{V}^{*(0)\beta}_{\mathrm{ext}}\left(R_{\beta}\right)\right]_{l''m''}$$

$$= \sum_{l''m''} \sum_{lm} R^2_{\beta} \sum_{im'} \zeta_{i,m'} \hat{\boldsymbol{e}}_i \left[\rho^{(0)}_{\mathring{\beta}}\left(R_{\beta}\right)\right]_{\lambda(l)} c^{\beta}_{\lambda(l)\mu(m)} \left[\boldsymbol{\nabla}^{\top} \boldsymbol{V}^{*(0)\beta}_{\mathrm{ext}}\left(R_{\beta}\right)\right]_{l''m''} \tag{7.164b}$$
$$\times \oint_{\beta} \mathrm{Y}^{*}_{l''m''}(\hat{\boldsymbol{r}}) \mathrm{Y}_{lm}(\hat{\boldsymbol{r}}) \mathrm{Y}_{1m'}(\hat{\boldsymbol{r}}) \, \mathrm{d}\Omega$$

$$= \sum_{l''m''} \sum_{lm} R^2_{\beta} \sum_{im'} \zeta_{i,m'} \hat{\boldsymbol{e}}_i \left[\rho^{(0)}_{\mathring{\beta}}\left(R_{\beta}\right)\right]_{\lambda(l)} c^{\beta}_{\lambda(l)\mu(m)} \left[\boldsymbol{\nabla}^{\top} \boldsymbol{V}^{*(0)\beta}_{\mathrm{ext}}\left(R_{\beta}\right)\right]_{l''m''} G^{m''\,m\,m'}_{l''\;l\;1} \, . \tag{7.164c}$$

This is analogous to the surface integrals discussed in equation (7.54). But here, the lattice-harmonic coefficients of the unperturbed-density are inserted (cf. equation (7.6c)).

Pulay Unit-Cell Integral Correction

Relative to equation (7.147), the IR integral is omitted according to equation (7.159). Furthermore, the MT integrals containing the linear potential variations are alleviated as in equation (7.156b). Finally, the first MT integral containing a gradient of the Hartree and the xc (Hxc) potentials stems from mitigating the MT integrals in the HF contribution (see equation (7.154f)). All in all, the Pulay-correction integral is reformulated to

$$\underline{D}^{\beta\alpha}_{\mathrm{Pl,dp}} = \sum_{\gamma} \int_{\gamma} \boldsymbol{\rho}^{*(1)}_{\gamma,\mathrm{Pl}}(\boldsymbol{r}; \boldsymbol{q}^{+}\beta) \left[\boldsymbol{V}^{(1)\gamma}_{\mathrm{eff}}(\boldsymbol{r}; \boldsymbol{q}^{+}\alpha) + \delta_{\gamma\alpha}\delta_{\beta\alpha} \boldsymbol{\nabla} V^{(0)\gamma}_{\mathrm{eff}}(\boldsymbol{r})\right]^{\top} \mathrm{d}^3 r \, , \tag{7.165a}$$

which Neukirchen has spitted in the implementation to

$$= \sum_{\gamma} \int_{\gamma} \boldsymbol{\rho}^{*(1)}_{\gamma,\mathrm{Pl,no}\boldsymbol{\nabla}}(\boldsymbol{r}; \boldsymbol{q}^{+}\beta) \left[\boldsymbol{V}^{(1)\gamma}_{\mathrm{eff}}(\boldsymbol{r}; \boldsymbol{q}^{+}\alpha) + \delta_{\gamma\alpha}\delta_{\beta\alpha} \boldsymbol{\nabla} V^{(0)\gamma}_{\mathrm{eff}}(\boldsymbol{r})\right]^{\top} \mathrm{d}^3 r \tag{7.165b}$$
$$- \sum_{\gamma} \int_{\gamma} \delta_{\beta\gamma} \boldsymbol{\nabla} \rho^{*(0)}_{\gamma}(\boldsymbol{r}) \left[\boldsymbol{V}^{(1)\gamma}_{\mathrm{eff}}(\boldsymbol{r}; \boldsymbol{q}^{+}\alpha) + \delta_{\gamma\alpha}\delta_{\beta\alpha} \boldsymbol{\nabla} V^{(0)\gamma}_{\mathrm{eff}}(\boldsymbol{r})\right]^{\top} \mathrm{d}^3 r \, .$$

In theses equations $\boldsymbol{\rho}^{*(1)}_{\gamma,\text{Pl}}(\boldsymbol{r};\boldsymbol{q}^{+}\beta)$ is defined as the sum of the third, fourth and fifth lines in equation (7.37a). In addition, $\boldsymbol{\rho}^{*(1)}_{\gamma,\text{Pl},\text{no}\boldsymbol{\nabla}}(\boldsymbol{r};\boldsymbol{q}^{+}\beta)$ denotes the sum of the third and fourth lines in equation (7.37a).

Pulay Matrix-Elements Correction

Resume

Omitting the respective terms from equations (7.153d) and (7.159) within equation (7.149a) yields

$$
\begin{aligned}
&\underline{D}^{\boldsymbol{k}n\beta\alpha}_{\text{Pu2b}}(\boldsymbol{q}^{+-}) && (7.166\text{a})\\
&\quad= \sum_{l'm'p'}\sum_{lmp}\sum_{\boldsymbol{G}'\boldsymbol{G}}\Bigg\{\\
&\qquad\Big(\boldsymbol{z}^{(1)}_{\boldsymbol{G}'}(\boldsymbol{k},n;\boldsymbol{q}\beta)a^{\boldsymbol{G}'\boldsymbol{k}\alpha}_{l'm'p'}(\boldsymbol{q})\mathrm{i}[\boldsymbol{k}+\boldsymbol{q}+\boldsymbol{G}']^{\top}\Big)^{*}\Big\langle\vec{\varphi}^{\,\mathring{\alpha}}_{l'm'p'}\Big|\mathscr{H}^{(0)}-\epsilon^{(0)}_{\boldsymbol{k},n}\Big|\vec{\varphi}^{\,\mathring{\alpha}}_{lmp}\Big\rangle_{\alpha}z^{(0)}_{\boldsymbol{G}}(\boldsymbol{k},n)a^{\boldsymbol{G}\boldsymbol{k}\alpha}_{lmp}\\
&\quad-\delta_{\beta\alpha}\Big(z^{(0)}_{\boldsymbol{G}'}(\boldsymbol{k},n)a^{\boldsymbol{G}'\boldsymbol{k}\alpha}_{l'm'p'}\Big)^{*}[\boldsymbol{k}+\boldsymbol{G}'][\boldsymbol{k}+\boldsymbol{G}']^{\top}\Big\langle\vec{\varphi}^{\,\mathring{\alpha}}_{l'm'p'}\Big|\mathscr{H}^{(0)}-\epsilon^{(0)}_{\boldsymbol{k},n}\Big|\vec{\varphi}^{\,\mathring{\alpha}}_{lmp}\Big\rangle_{\alpha}z^{(0)}_{\boldsymbol{G}}(\boldsymbol{k},n)a^{\boldsymbol{G}\boldsymbol{k}\alpha}_{lmp}\Bigg\}.
\end{aligned}
$$

Furthermore, equation (7.149b) simplifies to

$$
\begin{aligned}
&\underline{D}^{\boldsymbol{k}n\beta\alpha}_{\text{Pu2kO}}(\boldsymbol{q}^{-+}) && (7.166\text{b})\\
&\quad= \sum_{l'm'p'}\sum_{lmp}\sum_{\boldsymbol{G}'\boldsymbol{G}}\Bigg\{\\
&\qquad\Big(z^{(0)}_{\boldsymbol{G}'}(\boldsymbol{k},n)a^{\boldsymbol{G}'\boldsymbol{k}\beta}_{l'm'p'}\Big)^{*}\Big\langle\vec{\varphi}^{\,\mathring{\beta}}_{l'm'p'}\Big|\mathscr{H}^{(0)}-\epsilon^{(0)}_{\boldsymbol{k},n}\Big|\vec{\varphi}^{\,\mathring{\beta}}_{lmp}\Big\rangle_{\beta}a^{\boldsymbol{G}\boldsymbol{k}\beta}_{lmp}(\boldsymbol{q})\mathrm{i}[\boldsymbol{k}+\boldsymbol{q}+\boldsymbol{G}]\Big[\boldsymbol{z}^{(1)}_{\boldsymbol{G}}(\boldsymbol{k},n;+\boldsymbol{q}\alpha)\Big]^{\top}\\
&\quad-\delta_{\beta\alpha}\Big(z^{(0)}_{\boldsymbol{G}'}(\boldsymbol{k},n)a^{\boldsymbol{G}'\boldsymbol{k}\alpha}_{l'm'p'}\Big)^{*}[\boldsymbol{k}+\boldsymbol{G}][\boldsymbol{k}+\boldsymbol{G}]^{\top}\Big\langle\vec{\varphi}^{\,\mathring{\alpha}}_{l'm'p'}\Big|\mathscr{H}^{(0)}-\epsilon^{(0)}_{\boldsymbol{k},n}\Big|\vec{\varphi}^{\,\mathring{\alpha}}_{lmp}\Big\rangle_{\alpha}z^{(0)}_{\boldsymbol{G}}(\boldsymbol{k},n)a^{\boldsymbol{G}\boldsymbol{k}\alpha}_{lmp}\Bigg\}.
\end{aligned}
$$

and equation (7.149c) to

$$
\begin{aligned}
&\underline{D}^{\boldsymbol{k}n\beta\alpha}_{\text{Pu1bk}}(\boldsymbol{q}^{++}) && (7.166\text{c})\\
&\quad= \sum_{l'm'p'}\sum_{lmp}\sum_{\boldsymbol{G}'\boldsymbol{G}}\Bigg\{\\
&\qquad\frac{1}{2}\Big(z^{(0)}_{\boldsymbol{G}'}(\boldsymbol{k},n)a^{\boldsymbol{G}'\boldsymbol{k}\beta}_{l'm'p'}\mathrm{i}[\boldsymbol{k}+\boldsymbol{G}']\Big)^{*}\Big\langle\vec{\varphi}^{\,\mathring{\beta}}_{l'm'p'}\Big|\mathscr{H}^{(0)}-\epsilon^{(0)}_{\boldsymbol{k},n}\Big|\vec{\varphi}^{\,\mathring{\beta}}_{lmp}\Big\rangle_{\beta}\Big[\boldsymbol{z}^{(1)}_{\boldsymbol{G}}(\boldsymbol{k},n;\boldsymbol{q}\alpha)\Big]^{\top}a^{\boldsymbol{G}\boldsymbol{k}\beta}_{lmp}(\boldsymbol{q})\\
&\quad+\frac{1}{2}\Big(\boldsymbol{z}^{(1)}_{\boldsymbol{G}'}(\boldsymbol{k},n;\boldsymbol{q}\beta)a^{\boldsymbol{G}'\boldsymbol{k}\alpha}_{l'm'p'}(\boldsymbol{q})\Big)^{*}\Big\langle\vec{\varphi}^{\,\mathring{\alpha}}_{l'm'p'}\Big|\mathscr{H}^{(0)}-\epsilon^{(0)}_{\boldsymbol{k},n}\Big|\vec{\varphi}^{\,\mathring{\alpha}}_{lmp}\Big\rangle_{\alpha}\mathrm{i}[\boldsymbol{k}+\boldsymbol{G}]^{\top}z^{(0)}_{\boldsymbol{G}}(\boldsymbol{k},n)a^{\boldsymbol{G}\boldsymbol{k}\alpha}_{lmp}\\
&\quad+\delta_{\alpha\beta}\Big(z^{(0)}_{\boldsymbol{G}'}(\boldsymbol{k},n)a^{\boldsymbol{G}'\boldsymbol{k}\alpha}_{l'm'p'}\mathrm{i}[\boldsymbol{k}+\boldsymbol{G}']\Big)^{*}\Big\langle\vec{\varphi}^{\,\mathring{\alpha}}_{l'm'p'}\Big|\mathscr{H}^{(0)}-\epsilon^{(0)}_{\boldsymbol{k},n}\Big|\vec{\varphi}^{\,\mathring{\alpha}}_{lmp}\Big\rangle_{\alpha}z^{(0)}_{\boldsymbol{G}}(\boldsymbol{k},n)a^{\boldsymbol{G}\boldsymbol{k}\alpha}_{lmp}\mathrm{i}[\boldsymbol{k}+\boldsymbol{G}]^{\top}\Bigg\}.
\end{aligned}
$$

According to equation (7.128a), equations (7.166a), (7.166b), and (7.166c) must be summed, so

$$
\begin{aligned}
&\underline{D}^{\beta\alpha}_{\text{Pl,bk}}(\boldsymbol{q}) && (7.166\text{d})\\
&\quad:= \sum_{\boldsymbol{k},n}2f^{(0)}_{\boldsymbol{k},n}\Big(\underline{D}^{\boldsymbol{k}n\beta\alpha}_{\text{Pu2b}}(\boldsymbol{q}^{+-})+\underline{D}^{\boldsymbol{k}n\beta\alpha}_{\text{Pu2kO}}(\boldsymbol{q}^{-+})+2\underline{D}^{\boldsymbol{k}n\beta\alpha}_{\text{Pu1bk}}(\boldsymbol{q}^{++})\Big)\\
&\quad= \sum_{l'm'p'}\sum_{lmp}\sum_{\boldsymbol{G}'\boldsymbol{G}}\Bigg\{ && (7.166\text{e})
\end{aligned}
$$

$$
\begin{aligned}
&\left(\boldsymbol{z}^{(1)}_{\boldsymbol{G}'}\left(\boldsymbol{k}^{+}_{\mathrm{bf}}, n; \beta\right) a^{\boldsymbol{G}'\boldsymbol{k}^{+}_{\mathrm{bf}}\alpha}_{l'm'p'}\, \mathrm{i}\left[\boldsymbol{k}^{+}_{\mathrm{bf}} + \boldsymbol{G}'\right]^{\top} \right)^{*} \left\langle \vec{\varphi}^{\mathring{\alpha}}_{l'm'p'} \middle| \mathscr{H}^{(0)} - \epsilon^{(0)}_{\boldsymbol{k},n} \middle| \vec{\varphi}^{\mathring{\alpha}}_{lmp} \right\rangle_{\alpha} z^{(0)}_{\boldsymbol{G}}(\boldsymbol{k},n) a^{\boldsymbol{G}\boldsymbol{k}\alpha}_{lmp} \\
&+ \left(\boldsymbol{z}^{(1)}_{\boldsymbol{G}'}\left(\boldsymbol{k}^{+}_{\mathrm{bf}}, n; \beta\right) a^{\boldsymbol{G}'\boldsymbol{k}^{+}_{\mathrm{bf}}\alpha}_{l'm'p'} \right)^{*} \left\langle \vec{\varphi}^{\mathring{\alpha}}_{l'm'p'} \middle| \mathscr{H}^{(0)} - \epsilon^{(0)}_{\boldsymbol{k},n} \middle| \vec{\varphi}^{\mathring{\alpha}}_{lmp} \right\rangle_{\alpha} \mathrm{i}[\boldsymbol{k} + \boldsymbol{G}]^{\top} z^{(0)}_{\boldsymbol{G}}(\boldsymbol{k},n) a^{\boldsymbol{G}\boldsymbol{k}\alpha}_{lmp} \\
&+ \left(z^{(0)}_{\boldsymbol{G}'}(\boldsymbol{k},n) a^{\boldsymbol{G}'\boldsymbol{k}\beta}_{l'm'p'} \right)^{*} \left\langle \vec{\varphi}^{\mathring{\beta}}_{l'm'p'} \middle| \mathscr{H}^{(0)} - \epsilon^{(0)}_{\boldsymbol{k},n} \middle| \vec{\varphi}^{\mathring{\beta}}_{lmp} \right\rangle_{\beta} \mathrm{i}\left[\boldsymbol{k}^{+}_{\mathrm{bf}} + \boldsymbol{G}\right] \left[\boldsymbol{z}^{(1)}_{\boldsymbol{G}}\left(\boldsymbol{k}^{+}_{\mathrm{bf}}, n; \alpha\right)\right]^{\top} a^{\boldsymbol{G}\boldsymbol{k}^{+}_{\mathrm{bf}}\beta}_{lmp} \\
&+ \left(z^{(0)}_{\boldsymbol{G}'}(\boldsymbol{k},n) a^{\boldsymbol{G}'\boldsymbol{k}\beta}_{l'm'p'} \mathrm{i}[\boldsymbol{k} + \boldsymbol{G}'] \right)^{*} \left\langle \vec{\varphi}^{\mathring{\beta}}_{l'm'p'} \middle| \mathscr{H}^{(0)} - \epsilon^{(0)}_{\boldsymbol{k},n} \middle| \vec{\varphi}^{\mathring{\beta}}_{lmp} \right\rangle_{\beta} \left[\boldsymbol{z}^{(1)}_{\boldsymbol{G}}\left(\boldsymbol{k}^{+}_{\mathrm{bf}}, n; \alpha\right)\right]^{\top} a^{\boldsymbol{G}\boldsymbol{k}^{+}_{\mathrm{bf}}\beta}_{lmp} \\
&+ 2\delta_{\alpha\beta} \left(z^{(0)}_{\boldsymbol{G}'}(\boldsymbol{k},n) a^{\boldsymbol{G}'\boldsymbol{k}\alpha}_{l'm'p'} \mathrm{i}[\boldsymbol{k} + \boldsymbol{G}'] \right)^{*} \left\langle \vec{\varphi}^{\mathring{\alpha}}_{l'm'p'} \middle| \mathscr{H}^{(0)} - \epsilon^{(0)}_{\boldsymbol{k},n} \middle| \vec{\varphi}^{\mathring{\alpha}}_{lmp} \right\rangle_{\alpha} z^{(0)}_{\boldsymbol{G}}(\boldsymbol{k},n) a^{\boldsymbol{G}\boldsymbol{k}\alpha}_{lmp} \mathrm{i}[\boldsymbol{k} + \boldsymbol{G}]^{\top} \\
&- \delta_{\beta\alpha} \left(z^{(0)}_{\boldsymbol{G}'}(\boldsymbol{k},n) a^{\boldsymbol{G}'\boldsymbol{k}\alpha}_{l'm'p'} \right)^{*} [\boldsymbol{k} + \boldsymbol{G}'][\boldsymbol{k} + \boldsymbol{G}']^{\top} \left\langle \vec{\varphi}^{\mathring{\alpha}}_{l'm'p'} \middle| \mathscr{H}^{(0)} - \epsilon^{(0)}_{\boldsymbol{k},n} \middle| \vec{\varphi}^{\mathring{\alpha}}_{lmp} \right\rangle_{\alpha} z^{(0)}_{\boldsymbol{G}}(\boldsymbol{k},n) a^{\boldsymbol{G}\boldsymbol{k}\alpha}_{lmp} \\
&- \delta_{\beta\alpha} \left(z^{(0)}_{\boldsymbol{G}'}(\boldsymbol{k},n) a^{\boldsymbol{G}'\boldsymbol{k}\alpha}_{l'm'p'} \right)^{*} [\boldsymbol{k} + \boldsymbol{G}][\boldsymbol{k} + \boldsymbol{G}]^{\top} \left\langle \vec{\varphi}^{\mathring{\alpha}}_{l'm'p'} \middle| \mathscr{H}^{(0)} - \epsilon^{(0)}_{\boldsymbol{k},n} \middle| \vec{\varphi}^{\mathring{\alpha}}_{lmp} \right\rangle_{\alpha} z^{(0)}_{\boldsymbol{G}}(\boldsymbol{k},n) a^{\boldsymbol{G}\boldsymbol{k}\alpha}_{lmp} \Bigg\} .
\end{aligned}
$$

The last three lines can be further simplified by evaluating the outer products of the vectors and cancelling all terms containing the vector $\boldsymbol{k}$. This can be achieved by interchanging those terms proportional to $\boldsymbol{k}(\boldsymbol{G}')^{\top}$ and $\boldsymbol{G}\boldsymbol{k}^{\top}$ by their transposed complement, according to equation (7.123). Since $\alpha = \beta$, the atom index is not interchanged so that finally

$$
\begin{aligned}
&\underline{D}^{\beta\alpha}_{\mathrm{Pl,bk}}(\boldsymbol{q}) \qquad (7.166\mathrm{f}) \\
&= \sum_{l'm'p'} \sum_{lmp} \sum_{\boldsymbol{G}'\boldsymbol{G}} \Bigg\{ \\
&\quad \left(\boldsymbol{z}^{(1)}_{\boldsymbol{G}'}\left(\boldsymbol{k}^{+}_{\mathrm{bf}}, n; \beta\right) a^{\boldsymbol{G}'\boldsymbol{k}^{+}_{\mathrm{bf}}\alpha}_{l'm'p'} \right)^{*} \left\langle \vec{\varphi}^{\mathring{\alpha}}_{l'm'p'} \middle| \mathscr{H}^{(0)} - \epsilon^{(0)}_{\boldsymbol{k},n} \middle| \vec{\varphi}^{\mathring{\alpha}}_{lmp} \right\rangle_{\alpha} z^{(0)}_{\boldsymbol{G}}(\boldsymbol{k},n) a^{\boldsymbol{G}\boldsymbol{k}\alpha}_{lmp} \\
&\qquad\qquad\qquad\qquad\qquad\qquad\qquad\qquad\qquad\qquad \times \mathrm{i}\left[\boldsymbol{k} + \boldsymbol{G} - \boldsymbol{k} - \boldsymbol{q} - \boldsymbol{G}_{\mathrm{bf}} - \boldsymbol{G}'\right]^{\top} \\
&\quad + \mathrm{i}\left[\boldsymbol{k} + \boldsymbol{q} + \boldsymbol{G}_{\mathrm{bf}} + \boldsymbol{G} - \boldsymbol{k} - \boldsymbol{G}'\right] \\
&\qquad\qquad \times \left(z^{(0)}_{\boldsymbol{G}'}(\boldsymbol{k},n) a^{\boldsymbol{G}'\boldsymbol{k}\beta}_{l'm'p'} \right)^{*} \left\langle \vec{\varphi}^{\mathring{\beta}}_{l'm'p'} \middle| \mathscr{H}^{(0)} - \epsilon^{(0)}_{\boldsymbol{k},n} \middle| \vec{\varphi}^{\mathring{\beta}}_{lmp} \right\rangle_{\beta} \left[\boldsymbol{z}^{(1)}_{\boldsymbol{G}}\left(\boldsymbol{k}^{+}_{\mathrm{bf}}, n; \alpha\right)\right]^{\top} a^{\boldsymbol{G}\boldsymbol{k}^{+}_{\mathrm{bf}}\beta}_{lmp} \\
&\quad + 2\delta_{\beta\alpha} \left(z^{(0)}_{\boldsymbol{G}'}(\boldsymbol{k},n) a^{\boldsymbol{G}'\boldsymbol{k}\alpha}_{l'm'p'} \boldsymbol{G}' \right)^{*} \left\langle \vec{\varphi}^{\mathring{\alpha}}_{l'm'p'} \middle| \mathscr{H}^{(0)} - \epsilon^{(0)}_{\boldsymbol{k},n} \middle| \vec{\varphi}^{\mathring{\alpha}}_{lmp} \right\rangle_{\alpha} z^{(0)}_{\boldsymbol{G}}(\boldsymbol{k},n) a^{\boldsymbol{G}\boldsymbol{k}\alpha}_{lmp} \boldsymbol{G}^{\top} \\
&\quad - \delta_{\beta\alpha} \left(z^{(0)}_{\boldsymbol{G}'}(\boldsymbol{k},n) a^{\boldsymbol{G}'\boldsymbol{k}\alpha}_{l'm'p'} \boldsymbol{G}'\boldsymbol{G}'^{\top} \right)^{*} \left\langle \vec{\varphi}^{\mathring{\alpha}}_{l'm'p'} \middle| \mathscr{H}^{(0)} - \epsilon^{(0)}_{\boldsymbol{k},n} \middle| \vec{\varphi}^{\mathring{\alpha}}_{lmp} \right\rangle_{\alpha} z^{(0)}_{\boldsymbol{G}}(\boldsymbol{k},n) a^{\boldsymbol{G}\boldsymbol{k}\alpha}_{lmp} \\
&\quad - \delta_{\beta\alpha} \left(z^{(0)}_{\boldsymbol{G}'}(\boldsymbol{k},n) a^{\boldsymbol{G}'\boldsymbol{k}\alpha}_{l'm'p'} \right)^{*} \left\langle \vec{\varphi}^{\mathring{\alpha}}_{l'm'p'} \middle| \mathscr{H}^{(0)} - \epsilon^{(0)}_{\boldsymbol{k},n} \middle| \vec{\varphi}^{\mathring{\alpha}}_{lmp} \right\rangle_{\alpha} z^{(0)}_{\boldsymbol{G}}(\boldsymbol{k},n) a^{\boldsymbol{G}\boldsymbol{k}\alpha}_{lmp} \boldsymbol{G}\boldsymbol{G}^{\top} \Bigg\} \\
&= \sum_{l'm'p'} \sum_{lmp} \sum_{\boldsymbol{G}'\boldsymbol{G}} \Bigg\{ \qquad\qquad\qquad\qquad\qquad\qquad\qquad\qquad\qquad\qquad\qquad\qquad\qquad\qquad\qquad (7.166\mathrm{g}) \\
&\quad \left(\boldsymbol{z}^{(1)}_{\boldsymbol{G}'}\left(\boldsymbol{k}^{+}_{\mathrm{bf}}, n; \beta\right) a^{\boldsymbol{G}'\boldsymbol{k}^{+}_{\mathrm{bf}}\alpha}_{l'm'p'} \right)^{*} \left\langle \vec{\varphi}^{\mathring{\alpha}}_{l'm'p'} \middle| \mathscr{H}^{(0)} - \epsilon^{(0)}_{\boldsymbol{k},n} \middle| \vec{\varphi}^{\mathring{\alpha}}_{lmp} \right\rangle_{\alpha} \mathrm{i}\boldsymbol{G}^{\top} z^{(0)}_{\boldsymbol{G}}(\boldsymbol{k},n) a^{\boldsymbol{G}\boldsymbol{k}\alpha}_{lmp} \\
&\quad + \left(\boldsymbol{z}^{(1)}_{\boldsymbol{G}'}\left(\boldsymbol{k}^{+}_{\mathrm{bf}}, n; \beta\right) a^{\boldsymbol{G}'\boldsymbol{k}^{+}_{\mathrm{bf}}\alpha}_{l'm'p'} \mathrm{i}[\boldsymbol{G}' + \boldsymbol{G}_{\mathrm{bf}} + \boldsymbol{q}]^{\top} \right)^{*} \left\langle \vec{\varphi}^{\mathring{\alpha}}_{l'm'p'} \middle| \mathscr{H}^{(0)} - \epsilon^{(0)}_{\boldsymbol{k},n} \middle| \vec{\varphi}^{\mathring{\alpha}}_{lmp} \right\rangle_{\alpha} z^{(0)}_{\boldsymbol{G}}(\boldsymbol{k},n) a^{\boldsymbol{G}\boldsymbol{k}\alpha}_{lmp} \\
&\quad \times \left(\mathrm{i}\boldsymbol{G}' z^{(0)}_{\boldsymbol{G}'}(\boldsymbol{k},n) a^{\boldsymbol{G}'\boldsymbol{k}\beta}_{l'm'p'} \right)^{*} \left\langle \vec{\varphi}^{\mathring{\beta}}_{l'm'p'} \middle| \mathscr{H}^{(0)} - \epsilon^{(0)}_{\boldsymbol{k},n} \middle| \vec{\varphi}^{\mathring{\beta}}_{lmp} \right\rangle_{\beta} \left[\boldsymbol{z}^{(1)}_{\boldsymbol{G}}\left(\boldsymbol{k}^{+}_{\mathrm{bf}}, n; \alpha\right)\right]^{\top} a^{\boldsymbol{G}\boldsymbol{k}^{+}_{\mathrm{bf}}\beta}_{lmp} \\
&\quad \times \left(z^{(0)}_{\boldsymbol{G}'}(\boldsymbol{k},n) a^{\boldsymbol{G}'\boldsymbol{k}\beta}_{l'm'p'} \right)^{*} \left\langle \vec{\varphi}^{\mathring{\beta}}_{l'm'p'} \middle| \mathscr{H}^{(0)} - \epsilon^{(0)}_{\boldsymbol{k},n} \middle| \vec{\varphi}^{\mathring{\beta}}_{lmp} \right\rangle_{\beta} \mathrm{i}[\boldsymbol{G} + \boldsymbol{q} + \boldsymbol{G}_{\mathrm{bf}}] \left[\boldsymbol{z}^{(1)}_{\boldsymbol{G}}\left(\boldsymbol{k}^{+}_{\mathrm{bf}}, n; \alpha\right)\right]^{\top} a^{\boldsymbol{G}\boldsymbol{k}^{+}_{\mathrm{bf}}\beta}_{lmp} \\
&\quad + \delta_{\beta\alpha} \left(z^{(0)}_{\boldsymbol{G}'}(\boldsymbol{k},n) a^{\boldsymbol{G}'\boldsymbol{k}\alpha}_{l'm'p'} \boldsymbol{G}' \right)^{*} \left\langle \vec{\varphi}^{\mathring{\alpha}}_{l'm'p'} \middle| \mathscr{H}^{(0)} - \epsilon^{(0)}_{\boldsymbol{k},n} \middle| \vec{\varphi}^{\mathring{\alpha}}_{lmp} \right\rangle_{\alpha} z^{(0)}_{\boldsymbol{G}}(\boldsymbol{k},n) a^{\boldsymbol{G}\boldsymbol{k}\alpha}_{lmp} \boldsymbol{G}^{\top} \\
&\quad + \delta_{\beta\alpha} z^{(0)}_{\boldsymbol{G}}(\boldsymbol{k},n) a^{\boldsymbol{G}\boldsymbol{k}\alpha}_{lmp} \boldsymbol{G} \left(z^{(0)}_{\boldsymbol{G}'}(\boldsymbol{k},n) a^{\boldsymbol{G}'\boldsymbol{k}\alpha}_{l'm'p'} \boldsymbol{G}' \right)^{\dagger} \left\langle \vec{\varphi}^{\mathring{\alpha}}_{l'm'p'} \middle| \mathscr{H}^{(0)} - \epsilon^{(0)}_{\boldsymbol{k},n} \middle| \vec{\varphi}^{\mathring{\alpha}}_{lmp} \right\rangle_{\alpha}
\end{aligned}
$$

$$
\begin{aligned}
&- \delta_{\beta\alpha}\left(z^{(0)}_{\boldsymbol{G}'}(\boldsymbol{k},n)a^{\boldsymbol{G}'\boldsymbol{k}\alpha}_{l'm'p'}\boldsymbol{G}'\boldsymbol{G}'^{\top}\right)^{*}\left\langle\vec{\varphi}^{\mathring{\alpha}}_{l'm'p'}\middle|\mathscr{H}^{(0)} - \epsilon^{(0)}_{\boldsymbol{k},n}\middle|\vec{\varphi}^{\mathring{\alpha}}_{lmp}\right\rangle_{\alpha} z^{(0)}_{\boldsymbol{G}}(\boldsymbol{k},n)a^{\boldsymbol{G}\boldsymbol{k}\alpha}_{lmp}\\
&- \delta_{\beta\alpha}\left(z^{(0)}_{\boldsymbol{G}'}(\boldsymbol{k},n)a^{\boldsymbol{G}'\boldsymbol{k}\alpha}_{l'm'p'}\right)^{*}\left\langle\vec{\varphi}^{\mathring{\alpha}}_{l'm'p'}\middle|\mathscr{H}^{(0)} - \epsilon^{(0)}_{\boldsymbol{k},n}\middle|\vec{\varphi}^{\mathring{\alpha}}_{lmp}\right\rangle_{\alpha} z^{(0)}_{\boldsymbol{G}}(\boldsymbol{k},n)a^{\boldsymbol{G}\boldsymbol{k}\alpha}_{lmp}\boldsymbol{G}\boldsymbol{G}^{\top}\Big\}
\end{aligned}
$$

results. These are almost the equations which are implemented at the moment. Relative to equations (7.128b), (7.128c), and (7.128d), the number of terms has significantly decreased.

Assistance received

This statement also remains true if the derivation would begin from the formalism in section 7.6.4, which I have initially programmed. In order to implement the reformulations of section 7.6.5 and section 7.6.6, I have essentially deactivated already programmed terms. However, since the optimizations described in section 7.6.7 again make many terms obsolete, we decided that Neukirchen summarizes my routines of equations (7.149) in order to simplify the source code [256]. His subroutine is used for the final dispersion relations in section 7.7.2.

Symmetric kinetic energy

Moreover, we decided that only the IR kinetic energy operator is transformed from a Laplacian form, acting on the right, into a symmetric form, acting on the left and right, for a better numerical stability [68, 127, 256] (cf. section 5.11). Assuming Kohn–Sham wave functions which are expanded in the LAPW basis, leads to an additional surface term, stemming from the integration by parts [68]:

$$
\begin{aligned}
&\int_{\Omega}\Psi^{*(0)}_{\boldsymbol{k},n}(\boldsymbol{r})\overset{\rightharpoonup}{\Delta}\Psi^{(0)}_{\boldsymbol{k},n}(\boldsymbol{r})\,\mathrm{d}V && (7.167\mathrm{a})\\
&\quad= \int_{\mathrm{IR}}\left(\boldsymbol{\nabla}\Psi^{\dagger(0)}_{\boldsymbol{k},n}(\boldsymbol{r})\right)\boldsymbol{\nabla}\Psi^{(0)}_{\boldsymbol{k},n}(\boldsymbol{r})\,\mathrm{d}V + \sum_{\gamma}\int_{\gamma}\Psi^{*(0)}_{\boldsymbol{k},n}(\boldsymbol{r})\overset{\rightharpoonup}{\Delta}\Psi^{(0)}_{\boldsymbol{k},n}(\boldsymbol{r})\,\mathrm{d}V\\
&\qquad+ \sum_{\gamma}\oint_{\gamma}\Psi^{*(0)}_{\boldsymbol{k},n}(\boldsymbol{r})\frac{\partial\Psi^{(0)}_{\boldsymbol{k},n}(\boldsymbol{r})}{\partial r}\hat{\boldsymbol{r}}\,\mathrm{d}S\\
&\quad= \int_{\mathrm{IR}}\left(\boldsymbol{\nabla}\Psi^{\dagger(0)}_{\boldsymbol{k},n}(\boldsymbol{r})\right)\boldsymbol{\nabla}\Psi^{(0)}_{\boldsymbol{k},n}(\boldsymbol{r})\,\mathrm{d}V + \sum_{\gamma}\int_{\gamma}\Psi^{*(0)}_{\boldsymbol{k},n}(\boldsymbol{r})\overset{\rightharpoonup}{\Delta}\Psi^{(0)}_{\boldsymbol{k},n}(\boldsymbol{r})\,\mathrm{d}V && (7.167\mathrm{b})\\
&\qquad+ \sum_{l'm'p'}\sum_{lmp}\sum_{\gamma}A^{*\boldsymbol{k}\gamma n}_{l'm'p'}A^{\boldsymbol{k}\gamma n}_{lmp}\sum_{s}u^{\gamma s}_{l'p'}(r_{\nu\mathring{\gamma}})\frac{\partial u^{\gamma s}_{lp}(r_{\nu\mathring{\gamma}})}{\partial r_{\nu\mathring{\gamma}}}\oint_{\gamma}\mathrm{Y}_{l'm'}\left(\hat{\boldsymbol{r}}_{\mathring{\gamma}}\right)\mathrm{Y}_{lm}\left(\hat{\boldsymbol{r}}_{\mathring{\gamma}}\right)\hat{\boldsymbol{r}}\,\mathrm{d}S\\
&\quad= \int_{\mathrm{IR}}\left(\boldsymbol{\nabla}\Psi^{\dagger(0)}_{\boldsymbol{k},n}(\boldsymbol{r})\right)\boldsymbol{\nabla}\Psi^{(0)}_{\boldsymbol{k},n}(\boldsymbol{r})\,\mathrm{d}V + \sum_{\gamma}\int_{\gamma}\Psi^{*(0)}_{\boldsymbol{k},n}(\boldsymbol{r})\overset{\rightharpoonup}{\Delta}\Psi^{(0)}_{\boldsymbol{k},n}(\boldsymbol{r})\,\mathrm{d}V && (7.167\mathrm{c})\\
&\qquad+ \sum_{lmp'p}\sum_{\gamma}A^{*\boldsymbol{k}\gamma n}_{lmp'}A^{\boldsymbol{k}\gamma n}_{lmp}\sum_{s}u^{\gamma s}_{l'p'}(r_{\nu\mathring{\gamma}})\frac{\partial u^{\gamma s}_{lp}(r_{\nu\mathring{\gamma}})}{\partial r_{\nu\mathring{\gamma}}}\,.
\end{aligned}
$$

Although equation (7.166g) only comprises MT terms, the symmetrization is assumed for the complete formalism. Therefore, Neukirchen has programmed the last term in equation (7.167c) into each line of equation (7.166g). This means for example

$$
\left\langle\vec{\varphi}^{\mathring{\alpha}}_{l'm'p'}\middle|\mathscr{H}^{(0)} - \epsilon^{(0)}_{\boldsymbol{k},n}\middle|\vec{\varphi}^{\mathring{\alpha}}_{lmp}\right\rangle_{\alpha} \rightarrow \left\langle\vec{\varphi}^{\mathring{\alpha}}_{l'm'p'}\middle|\mathscr{H}^{(0)} - \epsilon^{(0)}_{\boldsymbol{k},n}\middle|\vec{\varphi}^{\mathring{\alpha}}_{lmp}\right\rangle_{\alpha} + \sum_{s}u^{\alpha s}_{l'p'}\frac{\partial u^{\alpha s}_{lp}}{\partial r}\,. \qquad (7.168)
$$

Performance optimization

In particular for the formalism in section 7.6.4, it was absolutely necessary to only calculate the small matching coefficients a at both $\boldsymbol{k}$ and $\boldsymbol{k}^{+}_{\mathrm{bf}}$ with the recycled routine `Abcof3` once. Then the different large matching coefficients are constructed by respective contractions, instead of calculating all of them by employing the recycled routine `Abcof`, which has turned out to be a performance bottleneck [127, 251]. Although the formalism for the dynamical matrix is now drastically simplified, it is still programmed in the aforementioned way.

Further possible optimization

Equation (7.166g), including the kinetic energy correction (7.168), can further be summarized. Since the dynamical matrix is self-adjoint in the end, the third and fifth lines of the aforesaid equation can be replaced by their adjoint complement with α and β interchanged. Then they equal the second and the fourth lines, respectively (vice versa is also possible). But, this becomes relevant in the future for polyatomic systems.

Matrix large matching coefficients

Now, the matrix-like matching coefficients are introduced in order to achieve a compacter notation

$$\underline{A}^{\boldsymbol{k}\alpha n}_{lmp} = \sum_{G} \boldsymbol{G}\boldsymbol{G}^{\top} z^{(0)}_{\boldsymbol{G}}(\boldsymbol{k}, n) a^{\boldsymbol{G}\boldsymbol{k}\alpha}_{lmp} \tag{7.169a}$$

$$\underline{A}^{\boldsymbol{k}^{+}_{\text{bf}}\alpha n}_{l'm'p'}(\beta) = \sum_{\boldsymbol{G}} \boldsymbol{z}^{(1)}_{\boldsymbol{G}}\left(\boldsymbol{k}^{+}_{\text{bf}}, n; \beta\right)\left[\boldsymbol{G} + \boldsymbol{G}_{\text{bf}} + \boldsymbol{q}\right]^{\top} a^{\boldsymbol{G}\boldsymbol{k}^{+}_{\text{bf}}\alpha}_{lmp} \,. \tag{7.169b}$$

Additionally, the vectorial and scalar matching coefficients in equations (7.36e), (7.36d), (7.36a), and (5.30) are required.

Final form

As a consequence, equation (7.166g) in combination with the substitution (7.168) can be rewritten as

$$\begin{aligned}
\underline{D}^{\beta\alpha}_{\text{Pl,bk}}(\boldsymbol{q}) = \sum_{l'm'p'} \sum_{lmp} \Bigg\{ & \\
& \boldsymbol{A}^{\boldsymbol{k}^{+}_{\text{bf}}\alpha n *}_{l'm'p'}(\beta) \left(\left\langle \vec{\varphi}^{\mathring{\alpha}}_{l'm'p'} \middle| \mathscr{H}^{(0)} - \epsilon^{(0)}_{\boldsymbol{k},n} \middle| \vec{\varphi}^{\mathring{\alpha}}_{lmp} \right\rangle_{\alpha} + \sum_{s} u^{\gamma s}_{l'p'} \frac{\partial u^{\gamma s}_{lp}}{\partial r} \right) \mathrm{i} \left[\boldsymbol{A}^{\boldsymbol{k}\alpha n}_{lmp} \right]^{\top} \\
& + \mathrm{i}^{*} \underline{A}^{*\boldsymbol{k}^{+}_{\text{bf}}\alpha n}_{l'm'p'}(\beta) \left(\left\langle \vec{\varphi}^{\mathring{\alpha}}_{l'm'p'} \middle| \mathscr{H}^{(0)} - \epsilon^{(0)}_{\boldsymbol{k},n} \middle| \vec{\varphi}^{\mathring{\alpha}}_{lmp} \right\rangle_{\alpha} + \sum_{s} u^{\gamma s}_{l'p'} \frac{\partial u^{\gamma s}_{lp}}{\partial r} \right) A^{\boldsymbol{k}\alpha n}_{lmp} \\
& + \mathrm{i}^{*} \left[\boldsymbol{A}^{\boldsymbol{k}\beta n}_{l'm'p'} \right]^{\dagger} \left(\left\langle \vec{\varphi}^{\mathring{\alpha}}_{l'm'p'} \middle| \mathscr{H}^{(0)} - \epsilon^{(0)}_{\boldsymbol{k},n} \middle| \vec{\varphi}^{\mathring{\alpha}}_{lmp} \right\rangle_{\beta} + \sum_{s} u^{\gamma s}_{l'p'} \frac{\partial u^{\gamma s}_{lp}}{\partial r} \right) \boldsymbol{A}^{\boldsymbol{k}^{+}_{\text{bf}}\beta n}_{lmp}(\alpha) \\
& + A^{*\boldsymbol{k}\beta n}_{l'm'p'} \left(\left\langle \vec{\varphi}^{\mathring{\alpha}}_{l'm'p'} \middle| \mathscr{H}^{(0)} - \epsilon^{(0)}_{\boldsymbol{k},n} \middle| \vec{\varphi}^{\mathring{\alpha}}_{lmp} \right\rangle_{\beta} + \sum_{s} u^{\gamma s}_{l'p'} \frac{\partial u^{\gamma s}_{lp}}{\partial r} \right) \mathrm{i} \underline{A}^{\boldsymbol{k}^{+}_{\text{bf}}\beta n}_{lmp}(\alpha) \\
& + \delta_{\beta\alpha} \boldsymbol{A}^{*\boldsymbol{k}\alpha n}_{l'm'p'} \left(\left\langle \vec{\varphi}^{\mathring{\alpha}}_{l'm'p'} \middle| \mathscr{H}^{(0)} - \epsilon^{(0)}_{\boldsymbol{k},n} \middle| \vec{\varphi}^{\mathring{\alpha}}_{lmp} \right\rangle_{\alpha} + \sum_{s} u^{\gamma s}_{l'p'} \frac{\partial u^{\gamma s}_{lp}}{\partial r} \right) \boldsymbol{A}^{\top\boldsymbol{k}\alpha n}_{lmp} \\
& + \delta_{\beta\alpha} \boldsymbol{A}^{\boldsymbol{k}\alpha n}_{lmp} \left[\boldsymbol{A}^{\boldsymbol{k}\alpha n}_{l'm'p'} \right]^{\dagger} \left(\left\langle \vec{\varphi}^{\mathring{\alpha}}_{l'm'p'} \middle| \mathscr{H}^{(0)} - \epsilon^{(0)}_{\boldsymbol{k},n} \middle| \vec{\varphi}^{\mathring{\alpha}}_{lmp} \right\rangle_{\alpha} + \sum_{s} u^{\gamma s}_{l'p'} \frac{\partial u^{\gamma s}_{lp}}{\partial r} \right) \\
& - \delta_{\beta\alpha} \underline{A}^{*\boldsymbol{k}\alpha n}_{l'm'p'} \left(\left\langle \vec{\varphi}^{\mathring{\alpha}}_{l'm'p'} \middle| \mathscr{H}^{(0)} - \epsilon^{(0)}_{\boldsymbol{k},n} \middle| \vec{\varphi}^{\mathring{\alpha}}_{lmp} \right\rangle_{\alpha} + \sum_{s} u^{\gamma s}_{l'p'} \frac{\partial u^{\gamma s}_{lp}}{\partial r} \right) A^{\boldsymbol{k}\alpha n}_{lmp} \\
& - \delta_{\beta\alpha} A^{*\boldsymbol{k}\alpha n}_{lmp} \left(\left\langle \vec{\varphi}^{\mathring{\alpha}}_{l'm'p'} \middle| \mathscr{H}^{(0)} - \epsilon^{(0)}_{\boldsymbol{k},n} \middle| \vec{\varphi}^{\mathring{\alpha}}_{lmp} \right\rangle_{\alpha} + \sum_{s} u^{\gamma s}_{l'p'} \frac{\partial u^{\gamma s}_{lp}}{\partial r} \right) \underline{A}^{\boldsymbol{k}\alpha n}_{lmp} \Bigg\} \,.
\end{aligned} \tag{7.170}$$

This form is implemented at the moment [256].

Performance optimization

Before the various matching coefficients can be contracted with the parentheses in the middle, the Hamiltonian and overlap matrix elements must be set up. The former decomposes into a contribution with the spherical Hamiltonian and one containing the non-spherical potential. Since they are similar in equation (7.167c) (only differ by their atom indices), they are only calculated once before the loop over the $\boldsymbol{k}$-points and the bands n. As a consequence, within the aforementioned loops only dot products and matrix products are required for the contraction with the aforementioned contracted large matching coefficients. These operations are highly optimized on modern processor architectures, and therefore this implementation scales well with the size of the $\boldsymbol{k}$-set.

Algorithm of Hamiltonian part

Evaluating the spherical Hamiltonian matrix element is exactly described by equation (5.60). The non-spherical part is basically equivalent to equations (5.62), as far as the derivation of the formalism is concerned. However, we omit the definition of the integrals $\Sigma^{pp'\gamma}_{ll'l''m''}$ and the non-spherical $t^{\text{full},pp'\gamma}_{\eta(l'm'lm)}$ matrices in contrast to the Sternheimer equation [127, 251]. This is due to performance and the natural integration of LOs at a later point [251]. The routines which have been recycled for the Sternheimer self-consistency cycle use mapping arrays, and only iterate over relevant index combinations. Basically, we iterate over all indices, neglecting Gaunt coefficient selection rules. These rules were applied in earlier days to avoid evaluating integrals which vanish anyway. For todays processor architectures, it is highly disadvantageous to employ if-directives within inner loops, as they hinder the compiler from implementing vectorization pragmas or other optimizations. Meanwhile, this has been optimized in more modern versions of `FLEUR` [127, 260]. So, here the non-spherical potential matrix element is calculated by evaluating the integral

$$\begin{aligned}&\int_{\gamma} \mathrm{d}^3 r_{\nu\mathring{\gamma}} \sum_{s} \varphi^{*s\mathring{\gamma}}_{l'm'p'}(\boldsymbol{r}_{\nu\mathring{\gamma}}) V^{(0)\gamma}_{\text{eff,nsph}}(\boldsymbol{r}_{\nu\mathring{\gamma}}) \varphi^{s\mathring{\gamma}}_{lmp}(\boldsymbol{r}_{\nu\mathring{\gamma}}) \\ &= \int_{0^+}^{R_{\mathring{\gamma}}} \mathrm{d}r_{\nu\mathring{\gamma}} \sum_{s} r_{\nu\mathring{\gamma}} u^{s\mathring{\gamma}}_{l'p'}(r_{\nu\mathring{\gamma}}) \left(\sum_{l''m''} \left[V^{(0)\gamma}_{\text{eff,nsph}}(r_{\nu\mathring{\gamma}}) \right]_{l''m''} r_{\nu\mathring{\gamma}} u^{s\mathring{\gamma}}_{lp}(r_{\nu\mathring{\gamma}}) G^{m',m'',m}_{l',\ l'',\ l} \right) .\end{aligned} \tag{7.171}$$

Relative to equations (5.62), the effective potential is unsymmetrized. Therefore, it is given in spherical instead of lattice harmonics, as well as for every atom instead of every atom type. The term within the parentheses is evaluated first, before being projected onto the radial solution. Moreover, complex integrations are performed by separate integrals for the real and imaginary parts. This first becomes necessary here, because the overlap and the spherical Hamiltonian matrix elements are real quantities.

Algorithm of overlap part

The overlap integral, which must be multiplied by the Kohn–Sham energy, is already discussed in detail within equation (5.57). However, guided by the principle of optimally cancelling mutual errors (see section 7.1.2), we have decided to not completely follow the evaluation presented in equation (5.57). The reason is that the overlap $N^{\mathring{\gamma}}_{ll'}$ constitutes a byproduct of a differential equation solved in `FLEUR`. We found that this is in general not precisely the same as the result that is calculated from [251]

$$\int_{\mathring{\gamma}} \mathrm{d}^3 r_{\nu\mathring{\gamma}} \sum_{s} \varphi^{*s\mathring{\gamma}}_{l'm'p'}(\boldsymbol{r}_{\nu\mathring{\gamma}}) \varphi^{s\mathring{\gamma}}_{lmp}(\boldsymbol{r}_{\nu\mathring{\gamma}}) = \delta_{ll'} \delta_{mm'} \int_{0^+}^{R_{\mathring{\gamma}}} \mathrm{d}r_{\nu\mathring{\gamma}} \sum_{s} r_{\nu\mathring{\gamma}} u^{s\mathring{\gamma}}_{l'p'}(r_{\nu\mathring{\gamma}}) r_{\nu\mathring{\gamma}} u^{s\mathring{\gamma}}_{lp}(r_{\nu\mathring{\gamma}}) . \tag{7.172}$$

To be consistent, we calculate this integral instead of using the aforementioned $N^{\mathring{\gamma}}_{ll'}$.

Surface-Integrals Correction

Final form

For the final form of the surface integrals, the surface terms from equation (7.153a) and equation (7.159) are omitted in equation (7.150b). Furthermore, the gradient in the xc terms is applied, using the chain rule and the product rule. This results in

$$
\begin{aligned}
&\underline{D}^{\beta\alpha}_{\text{sfO}}(\boldsymbol{q}^{+}) \qquad\qquad (7.173\text{a})\\
&= \sum_{\boldsymbol{k},n} f^{(0)}_{\boldsymbol{k},n} \sum_{\boldsymbol{G}'\boldsymbol{G}} \Big\{ -\boldsymbol{z}^{*(1)}_{\boldsymbol{G}'}(\boldsymbol{k},n;\boldsymbol{q}\beta) z^{(0)}_{\boldsymbol{G}}(\boldsymbol{k},n) \oint_{\partial\alpha} \phi^{*(0)\text{IR}}_{\boldsymbol{k}+\boldsymbol{q},\boldsymbol{G}'}(\boldsymbol{r}) \Big(\mathscr{H}^{(0)} - \epsilon^{(0)}_{\boldsymbol{k},n}\Big) \phi^{(0)\text{IR}}_{\boldsymbol{k},\boldsymbol{G}}(\boldsymbol{r}) \hat{\boldsymbol{r}}^{\top} \,\mathrm{d}S \\
&\quad - \delta_{\beta\alpha} \Big(\mathrm{i}(\boldsymbol{k}+\boldsymbol{G}') z^{(0)}_{\boldsymbol{G}'}(\boldsymbol{k},n)\Big)^{*} z^{(0)}_{\boldsymbol{G}}(\boldsymbol{k},n) \oint_{\partial\alpha} \phi^{*(0)\text{IR}}_{\boldsymbol{k},\boldsymbol{G}'}(\boldsymbol{r}) \Big(\mathscr{H}^{(0)} - \epsilon^{(0)}_{\boldsymbol{k},n}\Big) \phi^{(0)\text{IR}}_{\boldsymbol{k},\boldsymbol{G}}(\boldsymbol{r}) \hat{\boldsymbol{r}}^{\top} \,\mathrm{d}S \\
&\quad - \oint_{\partial\beta} \hat{\boldsymbol{r}} \phi^{*(0)\text{IR}}_{\boldsymbol{k},\boldsymbol{G}'}(\boldsymbol{r}) \Big(\mathscr{H}^{(0)} - \epsilon^{(0)}_{\boldsymbol{k},n}\Big) \phi^{(0)\text{IR}}_{\boldsymbol{k}+\boldsymbol{q},\boldsymbol{G}}(\boldsymbol{r}) \,\mathrm{d}S\, z^{*(0)}_{\boldsymbol{G}'}(\boldsymbol{k},n) \Big[\boldsymbol{z}^{(1)}_{\boldsymbol{G}}(\boldsymbol{k},n;\boldsymbol{q}\alpha)\Big]^{\top} \\
&\quad - \oint_{\partial\beta} \hat{\boldsymbol{r}} \delta_{\beta\alpha} \phi^{*(0)\text{IR}}_{\boldsymbol{k},\boldsymbol{G}'}(\boldsymbol{r}) \Big(\mathscr{H}^{(0)} - \epsilon^{(0)}_{\boldsymbol{k},n}\Big) \Big(\phi^{(0)\text{IR}}_{\boldsymbol{k},\boldsymbol{G}}(\boldsymbol{r})\Big) \,\mathrm{d}S\, z^{*(0)}_{\boldsymbol{G}'}(\boldsymbol{k},n) \mathrm{i}[\boldsymbol{k}+\boldsymbol{G}]^{\top} z^{(0)}_{\boldsymbol{G}}(\boldsymbol{k},n) \Big\} \\
&+ \oint_{\partial\beta} \delta_{\beta\alpha} \hat{\boldsymbol{r}} \Big(\rho^{(0)}_{\beta} \Big(\boldsymbol{\nabla}^{\top} V^{(0)\beta}_{\text{eff}}(\boldsymbol{r})\Big) - \rho^{(0)}_{\text{IR}}(\boldsymbol{r}) \Big(\boldsymbol{\nabla}^{\top} V^{(0)\text{IR}}_{\text{eff}}(\boldsymbol{r})\Big)\Big) \,\mathrm{d}S \\
&+ \delta_{\beta\alpha} \oint_{\partial\beta} \Big[\Big(\boldsymbol{\nabla} \rho^{(0)}_{\beta}(\boldsymbol{r}) \Big(V^{(0)\beta}_{\text{xc}}(\boldsymbol{r}) - V^{(0)\beta}_{\text{xc}}(\boldsymbol{r})\Big)\Big) + \rho^{(0)}_{\beta} \boldsymbol{\nabla}^{\top} V^{(0)\beta}_{\text{xc}}(\boldsymbol{r}) \\
&\qquad\qquad - \boldsymbol{\nabla} \Big(\rho^{(0)}_{\text{IR}}(\boldsymbol{r}) \Big(\epsilon^{(0)\text{IR}}_{\text{xc}}(\boldsymbol{r}) - V^{(0)\text{IR}}_{\text{xc}}(\boldsymbol{r})\Big)\Big) - \rho^{(0)}_{\text{IR}} \boldsymbol{\nabla}^{\top} V^{(0)\text{IR}}_{\text{xc}}(\boldsymbol{r}) \Big] \hat{\boldsymbol{r}}^{\top} \,\mathrm{d}S \\
&+ \delta_{\beta\alpha} \oint_{\partial\beta} \hat{\boldsymbol{r}} \Big[\rho^{(0)}_{\beta}(\boldsymbol{r}) \Big(2\Big[\boldsymbol{V}^{(1)\beta}_{\text{ext}}(\boldsymbol{r};\boldsymbol{q}^{+}\alpha)\Big]^{\top} + \Big[\boldsymbol{V}^{(1)\beta}_{\text{Har}}(\boldsymbol{r};\boldsymbol{q}^{+}\alpha)\Big]^{\top}\Big) \\
&\qquad\qquad - \rho^{(0)}_{\text{IR}}(\boldsymbol{r}) \Big(2\Big[\boldsymbol{V}^{(1)\text{IR}}_{\text{ext}}(\boldsymbol{r};\boldsymbol{q}^{+}\alpha)\Big]^{\top} + \Big[\boldsymbol{V}^{(1)\text{IR}}_{\text{Har}}(\boldsymbol{r};\boldsymbol{q}^{+}\alpha)\Big]^{\top}\Big) \Big] \,\mathrm{d}S \\
&+ \sum_{\boldsymbol{k},n} f^{(0)}_{\boldsymbol{k},n} \sum_{\boldsymbol{G}'\boldsymbol{G}} \Big\{ \boldsymbol{z}^{*(1)}_{\boldsymbol{G}'}(\boldsymbol{k},n;\boldsymbol{q}\beta) z^{(0)}_{\boldsymbol{G}}(\boldsymbol{k},n) \oint_{\partial\alpha} \phi^{*(0)\text{IR}}_{\boldsymbol{k}+\boldsymbol{q},\boldsymbol{G}'}(\boldsymbol{r}) \mathscr{V}^{(0)}_{\text{eff}} \phi^{(0)\text{IR}}_{\boldsymbol{k},\boldsymbol{G}}(\boldsymbol{r}) \hat{\boldsymbol{r}}^{\top} \,\mathrm{d}S \\
&\quad + \delta_{\beta\alpha} \Big(\mathrm{i}(\boldsymbol{k}+\boldsymbol{G}') z^{(0)}_{\boldsymbol{G}'}(\boldsymbol{k},n)\Big)^{*} z^{(0)}_{\boldsymbol{G}}(\boldsymbol{k},n) \oint_{\partial\alpha} \phi^{*(0)\text{IR}}_{\boldsymbol{k},\boldsymbol{G}'}(\boldsymbol{r}) \mathscr{V}^{(0)}_{\text{eff}} \phi^{(0)\text{IR}}_{\boldsymbol{k},\boldsymbol{G}}(\boldsymbol{r}) \hat{\boldsymbol{r}}^{\top} \,\mathrm{d}S \\
&\quad + \oint_{\partial\beta} \hat{\boldsymbol{r}} \phi^{*(0)\text{IR}}_{\boldsymbol{k},\boldsymbol{G}'}(\boldsymbol{r}) \mathscr{V}^{(0)}_{\text{eff}} \phi^{(0)\text{IR}}_{\boldsymbol{k}+\boldsymbol{q},\boldsymbol{G}}(\boldsymbol{r}) \,\mathrm{d}S\, z^{*(0)}_{\boldsymbol{G}'}(\boldsymbol{k},n) \Big[\boldsymbol{z}^{(1)}_{\boldsymbol{G}}(\boldsymbol{k},n;\boldsymbol{q}\alpha)\Big]^{\top} \\
&\quad + \oint_{\partial\beta} \hat{\boldsymbol{r}} \delta_{\beta\alpha} \phi^{*(0)\text{IR}}_{\boldsymbol{k},\boldsymbol{G}'}(\boldsymbol{r}) \mathscr{V}^{(0)}_{\text{eff}} \Big(\phi^{(0)\text{IR}}_{\boldsymbol{k},\boldsymbol{G}}(\boldsymbol{r})\Big) \,\mathrm{d}S\, z^{*(0)}_{\boldsymbol{G}'}(\boldsymbol{k},n) \mathrm{i}[\boldsymbol{k}+\boldsymbol{G}]^{\top} z^{(0)}_{\boldsymbol{G}}(\boldsymbol{k},n) \\
&\quad - \boldsymbol{z}^{*(1)}_{\boldsymbol{G}'}(\boldsymbol{k},n;\boldsymbol{q}\beta) z^{(0)}_{\boldsymbol{G}}(\boldsymbol{k},n) \oint_{\partial\alpha} \phi^{*(0)\alpha}_{\boldsymbol{k}+\boldsymbol{q},\boldsymbol{G}'}(\boldsymbol{r}) \mathscr{V}^{(0)}_{\text{eff}} \phi^{(0)\alpha}_{\boldsymbol{k},\boldsymbol{G}}(\boldsymbol{r}) \hat{\boldsymbol{r}}^{\top} \,\mathrm{d}S \\
&\quad - \delta_{\beta\alpha} \Big(\mathrm{i}(\boldsymbol{k}+\boldsymbol{G}') z^{(0)}_{\boldsymbol{G}'}(\boldsymbol{k},n)\Big)^{*} z^{(0)}_{\boldsymbol{G}}(\boldsymbol{k},n) \oint_{\partial\alpha} \phi^{*(0)\alpha}_{\boldsymbol{k},\boldsymbol{G}'}(\boldsymbol{r}) \mathscr{V}^{(0)}_{\text{eff}} \phi^{(0)\alpha}_{\boldsymbol{k},\boldsymbol{G}}(\boldsymbol{r}) \hat{\boldsymbol{r}}^{\top} \,\mathrm{d}S \\
&\quad - \oint_{\partial\beta} \hat{\boldsymbol{r}} \phi^{*(0)\beta}_{\boldsymbol{k},\boldsymbol{G}'}(\boldsymbol{r}) \mathscr{V}^{(0)}_{\text{eff}} \phi^{(0)\beta}_{\boldsymbol{k}+\boldsymbol{q},\boldsymbol{G}}(\boldsymbol{r}) \,\mathrm{d}S\, z^{*(0)}_{\boldsymbol{G}'}(\boldsymbol{k},n) \Big[\boldsymbol{z}^{(1)}_{\boldsymbol{G}}(\boldsymbol{k},n;\boldsymbol{q}\alpha)\Big]^{\top} \\
&\quad - \oint_{\partial\beta} \hat{\boldsymbol{r}} \delta_{\beta\alpha} \phi^{*(0)\beta}_{\boldsymbol{k},\boldsymbol{G}'}(\boldsymbol{r}) \mathscr{V}^{(0)}_{\text{eff}} \Big(\phi^{(0)\beta}_{\boldsymbol{k},\boldsymbol{G}}(\boldsymbol{r})\Big) \,\mathrm{d}S\, z^{*(0)}_{\boldsymbol{G}'}(\boldsymbol{k},n) \mathrm{i}[\boldsymbol{k}+\boldsymbol{G}]^{\top} z^{(0)}_{\boldsymbol{G}}(\boldsymbol{k},n) \Big\} .
\end{aligned}
$$

Additionally, in the last eight lines an “effective zero” is added, since these surface integrals only contain almost continuous quantities, such as the unperturbed effective potential and the LAPW basis functions [251]. Therefore, the sum of these surface terms is very small. Overall, the preceeding equations simplify to

$$
\begin{aligned}
&\underline{D}^{\beta\alpha}_{\text{sfO}}(\boldsymbol{q}^{+}) \qquad\qquad (7.173\text{b})\\
&= \sum_{\boldsymbol{k},n} 2 f^{(0)}_{\boldsymbol{k},n} \sum_{\boldsymbol{G}'\boldsymbol{G}} \Bigg\{ -\boldsymbol{z}^{*(1)}_{\boldsymbol{G}'}\Big(\boldsymbol{k}^{+}_{\text{bf}}, n; \beta\Big) z^{(0)}_{\boldsymbol{G}}(\boldsymbol{k}, n) \oint_{\partial\alpha} \phi^{*(0)\text{IR}}_{\boldsymbol{k}^{+}_{\text{bf}},\boldsymbol{G}'}(\boldsymbol{r}) \Big(\overset{\rightleftharpoons}{\mathscr{T}} - \epsilon^{(0)}_{\boldsymbol{k},n}\Big) \phi^{(0)\text{IR}}_{\boldsymbol{k},\boldsymbol{G}}(\boldsymbol{r}) \hat{\boldsymbol{r}}^{\top} \,\mathrm{d}S \\
&\qquad - \delta_{\beta\alpha} \Big(\mathrm{i}(\boldsymbol{k} + \boldsymbol{G}') z^{(0)}_{\boldsymbol{G}'}(\boldsymbol{k}, n)\Big)^{*} z^{(0)}_{\boldsymbol{G}}(\boldsymbol{k}, n) \oint_{\partial\alpha} \phi^{*(0)\text{IR}}_{\boldsymbol{k},\boldsymbol{G}'}(\boldsymbol{r}) \Big(\overset{\rightleftharpoons}{\mathscr{T}} - \epsilon^{(0)}_{\boldsymbol{k},n}\Big) \phi^{(0)\text{IR}}_{\boldsymbol{k},\boldsymbol{G}}(\boldsymbol{r}) \hat{\boldsymbol{r}}^{\top} \,\mathrm{d}S \\
&\qquad - \oint_{\partial\beta} \hat{\boldsymbol{r}} \phi^{*(0)\text{IR}}_{\boldsymbol{k},\boldsymbol{G}'}(\boldsymbol{r}) \Big(\overset{\rightleftharpoons}{\mathscr{T}} - \epsilon^{(0)}_{\boldsymbol{k},n}\Big) \phi^{(0)\text{IR}}_{\boldsymbol{k}^{+}_{\text{bf}},\boldsymbol{G}}(\boldsymbol{r}) \,\mathrm{d}S\, z^{*(0)}_{\boldsymbol{G}'}(\boldsymbol{k}, n) \Big[\boldsymbol{z}^{(1)}_{\boldsymbol{G}}\Big(\boldsymbol{k}^{+}_{\text{bf}}, n; \alpha\Big)\Big]^{\top} \\
&\qquad - \oint_{\partial\beta} \hat{\boldsymbol{r}} \delta_{\beta\alpha} \phi^{*(0)\text{IR}}_{\boldsymbol{k},\boldsymbol{G}'}(\boldsymbol{r}) \Big(\overset{\rightleftharpoons}{\mathscr{T}} - \epsilon^{(0)}_{\boldsymbol{k},n}\Big) \Big(\phi^{(0)\text{IR}}_{\boldsymbol{k},\boldsymbol{G}}(\boldsymbol{r})\Big) \,\mathrm{d}S\, z^{*(0)}_{\boldsymbol{G}'}(\boldsymbol{k}, n) \mathrm{i}[\boldsymbol{k} + \boldsymbol{G}]^{\top} z^{(0)}_{\boldsymbol{G}}(\boldsymbol{k}, n) \Bigg\} \\
&\quad - \oint_{\alpha} \boldsymbol{\rho}^{*(1)}_{\alpha,\text{Sh}}(\boldsymbol{r}; \boldsymbol{q}^{+}\beta) V^{(0)\alpha}_{\text{eff}}(\boldsymbol{r}) \hat{\boldsymbol{r}}^{\top} \,\mathrm{d}S \\
&\quad + \oint_{\partial\beta} \hat{\boldsymbol{r}} \Big[\rho^{(0)}_{\beta}(\boldsymbol{r}) \Big(\Big[\boldsymbol{V}^{(1)\beta}_{\text{C}}(\boldsymbol{r}; \boldsymbol{q}^{+}\alpha) + \delta_{\beta\alpha} \boldsymbol{\nabla} V^{(0)\beta}_{\text{C}}(\boldsymbol{r})\Big]^{\top} + \Big[\boldsymbol{V}^{(1)\beta}_{\text{ext}}(\boldsymbol{r}; \boldsymbol{q}^{+}\alpha)\Big]^{\top}\Big) \\
&\qquad\qquad - \rho^{(0)}_{\text{IR}}(\boldsymbol{r}) \Big(\Big[\boldsymbol{V}^{(1)\text{IR}}_{\text{C}}(\boldsymbol{r}; \boldsymbol{q}^{+}\alpha) + \delta_{\beta\alpha} \boldsymbol{\nabla} V^{(0)\text{IR}}_{\text{C}}(\boldsymbol{r})\Big]^{\top} + \Big[\boldsymbol{V}^{(1)\text{IR}}_{\text{ext}}(\boldsymbol{r}; \boldsymbol{q}^{+}\alpha)\Big]^{\top}\Big)\Big] \,\mathrm{d}S\ .
\end{aligned}
$$

Assistance and algorithm

The sixth line has been programmed by Neukirchen. Likewise, he substituted the Hamiltonians by the kinetic energy $\mathscr{T}$ within `juPhon`. While the evaluation of the last three lines is analogous to equations (7.163b) and (7.164c), the terms containing the kinetic energy operator must still be discussed. As the symmetric application of the IR kinetic energy is already prepared in equation (7.170), it can be applied to the surface integrals. Doing this, the phonon vector is also accounted for in the action of the kinetic energy. Therefore, the second line in equation (7.173b) is evaluated as

$$
\begin{aligned}
&\sum_{\boldsymbol{G}'\boldsymbol{G}} \boldsymbol{z}^{*(1)}_{\boldsymbol{G}'}\Big(\boldsymbol{k}^{+}_{\text{bf}}, n; \beta\Big) z^{(0)}_{\boldsymbol{G}}(\boldsymbol{k}, n) \oint_{\partial\alpha} \phi^{*(0)\text{IR}}_{\boldsymbol{k}^{+}_{\text{bf}},\boldsymbol{G}'}(\boldsymbol{r}) \Big(\overset{\rightleftharpoons}{\mathscr{T}} - \epsilon^{(0)}_{\boldsymbol{k},n}\Big) \phi^{(0)\text{IR}}_{\boldsymbol{k},\boldsymbol{G}}(\boldsymbol{r}) \hat{\boldsymbol{r}}^{\top} \,\mathrm{d}S \qquad (7.174)\\
&= \mathrm{i}\frac{4\pi R^{2}_{\mathring{\alpha}}}{\mathit{\Omega}} \sum_{\boldsymbol{G}'\boldsymbol{G}} \boldsymbol{z}^{*(1)}_{\boldsymbol{G}'}\Big(\boldsymbol{k}^{+}_{\text{bf}}, n; \beta\Big) z^{(0)}_{\boldsymbol{G}}(\boldsymbol{k}, n) \Big(\frac{1}{2}\Big(\boldsymbol{k}^{+}_{\text{bf}} + \boldsymbol{G}'\Big) \cdot (\boldsymbol{k} + \boldsymbol{G}) - \epsilon^{(0)}_{\boldsymbol{k},n}\Big) \mathrm{j}_{1}\Big(\big|\boldsymbol{G}'' - \boldsymbol{G}_{\text{bf}} - \boldsymbol{q}\big| R_{\mathring{\alpha}}\Big) \\
&\qquad\qquad \times \mathrm{e}^{\mathrm{i}\left(\boldsymbol{G}'' - \boldsymbol{G}_{\text{bf}} - \boldsymbol{q}\right)\cdot\boldsymbol{\tau}_{\alpha}} \sum_{im} \zeta^{*}_{i,m} \hat{\boldsymbol{e}}^{\top}_{i} \mathrm{Y}^{*}_{1m}\Big(\widehat{\boldsymbol{G}'' - \boldsymbol{G}_{\text{bf}} - \boldsymbol{q}}\Big)\ ,
\end{aligned}
$$

with $\boldsymbol{G}'' := \boldsymbol{G} - \boldsymbol{G}'$ and $\boldsymbol{G}_{\text{bf}}$ (cf. figure 7.2 for the latter), the third line as

$$
\begin{aligned}
&\sum_{\boldsymbol{G}'\boldsymbol{G}} \Big(\mathrm{i}(\boldsymbol{k} + \boldsymbol{G}') z^{(0)}_{\boldsymbol{G}'}(\boldsymbol{k}, n)\Big)^{*} z^{(0)}_{\boldsymbol{G}}(\boldsymbol{k}, n) \oint_{\partial\alpha} \phi^{*(0)\text{IR}}_{\boldsymbol{k},\boldsymbol{G}'}(\boldsymbol{r}) \Big(\overset{\rightleftharpoons}{\mathscr{T}} - \epsilon^{(0)}_{\boldsymbol{k},n}\Big) \phi^{(0)\text{IR}}_{\boldsymbol{k},\boldsymbol{G}}(\boldsymbol{r}) \hat{\boldsymbol{r}}^{\top} \,\mathrm{d}S \qquad (7.175)\\
&= \mathrm{i}\frac{4\pi R^{2}_{\mathring{\alpha}}}{\mathit{\Omega}} \sum_{\boldsymbol{G}'\boldsymbol{G}} \Big(\mathrm{i}(\boldsymbol{k} + \boldsymbol{G}') z^{(0)}_{\boldsymbol{G}'}(\boldsymbol{k}, n)\Big)^{*} z^{(0)}_{\boldsymbol{G}}(\boldsymbol{k}, n) \left(\frac{(\boldsymbol{k} + \boldsymbol{G}') \cdot (\boldsymbol{k} + \boldsymbol{G})}{2} - \epsilon^{(0)}_{\boldsymbol{k},n}\right) \mathrm{j}_{1}\Big(\big|\boldsymbol{G}''\big| R_{\mathring{\alpha}}\Big) \\
&\qquad\qquad \times \mathrm{e}^{\mathrm{i}\boldsymbol{G}''\cdot\boldsymbol{\tau}_{\alpha}} \sum_{im} \zeta^{*}_{i,m} \hat{\boldsymbol{e}}^{\top}_{i} \mathrm{Y}^{*}_{1m}\Big(\hat{\boldsymbol{G}}''\Big)\ ,
\end{aligned}
$$

the fourth line as

$$\begin{aligned}&\sum_{\boldsymbol{G}'\boldsymbol{G}}\oint_{\partial\beta}\hat{\boldsymbol{r}}\phi^{*(0)\mathrm{IR}}_{\boldsymbol{k},\boldsymbol{G}'}(\boldsymbol{r})\left(\overset{\rightleftharpoons}{\mathscr{T}}-\epsilon^{(0)}_{\boldsymbol{k},n}\right)\phi^{(0)\mathrm{IR}}_{\boldsymbol{k}^+_{\mathrm{bf}},\boldsymbol{G}}(\boldsymbol{r})\,\mathrm{d}S\,z^{*(0)}_{\boldsymbol{G}'}(\boldsymbol{k},n)\left[\boldsymbol{z}^{(1)}_{\boldsymbol{G}}\left(\boldsymbol{k}^+_{\mathrm{bf}},n;\alpha\right)\right]^\top \\ &=\mathrm{i}\frac{4\pi R^2_{\mathring{\alpha}}}{\Omega}\sum_{\boldsymbol{G}'\boldsymbol{G}}\left(\frac{(\boldsymbol{k}+\boldsymbol{G}')\cdot\left(\boldsymbol{k}^+_{\mathrm{bf}}+\boldsymbol{G}\right)}{2}-\epsilon^{(0)}_{\boldsymbol{k},n}\right)\sum_{im}\zeta^*_{i,m}\hat{\boldsymbol{e}}^\top_i\mathrm{j}_1\left(\left|\boldsymbol{G}''+\boldsymbol{G}_{\mathrm{bf}}+\boldsymbol{q}\right|R_{\mathring{\alpha}}\right) \\ &\qquad\times\mathrm{e}^{\mathrm{i}\left(\boldsymbol{G}''+\boldsymbol{G}_{\mathrm{bf}}+\boldsymbol{q}\right)\cdot\boldsymbol{\tau}_\alpha}\mathrm{Y}^*_{1m}\left(\widehat{\boldsymbol{G}''+\boldsymbol{G}_{\mathrm{bf}}+\boldsymbol{q}}\right)z^{*(0)}_{\boldsymbol{G}'}(\boldsymbol{k},n)\left[\boldsymbol{z}^{(1)}_{\boldsymbol{G}}\left(\boldsymbol{k}^+_{\mathrm{bf}},n;\alpha\right)\right]^\top ,\end{aligned} \tag{7.176}$$

and the fifth line as

$$\begin{aligned}&\sum_{\boldsymbol{G}'\boldsymbol{G}}\oint_{\partial\beta}\hat{\boldsymbol{r}}\delta_{\beta\alpha}\phi^{*(0)\mathrm{IR}}_{\boldsymbol{k},\boldsymbol{G}'}(\boldsymbol{r})\left(\overset{\rightleftharpoons}{\mathscr{T}}-\epsilon^{(0)}_{\boldsymbol{k},n}\right)\left(\phi^{(0)\mathrm{IR}}_{\boldsymbol{k},\boldsymbol{G}}(\boldsymbol{r})\right)\mathrm{d}S\,z^{*(0)}_{\boldsymbol{G}'}(\boldsymbol{k},n)\mathrm{i}[\boldsymbol{k}+\boldsymbol{G}]^\top z^{(0)}_{\boldsymbol{G}}(\boldsymbol{k},n) \\ &=\mathrm{i}\frac{4\pi R^2_{\mathring{\alpha}}}{\Omega}\sum_{\boldsymbol{G}'\boldsymbol{G}}\left(\frac{(\boldsymbol{k}+\boldsymbol{G}')\cdot(\boldsymbol{k}+\boldsymbol{G})}{2}-\epsilon^{(0)}_{\boldsymbol{k},n}\right)\mathrm{j}_1\left(\left|\boldsymbol{G}''\right|R_{\mathring{\alpha}}\right)\sum_{im}\zeta^*_{i,m}\hat{\boldsymbol{e}}^\top_i \\ &\qquad\times\mathrm{e}^{\mathrm{i}\boldsymbol{G}''\cdot\boldsymbol{\tau}_\alpha}\mathrm{Y}^*_{1m}\left(\hat{\boldsymbol{G}}''\right)z^{*(0)}_{\boldsymbol{G}'}(\boldsymbol{k},n)\mathrm{i}[\boldsymbol{k}+\boldsymbol{G}]^\top z^{(0)}_{\boldsymbol{G}}(\boldsymbol{k},n)\,.\end{aligned} \tag{7.177}$$

7.6.9 Tests

Test 33 and test 34 focus on the step function, which is vital for the evaluation of the IR integrals. Furthermore, the volume integrals (IR and MT spheres) can be checked analogous to test 22. Test 35 and test 36 deal with the Pulay matrix elements. Finally, test 37, test 38, and test 39 are concerned with the surface integrals.

Test 33: Converged Parameter for Interstitial Step Function

The integrity of the warping process and the quality of basis parameters such as G_{max} can be tested by comparing the results of a FFT and a "double-sum method" [127, 251]. For example, in the integral

$$\int_\Omega\rho^{(0)}_{\mathrm{IR}}(\boldsymbol{G})V^{(0)}_{\mathrm{eff}}(\boldsymbol{G})\,\mathrm{d}^3r=\sum_{\boldsymbol{G}'\boldsymbol{G}}\rho^{(0)}_{\mathrm{IR}}(\boldsymbol{G}')V^{(0)}_{\mathrm{eff}}(\boldsymbol{G})\int\mathrm{e}^{-\mathrm{i}(\boldsymbol{G}'-\boldsymbol{G})\cdot\boldsymbol{r}}\Theta(\boldsymbol{r})\,\mathrm{d}^3r \tag{7.178a}$$

$$=\Omega\sum_{\boldsymbol{G}'\boldsymbol{G}}\rho^{(0)}_{\mathrm{IR}}(\boldsymbol{G}')V^{(0)}_{\mathrm{eff}}(\boldsymbol{G})\Theta(\boldsymbol{G}'-\boldsymbol{G})\,\mathrm{d}^3r\ , \tag{7.178b}$$

the sums over the reciprocal lattice vectors $\boldsymbol{G}$ and $\boldsymbol{G}'$ can be evaluated. The Fourier coefficients of the step function coefficients are given in equation (5.48b). Alternatively, the effective potential can be warped, and the result summed with the charge density as in equation (7.161b).

Test 34: Converged Parameter for Convolution of Potential and Step Function

We defined one criterion for the FFT mesh so that it is large enough [127]. Within `FLEUR`, the IR effective potential expanded in stars is convoluted with the step function, exploiting the underlying symmetry. Therefore, errors of the FFT cancel each other and the warping is not so sensitive with respect to aliasing effects [127, 278]. The unwarped potential is stored in a file, and so is the warped potential (the latest names can be extracted from the documentation). Within this check, the effective unwarped potential is taken from this `FLEUR` file and translated from the star into the plane-wave representation. Then it is warped with the `juPhon` routine that has been written for unsymmetrized quantities. Its output is compared with the warped effective IR potential from `FLEUR`, which has been parsed from the respective file and translated into the plane-wave representation. The parameters `k1d`, `k2d`, and `k3d` must be large enough for this test to work. Organically, this is achieved by increasing G_{max}.

Test 35: Cross-checking the MT Hamiltonian and Overlap Matrix Element

The approaches to calculate the integral in equation (5.56), the expression (5.60b), and equation (7.171) either for the Sternheimer equation or the dynamical matrix are different. For the Sternheimer equation mainly subroutines from `FLEUR` are recycled. But for the dynamical matrix, I have programmed a more modular and versatile algorithm for satisfying the implementation demands of the dynamical matrix. Details of both methods can be found in section 7.4.3 and section 7.6.8. With these approaches, a matrix element as given in equation (5.53) is calculated. This check compares the results of both methods, which should be the same. In the future, only one Hamiltonian and overlap subroutine will be employed, making this test obsolete.

Test 36: Adding the IR part to the MT Hamiltonian and Overlap Matrix Element

As a supplement to test 35 an IR matrix element as in equation (5.49) can be added. The result of this sum should be zero to fulfill the Schrödinger equation of the Kohn–Sham Hamiltonian.

Test 37: Cross-Checking with Sternheimer Surface Integral

Two algorithms are employed in `juPhon` to calculate the surface integrals, which are of the form given in section 7.4.4. However, for the dynamical matrix the bands are equal (see section 7.6.8). So in the first implementation, I have written a simplified surface integral subroutine to avoid errors. Still, the general and the specified subroutine should deliver the same result, which is checked here. In the future, these two approaches will be unified.

Test 38: Cross-Checking of Surface Integrals with Almost Continuous Integrands

If the integrand is composed of quantities which are almost continuous, an IR surface integral should be almost the same as minus the MT sphere integral. The difference of them should be not significantly larger than the continuity of the quantities in the integrands. This check is not programmed in an separate subroutine, but intrinsically given by evaluating the last two lines of equation (7.173b).

Test 39: Analytical Goldstone Solution for Correction Terms

The second, third, fourth, and fifth lines in equation (7.166g) as well as the second, third, fourth, and fifth lines in equation (7.173b) are already checked by test 33, and test 34. However, the correct implementation of the wave-function expansion-coefficient contraction can also be tested by setting the first-order variation of the wave-function expansion coefficients to equation (7.30).

7.7 Phonon Dispersions

Outline

Although the formalism of Klüppelberg [88] is mainly correct, its dynamical-matrix part still comprises many terms that cancel each other analytically but *not* numerically. In this section, the impressive evolution of the phonon dispersions shall be shown, while reformulating his approach. Therefore, in section 7.7.1 examples for fcc Ne and fcc Al are given, essentially based on the equations until (i) section 7.6.4 and (ii) section 7.6.5. The latest phonon dispersions according to the approach in section 7.6.8 are finally presented in section 7.7.2. In addition to fcc Ne and fcc Al, the materials bcc Mo, fcc Au, fcc Ar, and fcc Cu are discussed there.

Calculation setups

Within all dispersion relations, my DFPT calculations from `juPhon` are compared to FD benchmarks generated by Alexander Neukirchen. Since I generated the DFPT results employing the nowadays crude $\mathrm{X}\alpha$ xc-potential approximation, contrasting these frequencies with experimental outcomes would be less informative. But, selecting the FD method as the benchmark enables me to start with the same input parameters and allows for basing both the FD and the DFPT approach upon the input data from the `FLEUR` code. The `juPhon` results are the acoustic modes of fourteen $\boldsymbol{q}$-values, which are incorporated in an $8 \times 8 \times 8$ Γ-centered discrete $\boldsymbol{q}$-mesh. These $\boldsymbol{q}$-vectors lie on characteristic high-symmetry points of fcc and bcc structures (see also table 7.8 for their definition) or on paths between them. I use the `FLEUR` version specified on page 112 to optimize the lattice constant of all discussed systems by a Birch–Murnaghan fit (see section 7.1.6). Overall, (i) for the aforementioned fit, (ii) for generating the input data for `juPhon`, and (iii) for the `juPhon` calculation itself, I employ an $8 \times 8 \times 8$ Γ-centered discrete $\boldsymbol{k}$-mesh. Furthermore, mainly I have converged the remaining input parameters for the fcc Ne and for the fcc Al systems. The parameters (except for the lattice constants) of bcc Mo, fcc Ar, and fcc Cu have been optimized by Neukirchen. Furthermore, he improved some nuances in the fcc Ne and fcc Al input parameters. All employed `FLEUR` input-generator input files can be found in appendix B. As far as the FD computations are concerned, Neukirchen employs `phonopy` [164] (version 2.9.3), which utilizes the output of a more modern `FLEUR`[30] code, still based on the aforementioned input-generator input files. It is important to know that in the aforesaid modern `FLEUR` version, the variable storing the constant for the speed of light is analogously increased by three orders of magnitude (cf. section 7.1.4). Additionally, it has proven sufficient to use only a $4 \times 4 \times 4$ Γ-centered discrete $\boldsymbol{k}$-mesh for the FD calculations [256]. The FD frequencies are interpolated and depicted as curves in the following dispersion relations. Furthermore, it must be considered

---

[30] This employed version can be found using the hash `0253eee4277e8dcd39a6940032373ba78f418441` within the `FLEUR` repository.

that `phonopy` corrects the frequencies in the end so that its Goldstone modes always vanish. Essentially, all frequencies are plotted in the unit cm^{-1} ($1\,\mathrm{cm}^{-1} \approx 0.124\,\mathrm{meV}$ [8]).

7.7.1 Evolution

Results after section 7.6.4

Rewriting the original dynamical-matrix approach of Klüppelberg [88] makes an impressive impact on the phonon dispersion-relations. Since it has turned out very early in the development that outer products of gradients are numerically hard or impossible to control, we decided against generating dispersion relations with this formalism [127]. However, I have calculated[31] the first dispersion relations for the approach explained in section 7.6.4. They are shown in figure 7.22 and figure 7.23 for fcc Ne and fcc Al, respectively. In general, it can be seen that the benchmark frequencies clearly differ from those calculated with `juPhon`. Still, it must be emphasized that the Goldstone condition (frequencies vanish) for Ne is already excellently fulfilled. The eigenvalues of the dynamical matrix from `juPhon` are at the order of magnitude 10^{-6} which is one order more than possible with the accuracy of the integration routines. Hence, it is in principle numerically zero, as expected for the Goldstone modes. However, for Al this is not the case. The frequencies at $\boldsymbol{q} = \mathbf{0}$ are imaginary and about $4.8\,\mathrm{meV}$. But, the degeneracy and splitting of the transversal modes (red and green) can already be seen for both systems. Nevertheless, for Ne the longitudinal mode (blue) is not as smooth as the transversal modes. Moreover, all `juPhon` frequencies for this system are imaginary, predicting material instabilities for every phonon vector. In contrast, some of the frequencies for Al are positive and from Γ to L the transversal modes are more consistent with the benchmark. Finally, the longitudinal mode is smoother relative to Ne.

Results after section 7.6.5

Avoiding also gradients of wave functions, as explained in section 7.6.5 leads to the phonon dispersions of Ne and Al in figure 7.24 and figure 7.25, respectively[32]. The transversal modes are now completely real (except for the Goldstone modes), whereas the longitudinal modes are still partially imaginary. Given Ne, the former match already perfectly with the benchmark on the path Γ to X, whereas the transversal modes of Al are at least closer to the benchmark curves. However, the Ne Goldstone modes worsen and are about $1.26\,\mathrm{meV}$ now, while those for aluminium do not change significantly and are still imaginary. In addition, the degeneracies of neon are well reproduced on Γ – X but poorly at W and especially on the path Γ – L (the colors have been chosen such that the path Γ – X, which appears more reliable, fits better). In contrast, the degeneracies of aluminium are as good as in figure 7.23. Still, the splitting is not as large as in the benchmark and smaller than in the aforementioned figure.

Results after section 7.6.6

If moreover the MT integrals are alleviated as expounded on in section 7.6.6, the modes of Ne deteriorate by becoming imaginary again. For Al, the longitudinal mode partly becomes

---

[31] The employed version can be found in the repository `juPhon`, when searching for the commit with the hash `21e11d729f64a934d403e768e4c1185773982c88`. The cutoff of the reciprocal energies in the Sternheimer equation that is discussed in section 7.4.1, is set to $1 \cdot 10^{-7}\,E_{\mathrm{h}}$, since there was no experience about its optimal value at this time. Finally, the outcome is divided by two, since this factor two in equation (7.123h) has not been considered for this commit, but it accounted for in the dispersion relations of section 7.7.2 [127, 256].

[32] The used version is given in the `juPhon` with the hash `df7f597115ec3d672ea18ff38a951575decf431b`. In order to profit from the experiences of Neukirchen, the reciprocal-energies cutoff is set to $5 \cdot 10^{-3}\,E_{\mathrm{h}}$ in this commit (cf. section 7.4.1) [256]. Furthermore, also here the dynamical matrices are divided by two, as already discussed in the previous footnote.

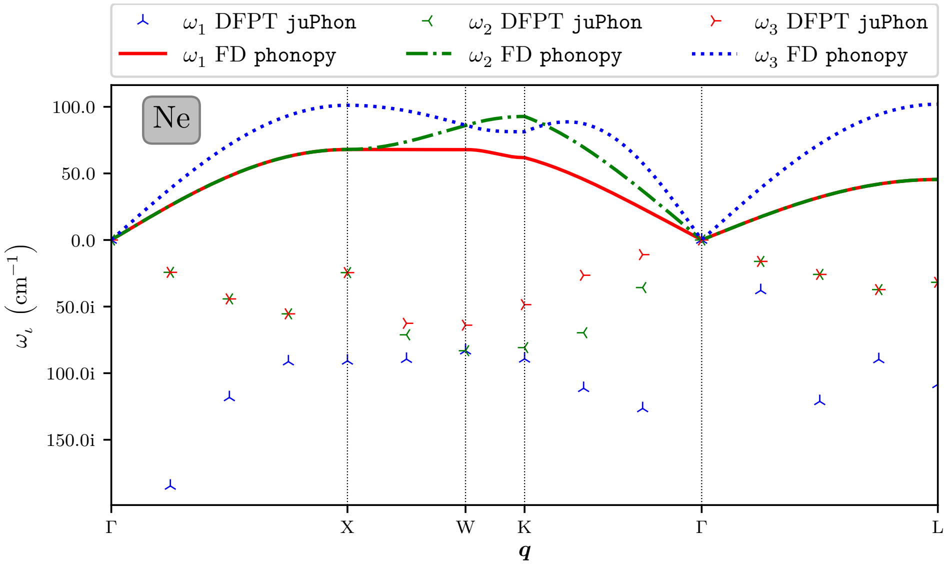

Figure 7.22: Dispersion relation of `juPhon` for fcc Ne according to section 7.6.4. My DFPT calculation with `juPhon` is conducted at $\boldsymbol{q}$-points (internal units) which are part of a discrete Γ-centered $8 \times 8 \times 8$ reciprocal mesh. These points lie on paths connecting the high-symmetry points defined in table 7.8, and are not interpolated (since this is not yet implemented). The curves show the results of a benchmark calculation by Alexander Neukirchen, employing the Finite Displacement implementation `phonopy` [164]. Both the `juPhon` and `phonopy` calculation use the same `FLEUR` input-generator input file provided in appendix B. However, the `juPhon` calculation utilizes an $8 \times 8 \times 8$ $\boldsymbol{k}$-set, while a $4 \times 4 \times 4$ $\boldsymbol{k}$-set proves to be sufficient for the FD calculation [256]. Moreover, the input of `juPhon` is from the old `FLEUR` version specified on page 112, while the FD calculation is based on a more modern `FLEUR` code (see page 261). Finally, ω_2 and ω_3 of `phonopy` is interchanged for the sake of a smoother dispersion between their two crossings close to W and K [119, 127]. This holds true for for all fcc dispersion relations in this subsection. In general, the DFPT frequencies deviate from the FD benchmark values and are imaginary. Still, the Goldstone modes already numerically vanish and the symmetry-dictated degeneracies and a splitting of the transversal modes are already reproduced.

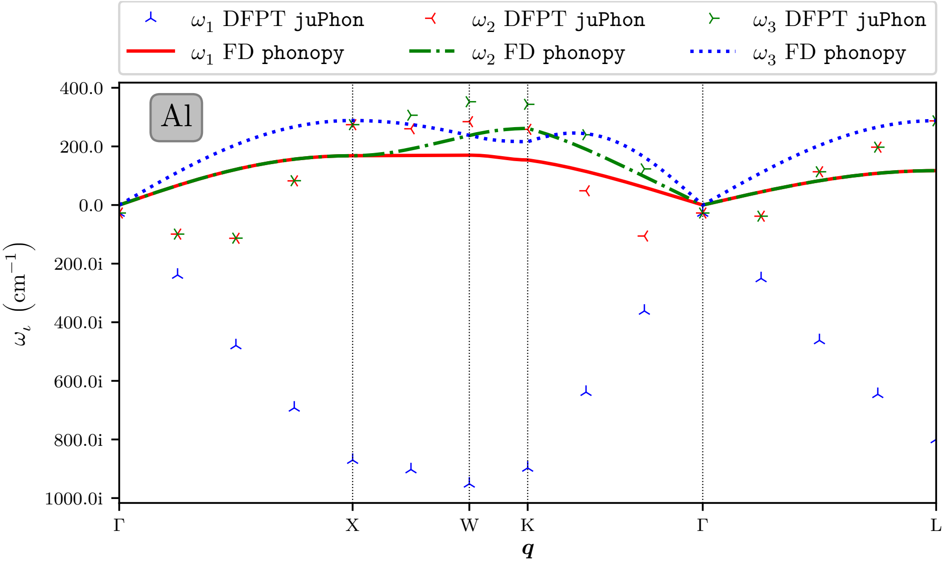

Figure 7.23: Dispersion relation of `juPhon` for fcc Al according to section 7.6.4. The details of calculating selected DFPT frequencies as well as the interpolated FD benchmark curves are already described in the caption of figure 7.22. The DFPT frequencies are different from the FD benchmark values, which is also the case for the Goldstone modes ($4.8\,\mathrm{meV}$ too large and imaginary). But relative to figure 7.22, some frequencies are real and the path Γ to L is more consistent with the benchmark. Additionally, the longitudinal mode is smoother. Finally, the degeneracy and splitting of the transversal modes already results.

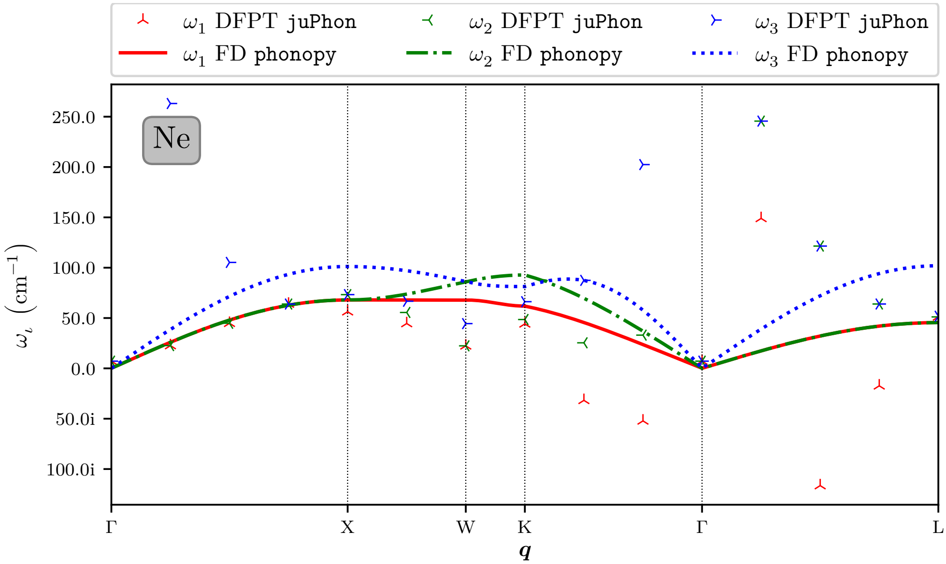

Figure 7.24: Dispersion relation of `juPhon` for fcc Ne according to the formalism after section 7.6.5. The details of calculating selected DFPT frequencies as well as the interpolated FD benchmark curves are already described in the caption of figure 7.22. Relative to figure 7.22, the transversal modes are now real and especially between Γ – X very close to the benchmark curves. But, the Goldstone modes have an offset of roughly $1.26\,\mathrm{meV}$ and the degeneracies worsen, in particular on the path Γ – L.

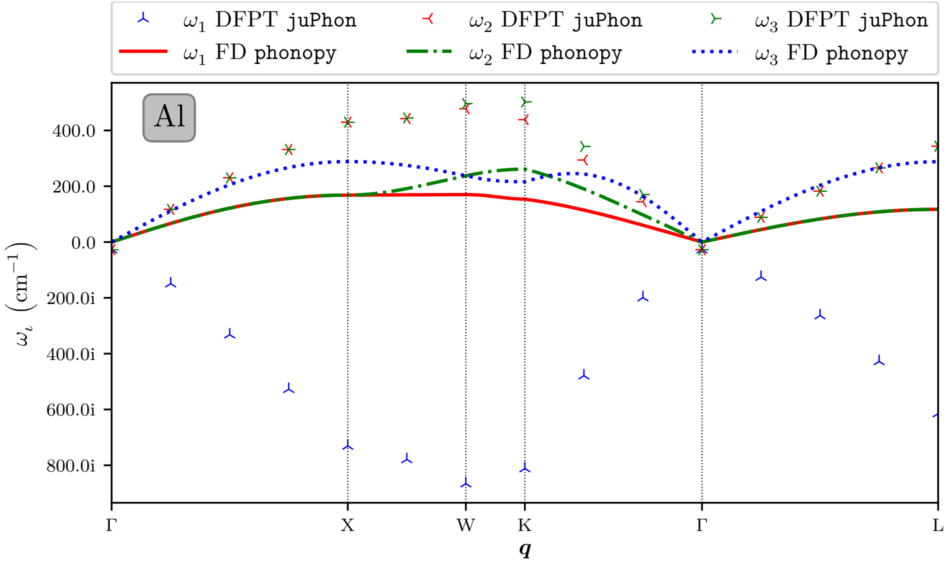

Figure 7.25: Dispersion relation of `juPhon` for fcc Al according to the formalism after section 7.6.5. The details of calculating selected DFPT frequencies as well as the interpolated FD benchmark curves are already described in the caption of figure 7.22. Compared to figure 7.23, the transversal modes are now real and considerably smoother. However, they overestimate the benchmark curves, while the longitudinal modes are still imaginary and thus far off.

real, but the transversal modes are again imaginary. Furthermore, the transversal frequencies are not as smooth as in figure 7.25. Thus, it has been necessary to improve the accuracy even further.

7.7.2 Status Quo

Calculation setup

Implementing the optimized framework from section 7.6.8 leads to significantly better phonon dispersion-relations. Overall, the `juPhon` calculations are very well in line with the FD benchmark results by Neukirchen. Details about the setup of the computations are already given in the introduction of this section. Furthermore, it is stated there that `phonopy` corrects the Goldstone modes so that they vanish. For the sake of an optimal comparison, the dynamical matrices from `juPhon` for finite $\boldsymbol{q}$-values are subtracted by the one for $\boldsymbol{q} = \mathbf{0}$, before they are diagonalized [256]. Furthermore, determining the frequencies from the eigenvalues is based on the same natural constants and unit conversion factors as employed by `phonopy` [256]. I follow these steps, from the correction of the dynamical matrices to the final `juPhon` frequencies shown in the following, using a post-processing script by Neukirchen [256]. Still the Goldstone modes that result from `juPhon` are provided in the captions of the figures to reveal the true quality of the `juPhon` calculation (or its input). Due to the arrangement of some equations in the programmed DFPT approach, I expect that inaccuracies of the Goldstone modes are also visible for finite $\boldsymbol{q}$-values. Furthermore, the core-tail corrections are deactivated, because they corrupt some degeneracies at the moment [256].

Copper

Gold

Aluminium

In figure 7.26, the phonon dispersion-relation of fcc Cu is displayed. Although the `juPhon` calculations almost perfectly correspond to the benchmark computations, overall the former overestimate the latter a bit, however, on average only by a few $\mu\mathrm{eV}$. Moreover, figure 7.27 displays the dispersion relation of Au. Relative to copper, the DFPT results overestimate the benchmark a little more, in particular at X and L (about $2.8\,\mathrm{meV}$). Still, the curvature and the degeneracies, which are governed by the intrinsic symmetry, are very consistent. The phonon dispersion-relation of fcc Al with a smaller over-estimation of the benchmark is shown in figure 7.28. One can see that the frequencies at the X point are roughly $6.2\,\mathrm{meV}$ larger than the benchmark, but this can also be found from FD and DFPT calculations with the `Elk` code [256]. Relative to copper, the consistency on the path X – W, at the point K, and on the path K – Γ is a bit poorer. However, the overall correspondence on the paths Γ – X and Γ – L, including the degeneracies, is comparable to the excellent results of copper. On the former path, the transversal modes perform better than the longitudinal ones, while on the latter the longitudinal modes are superior.

Molybdenum

In contrast to the previous fcc structures, figure 7.29 depicts the outcomes of bcc Mo. Before discussing this dispersion relation, it must be stated that the unperturbed wave-function expansion coefficients of the `FLEUR` calculation, preceding `juPhon`, are corrected, i.e., only their real parts are used. This is legitimate, because actually the coefficients must be real for materials featuring inversion symmetry, such as bcc Mo [127]. In this case, a special version of `FLEUR` is normally employed, ensuring real wave-function expansion coefficients, while the version I use is more general. Its diagonalization routine sometimes delivers wave-function expansion coefficients with the same real part but with an imaginary part, which is too large due to an aborted convergence (runtime optimization) [127]. Despite the imaginary part, the same charge density results and therefore this usually does not cause problems.

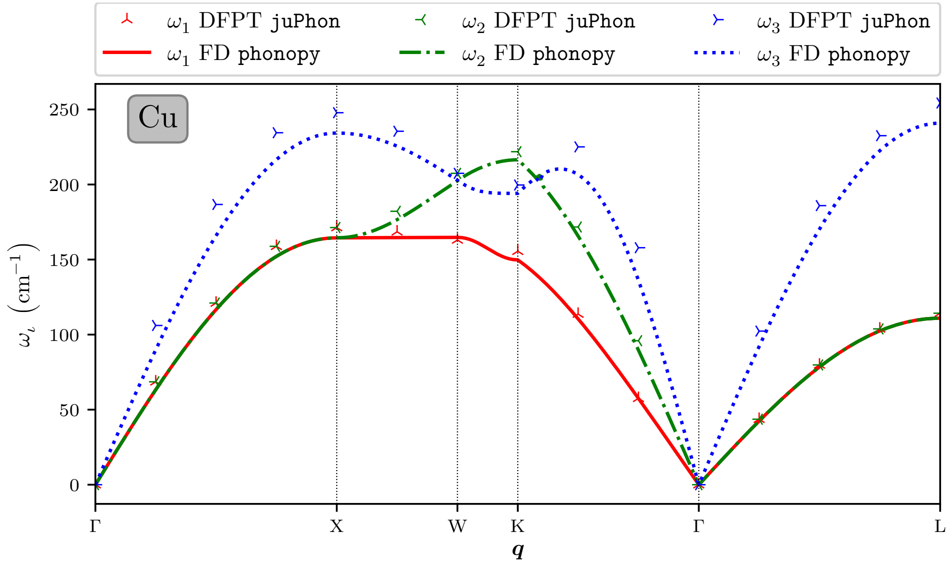

Figure 7.26: Final `juPhon` dispersion relation for fcc Cu compared with FD data. The outcome of `juPhon` is almost perfectly in line with the benchmark, it only deviates by about some μeV on average. Additionally, the degeneracy of the transversal modes along the Γ – X and Γ – L paths is excellently fulfilled. Between the two crossings of ω_2 and ω_3, the resulting (sorted) frequencies both for `juPhon` and for the FD benchmark are interchanged to achieve a smooth dispersion [119, 127]. This is done for all fcc dispersion relations in this subsection. The implemented formalism of `juPhon` is given in section 7.6.8. Furthermore, my DFPT calculation is performed at $\boldsymbol{q}$-points (internal units) which are part of a discrete Γ-centered $8 \times 8 \times 8$ reciprocal mesh. These points lie on paths connecting the high-symmetry points defined in table 7.8, and are not interpolated (since this is not yet implemented). The curves show the results of a benchmark calculation by Alexander Neukirchen, employing the FD implementation `phonopy` [164]. Both the `juPhon` and the `phonopy` calculation use the same `FLEUR` input-generator input file, provided in appendix B. However, the `juPhon` calculation utilizes an $8 \times 8 \times 8$ $\boldsymbol{k}$-set, while a $4 \times 4 \times 4$ $\boldsymbol{k}$-set proves to be sufficient for the FD calculation [256]. Moreover, the input of `juPhon` is from the old `FLEUR` version specified on page 112, while the FD calculation is based on a more modern `FLEUR` code (see page 261). It must be emphasized that the eigenvalues of the dynamical matrices from `juPhon` are corrected by their difference from zero at $\boldsymbol{q} = \boldsymbol{0}$, employing a post-processing script of Neukirchen. This causes a correction of the dispersion relation. However, it enables us a better comparison with the FD data, which is intrinsically corrected by `phonopy` so that forces sum rules are obeyed [256] and the Goldstone modes vanish. The original energy of the Goldstone frequencies from `juPhon` is at $2.81\,\mathrm{meV}$.

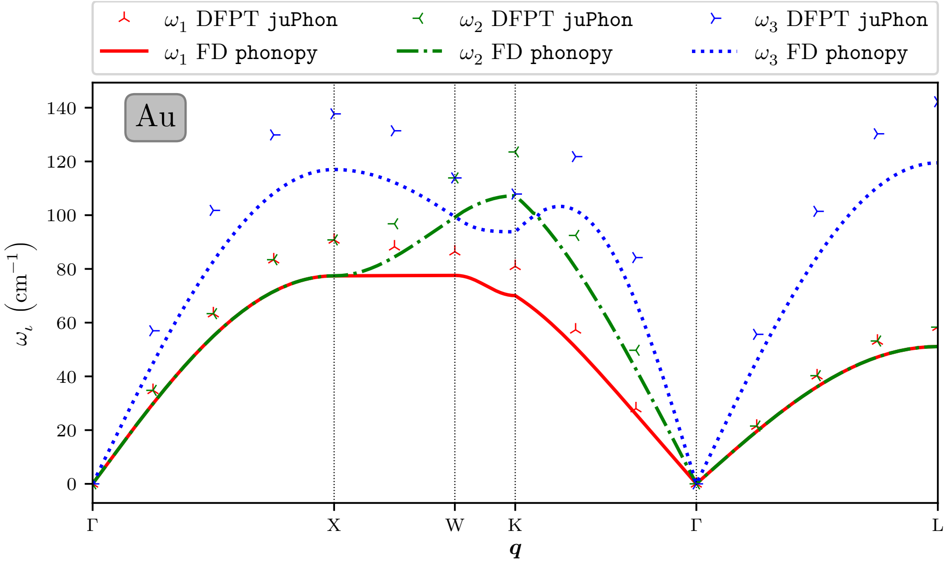

Figure 7.27: Final `juPhon` phonon dispersion-relation for fcc Au, compared with FD data. The details of calculating selected DFPT frequencies as well as the interpolated FD benchmark curves are already described in the caption of figure 7.26. Compared to copper, the DFPT frequencies overestimate the benchmark data a little, culminating at high-symmetry points, such as X and L. However, the curvature and the degeneracies are overall very consistent and the degeneracies along the $\Gamma - \mathrm{X}$ and $\Gamma - \mathrm{L}$ paths are perfectly reproduced. Finally, the original Goldstone frequencies of `juPhon` are at $8.82\,\mathrm{meV}$.

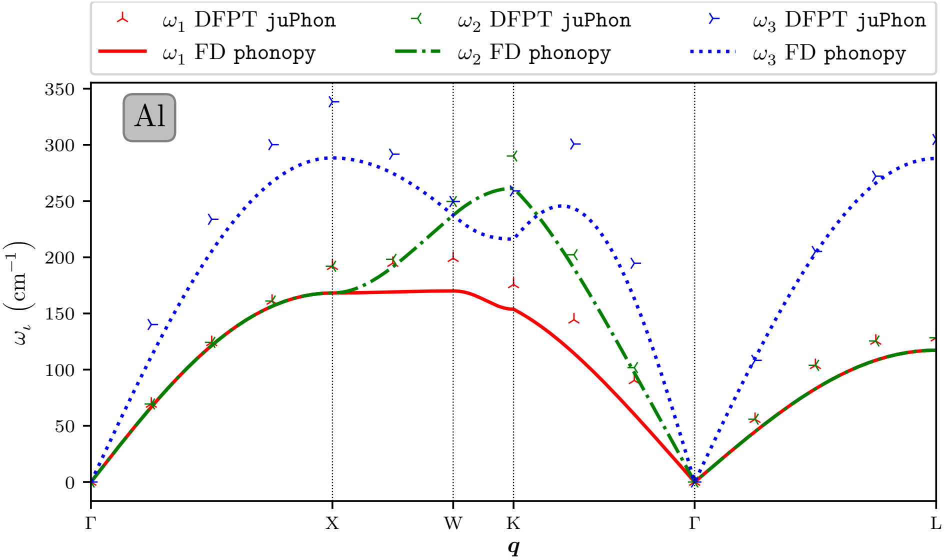

Figure 7.28: Final `juPhon` phonon dispersion-relation for fcc Al, compared with FD data. The details of calculating selected DFPT frequencies as well as the interpolated FD benchmark curves are already described in the caption of figure 7.26. The longitudinal mode along the path Γ – X is overestimated, to the largest extent at the X point (a few meV). The transversal modes on this path are better in line with the FD calculation, but also a bit too large at the X-point. In contrast, on the path Γ – L the longitudinal mode is very conform with the benchmark, whereas the transversal frequencies are little larger than the benchmark. The consistency on the path X – W, at K and on the path K – Γ is overall a little poorer compared to figure 7.26. But, on Γ–X and Γ–L, the degeneracies are very well reproduced. Finally, the original Goldstone frequency of `juPhon` is at 3.49 meV.

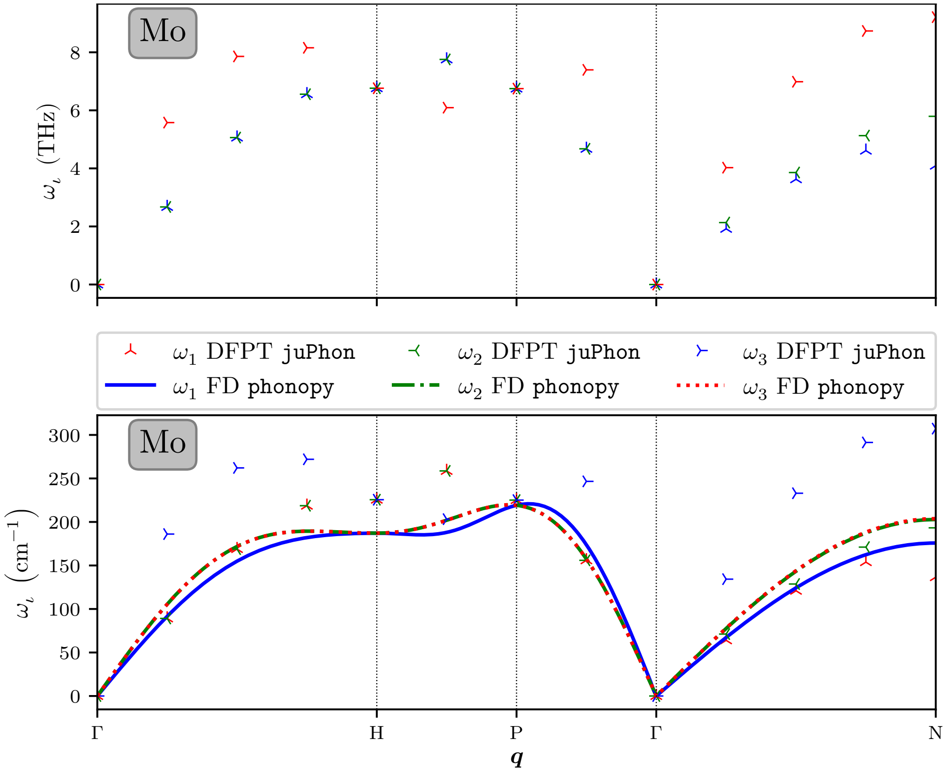

Figure 7.29: Final `juPhon` phonon dispersion-relation for bcc Mo, compared with FD and experimental reference data. The details of calculating selected DFPT frequencies as well as the interpolated FD benchmark curves are already described in the caption of figure 7.26. Apart from that, the imaginary parts of the input unperturbed wavefunction expansion coefficients from `FLEUR` are set to zero. Moreover, it is important to note that we substituted the high-symmetry point $\boldsymbol{q} = (-1/2, 1/2, 1/2)^{\top} a_0^{-1}$ by $\boldsymbol{q} = (1/2, 1/2, 1/2)^{\top} a_0^{-1}$, since negative $\boldsymbol{q}$ values are not realizable by `juPhon` at the moment. In addition, on H – Γ the `juPhon` frequencies are identified as transversal (red and green), provided they are degenerate, and longitudinal (blue) otherwise [127]. Relative to the fcc plots, the consistency with the benchmark (upper plot) is poorer. Especially, the longitudinal mode considerably differs. Furthermore, on Γ – N the degenerated transversal DFPT frequencies split, whereas the FD data does not show this, or only very poorly. But, it must explicitly be stressed that the consistency of the DFPT frequencies with experimental data is much better [127, 298]. In order to allow for a better comparison, the data of `juPhon` is converted to THz (lower plot), again using the post-processing script of Neukirchen. Although, the input data of `FLEUR` is provisionally fixed, and a non-realistic xc potential is utilized, the frequencies are very good line. In particular the two transversal modes between Γ – N are reproduced by the experiment. The original Goldstone frequencies of `juPhon` are 8.51 meV.

Likewise, the impact of the imaginary noise on the dispersion relations of other systems shown here seems not very relevant [256]. Nevertheless, Neukirchen found that for Mo it is enormous, e.g. at $\boldsymbol{q} = (1/8, 0, 0)^\top \boldsymbol{a}_0^{-1}$ frequencies of about $1.7 \cdot 10^5\,\mathrm{cm}^{-1}$ result [256]. But ignoring the imaginary part of the wave-function expansion-coefficients input, leads to the DFPT frequencies shown in figure 7.29. However, this can only be a quick-fix solution, because doing so causes slight inconsistencies, implying for example Kohn–Sham wave functions which are not perfectly orthogonal to each other. Still, the resulting frequencies are fairly consistent with the FD benchmark. But, it must be emphasized at this point that the FD benchmark does *not* perform very well. Although the DFPT frequencies are only based on a $X\alpha$ potential and despite the aforementioned correction of the input, they are significantly better in line with experimental results [127, 298]. In order to facilitate the comparison with the experiment, the DFPT frequencies are converted to THz in figure 7.29 (again using the aforesaid post-processing script of Neukirchen). The DFPT frequencies conform quantitatively very well with the experiment and especially the splitting of the transversal modes on the path Γ – N is predicted (this can not or only very poorly be seen in the FD benchmark). Furthermore, the longitudinal mode on the path Γ – N is larger than the transversal degenerate modes in the experiment which conforms better with the DFPT than with the FD results.

Neon In figure 7.30, the dispersion relation for fcc Ne can be found. It becomes obvious that especially close to the Γ point on the path Γ – X, the longitudinal mode (blue) diverges significantly from the benchmark (also for denser $\boldsymbol{q}$-meshes [256]). But this is not the case for the path Γ – L. We suppose that polarization effects could not sufficiently be taken into account, since Ne is an insulator [127]. Apart from that, the remaining frequencies are fairly good, and the degeneracies very well comparable with the reference calculation. But in contrast to the previous fcc systems in this subsection, the benchmark is underestimated instead of overestimated, for example regarding the longitudinal mode at the X and the L point (the latter does likewise not fit well to the curvature of the path). However, I indicate in particular the excellent realization of the Goldstone modes at an accuracy that is naturally given by the precision of the utilized integration routines. Argon Finally, the dispersion relation for fcc Ar is provided in figure 7.31. In contrast to fcc Ne in figure 7.30, there is no rapid change of the frequencies on the path Γ – X anymore. All in all, the `juPhon` frequencies lie very close to the interpolated FD curves. The Goldstone modes are again numerically perfect, analogously to fcc Ne. Relative to the other systems shown here, the phonon frequencies of the loosely bonded Ar and Ne are smaller. Therefore, the calculation must be more precise for reliable results. Particularly Ar with the smallest frequencies shown here substantiates that such results are possible with the `juPhon` implementation.

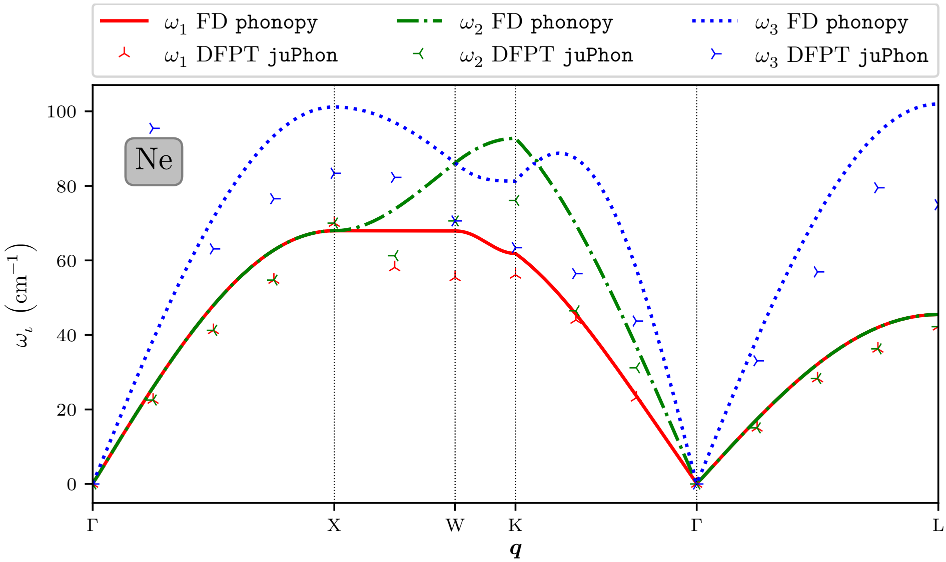

Figure 7.30: Final `juPhon` phonon dispersion-relation for fcc Ne, compared with FD data. The details of calculating selected DFPT frequencies as well as the interpolated FD benchmark curves are already described in the caption of figure 7.26. In contrast to aluminum, the benchmark is a bit underestimated. Furthermore, the curvature of the longitudinal mode at the L point is not well reproduced. Still, the overall consistency is fairly good, except for the longitudinal mode at $\boldsymbol{q} = (0, {}^{1}\!/_{8}, {}^{1}\!/_{8})^{\top} a_0^{-1}$. We suppose that polarization effects are not sufficiently considered for this insulator [127]. Apart from that, the degeneracy on the paths Γ – X and Γ – L are very good in line. Finally, it must be emphasized that the `juPhon` frequencies at Γ perfectly vanish within the best-possible numerical accuracy.

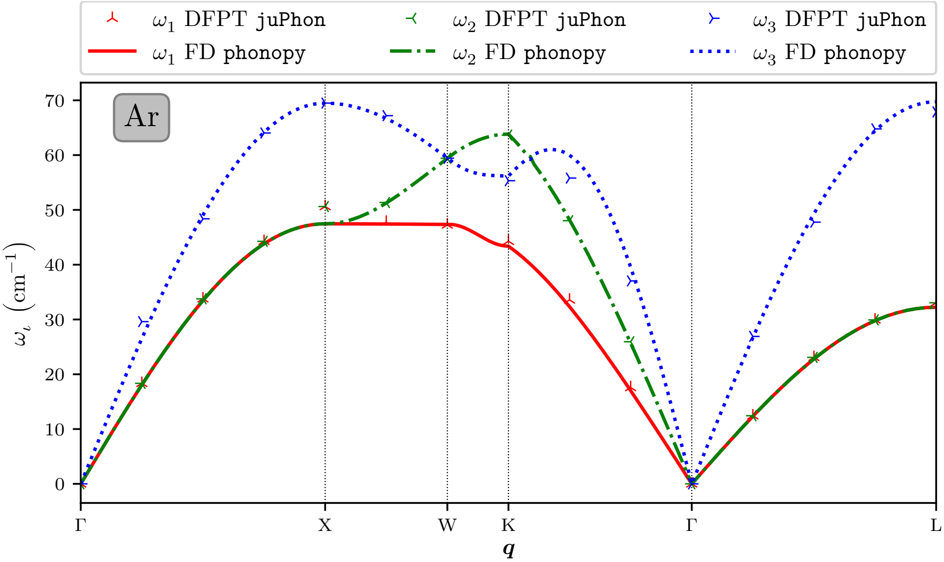

Figure 7.31: Final `juPhon` phonon dispersion-relation for fcc Ar, compared with FD data. The details of calculating selected DFPT frequencies as well as the interpolated FD benchmark curves are already described in the caption of figure 7.26. Relative to the outcome for fcc Ne in figure 7.30, the results are significantly better practically perfectly in line with the benchmark calculations. Furthermore, the degeneracies are well reproduced. Especially, the longitudinal mode close to the Γ point on the path Γ – X does not diverge. Again, the Goldstone modes of `juPhon` are with respect to the possible precision perfectly fulfilled.

Chapter 8

Conclusion

This thesis presents the necessary concepts and reformulations of the theoretical framework, and provides all details about the algorithm including its input in order to realize a successful implementation of the Density-Functional Perturbation Theory (DFPT) within the Density-Functional Theory (DFT) by means of the all-electron Full-Potential Linearized Augmented Plane-Wave (FLAPW) electronic-structure method for accurately calculating phonon dispersion-relations of solids from first-principles. This implementation is accomplished in the open-source code `juPhon`, which meets modern software-engineering standards (a link to its repository is given on page 112). The `juPhon` program is part of the `FLEUR` code family [69], since `juPhon` utilizes related subroutines and features an interface to the `FLEUR` program. The `FLEUR` framework is one particular realization of the FLAPW method, but `juPhon` can also be employed in combination with other FLAPW-method implementations, provided adequate interfaces are developed.

Although, currently, phonon spectra are only calculated in the harmonic approximation, for solids with one atom per unit cell, and for Slater's $\mathrm{X}\alpha$ approximation to the DFT exchange-correlation energy functional [123–125], all numerical and conceptual difficulties of `juPhon` have been resolved. This opens up the vista of calculating phonon spectra for complex solids with unit cells incorporating many atoms, which are arbitrary chemical elements of the periodic table. The `juPhon` implementation is a numerical realization of the DFPT [87] formalism within the FLAPW method formulated by Klüppelberg [88]. By means of `juPhon`, I have calculated the phonon dispersion-relations of fcc Cu, fcc Au, fcc Al, bcc Mo, fcc Ne, as well as fcc Ar and have compared them with experimental data and reference calculations, using the Finite Displacement method based on the output of the `FLEUR` code. We obtain consistent and reliable results.

Calculating phonon dispersion-relations from dynamical matrices, which are the second-order total energy changes with respect to infinitesimal displacements of the ion positions, is a significant challenge. We must compute the linear variations of (i) the wave-functions, (ii) the charge density, (iii) the Hartree, and (iv) the exchange-correlation potentials, each of them expanded in a section-wise defined LAPW basis set. The different definitions of the basis functions in different spatial regions of the unit cell, which are constructed to match at the muffin-tin (MT) sphere boundary, as well as the fact that the basis set is incomplete in the case of undergoing variations are ultimately the reason that determining the aforesaid quantities proves as a formidable task. Altogether, it simply adds up to many terms, the discussion and consideration of which makes the dissertation thesis a bit lengthy. Reaching the necessary accuracy for such a complex basis set has been the key to success, because the phonon energy per atom is about seven orders of magnitude smaller than the electronic energy. This was achieved by (i) analytically rearranging and reformulating terms featuring large values, such that they cancel analytically [88], (ii) simplifying the formalism [256], (iii) calculating correction terms like the Pulay contributions, (iv) taking into account discontinuities of linear and higher order at the MT sphere boundary, especially when atoms are moved, or (v) evaluating the Sternheimer equation in a Kohn–Sham wave-function representation instead of the LAPW basis-function one, which circumvents a costly and probably numerically-imprecise matrix inversion. As an example of simplification, significantly enhancing the numerical robustness, I have reformulated the equations of the dynamical matrix such that Hessian matrices are circumvented. For the new expressions, I have additionally proven that the dynamical matrix analytically vanishes for the Goldstone modes.

In general, testing is an important issue. Therefore, I have programmed a large test suite, which ensures the integrity of intermediate results. At the same time, it allows for flexibly adding new features to `juPhon` without corrupting old ones. For instance, since `juPhon` is compatible with the input of `FLEUR`, synergies will emerge from extending the former code to magnetic materials in the future. Finally, the correctness of the second-order ion–ion (nucleus–nucleus) interaction is verified for fcc Al and bcc Na by cross-checking it with a differing Ewald-type method, implemented in the `ABINIT` code.

In summary, this dissertation lays the computational and algorithmic foundations for analyzing the vibrational properties of electronically, structurally and chemically complex solids from first-principles by means of the all-electron FLAPW method.

Chapter 9

Outlook

The linear response of the charge density upon a change of an external parameter is a rather general issue in the DFT. So apart from phonons, the implementation of the Sternheimer equation and the entailed concepts may in the future be transferred to different perturbations (e.g. electric field). Due to the modular concept of `juPhon`, which permeates its complete structure, I consider this to be a straightforward project. Prospectively, the versatility of `juPhon` can be extended in various directions:

1. *To including more realistic and powerful exchange and correlation functionals.* This can be realized by updating the interface of `juPhon` to the latest `FLEUR` version (see reference [69]), because access to the `libxc` library is then automatically given.
2. *To calculating more complex materials systems with more atoms per unit cell and semi-core states.* Without great effort, calculations of (non-metallic) systems with a polyatomic basis can be made possible, now that the fundamental computational issues have been resolved. In the case of polyatomic metals, terms related to variations in the electron occupation numbers must be added, which have already been derived by Neukirchen [256].

   Adding local orbitals (LO) to the basis set allows the inclusion of advanced materials with semi-core states or states, which require more variational flexibility in the MT sphere. It can substitute for basis corrections beyond the Pulay terms (on condition that they should be necessary) [68, 88, 224].
3. *To relativistic, spin–orbit phenomena.* By checking the relativistic corrections, the treatment of heavy elements can be made useful as well as the treatment of phonon-induced spin-flip scattering and spin life-time effects.
4. *To magnetic systems.* The spin polarization and non-collinear magnetism should be implemented to investigate the magnon-phonon interaction and the Dzyaloshinskii–Moriya interaction in centro-symmetric systems.
5. *To lifting the frozen-core and the frozen-augmentation approximations of the radial basis functions.* It could be beneficial for the performance and accuracy of the Sternheimer equation to reflect the justification of these approximations. Relaxing them in the long-term will necessitate the core-electron response from a simplified Sternheimer

equation (no basis corrections are required for the pointwise core-electron wave functions) [251]. Maybe it is likewise possible to find well-educated guesses for the starting density-variations of the Sternheimer equation (apart from its analytical solution for the Goldstone modes) [251].

6. *To include symmetry rules.* In addition, reduced symmetry optimizations can be reintroduced for phonons and an interpolation of the phonon-dispersions can be realized. Further accuracy could be obtained from symmetrically arranging the $\boldsymbol{k}$- and $\boldsymbol{q}$-vectors around the Γ-point so that contributions numerically better cancel each other [127]. It is also possible to calculate an arbitrary $\boldsymbol{q}$-point beyond the given $\boldsymbol{k}$-set, but then additional $\boldsymbol{k}$-points must be added [251].
7. *To implement parallelization strategies.* Many sub-algorithms are ready to unleash their performance potential through a rigorous parallelization.

Appendix A

Installing and Employing `juPhon`

Installing

The program `juPhon` can be compiled by executing `make` in the console and then be found in the `build` folder. At the moment, some version of `ifort` [262] and the `Intel Math Kernel Library` (MKL) [296] are required, but open-source options will be provided very soon. Furthermore, the `FFTW3` [291] library should be installed. In general, the usage and installation of `juPhon` dynamically changes during its development. The latest requirements and manuals can thus be found in the `README.md` file.

Practical remarks

For the systems that have been investigated yet, the input parameters from the `FLEUR` input-file generator have almost been sufficient. But, in order to set an optimal $G_{\max}$ for the preceding `FLEUR` calculation and to avoid errors in the FFT routines of `juPhon`, test 34 must be executed. It passes as soon as $G_{\max}$ is large enough. Moreover, numerical problems are prevented, if the IR is not chosen too small. Some tests are very sensitive and require a well-converged `FLEUR` calculation. Therefore, I recommend a few more iterations after the `FLEUR` calculation has converged according to its log file. In addition, the size of the $\boldsymbol{q}$-point mesh within each dimension should be a factor of the respective $\boldsymbol{k}$-point mesh size, and the non-spherical $l_{\max,\mathring{\gamma}}$ must have the same value as the spherical $l_{\max,\mathring{\gamma}}$. Finally, the lattice constant should be optimally set (Birch–Murnaghan fit as described in section 7.1.6). Apart from that, the continuity of the unperturbed and perturbed quantities should be comparable [127, 251].

Appendix B

Applied Input Files

FLEUR input-generator input file employed for generating figure 7.3, figure 7.4, figure 7.10, figure 7.12, figure 7.14, figure 7.16, figure 7.22, figure 7.24, and figure 7.30 [256].

```
Ne fcc

0.0 1.0 1.0 ! a1
1.0 0.0 1.0 ! a2
1.0 1.0 0.0 ! a3
7.926224801 ! aa
0.5 0.5 0.5 ! scale

1 ! num atoms
10.1 0.0 0.0 0.0

&atom element='Ne' id=10.1 rmt=2.5 dx=0.012 jri=925 lmax=10 lnonsph=10 /
&comp kmax=4.0 gmax=15.7 gmaxxc=13.0/
&exco xctyp='x-a' /
&kpt div1=8 div2=8 div3=8 tkb=0.005 /
&end /
```

FLEUR input-generator input file of representative unit-cell for generating the `juPhon` part of figure 7.7, figure 7.8, and figure 7.9 [127].

```
sc Ne 1x1x1

&input film=f /

&lattice latsys=cP a0=1.0000000 a=5.12 /

1
10 0.0 0.0 0.0

```

```
&atom element='Ne' rmt=2.5 dx=0.012 jri=925 lmax=10 lnonsph=10 /
&comp kmax=4.0 gmax=15.7 gmaxxc=13.0 /
&exco xctyp='x-a' /
&kpt div1=8 div2=8 div3=8 /

&end /
```

FLEUR input-generator input file of reference supercell for figure 7.7 and figure 7.9 [127].

```
tP Ne 1x1x4 reference

&input film=f /

&lattice latsys=tP a0=1.0000000 a=5.12 c=20.48 /

4
10.000 0.0 0.0 0.0
10.001 0.0 0.0 0.25
10.002 0.0 0.0 0.5
10.003 0.0 0.0 0.75

&atom element='Ne' rmt=2.5 dx=0.012 jri=925 lmax=10 lnonsph=10 /
&comp kmax=4.0 gmax=15.7 gmaxxc=13.0 /
&exco xctyp='x-a' /
&kpt div1=8 div2=8 div3=2 /

&end /
```

FLEUR input-generator input file of supercell with displaced atoms for figure 7.7 and figure 7.9 [127].

```
tP Ne 1x1x4 displaced

&input film=f /

&lattice latsys=tP a0=1.0000000 a=5.12 c=20.48 /

4
10.000 0.0 0.0 0.00001
10.001 0.0 0.0 0.25
10.002 0.0 0.0 0.49999
10.003 0.0 0.0 0.75

&atom element='Ne' rmt=2.5 dx=0.012 jri=925 lmax=10 lnonsph=10 /
&comp kmax=4.0 gmax=15.7 gmaxxc=13.0 /
&exco xctyp='x-a' /
&kpt div1=8 div2=8 div3=2 /

&end /
```

FLEUR input-generator input file of reference supercell for figure 7.8 and figure 7.9 [127].

```
oP Ne 1x4x2 reference

&input film=f /

&lattice latsys=oP a0=1.0000000 a=5.12 b=20.48 c=10.24 /

8
10.0    0.0 0.0  0.0
10.0001 0.0 0.0  0.5
10.0002 0.0 0.25 0.0
10.0003 0.0 0.25 0.5
10.0004 0.0 0.5  0.0
10.0005 0.0 0.5  0.5
10.0006 0.0 0.75 0.0
10.0007 0.0 0.75 0.5

&atom element='Ne' rmt=2.5 dx=0.012 jri=925 lmax=10 lnonsph=10 /
&comp kmax=4.0 gmax=15.7 gmaxxc=13.0 /
&exco xctyp='x-a' /
&kpt div1=8 div2=2 div3=4 /

&end /
```

FLEUR input-generator input file of supercell with displaced atoms for figure 7.8 and figure 7.9 [127].

```
oP Ne 1x4x2 displaced

&input film=f /

&lattice latsys=oP a0=1.0000000 a=5.12 b=20.48 c=10.24 /

8
10.0    0.0 0.0   0.00001
10.0001 0.0 0.0   0.49999
10.0002 0.0 0.25  0.0
10.0003 0.0 0.25  0.5
10.0004 0.0 0.5  -0.00001
10.0005 0.0 0.5   0.50001
10.0006 0.0 0.75  0.0
10.0007 0.0 0.75  0.5

&atom element='Ne' rmt=2.5 dx=0.012 jri=925 lmax=10 lnonsph=10 /
&comp kmax=4.0 gmax=15.7 gmaxxc=13.0 /
&exco xctyp='x-a' /
&kpt div1=8 div2=2 div3=4 /
```

```

&end /
```

FLEUR input-generator input employed for generating figure 7.5, figure 7.6, figure 7.11, figure 7.13, figure 7.14, figure 7.16, figure 7.18, figure 7.20, figure 7.23, figure 7.25, figure 7.28.

```
Al fcc

0.0 1.0 1.0 ! a1
1.0 0.0 1.0 ! a2
1.0 1.0 0.0 ! a3
7.727075649 ! aa
0.5 0.5 0.5 ! scale

1 ! num atoms
13.1 0.0 0.0 0.0

&atom element="Al" id=13.1 rmt=2.38 lmax=10 lnonsph=10 dx=0.017 jri=885 /
&comp kmax=4.2 gmax=16.3 gmaxxc=14.5 /
&exco xctyp='x-a' /
&kpt div1=8 div2=8 div3=8 tkb=0.005 /
&end /
```

FLEUR input-generator input employed for generating figure 7.19 and figure 7.21 [127].

```
Na bcc

&input film=f /

&lattice latsys='bcc' a=4.2343794101 a0=1.8897161646320724 /

 1
11  0.0  0.0  0.0

&atom element="na" id=11 rmt=2.6 lmax=10 lnonsph=10 econfig="[Ne] | 3s1"/
&exco xctyp='x-a' /
&comp kmax=3.7 gmax=13.0 gmaxxc=10.5 /
&kpt div1=8 div2=8 div3=8 /

&end /
```

FLEUR input-generator input employed for generating figure 7.26 [256].

```
Cu fcc

0.0 1.0 1.0 ! a1
1.0 0.0 1.0 ! a2
```

```
1.0 1.0 0.0 ! a3
6.839983331 ! aa
0.5 0.5 0.5 ! scale

1 ! num atoms
29.1 0.0 0.0 0.0

&atom element="Cu" id=29.1 rmt=2.28 jri=981 lmax=10 lnonsph=10 /
&comp kmax=4.2 gmaxxc=12.5 gmax=21.0 /
&exco xctyp='x-a' /
&kpt div1=8 div2=8 div3=8 tkb=0.005 /
&end /
```

FLEUR input-generator input employed for generating figure 7.27 [256].

```
Au fcc

0.0 1.0 1.0 ! a1
1.0 0.0 1.0 ! a2
1.0 1.0 0.0 ! a3
8.221320368 ! aa
0.5 0.5 0.5 ! scale

1 ! num atoms
79.1 0.0 0.0 0.0

&atom element="Au" id=79.1 rmt=2.3 jri=981 lmax=10 lnonsph=10 /
&comp kmax=4.35 gmaxxc=12.5 gmax=20.0 /
&exco xctyp='x-a' /
&kpt div1=8 div2=8 div3=8 tkb=0.005 /
&end /
```

FLEUR input-generator input employed for generating figure 7.29.

```
Mo bcc

-1.0 1.0 1.0 ! a1
1.0 -1.0 1.0 ! a2
1.0 1.0 -1.0 ! a3
5.9679326711 ! aa
0.5 0.5 0.5  ! scale

1 ! num atoms
42.1 0.0 0.0 0.0

&atom element="Mo" id=42.1 rmt=2.5 jri=981 lmax=10 lnonsph=10  /
&comp kmax=4.0 gmaxxc=13.0 gmax=20.0 /
&exco xctyp='x-a' /
```

```
&kpt div1=8 div2=8 div3=8 tkb=0.005 /
&end /
```

`FLEUR` input-generator input employed for generating figure 7.31.

```
Ar fcc

0.0 1.0 1.0 ! a1
1.0 0.0 1.0 ! a2
1.0 1.0 0.0 ! a3
9.818181106 ! aa
0.5 0.5 0.5 ! scale

1 ! num atoms
18.1 0.0 0.0 0.0

&atom element="Ar" id=18.1 rmt=2.5 jri=981 lmax=10 lnonsph=10 /
&comp kmax=4.0 gmaxxc=11.0 gmax=16.5 /
&exco xctyp='x-a' /
&kpt div1=8 div2=8 div3=8 tkb=0.005 /
&end /
```

Appendix C

Gradient of a Muffin-Tin Function

This derivation is based on the diploma thesis of Betzinger [299], and essentially provided by him for me [251]. From equations (6.27) and (6.27c), the coordinate transformation

$$\begin{pmatrix} x_1 \\ x_2 \\ x_3 \end{pmatrix} = \frac{r}{\sqrt{2}} \begin{pmatrix} 1 & 0 & -1 \\ \mathrm{i} & 0 & \mathrm{i} \\ 0 & \sqrt{2} & 0 \end{pmatrix} \begin{pmatrix} \sqrt{\frac{4\pi}{3}} \mathrm{Y}_{l-1}(\hat{\boldsymbol{r}}) \\ \sqrt{\frac{4\pi}{3}} \mathrm{Y}_{l0}(\hat{\boldsymbol{r}}) \\ \sqrt{\frac{4\pi}{3}} \mathrm{Y}_{l1}(\hat{\boldsymbol{r}}) \end{pmatrix} =: \frac{1}{\sqrt{2}} \begin{pmatrix} 1 & 0 & -1 \\ \mathrm{i} & 0 & \mathrm{i} \\ 0 & \sqrt{2} & 0 \end{pmatrix} \begin{pmatrix} z_{-1} \\ z_0 \\ z_1 \end{pmatrix} \tag{C.1}$$

can be deduced. Inverting the Jacobian matrix leads to the inverse coordinate transformation

$$\boldsymbol{z} := \begin{pmatrix} z_{-1} \\ z_0 \\ z_1 \end{pmatrix} = \frac{1}{\sqrt{2}} \begin{pmatrix} 1 & -\mathrm{i} & 0 \\ 0 & 0 & \sqrt{2} \\ -1 & -\mathrm{i} & 0 \end{pmatrix} \begin{pmatrix} x_1 \\ x_2 \\ x_3 \end{pmatrix} =: \underline{\mathfrak{J}} \boldsymbol{x} \tag{C.2}$$

from the cartesian coordinates x_i to the so-called *natural* coordinates $z_{m''}$. The Jacobian $\underline{\mathfrak{J}}$ in equation (C.2) is likewise (almost) provided in Klüppelberg [88, equation (4.16)]. However, he has forgotten the minus sign before the imaginary unit in $\mathfrak{J}_{32}$ [261].

In order to elucidate the action of a cartesian gradient on a general function $\mathfrak{g}(\boldsymbol{z})$, the chain rule is employed so that

$$\boldsymbol{\nabla} \mathfrak{g}(\boldsymbol{z}) = \begin{pmatrix} \frac{\partial z_{-1}}{\partial x_1} & \frac{\partial z_0}{\partial x_1} & \frac{\partial z_1}{\partial x_1} \\ \frac{\partial z_{-1}}{\partial x_2} & \frac{\partial z_0}{\partial x_2} & \frac{\partial z_1}{\partial x_2} \\ \frac{\partial z_{-1}}{\partial x_3} & \frac{\partial z_0}{\partial x_3} & \frac{\partial z_1}{\partial x_3} \end{pmatrix} \begin{pmatrix} \partial_{z_{-1}} \\ \partial_{z_0} \\ \partial_{z_1} \end{pmatrix} \mathfrak{g}(\boldsymbol{z}) \tag{C.3a}$$

$$:= \frac{1}{\sqrt{2}} \begin{pmatrix} 1 & 0 & -1 \\ -\mathrm{i} & 0 & -\mathrm{i} \\ 0 & \sqrt{2} & 0 \end{pmatrix} \begin{pmatrix} \partial_{z_{-1}} \\ \partial_{z_0} \\ \partial_{z_1} \end{pmatrix} \mathfrak{g}(\boldsymbol{z}) \tag{C.3b}$$

$$:= \underline{T} \begin{pmatrix} \partial_{z_{-1}} \\ \partial_{z_0} \\ \partial_{z_1} \end{pmatrix} \mathfrak{g}(\boldsymbol{z}) =: \underline{T} \boldsymbol{\nabla}_{\mathfrak{n}} \mathfrak{g}(\boldsymbol{z}) \tag{C.3c}$$

results. This matrix $\underline{T}$ can also (almost) be found in Klüppelberg [88, equation (4.18)], but he forgets again two minus signs in $\underline{T}_{21}$ and $\underline{T}_{23}$ before the imaginary unit [261]. Using the inverse of $\underline{T}$, the relation

$$
\begin{aligned}
\boldsymbol{\nabla}_{\mathrm{n}}\mathfrak{g}(\boldsymbol{x}) &= \underline{T}^{-1}\boldsymbol{\nabla}\mathfrak{g}(\boldsymbol{x}) && \text{(C.4a)}\\
&= \frac{1}{\sqrt{2}}\begin{pmatrix} 1 & \mathrm{i} & 0 \\ 0 & 0 & \sqrt{2} \\ -1 & \mathrm{i} & 0 \end{pmatrix}\begin{pmatrix} \partial_{x_1} \\ \partial_{x_2} \\ \partial_{x_3} \end{pmatrix}\mathfrak{g}(\boldsymbol{x}) && \text{(C.4b)}
\end{aligned}
$$

holds true. Equations (C.2) as well as (C.4) and reference [299, equations (4.3.25)–(4.3.30)] are conform with each other.

After having elucidated the relation between the gradient in cartesian and natural coordinates, the focus changes to the action of the latter on a general function in spherical coordinates

$$
\boldsymbol{\nabla}_{\mathrm{n}}\mathfrak{g}(r,\theta,\phi) = \boldsymbol{\nabla}_{\mathrm{n}}\sum_{lm}[\mathfrak{g}(r)]_{lm}\mathrm{Y}_{lm}(\theta,\phi)\,, \tag{C.5}
$$

which is expanded in spherical harmonics (the MT part of the LAPW basis set). Expressing the cartesian gradient in spherical coordinates

$$
\begin{pmatrix} \partial_{x_1} \\ \partial_{x_2} \\ \partial_{x_3} \end{pmatrix} = \begin{pmatrix} \sin\theta\cos\phi \\ \sin\theta\sin\phi \\ \cos\theta \end{pmatrix}\partial_r + \frac{1}{r}\begin{pmatrix} \cos\theta\cos\phi \\ \cos\theta\sin\phi \\ -\sin\theta \end{pmatrix}\partial_\theta + \frac{1}{r\sin\theta}\begin{pmatrix} -\sin\phi \\ \cos\phi \\ 0 \end{pmatrix}\partial_\phi\,, \tag{C.6}
$$

while assuming

$$
\begin{pmatrix} x_1 \\ x_2 \\ x_3 \end{pmatrix} = \begin{pmatrix} r\sin\theta\cos\phi \\ r\sin\theta\sin\phi \\ r\cos\theta \end{pmatrix}\,, \tag{C.7}
$$

the components of $\boldsymbol{\nabla}_{\mathrm{n}}$ can be determined exploiting equations (C.4) and (C.6). This leads to

$$
\begin{aligned}
\partial_{z_{-1}} &= \frac{1}{\sqrt{2}}\left(\sin\theta\,\mathrm{e}^{\mathrm{i}\phi}\partial_r + \frac{1}{r}\mathrm{e}^{\mathrm{i}\phi}\left(\cos\theta\,\partial_\theta + \frac{\mathrm{i}}{\sin\theta}\partial_\phi\right)\right) && \text{(C.8a)}\\
\partial_{z_0} &= \cos\theta\,\partial_r - \frac{1}{r}\sin\theta\,\partial_\theta && \text{(C.8b)}\\
\partial_{z_1} &= -\frac{1}{\sqrt{2}}\left(\sin\theta\,\mathrm{e}^{-\mathrm{i}\phi}\partial_r + \frac{1}{r}\mathrm{e}^{-\mathrm{i}\phi}\left(\cos\theta\,\partial_\theta - \frac{\mathrm{i}}{\sin\theta}\partial_\phi\right)\right)\,, && \text{(C.8c)}
\end{aligned}
$$

and allows for an application to the aforementioned general function, which is expanded in spherical harmonics. Restricting to one summand with general orbital quantum number l and magnetic quantum number m reads

$$
\begin{aligned}
\partial_{z_{-1}}[\mathfrak{g}(r)]_{lm}\mathrm{Y}_{lm}(\theta,\phi) &= \frac{1}{\sqrt{2}}\sin\theta\,\mathrm{e}^{\mathrm{i}\phi}\mathrm{Y}_{lm}(\theta,\phi)\left(\frac{\partial[\mathfrak{g}(r)]_{lm}}{\partial r}\right) && \text{(C.9a)}\\
&\quad + \frac{1}{\sqrt{2}}\mathrm{e}^{\mathrm{i}\phi}\left[\cos\theta\,\partial_\theta + \frac{\mathrm{i}}{\sin\theta}\partial_\phi\right]\mathrm{Y}_{lm}(\theta,\phi)\frac{[\mathfrak{g}(r)]_{lm}}{r}\\
\partial_{z_0}[\mathfrak{g}(r)]_{lm}\mathrm{Y}_{lm}(\theta,\phi) &= \cos\theta\,\mathrm{Y}_{lm}(\theta,\phi)\partial_r[\mathfrak{g}(r)]_{lm} && \text{(C.9b)}\\
&\quad - \sin\theta\left(\partial_\theta\mathrm{Y}_{lm}(\theta,\phi)\right)\frac{[\mathfrak{g}(r)]_{lm}}{r}
\end{aligned}
$$

$$\begin{aligned}\partial_{z_1}[\mathfrak{g}(r)]_{lm}\mathrm{Y}_{lm}(\theta,\phi) = &-\frac{1}{\sqrt{2}}\sin\theta\,\mathrm{e}^{-\mathrm{i}\phi}\mathrm{Y}_{lm}(\theta,\phi)\partial_r[\mathfrak{g}(r)]_{lm} \\ &-\frac{1}{\sqrt{2}}\mathrm{e}^{-\mathrm{i}\phi}\Big[\cos\theta\,\partial_\theta - \frac{\mathrm{i}}{\sin\theta}\partial_\phi\Big]\mathrm{Y}_{lm}(\theta,\phi)\frac{[\mathfrak{g}(r)]_{lm}}{r}\,.\end{aligned} \tag{C.9c}$$

The angular parts can be reformulated, exploiting recursion relations that involve spherical harmonics and Legendre polynomials. These are for example given in Betzinger [299, equations (4.3.31) – (4.3.36)] (who refers to [300]), and read

$$\begin{aligned}\frac{1}{\sqrt{2}}\sin\theta\,\mathrm{e}^{\mathrm{i}\phi}\mathrm{Y}_{lm}(\theta,\phi) &= \eta^{-1}_{lm}\mathrm{Y}_{l+1,m+1}(\theta,\phi) \\ &\quad+ \upsilon^{-1}_{lm}\mathrm{Y}_{l-1,m+1}(\theta,\phi)\end{aligned} \tag{C.10a}$$

$$\begin{aligned}-\frac{1}{\sqrt{2}}\sin\theta\,\mathrm{e}^{-\mathrm{i}\phi}\mathrm{Y}_{lm}(\theta,\phi) &= \eta^{1}_{lm}\mathrm{Y}_{l+1,m-1}(\theta,\phi) \\ &\quad+ \upsilon^{1}_{lm}\mathrm{Y}_{l-1,m-1}(\theta,\phi)\end{aligned} \tag{C.10b}$$

$$\begin{aligned}\cos\theta\,\mathrm{Y}_{lm}(\theta,\phi) &= \eta^{0}_{lm}\mathrm{Y}_{l+1,m}(\theta,\phi) \\ &\quad+ \upsilon^{0}_{lm}\mathrm{Y}_{l-1,m}(\theta,\phi)\end{aligned} \tag{C.10c}$$

$$\begin{aligned}-\sin\theta\,\partial_\theta\mathrm{Y}_{lm}(\theta,\phi) &= -l\eta^{0}_{lm}\mathrm{Y}_{l+1,m}(\theta,\phi) \\ &\quad+ (l+1)\upsilon^{0}_{lm}\mathrm{Y}_{l-1,m}(\theta,\phi)\end{aligned} \tag{C.10d}$$

$$\begin{aligned}\frac{1}{\sqrt{2}}\mathrm{e}^{\mathrm{i}\phi}\Big[\cos\theta\,\partial_\theta + \frac{\mathrm{i}}{\sin\theta}\partial_\phi\Big]\mathrm{Y}_{lm}(\theta,\phi) &= -l\eta^{-1}_{lm}\mathrm{Y}_{l+1,m+1}(\theta,\phi) \\ &\quad+ (l+1)\upsilon^{-1}_{lm}\mathrm{Y}_{l-1,m+1}(\theta,\phi)\end{aligned} \tag{C.10e}$$

$$\begin{aligned}-\frac{1}{\sqrt{2}}\mathrm{e}^{-\mathrm{i}\phi}\Big[\cos\theta\,\partial_\theta - \frac{\mathrm{i}}{\sin\theta}\partial_\phi\Big]\mathrm{Y}_{lm}(\theta,\phi) &= -l\eta^{1}_{lm}\mathrm{Y}_{l+1,m-1}(\theta,\phi) \\ &\quad+ (l+1)\upsilon^{1}_{lm}\mathrm{Y}_{l-1,m-1}(\theta,\phi)\,.\end{aligned} \tag{C.10f}$$

The left-hand sides of these equations can be expressed as products of spherical harmonics

$$\frac{1}{\sqrt{2}}\sin\theta\,\mathrm{e}^{\mathrm{i}\phi}\mathrm{Y}_{lm}(\theta,\phi) = -\sqrt{\frac{4\pi}{3}}\mathrm{Y}_{11}(\theta,\phi)\mathrm{Y}_{lm}(\theta,\phi) \tag{C.11a}$$

$$-\frac{1}{\sqrt{2}}\sin\theta\,\mathrm{e}^{-\mathrm{i}\phi}\mathrm{Y}_{lm}(\theta,\phi) = -\sqrt{\frac{4\pi}{3}}\mathrm{Y}_{1,-1}(\theta,\phi)\mathrm{Y}_{lm}(\theta,\phi) \tag{C.11b}$$

$$\cos\theta\,\mathrm{Y}_{lm}(\theta,\phi) = \sqrt{\frac{4\pi}{3}}\mathrm{Y}_{10}(\theta,\phi)\mathrm{Y}_{lm}(\theta,\phi)\,. \tag{C.11c}$$

These products of spherical harmonics can be expanded in the spherical-harmonic basis:

$$\begin{aligned}\frac{1}{\sqrt{2}}\sin\theta\,\mathrm{e}^{\mathrm{i}\phi}\mathrm{Y}_{lm}(\theta,\phi) = &-\sqrt{\frac{4\pi}{3}}G^{m+1,m,1}_{l+1,\ \ l,\ 1}\mathrm{Y}_{l+1,m+1}(\theta,\phi) \\ &-\sqrt{\frac{4\pi}{3}}G^{m+1,m,1}_{l-1,\ \ l,\ 1}\mathrm{Y}_{l-1,m+1}(\theta,\phi)\end{aligned} \tag{C.12a}$$

$$\begin{aligned}-\frac{1}{\sqrt{2}}\sin\theta\,\mathrm{e}^{-\mathrm{i}\phi}\mathrm{Y}_{lm}(\theta,\phi) = &-\sqrt{\frac{4\pi}{3}}G^{m-1,m,-1}_{l+1,\ \ l,\ \ \ 1}\mathrm{Y}_{l+1,m+1}(\theta,\phi) \\ &-\sqrt{\frac{4\pi}{3}}G^{m-1,m,-1}_{l-1,\ \ l,\ \ \ 1}\mathrm{Y}_{l+1,m-1}(\theta,\phi)\end{aligned} \tag{C.12b}$$

$$\begin{aligned}\cos\theta\,\mathrm{Y}_{lm}(\theta,\phi) = {} & \sqrt{\frac{4\pi}{3}}G^{m,\ m,\ 0}_{l+1,\ l,\ 1}\mathrm{Y}_{l+1,m}(\theta,\phi) \\ & + \sqrt{\frac{4\pi}{3}}G^{m,\ m,\ 0}_{l+1,\ l,\ 1}\mathrm{Y}_{l+1,m}(\theta,\phi)\end{aligned} \tag{C.12c}$$

where many terms vanish because of the Gaunt selection rules addressed in section 7.3.1. Therefore, it is possible to identify

$$\eta^{-1}_{l'm'} = -\sqrt{\frac{4\pi}{3}}G^{m+1,m,1}_{l+1,\ \ l,\ 1} \qquad \upsilon^{-1}_{lm} = -\sqrt{\frac{4\pi}{3}}G^{m+1,m,1}_{l-1,\ \ l,\ 1} \tag{C.13a}$$

$$\eta^{0}_{l'm'} = \sqrt{\frac{4\pi}{3}}G^{m,\ m,\ 0}_{l+1,\ l,\ 1} \qquad \upsilon^{0}_{lm} = \sqrt{\frac{4\pi}{3}}G^{m,\ m,\ 0}_{l+1,\ l,\ 1} \tag{C.13b}$$

$$\eta^{1}_{l'm'} = -\sqrt{\frac{4\pi}{3}}G^{m-1,m,-1}_{l+1,\ \ l,\ \ \ 1} \qquad \upsilon^{1}_{lm} = -\sqrt{\frac{4\pi}{3}}G^{m-1,m,-1}_{l-1,\ \ l,\ \ \ 1}, \tag{C.13c}$$

when comparing equations (C.10a), (C.10b), and (C.10c) with (C.12). All in all,

$$\begin{aligned}\boldsymbol{\nabla}\mathfrak{g}(\boldsymbol{r}) = {} & \underline{T}\sum_{m''=-1}^{1}\hat{\boldsymbol{e}}_{m''}(-1)^{m''}\sqrt{\frac{4\pi}{3}}\sum_{lm}\mathrm{Y}_{lm}(\hat{\boldsymbol{r}})\sum_{l''|l''\in\{-1,1\}}G^{m,\ m+m'',\ -m''}_{l,\ \ \ l+l'',\ \ \ \ 1} \\ & \times\left[\frac{\partial[\mathfrak{g}(r)]_{l+l'',m'+m''}}{\partial r} - \left(-l''l + \frac{\left(\mathrm{i}\sqrt{3}\right)^{l''+1}l''-1}{2}\right)\frac{[\mathfrak{g}(r)]_{l+l'',m'+m''}}{r}\right]\end{aligned} \tag{C.14}$$

results, where the indices have been shifted according to $l := l' + l''$ and $m := m' - m''$, the unit vectors $\hat{\boldsymbol{e}}''_m$ span the natural basis (coordinates $z_{m''}$), and θ and ϕ have been expressed by the unit vector $\hat{\boldsymbol{r}}$.

Appendix D

Analytical Solution of the Monoatomic Sternheimer Equation for $q = 0$

Markus Betzinger suggested that the analytical solution of the Sternheimer equation for $\boldsymbol{q} = \boldsymbol{0}$ is given by equation (7.30). Consequently, equation (7.148) can be generalized according to the arguments around it, to cover the complete unit cell of monoatomic systems

$$\boldsymbol{V}_{\text{eff}}^{(1)}(\boldsymbol{r}; \boldsymbol{0}^{+}\alpha) = -\boldsymbol{\nabla}\boldsymbol{V}_{\text{eff}}^{(0)}(\boldsymbol{r})\,. \tag{D.1}$$

Hence, in order to prove the hypothesis of Betzinger for systems with a monoatomic lattice basis, equation (7.86a) can be rewritten for $\boldsymbol{q} = \boldsymbol{0}$, leaving out the third line (which is zero), and utilizing equations (7.30) as well as (D.1) [251]:

$$\begin{aligned}
&-\sum_{\boldsymbol{G}}\left\langle \phi_{\boldsymbol{k},\boldsymbol{G}'}^{(0)} \middle| \mathscr{H}^{(0)} - \varepsilon_{\boldsymbol{k},n}^{(0)} \middle| \phi_{\boldsymbol{k},\boldsymbol{G}}^{(0)} \right\rangle_{\Omega} \mathrm{i}(\boldsymbol{k}+\boldsymbol{G})\boldsymbol{z}_{\boldsymbol{G}}^{(0)}(\boldsymbol{k},n) \\
= -&\sum_{\boldsymbol{G}}\Bigg\{-\left\langle \phi_{\boldsymbol{k},\boldsymbol{G}'}^{(0)} \middle| \boldsymbol{\nabla}\mathscr{V}_{\text{eff}}^{(0)} - \delta_{\boldsymbol{q}\boldsymbol{0}}\epsilon_{\boldsymbol{k},n}^{(1)}(\boldsymbol{0}^{+}\alpha) \middle| \phi_{\boldsymbol{k},\boldsymbol{G}}^{(0)} \right\rangle_{\Omega} \\
&\quad - \left\langle \boldsymbol{\nabla}\vec{\phi}_{\boldsymbol{k},\boldsymbol{G}'}^{(0)} \middle| \mathscr{H} - \epsilon_{\boldsymbol{k},n}^{(0)} \middle| \vec{\phi}_{\boldsymbol{k},\boldsymbol{G}}^{(0)} \right\rangle_{\alpha} - \left\langle \vec{\phi}_{\boldsymbol{k},\boldsymbol{G}'}^{(0)} \middle| \mathscr{H}^{(0)} - \varepsilon_{\boldsymbol{k},n}^{(0)} \middle| \boldsymbol{\nabla}\vec{\phi}_{\boldsymbol{k},\boldsymbol{G}}^{(0)} \right\rangle_{\alpha} \\
&\quad + \mathrm{i}(\boldsymbol{k}+\boldsymbol{G}-\boldsymbol{k}-\boldsymbol{G}')\left\langle \vec{\phi}_{\boldsymbol{k},\boldsymbol{G}'}^{(0)} \middle| \mathscr{H}^{(0)} - \varepsilon_{\boldsymbol{k},n}^{(0)} \middle| \vec{\phi}_{\boldsymbol{k},\boldsymbol{G}}^{(0)} \right\rangle_{\alpha} \\
&\quad + \oint_{\partial\alpha} \vec{\phi}_{\boldsymbol{k},\boldsymbol{G}'}^{*(0)\alpha}(\boldsymbol{r})\left(\mathscr{H}^{(0)} - \varepsilon_{\boldsymbol{k},n}^{(0)}\right)\vec{\phi}_{\boldsymbol{k},\boldsymbol{G}}^{(0)\alpha}(\boldsymbol{r})\,\mathrm{d}\boldsymbol{S} \\
&\quad - \oint_{\partial\alpha} \phi_{\boldsymbol{k},\boldsymbol{G}'}^{*(0)\mathrm{IR}}\left(\mathscr{H}^{(0)} - \varepsilon_{\boldsymbol{k},n}^{(0)}\right)\phi_{\boldsymbol{k},\boldsymbol{G}}^{(0)\mathrm{IR}}\,\mathrm{d}\boldsymbol{S}\Bigg\} z_{\boldsymbol{G}}^{(0)}(\boldsymbol{k},n)\,.
\end{aligned} \tag{D.2a}$$

Now, a different supplementary zero is introduced by extending the matrix elements in the third and fourth lines from the displaced atom α to the complete unit cell Ω

$$\begin{aligned}
&-\sum_{\boldsymbol{G}}\left\langle \phi_{\boldsymbol{k},\boldsymbol{G}'}^{(0)} \middle| \mathscr{H}^{(0)} - \varepsilon_{\boldsymbol{k},n}^{(0)} \middle| \phi_{\boldsymbol{k},\boldsymbol{G}}^{(0)} \right\rangle_{\Omega} \mathrm{i}(\boldsymbol{k}+\boldsymbol{G})\boldsymbol{z}_{\boldsymbol{G}}^{(0)}(\boldsymbol{k},n) \\
= -&\sum_{\boldsymbol{G}}\Bigg\{-\left\langle \phi_{\boldsymbol{k},\boldsymbol{G}'}^{(0)} \middle| \boldsymbol{\nabla}\mathscr{V}_{\text{eff}}^{(0)} - \delta_{\boldsymbol{q}\boldsymbol{0}}\epsilon_{\boldsymbol{k},n}^{(1)}(\boldsymbol{0}^{+}\alpha) \middle| \phi_{\boldsymbol{k},\boldsymbol{G}}^{(0)} \right\rangle_{\Omega} \\
&\quad - \left\langle \boldsymbol{\nabla}\vec{\phi}_{\boldsymbol{k},\boldsymbol{G}'}^{(0)} \middle| \mathscr{H}^{(0)} - \epsilon_{\boldsymbol{k},n}^{(0)} \middle| \vec{\phi}_{\boldsymbol{k},\boldsymbol{G}}^{(0)} \right\rangle_{\Omega} - \left\langle \vec{\phi}_{\boldsymbol{k},\boldsymbol{G}'}^{(0)} \middle| \mathscr{H}^{(0)} - \varepsilon_{\boldsymbol{k},n}^{(0)} \middle| \boldsymbol{\nabla}\vec{\phi}_{\boldsymbol{k},\boldsymbol{G}}^{(0)} \right\rangle_{\Omega}
\end{aligned} \tag{D.2b}$$

$$\begin{aligned}
&+ \mathrm{i}(\boldsymbol{k}+\boldsymbol{G}-\boldsymbol{k}-\boldsymbol{G}')\left\langle \vec{\phi}^{(0)}_{\boldsymbol{k},\boldsymbol{G}'} \middle| \mathscr{H}^{(0)} - \varepsilon^{(0)}_{\boldsymbol{k},n} \middle| \vec{\phi}^{(0)}_{\boldsymbol{k},\boldsymbol{G}} \right\rangle_{\Omega} \\
&+ \oint_{\partial\alpha} \vec{\phi}^{*(0)\alpha}_{\boldsymbol{k},\boldsymbol{G}'}(\boldsymbol{r})\left(\mathscr{H}^{(0)} - \varepsilon^{(0)}_{\boldsymbol{k},n}\right)\vec{\phi}^{(0)\alpha}_{\boldsymbol{k},\boldsymbol{G}}(\boldsymbol{r})\,\mathrm{d}\boldsymbol{S} \\
&- \oint_{\partial\alpha} \phi^{*(0)\mathrm{IR}}_{\boldsymbol{k},\boldsymbol{G}'}\left(\mathscr{H}^{(0)} - \varepsilon^{(0)}_{\boldsymbol{k},n}\right)\phi^{(0)\mathrm{IR}}_{\boldsymbol{k},\boldsymbol{G}}\,\mathrm{d}\boldsymbol{S}\Bigg\} z^{(0)}_{\boldsymbol{G}}(\boldsymbol{k},n)\,.
\end{aligned}$$

Using the divergence theorem in the IR and the MT analogously to equation (7.153c), subtracting the contribution on the left-hand side of equation (D.2b) on both sides of it, and ignoring the first-order variation of the Kohn–Sham energy, because it vanishes for monoatomic systems, leads to

$$\begin{aligned}
0 = -\sum_{\boldsymbol{G}}\Bigg\{ &- \oint_{\partial\alpha} \vec{\phi}^{*(0)\alpha}_{\boldsymbol{k},\boldsymbol{G}'}(\boldsymbol{r})\left(\mathscr{H}^{(0)} - \varepsilon^{(0)}_{\boldsymbol{k},n}\right)\vec{\phi}^{(0)\alpha}_{\boldsymbol{k},\boldsymbol{G}}(\boldsymbol{r})\,\mathrm{d}\boldsymbol{S} \\
&+ \oint_{\partial\alpha} \phi^{*(0)\mathrm{IR}}_{\boldsymbol{k},\boldsymbol{G}'}\left(\mathscr{H}^{(0)} - \varepsilon^{(0)}_{\boldsymbol{k},n}\right)\phi^{(0)\mathrm{IR}}_{\boldsymbol{k},\boldsymbol{G}}\,\mathrm{d}\boldsymbol{S} \\
&- \mathrm{i}(\boldsymbol{k}+\boldsymbol{G}')\left\langle \vec{\phi}^{(0)}_{\boldsymbol{k},\boldsymbol{G}'} \middle| \mathscr{H}^{(0)} - \varepsilon^{(0)}_{\boldsymbol{k},n} \middle| \vec{\phi}^{(0)}_{\boldsymbol{k},\boldsymbol{G}} \right\rangle_{\Omega} \\
&+ \oint_{\partial\alpha} \vec{\phi}^{*(0)\alpha}_{\boldsymbol{k},\boldsymbol{G}'}(\boldsymbol{r})\left(\mathscr{H}^{(0)} - \varepsilon^{(0)}_{\boldsymbol{k},n}\right)\vec{\phi}^{(0)\alpha}_{\boldsymbol{k},\boldsymbol{G}}(\boldsymbol{r})\,\mathrm{d}\boldsymbol{S} \\
&- \oint_{\partial\alpha} \phi^{*(0)\mathrm{IR}}_{\boldsymbol{k},\boldsymbol{G}'}\left(\mathscr{H}^{(0)} - \varepsilon^{(0)}_{\boldsymbol{k},n}\right)\phi^{(0)\mathrm{IR}}_{\boldsymbol{k},\boldsymbol{G}}\,\mathrm{d}\boldsymbol{S}\Bigg\} z^{(0)}_{\boldsymbol{G}}(\boldsymbol{k},n)
\end{aligned} \tag{D.2c}$$

or evaluated to

$$0 = \sum_{\boldsymbol{G}} \mathrm{i}(\boldsymbol{k}+\boldsymbol{G}')\left\langle \vec{\phi}^{(0)}_{\boldsymbol{k},\boldsymbol{G}'} \middle| \mathscr{H}^{(0)} - \varepsilon^{(0)}_{\boldsymbol{k},n} \middle| \vec{\phi}^{(0)}_{\boldsymbol{k},\boldsymbol{G}} \right\rangle_{\Omega} z^{(0)}_{\boldsymbol{G}}(\boldsymbol{k},n) \tag{D.2d}$$

so that according to equation (2.3a)

$$0 = 0\,. \qquad \square \tag{D.2e}$$

Appendix E

Outer-Product Divergence Theorem

In section 7.6.3, I introduce the relation

$$\int_{\mathfrak{D}} \boldsymbol{\nabla}\left(\mathfrak{k}\boldsymbol{\nabla}^{\top}\mathfrak{g}\right)\mathrm{d}V = \int_{\partial\mathfrak{D}} \mathfrak{k}\hat{\boldsymbol{n}}\boldsymbol{\nabla}^{\top}\mathfrak{g}\,\mathrm{d}S\;, \tag{E.1}$$

in order to employ it throughout my dissertation. The following proof of equation (E.1) has completely been developed by Fabian Lux, who afterwards provided it for me [294].

In his proof, Lux starts with the general matrix element

$$\left[\boldsymbol{\nabla}\left(\mathfrak{k}\boldsymbol{\nabla}^{\top}\mathfrak{g}\right)\right]_{ij} = \partial_i\left(\mathfrak{k}\partial_j\mathfrak{g}\right) \tag{E.2}$$

of the left-hand side integrand in equation (E.1), and deduces an indexed differential form

$$\omega_{ij} = \frac{1}{2}\,\mathfrak{k}\,\partial_j\mathfrak{g}\,\epsilon^{ikl}\,\mathrm{d}x_k \wedge \mathrm{d}x_l\;, \tag{E.3}$$

the exterior derivative of which reads

$$\mathrm{d}\omega_{ij} = \partial_i\left(\mathfrak{k}\,\partial_j\mathfrak{g}\right)\mathrm{d}V\,, \tag{E.4}$$

where

$$\mathrm{d}V = \mathrm{d}x \wedge \mathrm{d}y \wedge \mathrm{d}z \tag{E.5}$$

is the volume form in a 3D Euclidian space. Moreover, it is important to know that equation (E.3) can be reformulated to

$$\omega_{ij} = \mathfrak{k}\,\partial_j\mathfrak{g}\;\mathrm{d}S_i \tag{E.6}$$

with the i-th surface area form

$$\mathrm{d}S_i = \frac{1}{2}\epsilon^{ikl}\,\mathrm{d}x_k \wedge \mathrm{d}x_l\;. \tag{E.7}$$

Now, he exploits Stoke's theorem for differential forms based on equations (E.4) as well as (E.6), and reformulates the resulting relations so that

$$\int_{\mathfrak{D}} \partial_i\left(\mathfrak{k}\,\partial_j\mathfrak{g}\right)\mathrm{d}V = \int_{\mathfrak{D}} \mathrm{d}\omega_{ij} \tag{E.8a}$$

$$= \int_{\partial\mathfrak{D}} \omega_{ij} \tag{E.8b}$$

$$= \int_{\partial\mathfrak{D}} \mathfrak{k}\,\partial_j\mathfrak{g}\,\mathrm{d}S_i \tag{E.8c}$$

$$= \int_{\partial\mathfrak{D}} \left(\mathfrak{k}\,\hat{\boldsymbol{e}}_i\partial_j\mathfrak{g}\right)\cdot\mathrm{d}\boldsymbol{S} \tag{E.8d}$$

$$= \int_{\partial\mathfrak{D}} \left(\mathfrak{k}\,\hat{\boldsymbol{e}}_i\partial_j\mathfrak{g}\right)\cdot\hat{\boldsymbol{n}}\,\mathrm{d}S \tag{E.8e}$$

$$= \int_{\partial\mathfrak{D}} \left(\mathfrak{k}\,(\hat{\boldsymbol{e}}_i\cdot\hat{\boldsymbol{n}})\partial_j\mathfrak{g}\right)\mathrm{d}S \tag{E.8f}$$

$$= \int_{\partial\mathfrak{D}} \left(\mathfrak{k}\,\hat{\boldsymbol{n}}_i\partial_j\mathfrak{g}\right)\mathrm{d}S \tag{E.8g}$$

$$= \int_{\partial\mathfrak{D}} [\mathfrak{k}\,\hat{\boldsymbol{n}}\boldsymbol{\nabla}\mathfrak{g}]_{ij}\,\mathrm{d}S\ . \qquad \square \tag{E.8h}$$

Since the left-hand side of equation (E.8a) equals the right-hand side of (E.8h) and equation (E.2) holds true, equation (E.1) can be implied.

Bibliography

[1] *ISO 80000 (Quantities and units — Part 2: Mathematics)*. Standard. Geneva, CH: International Organization for Standardization, Aug. 2019.

[2] Stefan Blügel et al. "Preface." In: *Computing Solids. Models, ab-initio methods and supercomputing*. Lecture Notes of the 45th IFF Spring School 2014. Ed. by Stefan Blügel et al. Vol. 74. Key Technologies. Forschungszentrum Jülich GmbH, 2014. ISBN: 978-3-89336-912-6. URL: `http://hdl.handle.net/2128/8540`.

[3] Richard M. Martin. *Electronic Structure: Basic Theory and Practical Methods*. 2nd ed. eBook. Cambridge University Press, 2020. ISBN: 9781108429900. DOI: `10.1017/9781108555586`.

[4] Vladimir V. Kiselev. *Collective Effects in Condensed Matter Physics*. Vol. 44. De Gruyter Studies in Mathematical Physics Series. De Gruyter, Inc., 2018. ISBN: 9783110586183.

[5] Gerald D. Mahan. *Many-Particle Physics*. 3rd ed. Physics of Solids and Liquids. Springer, Boston, MA. ISBN: 978-1-4757-5714-9. DOI: `10.1007/978-1-4757-5714-9`.

[6] *A Greek–English Lexicon by Liddell–Scott–Jones*. Perseus Collection. URL: `http://www.perseus.tufts.edu/hopper/morph?l=fwnh%2F&la=greek&can=fwnh%2F0#lexicon` (visited on 01/12/2021).

[7] Joginder Singh Galsin. *Solid State Physics*. Academic Press, 2019. ISBN: 978-0-12-817103-5. DOI: `10.1016/C2018-0-01175-5`.

[8] Giuseppe Grosso and Giuseppe Pastori Parravicini. *Solid State Physics*. 2nd ed. Academic Press, 2014. ISBN: 9780123850300. DOI: `10.1016/C2010-0-66724-1`.

[9] Sydney G. Davison and Maria Stęślicka. *Basic Theory of Surface States*. Vol. 46. Monographs on the Physics and Chemistry of Materials. Clarendon Press Oxford, 1992.

[10] James F. Scott. "Hot physics in the Cold War." In: *Nature Physics* 9.11 (2013), p. 691. DOI: `10.1038/nphys2802`.

[11] J. M. Ziman. *Principles of the Theory of Solids*. 2nd ed. Cambridge University Press, 1972. DOI: `10.1017/CBO9781139644075`.

[12] Neil W. Ashcroft and N. David Mermin. *Solid state physics*. Holt, Rinehart and Winston, 1976. ISBN: 0030839939.

[13] Matthieu J. Verstraete et al. "Density functional perturbation theory with spin-orbit coupling: Phonon band structure of lead." In: *Phys. Rev. B* 78.4 (July 2008), p. 045119. DOI: `10.1103/PhysRevB.78.045119`.

[14] Sebastian F. Maehrlein et al. “Dissecting spin-phonon equilibration in ferrimagnetic insulators by ultrafast lattice excitation.” In: *Science Advances* 4.7 (2018). DOI: 10.1126/sciadv.aar5164.

[15] Maria B. Lifshits and Michel I. Dyakonov. “Swapping Spin Currents: Interchanging Spin and Flow Directions.” In: *Phys. Rev. Lett.* 103.18 (Oct. 2009), p. 186601. DOI: 10.1103/PhysRevLett.103.186601.

[16] Atsufumi Hirohata and Koki Takanashi. “Future perspectives for spintronic devices.” In: *Journal of Physics D: Applied Physics* 47.19 (Apr. 2014), p. 193001. DOI: 10.1088/0022-3727/47/19/193001.

[17] Xiaoou Zhang et al. “Thermal Hall Effect Induced by Magnon-Phonon Interactions.” In: *Phys. Rev. Lett.* 123.16 (Oct. 2019), p. 167202. DOI: 10.1103/PhysRevLett.123.167202.

[18] Dongwook Go et al. “Orbitronics: Orbital currents in solids.” In: *EPL (Europhysics Letters)* 135.3 (Aug. 2021), p. 37001. DOI: 10.1209/0295-5075/ac2653.

[19] Wolfgang Nolting. *Theoretical Physics 9. Fundamentals of Many-body Physics*. English. Trans. German by William D. Brewer. 2nd ed. 2018. eBook. Cham: Springer, 2018. ISBN: 9783319983264. DOI: 10.1007/978-3-319-98326-4.

[20] M. Born and R. Oppenheimer. “Zur Quantentheorie der Molekülen.” In: *Annalen der Physik* 389.20 (1927), pp. 457–484. DOI: 10.1002/andp.19273892002.

[21] Max Born and Kun Huang. “Dynamical Theory of Crystal Lattices.” In: *The International Series of Monographs on Physics*. Ed. by N. F. Mott, E.C. Bullard, and D. H. Wilkinson. 1st ed. The International Series of Monographs on Physics. Oxford University Press, 1954.

[22] M. J. Verstraete and Z. Zanolli. “Density Functional Perturbation Theory.” In: *Computing Solids. Models, ab-initio methods and supercomputing*. Lecture Notes of the 45th IFF Spring School 2014. Ed. by Stefan Blügel et al. Vol. 74. Key Technologies. Forschungszentrum Jülich GmbH, 2014. ISBN: 978-3-89336-912-6. URL: http://hdl.handle.net/2128/8540.

[23] Rolf Heid. “Density Functional Perturbation Theory and Electron Phonon Coupling.” In: *Emergent Pheonomena in Correlated Matter*. Lecture Notes of the Autumn School Correlated Electrons 2013. Ed. by E. Pavarini, E. Koch, and U. Schollwöck. Vol. 3. Modeling and Simulation. Forschungszentrum Jülich GmbH, 2013. ISBN: 978-3-89336-884-6. URL: http://hdl.handle.net/2128/5389.

[24] Nicholas Metropolis et al. “Equation of State Calculations by Fast Computing Machines.” In: *The Journal of Chemical Physics* 21.6 (1953), pp. 1087–1092. DOI: 10.1063/1.1699114.

[25] C. Honerkamp. “Function renormalization group for weakly correlated systems.” In: *Computing Solids. Models, ab-initio methods and supercomputing*. Lecture Notes of the 45th IFF Spring School 2014. Ed. by Stefan Blügel et al. Vol. 74. Key Technologies. Forschungszentrum Jülich GmbH, 2014. ISBN: 978-3-89336-912-6. URL: http://hdl.handle.net/2128/8540.

[26] V. Meden. “The functional renormalization group approach to quantum many-body physics.” In: *Computing Solids. Models, ab-initio methods and supercomputing*. Lecture Notes of the 45th IFF Spring School 2014. Ed. by Stefan Blügel et al. Vol. 74. Key Technologies. Forschungszentrum Jülich GmbH, 2014. ISBN: 978-3-89336-912-6. URL: `http://hdl.handle.net/2128/8540`.

[27] Kenneth G. Wilson. “The renormalization group: Critical phenomena and the Kondo problem.” In: *Rev. Mod. Phys.* 47.4 (Oct. 1975), pp. 773–840. DOI: `10.1103/RevModPhys.47.773`.

[28] T. A. Costi. “Numerical Renormalization Group for Quantum Impurities.” In: *Computing Solids. Models, ab-initio methods and supercomputing*. Lecture Notes of the 45th IFF Spring School 2014. Ed. by Stefan Blügel et al. Vol. 74. Key Technologies. Forschungszentrum Jülich GmbH, 2014. ISBN: 978-3-89336-912-6. URL: `http://hdl.handle.net/2128/8540`.

[29] V. Fock. “Näherungsmethode zur Lösung des quantenmechanischen Mehrkörperproblems.” In: *Zeitschrift für Physik* 61.1 (1930), pp. 126–148. DOI: `10.1007/BF01340294`.

[30] M. Betzinger. “Hartree–Fock and Quantum Chemical Correlation Methods.” In: *Computing Solids. Models, ab-initio methods and supercomputing*. Lecture Notes of the 45th IFF Spring School 2014. Ed. by Stefan Blügel et al. Vol. 74. Key Technologies. Forschungszentrum Jülich GmbH, 2014. ISBN: 978-3-89336-912-6. URL: `http://hdl.handle.net/2128/8540`.

[31] Masuo Suzuki. “Relationship between d-Dimensional Quantal Spin Systems and (d+1)-Dimensional Ising Systems: Equivalence, Critical Exponents and Systematic Approximants of the Partition Function and Spin Correlations.” In: *Progress of Theoretical Physics* 56.5 (Nov. 1976), pp. 1454–1469. DOI: `10.1143/PTP.56.1454`.

[32] H. F. Trotter. “On the Product of Semi-Groups of Operators.” In: *Proceedings of the American Mathematical Society* 10.4 (1959), pp. 545–551. DOI: `10.2307/2033649`.

[33] Masuo Suzuki, Seiji Miyashita, and Akira Kuroda. “Monte Carlo Simulation of Quantum Spin Systems. I.” In: *Progress of Theoretical Physics* 58.5 (Nov. 1977), pp. 1377–1387. DOI: `10.1143/PTP.58.1377`.

[34] Anders W. Sandvik. “Computational Studies of Quantum Spin Systems.” In: *AIP Conference Proceedings* 1297.1 (2010), pp. 135–338. DOI: `10.1063/1.3518900`.

[35] H. G. Evertz. “The loop algorithm.” In: *Advances in Physics* 52.1 (2003), pp. 1–66. DOI: `10.1080/0001873021000049195`.

[36] S. Wessel. “Introduction to Quantum Monte Carlo.” In: *Computing Solids. Models, ab-initio methods and supercomputing*. Lecture Notes of the 45th IFF Spring School 2014. Ed. by Stefan Blügel et al. Vol. 74. Key Technologies. Forschungszentrum Jülich GmbH, 2014. ISBN: 978-3-89336-912-6. URL: `http://hdl.handle.net/2128/8540`.

[37] Walter Metzner et al. “Functional renormalization group approach to correlated fermion systems.” In: *Rev. Mod. Phys.* 84.1 (Mar. 2012), pp. 299–352. DOI: `10.1103/RevModPhys.84.299`.

[38] C. Platt, W. Hanke, and R. Thomale. “Functional renormalization group for multi-orbital Fermi surface instabilities.” In: *Advances in Physics* 62.4-6 (2013), pp. 453–562. DOI: `10.1080/00018732.2013.862020`.

[39] P. Hohenberg and W. Kohn. “Inhomogeneous Electron Gas.” In: *Phys. Rev.* 136.3B (Nov. 1964), B864–B871. DOI: 10.1103/PhysRev.136.B864.

[40] W. Kohn and L. J. Sham. “Self-Consistent Equations Including Exchange and Correlation Effects.” In: *Phys. Rev.* 140.4A (Nov. 1965), A1133–A1138. DOI: 10.1103/PhysRev.140.A1133.

[41] R. Zeller. “Introduction to Density-Functional Theory.” In: *Computational Condensed Matter Physics*. Lecture Manuscripts of the 37th Spring School of the Institute of Solid State Research. Ed. by Stefan Blügel et al. Vol. 32. Matter and Materials. Forschungszentrum Jülich GmbH, 2006. ISBN: 3-89336-430-7. URL: http://hdl.handle.net/2128/2396.

[42] Daniel Wortmann, Nicole Helbig, and Stefan Blügel. “Describing many-electron systems.” In: *Computing Solids. Models, ab-initio methods and supercomputing*. Lecture Notes of the 45th IFF Spring School 2014. Ed. by Stefan Blügel et al. Vol. 74. Key Technologies. Forschungszentrum Jülich GmbH, 2014. ISBN: 978-3-89336-912-6. URL: http://hdl.handle.net/2128/8540.

[43] J. P. Perdew and Alex Zunger. “Self-interaction correction to density-functional approximations for many-electron systems.” In: *Phys. Rev. B* 23.10 (May 1981), pp. 5048–5079. DOI: 10.1103/PhysRevB.23.5048.

[44] John P. Perdew and Yue Wang. “Accurate and simple analytic representation of the electron-gas correlation energy.” In: *Phys. Rev. B* 45.23 (June 1992), pp. 13244–13249. DOI: 10.1103/PhysRevB.45.13244.

[45] A. D. Becke. “Density-functional exchange-energy approximation with correct asymptotic behavior.” In: *Phys. Rev. A* 38.6 (Sept. 1988), pp. 3098–3100. DOI: 10.1103/PhysRevA.38.3098.

[46] Dorothea Golze, Marc Dvorak, and Patrick Rinke. “The GW Compendium: A Practical Guide to Theoretical Photoemission Spectroscopy.” In: *Frontiers in Chemistry* 7.377 (2019). DOI: 10.3389/fchem.2019.00377.

[47] E. K. U. Gross et al., eds. *Fundamentals of Time-Dependent Density Functional Theory [E-Book]*. 1st ed. Lecture Notes in Physics. Berlin, Heidelberg: Springer, 2012, XXXII, 559 pages, 72 illustrations. ISBN: 9783642235184.

[48] Carsten Ullrich. *Time-dependent density-functional theory : concepts and applications [E-Book]*. Oxford graduate texts. Oxford: Oxford University Press, 2012, xiv, 526 pages. DOI: 10.1093/acprof:oso/9780199563029.001.0001.

[49] Vladimir I. Anisimov, F. Aryasetiawan, and A. I. Lichtenstein. “First-principles calculations of the electronic structure and spectra of strongly correlated systems: the LDA+U method.” In: *Journal of Physics: Condensed Matter* 9.4 (Jan. 1997), pp. 767–808. DOI: 10.1088/0953-8984/9/4/002.

[50] Antoine Georges et al. “Dynamical mean-field theory of strongly correlated fermion systems and the limit of infinite dimensions.” In: *Rev. Mod. Phys.* 68.1 (Jan. 1996), pp. 13–125. DOI: 10.1103/RevModPhys.68.13.

[51] Reiner M. Dreizler. *Density Functional Theory: An Approach to the Quantum Many-Body Problem*. Ed. by Eberhard K. U. Gross. Berlin, Heidelberg: Springer, 1990, XI, 304 p., online resource. ISBN: 9783642861055. DOI: 10.1007/978-3-642-86105-5.

[52] W. Kohn. “Nobel Lecture: Electronic structure of matter—wave functions and density functionals.” In: *Rev. Mod. Phys.* 71.5 (Oct. 1999), pp. 1253–1266. DOI: `10.1103/RevModPhys.71.1253`.

[53] Axel D. Becke. “Perspective: Fifty years of density-functional theory in chemical physics.” In: *J. Chem. Phys.* 140.18A301 (2014). DOI: `10.1063/1.4869598`.

[54] R. O. Jones. “Density functional theory: Its origins, rise to prominence, and future.” In: *Rev. Mod. Phys.* 87.3 (Aug. 2015), pp. 897–923. DOI: `10.1103/RevModPhys.87.897`.

[55] X. Gonze et al. “First-principles computation of material properties: the ABINIT software project.” In: *Computational Materials Science* 25.3 (2002), pp. 478–492. DOI: `10.1016/S0927-0256(02)00325-7`.

[56] Aldo H. Romero et al. “ABINIT: Overview and focus on selected capabilities.” In: *The Journal of Chemical Physics* 152.12 (2020), p. 124102. DOI: `10.1063/1.5144261`.

[57] Xavier Gonze et al. “The Abinit project: Impact, environment and recent developments.” In: *Computer Physics Communications* 248 (2020), p. 107042. DOI: `10.1016/j.cpc.2019.107042`.

[58] G. Kresse and J. Furthmüller. “Efficient iterative schemes for ab initio total-energy calculations using a plane-wave basis set.” In: *Phys. Rev. B* 54.16 (Oct. 1996), pp. 11169–11186. DOI: `10.1103/PhysRevB.54.11169`.

[59] Paolo Giannozzi et al. “QUANTUM ESPRESSO: a modular and open-source software project for quantum simulations of materials.” In: *J. Phys.: Condens. Matter* 21.39 (Sept. 2009), p. 395502. DOI: `10.1088/0953-8984/21/39/395502`.

[60] Paolo Giannozzi et al. “Advanced capabilities for materials modelling with Quantum ESPRESSO.” In: *J. Phys.: Condens. Matter* 29.46 (Oct. 2017), p. 465901. DOI: `10.1088/1361-648x/aa8f79`.

[61] Paolo Giannozzi et al. “Quantum ESPRESSO toward the exascale.” In: *The Journal of Chemical Physics* 152.15 (2020), p. 154105. DOI: `10.1063/5.0005082`.

[62] B. Meyer et al. *FORTRAN90 Program for Mixed-Basis Pseudopotential Calculations for Crystals*. Max-Planck-Institut für Metallforschung, 1998.

[63] David Vanderbilt. “Soft self-consistent pseudopotentials in a generalized eigenvalue formalism.” In: *Phys. Rev. B* 41.11 (Apr. 1990), pp. 7892–7895. DOI: `10.1103/PhysRevB.41.7892`.

[64] M. Weinert. “Solution of Poisson’s equation: Beyond Ewald-type methods.” In: *J. Math. Phys.* 22.11 (1981), pp. 2433–2439. DOI: `10.1063/1.524800`.

[65] E. Wimmer et al. “Full-potential self-consistent linearized-augmented-plane-wave method for calculating the electronic structure of molecules and surfaces: O_2 molecule.” In: *Phys. Rev. B* 24.2 (July 1981), pp. 864–875. DOI: `10.1103/PhysRevB.24.864`.

[66] M. Weinert, E. Wimmer, and A. J. Freeman. “Total-energy all-electron density functional method for bulk solids and surfaces.” In: *Phys. Rev. B* 26.8 (Oct. 1982), pp. 4571–4578. DOI: `10.1103/PhysRevB.26.4571`.

[67] Hisazumi Akai et al. “Theory of Hyperfine Interactions in Metals.” In: *Progress of Theoretical Physics Supplement* 101 (Feb. 1990), pp. 11–77. DOI: `10.1143/PTP.101.11`.

[68] David J. Singh and Lars Nordström. *Planewaves¸ Pseudopotentials and the LAPW Method*. 2nd. 233 Spring Street, New York, NY 10013, USA: Springer Science + Business Media, Inc., 2006. ISBN: 978-0-387-28780-5. DOI: 10.1007/978-0-387-29684-5.

[69] Institute for Advanced Simulation 1 and Peter Grünberg Institut 1 at Forschungszentrum Jülich. *The FLEUR project*. URL: `www.flapw.de` (visited on 09/14/2021).

[70] Kurt Lejaeghere et al. "Reproducibility in density functional theory calculations of solids." In: *Science* 351.6280 (2016). DOI: 10.1126/science.aad3000.

[71] Stefan Blügel and Gustav Bihlmayer. "The Full-Potential Linearized Augmented Plane Wave Method." In: *Computational Nanoscience: Do It Yourself!* Lecture Notes of the Winter School 2006. Ed. by Johannes Grotendorst, Stefan Blügel, and Dominik Marx. Vol. 31. Publication Series of the John von Neumann Institute for Computing (NIC). NIC-Directors, 2006. ISBN: 3-00-017350-1.

[72] K. Kunc and R. M. Martin. "Ab Initio Force Constants of Germanium." In: *J. Phys. Colloques* 42.C6 (1981), pp. 649–651. DOI: 10.1051/jphyscol:19816189.

[73] K. Kunc and Richard M. Martin. "Ab Initio Force Constants of GaAs: A New Approach to Calculation of Phonons and Dielectric Properties." In: *Phys. Rev. Lett.* 48.6 (Feb. 1982), pp. 406–409. DOI: 10.1103/PhysRevLett.48.406.

[74] M. T. Yin and Marvin L. Cohen. "Ab initio calculation of the phonon dispersion relation: Application to Si." In: *Phys. Rev. B* 25.6 (Mar. 1982), pp. 4317–4320. DOI: 10.1103/PhysRevB.25.4317.

[75] Siqing Wei and M. Y. Chou. "Ab initio calculation of force constants and full phonon dispersions." In: *Phys. Rev. Lett.* 69.19 (Nov. 1992), pp. 2799–2802. DOI: 10.1103/PhysRevLett.69.2799.

[76] N. E. Zein. "Density Functional Calculations of Elastic Moduli and Phonon Spectra of Crystals." In: *Fiz. Tverd. Tela* 26 (1984), p. 3024. English Translation in Sov. Phys. Solid State 26.10 (1984), pp. 1825-1828.

[77] P. D. DeCicco, F. A. Johnson, and Robert Allan Smith. "The quantum theory of lattice dynamics." In: *Proceedings of the Royal Society of London*. Vol. A. IV 310. Mathematical and Physical Sciences, 1969. DOI: 10.1098/rspa.1969.0066.

[78] L. J. SHAM. "Electronic Contribution to Lattice Dynamics in Insulating Crystals." In: *Phys. Rev.* 188.3 (Dec. 1969), pp. 1431–1439. DOI: 10.1103/PhysRev.188.1431.

[79] Robert M. Pick, Morrel H. Cohen, and Richard M. Martin. "Microscopic Theory of Force Constants in the Adiabatic Approximation." In: *Phys. Rev. B* 1.2 (Jan. 1970), pp. 910–920. DOI: 10.1103/PhysRevB.1.910.

[80] Stefano Baroni, Paolo Giannozzi, and Andrea Testa. "Green's-function approach to linear response in solids." In: *Phys. Rev. Lett.* 58.18 (May 1987), pp. 1861–1864. DOI: 10.1103/PhysRevLett.58.1861.

[81] X. Gonze and J.-P. Vigneron. "Density-functional approach to nonlinear-response coefficients of solids." In: *Phys. Rev. B* 39.18 (June 1989), pp. 13120–13128. DOI: 10.1103/PhysRevB.39.13120.

[82] Xavier Gonze, Douglas C. Allan, and Michael P. Teter. “Dielectric tensor, effective charges, and phonons in α-quartz by variational density-functional perturbation theory.” In: *Phys. Rev. Lett.* 68.24 (June 1992), pp. 3603–3606. DOI: `10.1103/PhysRevLett.68.3603`.

[83] Xavier Gonze. “Perturbation expansion of variational principles at arbitrary order.” In: *Phys. Rev. A* 52.2 (Aug. 1995), pp. 1086–1095. DOI: `10.1103/PhysRevA.52.1086`.

[84] Xavier Gonze. “Adiabatic density-functional perturbation theory.” In: *Phys. Rev. A* 52.2 (Aug. 1995), pp. 1096–1114. DOI: `10.1103/PhysRevA.52.1096`.

[85] Xavier Gonze. “First-principles responses of solids to atomic displacements and homogeneous electric fields: Implementation of a conjugate-gradient algorithm.” In: *Phys. Rev. B* 55.16 (Apr. 1997), pp. 10337–10354. DOI: `10.1103/PhysRevB.55.10337`.

[86] Stefano de Gironcoli. “Lattice dynamics of metals from density-functional perturbation theory.” In: *Phys. Rev. B* 51.10 (Mar. 1995), pp. 6773–6776. DOI: `10.1103/PhysRevB.51.6773`.

[87] Stefano Baroni et al. “Phonons and related crystal properties from density-functional perturbation theory.” In: *Rev. Mod. Phys.* 73.2 (July 2001), pp. 515–562. DOI: `10.1103/RevModPhys.73.515`.

[88] Daniel Aaron Klüppelberg. “First-principle investigation of displacive response in complex solids.” PhD thesis. RWTH Aachen University, 2015. ISBN: 978-3-95806-123-1. URL: `http://hdl.handle.net/2128/10020`. Schriften des Forschungszentrums Jülich, Key Technologies Volume 119.

[89] D. A. Bozhko et al. “Magnon-phonon interactions in magnon spintronics (Review article).” In: *Low Temperature Physics* 46.4 (2020), pp. 383–399. DOI: `10.1063/10.0000872`.

[90] R. F. Sabiryanov and S. S. Jaswal. “Magnons and Magnon-Phonon Interactions in Iron.” In: *Phys. Rev. Lett.* 83.10 (Sept. 1999), pp. 2062–2064. DOI: `10.1103/PhysRevLett.83.2062`.

[91] Cassidy Berk et al. “Strongly coupled magnon-phonon dynamics in a single nanomagnet.” In: *Nature Communications* 10.1 (2019), p. 2652. DOI: `10.1038/s41467-019-10545-x`.

[92] Xavier Gonze, Gian-Marco Rignanese, and Razvan Caracas. “First-principle studies of the lattice dynamics of crystals, and related properties.” In: *Zeitschrift für Kristallographie - Crystalline Materials* 220 (Sept. 2009), pp. 458–472. DOI: `10.1524/zkri.220.5.458.65077`.

[93] R. Kouba et al. “Phonons and electron-phonon interaction by linear-response theory within the LAPW method.” In: *Phys. Rev. B* 64.18 (Aug. 2001), p. 184306. DOI: `10.1103/PhysRevB.64.184306`.

[94] Joo-Hyoung Lee, Young-Chung Hsue, and Arthur J. Freeman. “Magnetically induced variations in phonon frequencies.” In: *Phys. Rev. B* 73.17 (May 2006), p. 172405. DOI: `10.1103/PhysRevB.73.172405`.

[95] J. H. Lee. “First-principles Linear Response All-Electron FLAPW Study of Lattice Dynamics/phonons and the Effect of Magnetism.” PhD thesis. Northwesterns University, 2005.

[96] K. Dewhurst and S. Sharma. *The Elk LAPW Code*. URL: https://www2.mpi-halle.mpg.de/theory_department/research/elk_code_development/?L=0%27A%3D0 (visited on 09/14/2021).

[97] S. Y. Savrasov. "Linear-response theory and lattice dynamics: A muffin-tin-orbital approach." In: *Phys. Rev. B* 54.23 (Dec. 1996), pp. 16470–16486. DOI: 10.1103/PhysRevB.54.16470.

[98] Rici Yu and H. Krakauer. "Linear-response calculations within the linearized augmented plane-wave method." In: *Phys. Rev. B* 49.7 (Feb. 1994), pp. 4467–4477. DOI: 10.1103/PhysRevB.49.4467.

[99] Markus Betzinger et al. "Precise response functions in all-electron methods: Application to the optimized-effective-potential approach." In: *Phys. Rev. B* 85.24 (June 2012), p. 245124. DOI: 10.1103/PhysRevB.85.245124.

[100] Peter Blaha et al. "WIEN2k: An APW+lo program for calculating the properties of solids." In: *The Journal of Chemical Physics* 152.7 (2020), p. 074101. DOI: 10.1063/1.5143061.

[101] M. Weinert et al. "FLAPW: applications and implementations." In: *Journal of Physics: Condensed Matter* 21.8 (Jan. 2009), p. 084201. DOI: 10.1088/0953-8984/21/8/084201.

[102] Andris Gulans et al. "exciting: a full-potential all-electron package implementing density-functional theory and many-body perturbation theory." In: *Journal of Physics: Condensed Matter* 26.36 (Aug. 2014), p. 363202. DOI: 10.1088/0953-8984/26/36/363202. URL: http://exciting.wikidot.com (visited on 09/14/2021).

[103] P. Pulay. "Ab initio calculation of force constants and equilibrium geometries in polyatomic molecules." In: *Molecular Physics* 17.2 (1969), pp. 197–204. DOI: 10.1080/00268976900100941.

[104] Stefan Blügel and Gustav Bihlmayer. "Electronic Structure of Matter." In: *Memristive Phenomena. From Fundamental Physics to Neuromorphic Computing*. Lecture Notes of the 47th IFF Spring School 2016. Ed. by Rainer Waser and Matthias Wuttig. Vol. 113. Key Technologies. Forschungszentrum Jülich GmbH, 2016. ISBN: 978-3-95806-091-3. URL: http://hdl.handle.net/2128/10013.

[105] NobelPrize.org (NobelMedia AB 2021). *The Nobel Prize in Chemistry*. 1998. URL: https://www.nobelprize.org/prizes/chemistry/1998/summary/ (visited on 02/12/2021).

[106] Gabriel R. Schleder et al. "From DFT to machine learning: recent approaches to materials science–a review." In: *J. Phys. Mater.* 2.3 (May 2019), p. 032001. DOI: 10.1088/2515-7639/ab084b.

[107] L. H. Thomas. "The calculation of atomic fields." In: *Mathematical Proceedings of the Cambridge Philosophical Society* 23.5 (Jan. 1927), pp. 542–548. DOI: 10.1017/S0305004100011683.

[108] Enrico Fermi. "Un metodo statistico per la determinazione di alcune priopriet̀a dell'atomo." In: *Atti Accad. Naz. Lincei¸ Cl. Sci. Fis. Mat. Nat. Rend.* 6 (1927), pp. 602–607.

[109] P. A. M. Dirac. “Note on Exchange Phenomena in the Thomas Atom.” In: *Mathematical Proceedings of the Cambridge Philosophical Society* 26.3 (1930), pp. 376–385. DOI: 10.1017/S0305004100016108.

[110] Mel Levy. “Universal variational functionals of electron densities, first-order density matrices, and natural spin-orbitals and solution of the v-representability problem.” In: *Proceedings of the National Academy of Sciences* 76.12 (1979), pp. 6062–6065. DOI: 10.1073/pnas.76.12.6062.

[111] Mel Levy. “Electron densities in search of Hamiltonians.” In: *Phys. Rev. A* 26.3 (Sept. 1982), pp. 1200–1208. DOI: 10.1103/PhysRevA.26.1200.

[112] Mel Levy and John P. Perdew. “The Constrained Search Formulation of Density Functional Theory.” In: *Density Functional Methods In Physics*. Ed. by Reiner M. Dreizler and João da Providência. Boston, MA: Springer US, 1985, pp. 11–30. ISBN: 978-1-4757-0818-9. DOI: 10.1007/978-1-4757-0818-9_2.

[113] Elliott H. Lieb. In: *Physics as Natural Philosophy*. Ed. by A. Shimony and H. Feshbach. Cambridge: MIT Press, 1982, p. 111.

[114] Elliott H. Lieb. “Density Functionals for Coulomb Systems.” In: *International Journal of Quantum Chemistry* 24.3 (1983), pp. 243–277. DOI: 10.1002/qua.560240302.

[115] Elliott H. Lieb. “Density Functionals for Coulomb Systems.” In: *Density Functional Methods In Physics*. Ed. by Reiner M. Dreizler and João da Providência. Boston, MA: Springer US, 1985, pp. 31–80. ISBN: 978-1-4757-0818-9. DOI: 10.1007/978-1-4757-0818-9_3.

[116] N. David Mermin. “Thermal Properties of the Inhomogeneous Electron Gas.” In: *Phys. Rev.* 137.5A (Mar. 1965), A1441–A1443. DOI: 10.1103/PhysRev.137.A1441.

[117] J. C. Slater. “Wave Functions in a Periodic Potential.” In: *Phys. Rev.* 51.10 (May 1937), pp. 846–851. DOI: 10.1103/PhysRev.51.846.

[118] Marjana Ležaić and Yuriy Mokrousov. “Introduction to Density Functional Theory.” In: *Computing Solids. Models, ab-initio methods and supercomputing*. Lecture Notes of the 45th IFF Spring School 2014. Ed. by Stefan Blügel et al. Vol. 74. Key Technologies. Forschungszentrum Jülich GmbH, 2014. ISBN: 978-3-89336-912-6. URL: http://hdl.handle.net/2128/8540.

[119] Personal communication with Stefan Blügel.

[120] Mel Levy, John P. Perdew, and Viraht Sahni. “Exact differential equation for the density and ionization energy of a many-particle system.” In: *Phys. Rev. A* 30.5 (Nov. 1984), pp. 2745–2748. DOI: 10.1103/PhysRevA.30.2745.

[121] D. M. Ceperley and B. J. Alder. “Ground State of the Electron Gas by a Stochastic Method.” In: *Phys. Rev. Lett.* 45.7 (Aug. 1980), pp. 566–569. DOI: 10.1103/PhysRevLett.45.566.

[122] S. H. Vosko, L. Wilk, and M. Nusair. “Accurate spin-dependent electron liquid correlation energies for local spin density calculations: a critical analysis.” In: *Canadian Journal of Physics* 58.8 (1980), pp. 1200–1211. DOI: 10.1139/p80-159.

[123] J. C. Slater. “A Simplification of the Hartree-Fock Method.” In: *Phys. Rev.* 81.3 (Feb. 1951), pp. 385–390. DOI: 10.1103/PhysRev.81.385.

[124] Rajendra R. Zope and Brett I. Dunlap. “Slater’s Exchange Parameters α for Analytic and Variational Xα Calculations.” In: *J. Chem. Theory Comput.* 1.6 (Nov. 2005), pp. 1193–1200. DOI: `10.1021/ct050166w`.

[125] John W. D. Connolly. “The Xα Method.” In: *Semiempirical Methods of Electronic Structure Calculation: Part A: Techniques*. Ed. by Gerald A. Segal. Boston, MA: Springer US, 1977, pp. 105–132. ISBN: 978-1-4684-2556-7. DOI: `10.1007/978-1-4684-2556-7_4`.

[126] Frank Herman, John P. Van Dyke, and Irene B. Ortenburger. “Improved Statistical Exchange Approximation for Inhomogeneous Many-Electron Systems.” In: *Phys. Rev. Lett.* 22.16 (Apr. 1969), pp. 807–811. DOI: `10.1103/PhysRevLett.22.807`.

[127] Personal communication with Gustav Bihlmayer.

[128] Stefan Blügel. “Density Functional Theory in Practice.” In: *Computational Condensed Matter Physics*. Lecture Manuscripts of the 37th Spring School of the Institute of Solid State Research. Ed. by Stefan Blügel et al. Vol. 32. Matter and Materials. Forschungszentrum Jülich GmbH, 2006. ISBN: 3-89336-430-7. URL: `http://hdl.handle.net/2128/2396`.

[129] S. Blügel. *First principles calculations of the electronic structure of magnetic overlayers on transition metal surfaces*. Ed. by Verlag Jülich. Vol. 2197. Berichte der Kernforschungsanlage Jülich. Kernforschungsanlage Jülich, 1988. URL: `http://hdl.handle.net/2128/18476`.

[130] G. P. Kerker. “Efficient iteration scheme for self-consistent pseudopotential calculations.” In: *Phys. Rev. B* 23.6 (Mar. 1981), pp. 3082–3084. DOI: `10.1103/PhysRevB.23.3082`.

[131] P.-M. Anglade and X. Gonze. “Preconditioning of self-consistent-field cycles in density-functional theory: The extrapolar method.” In: *Phys. Rev. B* 78.4 (July 2008), p. 045126. DOI: `10.1103/PhysRevB.78.045126`.

[132] D. Wortmann. “DFT in practice.” In: *Computing Solids. Models, ab-initio methods and supercomputing*. Lecture Notes of the 45th IFF Spring School 2014. Ed. by Stefan Blügel et al. Vol. 74. Key Technologies. Forschungszentrum Jülich GmbH, 2014. ISBN: 978-3-89336-912-6. URL: `http://hdl.handle.net/2128/8540`.

[133] Stefan Blügel. “Complex Magnetism.” In: *Computing Solids. Models, ab-initio methods and supercomputing*. Lecture Notes of the 45th IFF Spring School 2014. Ed. by Stefan Blügel et al. Vol. 74. Key Technologies. Forschungszentrum Jülich GmbH, 2014. ISBN: 978-3-89336-912-6. URL: `http://hdl.handle.net/2128/8540`.

[134] G. Bihlmayer. “Magnetism in Density-Functional Theory.” In: *Computational Condensed Matter Physics*. Lecture Manuscripts of the 37th Spring School of the Institute of Solid State Research. Ed. by Stefan Blügel et al. Vol. 32. Matter and Materials. Forschungszentrum Jülich GmbH, 2006. ISBN: 3-89336-430-7. URL: `http://hdl.handle.net/2128/2396`.

[135] L. N. Oliveira, E. K. U. Gross, and W. Kohn. “Density-Functional Theory for Superconductors.” In: *Phys. Rev. Lett.* 60.23 (June 1988), pp. 2430–2433. DOI: `10.1103/PhysRevLett.60.2430`.

[136] M. Lüders et al. “Ab initio theory of superconductivity. I. Density functional formalism and approximate functionals.” In: *Phys. Rev. B* 72.2 (July 2005), p. 024545. DOI: `10.1103/PhysRevB.72.024545`.

[137] M. A. L. Marques et al. “Ab initio theory of superconductivity. II. Application to elemental metals.” In: *Phys. Rev. B* 72.2 (July 2005), p. 024546. DOI: `10.1103/PhysRevB.72.024546`.

[138] Antonio Sanna. “Introduction to Superconducting Density Functional Theory.” In: *The Physics of Correlated Insulators, Metals, and Superconductors*. Lecture Notes of the Autumn School on Correlated Electrons 2017. Ed. by Eva Pavarini et al. Vol. 7. Modeling and Simulation. Forschungszentrum Jülich GmbH, 2017. ISBN: 978-3-95806-224-5. URL: `http://hdl.handle.net/2128/15283`.

[139] Narbe Mardirossian and Martin Head-Gordon. “Thirty years of density functional theory in computational chemistry: an overview and extensive assessment of 200 density functionals.” In: *Molecular Physics* 115.19 (2017), pp. 2315–2372. DOI: `10.1080/00268976.2017.1333644`.

[140] Ryo Nagai, Ryosuke Akashi, and Osamu Sugino. “Completing density functional theory by machine learning hidden messages from molecules.” In: *npj Computational Materials* 6.1 (2020), p. 43. DOI: `10.1038/s41524-020-0310-0`.

[141] Sebastian Dick and Marivi Fernandez-Serra. “Machine learning accurate exchange and correlation functionals of the electronic density.” In: *Nature Communications* 11.1 (2020), p. 3509. DOI: `10.1038/s41467-020-17265-7`.

[142] K. Parlinski. “Lattice Dynamics: Vibrational Modes.” In: *Encyclopedia of Condensed Matter Physics*. Ed. by Franco Bassani, Gerald L. Liedl, and Peter Wyder. Oxford: Elsevier, 2005, pp. 98–102. ISBN: 978-0-12-369401-0. DOI: `10.1016/B0-12-369401-9/00509-X`.

[143] R H Olsson III and I El-Kady. “Microfabricated phononic crystal devices and applications.” In: *Measurement Science and Technology* 20.1 (Nov. 2008), p. 012002. DOI: `10.1088/0957-0233/20/1/012002`.

[144] Xiang Li et al. “Designing phononic crystal with anticipated band gap through a deep learning based data-driven method.” In: *Computer Methods in Applied Mechanics and Engineering* 361 (2020), p. 112737. DOI: `10.1016/j.cma.2019.112737`.

[145] B. N. Brockhouse and A. T. Stewart. “Scattering of Neutrons by Phonons in an Aluminum Single Crystal.” In: *Phys. Rev.* 100.2 (Oct. 1955), pp. 756–757. DOI: `10.1103/PhysRev.100.756`.

[146] B. N. Brockhouse et al. “Crystal Dynamics of Lead. I. Dispersion Curves at 100 °K.” In: *Phys. Rev.* 128.3 (Nov. 1962), pp. 1099–1111. DOI: `10.1103/PhysRev.128.1099`.

[147] Bertram N. Brockhouse. “Slow neutron spectroscopy and the grand atlas of the physical world.” In: *Rev. Mod. Phys.* 67.4 (Oct. 1995), pp. 735–751. DOI: `10.1103/RevModPhys.67.735`.

[148] B. Dorner et al. “First measurement of a phonon dispersion curve by inelastic X-ray scattering.” In: *Zeitschrift für Physik B Condensed Matter* 69.2 (1987), pp. 179–183. DOI: `10.1007/BF01307274`.

[149] R. Colella and B. W. Batterman. “X-Ray Determination of Phonon Dispersion in Vanadium.” In: *Phys. Rev. B* 1.10 (May 1970), pp. 3913–3921. DOI: `10.1103/PhysRevB.1.3913`.

[150] M. Mohr et al. “Phonon dispersion of graphite by inelastic x-ray scattering.” In: *Phys. Rev. B* 76.3 (July 2007), p. 035439. DOI: `10.1103/PhysRevB.76.035439`.

[151] J. T. Gourley and W. A. Runciman. “Multiphonon infrared absorption spectra of MgO and CaO.” In: *Journal of Physics C: Solid State Physics* 6.3 (Feb. 1973), pp. 583–592. DOI: `10.1088/0022-3719/6/3/021`.

[152] R. Saito et al. “Probing Phonon Dispersion Relations of Graphite by Double Resonance Raman Scattering.” In: *Phys. Rev. Lett.* 88.2 (Dec. 2001), p. 027401. DOI: `10.1103/PhysRevLett.88.027401`.

[153] J. Fritsch and U. Schröder. “Density functional calculation of semiconductor surface phonons.” In: *Physics Reports* 309.4 (1999), pp. 209–331. DOI: `10.1016/S0370-1573(98)00034-9`.

[154] J. M. Dickey and A. Paskin. “Computer Simulation of the Lattice Dynamics of Solids.” In: *Phys. Rev.* 188.3 (Dec. 1969), pp. 1407–1418. DOI: `10.1103/PhysRev.188.1407`.

[155] Jichen Li. “Simulations of inelastic neutron scattering spectra by molecular dynamics.” In: *Physica B: Condensed Matter* 263-264 (1999), pp. 404–407. DOI: `10.1016/S0921-4526(98)01397-0`.

[156] P. Heino. “Dispersion and thermal resistivity in silicon nanofilms by molecular dynamics.” In: *The European Physical Journal B* 60.2 (2007), pp. 171–179. DOI: `10.1140/epjb/e2007-00342-9`.

[157] Ling Ti Kong. “Phonon dispersion measured directly from molecular dynamics simulations.” In: *Computer Physics Communications* 182.10 (2011), pp. 2201–2207. DOI: `10.1016/j.cpc.2011.04.019`.

[158] Yoichiro Nambu. “Axial Vector Current Conservation in Weak Interactions.” In: *Phys. Rev. Lett.* 4.7 (Apr. 1960), pp. 380–382. DOI: `10.1103/PhysRevLett.4.380`.

[159] J. Goldstone. “Field theories with « Superconductor » solutions.” In: *Il Nuovo Cimento (1955-1965)* 19.1 (1961), pp. 154–164. DOI: `10.1007/BF02812722`.

[160] Marco Vallone. “Higgs and Goldstone Modes in Crystalline Solids.” In: *physica status solidi (b)* 257.3 (2020), p. 1900443. DOI: `10.1002/pssb.201900443`.

[161] M. T. Yin and Marvin L. Cohen. “Microscopic Theory of the Phase Transformation and Lattice Dynamics of Si.” In: *Phys. Rev. Lett.* 45.12 (Sept. 1980), pp. 1004–1007. DOI: `10.1103/PhysRevLett.45.1004`.

[162] K.-M. Ho, C. L. Fu, and B. N. Harmon. “Vibrational frequencies via total-energy calculations. Applications to transition metals.” In: *Phys. Rev. B* 29.4 (Feb. 1984), pp. 1575–1587. DOI: `10.1103/PhysRevB.29.1575`.

[163] K. -M. Ho et al. “Vibrational Frequencies and Structural Properties of Transition Metals via Total-Energy Calculations.” In: *Phys. Rev. Lett.* 49.9 (Aug. 1982), pp. 673–676. DOI: `10.1103/PhysRevLett.49.673`.

[164] A. Togo and I. Tanaka. “First principles phonon calculations in materials science.” In: *Scr. Mater.* 108 (Nov. 2015), pp. 1–5.

[165] Egil A. Hylleraas. “Über den Grundterm der Zweielektronenprobleme von H−, He, Li+, Be++ usw.” In: *Zeitschrift für Physik* 65.3 (1930), pp. 209–225. DOI: 10.1007/BF01397032.

[166] M. Yang, P. Senet, and C. Van Alsenoy. “DFT study of polarizabilities and dipole moments of water clusters.” In: *International Journal of Quantum Chemistry* 101.5 (2005), pp. 535–542. DOI: 10.1002/qua.20308.

[167] Yang Shen et al. “Phonon anharmonicity and components of the entropy in palladium and platinum.” In: *Phys. Rev. B* 93.21 (June 2016), p. 214303. DOI: 10.1103/PhysRevB.93.214303.

[168] Shobhana Narasimhan and Stefano de Gironcoli. “Ab initio calculation of the thermal properties of Cu: Performance of the LDA and GGA.” In: *Phys. Rev. B* 65.6 (Jan. 2002), p. 064302. DOI: 10.1103/PhysRevB.65.064302.

[169] Hans Hellmann. *Einführung in die Quantumchemie*. Deuticke, Leipzig, 1937.

[170] R. P. Feynman. “Forces in Molecules.” In: *Phys. Rev.* 56.4 (Aug. 1939), pp. 340–343. DOI: 10.1103/PhysRev.56.340.

[171] R. M. Sternheimer. “Electronic Polarizabilities of Ions from the Hartree-Fock Wave Functions.” In: *Phys. Rev.* 96.4 (Nov. 1954), pp. 951–968. DOI: 10.1103/PhysRev.96.951.

[172] Richard M. Martin, Lucia Reining, and David M. Ceperley. *Interacting electrons. Theory and Computational Approaches*. 1st ed. Cambridge University Press, 2016. ISBN: 9780521871501.

[173] Raffaele Resta. “Microscopic electronic screening in semiconductors.” In: *Festkörperprobleme 25: 5th General Conference of the Condensed Matter Division (CMD) 18–22 March 1985, Technische Universität Berlin (West) Plenary Lectures and Lectures held at the Symposia Sections of the CMD: Liquids Low Temperature Macromolecular Physics Magnetism Metals Semiconductors and Insulators Surfaces and Interfaces*. Ed. by P. Grosse. Berlin, Heidelberg: Springer Berlin Heidelberg, 1985, pp. 183–194. ISBN: 978-3-540-75361-2. DOI: 10.1007/BFb0108146.

[174] Mark S. Hybertsen and Steven G. Louie. “Ab initio static dielectric matrices from the density-functional approach. I. Formulation and application to semiconductors and insulators.” In: *Phys. Rev. B* 35.11 (Apr. 1987), pp. 5585–5601. DOI: 10.1103/PhysRevB.35.5585.

[175] Stephen L. Adler. “Quantum Theory of the Dielectric Constant in Real Solids.” In: *Phys. Rev.* 126.2 (Apr. 1962), pp. 413–420. DOI: 10.1103/PhysRev.126.413.

[176] Nathan Wiser. “Dielectric Constant with Local Field Effects Included.” In: *Phys. Rev.* 129.1 (Jan. 1963), pp. 62–69. DOI: 10.1103/PhysRev.129.62.

[177] C. Kittel. *Quantum Theory of Solids*. 2nd rev. ed. New York: John Wiley & Sons, Inc., 1964.

[178] W. Jones and N. H. March. *Theoretical Solid State Physics*. 2nd. New York: John Wiley & Sons, Inc., 1976.

[179] N. Marzari and D. J. Singh. “Dielectric response of oxides in the weighted density approximation.” In: *Phys. Rev. B* 62.19 (Nov. 2000), pp. 12724–12729. DOI: 10.1103/PhysRevB.62.12724.

[180] Phivos Mavropoulos. “Scattering theory of Bloch wavefunctions off defects in crystals.” In: *Computing Solids. Models, ab-initio methods and supercomputing*. Lecture Notes of the 45th IFF Spring School 2014. Ed. by Stefan Blügel et al. Vol. 74. Key Technologies. Forschungszentrum Jülich GmbH, 2014. ISBN: 978-3-89336-912-6. URL: `http://hdl.handle.net/2128/8540`.

[181] Changyol Lee and Xavier Gonze. “Ab initio calculation of the thermodynamic properties and atomic temperature factors of $\mathrm{SiO_2}$ α-quartz and stishovite.” In: *Phys. Rev. B* 51.13 (Apr. 1995), pp. 8610–8613. DOI: `10.1103/PhysRevB.51.8610`.

[182] S. Y. Savrasov and D. Y. Savrasov. “Electron-phonon interactions and related physical properties of metals from linear-response theory.” In: *Phys. Rev. B* 54.23 (Dec. 1996), pp. 16487–16501. DOI: `10.1103/PhysRevB.54.16487`.

[183] G. Grimvall. *The electron phonon interaction in metals*. Series of monographs on selected topics in solid state physics; Amsterdam: North Holland, 1981, XIV, 304 pages. ISBN: 9780444861054.

[184] Philip B. Allen and Božidar Mitrović. “Theory of Superconducting Tc.” In: *Solid State Physics*. Ed. by Henry Ehrenreich, Frederick Seitz, and David Turnbull. Vol. 37. Academic Press, 1983, pp. 1–92. DOI: `10.1016/S0081-1947(08)60665-7`.

[185] G. M. Eliashberg. “Interactions between electrons and lattice vibrations in a superconductor.” In: *Zh. Eksp. Teor. Fiz.* 38.3 (Sept. 1960), p. 966. English Translation in Sov. Phys. JETP 11 (1960), 696.

[186] W. L. McMillan. “Transition Temperature of Strong-Coupled Superconductors.” In: *Phys. Rev.* 167.2 (Mar. 1968), pp. 331–344. DOI: `10.1103/PhysRev.167.331`.

[187] P. B. Allen and R. C. Dynes. “Transition temperature of strong-coupled superconductors reanalyzed.” In: *Phys. Rev. B* 12.3 (Aug. 1975), pp. 905–922. DOI: `10.1103/PhysRevB.12.905`.

[188] J. M. Ziman. *Electrons and phonons : the theory of transport phenomena in solids*. Oxford classic texts in the physical sciences. Oxford: Clarendon Press, 2001, XIV, 554 pages. ISBN: 0198507798.

[189] Philip B. Allen. “Fermi-surface harmonics: A general method for nonspherical problems. Application to Boltzmann and Eliashberg equations.” In: *Phys. Rev. B* 13.4 (Feb. 1976), pp. 1416–1427. DOI: `10.1103/PhysRevB.13.1416`.

[190] P. B. Allen. “New method for solving Boltzmann’s equation for electrons in metals.” In: *Phys. Rev. B* 17.10 (May 1978), pp. 3725–3734. DOI: `10.1103/PhysRevB.17.3725`.

[191] P. B. Littlewood. “On the calculation of the macroscopic polarisation induced by an optic phonon.” In: *Journal of Physics C: Solid State Physics* 13.26 (Sept. 1980), pp. 4893–4903. DOI: `10.1088/0022-3719/13/26/011`.

[192] R. Resta and K. Kunc. “Self-consistent theory of electronic states and dielectric response in semiconductors.” In: *Phys. Rev. B* 34.10 (Nov. 1986), pp. 7146–7157. DOI: `10.1103/PhysRevB.34.7146`.

[193] H. Böttger. *Principles of the Theory of Lattice Dynamics*. Physik-Verlag, Weinheim, 1983.

[194] Stefano Baroni, Paolo Giannozzi, and Andrea Testa. “Elastic Constants of Crystals from Linear-Response Theory.” In: *Phys. Rev. Lett.* 59.23 (Dec. 1987), pp. 2662–2665. DOI: `10.1103/PhysRevLett.59.2662`.

[195] D. R. Hamann et al. “Metric tensor formulation of strain in density-functional perturbation theory.” In: *Phys. Rev. B* 71.3 (Jan. 2005), p. 035117. DOI: `10.1103/PhysRevB.71.035117`.

[196] Xifan Wu, David Vanderbilt, and D. R. Hamann. “Systematic treatment of displacements, strains, and electric fields in density-functional perturbation theory.” In: *Phys. Rev. B* 72.3 (July 2005), p. 035105. DOI: `10.1103/PhysRevB.72.035105`.

[197] S. Y. Savrasov. “Linear Response Calculations of Spin Fluctuations.” In: *Phys. Rev. Lett.* 81.12 (Sept. 1998), pp. 2570–2573. DOI: `10.1103/PhysRevLett.81.2570`.

[198] Felix Bloch. “Über die Quantenmechanik der Elektronen in Kristallgittern.” In: *Zeitschrift für Physik* 52.7 (1929), pp. 555–600. DOI: `10.1007/BF01339455`.

[199] Marvin L. Cohen. “Electronic structure of solids.” In: *Physics Reports* 110.5 (1984), pp. 293–309. DOI: `10.1016/0370-1573(84)90192-3`.

[200] Warren E. Pickett. “Pseudopotential methods in condensed matter applications.” In: *Computer Physics Reports* 9.3 (1989), pp. 115–197. DOI: `10.1016/0167-7977(89)90002-6`.

[201] J. C. Slater. “Wave Functions in a Periodic Potential.” In: *Phys. Rev.* 51.10 (May 1937), pp. 846–851. DOI: `10.1103/PhysRev.51.846`.

[202] J. C. Slater. “An Augmented Plane Wave Method for the Periodic Potential Problem.” In: *Phys. Rev.* 92.3 (Nov. 1953), pp. 603–608. DOI: `10.1103/PhysRev.92.603`.

[203] M. M. Saffren and J. C. Slater. “An Augmented Plane-Wave Method for the Periodic Potential Problem. II.” In: *Phys. Rev.* 92.5 (Dec. 1953), pp. 1126–1128. DOI: `10.1103/PhysRev.92.1126`.

[204] J. C. Slater. “Energy Band Calculations by the Augmented Plane Wave Method*.” In: *Advances in Quantum Chemistry*. Ed. by Per-Olov Löwdin. Vol. 1. Academic Press, 1964, pp. 35–58. DOI: `10.1016/S0065-3276(08)60374-3`.

[205] Terry L. Loucks. *Augmented Plane Wave Method. A Guide to Performing Electronic Structure Calculations*. Frontiers in physics. New York: W. A. Benjamin, 1967.

[206] O. Krogh Andersen. “Linear methods in band theory.” In: *Phys. Rev. B* 12.8 (Oct. 1975), pp. 3060–3083. DOI: `10.1103/PhysRevB.12.3060`.

[207] H. Bross et al. “New Version of the Modified Augmented-Plane-Wave Method.” In: *Phys. Rev. B* 2.8 (Oct. 1970), pp. 3098–3103. DOI: `10.1103/PhysRevB.2.3098`.

[208] D. D. Koelling and G. O. Arbman. “Use of energy derivative of the radial solution in an augmented plane wave method: application to copper.” In: *Journal of Physics F: Metal Physics* 5.11 (1975), p. 2041. DOI: `10.1088/0305-4608/5/11/016`.

[209] R. V. Kasowski. “Band Structure of NiS as Calculated Using a Simplified Linear-Combination-of-Muffin-Tin-Orbitals Method.” In: *Phys. Rev. B* 8.4 (Aug. 1973), pp. 1378–1382. DOI: `10.1103/PhysRevB.8.1378`.

[210] Paul M. Marcus. “Variational methods in the computation of energy bands.” In: *International Journal of Quantum Chemistry* 1.S1 (1967), pp. 567–588. DOI: `10.1002/qua.560010659`.

[211] H. A. Bethe and E. E. Salpeter. *Quantum Mechanics of One- and Two-Electron Systems*. Plenum, New York, 1977.

[212] Gustav Bihlmayer. “Relativistic effects in solids.” In: *Computing Solids. Models, ab-initio methods and supercomputing*. Lecture Notes of the 45th IFF Spring School 2014. Ed. by Stefan Blügel et al. Vol. 74. Key Technologies. Forschungszentrum Jülich GmbH, 2014. ISBN: 978-3-89336-912-6. URL: `http://hdl.handle.net/2128/8540`.

[213] D. D. Koelling and B. N. Harmon. “A technique for relativistic spin-polarised calculations.” In: *Journal of Physics C: Solid State Physics* 10.16 (Aug. 1977), pp. 3107–3114. DOI: `10.1088/0022-3719/10/16/019`.

[214] T. Takeda. “The scalar relativistic approximation.” In: *Zeitschrift für Physik B Condensed Matter* 32.1 (1978), pp. 43–48. DOI: `10.1007/BF01322185`.

[215] J. H. Wood and A. Michael Boring. “Improved Pauli Hamiltonian for local-potential problems.” In: *Phys. Rev. B* 18.6 (Sept. 1978), pp. 2701–2711. DOI: `10.1103/PhysRevB.18.2701`.

[216] H. Gollisch and L. Fritsche. “Relativistic one-particle equation for electron states of heavy metals.” In: *physica status solidi (b)* 86.1 (1978), pp. 145–150. DOI: `10.1002/pssb.2220860116`.

[217] Chun Li et al. “Magnetic anisotropy in low-dimensional ferromagnetic systems: Fe monolayers on Ag(001), Au(001), and Pd(001) substrates.” In: *Phys. Rev. B* 42.9 (Sept. 1990), pp. 5433–5442. DOI: `10.1103/PhysRevB.42.5433`.

[218] D. R. Hamann. “Semiconductor Charge Densities with Hard-Core and Soft-Core Pseudopotentials.” In: *Phys. Rev. Lett.* 42.10 (Mar. 1979), pp. 662–665. DOI: `10.1103/PhysRevLett.42.662`.

[219] David Singh. “Ground-state properties of lanthanum: Treatment of extended-core states.” In: *Phys. Rev. B* 43.8 (Mar. 1991), pp. 6388–6392. DOI: `10.1103/PhysRevB.43.6388`.

[220] E. Sjöstedt, L. Nordström, and D. J. Singh. “An alternative way of linearizing the augmented plane-wave method.” In: *Solid State Communications* 114.1 (2000), pp. 15–20. DOI: `10.1016/S0038-1098(99)00577-3`.

[221] Elisabeth Sjöstedt. “Augmented planewaves in the study of electronic structures.” Licentiate Thesis. Uppsala University, Department of Physics, 1999.

[222] José M. Soler and Arthur R. Williams. “Simple formula for the atomic forces in the augmented-plane-wave method.” In: *Phys. Rev. B* 40.3 (July 1989), pp. 1560–1564. DOI: `10.1103/PhysRevB.40.1560`.

[223] José M. Soler and Arthur R. Williams. “Augmented-plane-wave forces.” In: *Phys. Rev. B* 42.15 (Nov. 1990), pp. 9728–9731. DOI: `10.1103/PhysRevB.42.9728`.

[224] Rici Yu, D. Singh, and H. Krakauer. “All-electron and pseudopotential force calculations using the linearized-augmented-plane-wave method.” In: *Phys. Rev. B* 43.8 (Mar. 1991), pp. 6411–6422. DOI: `10.1103/PhysRevB.43.6411`.

[225] Ph. Kurz et al. “Ab initio treatment of noncollinear magnets with the full-potential linearized augmented plane wave method.” In: *Phys. Rev. B* 69.2 (Jan. 2004), p. 024415. DOI: `10.1103/PhysRevB.69.024415`.

[226] D. Wortmann, H. Ishida, and S. Blügel. “Ab initio Green-function formulation of the transfer matrix: Application to complex band structures.” In: *Phys. Rev. B* 65.16 (Mar. 2002), p. 165103. DOI: `10.1103/PhysRevB.65.165103`.

[227] D. Wortmann, H. Ishida, and S. Blügel. “Embedded Green-function approach to the ballistic electron transport through an interface.” In: *Phys. Rev. B* 66.7 (Aug. 2002), p. 075113. DOI: `10.1103/PhysRevB.66.075113`.

[228] E. E. Krasovskii. “Augmented-plane-wave approach to scattering of Bloch electrons by an interface.” In: *Phys. Rev. B* 70.24 (Dec. 2004), p. 245322. DOI: `10.1103/PhysRevB.70.245322`.

[229] Manabu Usuda et al. “All-electron GW calculation based on the LAPW method: Application to wurtzite ZnO.” In: *Phys. Rev. B* 66.12 (Sept. 2002), p. 125101. DOI: `10.1103/PhysRevB.66.125101`.

[230] Christoph Friedrich, Stefan Blügel, and Arno Schindlmayr. “Efficient implementation of the GW approximation within the all-electron FLAPW method.” In: *Phys. Rev. B* 81.12 (Mar. 2010), p. 125102. DOI: `10.1103/PhysRevB.81.125102`.

[231] H. Krakauer, M. Posternak, and A. J. Freeman. “Linearized augmented plane-wave method for the electronic band structure of thin films.” In: *Phys. Rev. B* 19.4 (Feb. 1979), pp. 1706–1719. DOI: `10.1103/PhysRevB.19.1706`.

[232] Y. Mokrousov, G. Bihlmayer, and S. Blügel. “Full-potential linearized augmented plane-wave method for one-dimensional systems: Gold nanowire and iron monowires in a gold tube.” In: *Phys. Rev. B* 72.4 (July 2005), p. 045402. DOI: `10.1103/PhysRevB.72.045402`.

[233] Philipp Kurz. “Non-Collinear Magnetism of Ultrathin Magnetic Films.” written at Institut für Festkörperforschung (IFF) Forschungszentrum Jülich. Diploma thesis. RWTH Aachen University, Jan. 1997.

[234] Philipp Kurz. “Non-collinear magnetism at surfaces and in ultrathin films.” PhD thesis. RWTH Aachen University, 2000. URL: `https://juser.fz-juelich.de/record/30593`. Berichte des Forschungszentrums Jülich; 3832.

[235] P. D. DeCicco. “Self-Consistent Energy Bands and Cohesive Energy of Potassium Chloride.” In: *Phys. Rev.* 153.3 (Jan. 1967), pp. 931–938. DOI: `10.1103/PhysRev.153.931`.

[236] N. Elyashar and D. D. Koelling. “Effect of non-muffin-tin terms on the electronic structure of transition metals: Niobium.” In: *Phys. Rev. B* 13.12 (June 1976), pp. 5362–5372. DOI: `10.1103/PhysRevB.13.5362`.

[237] T. Takeda and J. Kubler. “Linear augmented plane wave method for self-consistent calculations.” In: *Journal of Physics F: Metal Physics* 9.4 (1979), p. 661. DOI: `10.1088/0305-4608/9/4/013`.

[238] Michael E. Peskin and Daniel V. Schroeder. *An Introduction to Quantum Field Theory*. Ed. by David Pines. 1st ed. Westview Press, 1995.

[239] Boon K. Teo and Wai-Kee Li. “The Scales of Time, Length, Mass, Energy, and Other Fundamental Physical Quantities in the Atomic World and the Use of Atomic Units in Quantum Mechanical Calculations.” In: *J. Chem. Educ.* 88.7 (July 2011), pp. 921–928. DOI: `10.1021/ed100524t`.

[240] Francis Halzen and Alan D. Martin. *Quarks & Leptons : An Introductory Course in Modern Particle Physics*. John Wiley & Sons, Inc., 1984.

[241] Hiroshi Yamagami. "Fully relativistic noncollinear magnetism in spin-density-functional theory: Application to USb by means of the fully relativistic spin-polarized LAPW method." In: *Phys. Rev. B* 61.9 (Mar. 2000), pp. 6246–6256. DOI: `10.1103/PhysRevB.61.6246`.

[242] H. Ebert, D. Ködderitzsch, and J. Minár. "Calculating condensed matter properties using the KKR-Green's function method—recent developments and applications." In: *Reports on Progress in Physics* 74.9 (Aug. 2011), p. 096501. DOI: `10.1088/0034-4885/74/9/096501`.

[243] E. Wimmer, H. Krakauer, and A. J. Freeman. "Theory of Surface Electronic Structure." In: *Advances in Electronics and Electron Physics*. Ed. by Peter W. Hawkes. Vol. 65. Academic Press, 1985, pp. 357–434. DOI: `10.1016/S0065-2539(08)60881-1`.

[244] L. F. Mattheiss and D. R. Hamann. "Linear augmented-plane-wave calculation of the structural properties of bulk Cr, Mo, and W." In: *Phys. Rev. B* 33.2 (Jan. 1986), pp. 823–840. DOI: `10.1103/PhysRevB.33.823`.

[245] Jaejun Yu et al. "Origin of electric-field gradients in high-temperature superconductors: $\mathrm{YBa_2Cu_3O_7}$." In: *Phys. Rev. B* 43.1 (Jan. 1991), pp. 532–541. DOI: `10.1103/PhysRevB.43.532`.

[246] G. Lehmann and M. Taut. "On the Numerical Calculation of the Density of States and Related Properties." In: *physica status solidi (b)* 54.2 (1972), pp. 469–477. DOI: `10.1002/pssb.2220540211`.

[247] Peter E. Blöchl, O. Jepsen, and O. K. Andersen. "Improved tetrahedron method for Brillouin-zone integrations." In: *Phys. Rev. B* 49.23 (June 1994), pp. 16223–16233. DOI: `10.1103/PhysRevB.49.16223`.

[248] O. Jepson and O. K. Anderson. "The electronic structure of h.c.p. Ytterbium." In: *Solid State Communications* 9.20 (1971), pp. 1763–1767. DOI: `10.1016/0038-1098(71)90313-9`.

[249] D. J. Chadi and Marvin L. Cohen. "Special Points in the Brillouin Zone." In: *Phys. Rev. B* 8.12 (Dec. 1973), pp. 5747–5753. DOI: `10.1103/PhysRevB.8.5747`.

[250] Su-Huai Wei, Henry Krakauer, and M. Weinert. "Linearized augmented-plane-wave calculation of the electronic structure and total energy of tungsten." In: *Phys. Rev. B* 32.12 (Dec. 1985), pp. 7792–7797. DOI: `10.1103/PhysRevB.32.7792`.

[251] Personal communication with Markus Betzinger.

[252] M. Weinert and J. W. Davenport. "Fractional occupations and density-functional energies and forces." In: *Phys. Rev. B* 45.23 (June 1992), pp. 13709–13712. DOI: `10.1103/PhysRevB.45.13709`.

[253] George W. Hanson. *Operator Theory for Electromagnetics [E-Book] : An Introduction*. Ed. by Alexander B. Yakovlev. New York, NY: Springer, 2002, XIX, 634 p., 28 illus. ISBN: 9781475736793. DOI: `10.1007/978-1-4757-3679-3`.

[254] P. Ehrenfest. "Bemerkung über die angenäherte Gültigkeit der klassischen Mechanik innerhalb der Quantenmechanik." In: *Zeitschrift für Physik* 45.7 (1927), pp. 455–457. DOI: `10.1007/BF01329203`.

[255] Xavier Gonze and Changyol Lee. "Dynamical matrices, Born effective charges, dielectric permittivity tensors, and interatomic force constants from density-functional perturbation theory." In: *Phys. Rev. B* 55.16 (Apr. 1997), pp. 10355–10368. DOI: `10.1103/PhysRevB.55.10355`.

[256] Personal communication with Alexander Neukirchen.

[257] X. Gonze et al. "Interatomic force constants from first principles: The case of α-quartz." In: *Phys. Rev. B* 50.17 (Nov. 1994), pp. 13035–13038. DOI: `10.1103/PhysRevB.50.13035`.

[258] Tosio Kato. "On the eigenfunctions of many-particle systems in quantum mechanics." In: *Communications on Pure and Applied Mathematics* 10.2 (1957), pp. 151–177. DOI: `10.1002/cpa.3160100201`.

[259] Albert Danial. *cloc: v1.92*. Version v1.92. Dec. 2022. DOI: `10.5281/zenodo.5760077`.

[260] Personal communication with Daniel Wortmann.

[261] Personal communication with Aaron Klüppelberg.

[262] *Intel Fortran Compiler*. URL: `https://software.intel.com/content/www/us/en/develop/tools/oneapi/components/fortran-compiler.html#gs.ardytt` (visited on 09/14/2021).

[263] Robert C. Martin. *Clean code : a handbook of agile software craftmanship*. Ed. by Michael C. Feathers et al. Robert C. Martin series. Upper Saddle River, NJ: Prentice Hall, 2009. ISBN: 9780132350884.

[264] Guido Trensch and Wouter Klijn. "Software Development in Science." Lecture Notes of Training Course at Jülich Supercomputing Center. 2017.

[265] *ABINIT*. URL: `www.abinit.org` (visited on 09/14/2021).

[266] *TotalView*. HPC Debugging Software. URL: `https://totalview.io/products/totalview` (visited on 09/14/2021).

[267] Nicholas Nethercote and Julian Seward. "Valgrind: A Framework for Heavyweight Dynamic Binary Instrumentation." In: *Proceedings of ACM SIGPLAN 2007 Conference on Programming Language Design and Implementation (PLDI 2007)*. San Diego, California, USA, June 2007. URL: `https://www.valgrind.org/docs/valgrind2007.pdf`.

[268] Julian Seward and Nicholas Nethercote. "Using Valgrind to detect undefined value errors with bit-precision." In: *Proceedings of the USENIX'05 Annual Technical Conference*. Anaheim, California, USA, Apr. 2005.

[269] *Valgrind*. URL: `https://www.valgrind.org` (visited on 09/14/2021).

[270] Jan Kierfeld. "Computational Physics." Lecture Notes TU Dortmund University. 2017. URL: `http://t1.physik.tu-dortmund.de/files/kierfeld/teaching/LectureNotes/kierfeld_CompPhys.pdf` (visited on 09/07/2021).

[271] Rolf Rannacher. "Numerik 0." In: *Einführung in die Numerische Mathematik, Heidelberg*. Heidelberg University Publishing, 2017. DOI: `10.17885/heiup.206.281`.

[272] Thomas H. Cormen et al. *Introduction to Algorithms*. 3rd ed. The MIT Press Series. Cambridge, UNITED STATES: MIT Press, 2009.

[273] *Density Functional Theory and Electronic Structure (WS2020) – Tutorial. The Birch–Murnaghan equation of state*. FLEUR developed by IAS-1/PGI-1 at Forschungszentrum Jülich. URL: `https://www.flapw.de/master/DFT-2020-tut/latticeConstant/#12-the-birch-murnaghan-equation-of-state` (visited on 09/09/2021).

[274] Raymond Jeanloz. "Universal equation of state." In: *Phys. Rev. B* 38.1 (July 1988), pp. 805–807. DOI: `10.1103/PhysRevB.38.805`.

[275] D. G. Henshaw. "Atomic Distribution in Liquid and Solid Neon and Solid Argon by Neutron Diffraction." In: *Phys. Rev.* 111.6 (Sept. 1958), pp. 1470–1475. DOI: `10.1103/PhysRev.111.1470`.

[276] D. Roundy et al. "Ideal Shear Strengths of fcc Aluminum and Copper." In: *Phys. Rev. Lett.* 82.13 (Mar. 1999), pp. 2713–2716. DOI: `10.1103/PhysRevLett.82.2713`.

[277] R. W. G. Wyckoff. *Crystal Structure*. 2nd ed. New York: Interscience Publishers, 1963.

[278] Personal communication with Gregor Michalicek.

[279] E. P. Wigner. *Group theory and its application to the quantum mechanics of atomic spectra*. Pure and applied physics; New-York, NY: Academic Pr., 1959, XI, 372 pages.

[280] Milton Abramowitz. *Handbook of mathematical functions with formulas, graphs, and mathematical tables : Conference on Mathematical Tables : Cambridge, MA, 15.09.1954-16.09.1954*. Ed. by Milton Abramowitz and Irene A. Stegun. New-York, NY: Dover Publications, 1965.

[281] Wolfram Research Inc. *Mathematica*. Champaign, IL, 2018.

[282] Personal communication with Christoph Friedrich.

[283] John David Jackson. *Classical electrodynamics*. 3rd ed. New York, NY: Wiley, 1999, XXI, 808 pages. ISBN: 047130932X.

[284] Anton Kokalj. "Computer graphics and graphical user interfaces as tools in simulations of matter at the atomic scale." In: *Computational Materials Science* 28.2 (2003). Proceedings of the Symposium on Software Development for Process and Materials Design, pp. 155–168. DOI: `10.1016/S0927-0256(03)00104-6`.

[285] Anton Kokalj. "XCrySDen—a new program for displaying crystalline structures and electron densities." In: *Journal of Molecular Graphics and Modelling* 17.3 (1999), pp. 176–179. DOI: `10.1016/S1093-3263(99)00028-5`.

[286] J. D. Hunter. "Matplotlib: A 2D graphics environment." In: *Computing in Science & Engineering* 9.3 (2007), pp. 90–95. DOI: `10.1109/MCSE.2007.55`.

[287] Charles R. Harris et al. "Array programming with NumPy." In: *Nature* 585.7825 (Sept. 2020), pp. 357–362. DOI: `10.1038/s41586-020-2649-2`.

[288] Susi Lehtola et al. "Recent developments in libxc — A comprehensive library of functionals for density functional theory." In: *SoftwareX* 7 (2018), pp. 1–5. DOI: `10.1016/j.softx.2017.11.002`.

[289] Adly A. Girgis and Fredric M. Ham. "A Quantitative Study of Pitfalls in the FFT." In: *IEEE Transactions on Aerospace and Electronic Systems* AES-16.4 (1980), pp. 434–439. DOI: `10.1109/TAES.1980.308971`.

[290] Gregor Michalicek. “Extending the precision and efficiency of the all-electron full-potential linearized augmented plane-wave density-functional theory method.” PhD thesis. RWTH Aachen University, 2014. ISBN: 978-3-95806-031-9. URL: `http://hdl.handle.net/2128/8553`. Schriften des Forschungszentrums Jülich, Key Technologies Volume 102.

[291] Matteo Frigo and Steven G. Johnson. “The Design and Implementation of FFTW3.” In: *Proceedings of the IEEE* 93.2 (2005). Special issue on “Program Generation, Optimization, and Platform Adaptation”, pp. 216–231.

[292] Rossitza Pentcheva. “Ab-initio Rechnungen zum Zusammenhang zwischen Magnetismus und Struktur ultradünner Filme [E-Book].” German. Berichte des Forschungszentrums Jülich: Nr. 3364. Diploma thesis. Mar. 1997. URL: `http://hdl.handle.net/2128/21838`.

[293] Personal communication with Miriam Winkelmann.

[294] Personal communication with Fabian Lux.

[295] E. Anderson et al. *LAPACK Users’ Guide*. Third. Philadelphia, PA: Society for Industrial and Applied Mathematics, 1999. ISBN: 0-89871-447-8 (paperback).

[296] Endong Wang et al. “Intel Math Kernel Library.” In: May 2014, pp. 167–188. ISBN: 978-3-319-06485-7. DOI: `10.1007/978-3-319-06486-4_7`.

[297] Juris Meija et al. “Atomic weights of the elements 2013 (IUPAC Technical Report).” In: *Pure and Applied Chemistry* 88.3 (2016), pp. 265–291. DOI: `doi:10.1515/pac-2015-0305`.

[298] G. Simonelli, R. Pasianot, and E. J. Savino. “Phonon dispersion curves for transition metals within the embedded-atom and embedded-defect methods.” In: *Phys. Rev. B* 55.9 (Mar. 1997), pp. 5570–5573. DOI: `10.1103/PhysRevB.55.5570`.

[299] Markus Betzinger. “Efficient Implementation of the Non-Local Exchange Potential within the FLAPW Method.” written at Institut für Festkörperforschung (IFF) Forschungszentrum Jülich. Diploma thesis. RWTH Aachen University, Sept. 2007.

[300] R. Abt. PhD thesis. Universität Graz, Institut für Theoretische Physik, 2002.

Acknowledgements

First, I want to thank Prof. Dr. Stefan Blügel for giving me the great opportunity to write my dissertation in his institute, for supporting me in challenging situations, for inspiring me, for his helpful advice, and for writing the evaluation of my thesis. In this context, I likewise express my gratitude to the dean Prof. Dr. Carsten Honerkamp for having his consent that he draws up the second evaluation of my dissertation.

Furthermore, I thank Dr. Markus Betzinger for his assistance, for many fruitful discussions, and in particular for his loyalty after he has left science. I explicitly thank Dr. Gustav Bihlmayer who came to my aid, not hesitating to become my successive direct advisor during my plight after Markus Betzinger departed. Particularly, I appreciate the patience Gustav showed and his expert knowledge he provided in each of our discussions, as well as his open-door policy and support. Moreover, I thank Alexander Neukirchen for our discussions and his dedication and determined effort to improve `juPhon`, while I have been finishing my dissertation in the last months. Additionally, I am grateful for the IT support of Ingo Meyer and the assistance of Ute Winkler in administrative affairs. Apart from that, I would like to acknowledge discussions with Fabian Lux, Dr. Gregor Michalicek, Dr. Daniel Wortmann, and Miriam Winkelmann. Finally, I thank Prof. Dr. Stefan Blügel, Dr. Gustav Bihlmayer, Alexander Neukirchen, Ismo Toijala, Daniel Alexander Krużel, Dr. Mathias Christian Thomas David Müller, Elisabeth-Annemarie Gerhorst, Merlin Kallenborn, Dr. Maik Malki, and Dr. Jens Winkelmann for proofreading parts of my voluminous dissertation.

In particular, I wish to express my heartfelt thanks to my parents Sophia and Franz Paul, who enabled me to study and always give their active and enormous support in non-scientific affairs. Additionally, I express my thanks to my darling girlfriend Kim Alexa and to my sister Elisabeth-Annemarie for their whole-hearted support and for taking care of me. Particularly, I acknowledge the endless patience of Kim Alexa and her great sympathy. Moreover, I thank Dr. Matthias Heffinger, Dr. Mathias Christian Thomas David Müller, Stefan Rost, Dr. Gregor Michalicek, Jonas Langhabel, Andreas Landowski, and my remaining family and friends for encouraging me in writing my dissertation. I particularly thank my cousin Daniel Alexander Krużel who, as a native speaker, taught me the subtleties of the English language, and Ismo Toijala for providing me with his sophisticated LaTeX-macro framework. Finally, I would like to acknowledge my colleagues who created a good working atmosphere. Especially, I want to thank my office mate and friend Stefan Rost for the unforgettable and funny time we have spent together.

Schriften des Forschungszentrums Jülich
Reihe Schlüsseltechnologien / Key Technologies

Band / Volume 246
Tailoring neuroelectronic interfaces via combinations of oxides and molecular layers
X. Yuan (2021), 113 pp
ISBN: 978-3-95806-572-7

Band / Volume 247
Stoichiometric control and magnetoelectric coupling in artificial multiferroic heterostructures
P. Schöffmann (2021), vii, 176 pp
ISBN: 978-3-95806-575-8

Band / Volume 248
A Unified Framework for Functional Renormalisation Group Calculations and its Application to Three Dimensional Hubbard Models
J. Ehrlich (2021), xvi, 213 pp
ISBN: 978-3-95806-582-6

Band / Volume 249
Photoemission electron microscopy of magneto-ionic effects in $La_{0.7}Sr_{0.3}MnO_3$
M. Wilhelm (2021), 134 pp
ISBN: 978-3-95806-592-5

Band / Volume 250
Development of a Multiplexer System and Measurement of the Neutron Yield for a Low-Energy Accelerator-Driven Neutron Source
M. Rimmler (2021), v, 200 pp
ISBN: 978-3-95806-600-7

Band / Volume 251
Resolving interface effects in voltage controlled magnetic heterostructures using advanced neutron scattering and electron microscopy methods
T. Bhatnagar-Schöffmann (2021), ix, 171 pp
ISBN: 978-3-95806-604-5

Band / Volume 252
Strain development of *Gluconobacter oxydans* and *Pseudomonas putida* for production of the sweetener 5-ketofructose
K. Wohlers (2022), VI, 118 pp
ISBN: 978-3-95806-612-0

Band / Volume 253
Topological magnonic properties of two-dimensional magnetic materials
L. Zhang (2022), xx, 154 pp
ISBN: 978-3-95806-621-2

Band / Volume 254
Role of secondary metabolites in antiphage defense in *Streptomyces*
Aël Hardy (2022), IV, 193 pp
ISBN: 978-3-95806-633-5

Band / Volume 255
Neutron Scattering
Lectures of the JCNS Laboratory Course held at Forschungszentrum Jülich and at the Heinz-Maier-Leibnitz Zentrum Garching
edited by T. Brückel, S. Förster, M. Kruteva, M. Zobel, and R. Zorn (2022), ca. 300 pp
ISBN: 978-3-95806-634-2

Band / Volume 256
Magnetoelectric Interactions in Multiferroic Thin-film Heterosystems and Nanostructures
H. Gökdemir (2022), x, 140 pp
ISBN: 978-3-95806-635-9

Band / Volume 257
High-Performance Computing Approach to Hybrid Functionals in the All-Electron DFT Code FLEUR
M. Redies (2022), xi, 109 pp
ISBN: 978-3-95806-639-7

Band / Volume 258
Establishing regulatable expression systems in the acetic acid bacterium *Gluconobacter oxydans* 621H
P. M. Fricke (2022), VIII, 187 pp
ISBN: 978-3-95806-642-7

Band / Volume 259
Density-Functional Perturbation Theory within the All-Electron Full-Potential Linearized Augmented Plane-Wave Method: Application to Phonons
C.-R. Gerhorst (2022), xvi, 317 pp
ISBN: 978-3-95806-649-6

Weitere ***Schriften des Verlags im Forschungszentrum Jülich*** unter
http://wwwzb1.fz-juelich.de/verlagextern1/index.asp

Schlüsseltechnologien / Key Technologies
Band / Volume 259
ISBN 978-3-95806-649-6

Mitglied der Helmholtz-Gemeinschaft

JÜLICH
Forschungszentrum